Solar Thermal Propulsion for Microsatellite Manoeuvring

F.G. Kennedy

Submitted for the Degree of
Doctor of Philosophy
from the
University of Surrey

Surrey Space Centre
School of Electronics and Physical Sciences
University of Surrey
Guildford, Surrey GU2 5XH, UK

September 2004

© F.G. Kennedy 2004

Report Documentation Page	*Form Approved* *OMB No. 0704-0188*

Public reporting burden for the collection of information is estimated to average 1 hour per response, including the time for reviewing instructions, searching existing data sources, gathering and maintaining the data needed, and completing and reviewing the collection of information. Send comments regarding this burden estimate or any other aspect of this collection of information, including suggestions for reducing this burden, to Washington Headquarters Services, Directorate for Information Operations and Reports, 1215 Jefferson Davis Highway, Suite 1204, Arlington VA 22202-4302. Respondents should be aware that notwithstanding any other provision of law, no person shall be subject to a penalty for failing to comply with a collection of information if it does not display a currently valid OMB control number.

1. REPORT DATE **01 SEP 2004**	2. REPORT TYPE **N/A**	3. DATES COVERED **-**

4. TITLE AND SUBTITLE **Solar Thermal Propulsion for Microsatellite Manoeuvring**	5a. CONTRACT NUMBER 5b. GRANT NUMBER 5c. PROGRAM ELEMENT NUMBER
6. AUTHOR(S)	5d. PROJECT NUMBER 5e. TASK NUMBER 5f. WORK UNIT NUMBER
7. PERFORMING ORGANIZATION NAME(S) AND ADDRESS(ES) **University of Surrey**	8. PERFORMING ORGANIZATION REPORT NUMBER
9. SPONSORING/MONITORING AGENCY NAME(S) AND ADDRESS(ES)	10. SPONSOR/MONITOR'S ACRONYM(S) 11. SPONSOR/MONITOR'S REPORT NUMBER(S)

12. DISTRIBUTION/AVAILABILITY STATEMENT

Approved for public release, distribution unlimited

13. SUPPLEMENTARY NOTES

The original document contains color images.

14. ABSTRACT

15. SUBJECT TERMS

16. SECURITY CLASSIFICATION OF:			17. LIMITATION OF ABSTRACT	18. NUMBER OF PAGES	19a. NAME OF RESPONSIBLE PERSON
a. REPORT **unclassified**	b. ABSTRACT **unclassified**	c. THIS PAGE **unclassified**	**UU**	**381**	

Standard Form 298 (Rev. 8-98)
Prescribed by ANSI Std Z39-18

Abstract

Solar thermal propulsion (STP) is a 40-year-old concept that, despite substantial ground test heritage, still awaits its first flight experiment. It is simple in theory, relying neither on combustion nor electrical power to operate. Instead, incident sunlight, concentrated by a factor of 10,000 or more, heats a refractory metal or ceramic cavity receiver to temperatures of 2,000-3,000 K. A monopropellant—hydrogen being the most often proposed—is expelled through the receiver body and heated, then exhausted to provide thrust. Specific impulses of up to 1,000 s. are believed to be achievable. A more realistic approach for the near-term, proposed by the author, eschews hydrogen, which must be stored as a cryogenic liquid, for storable propellants such as ammonia or water, with the resultant decrease in specific impulse made up for by a concomitant decrease in system complexity. Nevertheless, propulsive performance is predicted to be on par with state-of-the-art chemical propulsion systems.

The thesis will trace the development of the microsatellite solar thermal engine from conception through mission analysis, design, modelling, fabrication, component, and system testing. On-sun testing of 14-cm and 56-cm diameter solar concentrating mirrors has clearly validated initial optical ray trace modelling and suggests that there is significant performance margin built into test concentrators. Electrical heating tests on two solar cavity receivers, the Mk. I and Mk. II, have demonstrated the designs' robustness at temperatures approaching 2,000 K, over many thermal cycles. Flow testing—in nitrogen, helium, and ammonia—demonstrated the Mk. I's excellent heat transfer capability and the Mk. II's survivability over multiple firing cycles. A novel solar thermal engine concept, utilising low-attenuation optical fibre for power transfer to a remote receiver, has been shown to permit the decoupling of the receiver from the concentrating mirror's focus, permitting multiple mirror inputs to heat a single receiver and allowing the receiver to be placed anywhere on the host spacecraft, minimising design and operational impacts. A variant of this engine is intended to fly aboard a Surrey satellite by 2006.

Key words: Solar thermal propulsion (STP). Microsatellites. Orbit transfer. Orbit maintenance. Manoeuvring. Refractory ceramics. Optical fibre.

Email: **f.kennedy@eim.surrey.ac.uk**

World Wide Web (WWW): **http://www.eps.surrey.ac.uk/**

“Don't tell me that Man doesn't belong out there. Man belongs wherever he wants to go - and he'll do plenty well when he gets there.”

—Wernher von Braun, New York, February 1958

“You can’t get to Venus on a…flashlight.”

—Terrence Murphy, Canoga Park, December 2003

Extended Abstract

While microsatellites have demonstrated ever-increasing capabilities for remote sensing and communications, their use has been heavily constrained and shaped by available launch opportunities, dictated by the large host satellites for which the launch vehicles are primarily intended. The secondary priority assigned to small satellites places them in orbits of opportunity that are often non-optimal, which in turn impacts the selection process of microsatellite mission designers, who refrain from planning missions to innovative orbits because such orbits are not obtainable in practice.

To overcome these limitations and to expand the options available to microsatellite mission designers, the author and the author's advisor, Dr. Philip Palmer, initiated a research programme in 2001 to develop a low-cost, lightweight, low-volume solar thermal engine (STE) suitable for use aboard satellites massing less than 100 kilograms.

The STE is conceptually simple, relying on a mirror or lens assembly to collect and concentrate incident solar radiation. This energy is focused, by a factor of more than 10,000, heating a blackbody cavity receiver to temperatures of 2,000-2,500 K. Propellant is then passed through a bed of thermal storage material inside the receiver, and exhausted to provide thrust. Up to 60 firing cycles are envisioned. While some propellants may decompose upon heating, the principal source of energy is the incident sunlight itself; no combustion takes place. The microscale STE system differs from previous concepts in that it trades performance for simplicity of design and ease of fabrication, test, and flight demonstration. The original proposals maximised performance, using liquid hydrogen propellant and operating at extremely high temperatures, nearing 3,000 K. The author selected a lower operating temperature range to increase material choice, and chose to substitute storable propellants, such as hydrazine, ammonia, and water, for liquid hydrogen, which is unsuitable for use aboard microsatellites.

With specific impulses approaching 400 seconds and thrust levels of several newtons, an STE offers the potential for low propellant consumption and reasonable transfer times to Geosynchronous Earth Orbit (GEO), lunar orbit, and near-earth asteroids. Velocity changes of up to 2,000 m/s, two orders of magnitude beyond anything attempted at Surrey, appear feasible.

The author examined a number of candidate missions, including lunar orbiters (e.g., the European Space Agency's SMART-1 mission), GEO missions, and Near Earth Object (NEO) probes. Three classes of microsatellite mission appear to benefit from the application of STP: (1) GEO insertion missions, (2) Near-Escape missions, and (3) Other Body (e.g., lunar) capture missions.

The author's detailed mission analysis reveals that many of these missions can be accomplished for under 2,000 m/s. Flight times range from 35 days (to GEO) to several hundred days (for lunar capture and NEO flybys). These missions form the basis for a set of key requirements for the STP system.

A detailed model of the solar thermal propulsion system was developed to permit the design of an STE while accounting for the complex interactions between critical subsystems. These three subsystems—the concentrator, receiver, and propellant storage assemblies—are modelled in sufficient detail to allow the user to modify their properties and observe system-level effects resulting from that modification. Concentrator parameters include reflectance, intercepted area, form and form error, and solar tracking accuracy. Receiver parameters include material thermal conductivity, heat capacity, sizing, flow restrictions, and receiver-propellant heat transfer modes. Propellant and storage system parameters include vehicle volume limitations, temperature- and pressure-dependent properties for several prospective propellants, and selected supply scheme (i.e., regulated or unregulated propellant feed). The model is composed principally of Visual Basic code but displays key output in Microsoft Excel.

Using this and other modelling tools, the author devised three preliminary designs for a microsatellite STE. Hydrazine (N_2H_4) was selected as the propellant; its catalytic decomposition permits propellant pre-heating and additional mass reduction of the propulsion system. Ammonia was chosen as the primary alternative. A rigid, fixed concentrator, diamond machined from aluminium, would heat a small cavity receiver to temperatures in excess of 2,000 K. The cavity receiver, fabricated from one of several monolithic ceramics, included both particle bed and channel heat transfer schemes. The selected receiver materials were highly resistant to corrosion, easily machined, and can withstand repeated thermal shock and high temperature.

Material survivability tests were conducted to determine the effect of high-temperature vacuum on candidate thermal storage materials. A composite ceramic composed of titanium diboride and boron nitride evidenced no mass loss or deformation after nearly an hour's exposure to vacuum, at temperatures of up to 2,300 K. Brazing trials were conducted at the University of Manchester to determine if a hermetic metal-to-ceramic seal could be achieved and survive in the harsh operating conditions of the STE. While the author was unable to achieve a leak-proof seal for the selected materials suite, strong bonds were obtained. After further consultation with expert ceramicists, the author devised a mechanical method for sealing, which is both simple to implement and has proven successful at temperatures of up to 2,000 K and pressures exceeding 10 bar.

Two solar receiver designs (denoted Mk. I and Mk. II) were constructed and tested in vacuum, electrically heated to temperatures of 1,500-2,000 K. The Mk. I system incorporated a particle bed for maximum wall-gas heat transfer; the Mk. II used a simpler, but less efficient single channel scheme. Both designs showed excellent mechanical stability and no mass loss after multiple heating cycles. The author then conducted full flow tests with representative propellants—nitrogen, helium, and ammonia---to assess the propulsive performance of the STE designs. Mass flow, pressure, temperature, and thrust data were collected over a number of engine firings. The Mk. I engine's measured propulsive efficiency—represented by its characteristic velocity, or c^*--and its predicted value diverged by only 2-5%. The Mk. II engine demonstrated a substantially lower value of c^*, primarily owing to its less efficient channel heat transfer scheme. This engine survived repeated firings with all propellants, with only minor evidence of damage. Some cracking of the ceramic was observed after five or more trials, although the cracks did not appear to result in any leakage.

A 56-centimetre diameter aluminium mirror was fabricated from a single billet via diamond-turning, with form errors approaching optical quality. On-sun testing of this mirror validated its performance. Concentration exceeded the target of 10,000, at a solar throughput of approximately 130 watts. Reflectance was measured as better than .85. Despite this mirror's excellent performance, its size and mass (15 kg) make it an unlikely addition to a small satellite propulsion suite. As mirror mass scales roughly with the fourth power of diameter, large-diameter mirrors become untenably heavy and expensive. The author proposed the following novel solution: Utilise multiple small mirrors and concatenate the inputs via ultra-low attenuation optical fibre. This approach, while attempted experimentally for surgical and material production applications, had not been applied to solar thermal propulsion. Initial tests demonstrated that throughput is strongly dependent on fibre alignment and tip quality. Proper polishing and careful handling of the fibre is essential. A final series of tests demonstrated that multiple small mirrors, ganged via fibre, can heat a small solar receiver to high temperatures. By decoupling the receiver from the focus of the concentrator, it can be placed anywhere on the satellite.

The multiple mirror/fibre coupling approach will be demonstrated in a flight demonstration of solar thermal propulsion aboard a Surrey microsatellite by 2006. A single-mirror, single-fibre system, using butane propellant, has been designed, fabricated, and tested on the ground, and is now planned to be tested in space; the predicted velocity change is expected to be on the order of 50 m/s. This will be the first ever space demonstration of solar thermal propulsion.

The following items are thought by the author to represent critical contributions to the state-of-the-art by this research:

- Development of a detailed integrated system model for microsatellite solar thermal propulsion systems, incorporating orbit transfer data, concentrator performance and pointing capabilities, receiver construction and properties, and propellant storage and feed system details. The integrated model permits the user to perform sensitivity analyses at a system level without continuous re-design and iteration with subsystem-level models;

- Innovative use of refractory ceramics and mechanical sealing methods to produce a low fabrication cost, ultra-high temperature capable solar receiver;
- First use of low-attenuation, high numerical aperture fibre optics for solar thermal propulsion, permitting decoupling of the solar receiver from the focus and multiple small mirrors in place of a single large mirror;
- The proposal to provide solar thermal augmentation for storable hypergolic propellants (i.e., hydrazine) to reduce overall propulsion system mass; and
- The development, test, and preparation for flight of a small proto-flight STE, suitable for microsatellite orbit transfer, which, to the author's knowledge, had not been previously proposed.

The author has published eight technical papers from 2001 through 2004. One of these, "Design and Proto-Flight Test Strategy for a Microscale Solar Thermal Engine," was re-published in the journal *Space Technology* in June 2003. A related paper, "Prometheus: A Low-Cost Microsatellite Flyby Mission of the Asteroid 4179 Toutatis," drawing on the mission analysis included in this research, was published in the *Journal of the British Interplanetary Society*, also in June 2003. Two others received awards: "A Comparison of Simulation and Test Campaign Results for a Microscale Solar Thermal Engine" received the British Interplanetary Society's Award for Best Technical Paper, 54th International Astronautical Conference, Bremen, Germany, 2003; and "Preliminary Analysis of Test Campaign Results for a Microscale Solar Thermal Engine" received First Prize at the 11th Annual Frank J. Redd Student Competition, Utah State University Small Satellite Conference, Logan, Utah, 2003.

This research effort received significant external contributions from the Boeing Company and the U.S. Air Force's European Office of Aerospace Research and Development (EOARD).

The views expressed in this document are those of the author and do not reflect the official policy or position of the United States Air Force, Department of Defense, or U.S. Government.

Acknowledgments

There are a number of people who deserve a great deal of thanks for their assistance over the past three years. These include Malcolm Paul, a rocket man with at least three doctorate-equivalents in Patience, Practicality and Common Sense, who helped make a difficult test campaign both bearable and doable; Dr. Ian Coxhill, renaissance man, rocket scientist, and physicist, who willingly acted as a sounding board, helped make several key tests work, and still managed to provide dozens of useful suggestions for keeping this research on track; Patrick Frye and Terry Murphy of the Boeing Company’s Rocketdyne Division, who provided essential funds and stuck to our plan even after a number of others fell by the roadside; Dr. Adam Baker, who pointed me in the right direction, materials-wise; Dave Gibbon, who overcame his natural conservative tendencies to help find ways to fly an “exotic” spacecraft propulsion system; Paul Henshall, who will hopefully carry this work to its natural completion, putting a solar thermal engine in space (where it belongs); and my academic advisor, Dr. Philip Palmer, who, while permitting me to exercise my initiative, offered some very sound course corrections at key intervals.

I would be remiss if I did not mention the assistance given to me by a number of people at the Surrey Space Centre and elsewhere: Dr. Hugh Newell, Peter Hurley, Dr. Guy Richardson, Paul Charman, Lee Cowie, Graham Eade, and Andy Phipps, Surrey Satellite Technologies, Ltd.; Dr. Julie Yeomans, Prof. John Watts, Dr. Neil Ward, Jan Fogg, and Gill Gibbs, at the University of Surrey; Mostyn Woodfield and the all-too-busy Russell Oliver of Sintec-Keramik, UK; Richard Parker, Dominic Whelton, Kevin Lee, and Lee Carey, of Precision Optical Engineering; Prof. Brian Derby of the University of Manchester’s Materials Science Centre; Dr. Ingrid Wysong, at the U.S. Air Force’s European Office of Aerospace Research and Development; Calvin Prentice, Qinetiq; Stephen Lyle, Saint-Gobain Advanced Ceramics; Andy Blackburn, MAST Carbon; and Richard White, Electron Beam Welding.

Lastly, a huge “thank you” to my wife and sons, who let me persuade them (somehow) to drag us all across the Atlantic for three years to study solar thermal propulsion systems in a region that only sees, on average, 150 sunny (bright?) days per year—and of which I’m ceaselessly reminded by various wags. I can’t express how much I appreciate the sacrifices you’ve all made on my behalf.

Contents

Abstract ii

Extended Abstract iii

Acknowledgments vii

Contents viii

List of Figures xi

List of Tables xxiii

Nomenclature xxv

1 Introduction 1

- 1.1 Propulsion as an Essential Adjunct to Advanced Microsatellites 1
- 1.2 Solar Thermal Propulsion 2
- 1.3 Scope of Research 4
- 1.4 Thesis Structure 5
- 1.5 Novel Work Undertaken 6

2 Literature Survey 9

- 2.1 Solar Thermal Propulsion Concepts and Heritage 9
  - 2.1.1 Solar Receiver Evolution 11
  - 2.1.2 Methods for Concentrating Sunlight 16
  - 2.1.3 Propellants and Propellant Storage 22
- 2.2 Solar Radiation 24
  - 2.2.1 Optical Fibre Transmission of Solar Radiation 26
  - 2.2.2 Alternative Concentration Schemes Applicable to Microsatellite Solar Thermal Propulsion 28
- 2.3 High-Temperature Materials and Joining Processes 31
- 2.4 Summary 34

3 Mission Analysis 36

3.1 Preliminary Mission Analysis 36
3.1.1 Review of Applicable Missions 36
3.1.2 First-Order Performance Comparison for a Solar Thermal Engine 42
3.1.3 Candidate Mission Selection 45
3.2 Detailed Mission Analysis 46
3.2.1 Geosynchronous Orbit Insertion 46
3.2.2 Near-Escape Missions 49
3.2.3 Lunar Capture 54
3.3 Summary 57
4 Preliminary Design 59
4.1 Rocket Propulsion Fundamentals 59
4.2 Baseline Engine Design 65
4.3 Concentrator Array Design 68
4.3.1 Concentrator Array Pointing Error 77
4.4 Receiver Design 81
4.4.1 Thermal Storage Media 83
4.4.2 Insulation 85
4.4.3 Sizing Considerations 86
4.4.4 Selection of a Heat Transfer Mode 87
4.5 Propellant Feed System Design 97
4.5.1 Propellant Feed System Configuration 102
4.6 Preliminary Design Summary 105
5 Integrated System Modelling and Detailed Design 108
5.1 Overview 108
5.2 Optical Performance Modelling with OSLO LT 108
5.3 Thermal Modelling with WinTherm 113
5.4 Constructing an Integrated System Model 116
5.5 Concentrator Subsystem Detailed Design 132
5.6 Receiver Subsystem Detailed Design 137
5.7 Detailed Design Summary 146
6 Component Test Campaign 147
6.1 Test Strategy 147
6.2 Receiver Testing 150
6.2.1 Material Survivability, Bonding, and Sealing Tests 151

6.2.2 Receiver Cavity Heating Profile and Survivability Tests 165
6.2.3 Receiver Cavity Hot Flow Tests 182
6.3 Concentrator Testing 211
6.3.1 Large Concentrator Properties Testing 213
6.3.2 Small and Ganged Mirror Testing 219
6.4 Summary of Test Results 232

7 Flight System Development 236

7.1 Mission Applications 236
7.1.1 A Microscale Solar Thermal Propulsion Experiment on DMC 238
7.1.2 An Operational Solar Thermal Propulsion Demonstrator on CFESat 242
7.2 Baseline Demonstrator Design Issues 251
7.3 Summary 253

8 Summary and Conclusions 255

8.1 Overview 255
8.2 Summary 255
8.3 Recommendations for Further Research 260

References 263

Research Publications 283

Appendix A: Astrodynamics 284

Appendix B: Development of a System Requirements Document 291

Appendix C: Engineering Drawings 328

List of Figures

Figure 1-1 Recent spacecraft propulsion systems tested at the Surrey Space Centre. 1
Figure 1-2 Solar Thermal Propulsion: a conceptual evolution. 3
Figure 2-1 Two depictions of an AFRPL conceptual design for a solar thermal engine, with dual off-axis inflatable concentrators, right [Etheridge, 1979][Holmes, 2001]..10
Figure 2-2 Deployed (left) and stowed (right) views of the proposed Solar Orbit Transfer Vehicle (SOTV), an Air Force Research Laboratory experiment [Partch, 1999]. 11
Figure 2-3 One solar cavity receiver/absorber concept, left. Rocketdyne's solar absorber/thruster assembly, right [Shoji, 1992][Shoji, 1983]. 12
Figure 2-4 Two windowed solar thermal propulsion concepts [Shoji, 1992]. 13
Figure 2-5 Reticulated, vitreous carbon foam, left [Ultramet 2, 2002]. "Inside-out" fabrication technique for subscale solar-powered rocket engine, right [DelaRosa, 1993]. 14
Figure 2-6 The ISUS Receiver-Absorber Converter [Partch, 1999] 15
Figure 2-7 Electrically heated "Wagon-wheel" solar receiver test article, with achieved peak temperatures (ºF), left [Tucker, 2001]. Hypothetical "Shooting Star" STE on Spartan free-flying experimental platform, depicting inflatable Fresnel lens concentrator [Shaltens, 2002]. 16
Figure 2-8 Theoretical receiver bulk temperature versus concentration ratio, for thermal storage ($\eta_c = 0$) and direct-gain ($\eta_c = 0.5$) receivers. 18
Figure 2-9 The 1996 Inflatable Antenna Experiment (IAE) on STS-77, deployed [L'Garde, 2004]. 19
Figure 2-10 The Jet Propulsion Laboratory's Inflatable Antenna Experiment, deployment scheme [Freeland, 1997]. 20
Figure 2-11 Two views of SRS Technologies' Flight Scale Concentrator (FSC-1) [Holmes, 2001]. 21
Figure 2-12 ISUS Ground Test Demonstration concentrator (left), and depiction of ISUS flight experiment with deployable, faceted concentrator arrays (right) [AFRL, 2004] 22
Figure 2-13 Unfurlable mesh reflectors [Harris, 2004]..22
Figure 2-14 Cryogenic liquid hydrogen long-term storage concept [Partch, 1999]. 23
Figure 2-15 Theoretical (blackbody) and measured power received at earth-sun separation distance, at wavelengths < 2,500 nm [NREL, 2001][Sears, 1975]. 25

Figure 2-16 Prototype nanomaterial production furnace utilising fibre-coupled solar radiation and a gold-coated photon regenerator (left), single fibre-optic mini-dish on solar tracking unit [Gordon 2, 2003]....26

Figure 2-17 Wavelength-dependent attenuation of two types of high numerical aperture optical fibre [Polymicro, 2004]....27

Figure 2-18 Paraboloidal mirror with second-stage concentrator (left) [Feuermann, 1999]. Compound Parabolic Concentrator (right) [Winston, 1974]....29

Figure 2-19 Collection efficiency versus relative concentration C_{rel}, for a single-mirror paraboloidal concentrator (left), and with the addition of Feuermann's Complementary Cassegrain Concentrator (CCC) (right) [Feuermann, 1999]....30

Figure 2-20 Refractive secondary concentrator concept, left [Donovan, 1997]. A compound parabolic concentrator trough with line-focus receiver, right [Winston, 1974]....30

Figure 2-21 Periodic table of the elements, illustrating melting temperature of individual species [Winter, 2001]....32

Figure 2-22 Density, decomposition temperature and room temperature specific heat for a variety of ceramic compounds [Lynch, 1966]....32

Figure 3-1 NASA Goddard Spaceflight Center's Magnetospheric Multi-Scale (MMS) four-phase mission scenario. MMS will explore various regions of the magnetosphere over a two-year period [NASA GSFC, 2002]....37

Figure 3-2 European Space Agency missions to the Moon and comets....38

Figure 3-3 GeMINI and MUSES-C missions....40

Figure 3-4 High-resolution radar image of 4179 Toutatis, taken by NASA's Goldstone radar in 1992 from a range of 4 million kilometres. [Ostro, 1995]....42

Figure 3-5 Two Surrey microsatellites, BilSAT and UoSAT-12....43

Figure 3-6 Geosynchronous Orbit Insertion....47

Figure 3-7 Toutatis Flyby Missions....50

Figure 3-8 High Altitude Phasing Orbit (HAPO)....53

Figure 3-9 The SMART-1 lunar orbiter trajectory requires multiple lunar swingbys [ESA, 2004]....55

Figure 3-10 Lunar Orbit Insertion Steps....56

Figure 3-11 Lunar capture with a low-thrust system, using seven insertion burns over approximately 20 hours. Final orbit is achieved through the use of two successive firings at perilune [STK Astrogator]....57

Figure 4-1 Burnout mass fraction (satellite mass following engine firing / m_i) for velocity changes of up to 3,000 m/s, for three representative propulsion systems: (1) the UK T5, an electrostatic ion engine, I_{sp} = 4,000 s; (2) the PPS 1350, a Hall effect thruster, I_{sp} = 1,600 s; and (3) a threshold performance STP-augmented hydrazine thruster, I_{sp} = 350 s....61

Figure 4-2 Mars orbiter utilising “ganged mirror” solar thermal propulsion for insertion firings..65
Figure 4-3 Top level options tree for STP engine design effort...65
Figure 4-4 Solar thermal engine configuration. 67
Figure 4-5 Solar thermal engine, receiver mounting detail..68
Figure 4-6 Fresnel lens and paraboloidal concentrators...68
Figure 4-7 Parabolic and spherical mirror profiles, indicating increasing divergence for larger radii (lower f-number). The parabolic mirror has a focal length (f) of unity; the spherical mirror’s radius of curvature is 2f = 2. 69
Figure 4-8 Key specifications for a parabolic point-focus mirror...70
Figure 4-9 Parabolic point-focus mirror concentration versus rim angle Φ 71
Figure 4-10 Developmental Comparative Active Telescope Testbed (DCATT) mirror fabrication. 72
Figure 4-11 Herschel advanced technology mirror elements...73
Figure 4-12 Specular reflectance of various optical coating materials for light at wavelengths of 200 nm < λ < 2,400 nm [Optiforms, 2001]...74
Figure 4-13 30-cm f/1 concentrating mirror. 75
Figure 4-14 57.6-cm f/.52 concentrating mirror. 76
Figure 4-15 Parabolic dish reflector...78
Figure 4-16 Intersection of parabolic dish acceptance regions and the solar disk. Light and dark gray areas represent the boundaries of the unity ($\theta = \theta_{s,min}$) and fractional ($\theta = \theta_{l,max}$) acceptance regions. 79
Figure 4-17 Incident sunlight reaching the receiver aperture, in suns, versus parabolic dish tracking error. $\Phi = 30^o$, C_g = 10,000. 81
Figure 4-18 Incident sunlight versus parabolic dish tracking error. $\Phi = 45^o$, C_g = 10,000. 81
Figure 4-19 Gas exit temperature vs. time, 750 N-s cavity receiver, 150 mN thrust, 5,000 second burn time. This sequence of curves represents bed lengths of 10 cm (top), 7.5 cm, 5 cm, and 2.5 (bottom)..89
Figure 4-20 Gas exit temperature vs. time, 2,808 N-s cavity receiver, 3 N thrust, 936- second burn time. This sequence of curves represents bed radii of 7 cm (top), 5.5 cm, 4.75 cm, and 4 cm (bottom)..90
Figure 4-21 Gas exit temperature vs. time, 428 N-s cavity receiver, 1 N thrust, 428- second burn time. The two curves represent initial bed temperatures of 2,500 K (top curve) and 1,950 K (bottom curve)..91
Figure 4-22 Cavity “hot wall” temperature vs. time, 2,760 N-s cavity receiver, fixed insolation of 333 W. The three curves represent insulation package thermal conductivities of 0.01, 0.05, and 0.2 W/m-K...92

Figure 4-23 Cavity “hot wall” temperature vs. time, 2,808 N-s cavity receiver, 3 N thrust, 936-second burn time. The four curves represent insolation values (solar energy input) of 333, 400, 466, and 533 W. 93

Figure 4-24 Cavity “hot wall” temperature vs. time, 750 N-s cavity receiver, 150 mN thrust, 5,000- second burn time. The three curves represent insolation values (solar energy input) of 200, 275, and 333 W. 94

Figure 4-25 Cavity “hot wall” temperature vs. time, 428 N-s cavity receiver, 1 N thrust, 428-second burn time. The four curves represent insolation values (solar energy input) of 100, 200, 250, and 300 W. 95

Figure 4-26 428 N-s cavity receiver details. 96

Figure 4-27 Fully assembled cutaway views of the 428 N-s cavity receiver, 5 cm outer radius, 8.9 cm insulation fitting length. 97

Figure 4-28 Gas exit temperature vs. time, 428 N-s receiver, 1 N thrust, 428- second burn time, 1,950 K initial bed temperature. The two curves represent hydrazine decomposition product input at 863 K (top) and ammonia at 300 K (bottom). Ammonia’s performance does not account for endothermic losses associated with H_2 and N_2 formation. 102

Figure 4-29 Schematic of feed system in blowdown mode. 103

Figure 4-30 Three possible propellant tank siting configurations for the SSTL enhanced microsatellite: (a) Spherical tanks in a cruciform configuration, (b) dual capped cylindrical tanks mounted transversely, and (c) six longitudinally mounted, capped cylinders. The view is along the satellite’s z-axis (looking towards nadir). 104

Figure 4-31 Solar thermal engine assembly layouts, preliminary design, single mirror approach. 105

Figure 5-1 Local slope error calculation for centreline ray (left), Hartmann test wavefronts (right), adapted from Malacara [1992]. 109

Figure 5-2 Representative screen shot of OSLO LT simulation, for 56-centimetre diameter, f/0.6 paraboloidal concentrating mirror. 111

Figure 5-3 Focal spot images, for perfect pointing (left), 0.5º offset (centre, spot moves 2.93 mm from optical axis), 1.0º offset (spot moves 5.87 mm from optical axis). 112

Figure 5-4 56-centimetre diameter paraboloidal concentrating mirror, perfect conic, 5mm spot (left) and imperfect, 9.2 mm spot (right), containing spherical and comatic aberrations. RMS wavefront error of mirror producing the image at right is 58 μm. 112

Figure 5-5 Sag versus radial position, 56-centimetre f/0.6 paraboloid. Equation 5-6 coefficients: a = -0.001, b = -1×10^{-6}, c = -9.5×10^{-8}, d = -5×10^{-11}, e = 4×10^{-12}, f = -8×10^{-15}. RMS form error = 1.5 μm. 113

Figure 5-6 WinTherm model of Mk. I cavity receiver in electrical heating test configuration, 325 W input power, left (one copper electrode shown in foreground). Temperature profile of solar receiver cavity external surface, insulation package external surface, and copper electrode, right. 114

Figure 5-7 WinTherm model of Mk. I cavity receiver (left) and test results (right), 600 W input power with high resistive losses in leads (250 W), electrode/lead contacts (100 W), and electrode (200 W). Receiver shell is enlarged to “compromise” diameter (average of internal and external surface diameters). Conductive coupling simulates resistive heating via copper electrodes (lower left), molybdenum leads, and a ceramic heating element (centre). 115

Figure 5-8 WinTherm model of Mk. I cavity receiver (left) and test results (right), 600 W input power, 250 W dissipation in molybdenum leads, 150 W dissipation in copper electrode/molybdenum contacts. This model is designed to accurately simulate external and internal radiative surfaces while modelling conduction through the thickness of the body using eight fins. 116

Figure 5-9 Screen shot of MSTISM Summary Input/Output Sheet. 117

Figure 5-10 Microscale Solar Thermal Integrated System Model schematic. 118

Figure 5-11 Screen shot of MSTISM Receiver Performance Input/Output Sheet. 119

Figure 5-12 Effective Biot number for several ceramic blackbodies (with characteristic lengths of 0.5, 5, and 50 cm). 120

Figure 5-13 First- and second-order reaction rate constants for ammonia decomposition [NIST, 2000]. ..125

Figure 5-14 Screen shot of MSTISM Propellant Management input/output worksheet. 126

Figure 5-15 MSTISM model of STP bulk receiver temperature, for 100-, 75-, 50-, and 30-cm mirror inputs. Solar flux = 1,353 W/m^2. Mirror reflectance = 0.90. 130

Figure 5-16 MSTISM model of STP bulk receiver temperature, for 30-cm mirror input. Solar flux = 1,353 W/m^2. Mirror reflectance = 0.90. Receiver diameter varies from 4 to 8.25 cm (x 5 cm length). 131

Figure 5-17 Cutaway of 56-cm diameter mirror, with radial ribs and lightweighting (left), and front face, with tripod support pass-throughs. Estimated mass, assuming a magnesium substrate: 8.8 kg, 36 kg/m^2. 133

Figure 5-18 MSTISM modelling, Mk. I cavity receiver under AM1.0 (1,353 W/m^2) and moderate terrestrial solar flux (750 W/m^2). Receiver mass = 1.157 kg. Insulation k = 0.06 W/m-K.134

Figure 5-19 Final mirror design submitted to Precision Optical Engineering (56-cm diameter aluminium, f/0.6 with no pass-throughs). 136

Figure 5-20 14-cm diameter solar concentrating mirror, *f*/0.6, intended for ganged-mirror operation with fibre-optic transmission. Both plastic and metal (aluminium) optics were constructed. 137

Figure 5-21 Baseline 428 N-s cavity receiver, B_4C particle bed in BN containment, surrounded by a ZrO_2/Al_2O_3 insulation package, left, and engineering drawing cutaway view, right (dimensions in millimetres). 138

Figure 5-22 Intermediate design, 428 N-s flanged cavity receiver, B_4C particle bed in BN containment, insulation package removed to illustrate mechanical sealing, left. Flanged cavity receiver, engineering drawing cutaway view, insulation package removed, right (dimensions in millimetres). 138

Figure 5-23 Maximum meridional and hoop stress in 80-mm O.D., thick-walled pressure vessel. 141

Figure 5-24 Mk. I cavity receiver, 1.3 kg, BN particle bed in ZSBN or IMC containment. Insulation package is 100% graphite foam. Mk. I cavity receiver in cross section, BN particle bed in ZSBN or IMC containment, graphite foam insulation. Dimensions in millimetres. 141

Figure 5-25 Mk. I cavity receiver in cross section, particle bed in ZSBN or IMC containment, ZrO_2 insulation later replaced with graphite foam (left). Feed line pass-through in fore face of receiver, showing brazed Mo fitting, right (all dimensions in millimetres). 142

Figure 5-26 Cavity receiver material samples, left photo: (1) Silica/boron nitride composite (M-26 60BN/40SiO_2, white block), (2) ZSBN (gray), and (3) BN/AlN (beige cylinder). Boron nitride particles and Mk. I receiver during fill process, right photo. Materials courtesy of St. Gobain Advanced Ceramics and Sintec Keramik. 144

Figure 5-27 Mk. II cavity receiver solid model cutaway (left) and engineering drawing (right). 144

Figure 5-28 Mk. II receiver heatup profile, 1,200 W input power (left), peak cavity temperature = 2,022 K after 30 minutes. Firing profile (right) demonstrates the heating efficiency of the receiver for two channel lengths (10 and 25 cm), with ammonia propellant. The 56 cm case is not shown; gas exit temperature tracks receiver body temperature. 145

Figure 6-1 SSTL vacuum test chamber with rotary first stage and oil diffusion pump. 148

Figure 6-2 Odeillo Solar Furnace Facility, near Perpignan, France. 149

Figure 6-3 Solar Simulator Test Chamber at the NASA Glenn Research Center. 150

Figure 6-4 Left: Pristine and heated samples of ZSBN ceramic composite, 40 minutes at 2,300 K, 20 mbar He environment, graphite furnace. Right: Fractured ZSBN specimen. 151

Figure 6-5 Left: Post-test samples of IMC ceramic composite, 40 minutes at 2,300 K, 20 mbar He environment, graphite furnace. Right: Close-up reveals evidence of graphite precipitation. 152

Figure 6-6 IMC (TiB_2/BN) solar receiver subcomponents during assembly and initial hermeticity testing. 153

Figure 6-7 Brazed feedline for high-temperature bond survivability 154

Figure 6-8 Brazing trials at the University of Manchester's Material Science Institute. 154

Figure 6-9 Post-furnace treatment of several braze specimens, University of Manchester. 155

Figure 6-10 MAST Carbon’s bonding attempt at 2,320 K melts molybdenum cap. 157
Figure 6-11 ZSBN ceramic post with Mo cap and Mo/MoSi$_2$/Si braze filler material. Graphite felt has bonded to bottom of ceramic post (right). 158
Figure 6-12 Screw-fit molybdenum cap and qualitative leak testing. 158
Figure 6-13 Mechanical feedline bonding with screwfit caps and graphite foil gaskets (Mk. II receiver). 160
Figure 6-14 Feedline post detail, Mk. I and Mk. II receivers. 161
Figure 6-15 Nozzle section, Mk. I and Mk. II receivers. 162
Figure 6-16 Normal shock formation in overexpanded nozzles. Dotted red line represents A_e/A_t = 33..163
Figure 6-17 Coefficient of thrust as a function of nozzle area ratio, indicating flow separation regime (γ = 1.2) [Zucrow, 1976]. 164
Figure 6-18 Packed bed preparation and assembly of Mk. I solar receiver for heating tests........166
Figure 6-19 Mk. I receiver in cavity heating rig (left). Cavity heating rig installed in chamber (right). 167
Figure 6-20 Thermocouple locations for Mk. I cavity heating profile tests (left). Resistance check on receiver heating element (right). 168
Figure 6-21 Vacuum heating test rig, Westcott E Site. 169
Figure 6-22 IMC heating element, tungsten leads (left). 2-path IMC heating element, 2nd version, tungsten leads (right). 170
Figure 6-23 Test 1 Heating Profile (Mk. I receiver, peak external cavity temperature (PECT) = 1,128 K, peak power dissipation in circuit = 704 W). Test date: 14 April 2003. 172
Figure 6-24 Test 2 Heating Profile (Mk. I receiver, PECT = 1,250 K, peak power dissipation in circuit = 872 W). Test date: 16 April 2003. MSTISM power = 595 W. 173
Figure 6-25 Test 10 Heating Profile (Mk. I receiver, PECT prior to first shutdown (85 minutes) = 1,047 K, peak power dissipation in circuit = 630 W; PECT following first shutdown = 1,077 K, peak power dissipation after first shutdown = 810 W). Test date: 13 May 2003. MSTISM power = 414 W. Dashed blue line: First shutdown (85 minutes). Dashed red line: Restart (87 minutes). 173
Figure 6-26 Eight-path graphite elements. 174
Figure 6-27 Test 14 Heating Profile (Mk. I receiver, PECT = 1,283 K, peak power dissipation in circuit = 1,267 W). Test date: 18 June 2003. MSTISM power = 939 W. 175
Figure 6-28 Test 17 Heating Profile (Mk. I receiver, PECT = 1,424 K, peak power dissipation before final ramp = 1,267 W; after ramp = 1,575 W). Test date: 27 June 2003. MSTISM power = 1,050 W. 176

Figure 6-29 Mk. I cavity receiver undergoing heating test in vacuum (left). Mk. II cavity receiver in similar test, showing lower (1) and upper (2) penetrations (right)....................................177

Figure 6-30 WinTherm overprediction of cavity temperature for a given circuit power dissipation. Test 17 (Mk. I receiver). MSTISM power = 1,050 W. WinTherm radiative power to receiver = 325 W. 178

Figure 6-31 Mk. I receiver after completion of Test 1 (left). Mk. I receiver at end of test series (right). 178

Figure 6-32 Mk. II receiver with insulation package sections, pre-assembly (left). Mk. II receiver on cavity heating rig prior to Test 18, insulation cap removed (right)..................................179

Figure 6-33 Test 21 Heating Profile (Mk. II receiver, PECT = 1,788 K, peak power dissipation (ramp 1) = 773 W; (ramp 2) = 1,080 W; (ramp 3) = 1,368 W). Test date: 10 July 2003. MSTISM power = 400 W. MSTISM power (2) = 654 W. MSTISM power (3) = 1,000 W. 180

Figure 6-34 Test 25 Heating Profile (Mk. II receiver, PECT = 1,974 K, peak power dissipation before final ramp = 1,080 W; after ramp = 1,429 W). Test date: 9 September 2003. MSTISM power = 1,000 W. MSTISM power (2) = 1,294 W...181

Figure 6-35 Mk. II cavity receiver following initial heating trials (Test 18/19), left. Mk. II cavity receiver after final heating trial (Test 25). 182

Figure 6-36 Rotary forepump (left) and forepump/blower assembly at Westcott F Site (right)...183

Figure 6-37 Westcott F Site high altitude test facility (HATF) chamber.....................................183

Figure 6-38 Initial flow characterisation test setup, Westcott F Site (left). Thrust stand electronics (right) with visual display on digital multimeter...184

Figure 6-39 Mass flow rate data versus inlet pressure (Tests 26-A, B results, 28-29 October 2003). 187

Figure 6-40 Derived vena contracta area (mm^2), Tests 26-A, B (28-29 October 2003). 188

Figure 6-41 Inlet pressure trace from Test 26-D, high temperature N_2 flow trial (29 October 2003). 190

Figure 6-42 Lower penetration temperature trace, Test 26-D, high temperature N_2 flow trial.....191

Figure 6-43 Ambient pressure drop trials, Mk. II receiver, Test 29 (19 November 2003). 191

Figure 6-44 Mk. II receiver undergoing N_2 flow testing (left). Residue observed on mounting plate beneath nozzle exit, following N_2 flow testing (right). 192

Figure 6-45 Heatup/cooldown profile for N2 flow trial, Test 26-D. Shaded area = flow test period. 192

Figure 6-46 Inlet pressure trace for N_2 flow trial, Test 26-D. Shaded area = flow test period. ...193

Figure 6-47 Estimated characteristic velocity profile for N_2 flow trial, Test 26-D.......................193

Figure 6-48 Calibration of Aalborg thermal mass flow meter versus catch-and-weigh, nitrogen gas (2-10 bar supply pressure)..194

Figure 6-49 Temperature and characteristic velocity (estimated and ideal), Test 27-A (3 November 2003). 194
Figure 6-50 Temperature and characteristic velocity (estimated and ideal), Test 27-B (3 November 2003). 195
Figure 6-51 Inlet pressure and mass flow (measured and adjusted), Test 27-B (3 November 2003). 195
Figure 6-52 Temperature and characteristic velocity (estimated and ideal), ammonia flow trial, Test 27-C (3 November 2003). 196
Figure 6-53 Inlet pressure and mass flow (measured and adjusted), Test 27-C (3 November 2003). 196
Figure 6-54 Boric oxide precipitate surrounding receiver nozzle exit (left) and dark globules on graphite foam insulation bottom (right) following Test 27-C (high-temperature NH_3 flow trial). 197
Figure 6-55 Mk. II receiver following Test 27-C (left). Detail of precipitate blisters near feedline (right). 198
Figure 6-56 Mk. II nozzle section (left) utilised for ambient pressure drop tests, with detail (right). 200
Figure 6-57 Cutaway view of Mk. II receiver with chamber pressure tap collar (left). Assembled receiver prior to beginning Test 30 series (right). 201
Figure 6-58 Flow testing with installed thrust stand. 202
Figure 6-59 Temperature and characteristic velocity (measured and ideal), nitrogen flow trial, Test 30-F (12 December 2003). 205
Figure 6-60 Mk. I receiver with chamber pressure tap collar. 205
Figure 6-61 Temperature and characteristic velocity (measured and ideal), ammonia flow trial, Test 30-H (8 January 2004). 206
Figure 6-62 Test 30-H detail, with ideal c^* estimates (no dissociation and partial dissociation). 207
Figure 6-63 Inlet and chamber pressure trace measurements, ammonia flow trial, Test 30-H.....207
Figure 6-64 Mk. II solar receiver, top surface detail showing circumferential and radial cracking (left). Mk. II receiver insulation package displaying white powder precipitate (right). 208
Figure 6-65 Temperature and characteristic velocity (measured and ideal), ammonia flow trial, Test 31-C (14 January 2004). 209
Figure 6-66 Inlet and chamber pressure trace measurements, ammonia flow trial, Test 31-C. 209
Figure 6-67 Mk. I receiver in ammonia flow testing (left) and following flange failure (right)...210
Figure 6-68 Mk. I receiver flange failure detail (left). Mk. I nozzle detail, post-firing (right). 211
Figure 6-69 Losmandy G-11 German Equatorial Mount, with declination/right ascension axes at right [Losmandy, 2004]. 212

Figure 6-70 Concentrator support structure for on-sun test, in single mirror configuration (left) and multiple small mirror configuration (right). 213
Figure 6-71 56-cm aluminium concentrating mirror on diamond turning tool following fabrication. 213
Figure 6-72 56-cm mirror form error (sag) data [Parker, 2003]. Bold line represents mirror centre. 215
Figure 6-73 Optical test rig mounted on Losmandy GM-11 mount. 215
Figure 6-74 RdF micro-foil heat flux sensor, Type 27133-1, 50 W/cm^2 maximum (left); sensor glue-mounted to copper target, prior to on-sun test (middle); and result of short on-sun exposure (right). 216
Figure 6-75 Photograph of centre of copper target during on-sun testing, through welding glass (left) and without (right). Spot size is clearly less than half the diameter of the inner ring, which is marked in yellow in the left-hand photo (10 mm). 217
Figure 6-76 Uncoated and coated (Al/MgF$_2$) 14-cm concentrating mirror (left). Mirror detail (right). 219
Figure 6-77 14-cm aluminium concentrator form error test results. Peak-to-Valley (PV) form error is 2.5 μm; RMS form error is significantly less, 0.57 μm (λ = 0.490 μm) [Whelton, 2003]. 220
Figure 6-78 Small PMMA mirrors undergoing spot size testing at SSTL solar simulator facility (left). Geometric concentration ratio estimate based on focal spot size measurement (right). 221
Figure 6-79 Focal spot size measurement, 14-cm aluminium mirror, utilising solar simulator (left). Optical fibre transmission testing with solar simulator (right). 222
Figure 6-80 0.75-mm (NA = 0.66) optical fibre heating test, using SSTL's solar simulator. 222
Figure 6-81 Optical fibre laser power throughput measurement test rig, University of Surrey Optoelectronics Laboratory (February 2004) [Lock, 2004]. 223
Figure 6-82 Incandescent lamp calibration for integrating sphere power throughput testing.......224
Figure 6-83 Interior of integrating sphere, demonstrating light baffling between source and sensor (left), 12-V test lamps (right). 225
Figure 6-84 Blackbody emission curves (monochromatic emissive power) for tungsten filament temperatures between 1,500 and 2,850 K. 226
Figure 6-85 Sphere multiplier and power dissipation (estimated and actual) versus predicted filament temperature, 1 and 4 May 2004. 227
Figure 6-86 Ganged mirror power throughput test, three optical fibres, 14 May 2004. 228
Figure 6-87 Ganged mirror power throughput test setup (left). Concentrated sunlight emerging from 0.75-mm core diameter optical fibre (NA = 0.66). 229

Figure 6-88 Fibre power transmission test results, 11 May 2004. 229

Figure 6-89 Graphite element heating with fibre-transmitted sunlight (left); detail of precision fibre placement rig (XY micrometer stage) with 14-cm plastic mirror and 0.75-mm fibre (right). 230

Figure 6-90 1-g graphite element heating test, single 750-micron optical fibre, NA = 0.66 (14 May 2004). 231

Figure 6-91 1-g graphite element heating test, direct heating (14 May 2004). 232

Figure 7-1 30-spacecraft Galileo navigation satellite constellation (left) and satellite detail (right). 237

Figure 7-2 Heatup (left) and firing profile (right) for baseline solar thermal demonstrator engine (15-minute charge, 1 minute delay, 40.4 s firing time). 240

Figure 7-3 Disaster Monitoring Constellation microsatellite augmented with microscale solar thermal propulsion experiment (space-facing facet detail, deployed configuration). 241

Figure 7-4 Propellant storage and feed system configuration, DMC experiment (left). Solar receiver mounting (right). 242

Figure 7-5 Orbital altitude versus time, initial spacecraft altitude = 560 km, planform area = 2 m^2, spacecraft mass = 150 kg . Solar maximum conditions assume a solar flux ($f_{10.7}$) of 225 SFU and a Geomagnetic A index (A_p) of 30. Solar minimum conditions assume a flux of 138 SFU and an A_p of 0. 244

Figure 7-6 Mission orbit re-acquisition delta-V requirements and mean time between firings versus orbital altitude, assuming solar maximum conditions. 245

Figure 7-7 Solar beta angle definition [Battin, 1987][Larson, 1992]. 246

Figure 7-8 Solar beta angle and zenith angle (φ) maxima and minima, 560 km circular orbit, 35.4° inclination, 1 October 2006 to 1 April 2007 (Mission Days 1-180). 247

Figure 7-9 Beta angle and zenith angle φ, Mission Days 20-22 (longest-duration thermal charging opportunity). 247

Figure 7-10 Heatup (left) and firing profile (right) for baseline solar thermal demonstrator engine (15-minute charge, 1 minute delay, 2.49 s firing time). 248

Figure 7-11 Orbital altitude versus time, drag makeup mission. Day 0 = MD 188 (7 April 2007). 249

Figure 7-12 Concentrator subassembly mounting schemes on CFESat space-facing facet: baseline 14-cm mirror, alt-azimuth mount (left), ganged mirror alternative, including four 7-cm mirrors (right). 250

Figure 7-13 EELV secondary payload adapter ring undergoing final machining, left [Ganley, 2002]. Example electrical harness layout, right [Goodwin, 2001]. 251

Figure 7-14 SSTL Fine Sun Sensor output, two axes and ratio (X/(X+Y)). 252

List of Tables

Table 3-1 Selection Matrix for Candidate Solar Thermal Propulsion Mission Scenarios 45

Table 3-2 Ariane ASAP, GTO to GEO..48

Table 3-3 Atlas IIAS, GTO to GEO..48

Table 3-4 Potential Candidates for NEO Flyby Missions, 2004-2006. [CfA, 2001] 50

Table 3-5 Mission to 4179 Toutatis. 51

Table 3-6 Mission to 2000 UK11. 52

Table 3-7 Effect of a 100-day hold on a highly elliptic (830 x 206,000 km) phasing orbit's elements. 52

Table 3-8 Ideal and simulated velocity change requirements for a GTO-to-Escape mission, given an initially unfavourable GTO. 54

Table 3-9 Lunar Capture Mission 56

Table 4-1 Density, I_{sp}, and Density-I_{sp}, for representative monopropellant and bipropellant combinations. 63

Table 4-2 Properties of Potential Thermal Storage Materials [Lienhard, 1987][Lynch, 1966][Pierson, 1996][MatWeb, 2002]...84

Table 4-3 Per-Orbit Impulse and Energy Storage Requirements for Thermal Storage Cavity Receiver 87

Table 4-4 Preliminary STE design points, with estimated concentrator size (assuming single mirrors and an optical efficiency of 0.8), "hot-start" charging times, and calculated peak temperatures achievable. 95

Table 5-1 Baseline LEO orbit raising mission, key parameters...129

Table 5-2 MSTISM performance sensitivity analysis, for mirror diameters of 100-, 75-, 50-, and 30 cm. Final payload mass excludes propellant and STP system mass. 130

Table 5-3 STP performance sensitivity analysis, for variable receiver sizes and a fixed mirror diameter of 30 cm. Final payload mass excludes propellant and STP system mass. 131

Table 5-4 Analysis for four candidate propellants, given a fixed receiver size (0.195 kg) and a fixed mirror diameter of 30 cm. Final payload mass excludes propellant, STP system mass. 132

Table 5-5 Aluminium 7075-T73 and magnesium properties [Matweb, 2002][Larson, 1992]......134

Table 6-1 Brazing filler metal liquidus temperatures [Rembar, 2002]. 154

Table 6-2 Mk. II receiver mass flow rate check..162

Table 6-3 Summary of cavity heating profile tests (April – September 2003). 171

Table 6-4 Ambient and high-temperature flow testing in Westcott F Site HATF (first series). ...187
Table 6-5 Test 26-C, Power-To-Flow test results. ...188
Table 6-6 Induction-coupled mass spectrometry results from Mk. I and Mk. II receiver samples. ...199
Table 6-7 Ambient (no heating) thrust measurement tests, Mk. II receiver, in nitrogen and helium. ...203
Table 6-8 Hot flow thrust measurement trials in helium, nitrogen, and ammonia. ...204
Table 6-9 Laser power meter characterisation of large (56-cm) concentrating mirror, 15 July 2003. ...219
Table 6-10 Incandescent lamp calibration test results, 1 and 4 May 2004. ...227
Table 7-1 SSTL microsatellites augmented with propulsion systems (current and planned). ...236
Table 7-2 Baseline parameters of a DMC de-orbit mission utilising solar thermal propulsion. Spacecraft “wet” mass = 100 kg. ...240
Table 7-3 Sensitivity of system performance to mirror diameter and propellant choice. The 60-cm option requires a larger receiver aperture (0.75 cm diameter) to accommodate the increase in focal spot size. ...241
Table 7-4 Baseline LEO drag makeup mission, key parameters. Spacecraft “wet” mass = 165 kg. ...248
Table 7-5 Sensitivity of STP system performance to mirror diameter. (*The 7-cm mirror option does not achieve the baseline minimum firing temperature (MFT) of 600 K; for this case only, MFT = 350 K). ...249

Nomenclature

a	Semi-major axis of elliptical orbit
a	Radius of receiver aperture
$[A]$	Concentration
A	Pre-exponential factor
A	Area of radiating surface
A_c	Concentrating mirror area
A_e	Nozzle exit area
AFRPL	Air Force Rocket Propulsion Laboratory
AlN	Aluminium nitride
AM0	Air Mass Zero
AM1.5	Air Mass 1.5
A_p	Planetary A index for geomagnetic activity
A_r	Receiver aperture area
ASAP	Ariane 5's Structure for Auxiliary Payloads
A_t	Nozzle throat area
AU	Astronomical Unit
b	radius of concentrating mirror
B^*	Pseudo ballistic coefficient
B.C.	Before Christ
Bi	Biot number
BN	Boron nitride
BNSC	British National Space Council
BOL	Beginning of Life
c	speed of light (2.9979×10^8 m/s)
C	Concentration ratio, based on the ratio of received power to incident flux

c^*	Characteristic velocity (m/s)
c_c	conic constant
C_D	Coefficient of drag (dimensionless)
C_f	Coefficient of thrust (dimensionless)
C_g	Geometric concentration ratio
C_{max}	Thermodynamically limited concentration ratio
$C_{max,flat}$	Maximum concentration ratio obtainable with a flat-plate absorber
C_p	Constant-pressure specific heat (J/kg-K)
C_v	Constant-volume specific heat (J/kg-K)
CfA	Harvard-Smithsonian Center for Astrophysics
CFESat	Cibola Flight Experiment Satellite
CHUPS	Cavity HeatUP Sequence
cm	centimetre
CONTOUR	Failed John Hopkins/Applied Physics Laboratory comet nuclei flyby mission
CPA	Coarse Pointing Assembly
CPC	Compound Parabolic Concentrator
C_{rel}	Ratio of average concentration to thermodynamic concentration limit
CRRES	Combined Release and Radiation Effects Satellite
CTE	Coefficient of Thermal Expansion
CVD	Chemical Vapour Deposition
D	Diameter of lens or mirror element
D	Hydraulic diameter
DARWIN	European Space Agency's proposed terrestrial planet finder mission
dB	Decibel
DC	Direct Current
delta-V	Velocity change (m/s)
DI_{sp}	Density-I_{sp}, g-s/cm^3
DMC	Disaster Monitoring Constellation

DoD	Department of Defense (U.S.)
D_p	Particle diameter
DSCS	Defense Satellite Communications System
DT	Diamond Turning
e	Eccentricity
e	Pointing error
E	Eccentric anomaly
E	Young’s Modulus
E	Per-mass augmentation power for electrothermally-augmented resistojets
E_a	Activation energy
EDX/SEM	Energy-Dispersive X-ray Scanning Electron Microscopy
EELV	Evolved Expendable Launch Vehicle
EPCRA	Emergency Planning and Community Right-to-Know Act
EOL	End of Life
ESA	European Space Agency
ESPA	EELV Secondary Payload Adapter
ETA	Electrothermal Augmentation
EUV	Extreme Ultraviolet
f	Darcy-Weisbach friction factor
f	focal length
$f/\#$	*f*-number, optical element focal length divided by diameter
F	Failure probability, for ceramic coupons
F	True anomaly
FPA	Fine Pointing Assembly
FSC	Flight Scale Concentrator
$f(t)$	space-facing facet normal
g	Gravitational acceleration at earth’s surface, 9.8 m/s^2
G	Gravitational constant (6.67×10^{-11} $N\text{-}m^2/kg^2$)

GAIA	European Space Agency's proposed mission for star mapping
GeMINI	Geosynchronous Minisatellite
GEO	Geosynchronous Earth Orbit
GSFC	Goddard Spaceflight Center
GSTB-v2	Galileo System Test Bed, version 2
GTO	Geosynchronous Transfer Orbit
h	Planck's constant, 6.6262 x 10^{-34} J/s
h	Altitude above earth's surface (m)
h	Surface sag (difference between ideal and actual mirror surface)
HAPO	High Altitude Phasing Orbit
HATF	High Altitude Test Facility
h-BN	Hexagonal boron nitride
h_c	heat transfer coefficient (W/m^2-K)
HEO	Highly Elliptical Orbit
HETO	Heliocentric Earth Trailing Orbit
i	Inclination (degrees)
I	Moment of inertia (m^4)
I	Intensity (W)
IAE	Inflatable Antenna Experiment
ICPMS	Induction-Coupled Plasma Mass Spectrometer
IMC	Intermetallic Composite (BN/TiB_2)
in.	inch (2.54 cm)
IR	Infrared
I_{sp}	Specific impulse (s)
ISUS	Integrated Solar Upper Stage
JPL	Jet Propulsion Laboratory
k	Reaction rate constant (cm^3/molecule-s)
k	Thermal conductivity, W/m-K

k	Boltzmann’s constant, 1.3806 x 10^{-23} J/K
K	Kelvin
kg	kilogram
kJ	Kilojoule
km	Kilometre
K_p	Equilibrium constant (based on mole fractions)
K_p	Equilibrium constant (based on partial pressures)
kW	Kilowatt
L2	One of the earth-moon LaGrange points
LAD	Liquid Acquisition Device
LAN	Longitude of the Ascending Node
LANL	Los Alamos National Laboratories
LEO	Low Earth Orbit
LGA	Lunar Gravity Assist
LISA	European Space Agency’s proposed gravity wave detector mission
LMO	Low Mars Orbit
LOI	Lunar Orbit Insertion
LVO	Low Venus Orbit
m	Weibull modulus
$\dot{m}$	mass flow rate (kg/s)
M	Moment (N-m)
M	Mean anomaly
M	Molecular weight (kg/kg-mol)
M	Central mass (kg)
M	Integrating sphere multiplier
M_e	Exit Mach number
MD	Mission Day
MEEGA	Mars-Earth-Earth Gravity Assist

MFT	Minimum Firing Temperature
m_i	initial mass of spacecraft
MJ	Megajoule
mm	millimetre
MMH	Monomethylhydrazine
MMS	Magnetospheric Multi-Scale
mN	Millinewton
MOID	Minimum Orbit Intersection Distance
m_p	propellant mass
MPa	Megapascal
mrad	milliradian
MSTISM	Microscale Solar Thermal Propulsion System Integrated System Model
MUSES-C	Japanese asteroid sample return mission
MW	Megawatt
mΩ	milliohm
n	Mean motion
n	Index of refraction
N	Newton
n_a	refractive index of air
NA	Numerical Aperture
NASA	National Aeronautics and Space Administration (U.S.)
n_{clad}	Optical fibre cladding refractive index
n_{core}	Optical fibre core refractive index
NEO	Near Earth Object
NERVA	Nuclear Engine for Rocket Vehicle Application
Nu_{Dp}	Nusselt number, based on particle diameter
OSLO	Optics Software for Layout and Optimisation
P	Probability

P	Power (W, kW, or MW)
P_a	Ambient pressure (MPa or psi)
P_c	Chamber pressure (MPa or psi)
P_e	Nozzle exit pressure (MPa or psi)
PBHT	Particle Bed Heat Transfer
PC	Polycarbonate
PECT	Peak External Cavity Temperature
PHA	Potentially Hazardous Asteroid
PICT	Peak Internal Cavity Temperature
PMD	Propellant Management Device
PMMA	Polymethyl Methacrylate
PPARC	Particle Physics and Astronomy Research Council
P-OE	Precision Optical Engineering
Pr	Prandtl number
psi	Pounds per square inch
PTLPB	Partial Liquid Transient Phase Bonding
PV	Peak to Valley
q	electron charge (1.6022×10^{-19} coulombs)
Q	Thermal quality (m^2-K/s)
Q	Radiative heat loss (W)
Qinetiq	Former Defence Evaluation and Research Agency (DERA) activity, now private
Q_{net}	Net heat deposited in a solar receiver, over one time step
R	Photodiode spectral responsivity (A/W)
R	Universal gas constant (8,314.3 J/kmol-K)
r_a	receiver aperture radius
RAAN	Right Ascension of the Ascending Node
RAC	Receiver/Absorber/Converter
R_c	Mirror radius of curvature

Re_{Dp}	Reynolds number, based on particle diameter
RMS	Root Mean Square
s	Second
s	scale factor (for pointing error calculations)
SFU	Solar Flux Unit
SIM	Space Interferometry Mission
SIMONE	Qinetiq proposal for a comet rendezvous mission utilising electric propulsion
SIP	Surrey Interplanetary Mission
SMART-1	European Space Agency's lunar mineralogy and space demonstration mission
SMART-2	European Space Agency's proposed pathfinder mission for LISA and DARWIN
SOI	Sphere of Influence
SOTV	Solar Orbit Transfer Vehicle
SPT	Stationary Plasma Thruster
SSC	Surrey Space Centre
SSME	Space Shuttle Main Engine
SSTL	Surrey Satellite Technologies, Ltd.
$s(t)$	solar vector
STA	Solar Thermal Augmentation
STE	Solar Thermal Engine
STK	Satellite Tool Kit
STP	Solar Thermal Propulsion
STP	Space Test Program
t	time (s)
T	Blackbody temperature (K)
T	Thrust (mN or N)
T_1	Radiating body temperature (K)
T_2	Background or "cold space" temperature (K)
T_b	Temperature of particle bed

T_c	Chamber temperature (K)
T/C	Thermocouple
TERC	Tailored Edge-Ray Concentrator
THz	Terahertz
TLI	Trans-Lunar Injection
T_m	Melting point
T_p	Temperature of propellant
T_r	Receiver equilibrium temperature (K)
TVS	Thermodynamic Vent System
UDMH	Unsymmetrical Dimethylhydrazine
u_e	Exit velocity (m/s)
UHF	Ultra-High Frequency
u_s	Superficial flow velocity (m/s)
V_a	Velocity at apogee
VFP	Vortex Flow Pancake
VHF	Very High Frequency
W	Wavefront aberration or error
W	Watt
WC	Tungsten carbide
WinTHERM	Thermal modelling software, Thermoanalytics, Inc.
WPM	Windowed Porous Material
WSB	Weak Stability Boundary
x	Distance along radius of mirror
XPS	X-ray Photoelectron Spectroscopy
y	Distance along mirror symmetry axis
z	Distance along mirror symmetry axis
ZSBN	Zirconia-Strengthened Boron Nitride (ZrO_2/BN/SiC)
α	Coefficient of thermal expansion (in./in./ ºC)

β	solar beta angle
γ	Ratio of specific heats
ΔP	Change in orbital period
ΔP	Pressure drop (MPa or psi)
Δu_{υ}	Spectral energy density (W/m^2-nm)
ΔV	Velocity change (m/s)
$\Delta V_{p.c.}$	ΔV required for plane change (m/s)
ε	Emissivity
ε	Particle bed porosity
λ	wavelength (nanometres or microns)
μ	Dynamic viscosity (Pa-s)
μm	micron (1 x 10^{-6} m)
μrad	microradian
η	thermal-to-electric conversion efficiency, for electric propulsion systems
η or η_o	Optical efficiency
η_q	Photodiode quantum efficiency
η_c	Collection efficiency
φ	Zenith angle between spacecraft space-facing facet normal and solar vector
Φ	Rim angle (degrees)
ψ	Incident ray azimuth angle
ψ	Optical fibre acceptance cone half-angle (degrees or radians)
Ψ	Optical fibre acceptance cone half-angle (sr)
π	Pi, 3.141592654…
ρ	Concentrating mirror radial position
ρ	Reflectance
ρ	Density (kg/m^3)
ρ_e	Resistivity ($\mu\Omega$-cm)

ρ_o	Standard earth atmospheric density at 120 km altitude
σ	standard deviation
σ	Stefan-Boltzmann constant, 5.6697 x 10^{-8} W/m^2-K^4
σ_o	Characteristic strength of material (psi or MPa)
σ_1	Meridional stress (Pa)
σ_2	Hoop stress (Pa)
σ_3	Radial stress (Pa)
σ_{min}	Minimum strength of material (psi or MPa)
τ	Orbital period
θ	Plane change (degrees or radians)
θ	Incident ray zenith angle
θ_{sun}	Half-angle of arc subtended by solar disk
θ_x	Mirror surface slope error
ν	Kinematic viscosity (m^2/s), equivalent to μ/ρ
ξ	Calculated slope error angle
ω	Argument of perigee
Ω	Right ascension (or longitude) of the ascending node

Chapter 1

1 Introduction

1.1 Propulsion as an Essential Adjunct to Advanced Microsatellites

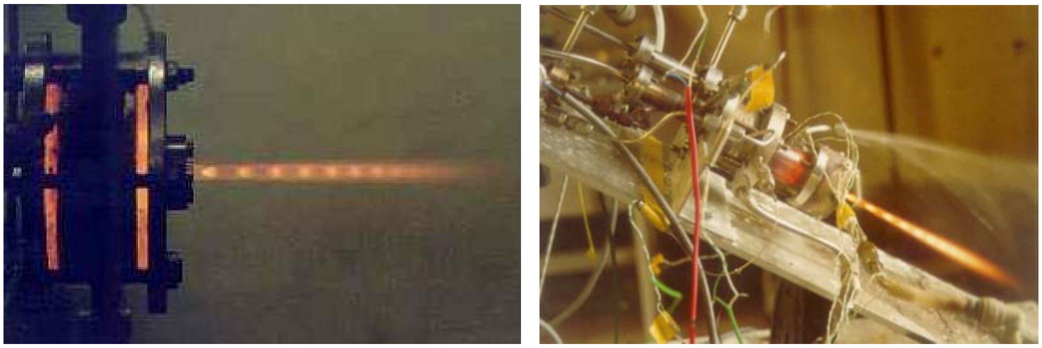

A Vortex Flow Pancake (VFP) hybrid rocket engine in test at Westcott "E" Site [Haag, 2001]

A H_2O_2/kerosene bipropellant rocket engine in test at "E" Site [Coxhill 2, 2002].

Figure 1-1 Recent spacecraft propulsion systems tested at the Surrey Space Centre.

The Surrey Space Centre has investigated a number of satellite propulsion concepts over the past decade, including cold gas systems, resistojets, mono- and bipropellant combinations (using nitrous oxide, N_2O, and hydrogen peroxide, H_2O_2), and hybrid gas oxidizer/solid fuel rockets [Sellers, 1996][Lawrence, 1998][Gibbon, 2000][Zakirov, 2001][Haag, 2001][Coxhill, 2002]. This ongoing effort is the result of a conscious decision to expand the utility of microsatellites. Haag [2000] notes:

> "'Small spacecraft' and 'propulsion' are two terms that are not commonly grouped together. There are several reasons why this is so. First, propulsion systems can be high-cost items whereas the small spacecraft mission is generally 'high-cost' intolerant. Secondly, there are mass and volume constraints…[along with] other considerations that serve to increase overall mission price (safety issues, environmental impact, etc.).
>
> There are many operational areas where a propulsive capability would serve to increase the utility of small spacecraft. Initial orbit manoeuvring, LEO drag compensation, constellation spacing, proximity operations, and de-orbit…"

Surrey's first satellite to incorporate a propulsion system was UoSAT-12, launched in 2000. UoSAT-12 included both a nitrogen cold gas system and a low-thrust N_2O resistojet for attitude control, momentum dumping, and a limited orbit changing capability. The total velocity change was 27 m/s [Haag, 2000].

Over the past several years, there has been a surging interest in using microsatellites to perform missions which, until now, have been regarded as the sole province of large (500 kg or greater) spacecraft. Such missions include major orbit transfers, to geosynchronous earth orbit (GEO) and the LaGrange points, lunar orbit, asteroids, and the inner planets (e.g., Mars, Venus). Jason [2000] examined a modified version of UoSAT-12 with a total velocity change capability of 1,700 m/s, sufficient to perform a number of the missions above. To produce a velocity change of this magnitude, high-efficiency propulsion is required.[1]

UoSAT-12's thrusters provide insufficient performance to perform manoeuvres of this kind; systems which might do so include hybrid and bipropellant hydrogen peroxide/kerosene (Figure 1-1) concepts pursued by Surrey, in addition to the ubiquitous bipropellant hydrazine/nitrogen tetroxide thruster (which has substantial flight heritage but are exceedingly expensive) [Sellers, 1996]. Electric propulsion systems, while potentially providing very high performance levels, are difficult to implement onboard small satellites, owing to their large power requirements. A relatively untested concept, solar thermal propulsion, promises higher performance (and therefore smaller propellant mass requirements) than any of Surrey's current stable of propulsion systems.[2]

1.2 Solar Thermal Propulsion

The solar thermal propulsion (STP) concept is a fairly basic one, relying on highly concentrated sunlight to heat a monopropellant to very high temperatures (typically approaching 3,000 K) and subsequently exhausting the propellant through a discharge nozzle to provide thrust. A typical solar thermal engine (STE) is composed of three primary components or subassemblies: a solar *concentrator*, which concentrates and focuses solar energy onto the receiver; the *receiver* itself, which acts as a heat exchanger for the propellant; and the *propellant storage and feed system*, which includes tankage and feed lines for routing propellant to the receiver. A fourth component, *control electronics*, is not considered here but is required to retrieve STP system telemetry, open and close valves, and (potentially) control both concentrator and receiver positioning.

---

[1] Figures of merit for propulsive efficiency, such as specific impulse (I_{sp}) and delta-V (ΔV), will be defined in Chapters 2 and 3.

[2] See Table 4.1 for information on the predicted performance for various propellants and propellant combinations, including electric propulsion systems, hybrid systems (H_2O_2/polyethylene) and H_2O_2/kerosene.

Various solar concentration schemes have been proposed, including lenses, deployable arrays, and inflatable arrays. All are tasked with the requirement of sufficiently concentrating available sunlight to heat the receiver to temperatures approaching material limits. The solar receiver collects radiant energy from the solar concentrator array and heats the propellant during thrusting. The United States Air Force's Integrated Solar Upper Stage (ISUS) used a thermal storage approach, relying on a coated graphite blackbody cavity receiver designed to withstand hydrogen attack on the graphite body, and minimise carbon loss [Frye, 1998]. A multilayer, refractory metal insulation package was devised to minimize radiative heat losses. Despite this, the ISUS ground demonstration at NASA's Lewis Research Center still suffered from greater heat losses (and thus achieved lower cavity temperatures) than models predicted.

Both ISUS and its follow-on, the Solar Orbit Transfer Vehicle (SOTV) [Kennedy, 1995][Kessler, 2000], are variants of the solar thermal engine which, when integrated with a satellite payload, would provide transfer to the satellite's intended orbit, and electrical power throughout the life of the satellite (Figure 1-2, left). This was analytically shown to further increase payload mass by using essentially the same hardware to provide both propulsive thrust and electrical power generation. An STP space experiment, originally scheduled for launch in the early 2000s, is now on hold due to funding limitations.

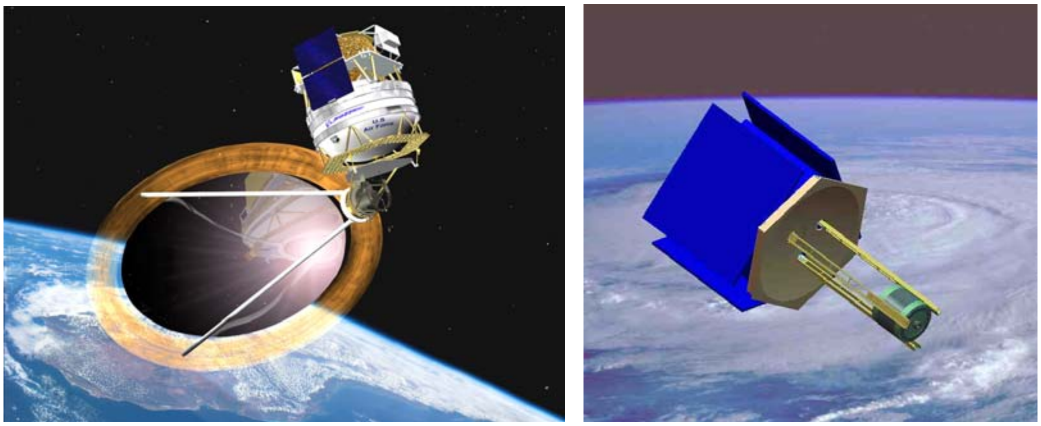

A Boeing/U.S. Air Force concept for a Solar Orbit Transfer Vehicle. [Boeing, 1999]

A low-cost solar thermal pathfinder hosted on a 20-kg microsatellite.

Figure 1-2 Solar Thermal Propulsion: a conceptual evolution.

In 2000, the author proposed a low-cost pathfinder to the Air Force experiment (Figure 1-2, right). This pathfinder, which would be hosted aboard a Surrey Satellite Technology, Ltd. (SSTL) micro- or mini-satellite, would demonstrate proof-of-concept in space, while still providing significant capability to the host satellite. It would eschew cryogenic hydrogen in favour of a storable propellant, rely on a small, fixed solar concentrator assembly, discard power production as a second mode, and maximize the use of off-the-shelf components in pursuit of a minimum-cost approach.

Given the severe mass and volumetric limitations imposed by the micro- and mini-satellite design, careful selection of propellants and engine cycle is essential. Surrey's enhanced microsatellite masses only 100 kilograms and is contained within a 60 x 60 x 80 centimetre volume, dictated by the stringent requirements imposed by Ariane 5's Structure for Auxiliary Payloads (ASAP) [Mugnier, 2000]. Thrust chamber temperature targets would be lowered from 3,000 K—which stretch material limits—to the 2,000-2,250 K regime. This reduces maximum achievable performance but allows for greater design flexibility in the selection of engine materials. A novel scheme for decoupling the receiver and concentrator, utilising optical fibre, permits a single large mirror to be replaced by an assembly of small mirrors, substantially reducing system weight.

This research has demonstrated the downward scalability of solar thermal propulsion and its applicability to small satellite platforms. Elements of the current research—to include the fibre-coupled receiver scheme—have been incorporated in a follow-on flight demonstration activity, which will provide an experimental propulsion capability aboard a Surrey microsatellite. This experimental payload is expected to fly in 2006.

Coupling a small satellite with STP could extend SSTL's capabilities into GEO-based telecommunications satellites and planetary exploration. Small satellite platforms, augmented by STP, provide the potential for low-cost access to GEO, the moon, and the inner solar system. Moreover, SSTL's capabilities offer the potential to jump-start solar thermal propulsion and permit a space demonstration significantly in advance of current plans—and at substantially lower cost.

1.3 Scope of Research

The scope of the present research effort includes the investigation of small solar thermal propulsion system, the detailed design and modelling of the integrated STP system and its key subsystems, their suitability for use aboard microsatellites, and their applicability to specific missions. The author's familiarity with the conceptual development of STP over the past forty years led to an interest in the implementation of several novel approaches that would permit a near-term space demonstration and provide residual utility to the host spacecraft. The author examined a number of existing and planned missions to determine if (a) the missions could be performed by microsatellite-based payloads, and (b) STP augmentation could enable or enhance the microsatellite missions under investigation.

Performance modelling included the use of standard, validated codes for optical ray tracing and thermal analysis. The author was directed to develop an integrated system model of the solar thermal propulsion system, incorporating orbital mechanics, propellant management, solar receiver characteristics, heating profile, and operation as a heat exchanger, in addition to attitude control effects and concentrator impacts.

As noted above, microsatellites impose stringent constraints on accessible payload volume, available surface area, cryogenic fluid use, spacecraft pointing, and engine firing. The author examined a number of innovative ways to achieve substantial performance gains over existing microsatellite propulsion options, while simultaneously adhering to the Surrey Space Centre's mantra of low-cost access to space. This dictated the use of storable monopropellants such as ammonia, in place of liquid hydrogen, to simplify ground handling, reduce cost, and permit long-term propellant storage. Various alternatives to the large, inflatable concentrating mirrors common to most STP concepts were examined; this effort culminated in the author's proposal to use multiple small, low-mass rigid metal mirrors, coupled with low-attenuation optical fibres, in place of large mirrors. These permit the solar receiver to be placed anywhere on the spacecraft, decoupling it from the mirror focal plane. On-sun testing revealed fibre transmission efficiencies approaching 40%, for unpolished fibres; polishing and precision alignment will undoubtedly improve performance. Refractory metal receivers, expensive and bulky, were rejected in favour of low-cost, all-ceramic devices fabricated from machinable structural composites such as TiB_2/BN and zirconia-strengthened boron nitride (ZSBN). These units performed well in vacuum, at temperatures of up to 2,000 K, and exposed to helium, nitrogen, and ammonia propellants at temperatures of up to 1,700 K.

Finally, this effort's scope included the investigation of methods that would permit the demonstration of a sub-scale STP system onboard a 100-kg Surrey microsatellite. Options for demonstration included the Disaster Monitoring Constellation and Cibola Flight Experiment spacecraft, both of which were shown to benefit from the inclusion of a small (14-cm) concentrating mirror system with a fibre-coupled solar receiver.

1.4 Thesis Structure

This thesis covers a three-year effort to design and demonstrate an innovative microscale solar thermal propulsion system suitable for deployment aboard microsatellites. The introductory material in this chapter provides a basic review of space propulsion research activities conducted at the Surrey Space Centre, how an investigation of solar thermal propulsion complements the existing research portfolio, and the scope and key contributions of this research activity.

Chapter 2, *Literature Survey*, discusses the history of the solar thermal propulsion concept, its key performance parameters, applications, and subsystems. Related areas of investigation, including high-temperature materials and methods for concentrating sunlight, are examined in detail.

Chapter 3, *Mission Analysis*, reviews a number of missions for microsatellite applicability and discusses the use of solar thermal propulsion as an augmentation, potentially allowing microsatellites to achieve high orbits (e.g., GEO, Earth escape) and perform entirely new missions. Several mission classes are identified as being both microsatellite-compatible and capable of enhanced performance through the use of STP systems.

Chapter 4, *Preliminary Design*, provides additional background on the assessment of solar thermal propulsion system performance. The chapter also discusses specific issues confronting the designer of highly-accurate concentrating mirrors, high-temperature solar receivers, and propellant management systems. Baseline system requirements and likely performance levels, predicted from simple subsystem models, are presented. This discussion feeds naturally into Chapter 5, *Integrated System Modelling and Detailed Design*, which examines the baseline system in more detail. Chapter 5 reviews the use of validated commercial codes for subsystem modelling and then proceeds to discuss the development of the author's Microscale Solar Thermal Propulsion System Integrated System Model (MSTISM), which builds on basic subsystem models to provide an overall picture of an STP system's performance. MSTISM was used to finalise the detailed design of the Mk. I and Mk. II solar receivers, as well as the large (56-centimetre diameter) and small (14-centimetre diameter) solar concentrators used during the test programme.

Chapter 6, *Component Test Campaign*, describes the efforts undertaken by the author to validate the subsystems developed in Chapter 5. This includes materials compatibility and bonding trials, hermetic sealing tests, electrical heating tests of full-scale solar receivers in vacuum, and full-flow testing—at temperature and in vacuum—with representative propellants. Results are compared to commercial and MSTISM predictions. The results of large and small concentrator testing, including ganged-mirror trials with optical fibre solar transmission, is also presented.

Chapter 7, *Flight System Development*, investigates the use of subscale demonstration STP systems aboard candidate Surrey microsatellites, and discusses specific design problems that will have to be resolved to permit a successful flight in the near-term (c. 2006). Chapter 8, *Summary and Conclusions,* draws the various strands of the research effort together, concluding that the initial hypothesis, that a microscale solar thermal propulsion system could be constructed with low-cost, readily available materials and elements, and usefully demonstrated in the near-term, is in fact true.

1.5 Novel Work Undertaken

The author has produced novel results in four specific areas:

(1) Mission utilisation of microsatellites augmented with solar thermal propulsion, to include:

   a. The use of low-eccentricity parking orbits in near-earth space, typically below 200,000 kilometres altitude, to permit low-thrust propulsion systems the capability to achieve escape or lunar orbit insertion without significant orbital element changes caused by lunar perturbations; and

   b. The use of high altitude phasing orbits (HAPOs), permitting earth escape and departure along any desired trajectory, thus permitting a microsatellite to be launched into an unfavourable initial orbit and still achieve escape or other-body capture.

(2) The development of a comprehensive integrated system model for microsatellite solar thermal propulsion systems, permitting the user to perform sensitivity analyses and conduct trades to optimise a microscale STP system for a given mission. Code results were validated through actual subsystem testing.

(3) The design of an innovative, all-ceramic solar thermal receiver, designed to store incident sunlight in an insulated body of thermal storage material and release it during engine firing. This includes:

   a. The use of high-temperature boron nitride-based composite ceramics, shown by the author to remain intact, suffering essentially zero mass loss and no mechanical failure, in vacuum and at temperatures of up to 2,273 K.

   b. The use of mechanical gasketing methods, using low-expansion molybdenum bolts and graphite seals to successfully bond and seal ceramic structures in compression at high temperatures (up to 2,000 K).

   c. The use of ultra high-temperature refractory metal brazes, including molybdenum-ruthenium, to bond composite ceramics at temperatures exceeding 2,000 K.

   d. The successful demonstration of the Mk. I and Mk. II solar receivers in vacuum, at temperatures of up to 1,700 K, utilising helium, nitrogen, and ammonia propellants, with a maximum achieved specific impulses of 237 s and thrust levels of up to 500 mN.

(4) The design and development of low-cost, low-mass concentrating mirrors, designed for ganged operation in conjunction with optical fibres. This approach, never before suggested in the literature, allows multiple small mirrors to duplicate the output of much larger mirrors, while permitting weight savings of up to 40%. Low-attenuation optical fibre permits remote location of the solar receiver; it no longer must be structurally supported at the mirror focal plane and can be mounted anywhere on the spacecraft, to

suit the microsatellite designer’s requirements. Small mirror and optical fibre tests demonstrated:

a. The utility of inexpensive, lightweight, highly accurate metal mirrors, providing peak concentration ratios approaching the theoretical limit for a given rim angle;

b. Fibre transmission efficiencies of up to 57%, observed in solar simulation and on-sun tests with 750-micron core diameter, high numerical aperture optical fibre;

c. As much as 2.2 W of optical power throughput from a combination of three 14-centimetre diameter mirrors and two types of optical fibre (750- and 1000-micron core diameter).

Chapter 2

2 Literature Survey

Spacecraft propulsion is a highly interdisciplinary enterprise; it requires a familiarity with compressible fluid flow, radiative, convective, and conductive heat transfer, thermochemistry and reaction kinetics, high-temperature materials behaviour, orbital mechanics, and spacecraft attitude control. Nuclear propulsion necessitates an understanding of nuclear reactor design and nuclear physics, while solar thermal propulsion—the focus of this research—demands a working knowledge of physical optics, lens and mirror design, and fibre optics. This chapter will focus on solar thermal propulsion concepts, their evolution over the past 40 years, and related disciplines. This material provides the essential background and base for the research described in further chapters.

2.1 Solar Thermal Propulsion Concepts and Heritage

In 1962, engineers at the U.S. Air Force's Rocket Propulsion Laboratory (AFRPL) at Edwards Air Force Base, California, successfully tested the first solar thermal rocket engine [Etheridge, 1979]. Using hydrogen as propellant, this system managed to achieve a specific impulse of 680 seconds (s). This level of performance is better than twice that of state-of-the-art bipropellant engines used for spacecraft manoeuvring, and 50% better than the most advanced chemical engine currently in service, the liquid hydrogen/oxygen fueled Space Shuttle Main Engine (SSME).

Specific impulse is commonly defined as thrust generated per unit weight of propellant mass [Humble, 1997]. It is therefore directly related to the amount of propellant required to accelerate a vehicle and produce a characteristic change in velocity, or delta-V (ΔV). For on-orbit manoeuvres, delta-V values can range from millimetres per second, in the case of small orbital corrections and attitude control burns, to multiple kilometres per second, in the case of significant transfers (e.g., low earth orbit to geosynchronous orbit, earth escape, or interplanetary trajectories). For small manoeuvres, variations in specific impulse tend to be unimportant; however, for high delta-V transfers, the difference in propellant mass can be substantial. At an I_{sp} of 320 s, a hydrazine/nitrogen tetroxide engine can transfer a 1,000-kg satellite from LEO to GEO in five hours, at a cost of over 2,800 kg of propellant.[3] Substituting a solar thermal engine (STE) with hydrogen propellant (I_{sp} = 680 s) reduces required propellant mass to just 900 kg. The two metric tons thus saved are made available to the mission designer for any number of purposes: heavier payloads and subsystems could be added, or the designer might decide to select a smaller, less expensive launch vehicle for a given payload mass. While this simple trade does not incorporate concept-specific complexities resulting from modified operations and hardware, it suggests that spacecraft designed to undertake high-cost orbital manoeuvres could be enhanced by augmentation with an appropriate solar thermal engine.

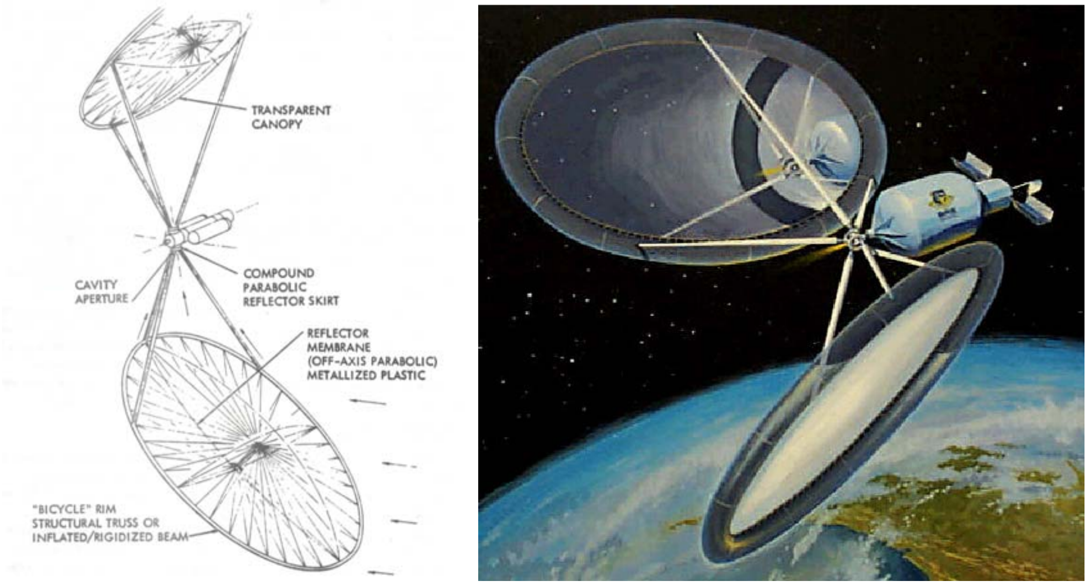
TRANSPARENT CANOPY
CAVITY APERTURE
COMPOUND PARABOLIC REFLECTOR SKIRT
REFLECTOR MEMBRANE (OFF-AXIS PARABOLIC) METALLIZED PLASTIC
"BICYCLE" RIM STRUCTURAL TRUSS OR INFLATED/RIGIDIZED BEAM

Figure 2-1 Two depictions of an AFRPL conceptual design for a solar thermal engine, with dual off-axis inflatable concentrators, right [Etheridge, 1979][Holmes, 2001].

Little data is available on 1960s-era analysis and testing programmes; Etheridge [1979] provides a very limited historical précis, but makes clear that early efforts to produce a flight-like solar thermal engine were overtaken by much larger and better-funded investigations in chemical, nuclear thermal, and electric propulsion. In 1973, following the cancellation of the U.S.'s Apollo programme, NASA stopped research to build a high-impulse nuclear thermal engine (i.e., the Nuclear Engine for Rocket Vehicle Application, or NERVA) and concentrated its resources on the development of the reusable Space Shuttle [Garber, 2002].

Etheridge's technical report is the seminal document in solar thermal propulsion system analysis, referenced by virtually all authors throughout the 1980s and 1990s. It examines the use of a solar thermal engine to transport a number of U.S. satellites from LEO to GEO and compares the performance of postulated STE configurations with conventional and advanced chemical, as well as electric, alternatives. Etheridge concludes that an STE, operating at propellant exit temperatures of up to 2,800 K, was attainable with 1970s–era technologies. This included the use of liquid hydrogen as primary propellant, refractory metal solar receivers, and large, inflatable concentrating mirrors—on the order of ten metres in diameter (Figure 2-1). A notable variant (Figure 2-2), utilising deployable, rigid optics and lower-temperature materials, was advanced in the mid-1990s [Kennedy, 1995]. To date, however, none of the concepts have been slated for space demonstration.

---

[3] This transfer typically demands two manoeuvres, totalling 4,200 m/s [Hill, 1992]. Details of these and other pertinent calculations are expounded upon in Chapter 4.

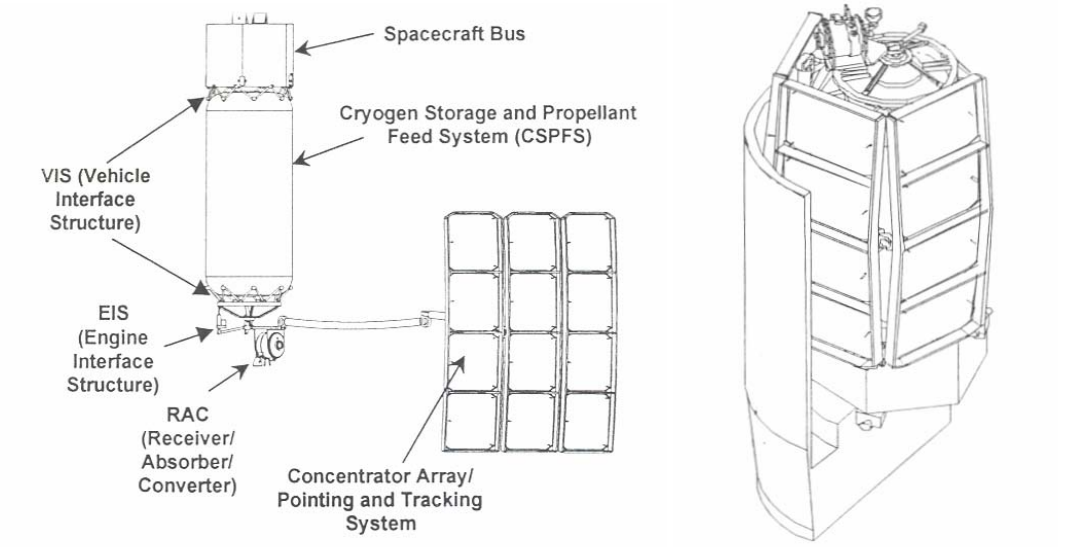
Spacecraft Bus
Cryogen Storage and Propellant Feed System (CSPFS)
VIS (Vehicle Interface Structure)
EIS (Engine Interface Structure)
RAC (Receiver/ Absorber/ Converter)
Concentrator Array/ Pointing and Tracking System

Figure 2-2 Deployed (left) and stowed (right) views of the proposed Solar Orbit Transfer Vehicle (SOTV), an Air Force Research Laboratory experiment [Partch, 1999].

2.1.1 Solar Receiver Evolution

Recommendations made in the Etheridge report guided solar thermal research for more than a decade after its publication, and continue to influence conceptual design to the present day. Shoji [1992], writing for Rockwell International's Rocketdyne Division, discusses highlights of the solar thermal engine research conducted in the 1980s at AFRPL, which focused on the development of a high-temperature solar receiver (Figure 2-3). Work at AFRPL's successor organizations, the Phillips Laboratory and Air Force Research Laboratory, has been joined worldwide by analytical investigations in the European Union [Calabro, 2001] and advanced refractory metal receiver trials in Japan [Shimizu, 1997].

As discussed in Section 1.2, solar thermal engines must operate at extremely high temperatures in order to be competitive with other propulsive options. Chemical propulsion systems can circumvent this problem to an extent; a chemical propellant's kinetic energy is derived from chemical energy released during decomposition or combustion. Thus, chemical propulsion system design focuses on minimising heat transfer from the hot propellant gases to the engine chamber and nozzle walls. This can be accomplished via several means, including regenerative cooling, wall film cooling [Coxhill, 2002], and off-stoichiometric operation [Hill, 1992]. Wall temperatures can be lowered dramatically, especially in cases where cryogenic fuels can be used.[4]

These options are unavailable to the STE designer. Energy must be deposited into the propellant from an external source; this can be done indirectly, through wall heating, or directly, via direct solar flux impinging on the propellant stream. Of the two options, only the first has been demonstrated successfully. These "windowless" systems use direct impingement by concentrated solar flux on high-temperature metal or ceramic walls, which then transfer heat to the propellant. Gas pressure and high operating temperature introduce stresses that ultimately limit the performance of such systems. Rocketdyne's rhenium coil thruster was intended to operate at 2,778 K.[5] The introduction of a quartz window was expected to equalise pressure on both sides of the cavity receiver wall, allowing higher-temperature operation.

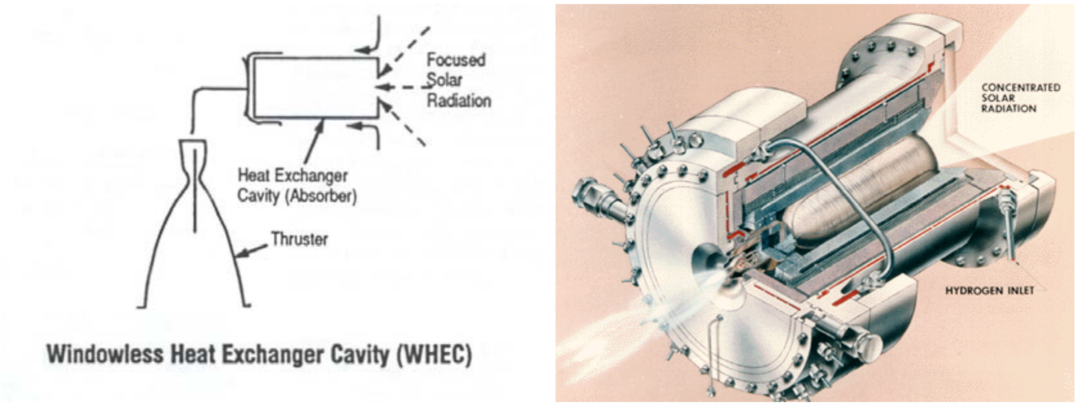

Figure 2-3 One solar cavity receiver/absorber concept, left. Rocketdyne's solar absorber/thruster assembly, right [Shoji, 1992][Shoji, 1983].

Direct gas heating requires windowed apertures (for propellant retention in the solar cavity) and the deposition of "seedant" particles in the propellant stream to increase absorptivity in the solar spectrum. As Venkateswaran [1992] notes, hydrogen, as well as a number of other candidate propellant gases, is very nearly transparent to solar radiation. Etheridge [1979] and Shoji [1983] discuss options for seedants, including a hydrogen gas/solid carbon particulate mixer upstream of the STE's heat exchanger, rotating seedant beds, and vortical gas injection (which would utilise vortex flow to retain seed particles at the periphery of the bed). These concepts, while potentially permitting higher peak gas temperatures—perhaps as high as 4,000 K—run afoul of a number of practical problems, including seedant deposition on concentrator surfaces and windows, spacecraft optical hardware, and other equipment, lowered specific impulse (due to the introduction of relatively high molecular weight seedant into the propellant stream), and, in the case of the rotating bed, the need for reliable high-temperature bearings and seals.

---

[4] For example, running a liquid hydrogen/oxygen engine "fuel-rich" lowers adiabatic flame temperature (reaction product temperature, assuming zero heat transfer) and decreases exhaust gas molecular weight.

Venkateswaran offers an alternative to the seedant bed, using alkali metal vapour in place of particulate seedant (Figure 2-4). A mixture of sodium, potassium, and caesium vapour is injected into the main propellant stream, increasing absorption from essentially zero to 30-60%. System modelling efforts coupled ray-tracing analyses (for incident solar radiation and absorption) with a two-dimensional, viscous flow simulation, examining high input power systems (1-10 MW). The inclusion of alkali metal raises the gas mixture's molecular weight, lowering specific impulse performance, but this approach might mitigate some of the operational problems associated with solid particulate seedants.[6]

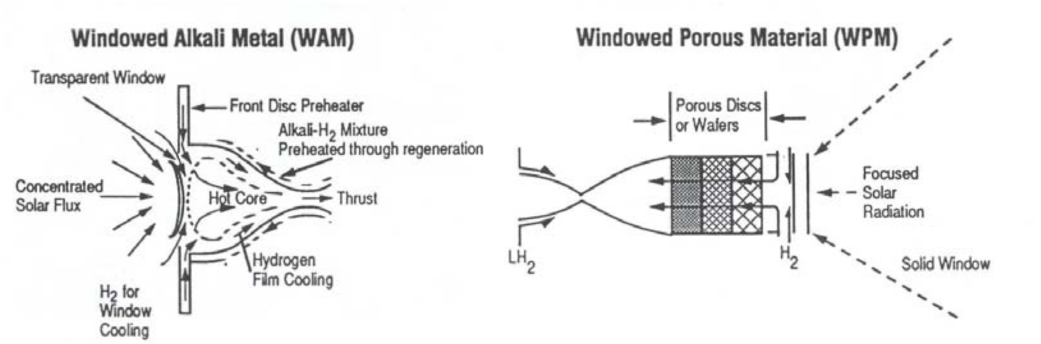
Windowed Alkali Metal (WAM)
Transparent Window
Front Disc Preheater
Alkali-H_2 Mixture Preheated through regeneration
Concentrated Solar Flux
Hot Core
Thrust
Hydrogen Film Cooling
H_2 for Window Cooling
Windowed Porous Material (WPM)
Porous Discs or Wafers
Focused Solar Radiation
LH_2
H_2
Solid Window

Figure 2-4 Two windowed solar thermal propulsion concepts [Shoji, 1992].

While this and other direct heating concepts have been extensively modelled, the author was unable to discover any published evidence of subsystem or element testing. Strongly similar to advanced nuclear propulsion concepts such as the open-cycle gas core rocket, which requires fluid dynamical containment of a fissioning uranium mass [McLafferty, 1970][Latham, 1971], they are sufficiently complex—and therefore costly—to have inhibited substantial practical development.

More recently, windowed porous material (WPM) concepts have been investigated [Shoji, 1986]. A series of reticulated foam disks, constructed of refractory metal carbide or other ceramic material, absorbs heat directly from impinging solar radiation. This structure acts only as a heat transfer device; it does not serve to confine high-pressure propellant gases and can be made

---

[5] The engine, designed and fabricated between 1982 and 1984, was tested "on-sun" for 65 hours, at up to 1,810 K [Shoji, 1992].

[6] Venkateswaran suggests that the Windowed Alkali Metal (WAM) concept is competitive at high power levels (1-10 MW thermal power) but cannot equal indirect (windowless, wall heating) system performance at lower input powers.

arbitrarily thin. This will further decrease stress in the porous strands making up the structure, owing to smaller temperature differentials across the strand walls. The WPM engine can theoretically be operated at very near its material limits (i.e., melting point) and has an inherently high surface area for gas-body heat transfer. Like all other windowed concepts, however, WPM suffers from potential window fouling by contaminants and heat stresses which could lead to failure of the window itself.

DelaRosa [1993] describes the fabrication of a prototype windowless thruster for the U.S. Air Force Phillips Laboratory,[7] using refractory rhenium foam (Figure 2-5). In this approach, a molybdenum mandrel is fitted with a rhenium sleeve and carbon foam torus. The foam is then chemically infiltrated with rhenium. A second outer sleeve is placed around the foam and the mandrel removed (via etching). This allows the production of a complex refractory metal/ceramic structure without precision machining.

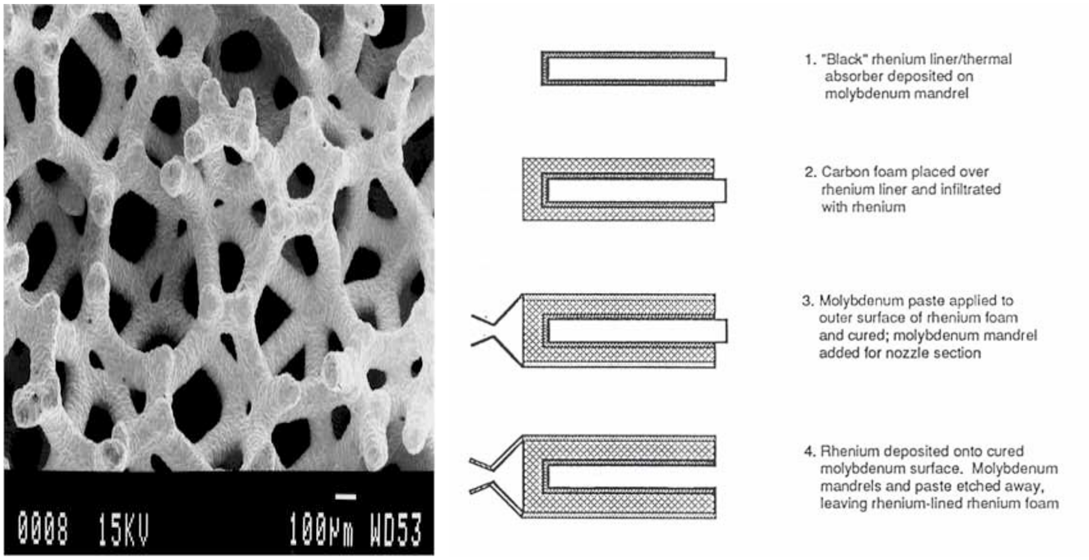
0008 15KV 100µm WD53
1. "Black" rhenium liner/thermal absorber deposited on molybdenum mandrel
2. Carbon foam placed over rhenium liner and infiltrated with rhenium
3. Molybdenum paste applied to outer surface of rhenium foam and cured; molybdenum mandrel added for nozzle section
4. Rhenium deposited onto cured molybdenum surface. Molybdenum mandrels and paste etched away, leaving rhenium-lined rhenium foam

Figure 2-5 Reticulated, vitreous carbon foam, left [Ultramet 2, 2002]. "Inside-out" fabrication technique for subscale solar-powered rocket engine, right [DelaRosa, 1993].

In 1995, engineers at the Phillips Laboratory's Kirtland Air Force Base in Albuquerque, New Mexico, designed and built several windowless solar receivers with the express purpose of producing both propulsive thrust and electrical power [Kennedy, 1995]. These efforts drew on recent advances made by the U.S. space nuclear power and propulsion community during the late 1980s, most notably in high-temperature materials research [El-Genk, 1994]. Unlike previous concepts, however, the Integrated Solar Upper Stage (ISUS) receivers relied on the interception and absorption of concentrated sunlight by a thermal storage material, making it possible to decouple thrusting and sun-pointing. This, in turn, permits higher-thrust firings (or smaller concentrator assemblies), as thrust is no longer limited by incident power. The ISUS system incorporated a rhenium-coated graphite cavity receiver surrounded by multiple sleeves composed of tungsten and molybdenum insulation (Figure 2-6). Incident sunlight would be absorbed by the cavity's walls and retained [Frye, 1998]. The high specific heat of graphite (2,000 J/kg-K), permits significant energy storage in a compact structure. This approach followed closely on NASA's proposals in the 1980s and 1990s to use phase-change thermal storage media in space-based solar dynamic power systems, intended for supplementary power onboard the International Space Station [Kerslake, 1993].

---

[7] More specifically, the Laboratory's Propulsion Directorate, located at Edwards Air Force Base, California.

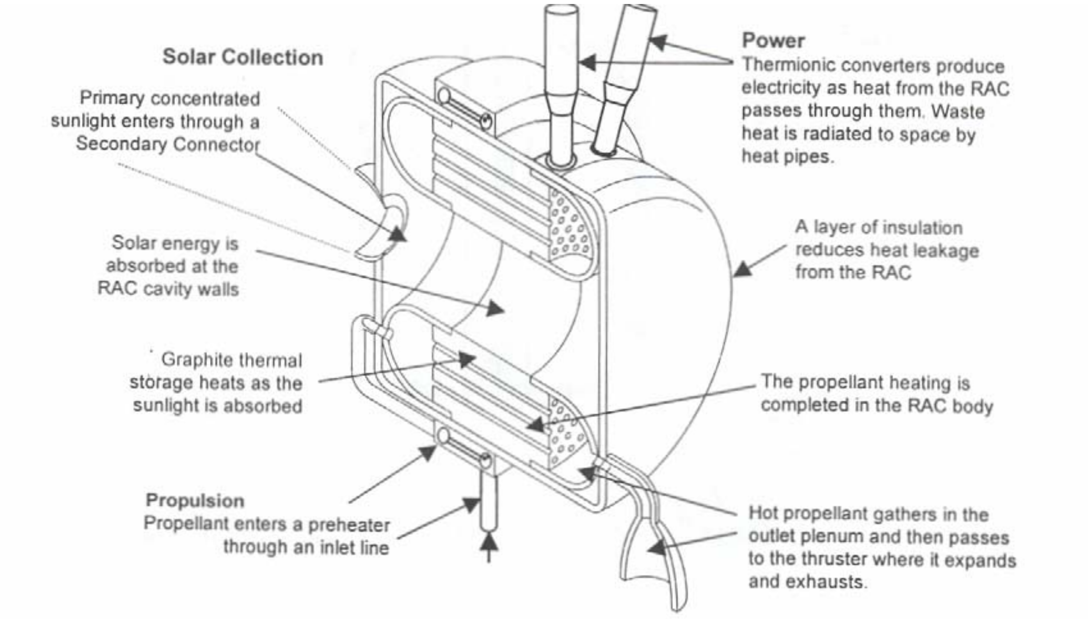
Solar Collection
Primary concentrated sunlight enters through a Secondary Connector
Solar energy is absorbed at the RAC cavity walls
Graphite thermal storage heats as the sunlight is absorbed
Propulsion
Propellant enters a preheater through an inlet line
Power
Thermionic converters produce electricity as heat from the RAC passes through them. Waste heat is radiated to space by heat pipes.
A layer of insulation reduces heat leakage from the RAC
The propellant heating is completed in the RAC body
Hot propellant gathers in the outlet plenum and then passes to the thruster where it expands and exhausts.

Figure 2-6 The ISUS Receiver-Absorber Converter [Partch, 1999]

In 1997, the ISUS Receiver-Absorber-Converter (RAC) was tested at NASA Lewis Research Center's Tank 6 facility. Tank 6, a high-vacuum chamber, contains nine 30-kilowatt (kW) xenon arc lamps and a collimated lens array, suitable for simulating sunlight in a space environment. The ISUS RAC was supplied with gaseous hydrogen and heated to temperatures in excess of 2,100 K, with an estimated specific impulse of 742 s [Frye, 1998]. While this ground demonstration was intended to reduce technical risk to a level sufficient to permit a near-term flight experiment, the ISUS follow-on activity, or Solar Orbit Transfer Vehicle (SOTV), has been unable to find sufficient funds to accomplish this.

Shooting Star, a short-lived programme at NASA's Marshall Spaceflight Center in Huntsville, Alabama, designed and fabricated a rhenium foam heat exchanger for solar thermal propulsion applications (Figure 2-7). This receiver was tested at temperatures of up to 3,000 ºF (1,922 K) with nitrogen propellant [Tucker, 2001].

In the past decade, there has been an upsurge of interest in the international community in developing a solar thermal thruster. While there has been some conceptual investigation in Europe, researchers at Japan's National Aerospace Laboratory succeeded in designing and fabricating 10-, 20-, and 50-mm diameter windowless receivers made from single-crystal molybdenum and coated with tungsten to prevent wall vaporisation at high temperatures ($\geq$ 2,500 K) [Shimizu, 2000]. Both nitrogen and helium propellants were tested, at receiver temperatures approaching 2,300 K. The large (50-mm) receiver was tested with nitrogen under vacuum conditions at Tohoku University's solar concentrator, reaching 2,000 K. Thrust data was considered suspect, as thrust stand temperature drift affected measurements. No specific impulse estimates for this final test were provided.

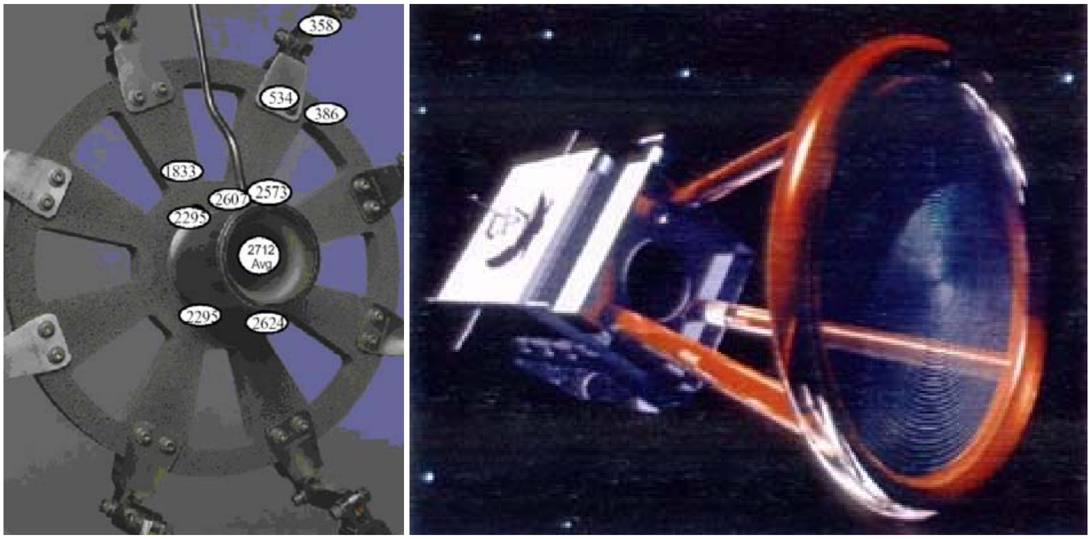

Figure 2-7 Electrically heated "Wagon-wheel" solar receiver test article, with achieved peak temperatures (ºF), left [Tucker, 2001]. Hypothetical "Shooting Star" STE on Spartan free-flying experimental platform, depicting inflatable Fresnel lens concentrator [Shaltens, 2002].

2.1.2 Methods for Concentrating Sunlight

Techniques for concentrating sunlight are centuries old. The apocryphal story of Archimedes' defeat of the Roman fleet at Syracuse in the 3rd century B.C., utilising "burning mirrors" to ignite the hulls of ships [Mills, 1992] illustrates mankind's long familiarity with the concept. The first practical attempts to harness solar power to perform mechanical work appear in the 17th century with the efforts of the Solomon de Caux in France; however, it was not until the late 19th century that mirrored-surface parabolic troughs and paraboloidal dishes were fabricated, and high concentration made possible [Ackermann, 1915]. Even at this relatively late date, dish concentrators were formed from individual plane mirror facets. The technology to produce mass-produce highly accurate paraboloidal surfaces (including lenses and mirrors) did not become readily available until the 1980s [Hecht, 1998].

As we have already seen, high-temperature operation is crucial to the success of the solar thermal engine. The strong temperature dependency of specific impulse (Section 4.1) dictates this strategy; for windowless receiver systems, propellant temperature will always be less than the receiver wall temperature. Kreider [1979] describes the relation between peak solar receiver temperature and concentration:

$$T_r = \left[\frac{(\eta_o - \eta_c)I}{\sigma\varepsilon}\right]^{\frac{1}{4}} \left[\frac{A_c}{A_r}\right]^{\frac{1}{4}} \qquad \textbf{(2-1)}$$

The receiver equilibrium temperature T_r is a function of the incident radiation I (in watts), the concentration ratio A_c/A_r (i.e., the quotient of concentrating mirror area to receiver aperture area), and two efficiency terms η_o and η_c. Optical efficiency (η_o) is the ratio of absorbed heat to incident flux available at the receiver aperture; collection efficiency (η_c) is the ratio of heat absorbed by the working fluid to the aperture flux.[8] This energy balance assumes receiver absorption of sunlight and energy transfer to the working fluid occurs simultaneously.[9]

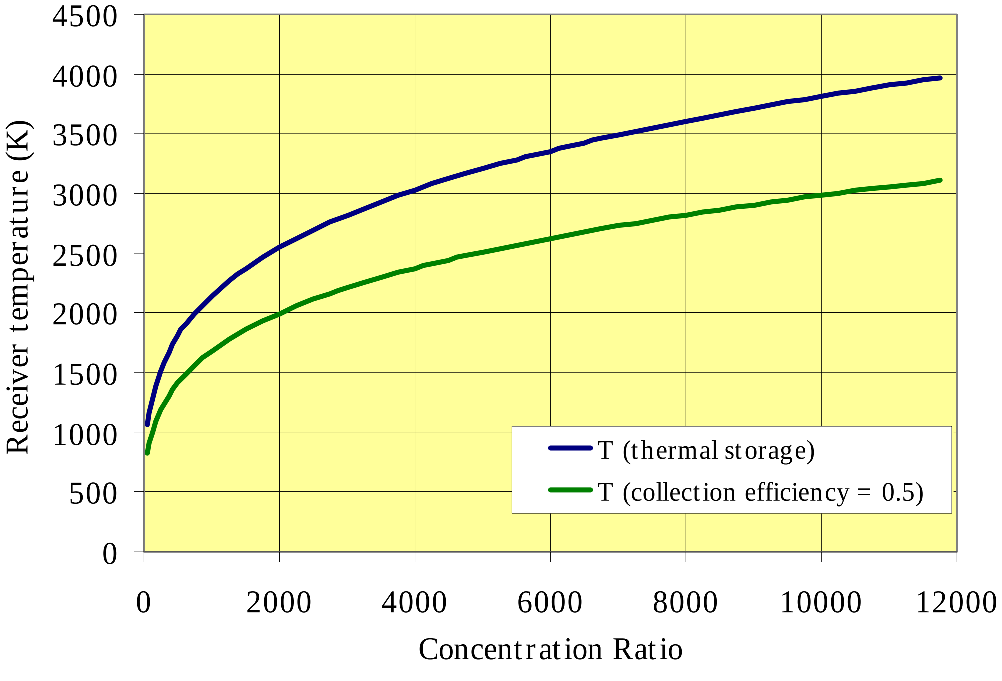

---

[8] Also included in this relation are the familiar Stefan-Boltzmann constant, σ, 5.6697 x 10-8 W/m^2-K^4, and the receiver emissivity ε.

[9] This is true for direct-gain systems, but not for thermal storage systems (see Chapter 4). Maximum achievable temperature with a thermal storage system is found by setting collection efficiency to zero (no flow during thermal charging).

Figure 2-8 Theoretical receiver bulk temperature versus concentration ratio, for thermal storage (η_c = 0) and direct-gain (η_c = 0.5) receivers.

Figure 2-8 illustrates the impact of concentration ratio on achievable temperature. For a high-absorptivity, non-selective receiver/absorber (ε = 0.9), and earth-orbit flux levels of roughly 1,350 W/m^2, concentration ratios of several thousand are needed to reach 2,000 K or higher. To achieve 3,000 K, a minimum concentration ratio of 10,000:1 is necessary. Note the difference in achievable temperatures between the *direct-gain* receiver (η_c = 0.5), which delivers heat directly to the propellant, and a thermal storage receiver (η_c = 0). The direct-gain receiver must support simultaneous radiative and conductive losses, lowering peak temperature. A thermal storage system, while capable of achieving higher peak temperatures, is handicapped by the decoupling of thermal charging and thrusting, which forces it to operate over a wide temperature range as it cools. The direct gain receiver can operate at a fixed temperature, providing a stable specific impulse performance.

Etheridge [1979] describes two dual-concentrator schemes for receiver heating. Both are large, in excess of 30 metres in diameter. As Venkateswaran [1992] notes:

> "The major drawbacks to solar propulsion arise because of the dilute energy density of solar radiation. Moderately sized rockets need large collectors to intercept sufficient quantities of energy, but, more importantly, the maximum energy remains quite low, even after focusing. This low intensity causes solar rockets to be relatively large in size, and makes it difficult to couple the solar energy into the thermal modes of the gas."

At 1,353 W/m^2, the accepted value of solar flux at an earth-sun separation distance of 150 million kilometres, a 30.5-m diameter concentrator will intercept roughly 1 MW of sunlight. Two mirrors of this size permit Etheridge to produce 44 lbf (196 N) of thrust with hydrogen propellant at an I_{sp} of 872 s.[10] This level of performance is sufficient to transfer a 10-metric ton payload from LEO to GEO in 14 days. If transfer time requirements can be relaxed to 40 days, Etheridge's baseline system can increase its payload delivery to GEO by 40%.

---

[10] Note that this system requires 7.33 m^2 of concentrator surface per newton of thrust produced.

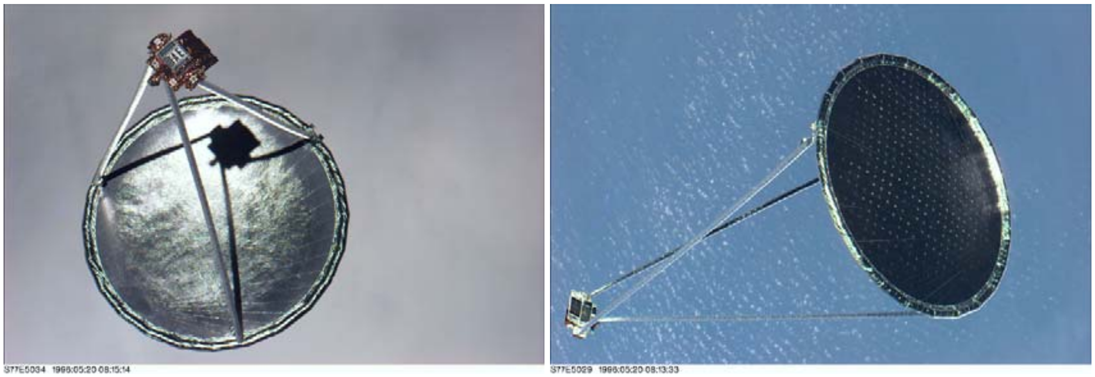

Figure 2-9 The 1996 Inflatable Antenna Experiment (IAE) on STS-77, deployed [L'Garde, 2004].

Direct-gain solar thermal engines demand relatively large concentrators. As discussed in the previous section, when incident solar energy is not stored and must be transferred directly to the propellant, thrust scales directly with concentrator size. To complicate the design problem, key requirements such as solar pointing accuracy (typically estimated at ±0.1°) and mirror form error (also on the order of ±0.1° root-mean-square, or RMS, slope error) do not relax for larger structures. Etheridge and his successors investigated a number of alternatives that might meet these and other stringent requirements.[11]These alternatives included (1) solid concentrators; (2) deployable petal structures; (3) tensioned membranes; (4) inflatables (with rigidizable and non-rigidizable supports); and (5) faceted systems (to include both Fresnel lenses and mirrors), which emulate the approach adopted by researchers for large ground-based concentrators (see Section 6.1). Fresnel lenses will require secondary optics for additional concentration.

Solid and petal systems, with areal densities of just 0.25 lbm/ft^2 (1.22 kg/m^2), were deemed to be excessively heavy and were rejected. Likewise, tensioned systems required a "complex deployment scheme," making them unsuitable [Etheridge, 1979]. The Etheridge analysis rapidly down-selected to the dual off-axis paraboloidal reflector scheme shown in Figure 2-1, utilizing inflatable, non-rigidized support and peripheral truss structures. Dual off-axis paraboloidal mirrors permit thrust vector pointing in all directions while simultaneously allowing for mirror sun-tracking. All successive efforts save ISUS appear to have followed Etheridge's lead [Holmes, 2001][Gierow, 2000].

---

[11] The assessment included radiation and meteorite damage, deployment, exhaust plume impingement, and eclipse effects.

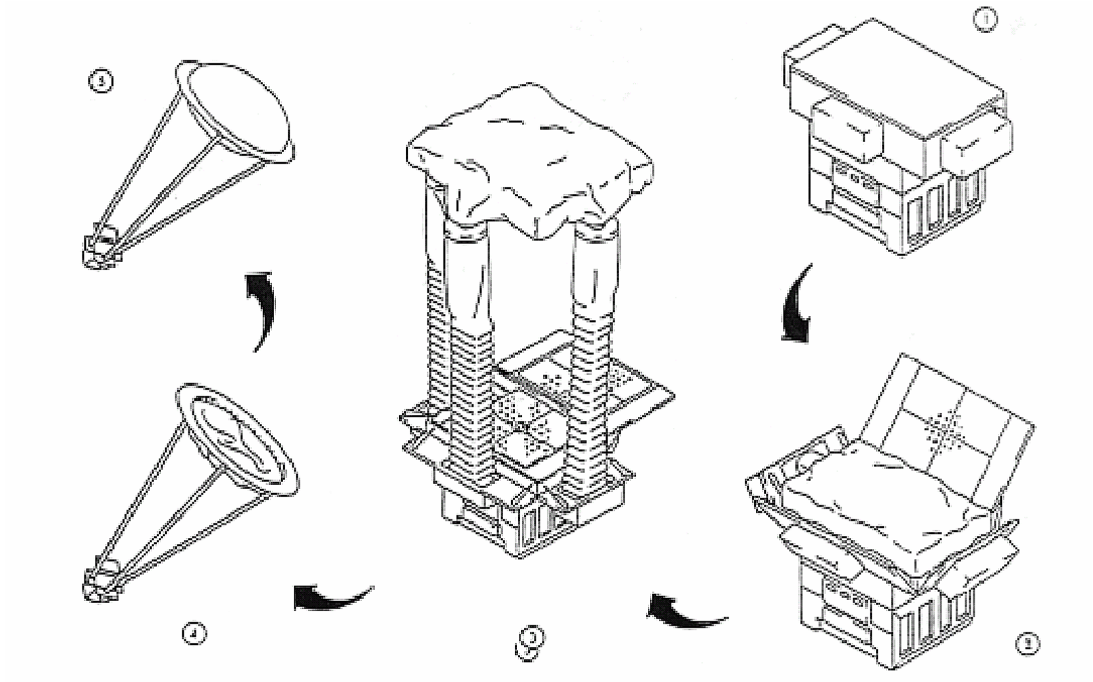

Figure 2-10 The Jet Propulsion Laboratory's Inflatable Antenna Experiment, deployment scheme [Freeland, 1997].

In May 1996, NASA's Jet Propulsion Laboratory, in conjunction with NASA's Goddard Spaceflight Center and L'Garde, Inc., fabricated and launched the 14-metre diameter Inflatable Antenna Experiment (IAE) aboard Space Shuttle mission STS-77 [Freeland, 1997]. While IAE was an on-axis paraboloid and designed for use at millimetre-wave communications rather than nanometer-wavelength optical applications, much of the underlying technology and deployment methodology would be applicable to space-based solar concentrators (Figure 2-9).

IAE was intended to measure surface form accuracy and thermal stability over a single orbital period, for various sun angles and antenna canopy inflation pressures, thus providing much-needed in-flight performance data applicable to future antennas, concentrators, and telescopes. After the stowed antenna was ejected from its packaging (Figure 2-10), the experiment's three struts were inflated and extended. Finally, the toroidal ring and antenna canopy (at left) would be inflated. High-resolution digital cameras were expected to image the antenna surface to permit characterisation of the deployed structure. Unfortunately, the antenna deployed far more quickly than was predicted, owing to residual gas in the struts and ring elements. Due to a malfunction in the inflation system, the ring was unable to fully inflate, making surface measurements impossible. No follow-on antenna or reflector experiment has yet been planned.

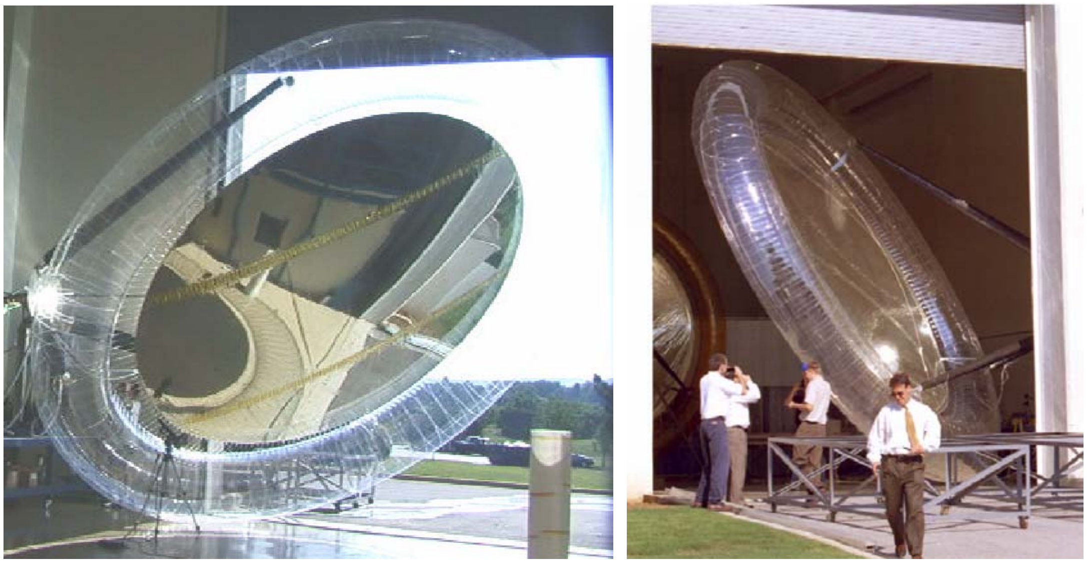

Figure 2-11 Two views of SRS Technologies' Flight Scale Concentrator (FSC-1) [Holmes, 2001].

Since 1996, the Air Force Research Laboratory has continued to invest in the development of lightweight inflatable concentrators. A division of SRS Technologies, based in Huntsville, Alabama, has manufactured a small (2 x 3 m) off-axis ground demonstration concentrator for deployment testing purposes [Gierow, 2000]. Larger inflatable structures have been tested by SRS (notably, an on-axis device at a diameter of 5 metres). Moore [1999] reports that a 1-mm (1,000 micron) RMS form error was obtained with the 5-m inflatable reflector. This is acceptable for communications applications, where wavelengths are on the order of the form error, but insufficient for optical imaging or solar concentration. Holmes [2001] indicates that a 4 x 6 metre "optical-quality" version of the SRS Flight Scale Concentrator (FSC-1), shown in Figure 2-11, was in fabrication and was due for testing later in 2001.

Figure 2-12 ISUS Ground Test Demonstration concentrator (left), and depiction of ISUS flight experiment with deployable, faceted concentrator arrays (right) [AFRL, 2004]

The Air Force Phillips Laboratory's Integrated Solar Upper Stage programme, in contrast to the preceding efforts, deliberately avoided the use of inflatable concentrators. Given the lack of on-orbit experimental data available in the mid-1990s, it was decided to examine options that would permit smaller, lower-technology concentrators within the current state-of-the-art (e.g., deployable, rigid structures).

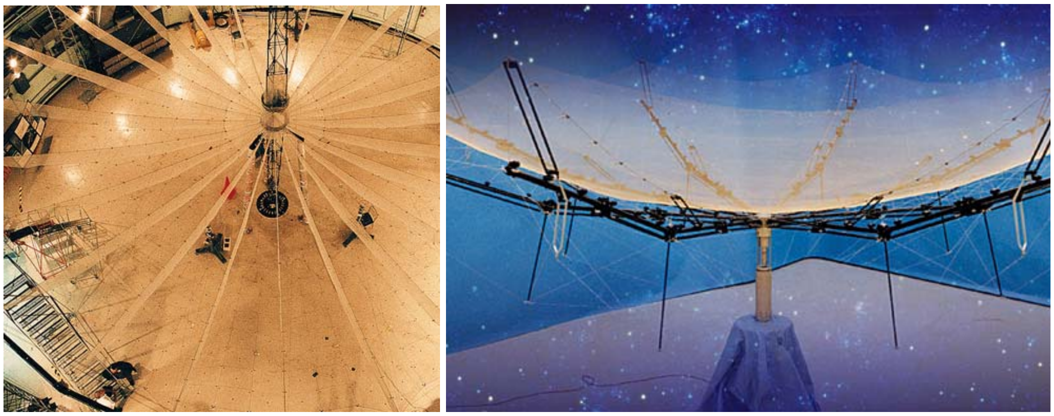

Figure 2-13 Unfurlable mesh reflectors [Harris, 2004].

The use of thermal storage media in favour of direct-gain receivers made these smaller concentrators feasible, accounting for weight penalties resulting from increased areal density [Frye, 1998]. The ISUS ground test demonstration at NASA's Lewis Research Center was conducted with a deployable, faceted concentrator prototype (Figure 2-12, left) similar to that proposed for a space-based solar thermal power system [Calogeras, 1992]. The baseline concentrator, a splined panel optic suggested by the Harris Corporation, is similar to the antenna illustrated in Figure 2-13. This concentrator, based on a 50-foot (15.2-metre) off-axis antenna design, was predicted to achieve an areal density of 1.0 kg/m^2.

2.1.3 Propellants and Propellant Storage

All solar thermal propulsion system concepts since Etheridge [1979] have baselined the use of hydrogen as primary propellant. This is unsurprising, as hydrogen—with a molecular weight of 2 kg/kg-mol—offers significantly higher specific impulse than any other available propellant for a given temperature [Hill, 1992]. Due to the square-root dependency of specific impulse on molecular weight, even the next lightest gas, helium, suffers from a 30% decrease in performance, and a correspondingly larger propellant mass for a given manoeuvre.

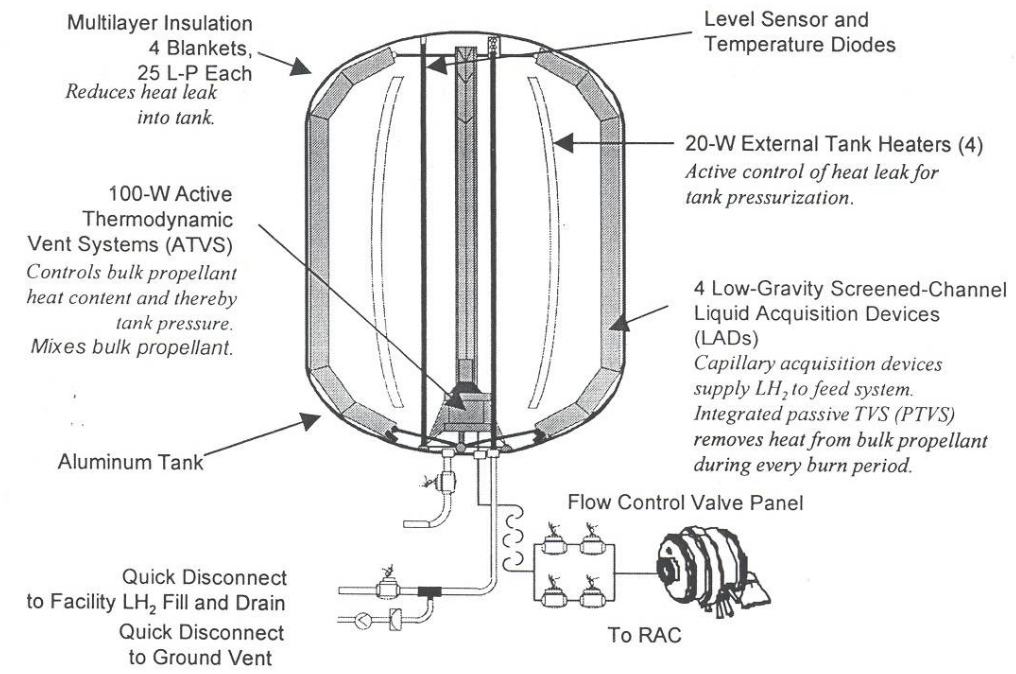
Multilayer Insulation
4 Blankets,
25 L-P Each
Reduces heat leak into tank.
Level Sensor and Temperature Diodes
20-W External Tank Heaters (4)
Active control of heat leak for tank pressurization.
100-W Active Thermodynamic Vent Systems (ATVS)
Controls bulk propellant heat content and thereby tank pressure.
Mixes bulk propellant.
4 Low-Gravity Screened-Channel Liquid Acquisition Devices (LADs)
Capillary acquisition devices supply LH_2 to feed system.
Integrated passive TVS (PTVS) removes heat from bulk propellant during every burn period.
Aluminum Tank
Flow Control Valve Panel
Quick Disconnect to Facility LH_2 Fill and Drain
Quick Disconnect to Ground Vent
To RAC

Figure 2-14 Cryogenic liquid hydrogen long-term storage concept [Partch, 1999].

Etheridge's analysis encountered immediate difficulties. Hydrogen's low storage density (4.4 lbm/ft^3 or 71 kg/m^3) makes it volumetrically inefficient for storage. The projected launch vehicle for the study, the Space Shuttle, was unable to simultaneously accommodate both the large storage tank and the payload. Additional investigations were performed which constrained the tank volume and examined the sensitivity of payload mass fraction to required delta-V. Etheridge was further directed to investigate the possibility of using alternate propellants, but after examining ammonia (I_{sp} = 440 s), he concluded that the system's performance was marginal, relative to state-of-the-art chemical systems, and that no additional analysis would be conducted on alternative propellants.

Cady [1996] discusses the use of passive and active thermal control for long-term storage of liquid hydrogen on the ISUS system (Figure 2-14). While conventional chemical upper stages such as Atlas Centaur only require short-term storage (on the order of hours), a solar thermal stage might require 30-60 days to achieve final orbit. Heat leakage into liquid hydrogen tanks must be absolutely minimised, or unacceptable boil-off (leading to pressure excursions and a possible catastrophic failure) and venting of propellant can result. Cady's solution involved the use of Joule-Thomson expansion of liquid hydrogen to subcool and collect counterflowing liquid hydrogen inside a liquid acquisition device (LAD). Subcooled hydrogen is then passed through a heat exchanger, picking up additional heat from the storage tank, and vaporised. As the LAD supplies hydrogen propellant to the solar receiver, all vented gas is used for thrusting operations;

no boil-off is jettisoned. A 71 ft^3 (2 m^3) tank with a storage capability of 284 lbm (129 kg) was successfully tested in vacuum at the Marshall Spaceflight Center following the ISUS Engine Ground Demonstration; safety concerns expressed by NASA Lewis Research Center staff prevented the installation of the liquid hydrogen tank in Lewis' Tank 6 vacuum chamber during testing [Cady, 1999].[12]

Storable propellants will not require the heroic insulation and cooling measures described above. Hydrazine (N_2H_4), a commonly used spacecraft propellant, is a moderate-density (1,004.5 kg/m^3) liquid that decomposes via catalysis into ammonia and nitrogen, releasing substantial energy. Ammonia itself can be used as a monopropellant, but not without an external heat source; it is a low-molecular weight liquid stored under its own vapour pressure (8 bar at 293 K), with a storage density of 630 kg/m^3. Unfortunately, it decomposes endothermically into hydrogen and nitrogen—a problem encountered in hydrazine monopropellant systems, which are designed to partially suppress ammonia dissociation and optimise specific impulse performance [Humble, 1995]. Water, investigated by Lawrence [1996] as a potential resistojet propellant at Surrey, has a slightly higher molecular weight than ammonia but a much improved storage density (1,000 kg/m^3). While none of these propellants can provide the level of propulsive efficiency achievable with hydrogen, they offer the possibility of simpler, more volumetrically-efficient storage solutions.

2.2 Solar Radiation

The sun is often described as a blackbody radiator at a temperature of 5,700-5,900 K. For its accepted diameter of 1.393 x 10^6 km, its output is estimated at nearly 3.65 x 10^{26} W. At a separation distance of 150 million kilometres, this flux is reduced to the extraterrestrial Air Mass Zero (AM0) value of 1,353 W/m^2 [Lienhard, 1987].[13] Figure 2-15 illustrates the difference between the theoretical (blackbody) solar spectrum and measured spectra, both in earth orbit and at the surface. The blackbody output, or spectral energy density Δu_ν over a frequency band $\Delta\nu$ can be estimated from Planck's Law [Sears, 1975]:

$$\Delta u_\nu = \frac{8\pi h}{c^3} \frac{\nu^3}{e^{(h\nu / kT)} - 1} \Delta \nu \qquad \textbf{(2-2)}$$

In this equation, h is Planck's constant (6.6262 x 10^{-34} J/s), c is the speed of light (2.9979 x 10^8 m/s), k is Boltzmann's constant (1.3806 x 10^{-23} J/K), and T is the blackbody temperature in degrees Kelvin. The resulting curve peaks at 2.0 W/m^2-nm around 600 THz (λ = 500 nm), in the blue-green portion of the visible spectrum.

---

[12] Following this test, the heat leak into the system was estimated at 6.7 W.

[13] The value currently "accepted by the space community" is 1,367 W/m^2 [NREL, 2001].

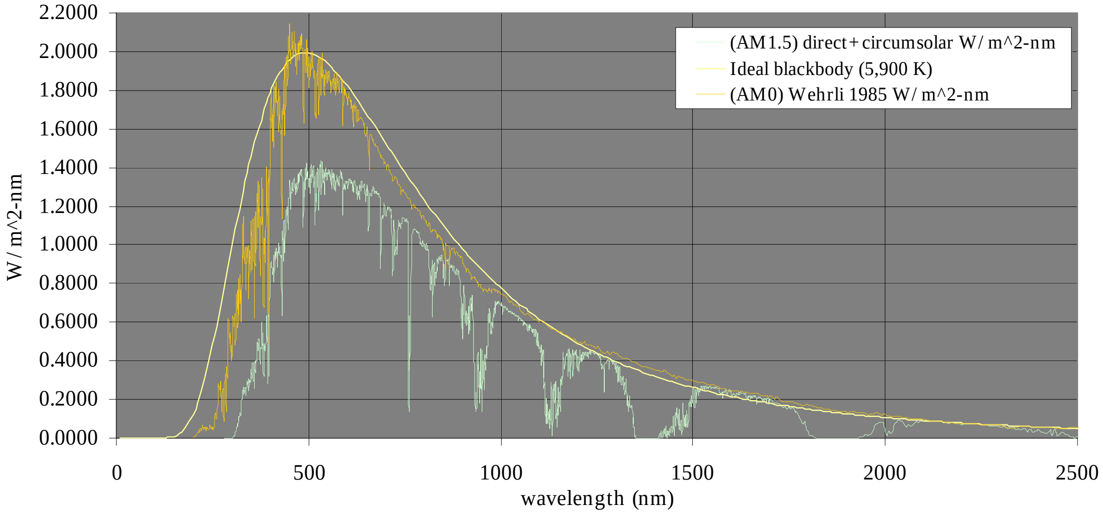

Figure 2-15 Theoretical (blackbody) and measured power received at earth-sun separation distance, at wavelengths ≤ 2,500 nm [NREL, 2001][Sears, 1975].

The AM1.5 curve in Figure 2-15 exhibits both a general reduction in flux over extraterrestrial values, a broader peak (500-550 nm), and specific low-transmission regions (notably, in the ultraviolet, below 400 nm, between 800 and 1,000 nm, 1,100 and 1,200 nm, and 1,300 to 1,500 nm). Many of these low-transmissivity bands are due to water and CO_2 absorption [Lienhard, 1987]. The impact on terrestrial flux levels is significant: only 47% of earth orbit flux, on average, reaches the ground. There are important implications for ground-based solar thermal engine testing utilising ambient sunlight: (1) such trials cannot be representative of space system performance, owing to lower flux levels available at the earth's surface, and (2) the increased infrared and ultraviolet content of extraterrestrial flux will have effects on the system that will be inadequately characterised at the surface.

Simulated sunlight, using lamps and collimated lens assemblies, is often used to circumvent operational difficulties associated with on-sun testing. Standard incandescent lamps operate at relatively low temperatures (2,000-2,900 K) and have spectral distributions shifted towards the infrared. Xenon arc lamps, which operate at colour temperatures of 5,500-6,000 K, have been used in a wide variety of solar simulation activities, including the ISUS Engine Ground Demonstration [Lot-Oriel, 2004][Frye, 1998].

2.2.1 Optical Fibre Transmission of Solar Radiation

Nakamura [1998] describes the use of low-attenuation optical fibres to transmit incident solar radiation for space-based plant growing applications:

> "…results obtained in the studies indicate that: (1) for solar power applications, the fused-silica optical fibres will have sufficiently high transmission characteristics for wavelengths between 0.5 and 2.2 mm; (2) concentrated solar radiation can be transmitted effectively (~95%) via commercially available optical fibres over the distance required for spacecraft applications (10-20 m); (3) the concentrator and optical fibres can be effectively integrated to input highly concentrated solar radiation (7,500-10,000 suns) into optical fibres; (4) aiming and tracking requirements can be significantly relaxed (accuracy $\Delta\theta = 5^{\circ}$) by using a two-stage concentration method with a steerable secondary concentrator attached to the fibre end; and (5) weight of the optical fibres…is not a significant penalty to the system."

The concentration levels described are on par with those required for solar thermal propulsion (10,000:1). Nakamura was able to demonstrate fibre power throughput efficiencies of 0.75 with system efficiencies of 0.32.

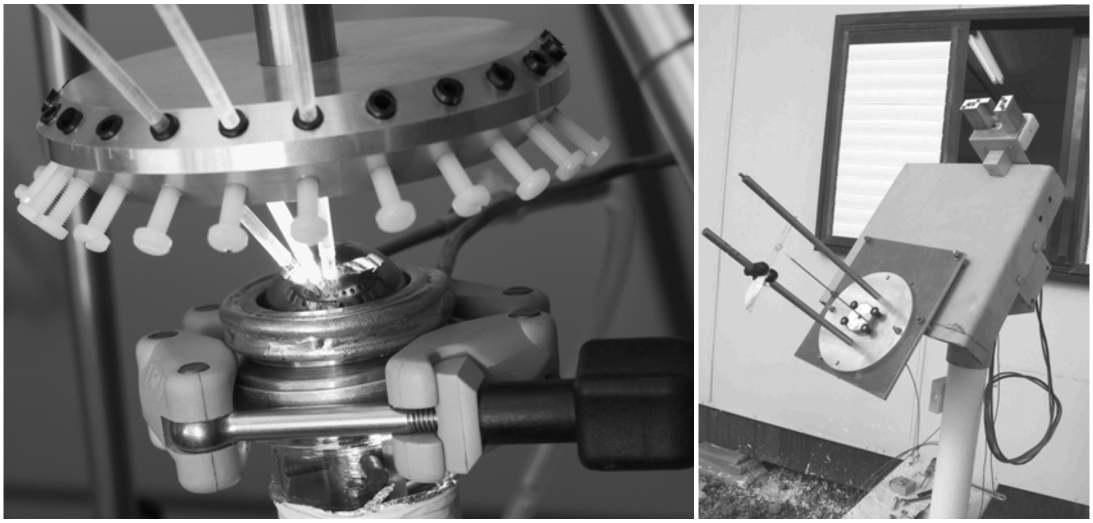

Figure 2-16 Prototype nanomaterial production furnace utilising fibre-coupled solar radiation and a gold-coated photon regenerator (left), single fibre-optic mini-dish on solar tracking unit [Gordon 2, 2003]

The first recorded efforts to transmit high-intensity solar power through optical fibre were conducted by Cariou [1982][1985]. Transmission efficiencies of 0.70, at power levels of 2 W, were experimentally demonstrated. Later efforts concluded that furnace temperatures of 1,500 ºC or greater were potentially achievable. Liang [1998], who reports power throughputs of up to 60 W with 19-fibre bundles at an efficiency of 0.60, remarks on the importance of fibre tip polishing to prevent scattering and drastic reductions in transmission efficiency. Gordon [2003] has performed extensive work on the transmission of concentrated sunlight for surgical and nanomaterial production applications. Using a single 20-cm diameter paraboloidal dish with a focal length of 12 cm, Gordon was able to demonstrate power throughput of approximately 8 W and an end-to-end system efficiency of 0.64, over a 20-m fibre run (Figure 2-16). Gordon estimated the power density at the focal spot of his mini-dish to exceed 15,000 suns at an ambient flux density of 840-930 W/m^2.[14]

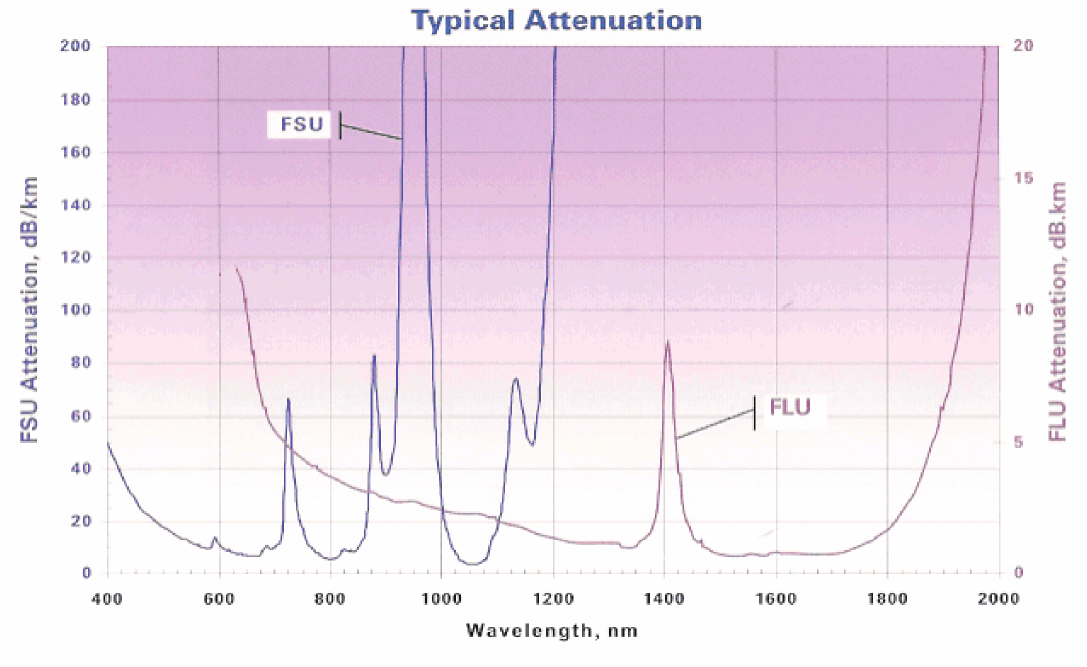

Figure 2-17 Wavelength-dependent attenuation of two types of high numerical aperture optical fibre [Polymicro, 2004].

The optical fibre, a high-purity silica variety obtained from Polymicro Technologies of Phoenix, Arizona, exhibited a numerical aperture of 0.66 and a core diameter of 1 mm. Numerical aperture describes the effective angular size (ψ = half-angle) of the fibre's acceptance cone:

$$NA = n_a \sin\psi = \sqrt{n_{core}^2 - n_{clad}^2} \tag{2-3}$$

The numerical aperture of the fibre is dependent on the refractive indices of the ambient medium (n_a), the fibre cladding (n_{clad}), and the fibre core (n_{core}). The Polymicro fibre acceptance cone is therefore 82.6º wide, capturing most (but not all) of the incident solar flux.[15] The mismatch between mini-dish and fibre can be estimated by noting that:

---

[14] At an ambient flux level of 900 W/m^2, flux density at the focal spot of 13.5 W/mm^2.

[15] Gordon's 20-cm mirror has an effective NA of 0.71.

$$\Psi = 2\pi(1 - \cos\psi) \qquad \textbf{(2-4)}$$

Here, Ψ is the solid angle measured in steradians (sr), subtended by the acceptance cone half-angle ψ. Incident sunlight from the mini-dish covers a solid angle of 1.84 sr, of which only 1.56 sr can be viewed by the fibre (85%). Mismatch of attainable focal spot size and fibre core diameter will lead to further losses. Gordon notes that care should be taken to (1) achieve extremely precise alignment of the fibre tip in the mirror's focal spot, since positioning tolerances appear to be on the order of ±0.1 mm; (2) procure high-attenuation optical fibres capable of withstanding high solar flux; and (3) use only high-accuracy solar tracking devices (±0.002 radians or 0.11°).

Figure 2-17 illustrates optical fiber attenuation over the most significant portion of the solar spectrum, in decibels per kilometre (dB/km). These particular species of fiber (FSU and FLU) exhibit very different attenuation curves—FSU is mostly transparent at optical and near-ultraviolet wavelengths, but opaque in the infrared, while FLU transmits a substantial amount of near infrared radiation (but displays poor performance near the solar irradiance peak of 500 nm).

2.2.2 Alternative Concentration Schemes Applicable to Microsatellite Solar Thermal Propulsion

As has been shown in Section 2.1.2, one of the distinguishing characteristics of past and present solar thermal concepts is the large primary mirror. Along with outsize cryogenic hydrogen storage tanks, the high-pointing accuracy, large-diameter deployable concentrating mirror represents a substantial technical risk that will require significant technological development to overcome.

A number of suggestions have been made to mitigate the development risk of the concentrator subsystem, including the leveraging of deployable antenna technologies [Borell, 1996] and the use of lower-concentration primaries coupled with secondary elements. Some of these approaches would permit substantial pointing inaccuracies, but at the cost of operation at lower peak temperatures and, therefore, lower attainable specific impulse.

Secondary concentrators can be used to improve both a primary concentrator's collection efficiency and its concentration ratio. Feuermann [1999] defines a relative concentration ratio C_{rel} as the average flux concentration divided by the thermodynamic limit to concentration, $(\sin^2 \theta_{sun})^{-1}$, and varies between zero and unity. θ_{sun} is the half-angle of the arc subtended by the solar disk, usually taken to be 0.25°. For a given paraboloidal dish rim angle Φ (Figure 2-18):

$$C_{rel} = \sin^2 \Phi \qquad \textbf{(2-5)}$$

Moderate rim angles (30 to 45º) provide high collection efficiency (Figure 2-18, right) but low average concentration.[16] Higher values of rim angle (70º or more) provide very high peak concentrations, approaching the thermodynamic limit, but low collection efficiency.

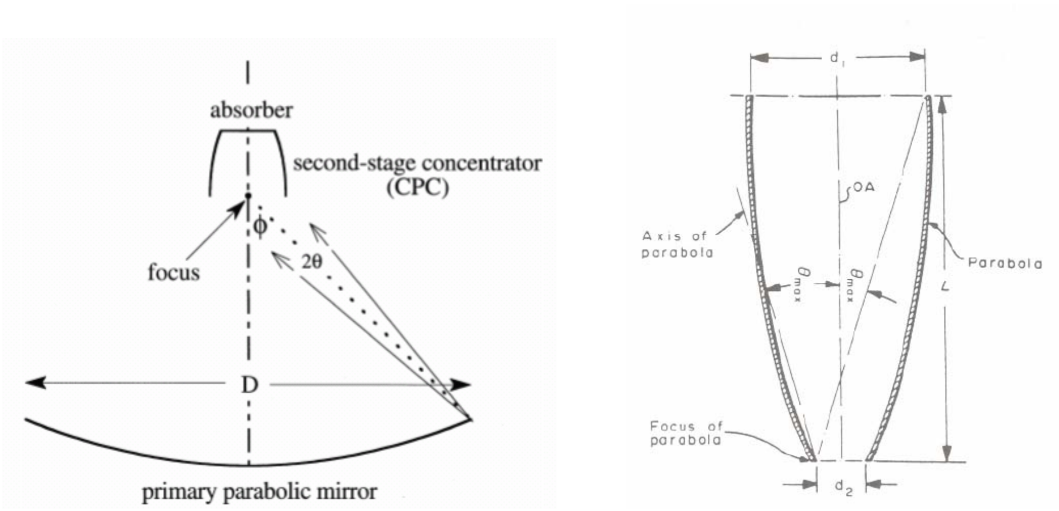

Figure 2-18 Paraboloidal mirror with second-stage concentrator (left) [Feuermann, 1999]. Compound Parabolic Concentrator (right) [Winston, 1974].

The addition of a secondary concentrator permits the interception of sunlight that would otherwise fall outside the receiver aperture and redirects it inside. While there are losses associated with multiple reflections (in mirror secondaries), as well as practical difficulties in placing reflective or refractive elements near high-temperature receivers, gains in collection efficiency can be substantial (Figure 2-19).

Some of the more well-known approaches include non-imaging designs such as the Compound Parabolic Concentrator (CPC), devised by Winston [1974], the Tailored Edge-Ray Concentrator (TERC) [Friedman, 1996], and hyperboloidal or "trumpet" secondaries. Other hyperboloidal secondaries may be used in Cassegrain (folded optics) schemes [Feuermann, 1979]. The CPC is often depicted in its two-dimensional form, the trough, and has been suggested for ground-based solar collection; its geometry permits reasonable concentration (~10:1) without solar tracking [Rabl, 1976]. While this falls far short of the concentration levels required for solar thermal propulsion (Figure 2-8), it suggests that improved concentration—with relaxed tracking constraints—are possible through the introduction of a CPC as a secondary concentrator.

---

[16] Collection efficiency can be defined as that fraction of incident sunlight reaching a disk of fixed diameter at the focal region.

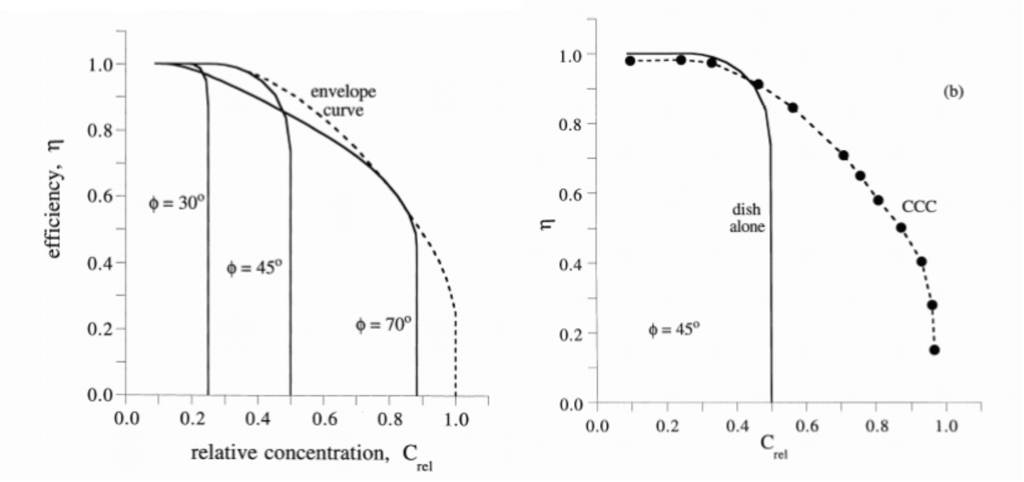

Figure 2-19 Collection efficiency versus relative concentration C_{rel}, for a single-mirror paraboloidal concentrator (left), and with the addition of Feuermann's Complementary Cassegrain Concentrator (CCC) (right) [Feuermann, 1999].

Refractive secondaries were proposed and tested in NASA's Shooting Star Solar Thermal Propulsion programme in the late 1990s [Soules, 1997]. Designed to enhance the concentration of a Fresnel lens primary (with theoretical peak concentration ratios of only ~1,000), the high-temperature sapphire refractive element shown in Figure 2-20 would exhibit little internal loss and might act to block infrared reflux from the receiver cavity and material losses at high temperature. Power throughput efficiencies were measured at 0.87. Expected throughput is as high as 0.93, assuming treatment of the sapphire element with an anti-reflective coating to reduce inlet losses [Wong, 2001].

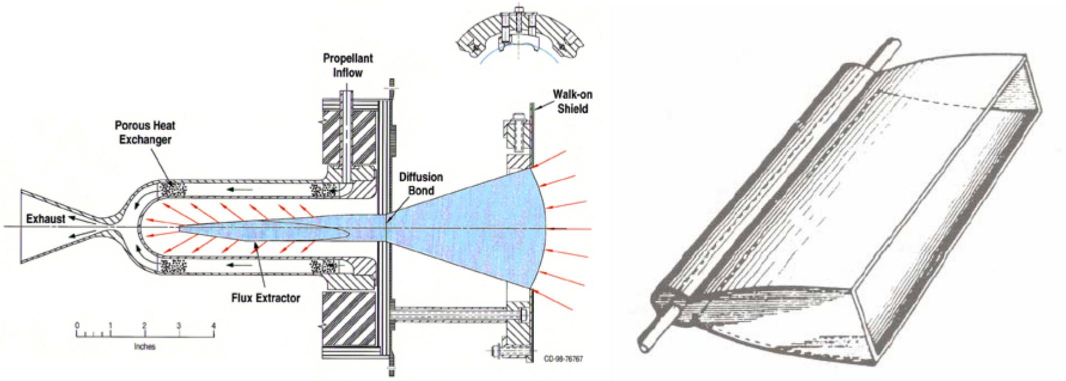

Figure 2-20 Refractive secondary concentrator concept, left [Donovan, 1997]. A compound parabolic concentrator trough with line-focus receiver, right [Winston, 1974].

For some space-based applications, two-dimensional troughs such as that depicted in Figure 2-20 (right) may be flown as demonstration systems if requirements are sufficiently relaxed. A CPC trough with a concentration ratio of 10:1, corresponding to an acceptance half-angle of nearly 6º, would permit a simple demonstration of solar thermal propulsion on a small satellite, without (1) demanding high-temperature materials, or (2) having to meet the stringent pointing requirements dictated by paraboloidal dish systems [Rabl, 1976]. Equation 2-1 indicates that an un-insulated tubular receiver placed at the trough's line focus could reach temperatures of more than 530 K. While the traceability of a demonstration of this type to larger, more capable STEs is clearly questionable, it does offer an opportunity for a low-cost starting point, if no other approach were achievable.

2.3 High-Temperature Materials and Joining Processes

Previous Surrey propulsion activities have refrained from the use of high temperature materials, owing to their scarcity (and cost), difficulty of machining, difficulty of bonding or joining, and a lack of comprehensive material performance data at temperatures of interest. As the author has suggested in Section 2.1.2, windowless solar receivers—the simplest to fabricate with present technologies—must always operate at temperatures in excess of the peak propellant temperature, which will nominally be above 2,000 K. There are only eighteen elements that remain in a solid phase at or above this temperature plateau, and just five (tantalum, osmium, rhenium, tungsten, and carbon) above 3,000 K. Carbon, with the highest decomposition temperature, does not actually melt but sublimates at 3,800 K.

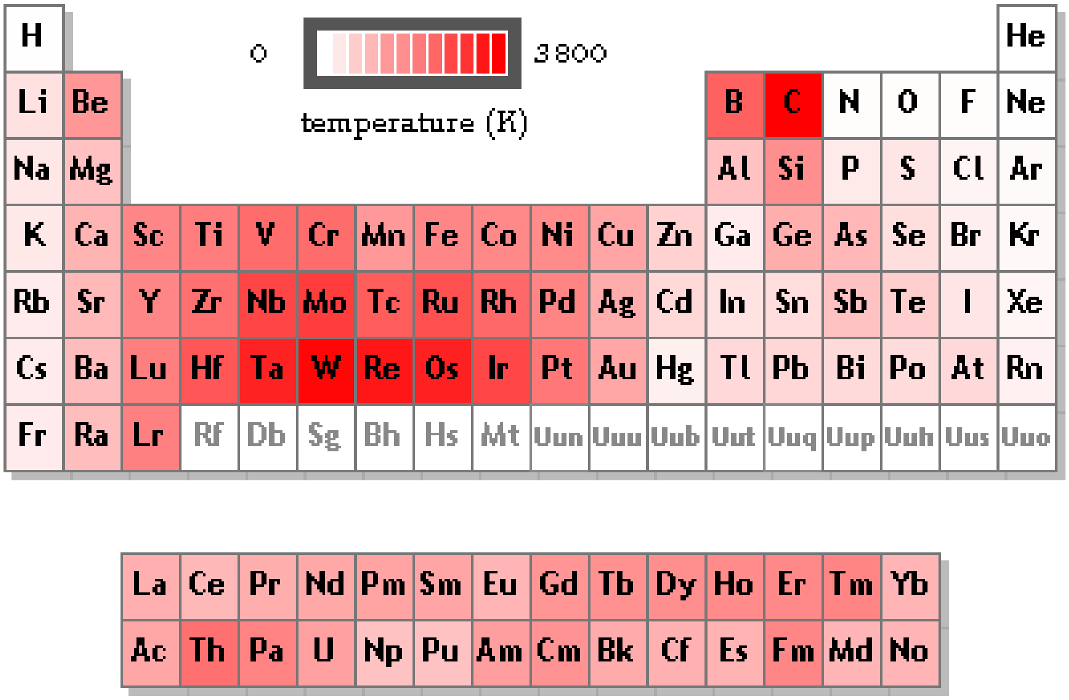

Figure 2-21 Periodic table of the elements, illustrating melting temperature of individual species [Winter, 2001]

In addition to these elemental species, there are a number of ceramic compounds that have melting or sublimation points above 2,000 K and which might be employed usefully in a solar thermal engine. These include various oxides, carbides, and nitrides of refractory metals such as tungsten, tantalum, zirconium, and hafnium (Figure 2-22, left). Tantalum carbide (TaC) and hafnium carbide (HfC) have the highest decomposition temperatures known, at nearly 7,100 ºF (4,200 K). However, TaC is attacked by hydrogen at temperatures exceeding 2,500 ºF (1,644 K) and HfC is reportedly “attacked by nitrogen at elevated temperatures.” [Lynch, 1966]

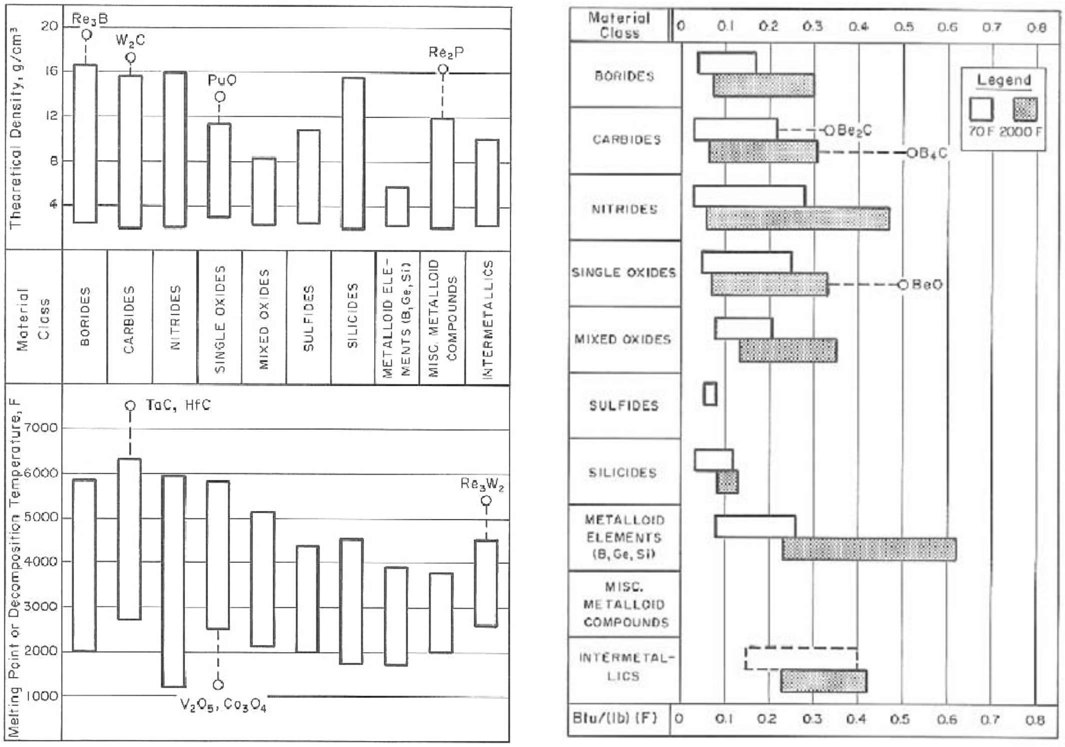

Figure 2-22 Density, decomposition temperature and room temperature specific heat for a variety of ceramic compounds [Lynch, 1966].

Refractory metals, such as molybdenum, rhenium, tantalum, and tungsten, typically have high thermal conductivities and very low specific heats; a detailed discussion is provided in Chapter 4. Unlike the pure metals, many ceramics offer much higher specific heats, allowing them to be used as efficient high-temperature thermal storage materials. Boron carbide, which finds favour in a host of applications, including sandblasting, armour plate, and neutron absorbers, has both a very high specific heat and high decomposition temperature [Nicholas, 1990]. The elemental species exhibiting high specific heat (≥ 1,000 J/kg-K at 25 ºC) include beryllium, boron, lithium, magnesium, and sodium; of these, only boron and carbon have melting points above 2,000 K

[Lide, 1995]. Boron is occasionally suggested as a high-temperature phase change thermal storage material, owing to its high melting point (2,348 K) and heat of fusion (4.5 MJ/kg) [Claasen, 1980][Lide, 1995].

Ceramics possess several useful properties for the STE designer but pose two distinct problems not shared by the majority of metals: (1) they are typically brittle and fracture in an unpredictable, sometimes catastrophic manner; and (2) traditional bonding methods (e.g., welding and brazing) are often ineffective with ceramics.

On the subject of failure prediction in ceramics, Green [1998] writes:

> "…ceramics contain flaws that can vary substantially in size and type, causing strength to vary significantly from sample to sample. This variability in strength is often expressed in terms of a failure probability. To describe a strength distribution at least two parameters are needed, to measure the width and magnitude of the distribution. The difficulty encountered is that the form of this distribution is not known a priori. For this reason, an empirical distribution, first suggested by Weibull (1951), is often used."

The three-parameter Weibull distribution for failure probability, *F*, can be defined as:

$$F = 1 - e^{\left[-\int_V \left(\frac{\sigma - \sigma_{\min}}{\sigma_o} \right)^m dV \right]} \tag{2-6}$$

Here, *m* denotes the Weibull modulus or width of the distribution, while the values σ_o and σ_{min} are the characteristic strength and minimum strength, respectively, of the material in question (in pounds per square inch, psi, or millions of Pascals, MPa). It is not unusual for 30 to 50 specimens to be broken in a test programme, before Weibull parameters are known with sufficient accuracy. Weibull plots are plotted logarithmically; while concrete specimens might exhibit $m = 5$ (± 30% variability in strength), state-of-the-art structural ceramics may exhibit *m* values of 10-15 or even higher, indicating a narrow distribution and good certainty regarding a material's performance, similar to ductile metals [UBC, 2004]. Munn [1999] discusses a set of strength measurements for zirconia specimens in which the Weibull modulus varied from a very high 92 (at room temperature) to just 9 at 600 ºC. Clearly, specific Weibull values must be understood within the context of the strength test that produced them.[17]

High-strength ceramics include tungsten carbide (WC) and aluminium nitride (AlN). WC has a high transverse rupture strength, 550 MPa [Pierson, 1996].[18] For comparison, titanium plate exhibits an ultimate strength in tension of 830 MPa, while the value for sheet aluminium alloy (7075-T73) is just 390 MPa [Larson, 1992]. The ultimate tensile strength of hexagonal boron nitride (h-BN) is quite low at room temperature: 40 MPa. However, at higher temperatures, h-BN's strength increases rapidly; at 2,400 K, its strength exceeds 120 MPa.

---

[17] Examples include three-point or four-point bending, pure bending, and tension [Green, 1998].

[18] Ceramic strength data is typically extracted from four-point bend tests [Nicholas, 1998].

Solar thermal receiver structures are likely to include a number of complex shapes, composed of dissimilar materials that will require permanent, reliable bonding and sealing to retain hot propellant gases. Refractory metal bonding is expensive but well within the state-of-the-art; a number of small machine shops and fabricators both within the United Kingdom and in the European Union are capable of welding (including electron beam welding) tungsten, rhenium, or molybdenum elements. Ceramic-to-ceramic, or ceramic-to-metal joining, however, poses unique problems. Nicholas [1998] identifies five common processes which may be utilised in metal-to-metal, ceramic-to-ceramic, and ceramic-to-metal bonding: (1) fusion welding, (2) diffusion bonding, in which solid surfaces are pressed together and heated, (3) brazing, using liquid metal to flow into a gap between two elements and solidify, (4) glazing or sealing, which uses glass in processes similar to welding and brazing, and (5) adhesive bonding.

Many ceramics sublimate instead of melting and therefore cannot be reliably welded. The number of available metal brazes for high-temperature use is quite small; above 2,000 K, the only non-proprietary braze filler metals are molybdenum-ruthenium and platinum-molybdenum [Rembar, 2001]. Adhesives fare similarly; the author was unable to uncover evidence of any adhesive solutions, apart from graphite-graphite bonding, that are viable above 2,000 K.

2.4 Summary

The conceptual design of solar thermal propulsion systems has evolved over the past forty years from high-risk, high-payoff schemes involving large deployable or inflatable concentrating mirrors and capable of specific impulses in excess of 1,000 s, to smaller, more incremental approaches which attempt to qualify critical elements or subscale systems. The Etheridge study [1979] epitomises the early approach; the Integrated Solar Upper Stage effort, conducted during the mid-1990s, sought a direction with decreased performance, but less inherent technical risk, in order to make space demonstration feasible [Kennedy, 1995]. Some of the key lessons of ISUS, including the use of thermal storage receivers to minimise concentrator mirror size and permit the use of multi-impulse trajectories (reducing delta-V requirements),[19] will be drawn on for use in the design and development of a microsatellite-based solar thermal propulsion system. Alternate concentrator approaches, to include optical fibre-coupled, multiple mirror designs and low-concentration ratio schemes (such as two-dimensional trough concentrators) have been investigated for their applicability. Various solar cavity receiver designs have been examined. A review of contemporary materials research and joining methods was also performed, in order to determine if improvements in technology might permit advanced structural ceramics to supplant expensive, difficult-to-machine refractory metal systems.

---

[19] See Appendix B.

Chapter 3

3 Mission Analysis

This section begins with a first-order examination of existing, planned, or potential missions that might benefit from the inclusion of a solar thermal propulsion system. These analyses lead the author to recommend a more detailed investigation into two or three missions and several possible solar thermal propulsion concepts.

Detailed mission analysis required the use of Analytical Graphics' Satellite Tool Kit (STK) [STK, 2002] to accurately assess candidate trajectories. STK's capabilities include orbit propagation using multiple central body models and including various forms of gravitational disturbances, which is essential for the types of missions under examination here. Astrogator, an STK module designed for satellite manoeuvre planning, was used extensively to assess required velocity changes, vectoring, and propellant consumption for a number of potential missions. It will be seen that candidate missions tend to require between 1,000 and 3,000 m/s of velocity change, and appear to be achievable with available technologies.

3.1 Preliminary Mission Analysis

This analysis contains a review of twelve missions, most slated for launch in the next decade. Several are nearing completion or have already flown. Solar thermal propulsion system performance is compared (at first order) to likely competing systems, assuming the host satellite is one of two Surrey small satellite platforms. Recommendations for more detailed analysis follow.

3.1.1 Review of Applicable Missions

Magnetospheric Multi-Scale (MMS). MMS's launch is estimated to occur in 2008. A four-phase mission, MMS requires four (originally five) spacecraft in formation (Figure 3-1). The first three phases use highly elliptical earth orbits, each focused on understanding a different region of the earth's magnetosphere. The third phase achieves a "deep tail" orbit of 120 earth radii via lunar gravity assist (LGA), while the fourth and final phase necessitates a second LGA to place MMS vehicles in a polar, 10 x 40 earth radii orbit. [NASA GSFC, 1999] The total velocity change for this mission is 1,100 m/s, assuming launch vehicle placement in the initial (1.2 x 12 earth radii) orbit. [NASA GSFC, 2002]

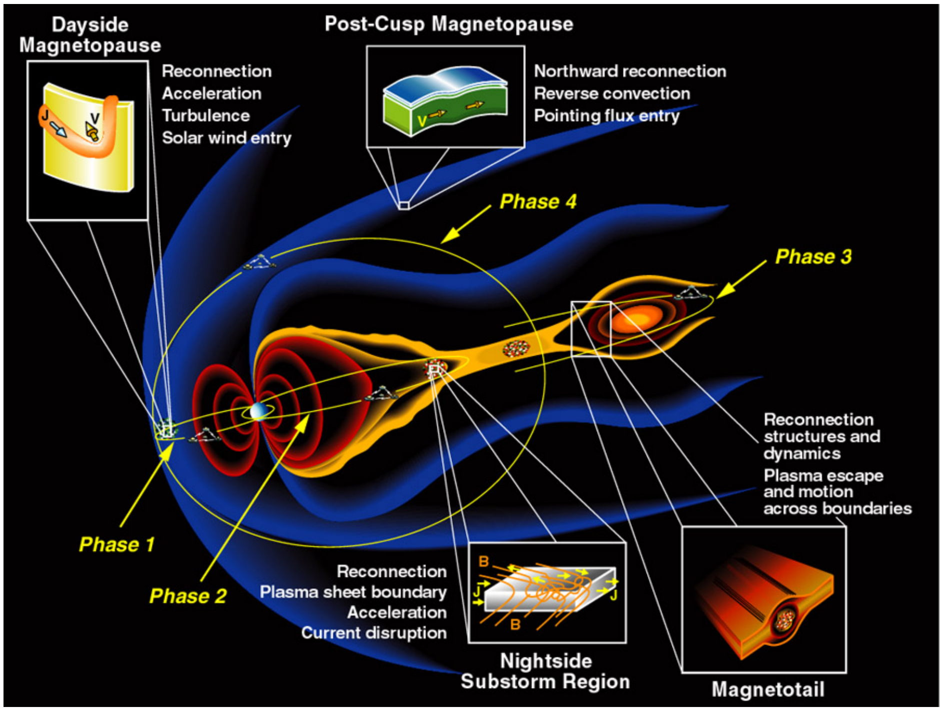
Dayside Magnetopause
Reconnection
Acceleration
Turbulence
Solar wind entry
Post-Cusp Magnetopause
Northward reconnection
Reverse convection
Pointing flux entry
V
J
Phase 4
Phase 3
Phase 1
Phase 2
Reconnection structures and dynamics
Plasma escape and motion across boundaries
Reconnection
Plasma sheet boundary
Acceleration
Current disruption
B
Nightside Substorm Region
Magnetotail

Figure 3-1 NASA Goddard Spaceflight Center's Magnetospheric Multi-Scale (MMS) four-phase mission scenario. MMS will explore various regions of the magnetosphere over a two-year period [NASA GSFC, 2002]

Cluster II. Cluster I was lost to a launch failure in 1996. The Cluster II mission, launched in 2000 aboard the Russia Soyuz/Fregat, utilizes four spacecraft injected into a near-GTO ellipse (251 km x 18,038 km altitude) at an inclination of 64.9º, then transferred to a polar, 4 x 19.6 earth radii ellipse via onboard propulsion. The constellation is intended to measure solar wind/magnetospheric interactions. [ESA (1), 2000][ESA (2), 2000] The author has estimated a velocity change (or delta-V, ΔV)[20] requirement for this mission (four apogee raising manoeuvres, one combined plane change and perigee raise) of 1,538 m/s. Cluster II used a conventional chemical bipropellant engine (hydrazine fuel, N_2H_4, and nitrogen tetroxide oxidixer, N_2O_4) to achieve this orbit.

---

[20] Velocity change, or delta-V (ΔV), is a key figure of merit in the design and analysis of rocket propulsion systems. It is directly related to propellant consumption—for a specific choice of propellant(s)—and is thus a critical factor in determining spacecraft size, or, conversely, determining whether a spacecraft of a given size and propellant loading can achieve a desired ΔV. Delta-V is usually given in meters/second.

Space Interferometry Mission (SIM). SIM is JPL's pathfinder for its Terrestrial Planet Finder mission. SIM's launch is intended for launch in either 2006 or 2009. Mission planners indicate a desire for direct injection into heliocentric earth trailing orbit (HETO). The spacecraft will slowly drift away from earth, achieving a maximum separation of 95 million km after five years. [JPL, 2001] Without direct injection, and assuming a shuttle launch to 185 km (circular) LEO, the required delta-V for an upper stage would be greater than 3,200 m/s.[21]

SMART-1. ESA's novel lunar mission is an auxiliary payload on Ariane 5, launched in September 2003. SMART-1 (Figure 3-2) is intended primarily for lunar mineralogy investigation and technology demonstration. SMART-1 will use a xenon-fueled Stationary Plasma Thruster (SPT) and a number of lunar gravity assists to get it into lunar orbit in approximately 15-17 months [Saccocia, 2000]. A comparable (non-spiral) earth-to-moon orbit insertion using impulsive manoeuvres would require on the order of 1,500 m/s to accomplish. This assumes a straightforward "drop-off" in GTO and no swingbys or use of Earth-Moon-Sun stability boundaries to decrease delta-V savings.

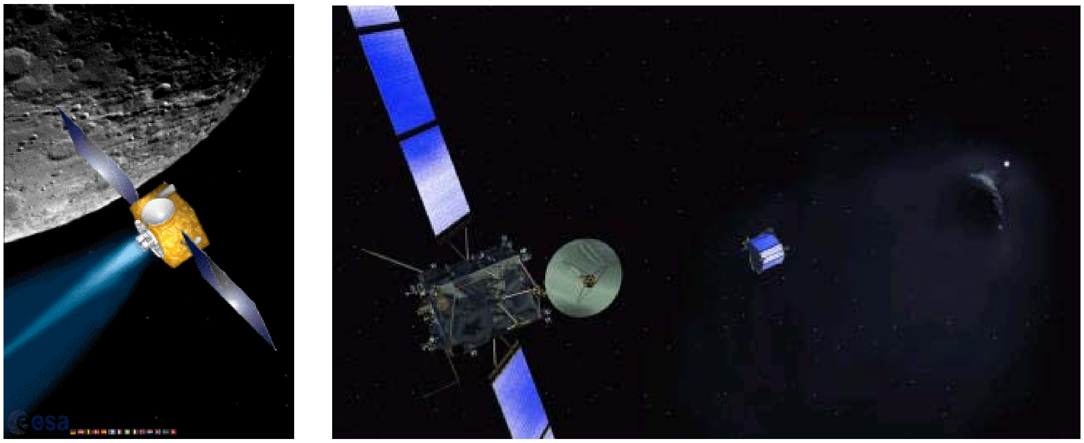

ESA's SMART-1 lunar mission [ESA, 2002]

ESA's ROSETTA rendezvous with the comet 67P/Churyumov-Gerasimenko in 2014 [ESA (3), 2000]

Figure 3-2 European Space Agency missions to the Moon and comets.

SMART-2. Planned for launch in 2006, ESA's SMART-2 is composed of two spacecraft "flying in formation," a testbed for LISA (a gravity wave detector) and DARWIN (a terrestrial planet finder), both of which require extremely accurate vehicle separation knowledge. SMART-2's potential mission orbits include HEO (perhaps GTO), Earth-Sun LaGrange points (L1 or L2),[22] GEO, or HETO. HETO is preferred, due to its relative stability. [ESA, 2001] An orbital scheme similar to SIM's (slowly drifting HETO) would require between 770 m/s (assuming an initial orbit in GTO) and 3,200 m/s (assuming a drop-off in low-inclination 185 km x 185 km LEO).

---

[21] See chapter 3 for a detailed discussion of this calculation. To provide some grounding, a typical monopropellant hydrazine thruster aboard a 100-kilogram spacecraft would have to expel approximately 75 kilograms of (decomposed) hydrazine to achieve this delta-V.

[22] L1 and L2 sit astride the Earth-Sun axis. L1 is between the Earth and Sun, L2 behind the Earth.

LunarSat. This satellite is a European conceptual study. It assumes a 100-kg. lunar polar orbiter, intended for south polar reconnaissance. (Indications of ice might eventually permit human habitation.) [LunarSat, 2002] The LunarSat mission planners investigated the use of *weak stability boundary* (WSB) transfers in order to reduce the required delta-V for this mission, which includes Ariane 5 insertion into GTO and a transfer time (GTO to Low Lunar Orbit, with high intermediate apogees of up to 1.4×10^6 km[23]) of up to 131 days [Biesbrock, 2001][Belbruno, 1993]. The delta-V requirement ranges between 1,170 and 1,325 m/s.

Rosetta. This ESA mission was originally intended to launch in January 2003; however, consecutive failures of the Ariane 5G launch vehicle forced ESA to postpone the launch until February 2004. Rosetta is now slated to encounter the comet 67P/Churyumov-Gerasimenko in 2014 (Figure 3-2). The present analysis was performed prior to the decision to delay launch and thus includes only an examination of Rosetta's initial mission profile, whose final destination was Comet 46P/Wirtanen [ESA (3), 2000]. This profile required Rosetta to perform a triple gravity assist (Mars-Earth-Earth, or MEEGA) and two asteroid flybys, one in 2006 (Otarawa) and the second in 2008 (Siwa). Ariane 5 and its upper stage provide a direct injection to escape (with sufficient excess velocity over escape to achieve a Mars rendezvous, roughly 3,400 m/s). Despite this, Rosetta still required 1,578 kg of propellant (54% of its wet mass). [Villefranche, 1997] Since most of the maneuvers planned prior to rendezvous with Wirtanen are for orbit correction, one can assume that the final rendezvous requires the vast majority of the propellant, and (at a specific impulse, or $I_{sp,}$[24] of between 240 and 292 seconds, approximating figures associated with N_2H_4—a monopropellant—and bipropellant N_2O_4/ N_2H_4) a delta-V of 1,850-2,250 m/s. Were Ariane to have deposited Rosetta into a standard GTO, the onboard propulsion would have to make up an additional 4,200 m/s to achieve the first insertion window at Mars.

Surrey Interplanetary Platform (SIP). Surrey Satellite Technology, Ltd.'s SIP is a 590-kg satellite sized to provide up to 3,200 m/s of propulsive capability. This is sufficient to perform transfers from GTO to either Low Mars Orbit (LMO) or Low Venus Orbit (LVO), with bipropellant N_2O_4 and monomethylhydrazine (MMH). Total payload in LMO/LVO will not exceed 20 kg. [Jason, 2000]

---

[23] This is nearly four times the Earth-Moon separation (384,400 km).

[24] Specific impulse, or I_{sp}, is another key figure of merit for a propulsion system. It is usually given in seconds, although a more accurate statement would be in Newton-seconds/kilogram (N-s/kg). The solar thermal propulsion systems under investigation are intended to provide up to 400 seconds of I_{sp}. Higher I_{sp} values allow for less propellant consumption, as will be seen later.

GAIA. ESA plans to launch this mission to the Earth-Sun L2 point, 1.5 x 10^6 km from the Earth, via Ariane 5 direct injection in 2009. GAIA will chart the "billion brightest objects in the sky," given its shielded orbital location. Since orbital velocity at L2 is only 45 m/s, GAIA only has to null this velocity to remain there (or nearly so, to orbit L2). [ESA (2), 2001] There are stability considerations regarding prolonged stays at L2 that are beyond the scope of this discussion, and are certainly not pertinent to this first-order analysis. Reaching L2 from GTO would require 745 m/s.

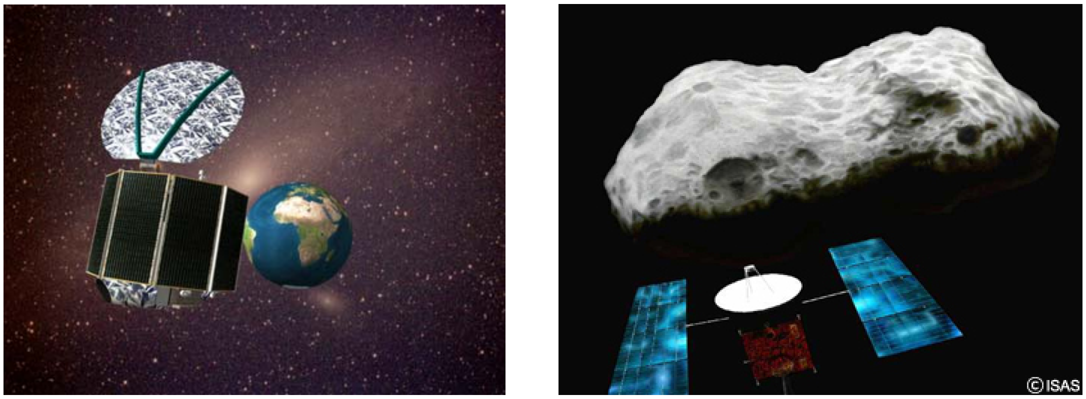

SSTL's proposed geosynchronous minisatellite, GEMINI. [SSTL, 2001]

Japan's MUSES-C rendezvous with 1998 SF36. [ISAS, 2002]

Figure 3-3 GeMINI and MUSES-C missions.

Herschel/Planck. A far IR and sub millimetre telescope package, 3.5 metres in diameter, paired with Planck, a 1.5-metre telescope intended to improve understanding of cosmic background radiation anisotropies. [ESA (4), 2000] Herschel and Planck will be launched in 2007 aboard Ariane 5 to the Earth-Sun L2 point. They will then separate and perform their separate missions. [Pilbratt, 2000] This is roughly the same mission profile as GAIA, above.

GEMINI. This Surrey mission concept includes a direct injection to GEO off of a Russian Proton booster (Figure 3-3). Based on a Surrey minisatellite concept, GEMINI's payload mass is just 110 kg. [SSTL, 2001] Were GEMINI examined as a low-inclination GTO insertion, the GTO-GEO delta-V would amount to roughly 1,500 m/s. This scenario requires significant perigee boosting—and lower thrust—since near-impulsive manoeuvres can be performed over longer times at apogee. A LEO-GEO transfer (expanding the choice of potential launch opportunities to include LEO-targeted boosters) would require an additional delta-V (LEO-GTO) of 2,500 m/s.

Near Earth Object (NEO) Flyby. There are several ongoing projects that propose to fly by or rendezvous with a Near Earth Object. These include (1) Japan's MUSES-C (Figure 3-3), which will return a sample of the asteroid 1998 SF36 to earth by 2007 [ISAS, 2002]; (2) Rosetta, discussed previously; (3) CONTOUR, a Johns Hopkins satellite intended to perform a flyby of two or perhaps three separate comet nuclei between 2003 and 2008 [APL, 2002]; and (4) SIMONE, a British proposal for a rendezvous with 4660 Nereus [Wells, 2001]. The British National Space Council (BNSC) and Particle Physics and Astronomy Research Council (PPARC) may be able to make funds available to perform a modest science mission to a candidate object. There are a number of opportunities to conduct a NEO flyby in the next few years. Some of them include the following close earth approaches:

1. 4179 Toutatis, a likely contact binary NEO (2.5 and 4 km diameter, respectively), which approaches within 1.5 x 10^6 km of Earth on 29 September 2004 (and which represents one of the closest known NEO approach for the next 60 years) [JPL, 2002];
2. 1862 Apollo (2-4 km diameter), which approaches within 1.1 x 10^7 km in November 2005;
3. 2000 AG6 (3.4 x 10^6 km closest approach, July 2005);
4. 1999 RQ36, a small (170-370 m diameter rock), with a close approach of 5 x 10^6 km in September 2005; and
5. 2000 PN9 (2-4 km diameter), 3 x 10^6 km closest approach, March 2006. [Harvard-Smithsonian Center for Astrophysics (CfA), 2001]

Toutatis (Figure 3-4) is an interesting choice and has been imaged in the past [JPL, 2002]. The approach of interest occurs soon after publication of this thesis. It is unlikely that a large-scale mission could have been built and launched in the allotted timeframe. At closest approach, Toutatis is racing through perihelion; the relative velocity of a probe with respect to Toutatis will be roughly 10,000 m/s.[25] There is thus little hope of achieving anything but a high-speed flyby. Options (2), (4), and (5) all are better options in terms of closing velocities, particularly (4), 1999 RQ36. This object, while small, has a nearly circular orbit (.898 x 1.36 astronomical units, or AU), making it a candidate for a potential rendezvous.

A flyby mission to Toutatis, assuming an injection by a booster to GTO, could *theoretically* cost as little as 770 m/s, provided the spacecraft is optimally phased in its initial orbit.[26] As this is just short of escape velocity, it might prove valuable to examine follow-on interplanetary targets.

The missions examined above can be roughly grouped into three "classes":

---

[25] Earth's velocity about the sun is approximately 30,000 m/s. At its perihelion, Toutatis will be moving at roughly 40,000 m/s with respect to the sun. Chapter 3 will discuss this and other calculations.

[26] Achieving this optimal phasing is, of course, the problem. The host satellites of interest (small platforms of 100 kg or less) are usually "piggyback" or secondary payloads with little say in the final mission orbit—this will be dictated by the needs of the primary payload. This in turn implies that an optimal orbit will be extremely hard to come by.

1. Near-Escape Missions, to include L2 orbiters (GAIA, Herschel/Planck), HETO (SIM), and "High HEO" (Cluster II, MMS, and NEO Flybys), with ideal[27] GTO-to-final orbit velocity increments of 700-1,200 m/s. These typically require short-duration perigee kicks to achieve final orbit.

2. Geosynchronous Earth Orbit (GEO) missions, such as GeMINI, with delta-V requirements (GTO-GEO) on the order of 1,500 m/s. This permits lower-thrust, apogee kicks to achieve final orbit.

3. Other Body Capture Missions, to include lunar orbiters (SMART-1, LUNARSAT), with ideal GTO-to-final orbit delta-Vs of 1,100 to 1,500 m/s, and interplanetary missions (Rosetta, Surrey Interplanetary Platform). The interplanetary missions examined here tend to be more energetic than their lunar counterparts, with delta-V requirements ranging up to 4,000 m/s. These will require a low-thrust system to provide a combination of perigee and apogee kicks.

Figure 3-4 High-resolution radar image of 4179 Toutatis, taken by NASA's Goldstone radar in 1992 from a range of 4 million kilometres. [Ostro, 1995]

Selecting one mission from each class, and subjecting it to further scrutiny, should provide substantial insight into the key trades and applicability of solar thermal propulsion.

3.1.2 First-Order Performance Comparison for a Solar Thermal Engine

The author has examined the use of two reference Surrey satellite platforms [Jason, 2000] in order to determine their relative utility for some of the missions outlined above. This first-order analysis concentrates on volumetric and mass availability onboard for a particular propellant and propulsion system combination. The two satellite platforms have the following features:

---

[27] The ideal analysis assumes "impulsive" (instantaneous) maneuvers, coplanar transfer orbits, and no third-body (e.g., sun, moon) or other perturbations. A detailed mission analysis—which is discussed in the next

1. Surrey Microsatellite: 100 kg initial mass, 60 x 60 x 80 cm dimensions, with 49 litres (.049 m^3) of propellant tankage permitted. The spacecraft is mass-limited to no more than 50 kg of propellant (Figure 3-5).
2. Surrey Minisatellite: 400 kg initial mass, 110 x 110 x 88.5 cm dimensions, with 180 litres (.18 m^3) of propellant tankage. No more than 200 kg of propellant is permitted aboard.

A third option, the Surrey Interplanetary Platform (SIP), is substantially larger—590 kg—and was not investigated here [Jason, 2000]. Its higher launch mass is a fair indicator that it is likely to be more expensive to build, test, integrate, and launch than either of the two options above. If neither smaller satellite provides an effective platform for solar thermal propulsion, it might be useful to pursue a SIP-based option. A fourth, smaller option is investigated as an experimental platform; details are provided in Appendix B.

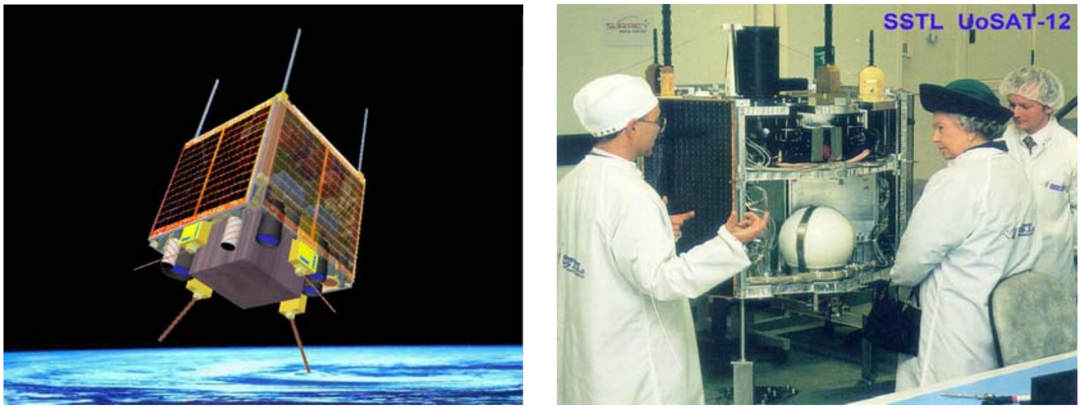

Turkey's BilSAT, an SSTL microsatellite launched in 2003 [SSTL (2), 2001]

Prof. Sir Martin Sweeting describing SSTL's UoSAT-12 minisatellite to Queen Elizabeth II [SSTL (3), 2001]

Figure 3-5 Two Surrey microsatellites, BilSAT and UoSAT-12.

The propellant and propulsion systems examined include the following (all STP monopropellants are liquids at room temperature, selected for low molecular weight):

1. An ammonia-based (NH_3) STP system, ideal specific impulse (I_{sp})= 407 seconds (s);
2. an STP-augmented hydrazine (N_2H_4) system, with roughly the same ideal I_{sp};[28]
3. a water-based (H_2O) STP system, ideal I_{sp} = 333 s.;
4. a bipropellant N_2O_4/MMH (monomethylhydrazine)[29] system, with an I_{sp} = 319 s.; and

---

chapter—will address these items in an effort to acquire more accurate delta-V requirements for the maneuvers under consideration.

[28] Hydrazine's ideal performance will fall somewhat short of ammonia's, due to the additional nitrogen content of the decomposed products—I_{sp} is inversely proportional to propellant molecular weight, and extra N_2 (28 grams/mole) will raise the average molecular weight of the product species from 8.5 to 10.7 grams/mole (g/mol). The author is assuming complete decomposition of hydrazine and/or ammonia (into N_2 and H_2) when making these calculations.

5. a bipropellant H_2O_2/kerosene system, I_{sp} = 298 s.

The author has neglected nozzle expansion and downstream thermochemistry considerations in the calculation of ammonia and augmented hydrazine specific impulses. These factors will tend to lower a given system's I_{sp}. It has been shown [Hastings, 1990] that an electrothermally augmented hydrazine thruster operating at a chamber temperature of 2,000 K and an area ratio (A_{exit}/A_t) of 50 can achieve 334 s. of I_{sp}.

This first-order analysis does not include alternate low-molecular weight STP propellants (hydrogen, H_2, and methane, CH_4). These were dropped from consideration due to storage difficulties and volumetric problems. Both hydrogen and methane are low-density cryogens (H_2: 71 kg/m^3, boiling point: 20 K [Humble, 1995]; CH_4: $\leq$ 400 kg/m^3, boiling point: 111.4 K [Lide, 1995]). Other candidate propellants (e.g., nitromethane (CH_3NO_2), unsymmetrical dimethylhydrazine,[30] and hydrogen peroxide, H_2O_2)—with higher molecular weights—were not considered, due to the long-term storage and handling difficulties they pose.

The author will defer a discussion of possible electric propulsion alternatives due to the very low electrical power available on these platforms; with only 100 W or less, transfer times (between initial and final orbits) become prohibitively large. A direct comparison is examined in detail in Appendix B. The standard formula for thrust power, *P*, is:

$$\eta P = \tfrac{1}{2} T c \qquad \textbf{(3-1)}$$

Here, *T* is engine thrust in newtons, η is an electrothermal arcjet's electric-to-thermal energy conversion efficiency, and *c* is exhaust velocity (m/s). [Martinez-Sanchez, 1990] For a representative ammonia arcjet (c = 4,890 m/s), and presuming 75% conversion efficiency of the host satellite's entire power production capability of 100 W, *T* = 30 milliNewtons (mN). For comparison, the solar thermal propulsion system under examination would provide roughly 500-3,000 mN of thrust.[31]

Given the mass and volume constraints imposed by the two platforms above, a maximum delta-V can be calculated.[32] Results follow:

1. STP-NH_3: This system delivers 1,389 m/s aboard a microsatellite, and 1,255 m/s aboard a minisatellite. Ammonia's low density (600 kg/m^3) tends to compromise this system's performance.
2. STP-N_2H_4: This system can deliver 2,702 m/s aboard a microsat, and 2,399 m/s on a minisatellite. Hydrazine's storage density (1,004.5 kg/m^3) is 1.7 times that of ammonia. This system takes advantage of the hydrazine decomposition reaction used in space-qualified

---

[29] MMH is a lower-density alternative to hydrazine. Its chemical formula is $CH_3NH\text{-}NH_2$ [Humble, 1995].
[30] UDMH, chemical formula $(CH_3)_2N\text{-}NH_2$, another alternative to pure hydrazine [Humble, 1995].
[31] This factor of 16-100 in thrust is directly related to time-to-orbit. See Appendix B.

monopropellant thrusters for years and adds additional heat (concentrated sunlight). This is required to "boost through" ammonia decomposition in the thrust chamber, which is highly endothermic. Electrically augmented systems have suffered due to high power requirements (and low power conversion efficiencies) [Martinez-Sanchez, 1990].

3. STP-H_2O: Delivers 2,197 m/s on a micro, 1,950 m/s on a mini. A water-based system is arguably the most environmentally sound approach, as water is universally available and not normally subject to usage restrictions. Water often suffers in more detailed comparisons, typically due to thrust chamber corrosion, freezing, and two-phase flow issues. [Lawrence, 1998]

4. N_2O_4/MMH: This bipropellant scheme delivers 2,167 m/s with a microsatellite, and 2,166 m/s on a minisatellite. There is significant space heritage in this system [Humble, 1995]. N_2O_4/MMH represents the most probable competitor to STP in this satellite weight class.

5. H_2O_2/kerosene: Delivers 2,024 m/s on either a mini- or microsatellite. Both this and the N_2O_4/MMH combination are mass-limited.

Both STP-N_2H_4 and STP-H_2O theoretically outperform their bipropellant counterparts. These two systems will therefore be investigated in greater detail in the following chapters. Both appear to provide sufficient delta-V to permit most of the missions outlined above to be performed on both mini- and microsatellites. In particular, STP-N_2H_4 offers an opportunity to integrate upper stage propulsion and onboard stationkeeping and attitude control, using the augmented system for orbit transfer and the unaugmented system for normal maintenance.

3.1.3 Candidate Mission Selection

Mission	Likelihood of Occurrence	Simplicity of Execution	Residual Value	Novelty	Compatibility with Microsatellites	TOTAL
MMS	**5**	**1**	**0**	**3**	**5**	**14**
Cluster II	**10**	**3**	**0**	**3**	**5**	**21**
SIM	**5**	**0**	**0**	**5**	**0**	**10**
SMART-1	**10**	**3**	**0**	**5**	**5**	**23**
SMART-2	**3**	**1**	**0**	**5**	**3**	**12**
LUNARSAT	**1**	**3**	**0**	**5**	**10**	**19**
Rosetta	**5**	**0**	**0**	**10**	**1**	**16**
SIP (Mars)	**1**	**3**	**0**	**5**	**10**	**19**
GAIA	**5**	**1**	**0**	**10**	**0**	**16**
Herschel/Planck	**10**	**1**	**0**	**5**	**0**	**16**
GeMINI	**3**	**3**	**5**	**3**	**10**	**24**
NEO Flyby	**1**	**3**	**3**	**5**	**10**	**22**

Table 3-1 Selection Matrix for Candidate Solar Thermal Propulsion Mission Scenarios

---

[32] Again, see chapter 3 for details.

Selection of one or two candidate mission scenarios were made on the basis of the following criteria: (1) Likelihood of mission occurrence; (2) relative simplicity; (3) value of the asset in its final orbit (residual operations); (4) novelty of the proposed mission; and (5) compatibility with a micro- or minisatellite platform. The assessments, while admittedly subjective, are based on the author's engineering experience and listed in Table 3-1. Values are assigned against the following scale:

0 = Very Low
1 = Low
3 = Moderate
5 = High
10 = Very high

The author has included Cluster II and SMART-1 (both on-orbit) simply for calibration. Several points emerge from this process: (1) Were either GeMINI or a NEO Flyby mission to become more likely, either would have received substantially higher totals than the remaining options. (2) LUNARSAT and SIP (Mars) also score relatively high, owing to their natural compatibility with small satellite platforms. Based on this ranking, the author selected three mission classes based on GeMINI (a GEO mission), a lunar orbiter, and a NEO flyby for more detailed analysis.

3.2 Detailed Mission Analysis

Using STK Astrogator, the author will provide greater detail for each of the three mission classes noted above. This will provide a starting point for system requirements definition.

3.2.1 Geosynchronous Orbit Insertion

Technically the simplest of the three mission classes, two GEO orbital insertions were examined: (1) Launch aboard an Ariane 5's ASAP (Ariane 5 Structure for Auxiliary Payloads) to a 350 x 35,717 km elliptical geosynchronous transfer orbit. Ariane delivers the host satellite to this orbit with an inclination of ~7º.[33] (2) Launch aboard Atlas IIAS to a 350 x 35,717 km GTO, with an inclination of 17º. Since this launch occurs at Cape Canaveral, Florida (latitude = 28.5 ºN), some inclination change is performed by the booster prior to separation.

This orbit (Figure 3-6) is similar to that of CRRES (Combined Release and Radiation Effects Satellite), launched into GTO via Atlas Centaur, in 1990. While the CRRES orbit is fairly stable, the following quote makes clear that perturbations (including Earth oblateness, solar, and lunar effects) nevertheless have a significant impact on its orbital elements:

---

[33] Kourou, French Guiana, Ariane's launch site, is at 5.5 ºN latitude. [Larson, 1992]

> “Perturbations to the CRRES orbit have played an important role in the design and planning of the CRRES mission. Specifically, perturbations due to the Earth's oblateness (J2 perturbations) cause cumulative secular variations (i.e., increasing with time) in the argument of perigee and the right ascension of the ascending node. These variations, coupled with the apparent 1°/day motion of the Sun, result in a new rotation of orbit perigee and apogee toward earlier local time, as the mission proceeds. Apsidal rotation also produces a periodic variation (36° peak to peak) in the latitude of perigee with a period of ~525 days. These two motions, given the initial local time of apogee, determined when and where, in local time and latitude, significant mission events such as the CRRES chemical releases occurred.
>
> Third body influences of the Sun and Moon, along with atmospheric drag, cause periodic and secular variations in the semi major axis, eccentricity, and inclination. Third body effects and atmospheric drag are highly coupled and can have a dramatic effect on the stability of high eccentricity orbits, especially those slightly more eccentric or inclined than CRRES. Thousands of orbits in the neighbourhood of the CRRES orbit were investigated in a study of high-eccentricity orbit stability and evolution. No eccentric re-entries were found to be possible for the range of CRRES orbits of interest.” [Johnson, 1992]

These effects, while relatively small for GEO transfers, become substantially more pronounced for the near-escape and lunar capture missions to be discussed presently.

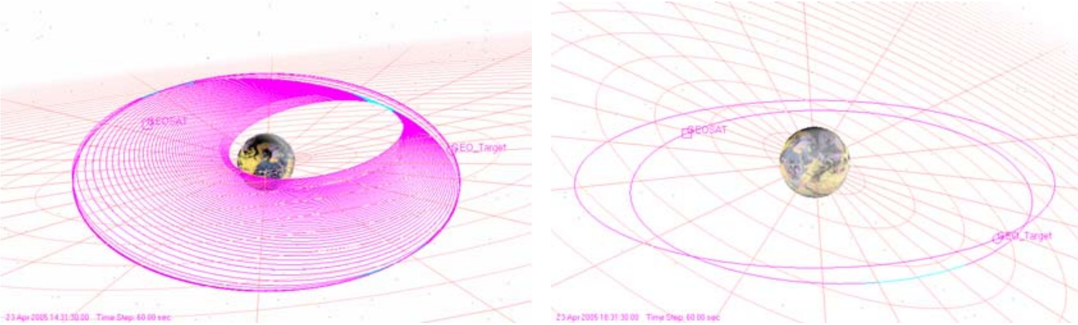

GTO-to-GEO Transfer [STK Astrogator]

Firing at nodal crossings reduces inclination prior to GEO insertion [STK Astrogator]

Figure 3-6 Geosynchronous Orbit Insertion.

Both GEO insertions were intended to place a 100-kg microsatellite in a GEO orbit of near-zero inclination and pre-specified longitude (116 °E). The first case modelled in STK Astrogator—from the lower-inclination Ariane GTO—required 58 individual manoeuvres to transfer the microsatellite to a geostationary position over the Far East. Details are provided in Table 3-2.

The microsatellite model assumes a ½-Newton solar thermal thruster with an average specific impulse of 400 s. This approximates the calculated performance of ammonia or augmented hydrazine propellant.[34] Burn times at apogee and at orbital nodes are limited to 5000 s (83 min.,

---

[34] As discussed in Chapter 1, a solar thermal augmented hydrazine thruster is assumed to have a performance similar (if slightly lower) than an ammonia thruster. The specific impulse figure of ~400 s. assumes complete dissociation of hydrazine, as well as its primary decomposition product, ammonia, into

20 s.) to minimize delta-V penalties associated with non-impulsive manoeuvring. Note that the delta-V figure obtained here is slightly higher than the ideal analysis in the previous section (~1,500 m/s). This results primarily from the 7º inclination change, which was not originally accounted for. However, there is a finite burn penalty associated with each apogee kick, including the inclination change burns at the nodes.

The second scenario—an Atlas IIAS launch to a 17º inclination GTO—is less favourable. This transfer is substantially more expensive than the first, due to the initial orbit's higher inclination. A number of additional plane change maneuvers were required to reduce this inclination over the course of the transfer. This added approximately 13 days to the overall scenario, and demands roughly 20 hours of additional operating time on the solar thermal engine.

Start Date	**1 April 2005, 00:00:00.00 (Julian Date 2453461.5)**
End Date	**6 May 2005, 09:11:16.96 (JD 2453496.88)**
Elapsed Time	**35 days, 9 hrs., 11 min.**
Number of Maneuvers	**58 (51 apogee kicks, 7 plane changes at node crossings).** **Two-orbit "hold" of 42 hrs., 20 min. introduced after apogee kick 48 to attain proper orbital phasing at GEO**
Total Velocity Change	**1,761 m/s**
Propellant Consumption	**36.184 kg**
Final Mass	**63.816 kg**
Engine "On-Time"	**80 hrs., 33 min.**

Table 3-2 Ariane ASAP, GTO to GEO.

Start Date	**1 April 2005, 00:00:00.00 (Julian Date 2453461.5)**
End Date	**19 May 2005, 00:11:44.39 (JD 2453509.47)**
Elapsed Time	**48 days, 0 hrs., 12 min.**
Number of Maneuvers	**73 (49 apogee kicks, 24 plane changes at node crossings).** **Six-day "hold" introduced after apogee kick 48 to attain proper orbital phasing at GEO**
Total Velocity Change	**2430 m/s**
Propellant Consumption	**46.206 kg**
Final Mass	**53.794 kg**
Engine "On-Time"	**101 hrs., 23 min.**

Table 3-3 Atlas IIAS, GTO to GEO

These two scenarios bound the likely performance requirements for a geosynchronous transfer. Details for this second mission are shown above (Table 3-3).

For comparison, a bipropellant N_2H_4/N_2O_4 system (I_{sp} = 319 s.) would consume 53 kg of fuel—7 kg more than the STP engine described above. On a microsatellite, this amount of weight represents substantial design margin—additional payloads, for example. A monopropellant N_2H_4 system (I_{sp} = 230 s.) would use 66 kg of fuel to complete this maneuver plan—leaving only 34 kg

---

N_2 and H_2. Ammonia decomposes via the following (endothermic) reaction: $2NH_3 \rightarrow N_2 + 3H_2$. [Martinez-Sanchez, 1990] for payload. This shows that an STP-augmented hydrazine thruster could mass as much as 20 kg *more* than the monopropellant system *by itself*, and still break even with the simpler system's unaided performance.

These analyses provide insight into a process for setting system mass targets; clearly, if the augmented STP system cannot achieve better performance than a simple hydrazine decomposition system due to its additional weight (or volume), it does not represent good value. Likewise, if an STP engine (augmented or unaugmented) fails to outperform a bipropellant N_2H_4/N_2O_4 system based on additional system mass requirements, it is unlikely to be pursued or adopted for use. The second of these potential criteria is the more stressing, due to the bipropellant's higher performance capability. Since the Atlas IIAS GTO-to-GEO mission has the highest delta-V requirement of any of the missions examined, a satisfactory STP system would have to be built for no more than ~7 kg more than the corresponding bipropellant scheme, to be considered effective. For delta-Vs of ~1500 m/s, this "margin" falls to 6.3 kg.

3.2.2 Near-Escape Missions

Near-escape missions are characterized by relatively short perigee kicks, which are used to increase the semi-major axis of the orbit and, if necessary, escape the earth's gravitational sphere of influence (SOI). The missions of interest can be classified as "near-escape" as they impart very little hyperbolic excess velocity to the host spacecraft. This results in a final heliocentric orbit that is nearly identical to that of the earth itself, and which, depending on the escape bearing, can result in earth return (or gravity assist) trajectories.

The use of near-escape trajectories is particularly useful for the study of Near Earth Object (NEO) missions—NEOs often pass close to earth and afford the mission planner the possibility of low (propellant) cost missions if timed correctly. The author has investigated a number of likely NEO candidates, to include several Potentially Hazardous Asteroids (PHAs),[35] which engage in close approaches to the earth and which, due to their size, might pose the threat of widespread catastrophe were it to impact [JPL (2), 2002]. Table 3-4 summarizes their characteristics.

Name or Designator	Perihelion and Aphelion (AU), Inclination (degrees)	Estimated Size (from absolute magnitude)	PHA	Close Approach Distance (AU) and Date
4179 Toutatis	**.918 x 4.102, 0.47**	**6.5 km[36]**	**Yes**	**.01, 29 Sep 04**
1992 UY4	**1.011 x 4.304, 2.83**	**1-2 km**	**Yes**	**.04, 8 Aug 05**

---

[35] Generally, a NEO is classified as a PHA if its absolute visual magnitude is greater than 22.0 (corresponding to a diameter of roughly 110-240 meters) and resides in an orbit characterized by an Earth Minimum Orbit Intersection Distance (MOID) of 0.05 AU (~7.5 million km). [JPL (3), 2002]

[36] Based on several radar observations, 4179 Toutatis might be a "contact binary" formed by two irregularly-shaped masses, totalling 4.6 km in length [JPL (1), 2002]

1999 RQ36	**.898 x 1.36, 6.02**	**170-370 m**	**Yes**	**.033, 20 Sep 05**
2000 AG6	**.822 x 1.208, 2.47**	**20-50 m**	**No**	**.022, 22 Jul 05**
2000 PH5	**.769 x 1.227, 2.07**	**85-190 m**	**No**	**.036, 26 Jul 05**
2000 UK11	**.665 x 1.104, 0.78**	**25-60 m**	**No**	**.03, 3 Nov 05**
1862 Apollo	**.647 x 2.295, 6.36**	**2-4 km**	**Yes**	**.075, 6 Nov 05**
2000 PN9	**.757 x 2.933, 51.3**	**2-4 km**	**Yes**	**.02, 6 Mar 06**
2001 FO127	**.743 x 1.028, 7.27**	**8-24 m**	**No**	**.029, 22 Mar 06**
2001 UP	**.634 x 1.138, 7.90**	**20-50 m**	**No**	**.035, 22 Oct 06**

Table 3-4 Potential Candidates for NEO Flyby Missions, 2004-2006. [CfA, 2001]

Two missions were examined: (1) an escape and encounter with 4179 Toutatis near its close approach to the earth in late 2004, and (2) an escape and subsequent encounter with the recently discovered NEO 2000 UK11, in late 2005. The Toutatis mission is of interest primarily because its target achieves one of the closest earth approaches of any known asteroid or comet for the next thirty years [JPL (1), 2002]. On 29 September 2004, it will approach within a scant 1.5 million kilometres of the earth, less than four times the distance between earth and Moon.

A 2005 mission to 2000 UK11 provides another opportunity to visit a low-inclination asteroid. Due to its much smaller apparent size, it represents a more difficult target; however, it will be moving at slower velocities than Toutatis near Earth. Toutatis, on earth approach, is near its perihelion and is moving at approximately 40,000 m/s. 2000 UK11 is closer to its aphelion at earth approach, and is travelling at somewhat slower speeds (24,600 m/s). The smaller difference in relative velocities between the asteroid and probe might allow for a longer "encounter" time at flyby.

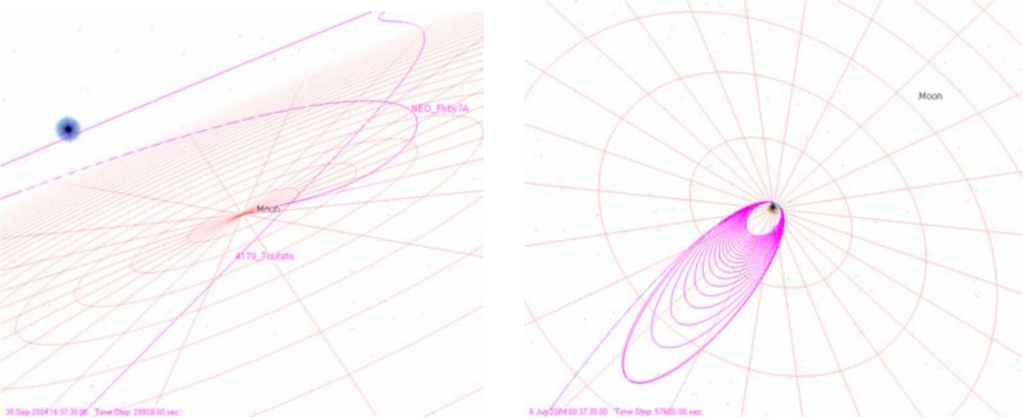
NEO_Flyby7A
Moon
4179_Toutatis
30 Sep 2004 16:37:30.00 Time Step: 28800.00 sec
Moon
6 Jul 2004 00:37:30.00 Time Step: 57600.00 sec

Flyby of 4179 Toutatis (the flyby occurs at the 2nd apparent intersection) [STK Astrogator]

4179 Toutatis Flyby mission phasing orbit and escape trajectory[STK Astrogator]

Figure 3-7 Toutatis Flyby Missions.

Details of the Toutatis mission are shown in Table 3-5. The spacecraft intercepts the asteroid approximately two weeks after earth close approach (Figure 3-7). The delta-V is nearly 2 ½ times the coplanar transfer assumption of 750 m/s, primarily due to gravity losses associated with the escape firings.[37]

The microsatellite model for Near-Escape missions to both Toutatis and 2000 UK11 (Table 3-6) assume a higher thrust than that used for GTO-to-GEO transfer—roughly six times higher (2980 mN). This is required in order to accomplish a significant velocity change in the smaller near-impulsive "window" at perigee. [Robbins, 1966] Thus, burn times are shorter, on the order of 920 seconds (~15 minutes). Average specific impulse remains the same, at 400 s. Both NEO mission profiles reveal much shorter total firing durations (12-13 hrs. vs. 80-100 hrs.) than their GEO counterparts. These missions are likely to be less stressing on the solar thermal engine, due to the reduced number of cycles and total thrusting time.

Start Date	**1 June 2004, 00:00:00.00 (Julian Date 2453157.5)**
End Date	**13 October 2004, 16:05:00.00 (JD 2453292.17)**
Elapsed Time	**134 days, 16 hrs., 5 min.**
Number of Manoeuvres	**55 (25 apogee and perigee kicks, 25 escape burns, 3 adjustment manoeuvres 60 days prior to encounter, 2 additional adjustments 30 days prior to encounter)**
Total Velocity Change	**1,770 m/s**
Propellant Consumption	**36.339 kg**
Final Mass	**63.661 kg**
Engine "On-Time"	**13 hrs., 12 min.**
Relative Velocity at Encounter	**8.539 km/sec**
Closest Approach	**3,995 km[38]**

Table 3-5 Mission to 4179 Toutatis.

Flyby missions to Near Earth Objects are highly dependent on the orbital elements of the initial geosynchronous transfer orbit. While inclination, eccentricity, and semi-major axis will be roughly similar for any GTO, the orbit's right ascension of the ascending node (Ω) and argument of perigee (ω) will determine whether or not the target lies in the narrow escape hyperboloid formed by the envelope of departure asymptotes –this window is narrow by necessity, since we are discussing "near escape" trajectories with very little excess velocity over that required to achieve escape. This limitation will make many GTOs unfavourable for specific NEO targets.

Start Date	**1 February 2005, 00:00:00.00 (Julian Date 2453402.5)**

---

[37] This delta-V penalty cannot easily be avoided. Severe lunar gravitational effects impact spacecraft loitering in higher-eccentricity orbits. One option for minimizing this penalty would be to increase burn times during the escape sequence, or raise the engine's thrust. For a solar thermal engine utilizing sensible heat thermal storage, longer burn times will translate to lower effective I_{sp}, due to operation at a reduced average temperature, but this is likely to be more than offset by a reduction in total delta-V. More work is needed to optimize escape trajectories.

[38] While this figure is higher than mission requirements are likely to permit (e.g., small satellite-capable optical cameras such as SMART-1's Asteroid-Moon Micro-Imager Experiment will have resolution and field-of-view requirements that demand an approach on the order of 100 km to achieve 10 m per pixel resolution), it is representative of the delta-V needed to achieve an approach of this kind. [ESA (5), 2000] Small corrections will allow for closer approaches—assuming the satellite's position determination system is sufficiently accurate.

End Date	**2 November 2005, 11:44:00.00 (JD 2453676.99)**
Elapsed Time	**274 days, 11 hrs., 46 min.**
Number of Manoeuvres	**52 (25 apogee and perigee kicks, 23 escape burns, 4 adjustment manoeuvres 10 days prior to encounter)**
Total Velocity Change	**1,696 m/s**
Propellant Consumption	**35.127 kg**
Final Mass	**64.873 kg**
Engine "On-Time"	**12 hrs., 34 min.**
Relative Velocity at Encounter	**7.08 km/sec**
Closest Approach	**3,659 km**

Table 3-6 Mission to 2000 UK11.

Since this limitation may very well be the overriding consideration in the choice of a specific target, the author has explored a method for attaining any desired "escape bearing," given an initial GTO. This involves a series of (primarily) perigee kicks to raise the spacecraft's orbit to a phasing orbit at approximately 830 x 206,000 km. At this apogee altitude, lunar perturbations are still sufficiently small that a hold in this orbit will not result in an eccentric re-entry. Table 3-7 illustrates an STK Astrogator simulation[39] of a 100-day hold in this orbit and the resulting change in orbital elements. There is a noticeable upward drift in inclination, in addition to slight decreases in both orbital eccentricity and semi-major axis. As a consequence, perigee altitude rises from 830 to slightly more than 2,100 km. This is in line with expectations. [Johnson, 1992]

	8 Apr 2005 18:30:00.00 (JD 2453469.3)	**18 Jul 2005 15:30:00.00 (JD 2453570.1)**
Semi-major axis (a), km	**106,550**	**106,247**
Eccentricity (e)	**.932338**	**.919370**
Inclination (i), degrees	**6.828**	**8.650**
Right Ascension of the Ascending Node (RAAN or Ω), degrees	**355.301**	**358.305**
Argument of Perigee (w), degrees	**190.519**	**190.569**
Mean Anomaly (M), degrees	**169.242**	**255.274**

Table 3-7 Effect of a 100-day hold on a highly elliptic (830 x 206,000 km) phasing orbit's elements.

Once this orbit is achieved, the orbit's inclination can be changed by up to 90 degrees for relatively low propellant cost (Figure 3-8). The maximum plane change cost is defined by:

$$\Delta V_{\text{p.c.}} = 2\, V_a \sin(\theta/2) \tag{3-2}$$

The velocity increment $\Delta V_{\text{p.c.}}$ required to perform an instantaneous plane change of angle θ is related to the orbital velocity at apogee V_a by the above trigonometric identity. [Bate, 1971] For the maximum plane change in the orbit of interest, orbital velocity at apogee is roughly 350 m/s, so the ideal (impulsive) $\Delta V_{p.c.}$ is 495 m/s. STK indicates that the actual cost of this plane change is 40% higher than the impulsive approximation suggests (Table 3-8).

---

[39] The force model used for these calculations includes lunar, solar, and all planetary perturbations (except Pluto), as well as zonal coefficients down to J4. [STK, 2002] A discussion of zonal coefficients can be found in Appendix A as well as [Battin, 1987].

Once the necessary plane change is performed, a series of apogee kicks are performed to circularise the orbit at roughly 206,000 km. Like the highly elliptical phasing orbit, this orbit is relatively stable for short duration.

A 10-day hold in this high circular orbit caused small eccentricity and inclination shifts. The orbit's semi-major axis climbed from 213,000 to 221,000 km during this hold. Its period is 12 ½ days—which sets an upper bound for waiting time in this orbit, since a hold of one full period will permit access to all possible escape bearings. At this altitude, escape requires a velocity increment of only 567 m/s (Figure 3-8). The total velocity change associated with this set of manoeuvres is illustrated below. The STK simulation will always be more expensive, as it is capable of accounting for penalties associated with third-body, zonal effects, and finite-duration burns (which the ideal calculations disregard).

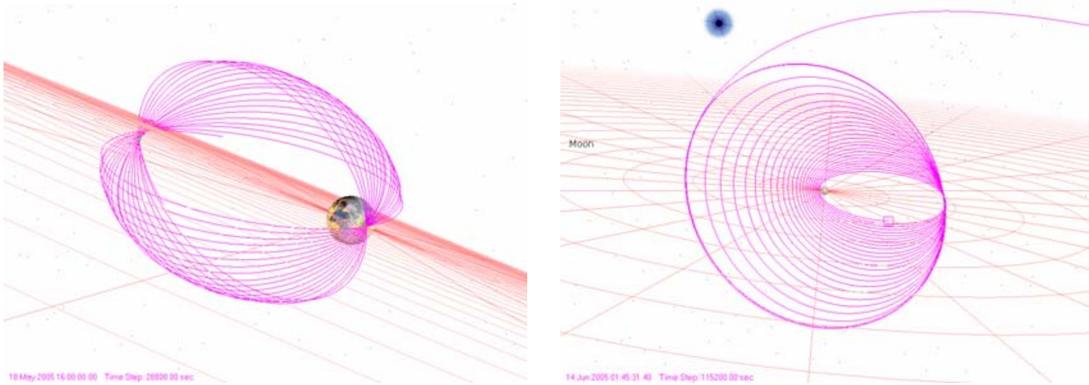
18 May 2005 16:00:00.00 Time Step: 28800.00 sec
Moon
14 Jun 2005 01:45:31.40 Time Step: 115200.00 sec

Multiple inclination change burns at high apogee [STK Astrogator]

Circularisation at 206,000 km and escape [STK Astrogator]

Figure 3-8 High Altitude Phasing Orbit (HAPO).

The total velocity change required to achieve any desirable escape bearing, from an initial (unfavourable) GTO, will fall between 2,300 (no plane change required) and 3,000 m/s (90º plane change). The STK simulation, which requires 267 days to achieve escape in this fashion, is a 78-burn transfer placing the host spacecraft in a hyperbolic orbit with an eccentricity of 1.05. This equates to a hyperbolic excess energy of just .045 km^2/s^2 or a v_∞ (hyperbolic excess velocity) of 299 m/s. For comparison, MUSES-C, Japan's NEO rendezvous mission slated for launch in 2002, receives an energetic boost from its upper stage, which provides 18 km^2/s^2 over escape (v_∞ = 6 km/sec)—significantly greater than the near-escape trajectory analysed here. [Kawaguchi, 1998]

	ΔV_1 (raise apogee)	$\Delta V_{p.c} = \Delta V_2$ (change plane)	ΔV_3 (raise perigee)	ΔV_4 (escape)	Total

Astrogator	**637 m/s**	**696**[40]	**1,083**	**607**	**3,023**
Ideal (Impulsive)	**609 m/s**	**≤495**	**1,032**	**567**	**≤ 2,703**

Table 3-8 Ideal and simulated velocity change requirements for a GTO-to-Escape mission, given an initially unfavourable GTO.

An alternative to the above approach[41] would be to make use of a lunar gravity assist (LGA) to achieve a specific escape trajectory. The value of this “high altitude phasing orbit” is that—while it is somewhat expensive—it should be applicable to any GTO in which a small satellite finds itself deposited. LGAs introduce several additional complications: lunar phasing (which reduces transfer opportunities), midcourse corrections to ensure the correct arrival asymptote in the lunar SOI, and the need for orbital planning inside the lunar SOI, prior to escape.

3.2.3 Lunar Capture

The instability of increasingly more eccentric transfer orbits becomes rapidly apparent when attempting to model earth escape or lunar capture missions. As the apogee of a spacecraft’s orbit approaches lunar altitude, perturbations become severe—long before the spacecraft ever enters the moon’s SOI. These perturbations are sufficient to cause large swings in the orbit’s semi-major axis, inclination, and eccentricity; this often results in re-entry at earth. The SMART-1 spacecraft uses lunar perturbations to its advantage (Figure 3-9).

---

[40] This STK simulation includes a plane change of 89.7 degrees.

[41] Which is notable in that it is, in essence, a lunar *avoidance* mission.

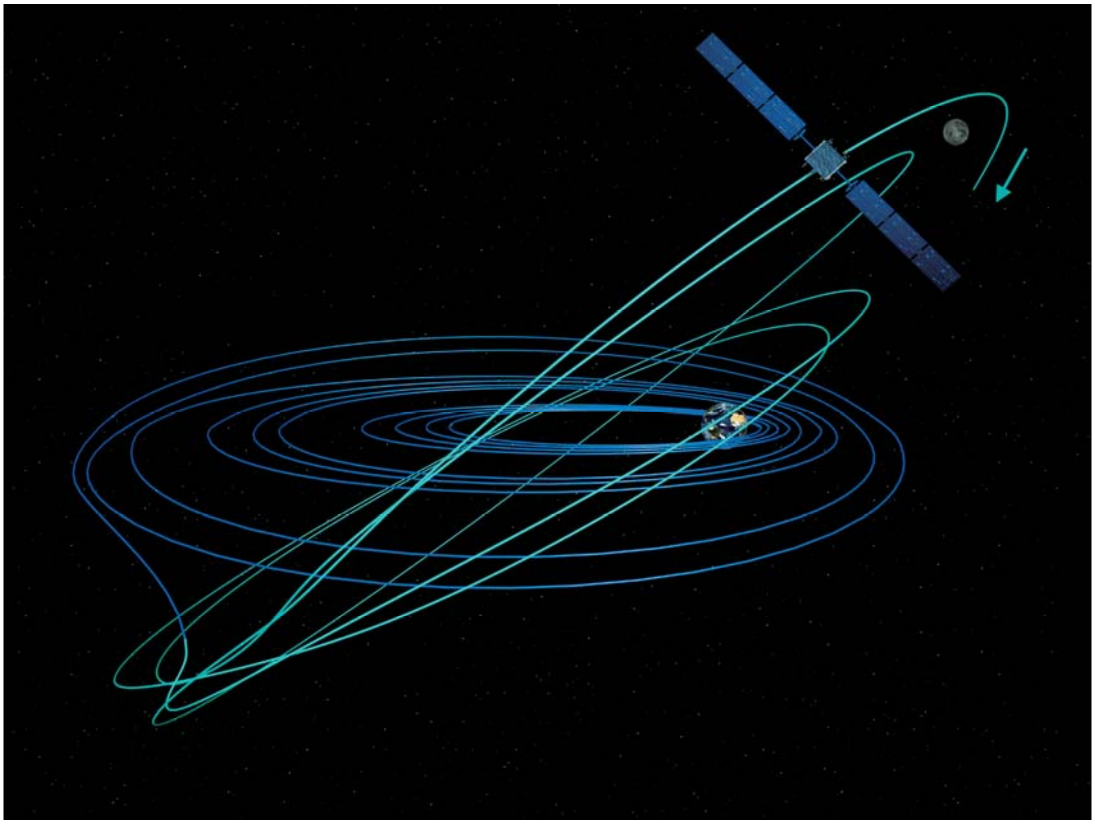

Figure 3-9 The SMART-1 lunar orbiter trajectory requires multiple lunar swingbys [ESA, 2004].

The solar thermal engine is a low-thrust, near-impulsive manoeuvring system capable of approximating "impulsive" performance via a series of perigee or apogee kicks. At near-lunar distances, a highly eccentric earth orbit has an apogee velocity of only 185 m/s. Since the moon is moving at slightly over 1,000 m/s in its orbit, the spacecraft, upon lunar approach, is moving at roughly 1,000 m/s relative to the moon—and accelerating rapidly as it moves closer. At low (earth-relative), high (moon-relative) approach velocities, a low-thrust engine is unable to impart a sufficient velocity change to close the orbit. Each 15-minute firing can produce only 25-55 m/s of delta-V. The result is a hyperbolic flyby.

It is possible to increase the approach orbit's energy—and thus its velocity at apogee—by increasing its perigee prior to lunar encounter. Table 3-9 illustrates the specifics of a successful lunar capture mission, simulated by STK Astrogator. A "full" Earth force model is used prior to close approach, at which point a selenocentric model is selected for orbital propagation. Final adjustment manoeuvres are also performed with the lunar model.[42]

Start Date	**1 March 2005, 00:00:00.00 (Julian Date 2453430.5)**
End Date	**22 August 2005, 22:36:00.00 (JD 2453608.44)**

---

[42] The lunar force model includes zonal coefficients up to and including J2. [STK, 2002]

Elapsed Time	**177 days, 22 hrs., 36 min.**
Number of Manoeuvres	**62 (21 perigee kicks, 28 apogee kicks, 4 trans-lunar injection burns, 7 lunar orbit insertion burns, and 2 final apolune-lowering burns)**
Total Velocity Change	**2,103 m/s**
Propellant Consumption	**41.5126 kg**
Final Mass	**58.4874 kg**
Engine "On-Time"	**13 hrs., 12 min.**
Final Orbit	**2,212 x 13,222 km, near-polar**

Table 3-9 Lunar Capture Mission

Prior to trans-lunar injection (TLI), the spacecraft is raised from its initial GTO to a 136,500 x 206,000 km elliptical orbit (Figure 3-10). The perigee of this orbit is sufficiently high to achieve substantially higher apogee velocity once the orbit is raised to lunar altitude.[43]

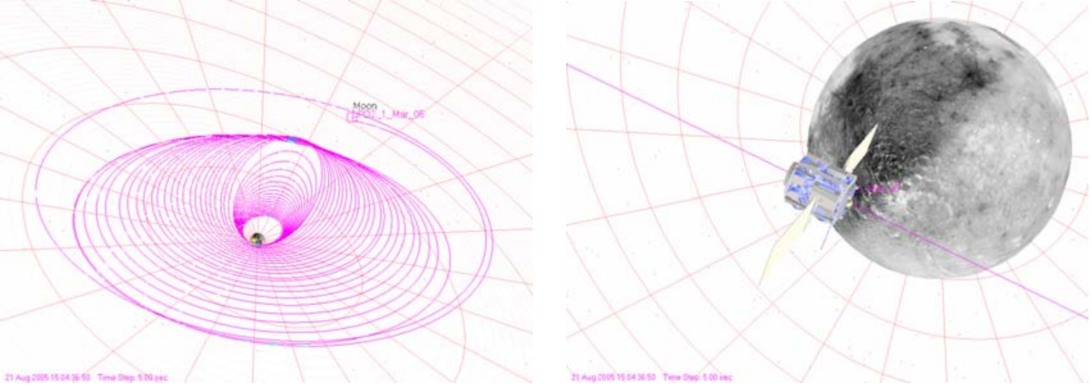
Moon
LPO2_1_Mar_05
21 Aug 2005 15:04:36.50 Time Step: 5.00 sec
21 Aug 2005 15:04:36.50 Time Step: 5.00 sec

Successive perigee and apogee firings boost a lunar orbiter to a 136,500 x 206,000 km phasing orbit [STK Astrogator]

A lunar orbiter passes under the moon's south pole prior to low-thrust orbital insertion [STK Astrogator]

Figure 3-10 Lunar Orbit Insertion Steps.

Following a 7-day hold (awaiting appropriate lunar phasing), the spacecraft fires at four discrete periods near perigee, three hours apart. 18 days later, the vehicle arrives at the moon, where it performs 7 lunar orbit insertion (LOI) firings—again, three hours apart (Figure 3-11). This permits the solar thermal engine to return to a "charging" or sun-pointing state, following the previous burn, with sufficient time to achieve maximum cavity receiver temperature.[44] Two final manoeuvres—both performed at sequential perilunes—slow the spacecraft into its final orbit around the moon. The required delta-V for this mission is 40% higher than the figure of 1,500 m/s discussed in the author's preliminary analysis. As has been noted, this is partially due to finite burn penalties associated with the TLI and LOI firings, although the greatest contribution arises from the need to achieve an intermediate staging orbit at 136,500 x 206,000 km.

---

[43] Apogee velocity in a 136,500 x 384,400 km orbit is 738 m/s.

[44] The author assumes the use of a thermal storage system (e.g., an insulated graphite block) for the purposes of this analysis. A direct-gain system would not require interim "recharges."

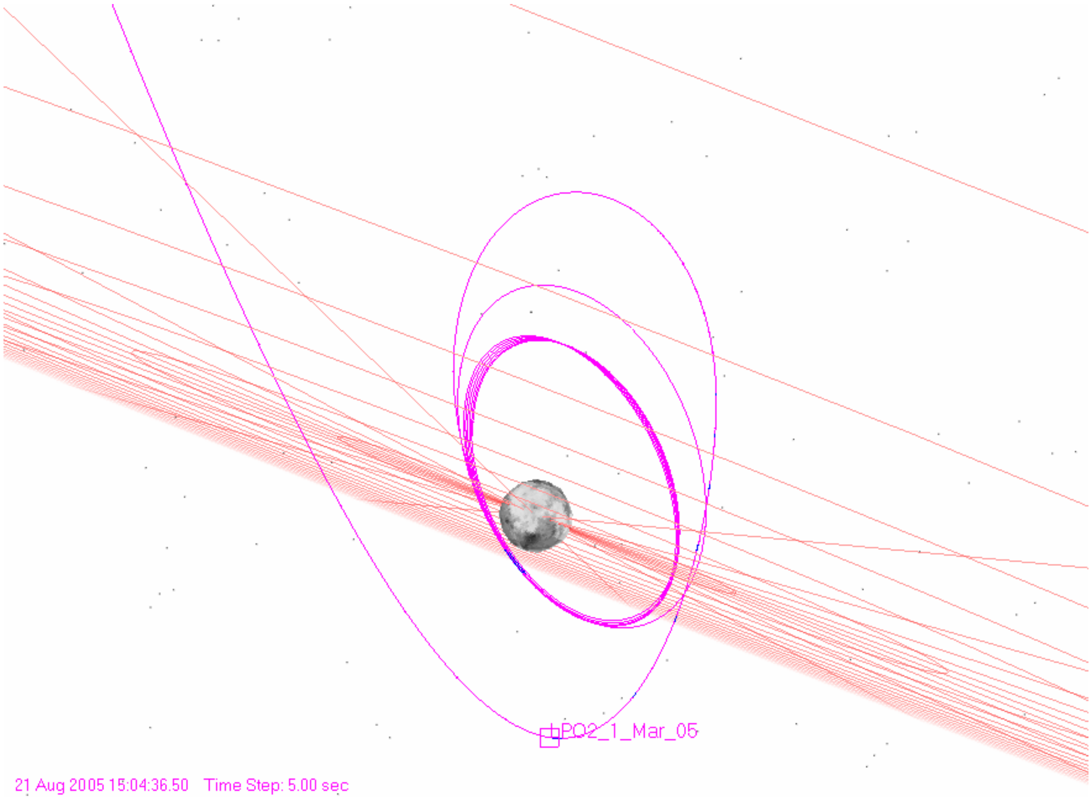

Figure 3-11 Lunar capture with a low-thrust system, using seven insertion burns over approximately 20 hours. Final orbit is achieved through the use of two successive firings at perilune [STK Astrogator]

3.3 Summary

A number of candidate missions have been reviewed to determine the applicability of solar thermal propulsion. Three mission classes were seen to benefit from the inclusion of STP—Geosynchronous, Near-Escape, and Other Body Capture—and realistic scenarios constructed using advanced trajectory analysis software. Generally, finite burn and third body perturbation considerations, which were not considered in the initial assessment, demonstrated that each of these missions will be more expensive than simple coplanar, ideal impulsive assumptions imply. For Near-Escape and Lunar Capture missions, lunar perturbations become sufficiently severe to warrant carefully selected phasing orbits to prevent eccentric reentry or—while potentially less catastrophic—substantial shifts in orbital elements. The author proposes a novel manoeuvring sequence to avoid these lunar perturbations and permit earth escape along any desired trajectory: the High Altitude Phasing Orbit (HAPO). While this set of manoeuvres is relatively expensive in terms of propellant consumption, it sets an upper bound on escape requirements for satellites lofted to (potentially unfavourable) geosynchronous transfer orbits, providing maximum flexibility to the mission designer. Most missions cluster around the 1,700-2,100 m/s regime. This is well within the capability of the solar thermal thruster schemes outlined in the preliminary analysis.

For lunar capture missions, the author proposes the use of intermediate, low-eccentricity phasing orbits in order to achieve low-thrust insertion upon lunar approach. This approach also limits lunar perturbations prior to the trans-lunar injection sequence.

Chapter 4

4 Preliminary Design

This chapter includes a discussion of the author's solar thermal propulsion system design philosophy, likely options, and potential trade spaces. The author provides a brief review of key rocket propulsion and astrodynamics concepts necessary to the discussion, then describes the design trades and analyses necessary for the formulation of the baseline preliminary design. The three final designs are based on requirements stated in Appendix B.

4.1 Rocket Propulsion Fundamentals

Simply put, rockets move spacecraft. Humble [1995] notes:

> "…A propulsion system accelerates matter to provide a force…that moves a vehicle or rotates it about its center of mass. Over the years, functions have been defined to more accurately describe what the propulsion system does. The main ones are (1) *Launch*, accelerating a vehicle from Earth, or near Earth, through the atmosphere to a desired orbit; (2) *Orbit insertion*, moving a vehicle from an initial orbit to a mission orbit; (3) *Orbit maintenance* and *manoeuvring*, keeping the space vehicle in the desired mission orbit or moving it to another desired orbit; and (4) *Attitude control*, providing torque to help keep a spacecraft pointed in the desired direction."

The author is primarily concerned with how to better implement functions (2) and (3). The solar thermal propulsion system—and many other low-to-moderate thrust systems intended as onboard spacecraft propulsion—are insufficiently powerful (by several orders of magnitude) to provide a launch capability. Orbit maintenance and attitude control require relatively small velocity changes and therefore do not generally call for high-performance (high specific impulse) propulsion systems. If thrusters are required,[45] schemes involving cold gas or monopropellant hydrazine are usually deemed sufficient to perform the task [Humble, 1995].

Substantial velocity changes—on the order of hundreds to thousands of meters per second—provide sufficient increases in orbital energy to move vehicles from low earth orbit to geosynchronous orbit, to the moon, near earth objects, and other planets. A minimum-energy, two-impulse, coplanar (i.e., Hohmann) transfer between low and geosynchronous orbits requires a velocity change (delta-V, or ΔV) of 4,200 m/s. A seven-day transfer from low earth orbit to lunar orbit is nearly the same—3,900 m/s. These classes of manoeuvres provide examples of what can be achieved with low-to-moderate thrust systems such as solar thermal propulsion.

---

[45] To despin momentum wheels, or to counteract small torques incurred during main engine firings (due to thrust vector misalignment).

More expensive (higher delta-V) missions permit outer planet and eccentric or highly-inclined near earth object rendezvous, or solar system escape. These scenarios have high delta-V requirements: For instance, launching a satellite into low earth orbit requires a ΔV of ~10,000 m/s.[46] Transfer from a low earth orbit to a solar escape orbit requires a minimum of 8,700 m/s [Hill, 1992].

The instantaneous velocity of a spacecraft relative to a central mass (e.g., the earth, moon, sun, or planetary body) can be calculated from the following relation, commonly known as the *vis-viva* integral [Battin, 1987] when solved for v^2:

$$v = \sqrt{GM\left(\frac{2}{r} - \frac{1}{a}\right)} \tag{4-1}$$

The spacecraft's velocity, v, is related to the gravitational constant G (6.67×10^{-11} N-m^2/kg^2), the central mass M (kg), the spacecraft's instantaneous separation from the central mass, r (m), and the spacecraft's orbital semi-major axis, a (m).[47]

A coplanar[48] transfer of a spacecraft to a new mission orbit requires a ΔV imparted by the vehicle's propulsion system. In order to provide a satellite in a circular low earth orbit a sufficient ΔV for it to leave the earth's gravitational sphere of influence (i.e., escape), the propulsion system must produce the following instantaneous change:

$$v_2 - v_1 = \sqrt{GM\left(\frac{2}{r_1} - \frac{1}{\infty}\right)} - \sqrt{GM\left(\frac{2}{r_1} - \frac{1}{r_1}\right)} = \left(\sqrt{2} - 1\right)\sqrt{\frac{GM}{r_1}} \tag{4-2}$$

---

[46] This includes gravity and drag losses sustained during the vehicle's ascent. However, it is not delta-V but thrust-to-weight ratio that prohibits the use of low-thrust systems in these mission scenarios.

[47] A vehicle in a 300-km altitude, circular low earth orbit travels at 7,723 m/s. The earth's mass (M) is 5.972×10^{24} kg. For a circular orbit (where $r = a$), *vis-viva* is simply:

$$v = \sqrt{\frac{GM}{r}} \tag{4-3}$$

[48] A non-coplanar transfer assumes a plane change (see Chapter 2). These are often quite expensive in terms of required delta-V.

Here, $r_2 = r_1$ (instantaneous velocity change), a_2 = infinity (parabolic orbit), and $a_1 = r_1$ (initial circular orbit). For an initial circular orbit altitude of 300 km (r_1 = 6,678 km), $v_2 - v_1 = \Delta V$ = 10,922 – 7,723 = 3,199 m/s. Initial orbits with higher energies—and correspondingly higher values of the vis-viva integral above—will lower this ΔV requirement. For example, a spacecraft in a highly elliptical geosynchronous transfer orbit (a = 24,355 km, perigee altitude r_1 = 300 km), moving at 10,147 m/s at perigee, must only increase its velocity by 775 m/s to escape.[49]

This is important inasmuch as a lower ΔV will necessitate a smaller propellant expenditure. The amount of propellant required to impart a specific ΔV can be calculated via the following relation:

$$m_p = m_i \left[1 - e^{\left(\frac{-\Delta V}{g I_{sp}} \right)} \right] \tag{4-4}$$

The propellant mass, m_p, required to produce a specified velocity change ΔV is related to the spacecraft's initial mass, m_i (prior to the firing), and the propulsion system's effective specific impulse, I_{sp}. This equation is credited to Tsiolkovskii [Brown, 1996]. The exponential nature of the relation is shown in Figure 3.1,[50] for selected propulsion systems.

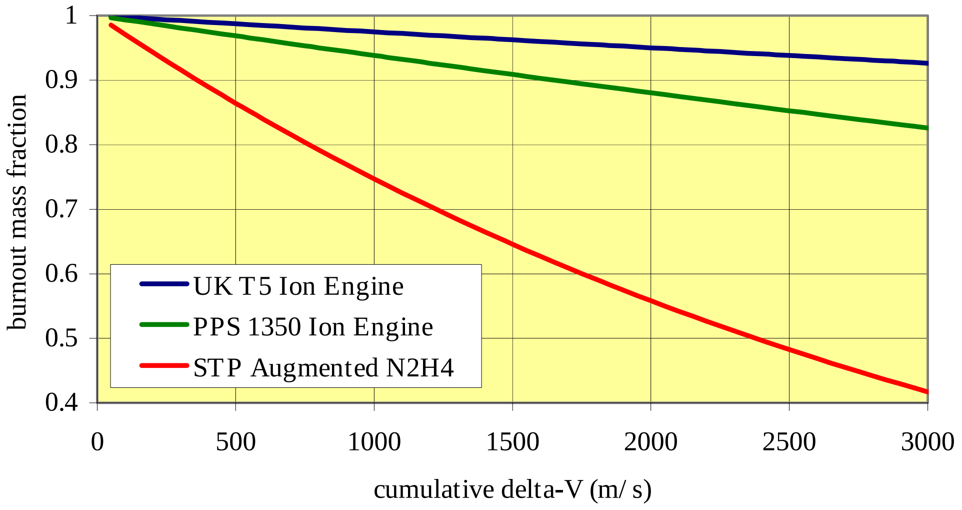

Figure 4-1 Burnout mass fraction (satellite mass following engine firing / m_i) for velocity changes of up to 3,000 m/s, for three representative propulsion systems: (1) the UK T5, an electrostatic ion

---

[49] *But it must do it at perigee.* As a consequence of orbital conservation of angular momentum, the spacecraft's velocity will begin to fall as it moves away from perigee, eventually reaching a minimum at apogee (in this particular case, apogee velocity is only 1,609 m/s). Therefore, near-impulsive manoeuvres are required to achieve escape with the velocity changes calculated above. Short-duration manoeuvres imply high thrust.

[50] Also Appendix B.

engine, I_{sp} = 4,000 s; (2) the PPS 1350, a Hall effect thruster, I_{sp} = 1,600 s; and (3) a threshold performance STP-augmented hydrazine thruster, I_{sp} = 350 s.

Figure 4-1 neatly encapsulates the potentially misleading nature of the simple calculations described above. While the electric propulsion alternatives provide high burnout mass fractions (80-95%) at delta-Vs of 3,000 m/s, what is not shown in this figure is the composition of the burnout mass. A substantial portion of this mass is in fact dedicated to the electrical power system required to produce the high voltages required for ionisation (in the case of an ion thruster) or a combination of ionisation and magnetic field sustainment (in the case of Hall effect thrusters). In either case, thrust levels—and thrust-to-weight ratios—are extremely low, which drives transfer times. This is exacerbated by the limited volume and surface area available for power production on small satellites. Appendix B provides additional information and a comparative look at EP and STP system performance on microsatellites.

Specific impulse, alluded to a number of times in previous chapters, is "the conventional method of comparing propellants, propellant combinations, and the efficiency of rocket engines." [Brown, 1996] It is simply defined as the thrust per unit weight propellant flow rate:

$$I_{sp} = \frac{T}{\dot{m}g} \tag{4-5}$$

A rocket's thrust, T, can be defined as:

$$T = \dot{m}u_e + \left(P_e - P_a\right)A_e \tag{4-6}$$

For an optimal expansion to ambient pressure P_a, the final term vanishes and I_{sp} can be seen to be the quotient of the effective exhaust velocity at the rocket nozzle exit plane, u_e, and gravitational acceleration g. Since u_e can be defined, given a specific set of assumptions,[51] as:

$$u_e = \sqrt{\frac{2\gamma R T_c}{(\gamma - 1)M}\left[1 - \left(\frac{P_e}{P_a}\right)^{\frac{\gamma-1}{\gamma}}\right]} \tag{4-7}$$

I_{sp} is therefore:

$$I_{sp} = \frac{u_e}{g} = \sqrt{\frac{2\gamma R T_c}{(\gamma - 1)g^2 M}\left[1 - \left(\frac{P_e}{P_a}\right)^{\frac{\gamma-1}{\gamma}}\right]} \tag{4-8}$$

---

[51] These include (1) homogenous, invariant propellant composition through the rocket's nozzle, (2) perfect gas behaviour, (3) no frictional losses at the walls, (4) adiabatic expansion, (5) steady, constant flow, (6) departure of all gases axially, and (7) uniformity of gas velocity across any section normal to the nozzle axis. [Brown, 1996]

Here, γ is the ratio of propellant specific heats C_p (constant pressure) and C_v (constant volume), nominally a figure between 1.10 and 1.67. R is the universal gas constant (8,314.3 J/kmol-K), and T_c is the "chamber temperature," or near-zero flow velocity (stagnation) temperature found in the engine prior to the convergent-divergent nozzle section. M is the propellant molecular weight (kg/kmol). Ammonia propellant—assuming little or no decomposition—at a chamber temperature of 2,000 K ($\gamma = 1.14$, $M = 17.03$) thus achieves an ideal[52] I_{sp} of 407 s.

Propellant Type	Density (g/cm^3)	I_{sp} (s)	DI_{sp} (g-s/cm^3)
Xe (3000 psi) [a]	2.0000	1600	3200
Xe (882 psi) [b]	1.1000	1600	1760
STP H_2 [c]	0.0710	917	65
STP-augmented N_2H_4 [c, e]	1.0045	402	404
STP NH_3 [c]	0.6000	449	270
STP H_2O [c]	1.0000	372	372
MMH/N_2O_4 [d]	1.1590	319	370
H_2O_2/Kerosene [d]	1.2790	305	390
Hybrid H_2O_2/ Polyethylene [d]	1.2970	300	389
N_2O	0.7500	206	155
H_2O_2 (89%)	1.3800	179	247

[a] 3000 psi storage pressure [Polyflex, 1999], UK T5 I_{sp} [Wells, 2001]
[b] 882 psi storage pressure [Gibbon, 2002], UK T5 I_{sp}
[c] heated to 2500 K. C_p and γ values are at 1500 K, ideal expansion to vacuum assumed
[d] oxidizer/fuel ratio optimised for maximum I_{sp}
[e] Complete dissociation of ammonia to N_2 and H_2 assumed

Table 4-1 Density, I_{sp}, and Density-I_{sp}, for representative monopropellant and bipropellant combinations.

The above equation strongly suggests the maximization of the quotient T_c/M, in order to achieve the highest possible I_{sp}. This has driven past designers of solar thermal engines (and nuclear rocket engines) to hydrogen propellant (M = 2 kg/kmol) and very high chamber temperatures (approaching 3,000 K). In theory—and practice—this has resulted in high performance levels. During ground tests in Nevada in the late 1960s and early 1970s, the NERVA (Nuclear Engine for

---

[52] "Ideal" here implies a perfect expansion to vacuum ($P_e = P_a$). The assumption of no decomposition is used only to provide an example; at this temperature, there will be substantial decomposition to N_2 and H_2, for nominal chamber pressures.

Rocket Vehicle Application) nuclear thermal rocket achieved a specific impulse of 835 s [Humble, 1995] with H_2 propellant. This is twice the performance of the best chemical upper stage[53] and provided high thrust levels (890 kN).

The solar thermal engine is capable of specific impulses in this range—however, the author has made a decision to bar the use of liquid hydrogen, due to incompatibility of the propellant with microsatellites. This incompatibility is twofold: (1) liquid H_2's storage density is extremely low, 71 kg/m^3 (one-fourteenth that of water), which indicates that very little could be stowed aboard a small satellite, and (2) the low storage temperature of the propellant—H_2 is a "hard" cryogen, boiling at just 20 K—which demands heroic measures to dam heat leakage and prevent boil-off [Cady, 1996].

Small satellites impose volumetric constraints that require a hybrid figure of merit that takes into account both the performance (I_{sp}) of a propellant and its storage density (ρ, kg/m^3). The product of a propellant's specific gravity ($\rho_{propellant}/\rho_{water}$) and its I_{sp}, occasionally referred to as the density-I_{sp} (DI_{sp}), provide a good indication of the volumetric compatibility of the propellant [Haag, 2001]. Representative propellants and their properties are shown in Table 4-1. When this product is taken into account, it can be seen that high-I_{sp} performers like H_2 become untenable for highly volume-constrained systems.

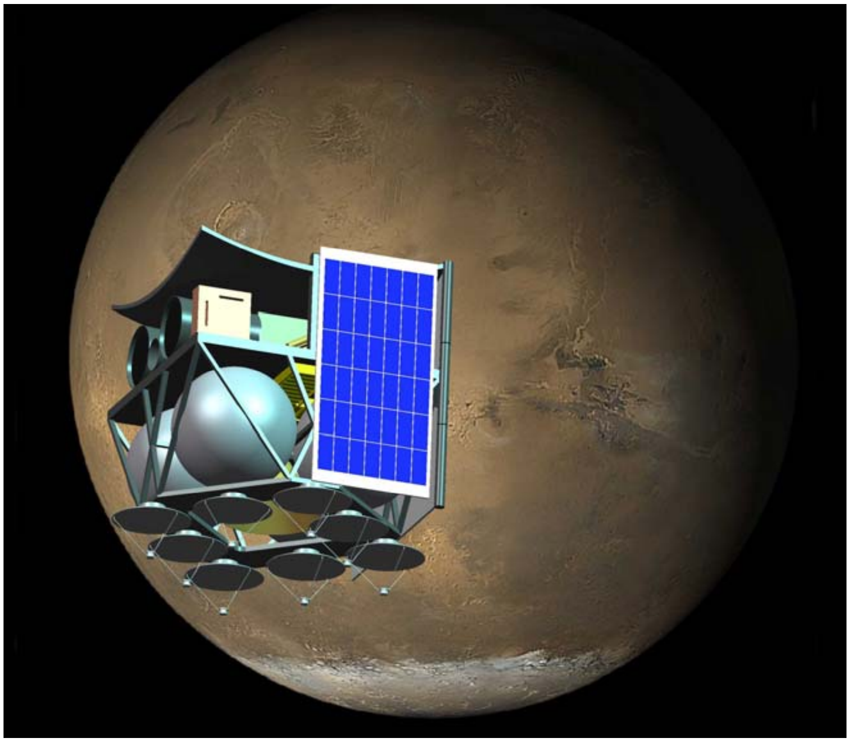

---

[53] Space Shuttle Main Engine (SSME), a liquid O_2/liquid H_2 chemical propulsion system, offers 455 s of I_{sp} [Hill, 1992].

Figure 4-2 Mars orbiter utilising "ganged mirror" solar thermal propulsion for insertion firings.

4.2 Baseline Engine Design

The baseline solar thermal propulsion system (Figure 4-2) will, of necessity, be compact, lightweight, low-cost, and high-performance. The degree to which compactness, lightness, cost reductions, and performance enhancement must be achieved is dictated by a set of baseline requirements in Appendix B (q.v.). These requirements, and the step-by-step option tree shown in Figure 4-3, provide a high-level framework for determining the general, and the more increasingly specific, details of the system under consideration.

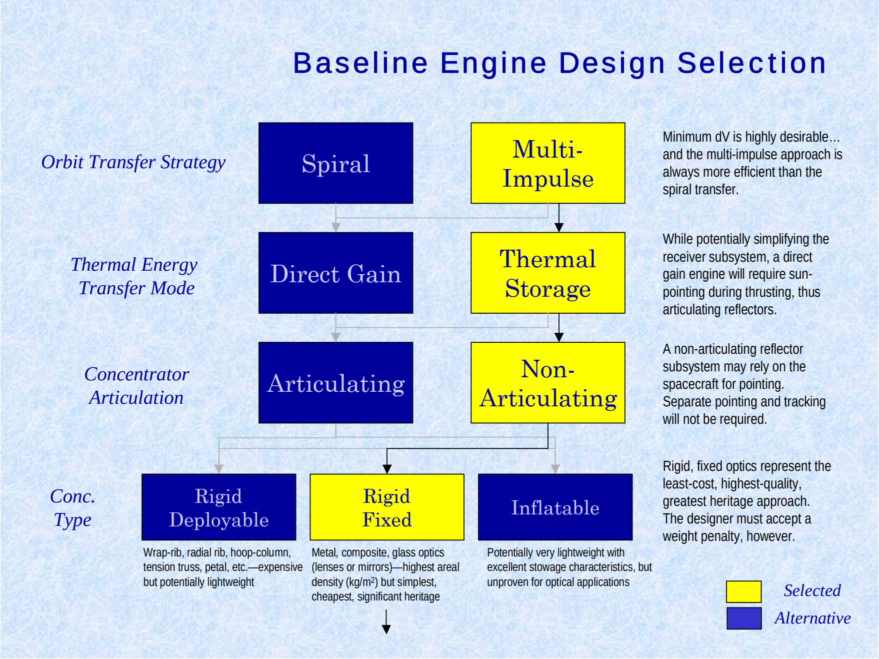
Baseline Engine Design Selection
Orbit Transfer Strategy
Spiral
Multi-Impulse
Thermal Energy Transfer Mode
Direct Gain
Thermal Storage
Concentrator Articulation
Articulating
Non-Articulating
Conc. Type
Rigid Deployable
Rigid Fixed
Inflatable
Selected
Alternative

Minimum dV is highly desirable… and the multi-impulse approach is always more efficient than the spiral transfer.

While potentially simplifying the receiver subsystem, a direct gain engine will require sun-pointing during thrusting, thus articulating reflectors.

A non-articulating reflector subsystem may rely on the spacecraft for pointing. Separate pointing and tracking will not be required.

Rigid, fixed optics represent the least-cost, highest-quality, greatest heritage approach. The designer must accept a weight penalty, however.

Wrap-rib, radial rib, hoop-column, tension truss, petal, etc.—expensive but potentially lightweight

Metal, composite, glass optics (lenses or mirrors)—highest areal density (kg/m^2) but simplest, cheapest, significant heritage

Potentially very lightweight with excellent stowage characteristics, but unproven for optical applications

Figure 4-3 Top level options tree for STP engine design effort.

The first trade involves the selection of an orbit transfer strategy—in this case, spiral (constant thrust) versus multi-impulse (apogee and perigee firings). The solar thermal engine concept is capable of fulfilling either strategy, or both. A spiral strategy has the advantage of permitting smaller engine components—and thus a system weight reduction—since the impulse provided by the engine can be "spread out" across a given orbit. However, selection of a spiral strategy requires the selection of a direct-gain engine. Such an engine would not store heat but would transfer it directly to the propellant while the engine's concentrating mirror is pointed at the sun. Since a spiral transfer will require constant sun-pointing, the potential complexity (in the form of independently articulating structures with high-accuracy pointing[54]) appears to rule out such an approach.

Furthermore, ruling out liquid hydrogen as a potential propellant—due to the host satellite's severe volumetric constraints, and the complexity of systems required to maintain it as a liquid—makes a spiral transfer strategy even less attractive. By foregoing H_2's high potential I_{sp}, and requiring the use of moderate molecular weight, storable propellants (NH_3, N_2H_4, or H_2O), the author is limited to specific impulses in the 400 s range. While relatively high, this is only 25% higher than conventional bipropellant systems—logical competitors for any fielded STP engine. Spiral transfer strategies will incur substantial delta-V penalties,[55] which, at these moderate specific impulses, cause the STP system to underperform relative to bipropellant N_2H_4/N_2O_4. These factors combine to necessitate the choice of a *multi-impulse transfer strategy*.

The second trade involves the selection of a thermal energy transfer mode to the propellant. There are two potential options available: direct gain and thermal storage. In the previous paragraph, the author has noted the principal objection to a direct-gain system, namely the requirement for a potentially expensive and complex set of articulating concentrators. A second pitfall is the low thrust power P (= ½ Tu_e) available with direct-gain systems; since the direct-gain solar thermal engine can only transfer as much incident solar radiation as falls on its concentrator surfaces, thrust power is limited to array input. This is not true of thermal storage systems, which take in energy over a longer period and can exhaust it at whatever power level is required, given the constraints of the design.

For comparison, the 30-cm mirror in Fig. 3.2 is assumed to impart 77 W of solar power to the engine's receiver. Were that receiver to be used in direct-gain mode, maximum thrust would be limited to 39 mN. This is on the order of electric propulsion systems proposed for small satellites; any transfer time advantage associated with using STP would be lost. In a thermal storage system, the receiver is heated over a specified period (in this case, 2.7 hrs.) and the actual firing conducted over just 428 s. The thrust level in this instance is 1,000 mN—25 times the direct-gain thrust.

The need to provide independently pointing concentrators, coupled with little if any mission advantage, points to the selection of a *thermal storage heat transfer approach*.

The author has ruled out concentrator articulation as an approach that is likely to be too expensive to implement aboard a small satellite. A key advantage to articulation is the decoupling of spacecraft power production and solar thermal engine pointing requirements—which will conflict if a non-articulating (fixed to satellite) concentrator is selected. Body-mounted photovoltaic arrays will receive little if any incident sunlight during the “charging period” for the solar thermal engine, since the vehicle will be required to point the concentrator at the sun. This could be resolved through provisions for additional battery power (to allow the satellite to ride out the artificial eclipse conditions), canted body panels, or a deployable panel (or panels) for power production during engine thermal charging.

---

[54] Pointing accuracies are likely to fall in the range of 0.1-0.25 degrees. This will be discussed in detail, later in this chapter.

The selection of a rigid, fixed concentrator—as opposed to inflatable and deployable[56] designs—is primarily driven by technical risk and cost. A rigid, fixed concentrator, mounted to one face of a microsatellite, is the simplest solution, with existing technologies (e.g., space telescope optics) providing substantial guidance for implementation. [Kasl, 1997] Deployable or inflatable optics allow for larger surfaces (and thus higher power input) and lighter structures, at higher complexity and cost. A notional mounting methodology is depicted in Figure 4-4 and Figure **4-5**. Selecting the rigid, fixed approach permits the satellite designer to preserve a known spacecraft structural configuration, prior to launch. A single mechanical configuration should also reduce test requirements.[57]

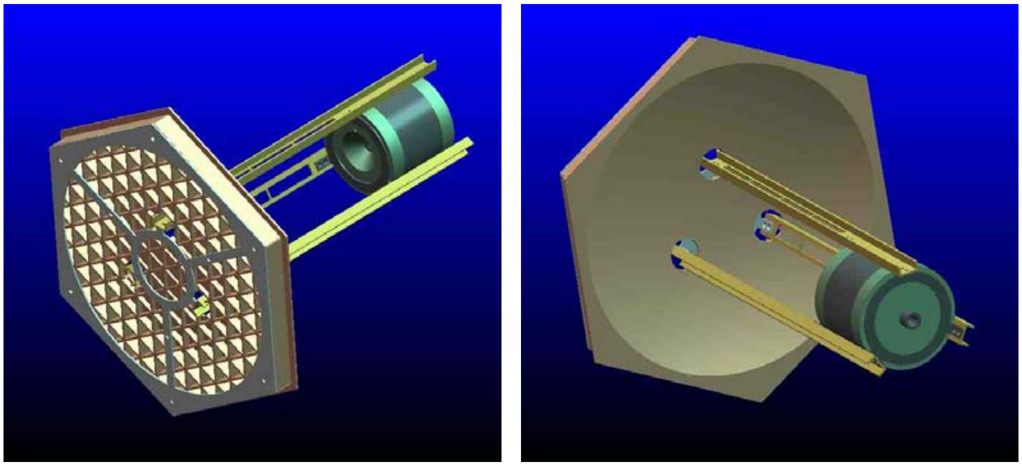

Notional solar thermal engine structural configuration. 30 cm mirror, 428 N-s receiver.

Solar thermal engine configuration, showing structural element pass-throughs in mirror.

Figure 4-4 Solar thermal engine configuration.

---

[55] Roughly a 40% increase in delta-V, for LEO-to-GEO transfers. Appendix B provides additional details.

[56] This must be distinguished from *articulating*. A *deployable* system will move—once.

[57] Although this approach might complicate satellite thermal management, as it will shadow the satellite during any thermal charging period. This might require additional power for electrical heaters, for systems susceptible to degradation as a result of temperature swings.

Additional top-level trades include the selection of a propellant (N_2H_4 being the nominal front-runner due to its high DI_{sp}), thermal storage receiver material selection, concentrator material and configuration selection, propellant feed system approach (blowdown or regulated), and the specific implications of these choices for testing and mission operations. These will be elaborated on throughout the remainder of this chapter.

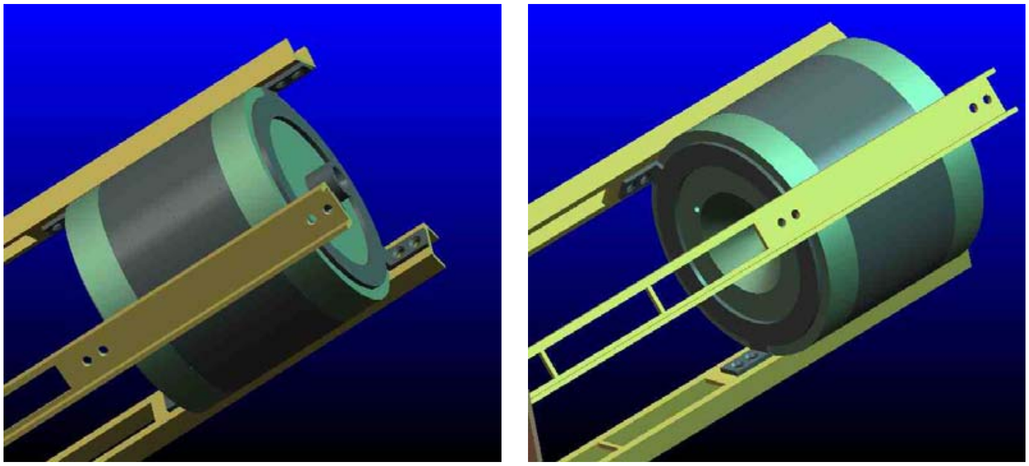

Detail of receiver body ring mount, showing aft receiver face and nozzle

Detail of receiver body ring mount, showing slotted "C" bar elements and fore receiver face

Figure 4-5 Solar thermal engine, receiver mounting detail.

4.3 Concentrator Array Design

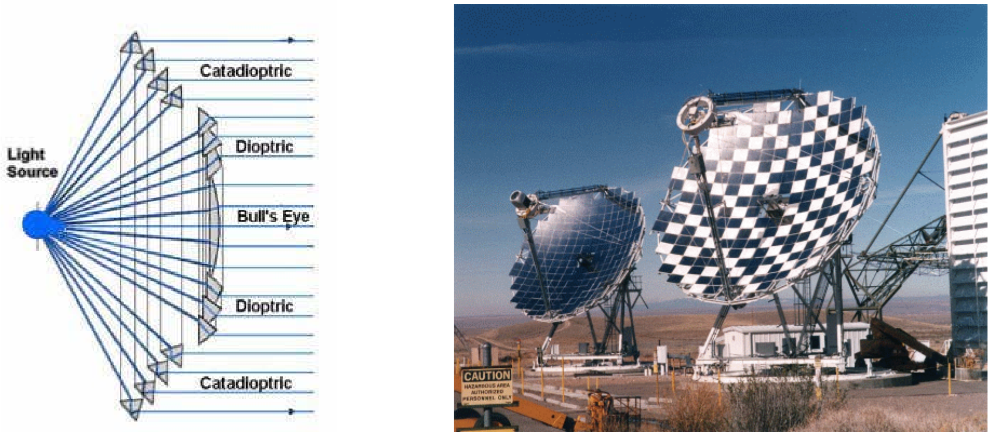

Fresnel lens schematic for lighthouse applications [Amass, 2000]

Large parabolic dish concentrators for terrestrial solar thermal energy production at JPL's Edwards Parabolic Dish Test Site [U. Missouri, 2002]

Figure 4-6 Fresnel lens and paraboloidal concentrators.

Several types of concentrator optics (Figure 4-6) theoretically permit a space-based solar thermal engine to achieve high concentration and, as a result, high propellant temperatures. These include parabolic point-focus dishes, spherical dishes, and Fresnel lenses or mirrors. Fresnel lenses, named for the French physicist Augustine Fresnel (1788-1827), are multiple-element optical systems that collimate light from a central source, or conversely, focus parallel rays from a distant source at a focal point [New Brunswick Lighthouses, 2001]. While Fresnel lenses can be produced inexpensively from lightweight plastic, they suffer from chromatic aberration; sunlight, which has a large wavelength distribution, is refracted at different angles according to the lens material index of refraction *(n)*. This limits its concentration ratio *(C)* to roughly 1,000 [Kreider, 1979].[58] Fresnel mirrors are composed of independently targetable segments that focus light on a central receiver; this is practical for terrestrial systems but overly complex for this application.

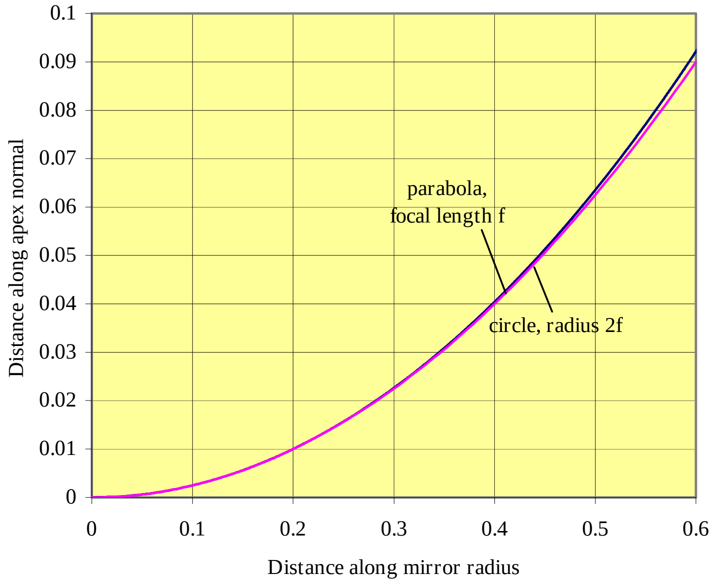

Figure 4-7 Parabolic and spherical mirror profiles, indicating increasing divergence for larger radii (lower f-number). The parabolic mirror has a focal length (f) of unity; the spherical mirror's radius of curvature is 2f = 2.

Spherical concentrators approximate parabolic systems, are easier and less expensive to construct than their aspheric counterparts, but themselves suffer from spherical aberration—rays from the outer edges of such a mirror will focus not at a point, but along a line [Pedrotti, 1993]. Without augmentation, they are capable of C values approaching 150 [Kreider, 1979]. Such mirrors can be constructed by hand: Amateur astronomers figure and polish glass substrates and apply reflective coatings to dishes of 30-50 cm diameter and even greater. Due to their relative ease of fabrication, mirrors with spherical curvature were among the first optical elements used in telescopes. For focal length-to-mirror diameter ratios greater than ~10, a spherical surface approximates the parabolic surface when the circle's radius is twice the parabola's focal length (Figure 4-7).[59]

---

[58] We will use different definitions for concentration ratio throughout this section. Here, we define *C* as the ratio of concentrator area to the area of the focused "spot" at the receiver, assuming that the spot encompasses all sunlight incident on the concentrator. Later we will define a geometric concentration ratio C_g that is dependent only on the areas of the concentrator and receiver.

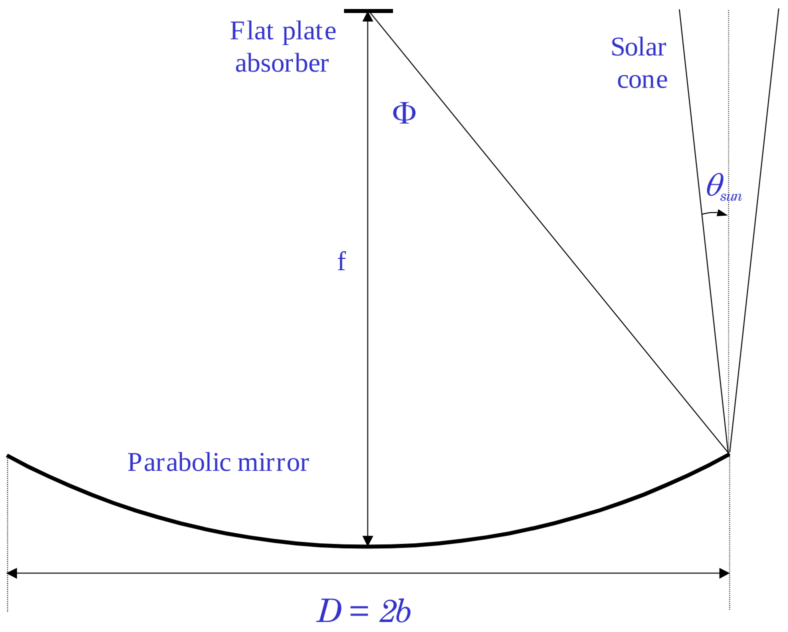

Figure 4-8 Key specifications for a parabolic point-focus mirror[60]

---

[59] One can confirm this by equating the slopes of parabolic (focal length = f) and spherical curves (radius = r) and assuming small values for maximum rim-to-mirror apex separation (z). For sufficiently high *f-numbers* (~f/10), the difference in z at the respective rims of a parabolic and spherical mirror is somewhat less than a quarter-wavelength of visible light (the human eye's maximum sensitivity occurs for $\lambda = 550$ nm [Pedrotti, 1993]). The quarter-wavelength rule is often used to define a threshold for quality telescopic optics—an RMS wavefront error of $\lambda/4$ (see Footnote 5), averaged over the mirror's surface, is considered sufficiently accurate that the optics are *diffraction-limited*—limited only by the wave nature of the incident light, and not by imperfections in the optical surface itself [Hecht, 1998].

[60] Mirror diameter D and focal length f are related through the optical element's *f-number* (f/#), where $f/\# = f/D$. For a parabolic mirror, the rim angle Φ is a somewhat more complicated function of f and D. A mirror with a rim angle of 30 degrees possesses an *f-number* of f/.933. This is an extremely "steep" optical surface, relative to commonly manufactured telescope optics, which are most often found in the range of f/4 to f/10 [Apogee, 2002]. These shallower parabolic mirrors are not useful for concentrating sunlight, due to the small rim angles and lower concentration ratios available for exploitation. Since spherical mirrors only approximate parabolic mirrors for higher *f-numbers* ($\geq f/10$), they are poor candidates for this application.

Parabolic point-focus mirrors (Figure 4-8) allow the highest concentrations, with local *C* approaching the thermodynamic limit. Of course, being neither spherical nor refracting elements, they do not suffer from either spherical or chromatic aberrations. Hottel [1967] has shown that the maximum achievable concentration ratio is defined by:

$$C_{\max} = \frac{n}{\sin^2 \theta_{sun}} \tag{4-9}$$

Here, θ_{sun} is the sun's subtended half-angle (0.25°) and *n* is the ambient index of refraction. For a flat absorber—or, alternatively, a thermal storage cavity aperture—an ideal concentrator of rim angle Φ may achieve concentration ratios equivalent to [Kreider, 1979]:

$$C_{\max,flat} = \frac{\sin^2 \Phi \cos^2\left(\Phi + \theta_{sun}\right)}{\sin^2 \theta_{sun}} \tag{4-10}$$

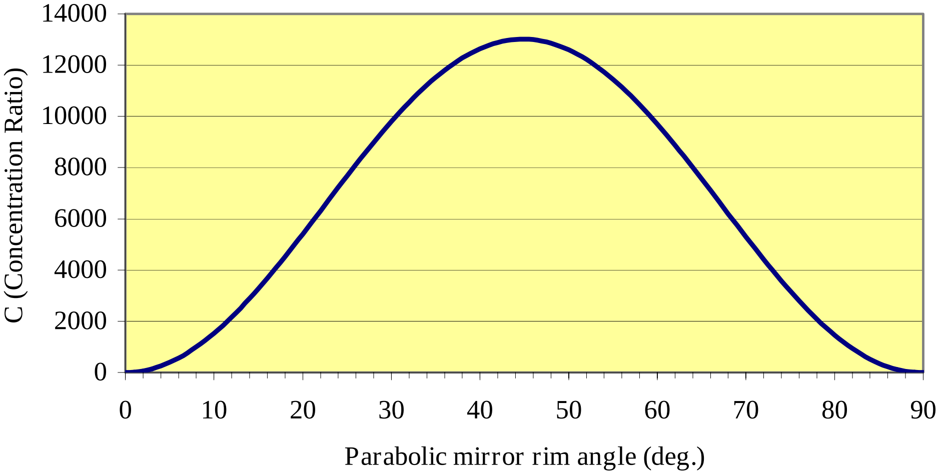

Figure 4-9 Parabolic point-focus mirror concentration versus rim angle Φ

Thus, while a *C* value of 52,000 is theoretically achievable (i.e., does not violate thermodynamic principles), the specific geometry of the parabolic mirror and receiver will limit practical *C* values. For instance, given a rim angle of 30°, the practical limit is 9,800. *C* reaches a maximum at Φ = 45°, where $C_{\max,flat}$ = .25 and $C_{\max}$ ~ 13,000. Kreider's equation represents a global value: It assumes that the flat plate receiver is sized to absorb (or admit) all light incident upon the parabolic mirror—thus, for very small values (~ 0°) and very large values (~ 90°) of Φ, the receiver aperture and parabolic mirror areas approach one another, and *C* approaches unity (Figure 4-9). Local concentration ratios for high-Φ dishes can be substantially higher, in some cases reaching an appreciable fraction of the thermodynamic limit [Jaffe, 1989][Kreider, 1979].

The parabolic mirror can be constructed from a wide variety of materials, including glass (e.g., Zerodur®, Pyrex® , etc.), metals[61], composites, and ceramics. Given the severe mass constraints imposed by small satellites, mirror areal density (kg/m^2) becomes an important figure of merit. Low thermal-expansion glass is perhaps the most commonly used material in amateur astronomy, although it is difficult to form minimum-thickness elements [Baker, 2002] due to distortion resulting from residual stress buildup in the optic. This results in relatively high areal densities.

Metal optics can be machined directly from blanks. Metal machining clearly offers significant heritage. Single-point diamond turning can produce RMS wavefront errors[62] of $\lambda/2$ (for a visible wavelength of 550 nm) and a microroughness[63] of 3 nm [Miller, 2000]. The author has investigated the procurement of a 30-cm diameter *f*/0.93 aluminum mirror from an American optical manufacturing vendor. A preliminary quote of $2,500 (£1,700) was obtained; however, this does not include additional costs associated with "lightweighting," (i.e., removal of excess backing material) coating, polishing, or allowances for mechanical attachments. Such a mirror—with .25-mm isogrid backing—would be 2.4 cm in thickness and mass 1.7 kg (24 kg/m^2). This compares favourably with highly lightweighted glass systems (e.g., Hextek's 18-in. (45.7 cm), 11.4 lb. (5.2 kg) Gas-Fusion™ mirror, at 32 kg/m^2) [Hextek, 2000].

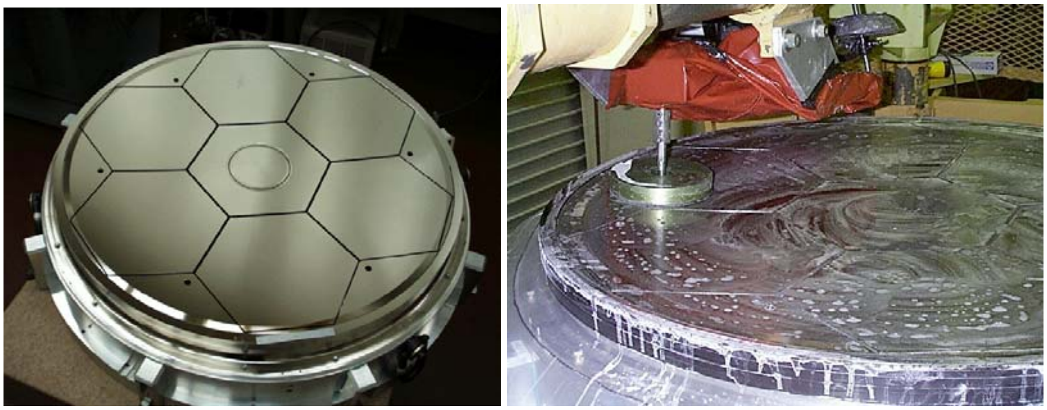

Initial figuring of the DCATT primary (T6061 Al)

DCATT primary mirror undergoing machine polishing

Figure 4-10 Developmental Comparative Active Telescope Testbed (DCATT) mirror fabrication.

---

[61] A good recent example of the use of metal optics in advanced applications is NASA Goddard Space Flight Center's Developmental Cryogenic Active Telescope Testbed (DCATT), which used a 90-cm segmented primary mirror constructed from diamond-turned T6061 aluminum. The mirror face was coated with nickel and polished (Figure 4-10). [Davila, 1998][DCATT web site, 2000]

[62] Root-mean-square (RMS) wavefront error is a global measure of quality for a specific optical element. The element's deviation from a parabolic ideal is measured for a variety of points across the surface of the mirror, and those data points are averaged to provide an RMS wavefront error figure.

[63] A measure of surface roughness, related to the optical element's *specularity*. The smaller the microroughness, the less diffuse (more specular) the reflection of light at the mirror surface. This results in higher image clarity in telescope systems.

Ceramics, such as SiC or C/SiC, have already been used in space-based telescope applications. ESA's Herschel far-infrared telescope—with a 3.5-meter SiC primary mirror (Figure 4-11, left), constructed from brazed segments—is slated for launch in 2007. [Pilbratt, 2001] Ultramet, an advanced materials vendor based in Pacoima, California, has fabricated "open-cell" mirror SiC test coupons at advertised areal densities of 10 kg/m^2. [Ultramet, 2001]. Despite their promise, these materials can still be considered "advanced," with relatively immature processes and high fabrication costs [Baker, 2002].

Composite Optics, Inc., a San Diego-based vendor of advanced structures for space applications, produced a 2.0-m, 35-kg. far-infrared demonstrator mirror for the FIRST (Far Infrared and Submillimeter Space Telescope, later Herschel) mission (Figure 4-11, right). The element—constructed from carbon fiber-reinforced polymer—has an areal density of 11 kg/m^2. The addition of carbon fibers to a polymer substrate permits control of the matrix material's coefficient of thermal expansion, which can be reduced to essentially zero. COI claims an RMS wavefront error of 2.1 μm. [COI, 2000]

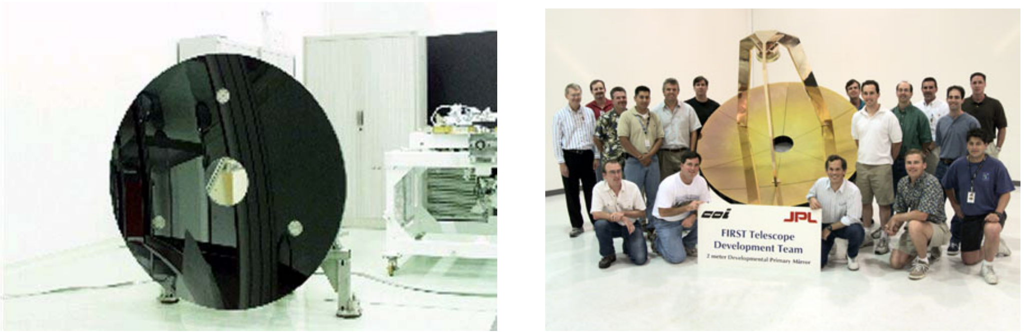

1.35-m SiC demonstrator mirror for Herschel telescope [Herschel web site]

2.0-m, 77-lb. (35 kg.) carbon fiber-reinforced polymer mirror [COI web site]

Figure 4-11 Herschel advanced technology mirror elements.

Plastic optics—machined from hard polymethyl methacrylate (PMMA), polycarbonate (PC), or polystyrene (PS)—would, in principle, allow for very low areal densities. PMMA and PC have specific gravities of 1.1-1.25 g/cm^3. While commonly available, easy to machine, and low-cost, plastics have poor thermal conductivity ($\leq$ 0.2 W/m/K), low stiffness, and high coefficients of thermal expansion relative to candidate reflective coatings (e.g., aluminium, nickel). These properties are a likely source of optical errors, due to (1) preferential expansion of a given sector of the plastic mirror ("warpage"), or (2) cracking of coatings due to CTE mismatch.

Based on the above data, the author has selected a machined metal optic for the baseline (preliminary) concentrator design, based primarily on long-established, widely-available machining and polishing capabilities, moderate areal densities, and low substrate material cost. Highly polished, protected aluminium provides reflectivities of roughly 90% through the visible spectrum. Other surface coating options include nickel, silver, and rhodium.[64] Mirror diameters of 60 cm are preferred, as they will conform to SSTL enhanced microsatellite volume constraints. To achieve near-maximum concentration ratios (C) of 10,000 or greater, as well as to minimize engine dimensions, the focal length of the optic must fall within the range 30 cm $< f <$ 60 cm, corresponding to f-numbers of $f/0.93$ to $f/0.6$ and Φ values of 30º to 45º. Faster (small integer or fractional f-number) mirrors will be steeper and may pose fabrication problems.[65] As depicted in Figure 4-12, C is maximized for a flat-plate receiver at $\Phi = 45^\circ$ ($f/0.6$).

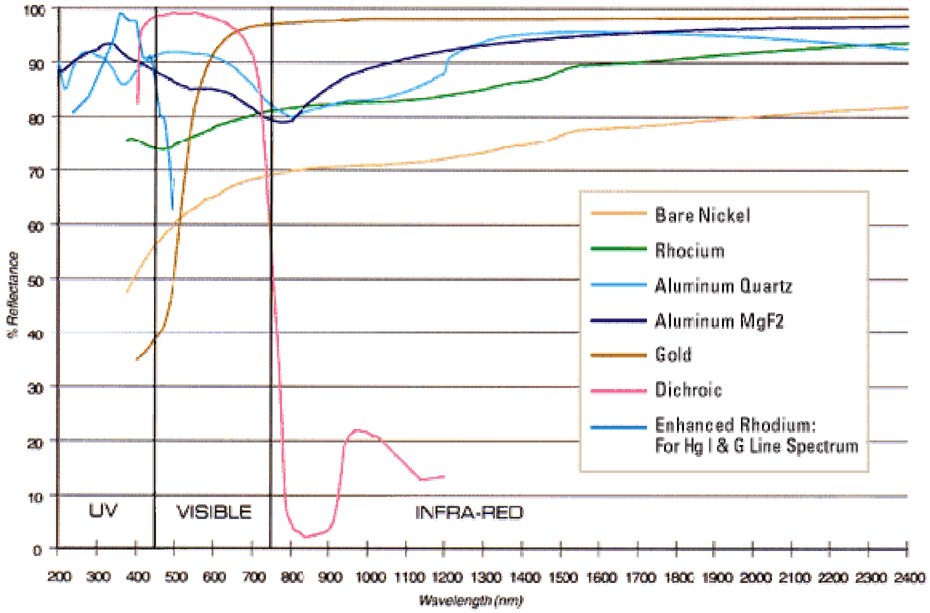

Figure 4-12 Specular reflectance of various optical coating materials for light at wavelengths of 200 nm $\leq \lambda \leq$ 2,400 nm [Optiforms, 2001]

Figure 4-13 shows notional Solid Edge models of a thin (2.5 mm) aluminium concentrator. The hexagonal backing structure is 36.95 cm across, vertex to vertex; total weight is roughly 1.7 kg (24 kg/m^2). No mounting locations are shown in this view. Given an optical efficiency of 0.8

---

[64] Nickel is often selected due to its hardness and resistance to scratching during normal handling, at reduced reflectivities relative to aluminium; however, nickel possesses a CTE value which is approximately half that of its aluminium substrate. Silver offers very high reflectivities but is susceptible to tarnishing and is extremely soft. Rhodium is hard, with higher reflectivity than nickel.

[65] E.g., NASA Goddard is exploring "superpolishing" of aluminium optics to very small surface roughnesses—as little as 0.8 nm RMS. [Content, 2001] However, Goddard's experience is only with aspheres slower than $f/3$, unsuitable for this application. Additional effort would be required to achieve superpolished, fractional f-number aluminium optics.

(including a reflectance of 0.9), this mirror should be capable of relaying approximately 77 W of solar input into an appropriately designed receiver.[66]

Figure 4-14 illustrates a larger concentrator assembly, 57.6 cm in diameter, with an alternate (sparser web) backing structure composed of 5 mm-thick ribs and torsion rings. This mirror is *f*/0.6 ($\Phi = 45^{\circ}$), masses 6 kg (23 kg/m^2), and has its central section removed to facilitate placement on the nadir face of a microsatellite.[67] This mirror's estimated power input, at an optical efficiency of 0.8—not accounting for the central hole—is 282 W.

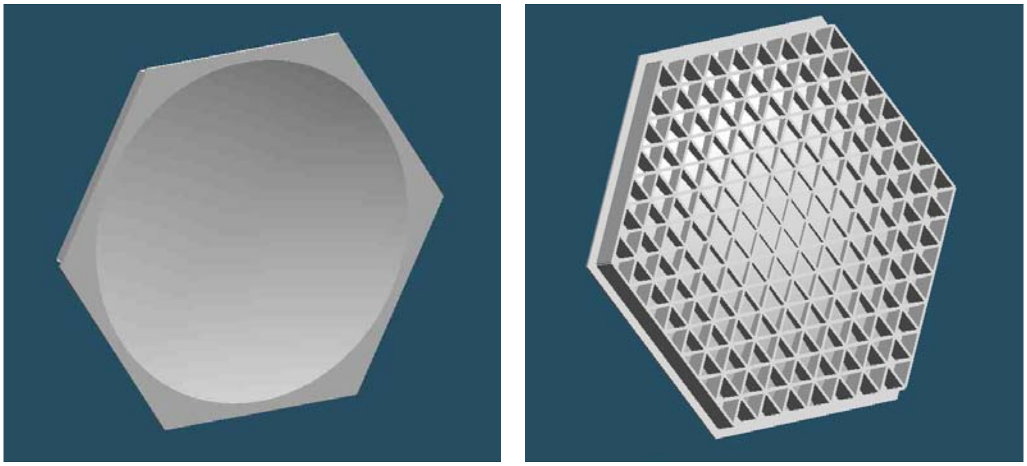

30-cm f/1 concentrator, aluminium substrate

Rear face of 30-cm f/1 concentrator, 2.5 mm isogrid back

Figure 4-13 30-cm f/1 concentrating mirror.

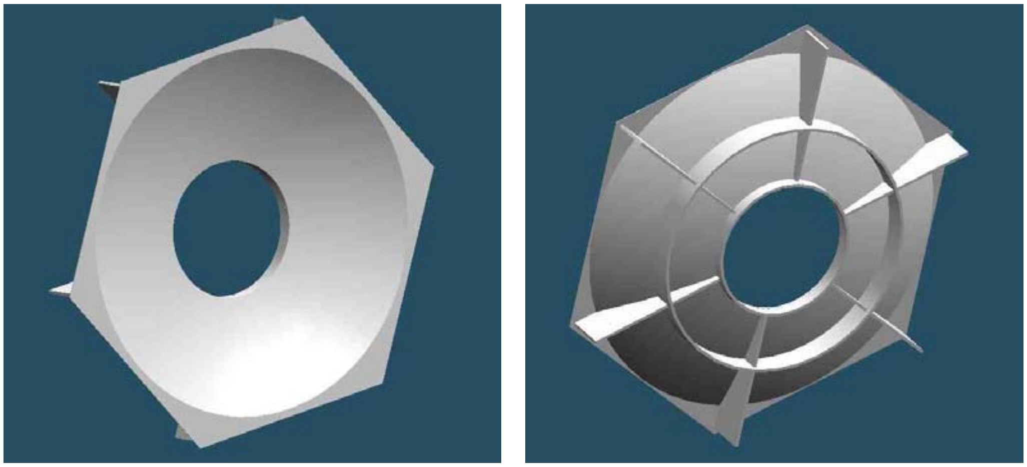

---

[66] There is a ~10 W loss due to the central obscuration of the receiver. The target input for this system (100 W) can be met by increasing the mirror diameter from 30 to 34 cm.

[67] This is very nearly the largest mirror that can be accommodated by the Ariane 5 ASAP's volumetric requirements (60 cm x 60 cm footprint) without a waiver. The receiver body would hang through the central hole, inside the microsatellite adapter ring. The receiver would mount directly to the satellite's nadir face panel itself, or to an intermediate mounting ring on the face panel.

57.6-cm f/.52 concentrator, aluminium substrate

Rear face of 57.6-cm f/.52 mirror, rib and ring backing

Figure 4-14 57.6-cm f/.52 concentrating mirror.

As will be seen later in Section 4.6, the decision to use rigid metal optics (rather than low areal density ceramic or carbon fibre systems) incurs a serious weight penalty. A lightweighted, 79-cm diameter aluminium optic, constructed at a highly optimistic areal density of 20 kg/m^2, would still mass almost 11 kilograms. An alternative concentration scheme, discussed in Chapter 2, would replace the single, large metal mirror with multiple smaller mirrors. This would be achieved through the concatenation of focused sunlight via low-attenuation optical fibres [Feuermann, 1999][Cariou, 1985]. This approach, first broached by Kato and Nakamura for terrestrial solar thermal applications, has been made feasible in the intervening three decades by advances in optical fibre processing. Fibre light attenuation results partially from impurities in the base fibre material and partially from flaws in processing. In the 1970s, Kato [1976] speculated on the use of fused-silica and soda-lime-silicate (SLS) glass fibres for passing visible wavelengths (λ = 200-1,000 nm), noting, "…the transmission of more than 80% of solar radiation over [a] length of about 40 metres is possible…using fused-silica core optical fibres." Due to spectral shift of the incident light towards the infrared—and preferential absorption of specific wavelengths—energy dissipation falls away rapidly after the first few metres; the "surviving" flux encounters reduced absorption over the remaining length of fibre. Thus, while a straight-line extrapolation of the 80% figure would lead one to estimate a per-kilometre transmission of just 0.3% (-25 dB/km), Nakamura demonstrates that the figure is much closer to 20% (-7 dB/km). This is in line with current state-of-the-art [Polymicro, 2004].

Assuming fibre transmission efficiencies of 80%, a single 57.6-cm mirror can be replaced by ten 20-cm mirrors. Both Lee [1998] and Ashby [1980] note that space mirror mass m_m tends to scale nonlinearly with diameter D_m. Lee suggests the relation $m_m = f(D_m^{2.7})$, while Ashby is more conservative, using the relation $m_m = f(D_m^4)$. A 20-cm mirror would therefore mass between 1.5 and 6% that of a 57.6-cm mirror.[68] Since intercepted area scales with the square of diameter, multiple small mirrors should save significant mass.

---

[68] Each of the ten 20-cm diameter mirrors are predicted to mass 360 grams, for a total mass of 3.6 kg. This represents a 40% weight savings over the larger mirror the ganged assembly replaces. Twenty mirrors of this diameter could be substituted for the large (79-cm) concentrator discussed at the end of the chapter, saving almost 4 kilograms (35%).

4.3.1 Concentrator Array Pointing Error

Bendt and Rabl [1981] provide a useful framework for analysing the optical performance of a parabolic dish concentrator. Given "perfect" (i.e., zero slope error) optics, an angular acceptance function, f(θ), can be derived which represents the fraction of incident light at zenith angle θ reaching a receiver aperture of pre-determined size (Figure 4-15). For point-focus concentrators, θ is small—permitting the approximation sin θ = θ.

An arbitrary point *P* on the dish can be defined in the coordinate system:

$$P = \left(\rho, \alpha, z = \frac{\rho^2}{4} \right) \tag{4-11}$$

Here, *a* is the receiver radius and *b* the dish radius. A local rim angle ϕ is also defined; ϕ reaches its maximum ($\phi = \phi_{max} = \Phi$) at the dish's rim. A ray incident at *P*, with zenith angle θ and azimuth angle ψ, defines a point acceptance function:

$f_p(\theta,\psi,\rho,\alpha) = 1$, *if the incident ray reaches the receiver*

$= 0$, *if the ray misses the receiver*

Integration of this function over, and subsequent division by, the dish area—provides an average angular acceptance over the entire aperture. After introducing a new angle β = ψ – α, Bendt and Rabl note that, due to azimuthal symmetry, angular acceptance is not dependent on ψ (i.e., f(θ,ψ) = f(θ)). They continue:

> "The function f_p was defined with respect to radiation incident on the receiver. However, reversing the direction of the rays does not change the path. Hence one can treat the receiver as an emitter and ask whether any ray originating from the receiver and reflected at P leaves the aperture in the direction (θ, β). The answer is
>
> $f_p(\theta,\beta,\rho,\alpha) = 1$, if yes
>
> $= 0$, if no
>
> Because of azimuthal symmetry, it is sufficient to evaluate fp(θ,β,ρ,α) only on one radius line, α = 0…" [Bendt, 1981]

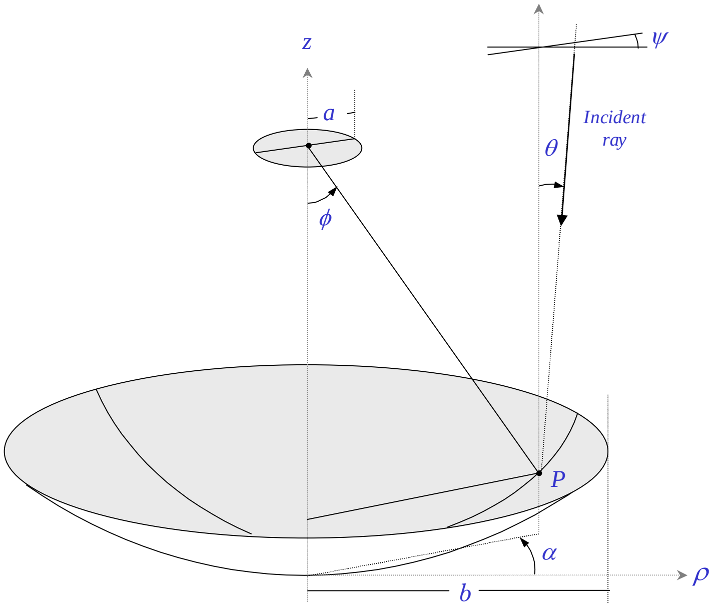

Figure 4-15 Parabolic dish reflector

For a flat plate or cavity receiver, rays emerging from the receiver and reflecting at *P* form an elliptical cone defined by two critical angles, θ_s and θ_l. These are the angular minor and major axes of the elliptical cone, and can be determined from the dish geometry to be:

$$\theta_s = \frac{a}{1+z}\cos\phi \quad \textbf{and} \quad \theta_l = \frac{a}{1+z} \qquad \textbf{(4-12,-13)}$$

If we note that (1) we can minimize θ_s by substituting $z_{max} = b^2/4$ and $\phi_{max} = \Phi$, and (2) maximize θ_l through the substitution of $z_{min} = 0$, some additional algebraic manipulation and the application of trigonometric identities produces the following:

$$\theta_{s,\min} = \frac{a}{b}\sin\Phi\cos\Phi = \frac{\sin\Phi\cos\Phi}{\sqrt{C_g}}\text{, and} \qquad \textbf{(4-14)}$$

$$\theta_{l,\max} = a = \frac{b}{\sqrt{C_g}} = \frac{2}{\sqrt{C_g}}\tan\frac{\Phi}{2} \qquad \textbf{(4-15)}$$

C_g, the geometric concentration ratio discussed previously, is equal to b^2/a^2. The smaller of these, $\theta_{s,min}$, defines the boundary of the parabolic dish's *unity acceptance region*. For $\theta \leq \theta_{s,min}$, all incident rays will reach the receiver. This implies that, if any part of the solar disk lies within $\theta_{s,min}$ of the dish's zenith, the whole of that portion of the sun's incident radiation will reach the aperture. The larger angle, $\theta_{l,max}$, defines the boundary between a *fractional acceptance region*—

where some, but not all, of the incident energy reaches the receiver, and the *zero acceptance region*.

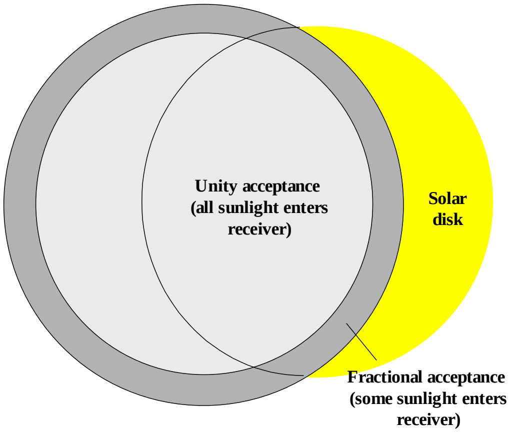
Unity acceptance (all sunlight enters receiver)
Solar disk
Fractional acceptance (some sunlight enters receiver)

Figure 4-16 Intersection of parabolic dish acceptance regions and the solar disk. Light and dark gray areas represent the boundaries of the unity ($\theta = \theta_{s,min}$) and fractional ($\theta = \theta_{l,max}$) acceptance regions.

The balance of Bendt and Rabl's effort is directed towards precise calculation of $f(\theta)$ in the fractional acceptance region ($\theta_{s,min} \leq \theta \leq \theta_{l,max}$)—which, as they note, is not susceptible to analytic determination.[69] To simplify, the author will take the average value of $f(\theta)$ within the fractional acceptance region to be approximately 0.5.For a given geometric concentration ratio C_g and dish rim angle Φ, the angles $\theta_{s,min}$ and $\theta_{l,max}$ define two concentric circles centred on the dish's zenith. The intersection of these circles and the solar disk results in incident radiation reaching the receiver (Figure 4-16).

The author has assumed a "pillbox" or flat solar intensity profile (no degradation towards the periphery). Further, the author has assumed an apparent solar diameter of .53°—slightly larger than Kreider [1979]. For a given separation distance, the common area of the three circles can be calculated, and, combined with the pillbox and fractional acceptance average value assumptions, total incident sunlight can be determined.[70] For a parabolic dish with rim angle $\Phi = 30^o$ and a concentration ratio of 10,000—very close to the theoretical maximum for this Φ [Feuermann, 1999]—the author has plotted the incident radiation (in suns) versus concentrator misalignment or off-pointing angle θ (Figure 4-17). Note that, even for perfect alignment (θ = 0º), the received radiation is only .93 suns—this is a consequence of the specific choices of Φ and desired C_g.[71] For the selected values, the solar disk is slightly larger than the unity acceptance circle but smaller than the fractional acceptance circle, so a portion of the sun's energy, incident from its rim, does not intercept the receiver. Increasing Φ to 45º increases intercepted input to ~0.9 suns at a 0.1º offset (

---

[69] When combined with certain assumptions regarding both optical errors and the source (e.g., the Sun), an intercept factor, defined as the fraction of the incident flux intercepted at the receiver, can be calculated. [Bendt, 1981]

[70] The area of two overlapping circles can be calculated from the following equation, where r and R are the radii of the circles, and d is the separation distance between the two circles' centres [Weisstein, 1999]:

Figure **4-18**).[72]

An energy balance, equating incident sunlight for a given tracking error θ, with estimated losses (aperture re-radiation, radiation losses through the insulation package, convective losses during testing in air), should provide a maximum achievable receiver temperature and, consequently, maximum engine specific impulse. The author's Cavity Heat Up Sequence (CHUPS) Visual Basic code, described in the next section, addresses these issues—maximum achievable receiver temperature appears to be fall in the range of 2,400-2,500 K for threshold charging times.[73]

$$A = r^2 \cos^{-1}\left(\frac{d^2 + r^2 - R^2}{2dr}\right) + R^2 \cos^{-1}\left(\frac{d^2 + R^2 - r^2}{2dR}\right) - \frac{1}{2}\sqrt{(-d + r + R)(d + r - R)(d - r + R)(d + r + R)} \tag{4-16}$$

[71] Selection of a smaller C_g (say, 5,000) would allow interception of all incident sunlight at perfect alignment, but would result in a larger receiver aperture, higher re-radiation, and lower achievable temperatures. A better alternative is a larger Φ (Fig. 3.9)

[72] Combined with an aluminium optic's reflectivity of ~0.9, selecting a maximum offset angle of 0.1 degrees (for Φ = 45 deg., C_g = 10,000) provides a net optical efficiency (solar input into receiver divided by solar input into concentrator) of ~0.8.

[73] That is, the time required to heat the receiver from its nominal "hot start" temperature (863 K for an engine using hydrazine's ultimate decomposition products, nitrogen and hydrogen) to its maximum temperature.

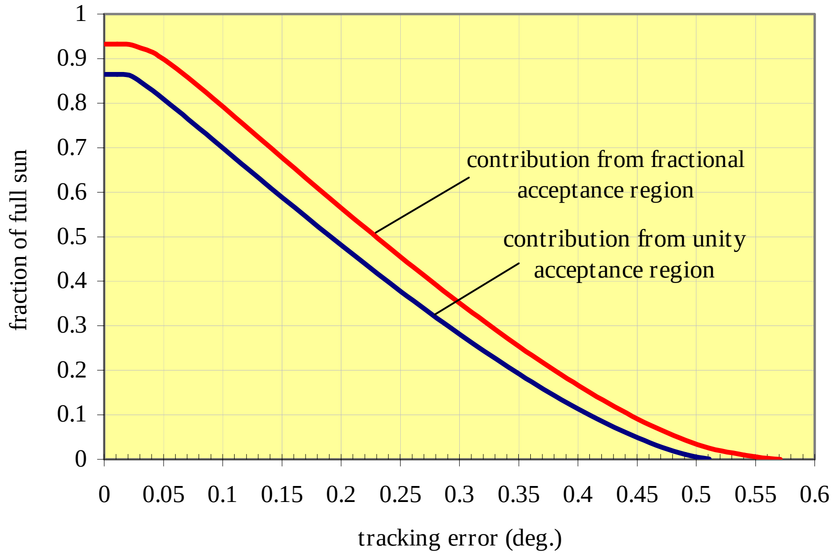

Figure 4-17 Incident sunlight reaching the receiver aperture, in suns, versus parabolic dish tracking error. $\Phi = 30^o$, $C_g = 10,000$.

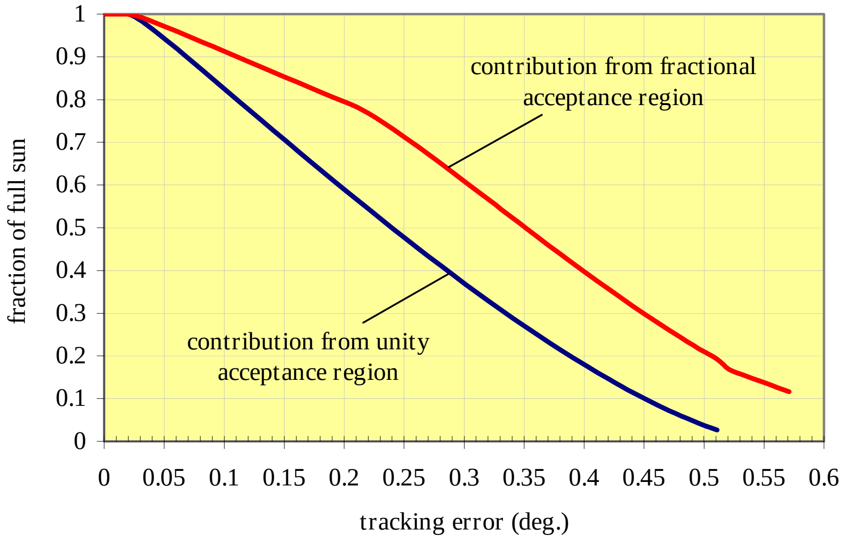

Figure 4-18 Incident sunlight versus parabolic dish tracking error. $\Phi = 45^o$, $C_g = 10,000$.

4.4 Receiver Design

The solar thermal propulsion receiver is a high-temperature heat exchanger, imparting concentrated radiant energy to a propellant. Two types of receivers—*direct-gain* and *thermal storage*—have been proposed for use in solar thermal power and propulsion systems. Until fairly recently, virtually all of the options considered for propulsion were “direct-gain,” i.e., systems that transfer solar energy directly to a propellant, via solid wall heating [Shoji, 1985] or through various windowed, seeded-bed or porous wall approaches [Shoji, 1986]. Direct-gain systems are constrained by the power input of the system’s concentrator, since no energy is stored. This not only constrains available thrust but demands sun-pointing while manoeuvring. This dictates articulating, deployable concentrator arrays with an independent pointing capability. While complicating the concentrator design, direct-gain systems permit, in principle, relatively simple, lightweight receiver designs; the system is heated to temperature only during thrusting, permitting the propellant to act as a natural coolant along problematic conductive thermal paths such as propellant lines.

Thermal storage systems, while investigated for space solar dynamic power applications [NASA GRC, 2000], have only recently been considered for onboard propulsion. The Integrated Solar Upper Stage and Solar Orbit Transfer Vehicle [Frye, 1998][Partch, 1999] concepts both employ thermal storage to decouple thrusting and sun pointing, increasing available thrust levels and thus reducing orbit transfer times. Implementation of the receiver is complicated by the need for insulation as well as thermal dams along likely leak paths, not to mention higher overall weight (owing to the use of thermal storage material). There are several options available for thermal storage:

> *Sensible heat* storage, which uses the heat capacity of a single-phase material such as graphite (C_p = 2.09 kJ/kg K at 20 ºC [Lienhard, 1987]) to store incident heat across a wide temperature range;
>
> *Phase change* or *latent heat* storage, which offers the attractive possibility of extremely high energy density, such as lithium fluoride (h_f = 1.05 MJ/kg at its melting point of 1121 K [Pletka, 1998]). NASA’s Glenn Research Center examined the use of a eutectic salt (LiF/CaF_2) for thermal storage. Elemental boron, which melts at 2348 K, possesses an h_f of 4.65 MJ/kg. Elemental silicon melts at 1687 K and possesses an h_f of 1.79 MJ/kg. [Lide, 1995]
>
> *Thermochemical* storage offers “…high energy density in the storage medium…” combined with room-temperature storage capability [Claasen, 1980]. The reaction must be reversible, and, to minimize mass, the heat of reaction must be substantial. Claasen indicates that the following reaction is promising, representing approximately 1.23 MJ/kg of thermal storage:

$$2SO_2 + O_2 \rightarrow 2SO_3 + 98.3\text{ kJ/mol}$$

The author has selected a sensible heat storage system due to its relative simplicity of design and moderate but acceptable performance levels. Over a 500-degree temperature range, sensible heat thermal storage in graphite represents approximately 1.05 MJ/kg. This is nearly on a par with phase change or thermochemical storage. While the latter two modes offer the possibility of very high energy densities (and very small receivers), they incur substantial difficulties. Phase change systems suffer from containment structure bursting and void formation [Kerslake, 1993]. Thermochemical storage presents the problem of containment of the separated products, as well as selection of appropriate catalysts for the reversible reactions of interest.

4.4.1 Thermal Storage Media

A material selection matrix (Table 4-2) provides insight into materials that might be used for a sensible heat storage receiver. Key factors include high specific heat, high melting point, low thermal expansion in the temperature range of interest, and high thermal conductivity. Thermal conductivities are typically given at or near 273.15 K (0 ºC). Coefficients of thermal expansion are given at the highest temperature range for which data is available. The product $\rho C_p T_m$ is provided as a useful figure of merit, as it represents a characterisic material energy density. Several high-temperature elements—both metallic and metalloid—are considered. In addition, a number of refractory ceramic materials are examined for potential use. Most of the data in Table 4-2 is drawn from [Lynch, 1966].

Beryllia (BeO) offers high energy densities but is expensive, toxic when particles are inhaled during machining or grinding processes, and highly regulated due to its status as a known human carcinogen [Brush Wellman, 2002]. The refractory metals are relatively poor performers, despite their high densities and very high melting points; their low heat capacities make them weak candidates for thermal storage. Other metals will provide less performance than those shown. Silicon, boron, and alumina (Al_2O_3) all have melting points at or below the peak receiver temperature target of 2,500 K—thus, while they remain potential candidates for use at lower temperatures, or for systems incorporating phase change storage, they do not appear to be useful for the application at hand.

Of the remaining materials, graphite (C) is the least expensive, easy to machine, and available from a number of sources both in the UK and overseas. The US Air Force’s ISUS program selected a coated graphite cavity for its recent ground testing at Edwards Air Force Base and the NASA Glenn Research Center [Westerman, 1998]. The primary drawback to graphite is its potential for reactivity with propellants of interest at high temperatures—in this case, ammonia, hydrazine, or water. A non-reactive coating (e.g., ISUS selected a rhenium coat) potentially serves as an effective propellant barrier, but adds questions of differential thermal expansion and cracking of the coating during thermal cycling, as well as the selection of a reliable coating method (of which there are a number to choose from, including sputtering, thermal spray, ion plating, and chemical vapor deposition, or CVD). [Pierson, 1996]

Material	Density (kg/m^3)	Specific Heat	Melting Point (K)	Thermal Conductivity	Coefficient of Thermal Expansion	Material Energy Density

		(J/kg-K)		(W/m-K)	(μm/m-K)	(GJ/m^3)
C	**2,100**	**2,091** [a]	**3,923**	**24**	**2**	**17.2**
B	**2,350**	**2,930** [a]	**2,348**	**0.7-1.9**	**7**	**16.9**
Si	**2,330**	**963** [b]	**1,685**	**156**	**4**	**3.8**
B_4C	**2,520**	**2,511**[a]	**2,700**	**30**	**6**	**17.1**
BN	**2,270**	**1,988** [a]	**3,273**	**17**	**0**[c]	**14.8**
BeO	**3,008**	**2,428** [a]	**3,010**	**207**	**13.5**	**22.0**
Al_2O_3	**3,980**	**1,360** [d]	**2,322**	**33**	**11.9**	**12.6**
SiC	**3,210**	**1,465** [e]	**2,818**	**173**	**5.4**	**13.3**
W	**19,300**	**134** [f]	**3,643**	**163**	**4.4**	**9.4**
Re	**21,030**	**150** [g]	**3,453**	**40**	**6.7**	**10.9**
Mo	**10,022**	**255**	**2,890**	**138**	**6.5**	**7.4**

[a] At 2000 K.
[b] At 1367 K.
[c] Hot-pressed BN [Pierson, 1996].
[d] At 1644 K.
[e] At 1922 K.
[f] Over the range 293-393 K.
[g] At 1273 K.

Table 4-2 Properties of Potential Thermal Storage Materials

[Lienhard, 1987][Lynch, 1966][Pierson, 1996][MatWeb, 2002]

Boron carbide (B_4C) has a very high heat capacity at temperature, nearly 20% greater than graphite at 2,000 K, reactivity concerns similar to that of graphite, and extremely high hardness (with concomitant difficulties in machining).[74] B_4C's high heat capacity makes it an extremely attractive thermal storage medium, if it can be isolated from the propellant stream. Lawrence [1998] experimented with unprotected B_4C particles in a fixed bed for heat transfer to water propellant; the B_4C reacted with the water to produce a slurry of boric oxide (B_2O_3).

Boron nitride (BN) is another high-temperature capable, high-specific heat material (roughly that of graphite) which could be used for either thermal storage or for containment. Hexagonal BN is an electrical insulator with a structure very similar to graphite, but with greater oxidation resistance. [Lynch, 1966] It is also resistant to chemical attack by nitrogenous and hydrogenous compounds (i.e., ammonia, hydrazine) at very high temperatures—making it a useful choice for coatings or receiver structure.[75] The material is soft and easily machined. Cubic BN, which is produced via high-pressure, high-temperature treatment of hexagonal BN, is structurally similar to diamond and extremely expensive.

Silicon carbide (SiC) is characterized by moderate specific heat at 2,000 K, good oxidation resistance, and significant industrial acceptance (as an abrasive). With its excellent stiffness-to-density ratio and high thermal conductivity, SiC has been proposed for use onboard ESA's Herschel space telescope, as the substrate material for the primary mirror. [Safa, 1997] As it is readily attacked by nitrogen above 1670 K, it would—like B_4C—necessitate a material barrier (BN, for example) in order to consider it for long-term use in an atmosphere of high-temperature ammonia or hydrazine decomposition products. [Lynch, 1966]

---

[74] Only cubic boron nitride (BN) and diamond are harder.
[75] BN is stable in nitrogen to 2673 K. [American Ceramic Society, 1994]

Based on these factors, the author has selected B_4C as the primary thermal storage medium—its high heat capacity at peak temperatures permits the design of a relatively small receiver subsystem. Carbon and silicon carbide are possible alternatives, although neither matches boron carbide's energy density. The B_4C will be separated from the incoming propellant by a BN barrier. In the baseline receiver case, this will require either (1) small boron carbide particles to be coated with a layer BN, or (2) a monolithic boron carbide structure to be overlaid with a BN coat. The B_4C/BN particle container or "can" will be hot-pressed BN, known for its low (near-zero) coefficient of thermal expansion.[76] An alternate plan[77] would be to remove B_4C from the design altogether, substituting BN as the thermal storage medium. Due to BN's lower heat capacity, this substitution would require a slightly larger receiver, but would remove any possibility of ammonia or hydrazine product degradation of B_4C elements.

4.4.2 Insulation

Very high-temperature, low thermal conductivity materials are required to insulate the hot (2,000-2,500 K) receiver prior to firing. At these temperatures, radiative losses are quite substantial; an uninsulated 10 cm (length) by 10 cm (radius) cylinder at 2,000 K radiates approximately 114 kW to a uniform 290 K background, according to [Lienhard, 1987]:

$$Q = A\varepsilon\sigma(T_1^4 - T_2^4) \tag{4-17}$$

Where Q is the radiative heat loss in watts, ε is the cylinder's effective emissivity (here taken to be equal to 1), σ is Boltzmann's constant (5.6697 x 10^{-8} W/m^2-K^4), and T_1 and T_2 represent the cylinder and "cold space" temperatures, respectively. In order to maintain this cylinder at 2,000 K, the radiative loss would have to be countered by an equivalent solar input; in near-Earth space, this would necessitate the use of a large solar concentrator, nearly 85 m^2 in area.

At an external surface temperature of 400 K, this same cylinder sheds only 130 W—this loss can be countered by a relatively small amount of incident sunlight, roughly equivalent to a tenth of a square meter. One can estimate the needed thermal conductivity (k, W/m-K) of an insulation package for a hot receiver by assuming one-dimensional, steady radial conduction through a thick-walled cylinder [Lienhard, 1987]:

---

[76] The use of low-CTE, hot-pressed BN for the receiver structure will minimize thermal "walk" by the receiver with respect to the concentrator mirror.

[77] In the event that BN coating provides unacceptable performance.

$$Q = \frac{2\pi k l \Delta T}{\ln\left(\frac{r_o}{r_i}\right)} \tag{4-18}$$

For an internal radius (r_i) of 7 cm, maximum heat dissipation of 130 W and a temperature difference of roughly 1,600 K, the cylinder's required k can be calculated to be $\leq$ 0.072 W/m-K. While certainly low, this figure falls within the realm of a number of high temperature insulation materials, including various ceramic fibers and powders. Current Space Shuttle tiles are composed primarily of silica (SiO_2) fibers and intended for thermal protection during vehicle re-entry.[NASA Spaceflight, 2001] Advanced alternatives, such as NASA Ames' AETB-12 tiles, are composed of silica, alumina, and aluminoborosilicate fibers, useable to 1800 K and offering k values of 0.06 W/m-K. [NASA, 2001] The U.S. Air Force Research Laboratory's Solar Orbit Transfer Vehicle (SOTV) is considering the use of graphite felt and tungsten multilayer insulation to shield its cavity, a large graphite monolith. [Partch, 1999] Other high temperature options include zirconia (ZrO_2) foam—with thermal conductivities on the order of 0.1-0.2 W/m-K [Lynch, 1966]. Ultramet [2002], a California-based materials vendor, indicates that zirconia foam offers Shuttle tile insulative capability at "…1,000 ºF [560 K] higher operating temperature."

The author selected a jacketed insulation package composed of (1) a zirconia inner shell, for high-temperature use (near peak receiver temperatures of 2,500 K), and (2) an alumina- or alumina/silica fiber outer shell, with reduced temperature capability but improved (lower) thermal conductivity. This was eventually replaced with a simpler, machinable graphite foam package with higher thermal conductivity.

4.4.3 Sizing Considerations

Appendix B provides details of the microscale solar thermal engine's specific impulse, thrust, charging time, and firing duration requirements for three missions (GTO-to-GEO, GTO-to-Near Escape, and LEO orbit raising). These figures were translated directly into requirements for peak receiver temperature, energy storage, and maximum heat dissipation.

The first (derived) figure of merit is total impulse per orbit, which, for constant thrust systems, is simply thrust multiplied by burn time. Table 4-3 provides total per-orbit impulse and related threshold requirements for the three missions of interest.

Coupled with minimum acceptable specific impulse (350 s.), the per-orbit impulse permits an estimate of thermal storage receiver size. The jet power *(P)* of the solar thermal engine is:

$$P = \frac{1}{2} T u_e \tag{4-19}$$

Here, T is thrust and u_e is the propellant exit velocity. The product of power and burn time provides an estimate of the total energy removed from the receiver during each burn. This calculation actually overpredicts the removed power, since the incoming propellant has substantial initial energy even at its storage temperature (ammonia and water at 300 K, or hydrazine decomposition products at 863 K). Higher inlet temperatures are clearly desirable; a substantial portion of the heating of hydrazine products is performed via its decomposition, whereas incoming ammonia or water will have to be heated from ambient conditions—driving a requirement for greater receiver heat storage. Nevertheless, the simple calculation suggests that a mass of no more than 1.63 kg of boron carbide is sufficient to provide 2,970 N-s of impulse at an I_{sp} of 350 s.[78]

Mission	Thrust (N)	Charging Time (hrs.)	Firing Duration (s.)	Per-Orbit Impulse (N-s)	Energy Removed Per Burn (MJ)
GTO-to-GEO	**0.15**	**4**	**5,000**	**750**	**1.29**
GTO-to-Near Escape	**5.2**	**5**	**540**	**2,970**	**4.82**
LEO Orbit Raising	**1**	**2**	**428**	**428**	**0.73**

Table 4-3 Per-Orbit Impulse and Energy Storage Requirements for Thermal Storage Cavity Receiver

Substituting boron nitride for B_4C would raise the thermal storage mass required to 1.9 kg.[79] Higher heat capacities lead to smaller receiver masses, smaller volumetric displacements, and smaller overall receiver surface areas, lowering radiative losses and allowing higher peak temperatures to be reached.

4.4.4 Selection of a Heat Transfer Mode

The solar thermal receiver is intended to efficiently transfer—via convection—heat from a thermal storage medium (e.g., boron carbide, graphite, or boron nitride) to a gaseous-phase propellant. The simplest approach would be a set of single-pass channels through a monolithic block of the thermal storage material; multiple passes complicates plumbing and requires additional plena to contain propellant. Lawrence [1998] examined various approaches for nitrous oxide and water resistojets and concluded that packed, fixed beds of small (submillimeter) particles offer high-efficiency heat transfer (due to high surface area) combined with simplicity of construction, providing significant advantage over channels or tubes.[80] Packed beds are immune to thermal shock and expansion difficulties that monolithic structures encounter; any stresses generated in the bed material are alleviated *locally*. Such beds do have disadvantages, including relatively high pressure drops (due to high frictional losses), and *channelling* (preferential flow through sections of the bed, resulting in inefficient heat transfer). Nevertheless, the need for maximal heat transfer in a small volume has led the author to select a packed bed for the baseline design.[81]

---

[78] Assuming an average heat capacity of 1,805 J/kg-K, peak receiver and propellant inlet temperatures of 2,500 K and 863 K, respectively. B_4C's heat capacity at low (room) temperatures (300 K) is roughly 800 J/kg-K, [Lynch, 1966] rising to over 2,400 J/kg-K at 2,500 K. The author's firing simulation program indicates that less than half this amount (1.15 kg) is needed to heat hydrazine decomposition products from 863 K to receiver temperature and achieve the threshold I_{sp} requirement.

[79] SiC has a C_p of 670 J/kg-K at 300 K, 1,465 J/kg-K at 1,922 K [Lynch, 1966]. The author assumes an average C_p of 1,347 J/kg-K.

There are multiple correlations available for particle bed heat transfer. Lawrence [1998] provides the Achenbach correlation:

$$Nu_{D_p} = \frac{1-\varepsilon}{\varepsilon}\left\{ .622926\left(\frac{\mathrm{Re}_{D_p}}{1-\varepsilon}\right)^{2.32} + 6.44603\times10^{-4}\left(\frac{\mathrm{Re}_{D_p}}{1-\varepsilon}\right)^{3}\right\}^{0.25}\mathrm{Pr}^{0.33} \tag{4-20}$$

Here, heat transfer is related to the bed porosity (void volume/bed volume) ε and the characteristic Nusselt number (Nu_{Dp}),[82] where Nu is defined as:

$$Nu_{D_p} = \frac{h_c D_p}{k} \tag{4-21}$$

In this formulation, the Nusselt number (based on a characteristic length, which in this instance is the average particle diameter) is computed from the product of the bed heat transfer coefficient h_c, the average particle diameter D_p, and the bed material thermal conductivity k. The correlation itself is an empirical one, related to the flow Reynolds number:

$$\mathrm{Re}_{D_p} = \frac{\rho u_s D_p}{\mu} \tag{4-22}$$

Where u_s is the flow superficial velocity, or the velocity of the flow in the absence of the particle bed. Dynamic viscosity, or μ, represents viscous forces. Small values indicate the dominance of viscous forces, and the presence of laminar (non-turbulent, non-mixing) flow regimes. This correlation also includes reference to the flow Prandtl number:

---

[80] Reticulated foams—randomly connected open cells inside a material matrix—are another high efficiency heat transfer option which has been examined for numerous applications, including fuel cells [Haack] and high temperature insulation [Ultramet, 2002].

[81] The author has computed the heat transfer coefficient for a monolithic block-and-channel configuration with hydrazine decomposition product propellant at high pressure. The value—assuming 100 1-mm bore channels—is ~2,000 W/m^2-K. While this is on the order of the figures obtained for packed bed coefficients, the relative area for heat transfer (pipe wall vs. particle surfaces) in channel flow is substantially smaller.

[82] The Nusselt number is a non-dimensional grouping which is inversely proportional to the thickness of the thermal boundary layer near a convectively-cooled (or heated) body of interest [Lienhard, 1986]. Other values in this equation include the flow Reynolds' number (Re), also based on particle diameter, which indicates the relative magnitude of inertial forces to viscous forces within a fluid, and the flow Prandtl number (Pr), which indicates the relative magnitude of thermal and viscous boundary layers. Pr is roughly on the order of unity for gases—0.67 for diatomic gases, specifically.

$$\mathrm{Pr} = \frac{\mu C_p}{k} \tag{4-23}$$

This relation also includes μ, as well as the fluid's specific heat, C_p. This correlation provides an estimate of the bed/fluid heat transfer coefficient h_c via empirical calculation of the Nusselt number. The figure for h_c can then be used to determine heat transfer via [Lienhard, 1987]:

$$Q = h_c A(T_b - T_p) \tag{4-24}$$

Throughout the duration of a firing, the receiver will lose heat through convective processes to the propellant. Propellant exit temperature, and therefore instantaneous specific impulse, will fall in line with the receiver temperature. Eventually, the receiver body will fall to the propellant inlet temperature, and will no longer transfer heat to the propellant. The effective specific impulse of the solar thermal engine will be the time-averaged specific impulse through the course of the firing. This effective I_{sp} must exceed the minimum (threshold) requirement of 350 s. to be considered fully successful.

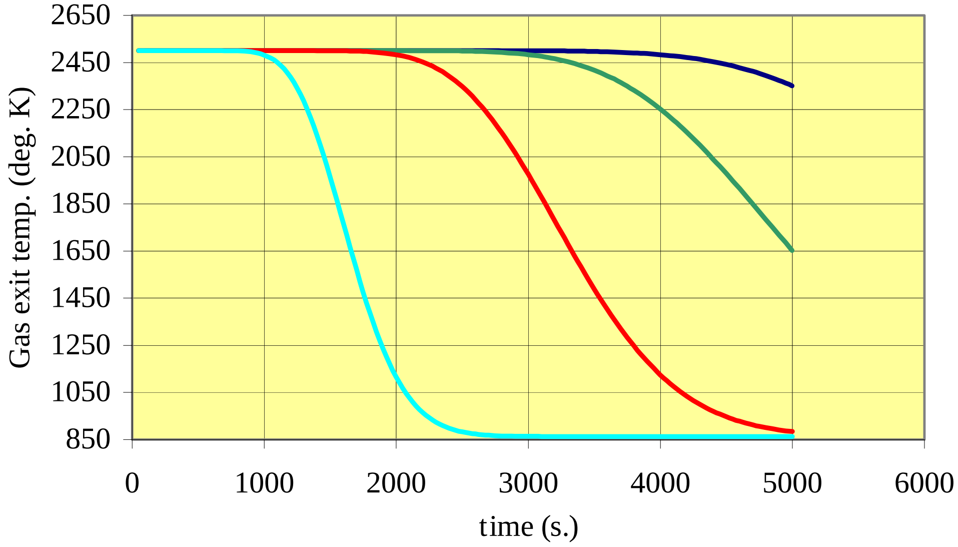

Figure 4-19 Gas exit temperature vs. time, 750 N-s cavity receiver, 150 mN thrust, 5,000 second burn time. This sequence of curves represents bed lengths of 10 cm (top), 7.5 cm, 5 cm, and 2.5 (bottom).

To aid the process of preliminary design, author has constructed a simple Visual Basic simulation of a particle bed cavity heat exchanger. In this simulation, the particle bed is divided into thin slices and an energy balance performed on each slice (and each element of propellant) at each time step. Convective heat transfer between slice and propellant slug is calculated for a given time step,[83] and a new temperature distribution (gas and bed) determined. Radiative and conductive losses are neglected for purposes of the simulation but could be included; the primary heat transfer mechanism—for short durations—is convective, between bed and propellant. The user may select a number of bed and propellant characteristics, including bed and propellant densities, thermal conductivities, specific heats, and bed dimensions. An initial bed temperature and propellant inlet temperature are also determined prior to starting the simulation. Finally, the user must select a time constant for the simulation; this value must be sufficiently small to permit the linearized form of the heat transfer equation to return valid results. Too large a time constant will cause the solution to oscillate or diverge.[84]

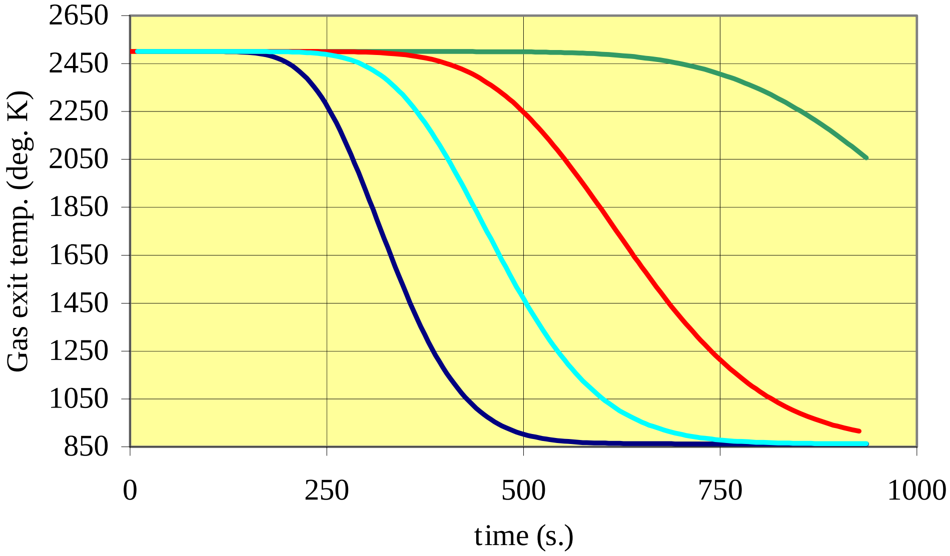

Figure 4-20 Gas exit temperature vs. time, 2,808 N-s cavity receiver, 3 N thrust, 936- second burn time. This sequence of curves represents bed radii of 7 cm (top), 5.5 cm, 4.75 cm, and 4 cm (bottom).

Figure 4-19 illustrates the performance of various receiver configurations for the GTO-to-GEO mission. This mission requires a nominal per-orbit impulse of 750 N-s, equivalent to a constant 150-mN thrust level over 5,000 seconds. All cases are identical save for bed length. The longest

---

[83] In this case, using the Whitaker correlation, an alternative (but similar) formulation to Achenbach:

$$Nu_{D_p} = \frac{1-\varepsilon}{\varepsilon}\left\{0.5\left(\mathrm{Re}_{D_p}\right)^{0.5} + 0.2\left(\mathrm{Re}_{D_p}\right)^{0.67}\right\}\mathrm{Pr}^{0.33} \qquad (4\text{-}25)$$

This correlation is taken from Kreith and Bohn [1997]. Others include Upadhyay {Kreith, 1997] and Kunii/Levenspiel [Rhodes, 2001]. Most of these correlations provide regimes of applicability, in terms of the flow Reynolds' number. This must be considered when attempting to simulate a given bed geometry and propellant type.

[84] The algorithm (Particle Bed Heat Transfer, or PBHT) is relatively simple. It determines the energy and temperature profiles of the bed and resident propellant at time *t* + *dt* from values known at time *t*; thus, the

(10-cm) bed provides an average I_{sp} of 401 s, nearly the ideal value for this propellant (decomposed N_2H_4) and initial bed temperature. As the bed length is reduced to smaller and smaller values, the total amount of thermal energy resident in the bed declines. The very high values of h_c (on the order of several hundred W/m^2-K for this configuration) drive the gas to near-bed temperatures after traversing only a fraction of the bed; the exit end of the bed (and gas exit temperature) thus remains near its peak for a substantial fraction of the burn time, for long bed lengths. At 2.5 cm, however, the bed configuration produces an average I_{sp} of only 301 s—fully half of the burn is spent at the minimum (gas inlet) temperature of 863 K. The 5-cm configuration produces an average I_{sp} of 355 s.

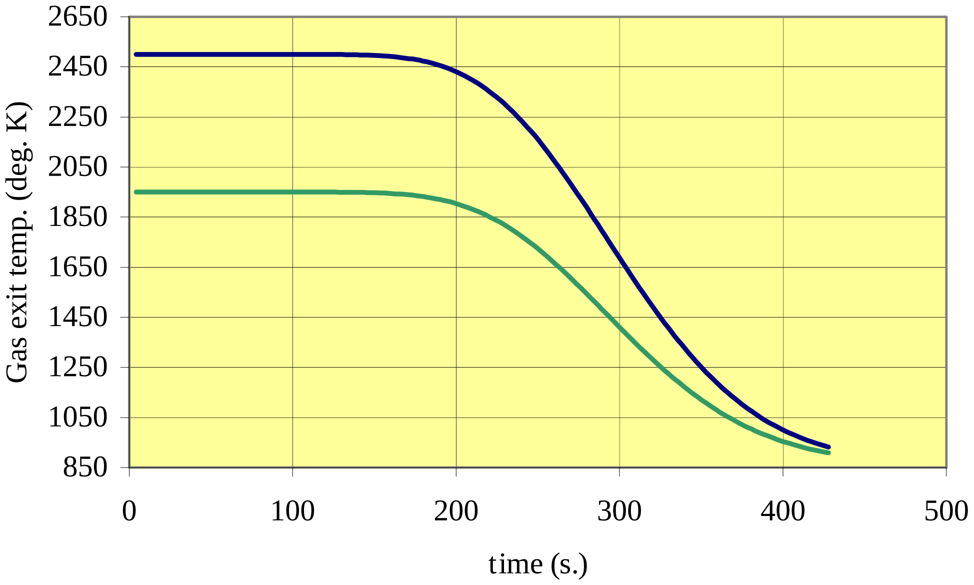

Figure 4-21 Gas exit temperature vs. time, 428 N-s cavity receiver, 1 N thrust, 428- second burn time. The two curves represent initial bed temperatures of 2,500 K (top curve) and 1,950 K (bottom curve).

Figure 4-20 and Figure 4-21 provide similar information for large (2,808 N-s) and “micro” (428 N-s) impulse cavity receiver configurations. These are sized to fulfil (1) a GTO-to-Near-Escape role, and (2) a LEO orbit-raising role, as per the stated requirements in Appendix B. The sensitivity of large cavity gas exit temperature to changes in bed radius is explored in Figure 4-20. The top curve represents the largest radius—7 cm—while the bottom curve represents the performance of a bed radius of 4 cm. Average specific impulse (for a nominal 936-second burn) range between 305 s. (4 cm) and 397 s. (7 cm). The design point radius (5.5 cm) provides an average I_{sp} of 359 s. In Figure 4-21, the 428 N-s receiver performance is provided for 2,500 K

---

code is explicit and subject to instability. While implicit methods could be used to create an inherently and 1,950 K peak temperatures, corresponding to average I_{sp} figures of 361 s and 325 s, respectively.[85]

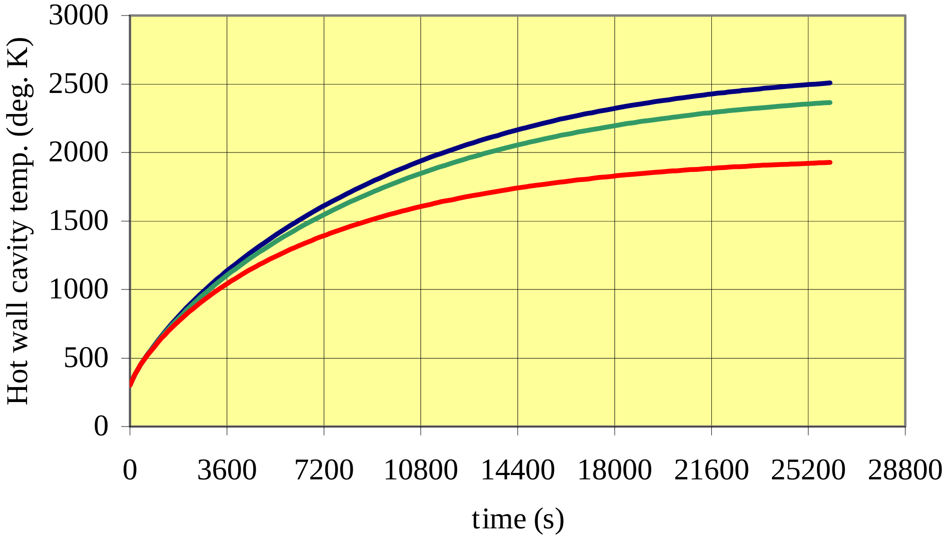

Figure 4-22 Cavity "hot wall" temperature vs. time, 2,760 N-s cavity receiver, fixed insolation of 333 W. The three curves represent insulation package thermal conductivities of 0.01, 0.05, and 0.2 W/m-K.

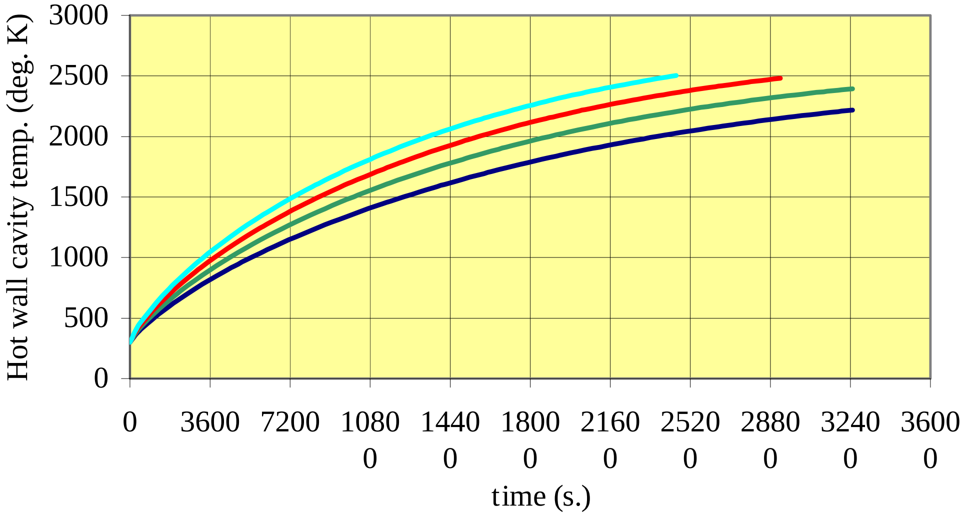

---

stable algorithm, this was not deemed necessary. More information is available in Appendix E.

[85] Note that the performance level of this receiver, at a peak operating temperature of 1,950 K, is somewhat below the threshold value of 350 s., specified in Appendix B.

Figure 4-23 Cavity "hot wall" temperature vs. time, 2,808 N-s cavity receiver, 3 N thrust, 936- second burn time. The four curves represent insolation values (solar energy input) of 333, 400, 466, and 533 W.

Figure 4-22 shows the impact of exterior insulation on achievable receiver temperature, utilizing the CHUPS (Cavity HeatUP Sequence) code, discussed in Appendix E. CHUPS is a combined radiative/conductive heat transfer model, constructed by the author and applicable to cylindrical heat exchangers. The user inputs receiver geometry and material data, as well as simulation constraints and external data (e.g., insolation, rejection temperatures for radiative surfaces). The program output provides some insight into the duration of the heatup, or charging, sequence prior to firing.[86] Output from this preliminary effort with the CHUPS code will be compared to similar output from WinTherm, a commercial thermal modeller obtained by the author, and MSTISM (Microscale Solar Thermal Integrated System Model), devised by the author, in Chapter 5.[87] After seven hours of direct insolation, a receiver containing insulation having the lowest thermal conductivity (*k*, 0.01 W/m-K, top curve) reaches a peak temperature of 2,500 K. Increasing k to 0.05 decreases this maximum to 2,365 K. A further increase (to 0.2 W/m-K) constrains the receiver from getting much higher than 2,000 K.

Figure 4-23 illustrates the effect of insolation on the large (GTO-to-Near-Escape) cavity. A larger insolation (i.e., larger concentrator input) can substantially reduce charging time; at 533 W—60% more than the nominal (default) figure of 333 W—charging time (ambient to 2,500 K) is reduced to 7 hours. A "hot start," or charge from 863 K to 2,500 K, requires 6.2 hours.[88]

Similar analyses can be performed for the small (750 N-s) and "micro" (428 N-s) cavities (Figure 4-24, Figure 4-25). The small, GTO-to-GEO capable receiver reaches 2,500 K from ambient in 3 hrs., 20 min., with an insolation of 333 W. Its hot-start recharge time is 3 hrs., 5 min. At 275 W, these figure rise to over 5 ½ hours (ambient-to-2,500 K) and 5 hrs., 5 min. (hot-start). At 200 W, insolation is insufficient to allow the peak temperature to be reached for any charging duration.

---

[86] Charging times are constrained in Appendix B to threshold values of 4 hours (GTO-to-GEO), 5 hours (GTO-to-Near Escape), and 2 hours (LEO Orbit Raising), respectively.

[87] CHUPS and WinTherm output generally agree, but underpredict the amount of incident power required to achieve a given peak temperature. MSTISM and test results agree well. See Chapters 5 and 6.

[88] This is approximately one hour longer than the requirement in Appendix B. At an optical efficiency of 0.8, a 533-W input requires a mirror with nearly half a square meter of intercepted surface area, or a diameter of 79 cm. This is larger than the Ariane 5 ASAP footprint of 60 cm x 60 cm, and would either require a waiver or necessitate folding of the structure (which would be clearly undesirable).

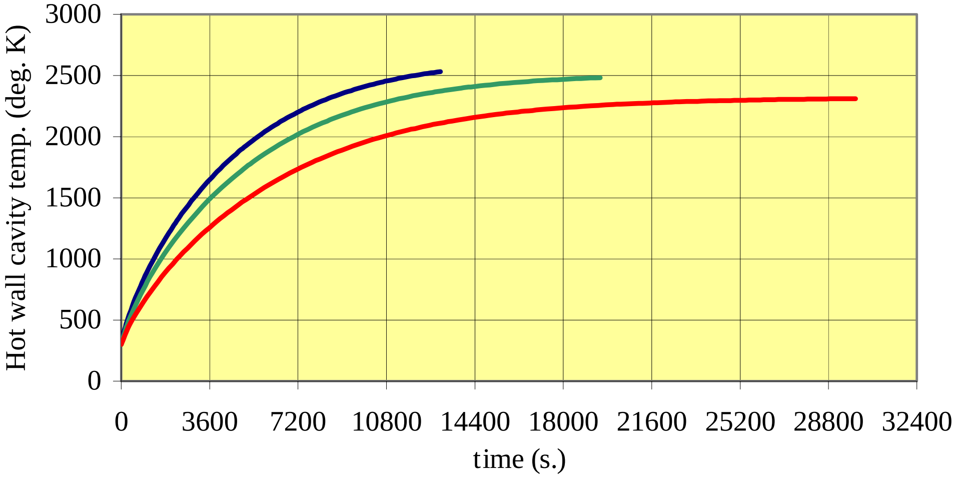

Figure 4-24 Cavity "hot wall" temperature vs. time, 750 N-s cavity receiver, 150 mN thrust, 5,000-second burn time. The three curves represent insolation values (solar energy input) of 200, 275, and 333 W.

The micro receiver's charging performance (Figure 4-25) is shown with insolation figures of 100 (lower curve), 200, 250, and 300 W (upper curve). At the minimum solar input level of 100 W, CHUPS indicates that the receiver hot wall could reach 2,000 K after 3 ½ hours.[89] At 250 W, the receiver is predicted to reach 2,500 K, but only after almost 5 hours. The receiver "hot start" capability at 250 W input is still over 5 hours. If the peak temperature requirement is relaxed to 2,000 K, charging time (ambient to 2,000 K) performance improves substantially: 3 ½ hours at 100 W, and slightly more than an hour, at 300 W.

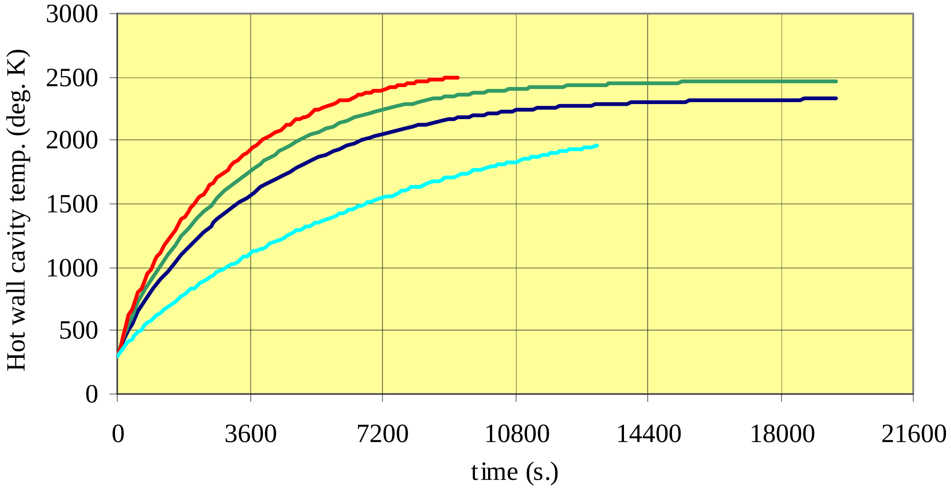

---

[89] Following the same procedure as above, at an optical efficiency of 0.8, a 100-W input will require 0.09 m^2 of surface area—a mirror of 34 cm diameter.

Figure 4-25 Cavity "hot wall" temperature vs. time, 428 N-s cavity receiver, 1 N thrust, 428- second burn time. The four curves represent insolation values (solar energy input) of 100, 200, 250, and 300 W.

As will be shown in the next chapters, the relatively simple PBHT and CHUPS codes used for the preliminary design phase provided an overly optimistic assessment of incident power required to achieve a specific performance plateau (i.e., peak external cavity temperature). For example, the simple PBHT code used here assumed no radiative losses from the cavity receiver during firing, although such losses are shown to be significant in Chapters 5 and 6. The CHUPS code, a one-dimensional coupled conduction/radiation model, accounts for only part of the radiative losses in the receiver and uses an oversimplified model for heat transfer between receiver and insulation slices.[90] CHUPS therefore does not properly account for cylindrical geometry, and, for a fixed input power, overpredicts peak cavity temperature. This overprediction results in a preliminary estimate for required mirror diameter that is low by a factor of approximately 2 (Table 4-4). The detailed design (Chapter 5) addresses these issues.

The table below summarizes the key performance parameters of the micro, small, and large solar thermal engine model baseline. These parameters were used to construct preliminary solid models of the system components, intended to throw light on potential fabrication problems, joining and sealing, and satellite vehicle compatibility issues. The baseline design for the receiver assumes a boron nitride-coated boron carbide particle bed contained within a boron nitride can (in orange, Figure 4-26). Zirconia spacers separate the can from the insulation package, which is composed of zirconia foam (inner shell) and silica/alumina fibre (outer shell). The cavity would be sleeved with boron carbide to maximize absorptivity.

Mission	Thrust (N)	Per-Orbit Impulse (N-s)	Firing Duration (s)	Receiver Mass (g)	Required Insolation (W)/ Estimated Mirror Diameter (cm)	Charging Time (hrs.)/Peak Temp (K)
GTO-to-GEO	**0.15**	**750**	**5,000**	**1,002**	**333 / 63**	**3.1 / 2,501**
GTO-to-Near Escape	**3.0**	**2,808**	**936**	**2,745**	**533 / 79**	**5.4 / 2,408**[a]
LEO Orbit Raising	**1**	**428**	**428**	**712**	**100 / 34**	**2.7 / 1,957**

[a] Decreased below 2,500 K to reduce charging time.

Table 4-4 Preliminary STE design points, with estimated concentrator size (assuming single mirrors and an optical efficiency of 0.8), "hot-start" charging times, and calculated peak temperatures achievable.

---

[90] utilising the thermal resistance of a plane wall (L/kA) in place of that for a cylinder ($\ln R/2\pi kl$). Here, $R = r_o / r_i$, where r_o is the slice's outer radius and r_i the inner radius.

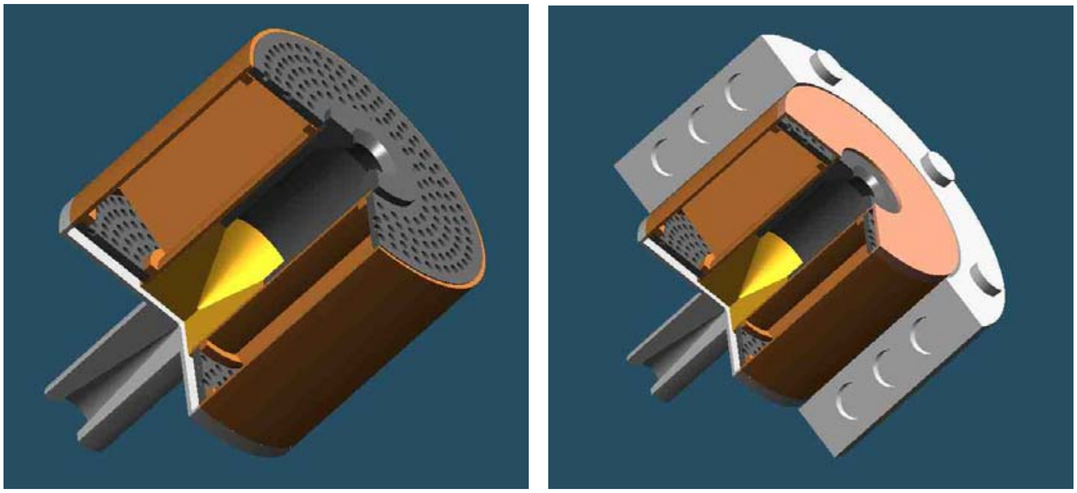

428 N-s cavity receiver, insulation package and fore plenum removed to show fore injector detail.

428 N-s cavity receiver, view selected to reveal details of the insulation package's construction.

Figure 4-26 428 N-s cavity receiver details.

Figure 4-26 and Figure 4-27 illustrate details of the "micro" receiver's construction. The aft end or cavity plug (yellow) will be machined to remove a conical section, reducing direct re-radiation of near-paraxial light impinging on the aft section of the cavity. There are two identical "injector plates," each with several hundred countersunk holes with diameters of 2 mm (countersink) and 0.2 mm (hole). The final diameter is slightly less than half the diameter of the selected bed particles (500 μm), allowing for particle retention. The aft plenum couples to a 200:1 area ratio nozzle—protruding several centimetres beyond the aft insulation face. As will be seen in the next chapter, this nozzle configuration, while plausible, represents a significant source of radiative loss during heatup.

The insulation package is a four-piece assembly with dowel-and-hole construction for ease of alignment. In the case of the micro cavity, this insulation is uniformly 16.5 mm thick,[91] save only at the nozzle exit plane and near the cavity aperture. A single propellant feed line (not visible in the cutaway figures above) is routed through a hole in the fore insulation cap and through the fore plenum.

The receiver structure is essentially an amalgam of ceramic materials, primarily BN and B_4C. The only metal items to be included are (1) the propellant feed line into the fore insulation cap, which will be a high-temperature metal (W, Re, or Mo are likely choices), and (2) the mounting structure—not shown here—which will clamp to the exterior surface of the insulation package.

---

[91] 6.5 mm of ZrO_2, 10 mm of alumina fiber.

Aluminium alloy (e.g., T6061), equivalent to that used in the concentrator substrate, was baselined.

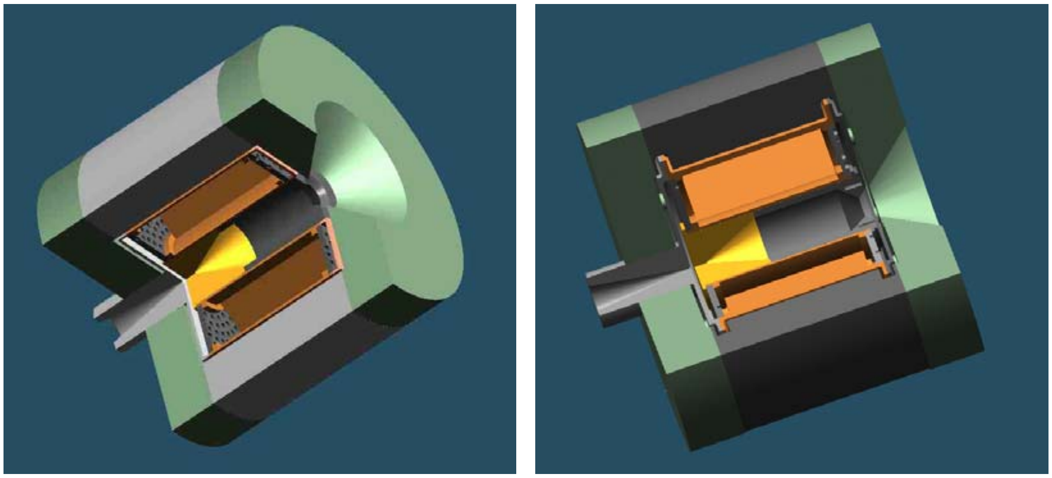

Figure 4-27 Fully assembled cutaway views of the 428 N-s cavity receiver, 5 cm outer radius, 8.9 cm insulation fitting length.

There are four options available to the ceramicist for joining ceramic items [Schwartz, 1990]. These include mechanical methods (bolts, screws, tie-downs, or other fasteners), brazing, welding, and sealant bonding. Mechanical bonding was initially dismissed as the least likely approach for achieving a hermetic seal between ceramic/ceramic and ceramic/metal interfaces.[92] Sealants (e.g., cements) were seen to provide relatively low strength bonds at low temperatures (< 1,430 ºC), but only a very few were rated to survive the high peak temperatures needed in the cavity receiver. Refractory metal alloy brazing showed the greatest promise for strong, hermetic joints. This led to a series of bonding trials, discussed in detail in Chapter 6.[93]

4.5 Propellant Feed System Design

Before embarking on a detailed description of the propellant storage and feed system, it is first necessary to revisit the issue of propellant selection. Unlike the vast majority of rocket propulsion systems in use today, solar thermal propulsion system does not rely on conventional chemical reactions to produce high-temperature exhaust. A low-molecular weight monopropellant is heated to very high temperature within the STP engine's receiver and is exhausted to produce thrust at high specific impulse. The ubiquitous choice has long been hydrogen (H_2), due to its low molecular weight and potential for high specific impulse—perhaps as high as 1,000 s. Earlier in this chapter, the author indicated that H_2 is not a candidate for use, owing to specific storage concerns (i.e., cryogenic storage temperatures) and volumetric constraints it imposes on a small satellite.[94] This will also be true of helium (which has a lower boiling point than H_2) and methane (CH_4[95], which boils at 112 K at 1 bar [CGA, 1966]). Liquefied petroleum gases (e.g., butane, C_4H_{10}; propane, C_3H_8; propylene, C_3H_6; and various butylenes) all have specific gravities on the order of 0.6, relative to water—approximately that of ammonia. Unlike ammonia, however, these hydrocarbons will evolve hydrogen gas and carbon particulate upon decomposition—a phenomenon that can coat and eventually block flow passages (or the engine throat) and which is clearly something to be avoided.

---

[92] Note that there are cases—such as the fitting together of insulation package elements—which lends itself to mechanical bonding.

[93] Ceramics (such as BN or SiC) that sublime, rather than melt, are not candidates for welding. [Schwartz, 1990] The number of very high temperature brazing systems is extremely limited [REMBAR, 2002].

Other, more obscure possibilities such as nitromethane (CH_3NO_2), diborane (B_2H_6), and pentaborane (B_5H_9) were all briefly reviewed and dismissed. Nitromethane has a high storage density (1,140 kg/m^3) but is susceptible to detonation [Baker, 2000]. Diborane, which can be expected to decompose in a similar manner to methane, liberating boron and hydrogen gas, is listed as an Extremely Hazardous Substance under the U.S. Emergency Planning and Community Right-to-Know Act (EPCRA) and may autoignite [Voltaix, 2000]. Pentaborane is perhaps even more hazardous; the last remaining U.S. stockpile of B_5H_9 was recently destroyed, due to toxicological concerns [USACE, 2001].

Nitrous oxide (N_2O), a propellant option with some history at Surrey, will decompose to N_2 and O_2 above 793 K [Zakirov, 2001]. Its storage density[96] of 785 kg/m^3 is higher than the hydrocarbons and ammonia, but lower than water, hydrazine, and hydrogen peroxide. Its relatively poor performance (I_{sp} = 206 s. at its adiabatic flame temperature of 1,913 K) is due to the high molecular weight of its decomposition products. This, in addition to the large amount of free oxygen evolved—which is likely to corrode most materials at the STP engine's operating temperature—does not recommend N_2O. While certain coatings (e.g., iridium) can mitigate the erosive effects of oxygen [Ultramet, 2002], propellants with no oxygen content are desired.

Other room-temperature storable, low-molecular weight liquids include water, ammonia, hydrogen peroxide, and hydrazine. Like N_2O, hydrogen peroxide suffers from the high average molecular weight of its exhaust products (H_2O and O_2 [Clark, 1972]), as well as its oxygen content and potential for engine material corrosion. Water is an extremely stable molecule with moderate molecular weight (18 g/mol) and high storage density at room temperature—1,000 kg/m^3. It offers the possibility of high specific impulse (372 s. at 2,500 K), and decomposes via the following reaction [Humble, 1995]:

---

[94] Recall that liquid H_2's density is approximately 71 kg/m^3.

[95] Methane—for terrestrial use—is typically stored in cylinders as a non-liquefied compressed gas at pressures of 2,000 psi (136 bar) at 294 K (21 degrees C). Methane has a specific gravity, relative to air (1.21 kg/m^3 at sea level), of 0.55491 at 289 K (16 degrees C) and 1 bar [CGA, 1966]. Given perfect gas behavior, this permits storage densities on the order of (2000/14.7) x 1.21 kg/m^3 = 160 kg/m^3, more than a factor of two better than liquid hydrogen but only 16% that of liquid water.

[96] At 293 K (20 degrees C) and 50 bar [CGA, 1966].

$$2H_2O\ (g) \rightarrow 2H_2\ (g) + O_2\ (g) + 483{,}860\ J$$

Catalysis or very high temperatures are required to allow this highly endothermic reaction to proceed.[97] In the presence of most materials, however, water is highly corrosive at temperatures of interest. Katscher [1986] indicates the following reaction is responsible for erosion of graphite in certain "high"-temperature (950-1,200 K) nuclear reactor systems:

$$C + H_2O\ (g) \rightarrow CO\ (g) + H_2\ (g) + 131{,}000\ J$$

This would clearly present a problem in an uncoated graphite receiver. An oxidation-resistant coating would be required. Similarly, Lawrence [1998] found that uncoated boron carbide particles and water propellant proved incompatible, at temperatures above 570 K. Boric oxide is produced, along with other products, according to Fujii [1991]:

$$B_4C + 6H_2O \rightarrow 2B_2O_3 + 6H_2 + C$$

Despite its touted oxidation resistance [Lynch, 1966], boron nitride—the selected primary receiver material—is likely to encounter similar boric oxide formation [Pierson, 1996] at sufficiently elevated temperatures in steam. In general, water is a highly corrosive molecule that is likely to erode most of the substances deemed useful for receiver structure or thermal storage. A refractory metal, metal oxide, or specific metal carbide (e.g., HfC, ZrC [Ultramet, 2002]) coating would be required to permit the use of water. The author reserves the use of water as an alternate, but cannot baseline it due to the additional design constraints it imposes.

Ammonia (NH_3), a low density liquefied gas (600 kg/m^3), is stored under its own vapor pressure of 8 bar at 294 K (21 ºC). This is highly advantageous from a design standpoint; no separate expulsion method (pressurant gas or pumping) is required to move the propellant from tank to receiver. It is nominally capable of achieving an ideal I_{sp} of 400 s, assuming no decomposition. However, ammonia decomposition is a fact of life; state-of-the-art hydrazine thrusters are designed to maximize temperature (and therefore I_{sp}), given a known level of ammonia decomposition in the thrust chamber [Humble, 1995]. Like water, ammonia decomposes to N_2 and H_2 endothermically, robbing the propellant flow of energy.

---

[97] Complete dissociation via thermal decomposition would require an enthalpy change of 13.4 MJ/kg. The corresponding temperature rise (assuming an average Cp of 2,500 J/kg-K [Lide, 1995]) is over 5,000 K. The H_2-O_2 reaction's adiabatic flame temperature (stoichiometric) is roughly 3,500 K. As the baseline system will not approach these temperatures, there is unlikely to be any significant water dissociation.

Ammonia (and its decomposition products) are compatible with the baseline receiver design. The primary structure (BN) and particle bed (BN-coated B_4C) are resistant to hot hydrogen, hot ammonia, and hot nitrogen at high temperatures.[98] Lynch [1966] notes that BN, in hydrogen, "may be used effectively above 3,500 F [2,200 K]." Due to its high-temperature compatibility with the baseline design, and despite its relatively low DI_{sp} (Table 3.0) ammonia is a strong contender aboard missions whose margins permits the use of a low-density propellant.

Hydrazine (N_2H_4) is a common spacecraft propellant with a long heritage, used in both monopropellant systems (via decomposition) and bipropellant systems (with an oxidizer, typically nitrogen tetroxide, N_2O_4). It has a high storage density (1,004.5 kg/m^3) but requires a pressurant for use. It is moderately toxic, has been declared a probable human carcinogen, and is flammable as well as shock-sensitive [ATSDR, 1997]. On its own, it is capable of I_{sp} figures approaching 230 s, but this is limited by ammonia decomposition [Humble, 1995]:

$$3N_2H_4 \rightarrow 4NH_3 + N_2 - 336{,}280\ J$$

$$4NH_3 \rightarrow 2\ N_2 + 6H_2 + 184{,}400\ J$$

The first (exothermic) reaction produces ammonia and nitrogen gas with an adiabatic flame temperature of 1,650 K. The second (endothermic) reaction produces additional nitrogen in addition to hydrogen gas—this tends to lower the exhaust product temperature substantially [Hastings, 1990].[99] The average molecular weight of the decomposed products (10.67 g/mol) is slightly higher than that of ammonia's decomposed products (8.5 g/mol).

The first reaction holds significant promise, however, for a method by which a solar thermal propulsion system could augment—in much the same way as an electrothermally augmented (ETA) hydrazine thruster[100] augments—the chemical system's base performance. The novelty in such an approach is the solar thermal engine's much higher efficiency of energy transmission, relative to its electrothermal cousin: Unlike the classical ETA thruster, which suffers from solar cell efficiencies on the order of 14-35% [Larson, 1992][Wells, 2001], and additional transmission line, power conversion, and heater efficiencies (~75% [Hastings, 1990]), the STP system offers direct solar energy input at very high efficiencies, perhaps approaching 80% or higher—assuming high-reflectance materials ($r > 0.9$), negligible contamination and shading effects, and reasonable pointing accuracies (<0.1º). Solar thermal augmented (STA) hydrazine would raise the decomposed products (NH_3, N_2, and H_2) to temperatures as high as 2,500 K, and specific impulses approaching 400 s. The author is not aware of any previous proposals to use solar heating as a chemical propulsion augmentation system.[101]

---

[98] Further investigation will be required to determine the porosity of BN coatings and their effectiveness as barriers to various propellant components (e.g., H_2O, O_2, N_2, H_2).

[99] Full decomposition of ammonia leads to an adiabatic flame temperature of 863 K.

[100] Brown [1996] describes Intelsat V's 414-W electrothermal hydrazine thruster, which achieves a specific impulse of 295 s and a maximum heater temperature of slightly more than 2,200 K.

The primary advantage of hydrazine over the other propellants under investigation is its large, exothermic heat of decomposition. While water and ammonia will enter the receiver at their storage temperatures (300 K), hydrazine's products will enter at roughly 860 K. This temperature difference (560 K) represents an additional 2.2 MJ/kg[102] of energy that is available for heating propellant. This is substantial; for a micro receiver (428 N-s impulse), the total per-burn propellant consumption is approximately one-tenth of a kilogram and the total energy storage capacity on the order of 1.5 MJ. The "savings" (0.22 MJ) is a substantial fraction—15%—of the total capacity. This can be seen in Figure 4-28, in which the additional energy made available in the hydrazine case (burn average I_{sp} = 325 s) allows it to roughly match ammonia's performance (burn average I_{sp} = 329 s), despite hydrazine's molecular weight disadvantage. In actuality, ammonia decomposition (and resultant endothermic losses associated with H_2 and N_2 formation) will apply equally to the ammonia case, which means that the calculated I_{sp} above is somewhat higher than what could be achieved in reality. Thus, the hydrazine case is likely to be superior.

On the basis of the above analysis, the author has selected hydrazine as the primary propellant for all missions under scrutiny. Its high density I_{sp}, coupled with its long-standing heritage as a spacecraft propellant, offsets its well-known toxicity and handling problems. Furthermore, hydrazine's decomposition offers the possibility for a significant boost in propellant inlet temperatures at the receiver, reducing the amount of energy required for storage in the cavity receiver. Ammonia, which offers higher specific impulse but demands greater storage volume, is an alternate choice which will also be useful as a ground test propellant—owing to its decomposition product similarity to hydrazine and simpler handling requirements. Nitrogen,

---

[101] For comparison, Hastings [1990] provides an example ETA system for the U.S. DSCS III (Defense Satellite Communications System) satellite. For a supplied electrical input power of 1 kW and a desired I_{sp} of 315 s, he shows:

$$T = \frac{\eta P}{E} g I_{sp} \tag{4-27}$$

Here, the ETA system's thrust (T) is the product of the heater efficiency, η, the supplied electrical power, P, and the exhaust velocity u_e (= gI_{sp}), divided by the per-mass augmentation power required, E, in MJ/kg. Hastings calculates a thrust figure of 813 mN. Assuming a solar cell conversion efficiency of 14%, and no other losses, the required solar cell array area is over 5 m^2. This system is clearly inapplicable to small satellites—they are simply too power-limited (by virtue of volume and surface area constraints) to take advantage of this capability. The micro STP cavity receiver (428 N-s) discussed in the previous section provides a similar (1,000 mN) thrust level for a firing time of over 400 seconds. The receiver mass is estimated at 500 grams; the concentrator (34 cm diameter) will mass roughly 2 kg. The system should be able to repeat its performance after a 2.7-hour thermal charging period. No electrical power input is required; the only major concessions to satellite design will be (1) reserving the nadir face for the concentrator mirror, and (2) the need to provide accurate pointing for STP thermal charging.

[102] Assuming ammonia's specific heat of 3,910 J/kg-K, at 1,500 K. Water at 1,500 K and 10 bar pressure has a somewhat lower specific heat, 2,618 J/kg-K. [Lide, 1995]

hydrogen, or inert gases (Ar, He) may also be used during ground testing to demonstrate receiver heat transfer and propellant feed system flow characteristics.

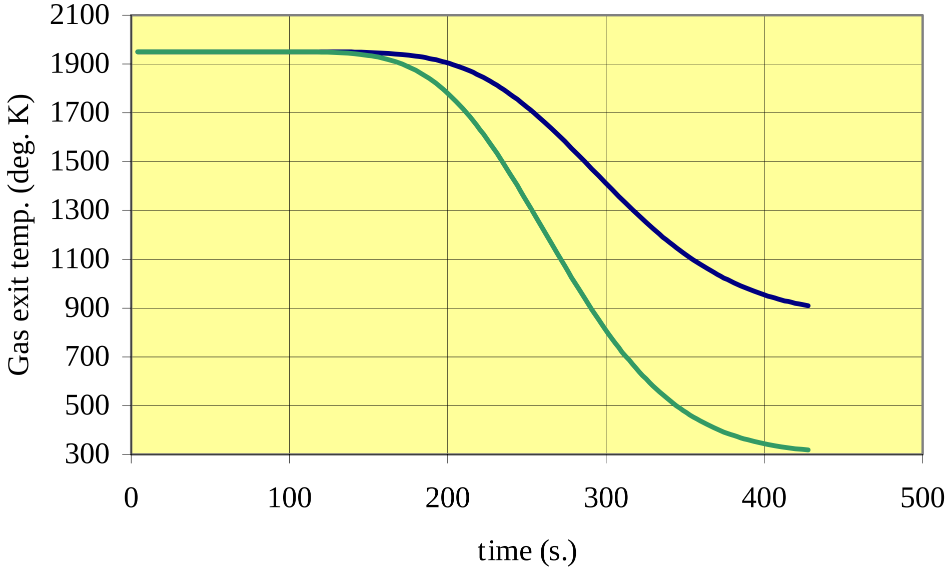

Figure 4-28 Gas exit temperature vs. time, 428 N-s receiver, 1 N thrust, 428- second burn time, 1,950 K initial bed temperature. The two curves represent hydrazine decomposition product input at 863 K (top) and ammonia at 300 K (bottom). Ammonia's performance does not account for endothermic losses associated with H_2 and N_2 formation.

4.5.1 Propellant Feed System Configuration

For small spacecraft propulsion systems, simplicity and cost drive the selection of a specific feed system configuration. The two potential choices are (1) a blowdown (unregulated) system, and (2) a regulated system. The blowdown system consists of a single propellant tank shared by the propellant (i.e., hydrazine) and the pressurant (e.g., He, N_2, or H_2). While simpler than the regulated system, feed pressure will fall as propellant is expelled from the tank. This will result in a decrease in thrust over time, thus complicating mission operations somewhat—a fixed-burn time firing will deliver smaller and smaller impulse bits as the mission progresses.[103] A regulated system uses a mechanical or computer-controlled regulator to deliver propellant to the engine at a fixed, predetermined pressure. This requires the addition of a pressurant tank (nominally pressurized to very high values, 200-340 bar [Brown, 1996]) and additional flow control devices and fittings. Propellant management devices or PMDs (e.g., bellows, diaphragms, pistons, vanes, or wicking screens) are required to ensure separation of liquid propellant from the gas pressurant during zero gravity operation. The author has tentatively selected a rolling diaphragm positive expulsion device and a blowdown mode for the baseline propellant management system, based on Humble [1996]: The rolling diaphragm tends to be a low-mass, low-cost design.

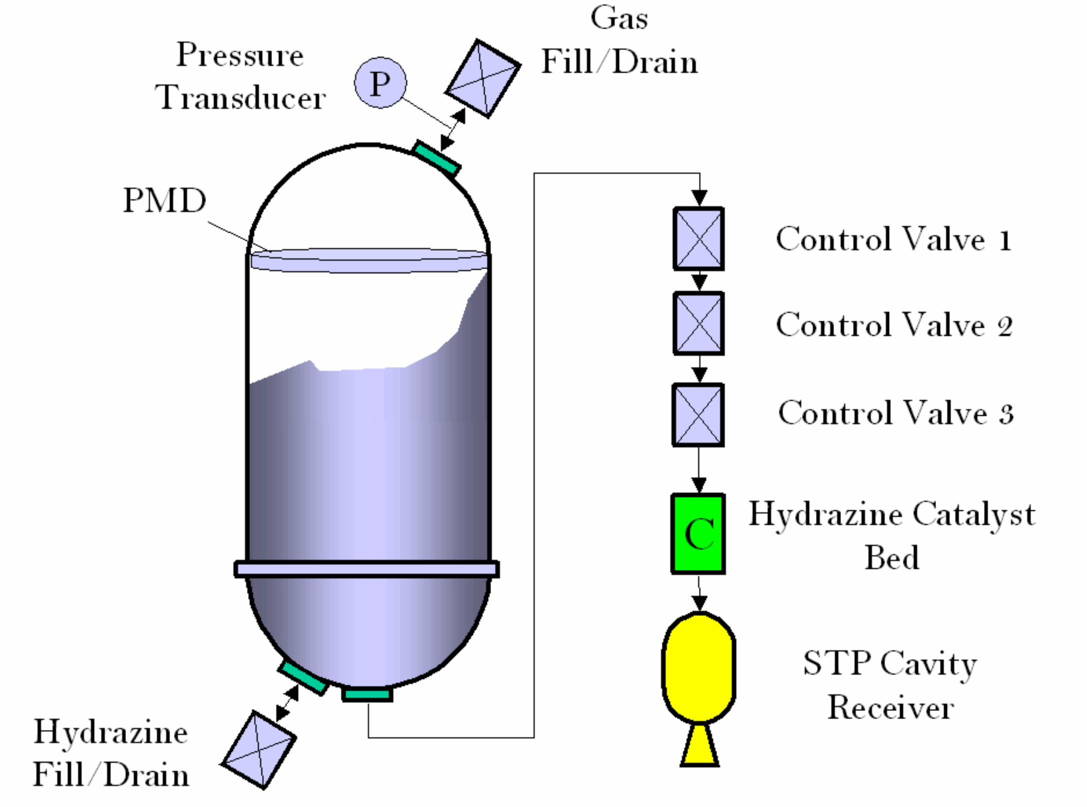
Gas
Fill/Drain
Pressure
Transducer
P
PMD
Control Valve 1
Control Valve 2
Control Valve 3
C
Hydrazine Catalyst
Bed
STP Cavity
Receiver
Hydrazine
Fill/Drain

Figure 4-29 Schematic of feed system in blowdown mode.

A representative blowdown system operating at a beginning of life (BOL) pressure of 350 psi (24 bar) and an end-of-life (EOL) pressure of 100 psi (6.8 bar) will allow the micro STP system to provide between 500 (EOL) and 1800 mN (BOL) of thrust, according to the standard equation for thrust (Equation 4-6) and:

$$\dot{m} = \frac{P_c A_t}{c^*} \tag{4-28}$$

Here, c^* is the characteristic velocity[104] of the propellant, which, in this case, is decomposed hydrazine; P_c is the chamber pressure, and A_t is the nozzle throat area [Humble, 1995]. For hydrazine decomposition products at 2,500 K, c^* is approximately 2,100 m/s. The micro engine's

---

[103] Alternately, a fixed-impulse scheme could be created in which burn times are increased over the duration of the mission.

[104] The characteristic velocity is a function of chamber conditions and propellant only.

design throat area, A_t, is 3.89 x 10^{-7} m^2 (corresponding to a radius of .35 mm). The author estimates that a spherical aluminium tank (30.75 cm outer diameter) with 1 mm sidewalls will mass 830 g and hold 11.75 kg[105] of N_2H_4. This does not include structural attachments, propellant management devices, bosses, or fittings, which tend to significantly increase a tank's mass. Humble [1995] notes that the addition of these items typically results in a tank mass of two to two-and-one-half times the tank shell mass (<2.075 kg for this design). Figure 4-29 illustrates a possible layout for this feed system.

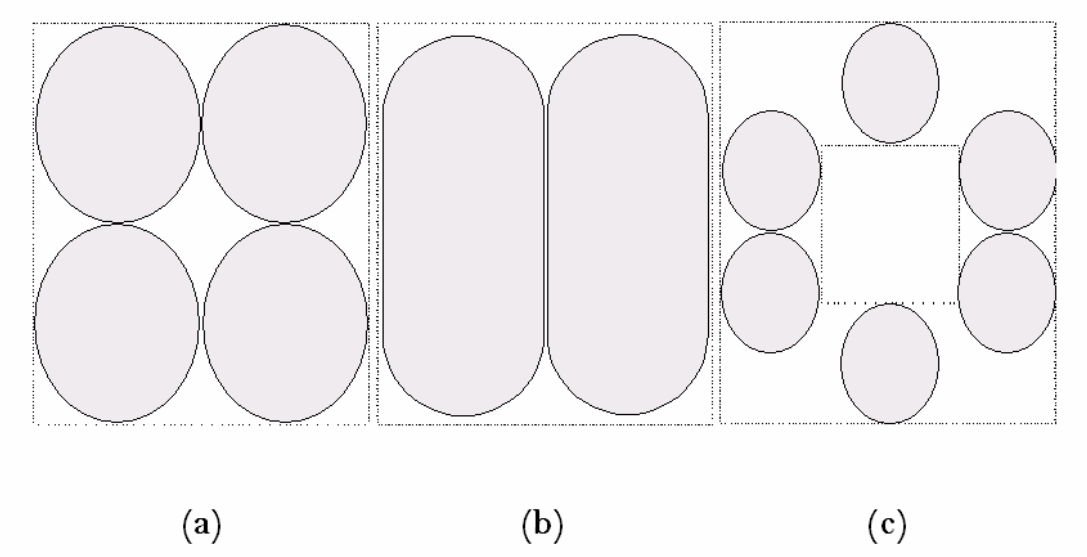

Figure 4-30 Three possible propellant tank siting configurations for the SSTL enhanced microsatellite: (a) Spherical tanks in a cruciform configuration, (b) dual capped cylindrical tanks mounted transversely, and (c) six longitudinally mounted, capped cylinders. The view is along the satellite's z-axis (looking towards nadir).

The small (100 kg microsatellite, GTO-to-GEO, 1,761 m/s, burn-average I_{sp} = 355 s) and large (100 kg, Near Escape, 1,770 m/s, burn average I_{sp} = 359 s) engines require correspondingly larger tanks to accomplish their missions. With a 10% margin and an equivalent blowdown ratio[106] of 3.5:1, these mission require 43.7 and 43.5 kg of hydrazine, respectively. Given SSTL's enhanced microsatellite volumetric constraints (Appendix B, q.v.), multiple tanks will be required. Configurations (Figure 4-30) for a 43.7 kg propellant loading include (1) four spherical tanks in a cruciform configuration on a reserved platform ("propulsion shelf") under the electronics stack,[107] each 30 cm in diameter, massing 1.9 kg (4.75 kg with factor of 2.5) in total and holding 10.93 kg of propellant each, (2) two hemispherical-capped cylindrical tanks on a propulsion shelf below the electronics stack, 28 cm x 55.6 cm, mounted transversely to the satellite +z axis, together massing 2.7 kg (6.75 kg with factor of 2.5) and holding 21.85 kg of hydrazine each (3) six capped cylinders, mounted parallel to the satellite +z axis and around the electronics stack central "keep-out" zone, massing 4.96 kg (12.4 kg with factor of 2.5) in total, holding 7.3 kg of propellant each, and measuring 13.75 cm x 68.3 cm. This last configuration adheres to the enhanced microsatellite internal volume (as well as the Ariane ASAP footprint) constraints, but its relatively high tankage mass detracts from its utility.

---

[105] This is based on the LEO orbit raising mission (352 to 704 km), a cumulative delta-V requirement of 193.6 m/s, a burn average I_{sp} of 325 s, He fill gas at an initial pressure of 350 psi (24 bar), and includes a 10% margin to cover ullage, trapped propellant volumes, and any contingency firing.

[106] Blowdown ratio = BOL tank pressure / EOL tank pressure.

[107] This configuration might not be achievable, given the 60 x 60 cm ASAP footprint.

4.6 Preliminary Design Summary

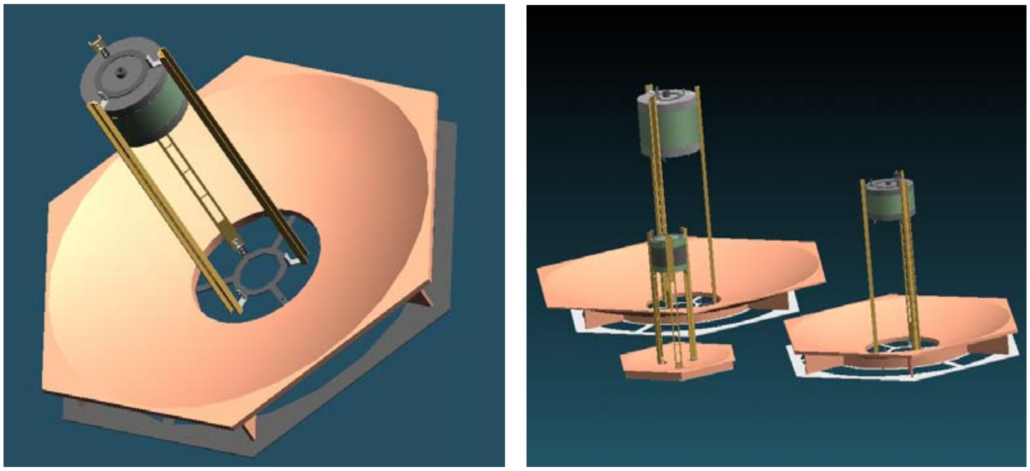

STP small engine assembly, 12 kg, 63-cm concentrator. This system provides 150 mN of thrust for up to 5,000 s (83 min.) at an average specific impulse of 355 s, with hydrazine propellant.

Relative size of micro (foreground, left), small (right), and large engine assemblies (background, left). Preliminary mass estimates range from 3 (micro engine) to 20 kg (large engine).

Figure 4-31 Solar thermal engine assembly layouts, preliminary design, single mirror approach.

The author has provided a detailed account of the preliminary design for a set of solar thermal propulsion systems (Figure 4-31), applied to the three mission classes described in Chapter 3. Specific requirements for these missions can be found in Appendix B. In most cases, the author was able to meet the threshold requirements for I_{sp} and total impulse per firing.[108] There are several instances of shortfalls, discussed below.

The preliminary modelling suggested that system dry mass requirements could be met for the micro and small engine configurations. The large engine—at 19 kg—was found to be overweight as a result of its outsize metal mirror, which masses 10.5 kg. As the author has mentioned previously, simplifications in the preliminary receiver heating model show that even these relatively large mirrors would not be large enough to heat the three receiver types to operating temperature. Finding a means to resolve this dilemma became one of the principal tasks of the detailed design phase. While there are options available for decreasing this mass, the most commonly suggested alternatives, are also the most expensive.[109]

A ganged mirror assembly, consisting of twenty 20-cm diameter paraboloidal dishes, provides a received power (at the cavity aperture) equivalent to a single 79-cm mirror. An example is shown in Figure 4-2. Optical fibre runs would transmit the incident solar radiation to a single solar receiver, thus decoupling the receiver from the concentrator focus and allowing it to be placed anywhere on the spacecraft. Since a rigid, fixed 79-cm mirror is larger than the ASAP footprint—a key constraint—deployable shelves of 20-cm mirrors represent a plausible alternative that both saves mass (nearly 4 kilograms, in this instance) and permits stowage within the volumetric limitations of the most likely host launcher. While solar radiation transmission has been suggested for terrestrial applications and for space-based plant growth, the author is unaware of any previous suggestions to apply this technology to solar thermal propulsion.

Spacecraft internal volume presented difficulties—available propellant tank space is at a premium on SSTL's microsatellites, and strict adherence to keep-out zones will require high-aspect ratio, inefficient tank configurations. Launch constraints—which determine maximum concentrator size and thus limit total solar input power for rigid, fixed mirror assemblies—are the greatest source of difficulty, as they drive thermal storage charging times to their thresholds and, in several cases, beyond. While maximum receiver temperatures can be lowered to reduce charging time, this adversely impacts specific impulse performance. Longer charging times have additional effects, including missed firing opportunities and longer transfer times. For example, the micro engine, sized to provide 428 N-s of impulse per firing, requires nearly three hours of charging and can only fire on every third pass.[110] This demands a 17-day transfer between 352 and 704 km. The small engine, which provides 750 N-s of impulse per firing, is not constrained by its charging duration and should be capable of achieving a GTO-to-GEO transfer in 117 days—approximately

---

[108] These three drive propellant consumption (therefore volume) and transfer times, the key figures of merit. Per-burn total impulse is a concatenation of thrust and firing duration requirements—with longer firing durations offsetting decreased thrust.

[109] A a lighter-weight mirror solution (e.g., carbon-fiber reinforced polymers), would lower the areal density of the 79-cm mirror from its present 21.2 kg/m^2 to ~10 kg/m^2. This would reduce the mirror mass by more than 5 kg, reducing the system mass figure to 13.4 kg (below the threshold target of 15 kg).

[110] The initial orbit's (352 km circular) period is 92 minutes, of which 36 minutes is spent in eclipse. The remaining 56 minutes are available for thermal storage mass charging. Three consecutive charging periods—assuming minimal radiative loss in eclipse—are sufficient to permit a firing at design average specific impulse (325 s).

20% greater than the threshold requirement. The large (2,808 N-s) engine is tasked to perform more complicated manoeuvring: (1) a lunar orbit insertion, and (2) a NEO flyby.

The flyby mission scenario includes 25 escape burns separated by three hours, and cannot be accomplished by the large engine (which requires over five hours to recharge). This is not likely to be critical for the flyby mission, however; additional wait time between firings at escape may require a slightly larger delta-V (as the majority of firings will be conducted farther from perigee), but the overall mission profile is not compromised. The lunar capture mission is less forgiving. A low-thrust insertion at the moon requires multiple, closely spaced firings to permit capture; the seven-burn insertion sequence (see Chapter 3) is unlikely to permit a doubling of wait time between firings. To preserve the mission profile, charging time can be restricted to three hours for critical phases (TLI, LOI). This reduces maximum achievable receiver temperature for affected manoeuvres to approximately 2,000 K (Fig. 3.30) and average I_{sp} to roughly 325 s.[111]

---

[111] Assuming performance similar to that of the micro engine, which also has a peak temperature of 2,000 K and an average I_{sp} of 325 s. This translates to an additional 1.6 kg of hydrazine propellant to balance the reduced specific impulse.

Chapter 5

5 Integrated System Modelling and Detailed Design

5.1 Overview

This chapter begins with concentrator and receiver subsystem modelling using the validated, commercially available codes OSLO LT (a ray-trace simulator for optical systems) and WinTherm (a coupled-mode heat transfer simulator, utilised frequently in the automotive industry). A description of the author's Microscale Solar Thermal Integrated System Model (MSTISM), a system-level code intended to permit detailed modelling and sensitivity analyses for detailed solar thermal engine design, follows the results of proprietary code modelling. Finally, the author describes the process and outcome of the detailed engine design activity, building on the preliminary design results obtained in Chapter 4. These designs were subsequently fabricated and tested, with results available in the next chapter.

5.2 Optical Performance Modelling with OSLO LT

The form, or surface slope error of a concentrating mirror determines its ultimate efficacy as a power transmission device. Small "hills" and "valleys," no more than several tens of nanometres in height or depth, can significantly impact the performance of optical imaging elements. As noted in Chapter 4, telescopes and other imaging devices often quote a wavefront error of $\lambda/4$ (equivalent to a surface form error of $\lambda/8$). While solar concentration does not demand diffraction-limited optics and wavefront errors on the order of the wavelength of light transmitted, poor mirror surface preparation can result in ray deviations, scattering, and low optical efficiencies. Etheridge [1979] and Partch [1999] both detail pointing budgets that include mirror slope error requirements of between 0.1º (1.7 milliradians, or mrad) and 0.5º (8.7 mrad, integrated over the entire mirror surface). Other budget elements include pointing errors, discussed in Chapter 4.

From geometrical principles, one can estimate the maximum local slope error that will still permit an incident ray to be received by an aperture of fixed radius r_a. A centreline ray (one emanating from the centre of the solar disk) strikes a parabolic mirror at point *P*, a radial distance *x* from the normal to its apex (Figure 5-1) and is reflected. For zero slope error, the reflected ray will arrive at point *O*. For maximum permissible slope error, the reflected ray will just intercept the aperture's edge, at *A*. For this value of slope error, 50% of the incident power will miss the aperture; light from the far edge of the solar disk will fall on the centreline of the aperture. Applying the law of cosines to the triangle *OAP* in the figure, and solving for the included angle ξ, allows one to deduce the permissible slope error. This is simply:

$$\xi = \cos^{-1}\left(\frac{r_a^2 - OP^2 - AP^2}{-2(OP)(AP)}\right) \qquad \textbf{(5-1)}$$

Where:

$$AP = \sqrt{(f-y)^2 + (x-r_a)^2} \qquad \textbf{(5-2)}$$

And:

$$OP = \sqrt{(f-y)^2 + x^2} \qquad \textbf{(5-3)}$$

For a 30º rim angle (f/.866), and a geometric concentration ratio of 10,000:1, the maximum permissible slope error for a ray incident near the mirror periphery is 0.115º (2 mrad).

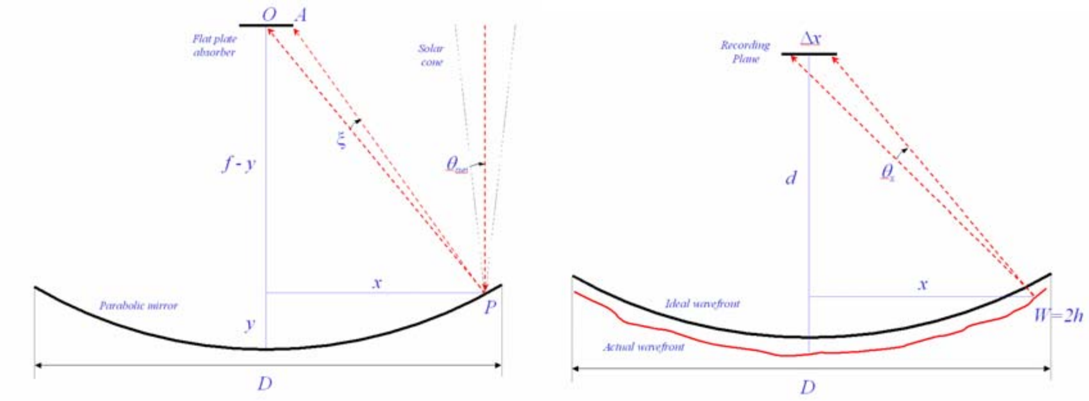

Figure 5-1 Local slope error calculation for centreline ray (left), Hartmann test wavefronts (right), adapted from Malacara [1992].

For comparison, Etheridge estimates that his primary mirror is capable of a concentration ratio approaching 4,000, for a form error of 0.5º [1979]. At 0.25º, *C* rises to nearly 7,000; at 0.13º, *C* is over 12,000. Malacara [1992] provides the following approximate relation between wavefront aberration or error *W* and ray deviation Δ*x* at a "recording" plane (Figure 5-1, right):

$$W = \frac{1}{d}\int_0^x \Delta x dx \qquad \textbf{(5-4)}$$

Malacara's formulation includes the assumption that the distance from the recording plane to the mirror surface, *d*, is constant; while this might be approximately true for long focal length (high *f*/#) mirrors, it is not the case for fractional *f*/# paraboloidal mirrors. For the case at hand, then, $d = f - y(x)$ is clearly a function of lateral travel *x* and cannot be brought outside the integrand. If Δx can be approximated with reasonable accuracy by a polynomial function in *x*, a direct correspondence between wavefront error[112] and surface slope error θ_x can be found:

$$\frac{\Delta x(x)}{f - y(x)} = \sin\theta_x \qquad \textbf{(5-5)}$$

Using equations 5-4 and 5-5, it can be demonstrated that a 63-centimetre diameter mirror, *f*/0.6, produces a wavefront error on the same order as the ray deviation, if one assumes a fixed value for the deviation ($\Delta x = 3.15$ mm).[113] This in turn equates to a surface slope error at the periphery of the mirror of 0.58º (10 mrad). For a ray deviation that instead increases linearly in *x*, or for deviations with higher-order terms, much smaller wavefront errors are capable of producing ray deviations of this magnitude.

Shape, form error, wavefront error, and resultant ray deviation will be unique to specific mirrors. it is, however, possible to specify a base mirror surface and introduce aberrations to determine the effect of imperfect fabrication or pointing on focal spot size, and, therefore, concentration ratio. The freely available ray-tracing tool OSLO[114] LT, a Microsoft Windows based application with a spreadsheet-based graphical user interface, allows a user to simulate and analyse optical systems composed of up to ten refractive or reflective surfaces [Sinclair Optics, 2001].

The theory of ray-tracing, and the details of its implementation in OSLO LT, will not be described here, although Hecht [1998], Pedrotti [1993], and Lambda Research Corporation's OSLO reference manual [2001] provide substantial background information. Fundamentally, as Pedrotti [1993] notes:

> "If the quality of an image is to be improved…ways must be found to reduce the ever-present aberrations that arise from the presence of rays deviating, more or less, from [the paraxial ideal]. To determine the path of individual rays of light through an optical system, each ray must be traced, independently, using only the laws of reflection and refraction together with geometry. This technique is called ray-tracing because it was formerly done by hand, graphically, with ruler and compass…"

---

[112] The resultant height (i.e., the difference between the ideal and actual surfaces, or form error), *h*, is ½ *W*.

[113] For a ray deviation of 3.15 mm (equivalent to the focal spot radius for $C = 10{,}000$), $W = 2.8$ mm.

Meridional rays, those that pass through the system's optical axis, are easier to analyse than skew rays (those that do not pass through the optical axis), as meridional rays permit a two-dimensional treatment and therefore a simplification of the calculations involved [Pedrotti, 1993].

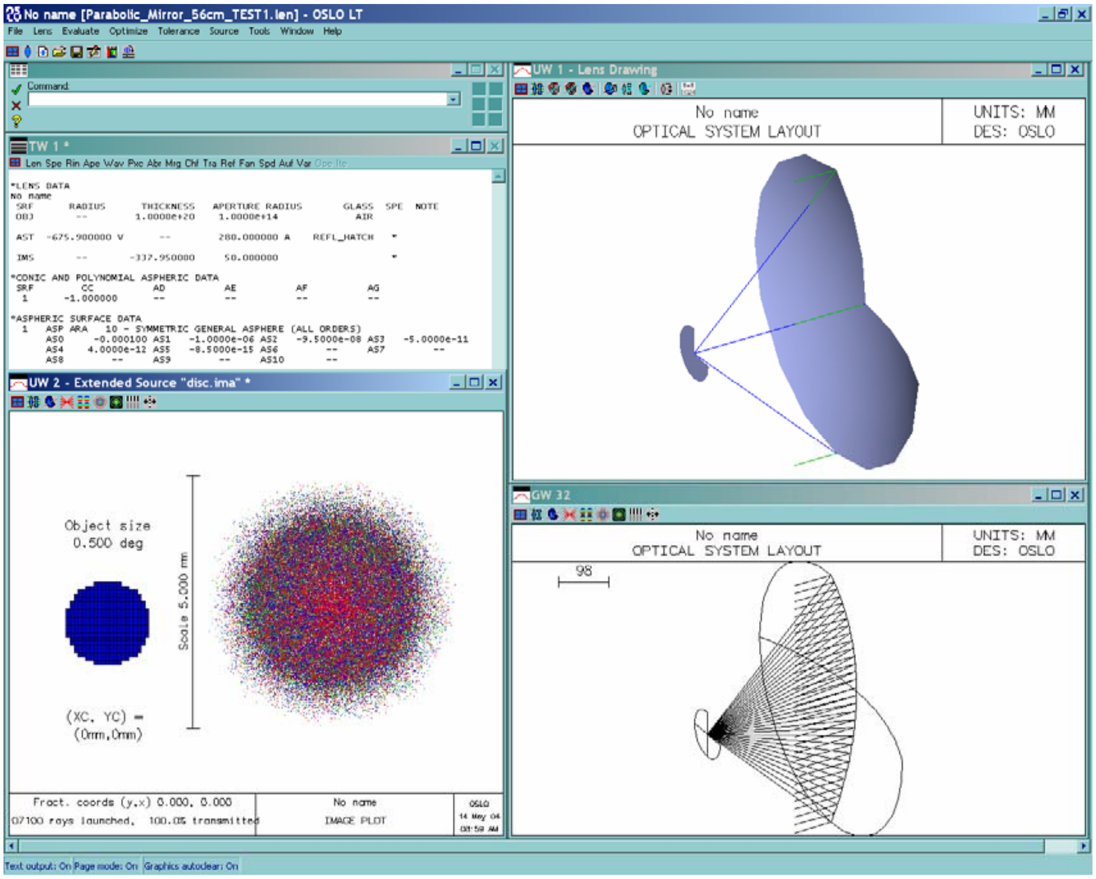

No name [Parabolic_Mirror_56cm_TEST1.len] - OSLO LT
File Lens Evaluate Optimize Tolerance Source Tools Window Help
Command
TW 1 *
Len Spe Rin Ape Wav Pxc Abr Mrg Chf Tra Ref Fan Spd Auf Var Ope Ite
UW 1 - Lens Drawing
No name
OPTICAL SYSTEM LAYOUT
UNITS: MM
DES: OSLO
UW 2 - Extended Source "disc.ima" *
Object size
0.500 deg
Scale 5.000 mm
(XC, YC) =
(0mm,0mm)
GW 32
No name
OPTICAL SYSTEM LAYOUT
UNITS: MM
DES: OSLO
98

```
*LENS DATA
No name
 SRF      RADIUS      THICKNESS    APERTURE RADIUS       GLASS   SPE   NOTE
 OBJ        --        1.0000e+20    1.0000e+14             AIR

 AST   -675.900000 V      --        280.000000 A    REFL_HATCH   *

 IMS        --       -337.950000     50.000000                  *

*CONIC AND POLYNOMIAL ASPHERIC DATA
 SRF         CC          AD            AE            AF            AG
  1      -1.000000       --            --            --            --

*ASPHERIC SURFACE DATA
  1    ASP ARA    10 - SYMMETRIC GENERAL ASPHERE (ALL ORDERS)
       AS0      -0.000100 AS1    -1.0000e-06 AS2    -9.5000e-08 AS3    -5.0000e-11
       AS4     4.0000e-12 AS5    -8.5000e-15 AS6         --     AS7         --
       AS8         --     AS9         --     AS10        --
```

```
Fract. coords (y,x) 0.000, 0.000
07100 rays launched,  100.0% transmitted
No name
IMAGE PLOT
OSLO
14 May 04
08:59 AM
```

Text output: On Page mode: On Graphics autoclear: On

Figure 5-2 Representative screen shot of OSLO LT simulation, for 56-centimetre diameter, f/0.6 paraboloidal concentrating mirror.

Lens or reflective (mirror) element data is entered in a data entry spreadsheet window, to include each surface and its properties (e.g., radius, thickness, aperture radius, and composition). As OSLO is used primarily for lens design, default surfaces are refractive and elements are composed of glass. Figure 5-2 shows a 56-centimetre diameter paraboloidal mirror with a focal length of 33.6 centimetres; simulated fabrication error has been introduced in the form of comatic and spherical aberration.[115] A pixellated disk representing the sun, subtending an arc of 0.50º, has been placed on the object plane (at infinity). OSLO produces an image plot (lower left hand

---

[114] Optics Software for Layout and Optimisation (OSLO).

[115] Spherical aberration results from a mirror's failure to focus rays at a single axial location; rays tend to spread longitudinally, producing a line focus. Comatic aberration, or coma, results from a variation in effective focal length for object points not on the optical axis. These and other *Seidel aberrations* result from expansion of *sin* θ (usually approximated as θ) in Snell's law to include higher-order (θ^3, θ^5, …) terms [Hecht, 1998].

corner of figure) demonstrating that the focal spot produced by this mirror is slightly less than 5 mm in diameter, in the case of perfect pointing. This and other analyses were used to validate the large mirror design prior to fabrication. The effective concentration ratio for this system is better than 12,500.

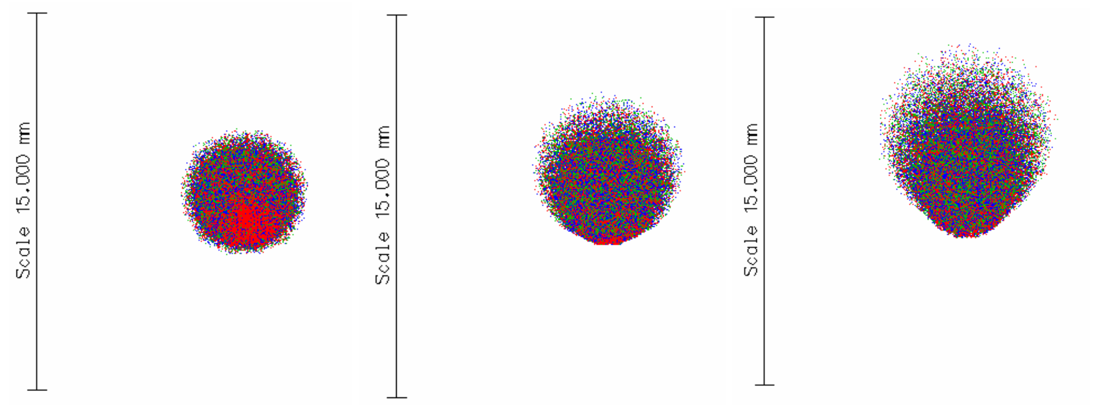

Figure 5-3 Focal spot images, for perfect pointing (left), 0.5° offset (centre, spot moves 2.93 mm from optical axis), 1.0° offset (spot moves 5.87 mm from optical axis).

OSLO also permits an assessment of pointing error on focal spot size (Figure 5-3). As pointing offset increases, the focal spot translates and acquires a coma (tail), the hallmark of comatic aberration. At an offset of 1°, the spot has grown from 5 mm in diameter along the vertical axis to nearly 8 mm, and has moved almost 6 mm off-centre. Since the diameter of the receiver aperture (8 mm), described later in this chapter, is designed to limit radiative losses from its interior and permit high peak temperatures, it can be seen that off-pointing of this magnitude will result in substantial losses and unacceptably poor performance. Pointing accuracies of ±0.1° or better will be required to maximise power transfer while allowing a minimum aperture diameter.

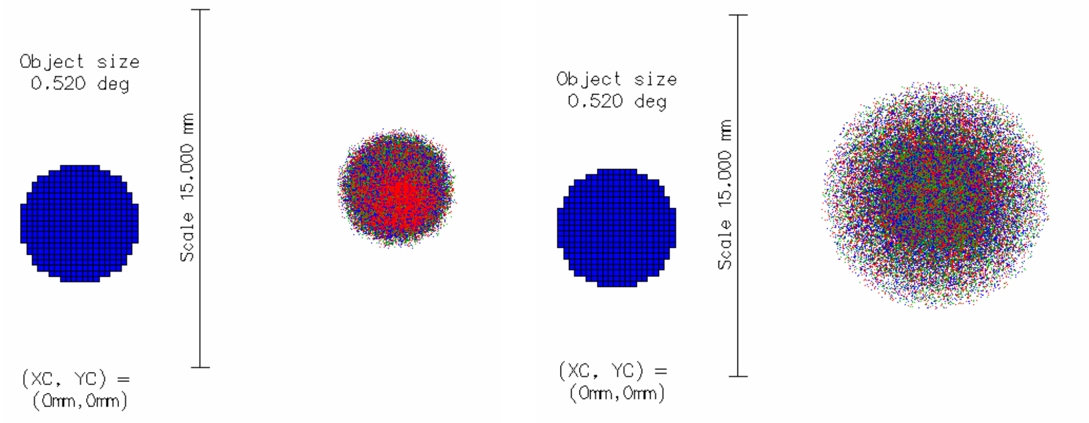

Figure 5-4 56-centimetre diameter paraboloidal concentrating mirror, perfect conic, 5mm spot (left) and imperfect, 9.2 mm spot (right), containing spherical and comatic aberrations. RMS wavefront error of mirror producing the image at right is 58 µm.

To model the effects of aberrations, it is useful to establish the departure or "sag," *h*, of the real optical surface from the ideal:

$$h = \frac{R_c x}{1+\sqrt{1-R_c(c_c+1)x^2}} + ax + bx^2 + cx^3 + dx^4 + \ldots \qquad \textbf{(5-6)}$$

The sag is therefore a function of the real surface's radius of curvature R_c, its conic constant c_c (-1 for paraboloidal elements), and the lateral distance from the mirror apex *x*. The first term describes the base mirror. The coefficients *a*, *b*, *c*, *d*, … in combination with the linear and higher-order terms in *x* describe deviations from this ideal surface [LRC, 2001]. A representative plot of sag versus radial position is shown in Figure 5-5. A mirror with this sag profile will have a root-mean-square form error of 1.49 microns, or an RMS wavefront error of 3 microns.

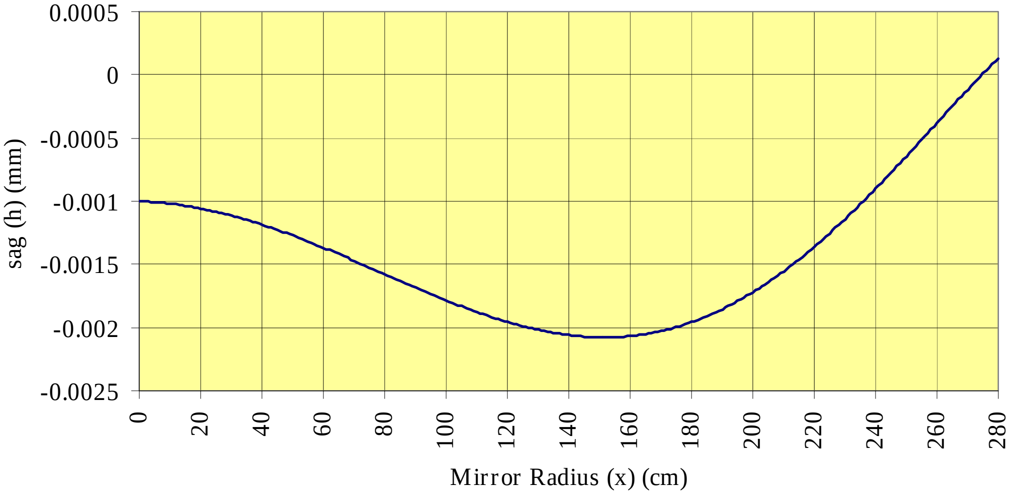

Figure 5-5 Sag versus radial position, 56-centimetre f/0.6 paraboloid. Equation 5-6 coefficients: a = -0.001, b = -1×10^{-6}, c = -9.5×10^{-8}, d = -5×10^{-11}, e = 4×10^{-12}, f = -8×10^{-15}. RMS form error = 1.5 µm.

A similar profile, but with exaggerated sag, was used to produce the focal spot image data in Figure 5-4, for the 58-µm RMS wavefront error mirror. This analysis shows that concentrating systems are capable of tolerating large wavefront errors—for some sag profiles, up to 100 times the primary light wavelength (588 nm). This will result in relaxed specifications for fabricators and substantially reduced cost.

5.3 Thermal Modelling with WinTherm

Thermoanalytics, Inc., WinTherm [2001] thermal modelling software was used to validate previous solar receiver thermal charging simulations with the CHUPS code (Chapter 4) and as a benchmark for actual heating profiles found in receiver tests (Chapter 6). WinTherm is capable of simulating conduction, convection, and radiation heat transport in and over shell structures of the type displayed in Figure 5-6. The heat diffusion equation [Lienhard, 1987], a parabolic differential equation, is typically posed as:

$$\vec{\nabla}\cdot(k\vec{\nabla}T)+\dot{q}=\rho C_p\frac{\partial T}{\partial t} \tag{5-7}$$

Radiation at a boundary can be expressed by a boundary condition of the third kind:

$$-k\frac{\partial T}{\partial x}=\varepsilon\sigma\left(T^4-T_{ambient}^4\right) \tag{5-8}$$

WinTherm utilises a time-averaging finite difference scheme, the Crank-Nicholson method, to simultaneously solve for the three modes of heat transport, thus permitting the determination of the modelled objects' temperature profile over time. Crank-Nicholson is implicit, requiring the solution of a linear system of equations at each time step, and is therefore unconditionally stable.

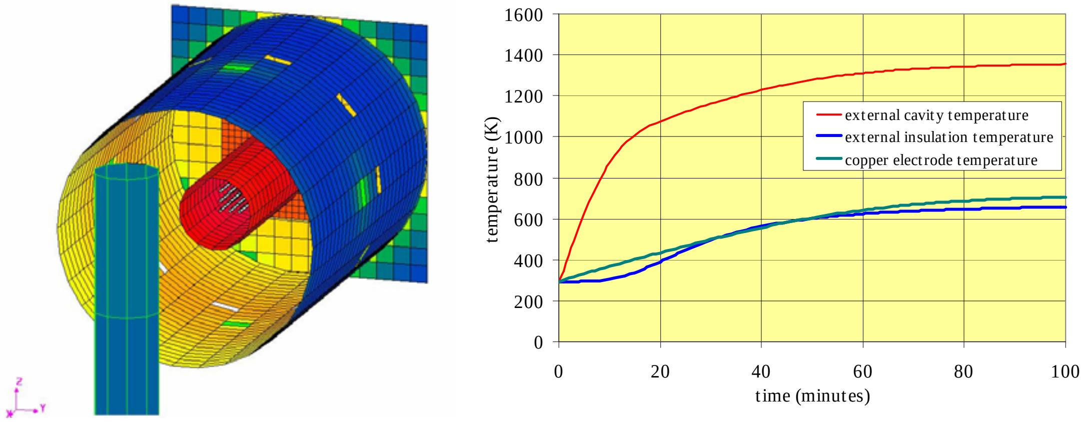

Figure 5-6 WinTherm model of Mk. I cavity receiver in electrical heating test configuration, 325 W input power, left (one copper electrode shown in foreground). Temperature profile of solar receiver cavity external surface, insulation package external surface, and copper electrode, right.

WinTherm first calculates radiation view factors for each pair of elements, by generating a number of simulated rays at the first element and determining how many rays intersect the second. Unfortunately, WinTherm does not take into account element thickness when modelling radiation view factors (although it does use user-inputted thickness data to determine conduction through individual elements). WinTherm wrongly assumes that a structure's inner and outer radiating surfaces are the same; therefore, the code's results suffer from significant inaccuracies when modelling thick structures in radiation-dominant problems, such as that occurring in high-temperature solar receivers. The small receiver structure (inner cylinder in Figure 5-6) accurately simulates the inner receiver surface but underpredicts radiative transfer (due to the smaller-than-actual external surface area) between the outer surface of the receiver and the insulation package, producing higher receiver temperatures for a given power dissipation than is actually observed. Test results, discussed in Section 6.2.2 bear this out.

Attempts were made to predict both ideal (in-space) and ground testing results. Figure 5-7 illustrates a resistive element heating model of the Mk. I cavity receiver.[116] The inner diameter of the cavity is 22.5 mm; the outer diameter is 85 mm. To overcome WinTherm's inherent problems with modelling thick bodies, a compromise diameter of 54 mm was used to model radiative heat transfer between (1) resistive heating elements and the receiver's inner surface, and (2) the receiver's outer surface and the insulation package's inner surface. Vacuum chamber walls, as well as front receiver body and insulation covers, are included in the model but not shown in the figure.

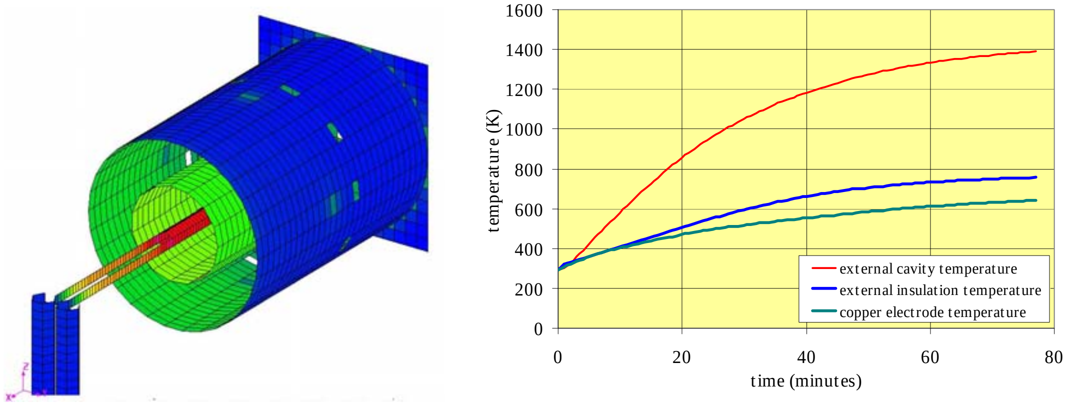

Figure 5-7 WinTherm model of Mk. I cavity receiver (left) and test results (right), 600 W input power with high resistive losses in leads (250 W), electrode/lead contacts (100 W), and electrode (200 W). Receiver shell is enlarged to "compromise" diameter (average of internal and external surface diameters). Conductive coupling simulates resistive heating via copper electrodes (lower left), molybdenum leads, and a ceramic heating element (centre).

Improved simulation results, such as those shown in Figure 5-7, were compared to test data but still failed to properly predict the temperature profiles of key elements. Sensitivity analyses were performed to determine the effect of higher-than-predicted insulation thermal conductivities and anomalous power dissipation in electrodes, leads, and contacts. Results from this investigation indicated that, even for cases with high insulation *k* values (≥ 0.3 W/m-K), and with significant, remote resistive losses in the heating element circuit, it was not possible to achieve congruence between model and test output. A final modelling attempt (Figure 5-8) was made to resolve the disparity between WinTherm and test data; this simulation incorporated high-conductance fins to transfer heat between an appropriately sized inner receiver surface and outer surface. While this approach provided substantially improved agreement over previous models, its form deviates substantially from the actual physical layout of the Mk. I and Mk. II receivers.

---

[116] Design details for the Mk. I and Mk. II receivers can be found in Section 5.6.

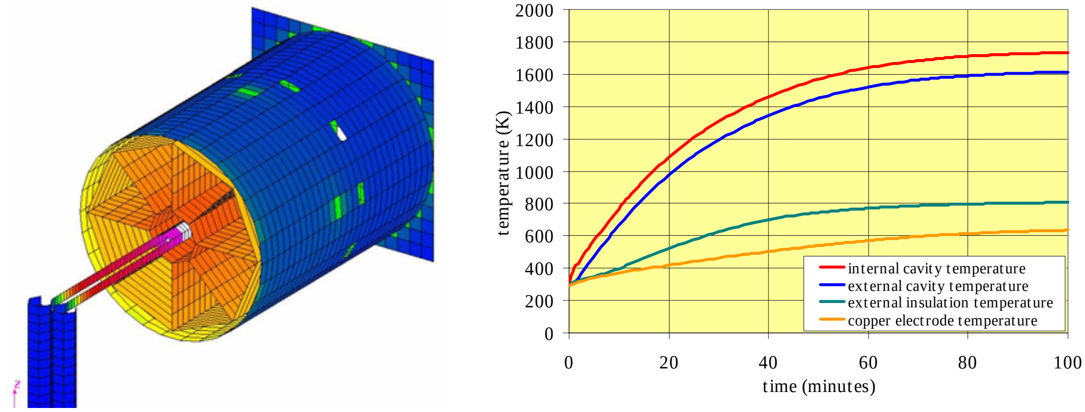

Figure 5-8 WinTherm model of Mk. I cavity receiver (left) and test results (right), 600 W input power, 250 W dissipation in molybdenum leads, 150 W dissipation in copper electrode/molybdenum contacts. This model is designed to accurately simulate external and internal radiative surfaces while modelling conduction through the thickness of the body using eight fins.

WinTherm was used successfully to model copper target heating by a large (56-centimetre diameter) solar concentrating mirror under both atmospheric (with natural convection) and space conditions. Section 6.3.2 provides details.

5.4 Constructing an Integrated System Model

The OSLO NT and WinTherm codes provide for high-fidelity analysis in two very narrow areas: optical surface performance verification and coupled convective/radiative/conductive heat transfer simulation in shell structures. While potentially very accurate, these models (in particular, WinTherm) were cumbersome to initialise and time-consuming to run. The more complicated of the WinTherm simulations required as much as an hour to process a receiver heating profile.

More importantly, neither OSLO nor WinTherm was capable of outputting data automatically into another code for iterative analysis of the entire solar thermal propulsion system, to include not just the receiver structure and concentrator but also tankage and propellant management, satellite attitude control, firing profiles, and orbit changes resulting from STE use. To address this deficiency, a whole-system simulation of the STE was constructed, the Microscale Solar Thermal Integrated System Model, or MSTISM (Figure 5-9). MSTISM was built and operated within the commonly available spreadsheet programme, Microsoft Excel (v9.0.3821 SR-1), and was augmented with a number of Visual Basic scripts. These scripts assign values to spreadsheet cells and perform complex, iterative calculations for heating and convective cooling—a task that Excel is not particularly well suited for.

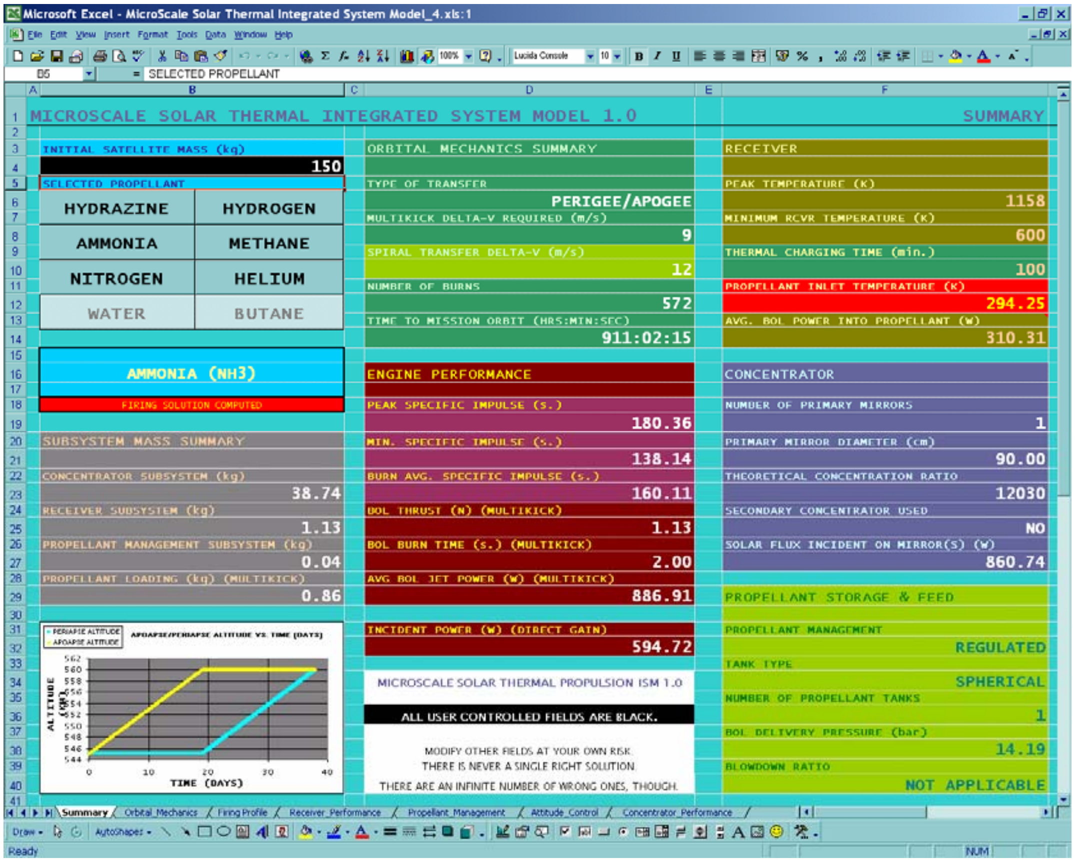
Microsoft Excel - MicroScale Solar Thermal Integrated System Model_4.xls:1
File Edit View Insert Format Tools Data Window Help
100%
Lucida Console
10
B5
A
B
C
D
E
F
Summary
Orbital_Mechanics
Firing Profile
Receiver_Performance
Propellant_Management
Attitude_Control
Concentrator_Performance
Draw
AutoShapes
Ready
NUM
PERIAPSE ALTITUDE
APOAPSE ALTITUDE
APOAPSE/PERIAPSE ALTITUDE VS. TIME (DAYS)
562
560
558
556
554
552
550
548
546
544
ALTITUDE (KM)
0
10
20
30
40
TIME (DAYS)

= SELECTED PROPELLANT

MICROSCALE SOLAR THERMAL INTEGRATED SYSTEM MODEL 1.0

SUMMARY

INITIAL SATELLITE MASS (kg): 150

SELECTED PROPELLANT

HYDRAZINE	HYDROGEN
AMMONIA	METHANE
NITROGEN	HELIUM
WATER	BUTANE

AMMONIA (NH3)

FIRING SOLUTION COMPUTED

SUBSYSTEM MASS SUMMARY

CONCENTRATOR SUBSYSTEM (kg): 38.74

RECEIVER SUBSYSTEM (kg): 1.13

PROPELLANT MANAGEMENT SUBSYSTEM (kg): 0.04

PROPELLANT LOADING (kg) (MULTIKICK): 0.86

ORBITAL MECHANICS SUMMARY

TYPE OF TRANSFER: PERIGEE/APOGEE

MULTIKICK DELTA-V REQUIRED (m/s): 9

SPIRAL TRANSFER DELTA-V (m/s): 12

NUMBER OF BURNS: 572

TIME TO MISSION ORBIT (HRS:MIN:SEC): 911:02:15

ENGINE PERFORMANCE

PEAK SPECIFIC IMPULSE (s.): 180.36

MIN. SPECIFIC IMPULSE (s.): 138.14

BURN AVG. SPECIFIC IMPULSE (s.): 160.11

BOL THRUST (N) (MULTIKICK): 1.13

BOL BURN TIME (s.) (MULTIKICK): 2.00

AVG BOL JET POWER (W) (MULTIKICK): 886.91

INCIDENT POWER (W) (DIRECT GAIN): 594.72

MICROSCALE SOLAR THERMAL PROPULSION ISM 1.0

ALL USER CONTROLLED FIELDS ARE BLACK.

MODIFY OTHER FIELDS AT YOUR OWN RISK.
THERE IS NEVER A SINGLE RIGHT SOLUTION.
THERE ARE AN INFINITE NUMBER OF WRONG ONES, THOUGH.

RECEIVER

PEAK TEMPERATURE (K): 1158

MINIMUM RCVR TEMPERATURE (K): 600

THERMAL CHARGING TIME (min.): 100

PROPELLANT INLET TEMPERATURE (K): 294.25

AVG. BOL POWER INTO PROPELLANT (W): 310.31

CONCENTRATOR

NUMBER OF PRIMARY MIRRORS: 1

PRIMARY MIRROR DIAMETER (cm): 90.00

THEORETICAL CONCENTRATION RATIO: 12030

SECONDARY CONCENTRATOR USED: NO

SOLAR FLUX INCIDENT ON MIRROR(S) (W): 860.74

PROPELLANT STORAGE & FEED

PROPELLANT MANAGEMENT: REGULATED

TANK TYPE: SPHERICAL

NUMBER OF PROPELLANT TANKS: 1

BOL DELIVERY PRESSURE (bar): 14.19

BLOWDOWN RATIO: NOT APPLICABLE

Figure 5-9 Screen shot of MSTISM Summary Input/Output Sheet.

MSTISM is logically divided into seven input/output sheets (Figure 5-10): (1) *Summary*, which takes preliminary input from the user (e.g., microsatellite mass and STE propellant type) and displays results from most of the other sheets; (2) *Orbital Mechanics*, which permits the user to specify initial and final orbital parameters and outputs delta-V requirements; (3) *Concentrator Performance*, which accepts input regarding ambient solar flux, concentrator properties and geometry, and outputs key parameters such as received power and spot size; (4) *Attitude Control*, which allows the user to specify satellite or mirror pointing error and its distribution (which is then factored into concentrator performance); (5) *Receiver Performance*, which accepts inputs in the form of material properties and geometry, channel flow or particle bed heat exchange scheme selection, and concentrator power, then outputs both a heating and firing profile; (6) *Propellant Management*, which takes propellant type input from the Summary sheet and tank constraints from the user, then calculates tank numbers, masses, and volumes; and, finally, (7) *Firing Profile*, which allows the user to select firing type (i.e., periapse or apoapse) based on estimated engine performance, and assign burn times to individual manoeuvres, if required.

The top, or *Summary*, sheet, requires only two inputs from the user: a starting (wet) satellite mass and a choice of propellant. Selecting a propellant type initiates a Visual Basic script, which deposits temperature-dependent gas property data on several other sheets. This data includes viscosity, specific heat, and thermal conductivity, all derived from validated online databases [NIST, 2000]. Available propellants include hydrazine, hydrogen, ammonia, methane, nitrogen, and helium, with the option to add others.[117] *Summary* also contains key parameters from other sheets, including a graphical display of the manoeuvre profile, estimated system mass properties, performance (including time-to-final-orbit, specific impulse, and thrust), and subsystem details such as receiver peak temperature, incident power at the receiver aperture, and propellant tank supply pressure. If the user selects a new propellant, *Summary* provides a warning that the displayed data has not been updated to conform to this choice, and directs the user to perform additional actions.

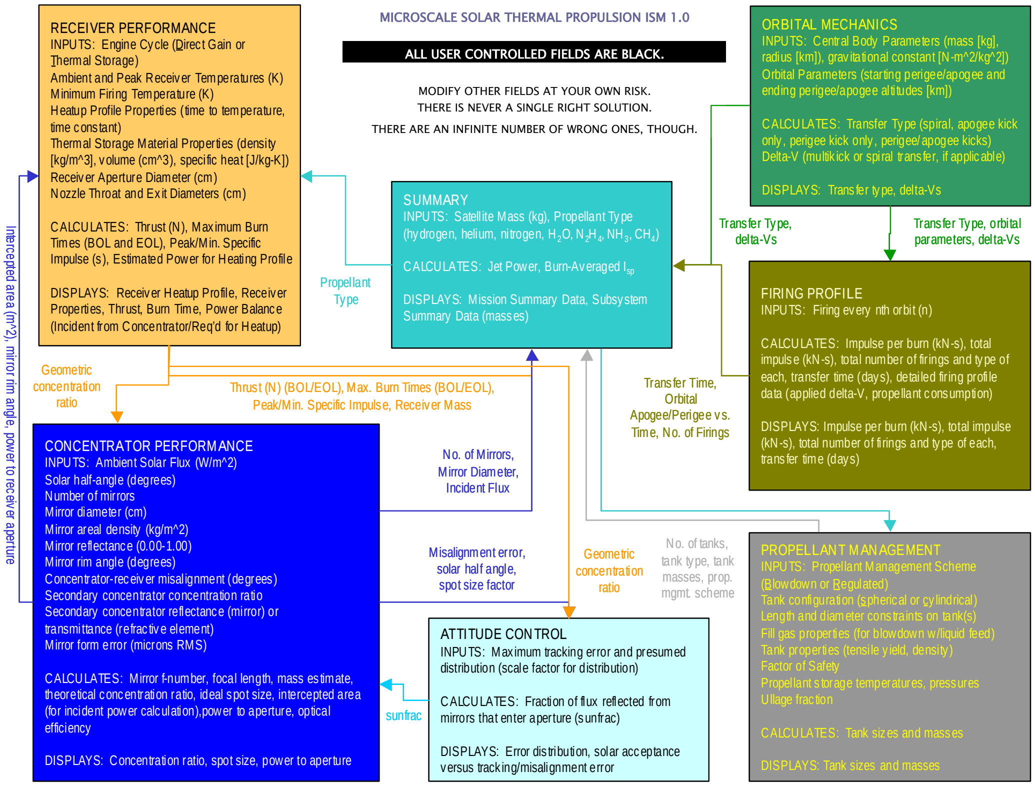
RECEIVER PERFORMANCE
INPUTS: Engine Cycle (Direct Gain or Thermal Storage)
Ambient and Peak Receiver Temperatures (K)
Minimum Firing Temperature (K)
Heatup Profile Properties (time to temperature, time constant)
Thermal Storage Material Properties (density [kg/m^3], volume (cm^3), specific heat [J/kg-K])
Receiver Aperture Diameter (cm)
Nozzle Throat and Exit Diameters (cm)
CALCULATES: Thrust (N), Maximum Burn Times (BOL and EOL), Peak/Min. Specific Impulse (s), Estimated Power for Heating Profile
DISPLAYS: Receiver Heatup Profile, Receiver Properties, Thrust, Burn Time, Power Balance (Incident from Concentrator/Req'd for Heatup)
MICROSCALE SOLAR THERMAL PROPULSION ISM 1.0
ALL USER CONTROLLED FIELDS ARE BLACK.
MODIFY OTHER FIELDS AT YOUR OWN RISK.
THERE IS NEVER A SINGLE RIGHT SOLUTION.
THERE ARE AN INFINITE NUMBER OF WRONG ONES, THOUGH.
ORBITAL MECHANICS
INPUTS: Central Body Parameters (mass [kg], radius [km]), gravitational constant [N-m^2/kg^2])
Orbital Parameters (starting perigee/apogee and ending perigee/apogee altitudes [km])
CALCULATES: Transfer Type (spiral, apogee kick only, perigee kick only, perigee/apogee kicks)
Delta-V (multikick or spiral transfer, if applicable)
DISPLAYS: Transfer type, delta-Vs
Propellant Type
SUMMARY
INPUTS: Satellite Mass (kg), Propellant Type (hydrogen, helium, nitrogen, H_2O, N_2H_4, NH_3, CH_4)
CALCULATES: Jet Power, Burn-Averaged I_{sp}
DISPLAYS: Mission Summary Data, Subsystem Summary Data (masses)
Transfer Type, delta-Vs
Transfer Type, orbital parameters, delta-Vs
FIRING PROFILE
INPUTS: Firing every nth orbit (n)
CALCULATES: Impulse per burn (kN-s), total impulse (kN-s), total number of firings and type of each, transfer time (days), detailed firing profile data (applied delta-V, propellant consumption)
DISPLAYS: Impulse per burn (kN-s), total impulse (kN-s), total number of firings and type of each, transfer time (days)
Intercepted area (m^2), mirror rim angle, power to receiver aperture
Geometric concentration ratio
Thrust (N) (BOL/EOL), Max. Burn Times (BOL/EOL), Peak/Min. Specific Impulse, Receiver Mass
Transfer Time, Orbital Apogee/Perigee vs. Time, No. of Firings
CONCENTRATOR PERFORMANCE
INPUTS: Ambient Solar Flux (W/m^2)
Solar half-angle (degrees)
Number of mirrors
Mirror diameter (cm)
Mirror areal density (kg/m^2)
Mirror reflectance (0.00-1.00)
Mirror rim angle (degrees)
Concentrator-receiver misalignment (degrees)
Secondary concentrator concentration ratio
Secondary concentrator reflectance (mirror) or transmittance (refractive element)
Mirror form error (microns RMS)
CALCULATES: Mirror f-number, focal length, mass estimate, theoretical concentration ratio, ideal spot size, intercepted area (for incident power calculation), power to aperture, optical efficiency
DISPLAYS: Concentration ratio, spot size, power to aperture
No. of Mirrors, Mirror Diameter, Incident Flux
Misalignment error, solar half angle, spot size factor
Geometric concentration ratio
No. of tanks, tank type, tank masses, prop. mgmt. scheme
PROPELLANT MANAGEMENT
INPUTS: Propellant Management Scheme (Blowdown or Regulated)
Tank configuration (spherical or cylindrical)
Length and diameter constraints on tank(s)
Fill gas properties (for blowdown w/liquid feed)
Tank properties (tensile yield, density)
Factor of Safety
Propellant storage temperatures, pressures
Ullage fraction
CALCULATES: Tank sizes and masses
DISPLAYS: Tank sizes and masses
sunfrac
ATTITUDE CONTROL
INPUTS: Maximum tracking error and presumed distribution (scale factor for distribution)
CALCULATES: Fraction of flux reflected from mirrors that enter aperture (sunfrac)
DISPLAYS: Error distribution, solar acceptance versus tracking/misalignment error

Figure 5-10 Microscale Solar Thermal Integrated System Model schematic.

---

[117] Water and butane are "greyed-out" propellant options. Water was not included owing to difficulties in modelling two-phase liquid/gas flow in the receiver. Butane (C_4H_{10}), while used operationally by SSTL for low-temperature resistojets on multiple spacecraft, dissociates above approximately 450 °C (723 K). Butane has a complicated decomposition chain with a number of hydrocarbon products emerging at various temperatures [Gibbon, 2000][NIST, 2000].

The second, or *Orbital Mechanics*, sheet, defaults to a low earth-centred circular starting orbit. The user can modify central body properties to simulate heliocentric (or selenocentric) manoeuvres, but trajectories transiting between spheres of influence (e.g., earth-centred to moon-centred) are not permitted.[118] The user can select starting and final orbital parameters, as well as finite burn penalties, delta-Vs supplied by other codes such as STK Astrogator, and starting orbital inclination. *Orbital Mechanics* will then proceed to calculate delta-V requirements for periapse and/or apoapse transfers, according to orbital energies determined by the *vis-viva* integral (Equation 4-1). This information is handed off to other sheets, used to determine required propellant mass, tankage properties, and firing profile details.

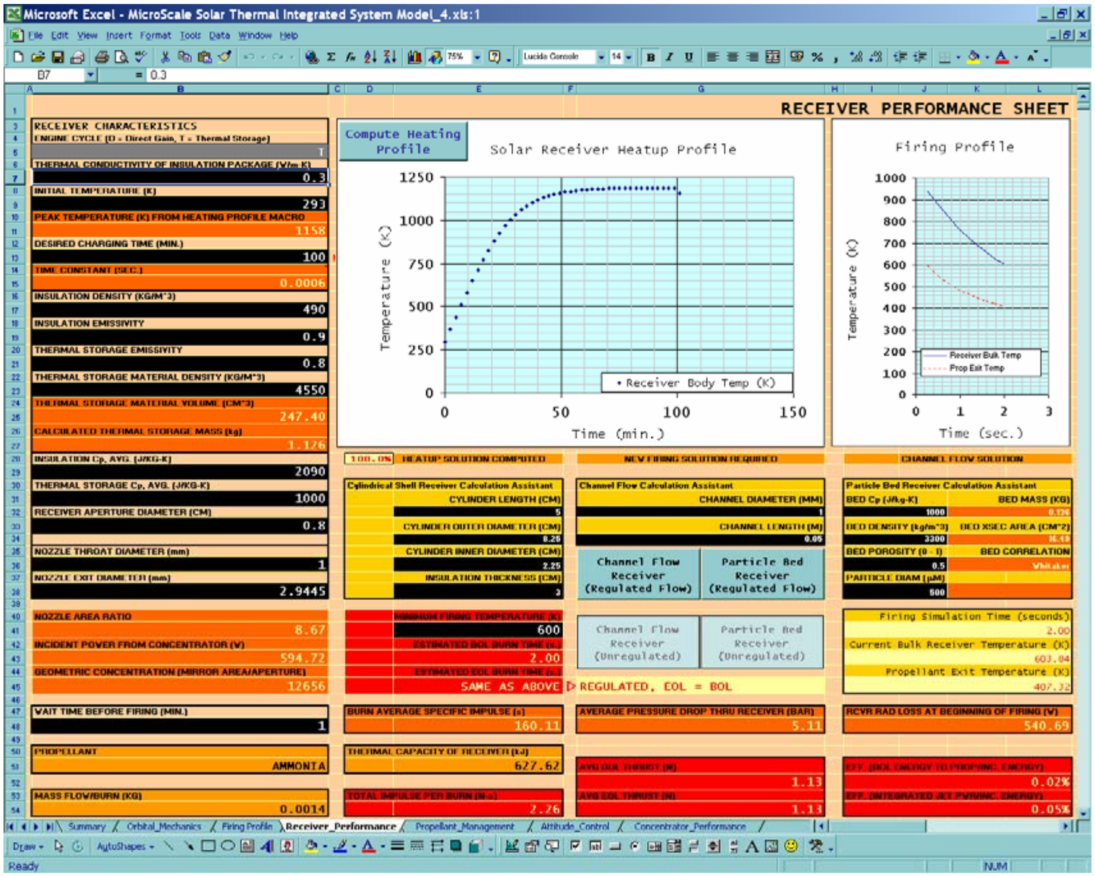
Microsoft Excel - MicroScale Solar Thermal Integrated System Model_4.xls:1
File Edit View Insert Format Tools Data Window Help
B7
= 0.3
RECEIVER PERFORMANCE SHEET
Compute Heating Profile
Solar Receiver Heatup Profile
Temperature (K)
1250
1000
750
500
250
0
0
50
100
150
Time (min.)
• Receiver Body Temp (K)
Firing Profile
Temperature (K)
1000
900
800
700
600
500
400
300
200
100
0
0
1
2
3
Time (sec.)
Receiver Bulk Temp
Prop Exit Temp
Channel Flow Receiver (Regulated Flow)
Particle Bed Receiver (Regulated Flow)
Channel Flow Receiver (Unregulated)
Particle Bed Receiver (Unregulated)
Summary
Orbital_Mechanics
Firing Profile
Receiver_Performance
Propellant_Management
Attitude_Control
Concentrator_Performance
Draw
AutoShapes
Ready
NUM

RECEIVER CHARACTERISTICS	
ENGINE CYCLE (D = Direct Gain, T = Thermal Storage)	T
THERMAL CONDUCTIVITY OF INSULATION PACKAGE (W/m-K)	0.3
INITIAL TEMPERATURE (K)	293
PEAK TEMPERATURE (K) FROM HEATING PROFILE MACRO	1158
DESIRED CHARGING TIME (MIN.)	100
TIME CONSTANT (SEC.)	0.0006
INSULATION DENSITY (KG/M^3)	490
INSULATION EMISSIVITY	0.9
THERMAL STORAGE EMISSIVITY	0.8
THERMAL STORAGE MATERIAL DENSITY (KG/M^3)	4550
THERMAL STORAGE MATERIAL VOLUME (CM^3)	247.40
CALCULATED THERMAL STORAGE MASS (kg)	1.126
INSULATION Cp, AVG. (J/KG-K)	2090
THERMAL STORAGE Cp, AVG. (J/KG-K)	1000
RECEIVER APERTURE DIAMETER (CM)	0.8
NOZZLE THROAT DIAMETER (mm)	1
NOZZLE EXIT DIAMETER (mm)	2.9445
NOZZLE AREA RATIO	8.67
INCIDENT POWER FROM CONCENTRATOR (W)	594.72
GEOMETRIC CONCENTRATION (MIRROR AREA/APERTURE)	12656
WAIT TIME BEFORE FIRING (MIN.)	1
PROPELLANT	AMMONIA
MASS FLOW/BURN (KG)	0.0014

100.0% HEATUP SOLUTION COMPUTED

NEW FIRING SOLUTION REQUIRED

CHANNEL FLOW SOLUTION

Cylindrical Shell Receiver Calculation Assistant	
CYLINDER LENGTH (CM)	5
CYLINDER OUTER DIAMETER (CM)	8.25
CYLINDER INNER DIAMETER (CM)	2.25
INSULATION THICKNESS (CM)	3

Channel Flow Calculation Assistant	
CHANNEL DIAMETER (MM)	1
CHANNEL LENGTH (M)	0.05

Particle Bed Receiver Calculation Assistant	
BED Cp (J/kg-K)	1000
BED MASS (KG)	[illegible]
BED DENSITY (kg/m^3)	3300
BED XSEC AREA (CM^2)	[illegible]
BED POROSITY (0 - 1)	0.5
BED CORRELATION	Whitaker
PARTICLE DIAM (μM)	500

MINIMUM FIRING TEMPERATURE (K)	600
ESTIMATED BOL BURN TIME (s.)	2.00
ESTIMATED EOL BURN TIME (s.)	SAME AS ABOVE

▷ REGULATED, EOL = BOL

Firing Simulation Time (seconds)	2.00
Current Bulk Receiver Temperature (K)	603.84
Propellant Exit Temperature (K)	407.32

BURN AVERAGE SPECIFIC IMPULSE (s)	160.11
AVERAGE PRESSURE DROP THRU RECEIVER (BAR)	5.11
RCVR RAD LOSS AT BEGINNING OF FIRING (W)	540.69
THERMAL CAPACITY OF RECEIVER (kJ)	627.62
TOTAL IMPULSE PER BURN (N-s)	2.26
AVG BOL THRUST (N)	1.13
AVG EOL THRUST (N)	1.13
EFF. (BOL ENERGY TO [illegible] ENERGY)	0.02%
EFF. (INTEGRATED JET PWR/INC. ENERGY)	0.05%

Figure 5-11 Screen shot of MSTISM Receiver Performance Input/Output Sheet.

The third, or *Concentrator Performance*, sheet, requests a substantial amount of user input, including apparent solar disk half-angle and incident solar flux at the orbit of interest, the number and properties of the system's concentrating mirrors, and potential sources of error. The sheet calculates theoretical concentration ratio (according to Kreider [1979], using Equation 4-10) and ideal spot size. An empirical spot size factor, based on OSLO LT model results for form errors of up to 60 microns, is applied to the ideal calculation. Changes in the shape of the spot are not taken into account; comatic spot deformation is not significant unless the tracking error becomes severe (0.5° or greater, see Figure 5-3). The code then estimates the amount of radiant energy intercepted by the solar receiver's aperture, taking into account losses associated with Bendt and Rabl's analysis of fractional acceptance regions (based on pointing errors, see Section 4.3.1). *Concentrator Performance* displays theoretical and geometric concentration ratios, as well as optical efficiency and the selected mirror profile.

---

[118] The addition of a patched-conic trajectory modeller for interplanetary (or earth-moon) orbit transfer was

The fourth sheet, *Attitude Control*, is closely coupled to *Concentrator Performance*. At present, it uses a simple Gaussian distribution[119] to predict mean pointing accuracy, assuming two user inputs: maximum pointing error and a scale factor. The mean accuracy figure is then used to estimate the mean fraction of incident light reaching the receiver (via Equation 4-16)—this critical value is passed to the *Receiver Performance* sheet. Subsystem mass data is displayed on *Summary*.

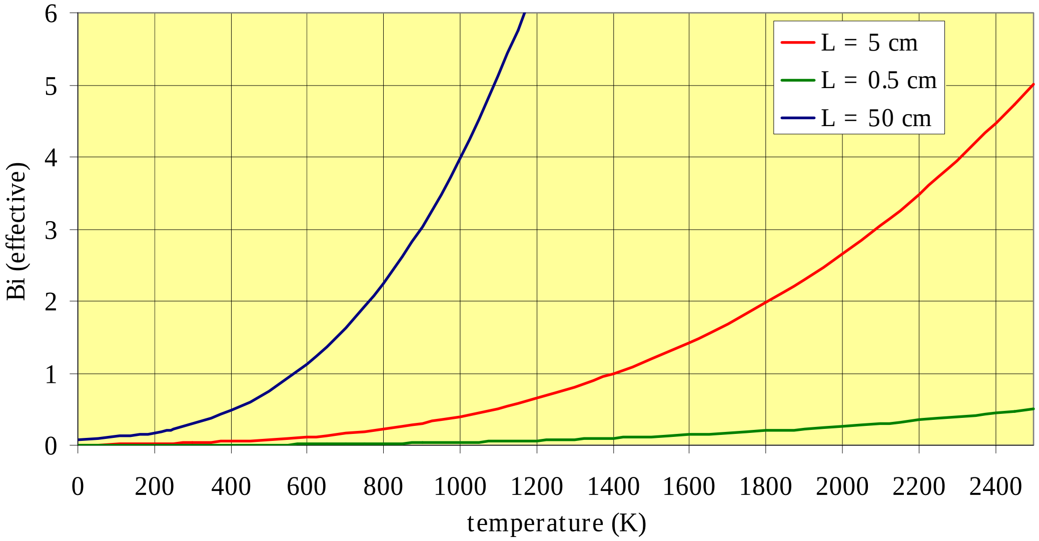

Figure 5-12 Effective Biot number for several ceramic blackbodies (with characteristic lengths of 0.5, 5, and 50 cm).

The fifth sheet, *Receiver Performance*, is the heart of the MSTISM model (Figure 5-11). The user is required to input a number of key parameters: (1) receiver body properties (to include material

---

deemed a possible (but unnecessary) addition.

[119] For a given pointing error *e*, the probability *P* that the system will be found in a given pointing state is represented by:

$$P = \frac{e^{-\left(e^2/2s^2\right)}}{\sqrt{2\pi}} \qquad (5\text{-}9)$$

Here, s is the scale factor selected by the user.

thermal conductivity, specific heat, and geometry), (2) insulation package properties, (3) nozzle properties, (4) charging time and wait time prior to firing, and (5) minimum receiver body (or cut-off) firing temperature. Once these parameters are set, the user must run a Visual Basic script containing a modified version of the CHUPS code (see Chapter 4). This script estimates the time-dependent temperature profile of the receiver, for selected charging and wait times, and takes several minutes to run.[120] The user is then requested to specify a choice of heat transfer mode—channel or packed bed heat transfer—by selecting and running an appropriate Visual Basic script.

Unlike the CHUPS code, MSTISM uses a simplified (lumped-capacity) model of the receiver body in place of a series of concentric shells. For small ceramic bodies at moderate temperatures, this can be shown to be a reasonable approximation. An effective Biot number, *Bi*, can be defined to determine the importance of internal conduction within the receiver body relative to surface radiative cooling [Blanchard, 1994]. Typically, the Biot number has been used to uncover the relative importance of internal conduction and external convection; however, in the case at issue, the receiver body is in vacuum and no convection occurs. For small values of the Biot number (<<1), the temperature distribution within the body is flat and lumped-capacity solutions apply. For large values (>>1), the temperature distribution is significant and other methods (i.e., finite difference conduction models) are necessary for an adequate simulation.[121] Blanchard defines Bi_e as:

$$Bi_e = \frac{\varepsilon\sigma\left(T_b^{\,2} + T_a^{\,2}\right)\left(T_b + T_a\right)L}{k} \tag{5-10}$$

Bi_e is therefore a function of body temperature (T_b) and ambient (or background) temperature (T_a), as well as the body's characteristic dimension L, and its thermal conductivity k. For a small, black ceramic body ($\varepsilon = 1.0$, $L = 5$ cm, $k = 10$ W/m-K), Bi_e ranges from 0.03 at 293 K to 2.66 at 2,000 K. This would appear to imply that the lumped-capacity solution is relatively sound for small bodies throughout the temperature range of interest. At high temperatures (above 1,400 K), MSTISM will tend to underpredict peak receiver temperature, providing a conservative estimate. Figure 5-12 illustrates the variation of Biot number with characteristic length.

The core of the MSTISM heating algorithm is an energy balance:

$$Q_{net} = Q_{in} - (Q_{insulation} + Q_{aperture} + Q_{cap}) \tag{5-11}$$

---

[120] Like CHUPS, the MSTISM heatup script uses an Eulerian (explicit) solver, which, for large time steps, can become unstable. The script was designed to select a time constant sufficiently small to ensure convergence, but this increases the number of computations and demands two to five minutes to process the solution.

[121] In the large *Bi* case, a lumped-capacity solution will overestimate a body's surface temperature, radiating more heat to the surroundings than the actual body, and underestimating peak body temperature.

Q_{net} is the amount of heat deposited in the receiver structure over a time τ, calculated from the difference between concentrator input Q_{in} and the radiative loss terms $Q_{insulation}$, $Q_{aperture}$, and Q_{cap}. The change in receiver body temperature over the time period t to t + τ is then calculated from the lumped-capacity relation:

$$T_{b,t+\tau} - T_{b,t} = \frac{Q_{net}}{\rho_b V_b C_p} \tag{5-12}$$

The MSTISM model does not incorporate temperature-dependent specific heat for receiver materials; the user is required to input an estimated average C_p based on the temperature excursion seen by the receiver. MSTISM clearly cannot dispense with the concentric shell model where it is most important—in the insulation package. Here, the temperature distribution can be extreme, with interior-to-exterior surface temperature variations of more than 1,500 K, and Biot numbers in the hundreds. The receiver's insulation package is therefore divided into four shells of equal thickness t_{shell} and thermal conductivity k_{shell}. An energy balance similar to that in Equation 5-11 is applied to each of the shells in succession. To inhibit divergence in what is essentially an explicit formulation, the code selects a value for τ based on the thickness of the insulation package, typically on the order of 3 x 10^{-4} seconds.

Two independent (but similar) Visual Basic scripts allow MSTISM to simulate channel flow or packed bed heat transfer for a variety of propellant choices. Several of these choices (hydrogen, nitrogen, and helium) are stable species over the temperature regime of interest, and do not require decomposition product modelling. However, even these propellants experience significant variations in key parameters; namely, specific heat, viscosity, and thermal conductivity, as the temperature of the propellant rises over its passage through the solar receiver body. Empirical curve fits of NIST [2000] correlations were used to track gas properties at various stations in the receiver.

Both scripts were based on the author's PBHT code for heat transfer modelling. Originally developed to predict performance for packed beds, the code was modified to allow simulation of channel flow. Both rely on local estimations of Reynolds, Prandtl, and Nusselt numbers (Equations 4-20, -21, -22, -23, and –24). Once the local Nusselt number is determined, a gas-body heat transfer coefficient is calculated and the total energy transferred (from receiver section to gas slug) can be estimated. Equation 4-20 gives the Nusselt number for a packed bed. This can be replaced with Petukhov's expression for a channel flow heat exchanger [Lienhard, 1987]:

$$Nu = \frac{f}{8} \frac{\mathrm{Re}\,\mathrm{Pr}}{\left(1.07 + 12.7\sqrt{\frac{f}{8}}\left(\mathrm{Pr}^{2/3} - 1\right)\right)} \tag{5-13}$$

In this instance, Re, Pr, and Nu are based on the characteristic length of the heat exchanger (which, in this case, is the channel's hydraulic diameter). The Darcy-Weisbach friction factor *f* is estimated using:

$$f = \frac{1}{\left(1.82\log_{10}\mathrm{Re} - 1.64\right)^2} \qquad \textbf{(5-14)}$$

Since channel flow and particle bed heat exchangers can be susceptible to sizeable pressure drops, the measured supply pressure and the pressure in the receiver plenum (i.e., chamber pressure, or P_c) may be substantially different. This is critical to proper estimation of characteristic velocity (Equation 4-28), and, thus, specific impulse. Pressure drop through a packed bed receiver can be estimated with the use of the Ergun equation:

$$\frac{\Delta P}{L} = 150\frac{\mu(1-\varepsilon)u_s}{\varepsilon^3 D_p^2} + 1.75\frac{(1-\varepsilon)\rho u_s^2}{\varepsilon^3 D_p} \qquad \textbf{(5-15)}$$

The pressure drop over a fixed length *L* is dependent on flow density ρ and dynamic viscosity μ, the superficial velocity (u_s), bed porosity ε, and particle diameter D_p, all described in Chapter 4. Conversely, for a channel flow heat exchanger,

$$\frac{\Delta P}{L} = f\,\frac{\rho u^2}{2D} \qquad \textbf{(5-16)}$$

This relation makes use of the friction factor (Equation 5-x), local flow velocity *u*, and the hydraulic diameter *D*.

Estimating local gas-body heat transfer requires precise knowledge of gas properties, which, in the case of propellants susceptible to dissociation, involve mixtures and are highly variable. While some propellant selections available to the MSTISM user are stable even at very high temperatures, hydrazine (N_2H_4), methane (CH_4) and ammonia (NH_3) will decompose. The decomposition is modelled in MSTISM as an equilibrium process without any intermediate products; at any position in the receiver flow path (channel or packed bed), an equilibrium constant K_p can be defined [Hill, 1992]:

$$K_p(T) = \frac{p_M^{\mu}\, p_N^{\nu}}{p_A^{\alpha}\, p_B^{\beta}} \qquad \textbf{(5-17)}$$

Here, K_p is a function of the various partial pressures of a reaction's products (p_M, p_N) and reactants (p_A, p_B) raised to the stoichiometric exponents α, β, μ, and ν:

$$\alpha A + \beta B \leftrightarrow \mu M + \nu N$$

These are tabulated for a variety of reactions across a wide range of temperatures, and include ammonia and methane decomposition. One can also define an equilibrium constant K_n based on mole fraction:

$$K_n(T) = \frac{\chi_M^{\mu}\chi_N^{\nu}}{\chi_A^{\alpha}\chi_B^{\beta}} \tag{5-18}$$

Then, applying the well-known Gibbs-Dalton Law,[122]

$$K_n = p_m^{\alpha+\beta-\mu-\nu}K_p \tag{5-19}$$

This permits the calculation of relative concentration (mole fraction) for each constituent, for a known temperature and pressure. In the case of ammonia,

$$\frac{x}{2}N_2 + \frac{3x}{2}H_2 \leftrightarrow xNH_3$$

The number of NH_3 moles present at equilibrium (x) can be found by applying reaction stoichiometry and equating equilibrium constants K_p and K_n, then iteratively solving for x:

$$K_n = \frac{\chi_{N_2}^{1/2}\chi_{H_2}^{3/2}}{\chi_{NH_3}} = \frac{\left(\dfrac{x}{2-x}\right)}{\left(\dfrac{1/2-x/2}{2-x}\right)\left(\dfrac{3/2-3x/2}{2-x}\right)} = p_m^{-1}K_p \tag{5-20}$$

Wysong [2004] and Humble [1995] note that equilibrium calculations such as these are somewhat optimistic, in that the rate of reaction is often insufficient to allow the decomposition to proceed to completion. In the particular case of ammonia, decomposition is highly desirable because the molecular weight of the products (N_2 and H_2) is only half that of the reactants (NH_3)—which strongly drives achievable specific impulse. While reaction rate and propellant gas residence time was not accounted for in the MSTISM simulation, it will be seen later (in Chapter 6) that, for intermediate temperature regimes, ammonia decomposition does not go to completion prior to exiting the receiver body, and an estimation of propellant composition is critical to accurately assessing performance (i.e., characteristic velocity and specific impulse).

Atkins [1997] defines a reaction's rate constant k, in cm^3/molecule-s, as:

$$k = Ae^{-E_a/RT} \tag{5-21}$$

Arrhenius first proposed this formulation in 1889 as an application of collision theory. The rate constant depends on a pre-exponential factor A (which accounts for molecular collision rates), the activation energy E_a (the minimum energy required for decomposition to take place), and the product of the gas constant *R* and ambient temperature *T*. Tabulations of *k* for various reactions are maintained on the National Institute of Standards and Technology (NIST) web site for chemical kinetics [NIST, 2000]. Several of these are depicted in Figure 5-13.[123] Note that the second-order reactions (the lower two curves) are substantially slower than the first-order reactions.

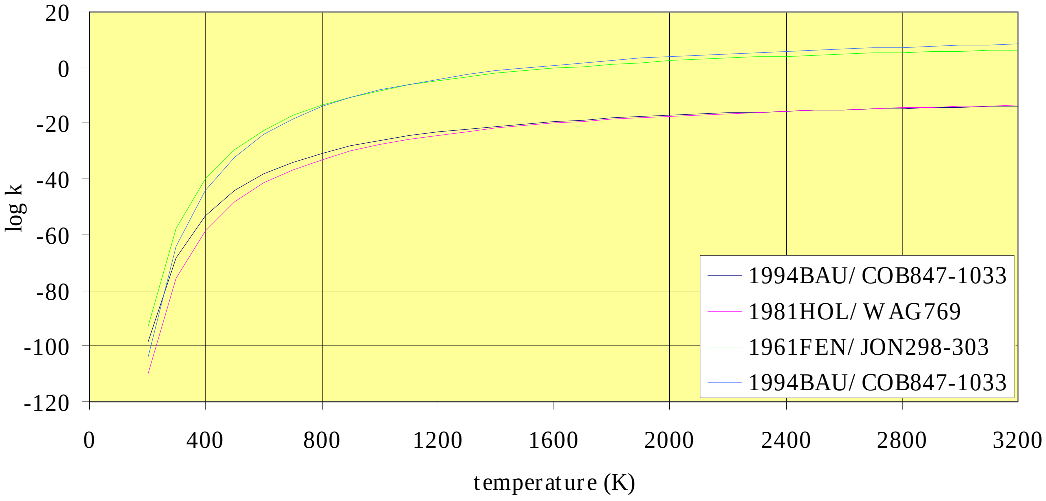

Figure 5-13 First- and second-order reaction rate constants for ammonia decomposition [NIST, 2000].

The rate constant *k* plays a crucial role in determining molar concentration $[A]_t$ given at any time *t*. An integrated rate law for a first-order reaction can be written as:

$$[A]_t = [A_o]e^{-kt} \tag{5-22}$$

Here, $[A]_t$ is simply a function of the initial concentration $[A_o]$ and the declining exponential term $-kt$. At low temperatures, ammonia's rate of decomposition is extremely low, only becoming appreciable above approximately 1,600 K. Since gas residence times in the solar thermal receiver body are relatively short (< .01 s), significant first-order decomposition only takes place when temperatures exceed 1,800 K.[124] Above these temperatures, even the short stay times seen in

---

[122] Gibbs-Dalton states that the mole fraction of the ith species is related to the ratio of the partial pressure of that species (p_i) and the total pressure p_m.

[123] For instance, NIST [2000] cites a 1994 reference by D. Baulch and C. Cobos (et. al.) for ammonia decomposition valid over the temperature range 2,000-3,000 K. The authors' observations led them to select the following values for the rate constant formula: pre-exponential A = 8.3x10^{15} s^{-1}, E_a = 458.959 kJ/mole. This is a first-order reaction.

[124] At 1,725 K, the Baulch/Kobos (1994BAU/COB847-1033) rate constant is 65.6. For a residence time in the receiver of 0.006 s, approximately one-third of the ammonia propellant will have dissociated. At 1,800 K, this fraction rises to over 90%.

channel flow heat exchangers will permit near-complete dissociation. The transition regime (1,600-1,800 K), while not addressed by MSTISM, will figure in the analysis of test results.

The MSTISM *Receiver Performance* heat transfer scripts subdivide the heat exchanger into 100 sections for analysis. Gas slugs are passed from section to section, and gas properties recalculated in each section. Dissociation losses—based on equilibrium constant calculations—are added to convective heat transfer figures. As each slug emerges, the integrated power transfer from receiver body to gas is determined and the body temperature recalculated to reflect energy loss. Unlike the PBHT code, MSTISM does not retain section temperature information for each gas flow iteration—it is assumed, due to the small body size and moderate thermal conductivity, that the receiver remains roughly isothermal throughout a firing. Gas flow simulation continues until the prescribed burn time expires or until receiver temperature drops below the user-specified minimum. Radiative losses are accounted for during firings. Chamber temperatures (gas and body) and mass flow rates are tabulated out-of-view on *Receiver Performance* and a number of performance parameters calculated, including integrated mass flow, thrust coefficient, characteristic velocity, thrust, impulse, and specific impulse.

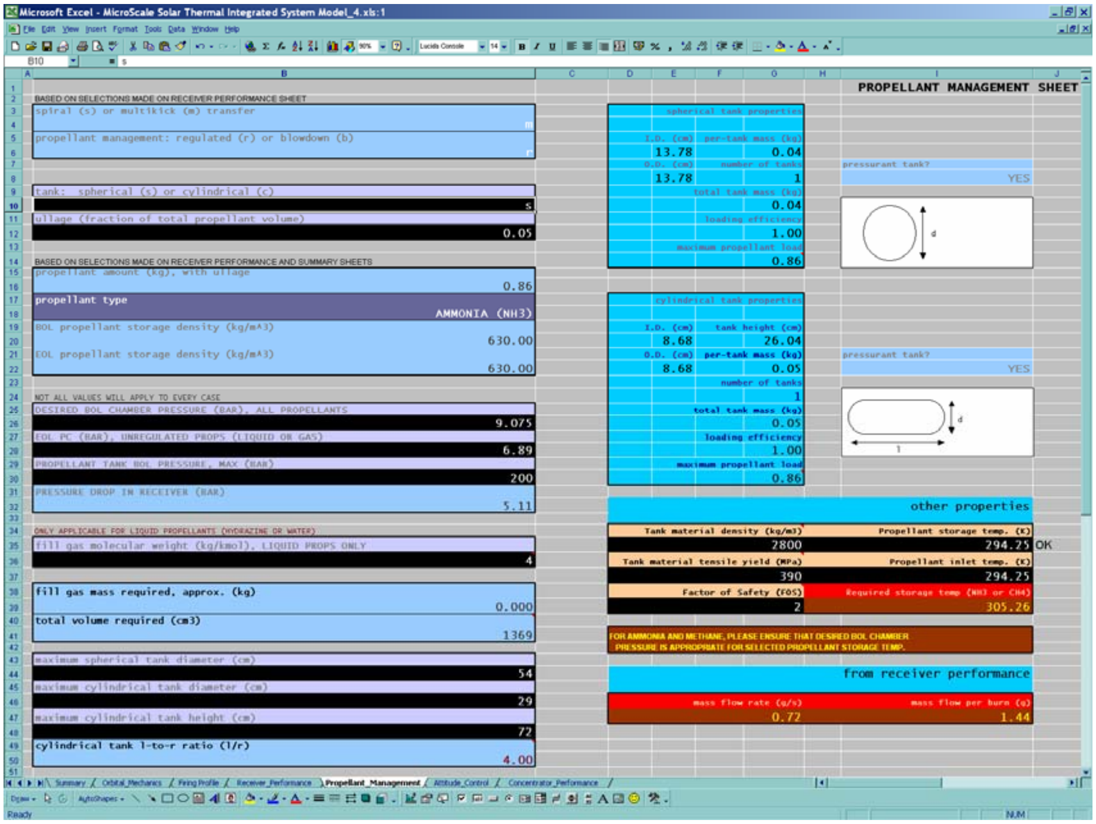

PROPELLANT MANAGEMENT SHEET

BASED ON SELECTIONS MADE ON RECEIVER PERFORMANCE SHEET

spiral (s) or multikick (m) transfer: m

propellant management: regulated (r) or blowdown (b): r

tank: spherical (s) or cylindrical (c): s

ullage (fraction of total propellant volume): 0.05

BASED ON SELECTIONS MADE ON RECEIVER PERFORMANCE AND SUMMARY SHEETS

propellant amount (kg), with ullage: 0.86

propellant type: AMMONIA (NH3)

BOL propellant storage density (kg/m^3): 630.00

EOL propellant storage density (kg/m^3): 630.00

NOT ALL VALUES WILL APPLY TO EVERY CASE

DESIRED BOL CHAMBER PRESSURE (BAR), ALL PROPELLANTS: 9.075

EOL PC (BAR), UNREGULATED PROPS (LIQUID OR GAS): 6.89

PROPELLANT TANK BOL PRESSURE, MAX (BAR): 200

PRESSURE DROP IN RECEIVER (BAR): 5.11

ONLY APPLICABLE FOR LIQUID PROPELLANTS (HYDRAZINE OR WATER)

fill gas molecular weight (kg/kmol), LIQUID PROPS ONLY: 4

fill gas mass required, approx. (kg): 0.000

total volume required (cm3): 1369

maximum spherical tank diameter (cm): 54

maximum cylindrical tank diameter (cm): 29

maximum cylindrical tank height (cm): 72

cylindrical tank l-to-r ratio (l/r): 4.00

spherical tank properties

I.D. (cm): 13.78

per-tank mass (kg): 0.04

O.D. (cm): 13.78

number of tanks: 1

total tank mass (kg): 0.04

loading efficiency: 1.00

maximum propellant load: 0.86

pressurant tank?: YES

cylindrical tank properties

I.D. (cm): 8.68

tank height (cm): 26.04

O.D. (cm): 8.68

per-tank mass (kg): 0.05

number of tanks: 1

total tank mass (kg): 0.05

loading efficiency: 1.00

maximum propellant load: 0.86

pressurant tank?: YES

other properties

Tank material density (kg/m3): 2800

Propellant storage temp. (K): 294.25 OK

Tank material tensile yield (MPa): 390

Propellant inlet temp. (K): 294.25

Factor of Safety (FOS): 2

Required storage temp (NH3 or CH4): 305.26

FOR AMMONIA AND METHANE, PLEASE ENSURE THAT DESIRED BOL CHAMBER PRESSURE IS APPROPRIATE FOR SELECTED PROPELLANT STORAGE TEMP.

from receiver performance

mass flow rate (g/s): 0.72

mass flow per burn (g): 1.44

Figure 5-14 Screen shot of MSTISM Propellant Management input/output worksheet.

Following a simulated firing, burn-average specific impulse, total impulse, thrust, mass flow per burn, and efficiency estimates are displayed on *Receiver Performance*. These figures of merit are also passed to *Firing Profile* to permit estimates of time-to-orbit (based on the number of required firings). Propellant usage estimates also permit *Propellant Management* to properly size tanks for the user-specified mission.

Propellant Management (Figure 5-14) requires the user to specify tank type (spherical or cylindrical), ullage fraction (default of 5%), a desired chamber pressure, maximum tank pressure (for tensile yield considerations), and tank size constraints.

Propellant data is supplied by the user selection on the *Summary* sheet. A regulated supply pressure is found by adding the specified chamber pressure to the pressure drop calculated by *Receiver Performance*. Tank specifications are determined from propellant mass and storage densities, as well as user selections for tank material yield strength, structure density, and requisite factor of safety. For self-pressurised propellants (vapour pressure supply), the Visual Basic scripts in *Receiver Performance* will automatically calculate an appropriate storage temperature for the selected supply pressure; if this is within ±10% of the expected storage temperature, *Propellant Management* will register “OK.” Tank masses so calculated are displayed on *Propellant Management* and *Summary*.Burn time, applied thrust, and specific impulse information passed from *Receiver Performance* to *Firing Profile* permit an estimate to be performed of delta-V per individual firing. *Firing Profile* allows the user to override the automatically assigned burn times and firing types (apoapse or periapse) as required. Orbital parameters are recalculated following each firing, and the full mission profile, as well as time-to-final-orbit, displayed both on *Firing Profile* and *Summary*. For near-circular orbits, eclipse duration *t* can be calculated from [Larson, 1992]:

$$t = \cos^{-1}\left(\frac{\sqrt{1 - r_{eq}^2 / r_{sat}^2}}{\cos\beta}\right)\frac{\tau}{\pi} \tag{5-23}$$

Here, β represents the solar/orbit plane angle (i.e., the “beta” angle), τ is the satellite’s orbital period, and r_{eq}^2/r_{sat}^2 is the ratio of the squares of equatorial planetary radius to satellite orbital radius. The sheet will display a warning if charging time exceeds the available orbital time in sunlight, prompting the user to correct the entry.

Proper use of the MSTISM code requires adherence to the following procedural steps:

(1) Code startup: The user must enable the use of macros (Visual Basic scripts). If the displayed page is other than *Summary*, the user should select the *Summary* tab at the bottom of the window.

(2) *Summary*: The user should select a “wet” spacecraft mass (i.e., including propellant) and a propellant type from the set of available options at the worksheet’s top left.

(3) *Orbital Mechanics*: The user should select a periapse and apoapse for both starting and ending orbits. The code will assume a multi-impulse transfer, but will also estimate a spiral delta-V requirement for comparison, for circular-to-circular orbit transfers. This sheet will also warn the user if the STP system's performance will require more than 2,500 firings to achieve final orbit.

(4) *Concentrator Performance*: The user should select a mirror diameter, areal density, reflectance, and desired mirror rim angle. Multiple mirror inputs can be concatenated, although losses associated with fibre-optic coupling are not addressed by this code.

(5) *Attitude Control*: Default values assume a 0.3° maximum error in pointing accuracy, with a root-mean-square (RMS) tracking error of 0.13°. The user is free to modify both the maximum error and the RMS error (via the scale factor mentioned previously).

(6) *Propellant Management*: The user can now select specific tank constraints and set chamber pressure to a desired value.

(7) *Receiver Performance*: The user should select thermal conductivity, specific heat, density, emissivity, thermal charging time, wait time, and geometric properties of the receiver and insulation package prior to initiating the heatup profile script via the button labelled "Compute Heating Profile." It is possible for the user to introduce values that will stop the heatup profile script: zero-thickness insulation packages and negative-thickness receiver structures are examples.

(8) *Receiver Performance*: Once the heatup script has generated a profile of receiver temperature vs. time, the user should select (1) an appropriate nozzle throat and nozzle exit diameter, (2) minimum (cutoff) receiver firing temperature, and (3) heat exchanger geometric details, potentially including channel length and diameter, packed bed particle size, porosity, and other properties. The user can then select a firing solution script via one of the two buttons: "Channel Flow Receiver (Regulated Flow)," or "Particle Bed Receiver (Regulated Flow)." Either script will produce a temperature profile for both the propellant gas and receiver body.

(9) *Firing Profile*: Once heatup and firing scripts have been run, a fixed firing profile is used repeatedly to achieve the user's selected orbit transfer. Each firing is user-modifiable.

Changing propellant selections, concentrator power input, or receiver properties will require the user to rerun the heatup and firing scripts before results (shown on *Summary*) are accurate. Representative results from MSTISM runs are shown below.

The principal advantage of the MSTISM code over more capable, but more narrowly applicable, individual codes is its capability to provide a broad assessment of system performance and its implications for mission success. To illustrate the utility of the MSTISM programme, the author has performed a sensitivity analysis for a modest delta-V LEO orbit raising mission (460 km circular to 560 km circular). Baseline mission parameters are shown in Table 5-1.

Start Orbit	**460 x 460 km circular**
Mission Orbit	**560 x 560 km circular**
Elapsed Time	**69 hrs., 36 min.**
Number of Manoeuvres	**45 (22 apogee kicks, 23 perigee kicks).**
Total Velocity Change	**58 m/s**
Propellant Consumption	**2.51 kg (ammonia)**
Final Mass	**97.49 kg**
Engine "On-Time"	**1 hr., 17 min.**

Table 5-1 Baseline LEO orbit raising mission, key parameters.

The baseline STP system assumes an 8-kg, 100-cm diameter mirror[125] supplying 790 W to an insulated, all-ceramic (TiB_2/BN) solar receiver. The receiver structure masses 1.13 kg and reaches a maximum temperature of 1,250 K in 50 minutes. With ammonia propellant, this system's burn-average I_{sp} was calculated to be 245 s. The STP system's total mass (propellant excluded) was less than 9.5 kg. The baseline mirror is large—too large, in fact, to be stowed inside an ASAP footprint without folding. Since this contributes significantly to overall system complexity (and cost), it would be useful to find an alternative configuration that meets mission requirements without demanding high solar input. Figure 5-15 demonstrates the results of mirror downsizing, holding thermal charging time constant at 50 minutes.

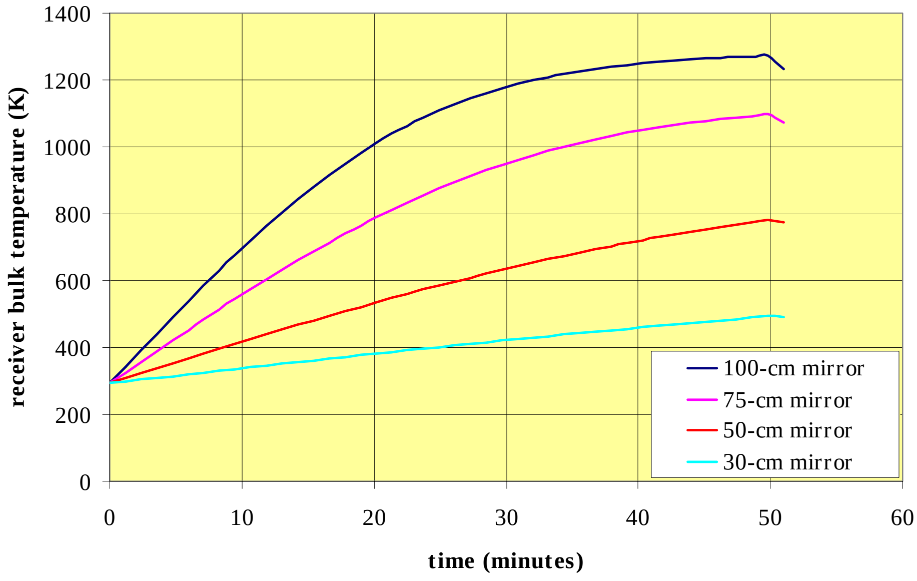

---

[125] This assumes an advanced mirror, ceramic or carbon fibre composite, with an areal density = 10 kg/m^3.

Figure 5-15 MSTISM model of STP bulk receiver temperature, for 100-, 75-, 50-, and 30-cm mirror inputs. Solar flux = 1,353 W/m^2. Mirror reflectance = 0.90.

In Chapters 3 and 4, it was noted that the concentrating mirror was the primary mass driver, even for high delta-V missions; this is even clearer for low delta-V, as seen in Table 5-2. Yet, for the relatively low velocity change required by this mission, it can be seen that mirror downsizing does not adversely affect system performance. The downward trend in mirror mass more than makes up for the very slight increase in propellant mass needed to offset the significant specific impulse penalty. At a diameter of 30 centimetres, the mirror input power is insufficient to heat the receiver to the minimum firing (or cutoff) temperature of 600 K used in the other simulation runs; in this case, the cutoff temperature was lowered to 350 K so that a comparison could be achieved. While this results in a drastically reduced I_{sp}, the impact on final payload delivered to orbit is minimal.

Concentrator diameter	100 cm	75	50	30
Input power (W)	790	513	239	86
Elapsed time to orbit (hrs.)	69.6	88.5	227.6	98.0
Number of manoeuvres (apogee/perigee)	45 (22/23)	57 (29/28)	145 (74/71)	63 (32/31)
Total velocity change (m/s)	58	58	58	58
Propellant Consumption (ammonia, kg)	2.51	2.61	2.88	4.42
Engine “On-Time” (hrs.)	1.28	1.27	1.28	1.20
Burn-average I_{sp} (s)	245	235	213	138
Mirror mass (kg)	7.97	4.48	1.99	0.72
Dry STP system mass (kg)	9.50	5.73	3.26	2.06
Final payload mass (kg)	87.99	91.66	93.86	93.52

Table 5-2 MSTISM performance sensitivity analysis, for mirror diameters of 100-, 75-, 50-, and 30 cm. Final payload mass excludes propellant and STP system mass.

The second stage of this analysis examines modifications to the receiver, presuming a 30-cm concentrating mirror supplying 86 W of input power. Smaller receivers (with a constant area aperture) of external diameters between 4 and 8.25 cm (Figure 5-16) were analysed. As shown in Table 5-3, a 20% increase in I_{sp} can be gained through decreasing thermal storage mass, at the cost of tripling transfer time between the starting and final altitude orbits.

A final sensitivity analysis examines the contribution of propellant type. The model will replace the baseline propellant, ammonia, with nitrogen, helium, and hydrazine, while fixing concentrator size at 30 cm and receiver diameter at 4 cm. Although the low velocity change requirement tends to obscure the differences in performance among these propellant types, the relative final payload mass values are instructive. Hydrazine, which is presumed to decompose in a catalyst pack prior to entry into the receiver, enters at 863 K; therefore, unlike the other propellants, the user-selected minimum firing temperature is substantially higher (and the burn-average specific impulse is likewise higher).[126]

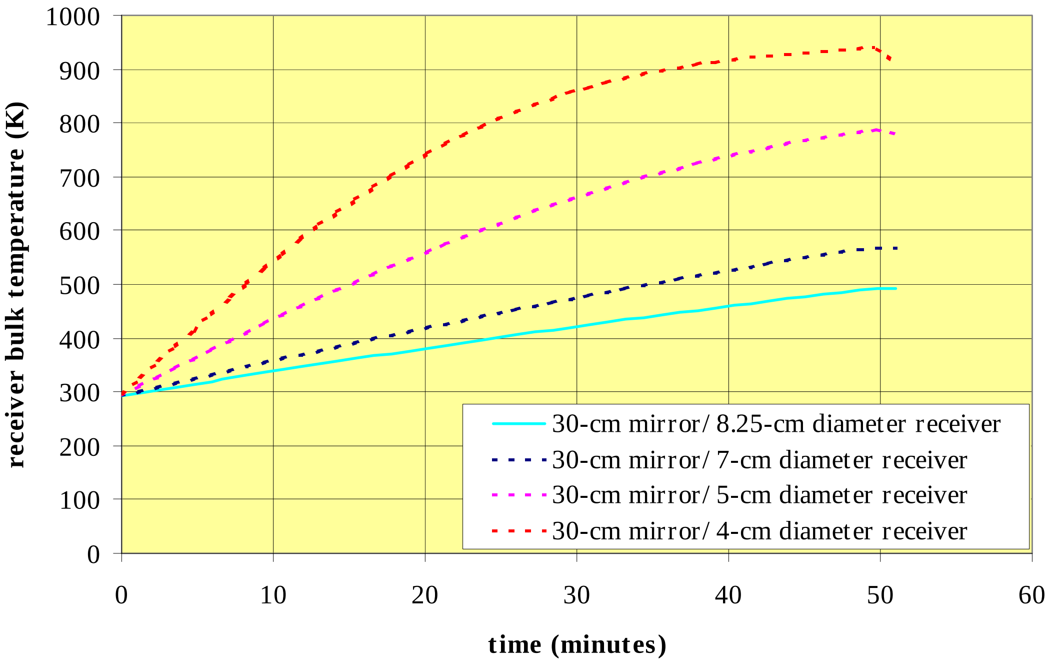

Figure 5-16 MSTISM model of STP bulk receiver temperature, for 30-cm mirror input. Solar flux = 1,353 W/m^2. Mirror reflectance = 0.90. Receiver diameter varies from 4 to 8.25 cm (x 5 cm length).

Concentrator diameter Receiver diameter	30 cm 8.25 cm	30 7.00	30 5.00	30 4.00
Input power (W)	86	86	86	86
Elapsed time to orbit (hrs.)	98.0	115.4	177.1	271.9
Number of manoeuvres (apogee/perigee)	63 (32/31)	74 (38/36)	113 (57/56)	173 (88/85)
Total velocity change (m/s)	58	58	58	58
Propellant Consumption (ammonia, kg)	4.42	4.25	3.85	3.64
Engine "On-Time" (hrs.)	1.20	1.20	1.22	1.22
Burn-average I_{sp} (s)	138	143	158	167
Mirror mass (kg)	0.72	0.72	0.72	0.72
Dry STP system mass (kg)	2.06	1.71	1.26	1.09
Final payload mass (kg)	93.52	94.04	94.89	95.27

Table 5-3 STP performance sensitivity analysis, for variable receiver sizes and a fixed mirror diameter of 30 cm. Final payload mass excludes propellant and STP system mass.

This round of sensitivity studies reveals: (1) high input power confers no advantage for low delta-V missions, even if low areal density concentrating mirrors are used; (2) decreasing thermal storage receiver mass for a fixed input power permits higher peak temperature (and higher specific impulse) and is advantageous if a transfer time penalty can be accepted; and (3) for low delta-V missions and low input powers, the augmented hydrazine system provides performance superior to the other propellant choices. The difference between the baseline and the hydrazine system's performance, in terms of overall payload delivered to orbit, is over 6 kilograms.

---

[126] While MSTISM does not account for ancillary hardware (e.g., feedlines, valves, tank bosses), the code

Concentrator diameter	**30 cm**	**30**	**30**	**30**
Receiver diameter	**4.00 cm**	**4.00**	**4.00**	**4.00**
Propellant	**ammonia**	**nitrogen**	**helium**	**hydrazine**
Input power (W)	**86**	**86**	**86**	**86**
Elapsed time to orbit (hrs.)	**271.9**	**53.8**	**121.7**	**3,305**
Number of manoeuvres (apogee/perigee)	**173 (88/85)**	**35 (18/17)**	**78 (40/38)**	**2,092 (88/85)**
Total velocity change (m/s)	**58**	**58**	**58**	**58**
Propellant Consumption (ammonia, kg)	**3.64**	**5.90**	**2.65**	**3.05**
Engine "On-Time" (hrs.)	**1.22**	**1.26**	**1.41**	**1.31**
Burn-average I_{sp} (s)	**167**	**102**	**231**	**200**
Mirror mass (kg)	**0.72**	**0.72**	**0.72**	**0.72**
Dry STP system mass (kg)	**1.09**	**1.42**	**2.42**	**1.01**
Final payload mass (kg)	**95.27**	**92.68**	**94.93**	**95.94**

Table 5-4 Analysis for four candidate propellants, given a fixed receiver size (0.195 kg) and a fixed mirror diameter of 30 cm. Final payload mass excludes propellant, STP system mass.

The MSTISM code is valuable in that it permits a rapid comparison between design points along multiple dimensions (including propellant selection; insulation and thermal storage material type, receiver and nozzle geometry, attitude control accuracy; size, type, and number of concentrating mirrors) without necessitating the use of separate, complex codes to optimise subsystems separately. As will be seen in Chapter 6, its ability to model receiver heating profiles is more accurate than WinTherm's.

5.5 Concentrator Subsystem Detailed Design

Two concentration schemes were carried forward into the detailed design phase—a rigid, fixed metal primary mirror (56-cm diameter) designed for direct mounting to a satellite facet, and a smaller (14-cm) rigid metal primary, intended to couple incident sunlight into optical fibres. No secondary concentration was envisioned; both mirrors were designed to provide concentration ratios of 10,000:1 or greater. The small primary's intercepted area is slightly in excess of 6% of the larger mirror.

---

does permit the user to determine the *relative* mass efficacy of various design choices.

In order to maximize the large mirror's potential for both test and potential flight opportunities, the author procured a near maximum-diameter concentrator. The design's 56-centimetre diameter represents an approximate upper limit on two separate counts: (1) a substantially larger non-deployable mirror will not be able to be mounted on a standard Surrey enhanced microsatellite face (dimensions 60 cm x 60 cm) [Mugnier, 2000] and (2) local (UK) vendors were unable to produce diamond-turned optics of greater size. For example, University College (London) possessed the capability to machine diamond-turned (DT) aluminium optics at diameters of up to 20 cm and mechanically polish optics of up to 60 cm diameter [Brooks, 2002]. Prior to 2003, Precision Optical Engineering of Hitchin, Hertsfordshire, was capable of manufacturing DT optics of up to 56 cm diameter [POE, 2002].

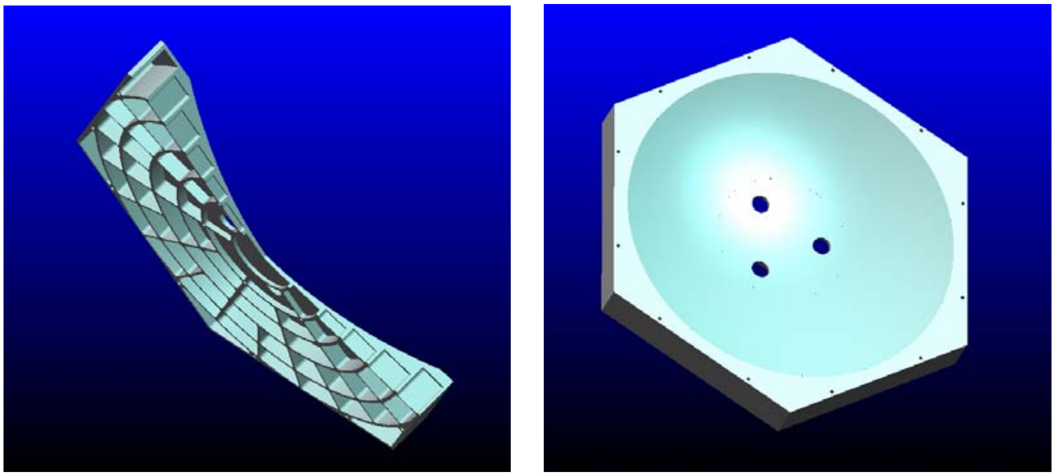

Figure 5-17 Cutaway of 56-cm diameter mirror, with radial ribs and lightweighting (left), and front face, with tripod support pass-throughs. Estimated mass, assuming a magnesium substrate: 8.8 kg, 36 kg/m^2.

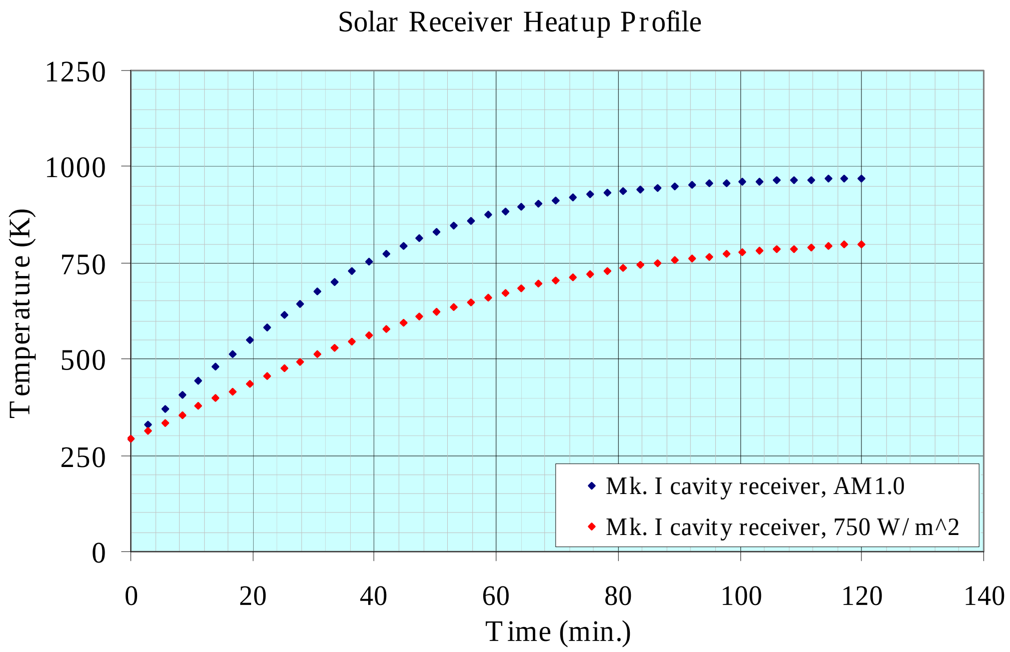

Figure 5-18 MSTISM modelling, Mk. I cavity receiver under AM1.0 (1,353 W/m^2) and moderate terrestrial solar flux (750 W/m^2). Receiver mass = 1.157 kg. Insulation k = 0.06 W/m-K.

The 56-cm diameter optic can be masked in radius to determine the effect of reduced solar input on thermal charging time and maximum achievable receiver temperature, thus allowing for correction of the receiver thermal model. Under AM0[127] conditions, this mirror is expected to capture 333 W of incident sunlight and—at an optical efficiency of 0.8—reflect 267 W through an appropriately sized receiver aperture (0.64 cm diameter). Using the MSTISM model, this was shown to be sufficient power to heat the nominal micro cavity receiver (500 g) to 1,100 K in two hours.[128] The Mk. I cavity receiver (1.15 kg as designed), described in the next section, can be heated by this mirror to 971 K at AM0, or 800 K under terrestrial conditions (Figure 5-18).

	Al 7075-T73	**Mg**
Density, ρ (kg/m^3)	**2,800**	**1,770**
Thermal conductivity, k (W/m-K)	**155**	**159**
Specific heat, C_p (J/kg-K)	**960**	**1,030**
Young's Modulus, E (GPa)	**71**	**45**
Coefficient of Thermal Expansion, CTE (in./in/°C), α	**2.21×10^{-5}**	**2.61×10^{-5}**

Table 5-5 Aluminium 7075-T73 and magnesium properties [Matweb, 2002][Larson, 1992].

A more traditional approach, suggested by Brooks, involves a "rough cut" of the mirror surface (to approximately the correct form), followed by grinding to the exact form. A ground mirror would then be coated with a hard metal (e.g., Ni, usually by chemical bath deposition or electroplating) to facilitate polishing. The polishing—which could be performed either by hand, with a polishing "lap" tool, or via an automated polishing machine, eliminates pitting and other signs of microroughness (thus minimising diffuse reflection). The polished Ni coat would be recoated twice, first with Al (which has a higher reflectivity than Ni) and then with MgF_2. Unlike diamond turning, which is not conducive to overcoating, this approach lends itself to the use of a different metallic substrate. Magnesium—with a density of only 1,770 kg/m^3—provides similar specific stiffness (E/ρ) to aluminium at only two-thirds the mass. An Mg version of the mirror depicted in Fig. 4 would mass only 8.8 kg (42.6 kg/m^2). Another key figure of merit, thermal quality, is defined by [Roberts, 2001]:

---

[127] See Section 2.2. An extraterrestrial flux level of 1,353 W/m^2 is assumed.

[128] This calculation assumes a ~4σ pointing error of ±0.30° and an RMS pointing error of ±0.18°.

$$Q = \frac{k}{\alpha C_p \rho} \qquad \textbf{(5-24)}$$

Again, magnesium and aluminium (Table 5-5) have comparable thermal quality figures—3.34 and 2.61 m^2-K/s, respectively. The higher the quality, the better the thermal performance (i.e., less propensity for warpage due to uneven heating or cooling) offered by the metal substrate. Note the thermal quality of these metals in relation to other options: (1) beryllium (5.33 m^2-K/s), a high-cost, high-performance mirror material; (2) steel (1.15), typically not considered; and (3) Schott's Zerodur® (fused silica) and Corning's ULE® (Ultra-Low Expansion borosilicate glass) used for telescope optics, with thermal qualities of 15.85 and 25.32 m^2-K/s, respectively [Corning, 2002][Schott, 2002]. While glass optics are acceptable for ground-based mirrors, they are generally too heavy for microsatellite applications, with areal densities on the order of 40+ kg/m^2. Finally, beryllium, while attractive from an areal density standpoint, is very expensive to procure and necessitates special precautions during machining [Dierickx, 2000].

Equation 5-6 provides the standard relation for the mirror surface. For a 56-cm diameter mirror with a 45º-rim angle (corresponding to an *f/#* of *f/*0.604), the focal length is 33.8 cm and the base sphere radius is 2*f*, or 67.6 cm. The equation takes the specific form (in cm):

$$h = \frac{(0.0147939)x^2}{1+\sqrt{1-(0)(0.0147939)^2 x^2}} = \frac{x^2}{135.19} \qquad \textbf{(5-25)}$$

Masking this mirror at the preliminary design diameter of 34 cm will simulate an *f/*1 (Φ = 30º) optic. The geometric concentration ratio C_g, assuming a receiver cavity aperture of 0.64 cm diameter, is on the order of 7,700. When masked at 34 cm diameter, C_g = 2,800. The final mirror design (Figure 5-19) eliminated the hexagonal planform of the original, and excluded tripod pass-throughs.[129] Aluminium was selected over magnesium, in part due to the fabricator's long experience with the former metal. No vendor would agree to turn a magnesium billet without substantial preparatory efforts [Brooks, 2002][POE, 2002]. Fabrication results, including form error testing, are discussed in the next chapter.

---

[129] This was done to simplify fabrication of the mirror on the diamond turning tool. The fabricator suggested that the hexagonal planform might introduce zonal asymmetries into the final mirror form, and

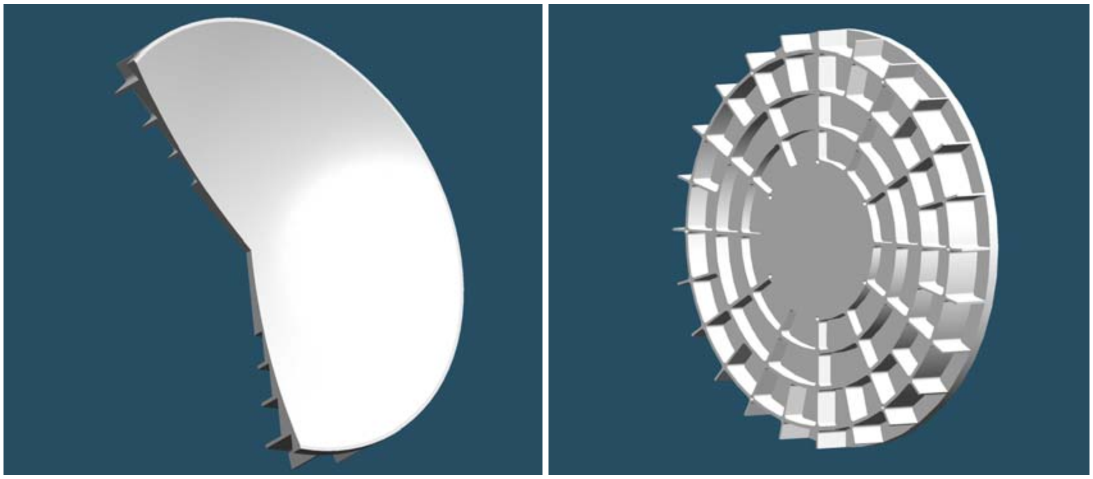

Figure 5-19 Final mirror design submitted to Precision Optical Engineering (56-cm diameter aluminium, f/0.6 with no pass-throughs).

An identical, but smaller, mirror form was supplied to Precision Optical Engineering and Carville, Ltd., for the production of multiple 14-centimetre diameter mirrors (Figure 5-20), in support of the ganged-mirror scheme utilising optical fibre transmission. Carville was requested to produce ten mirrors machined from polymethyl methacrylate (PMMA); Precision Optical was asked to fabricate three mirrors from aluminium. The PMMA mirrors would be overcoated with aluminium and a magnesium fluoride protectant layer. Results of both of these fabrication processes are discussed in Section 6.3.

---

that a circular plan was to be preferred. The fabricator also demanded the elimination of pass-through holes, in order to use a vacuum chuck for rear mirror support.

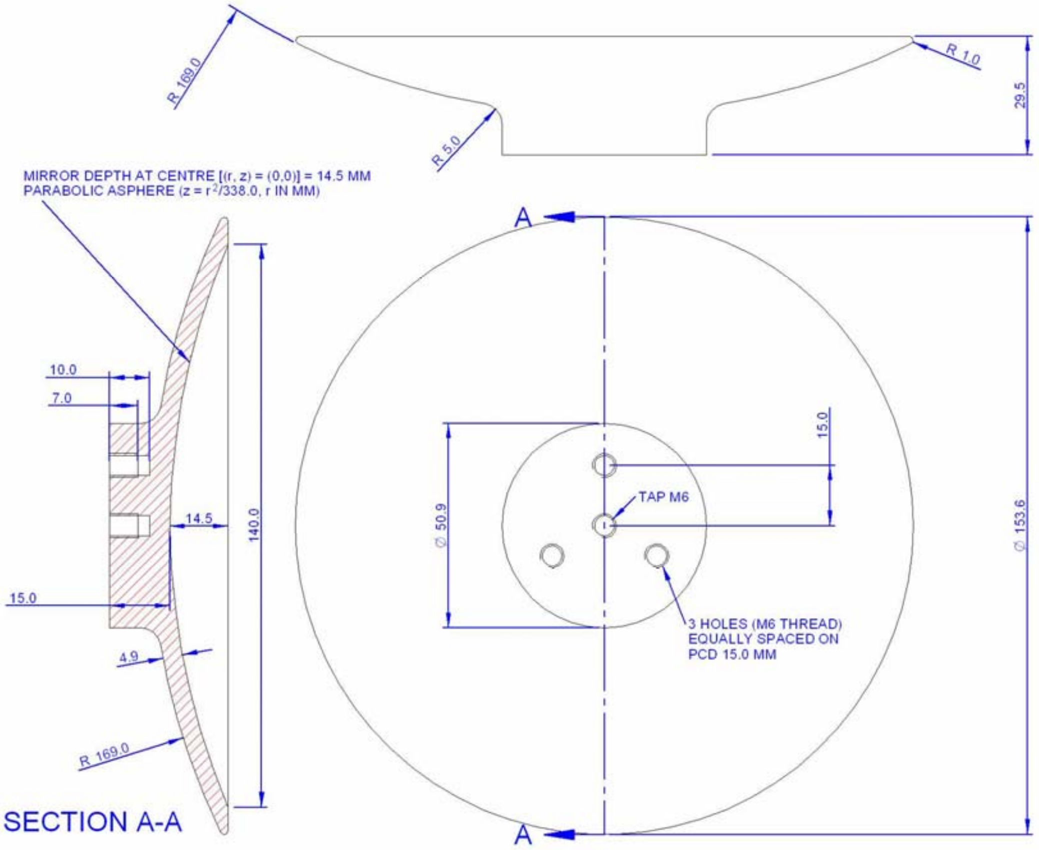
R 169.0
R 5.0
R 1.0
29.5
MIRROR DEPTH AT CENTRE [(r, z) = (0,0)] = 14.5 MM
PARABOLIC ASPHERE (z = r²/338.0, r IN MM)
A
10.0
7.0
14.5
140.0
15.0
4.9
R 169.0
SECTION A-A
∅ 50.9
15.0
TAP M6
∅ 153.6
3 HOLES (M6 THREAD)
EQUALLY SPACED ON
PCD 15.0 MM
A

Figure 5-20 14-cm diameter solar concentrating mirror, *f*/0.6, intended for ganged-mirror operation with fibre-optic transmission. Both plastic and metal (aluminium) optics were constructed.

5.6 Receiver Subsystem Detailed Design

Only the micro receiver, initially designed to provide 428 N-s of impulse per burn—was selected for detailed design and analysis. The small (750 N-s) and large (2,808 N-s) systems were not carried forward. While the larger engine types are of interest for providing high delta-V capability to standard (100 kg) microsatellites, it was decided that the smallest, lightest system would be of greater interest; it can be flight-tested aboard a small (20- to 100-kg) platform and is likely to be the lowest-cost of the three. Two versions were designed, built, and tested: the particle-bed heat exchanger (Mk. I), and a smaller, channel-flow heat exchanger (Mk. II). Graphite foam insulation, easier to obtain and machine, was substituted for zirconia/alumina foam.

The author conferred with a number of ceramic materials experts [Woodfield, 2002][Oliver, 2003][Morrell, 2002][Yeomans, 2002] during the detailed design phase. These individuals pointed out a number of practical difficulties with the baseline receiver design, illustrated in

Figure 5-21. These included: (1) severe difficulties encountered when attempting to bond BN surfaces to other BN elements or different ceramic materials through brazing or hot-pressing, due to BN's inertness; (2) thin walls, potentially too thin to manufacture reliably; (3) significant material porosity (for high-purity BN) and therefore likely propellant leakage during thrusting; and (4) potentially catastrophic thermal expansion differences between BN and B_4C structures.

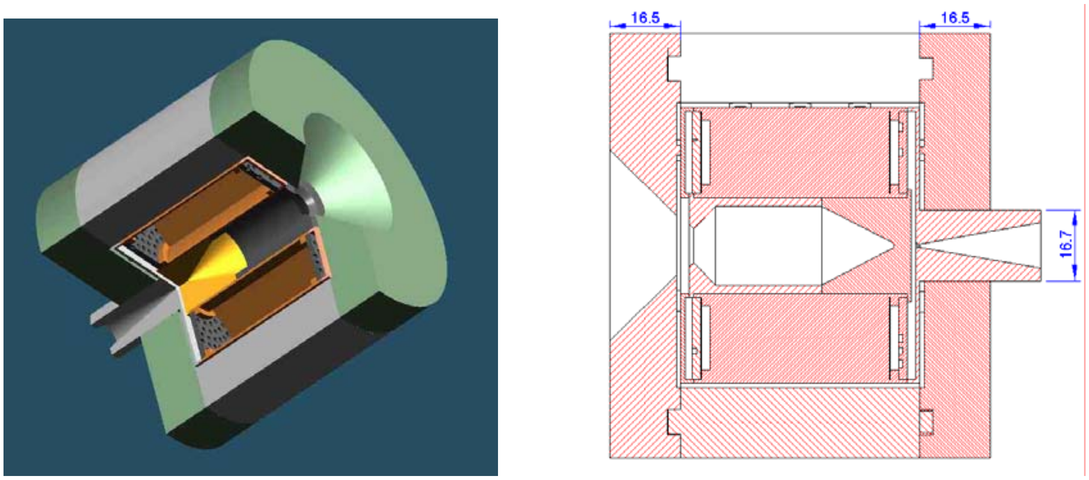

Figure 5-21 Baseline 428 N-s cavity receiver, B_4C particle bed in BN containment, surrounded by a ZrO_2/Al_2O_3 insulation package, left, and engineering drawing cutaway view, right (dimensions in millimetres).

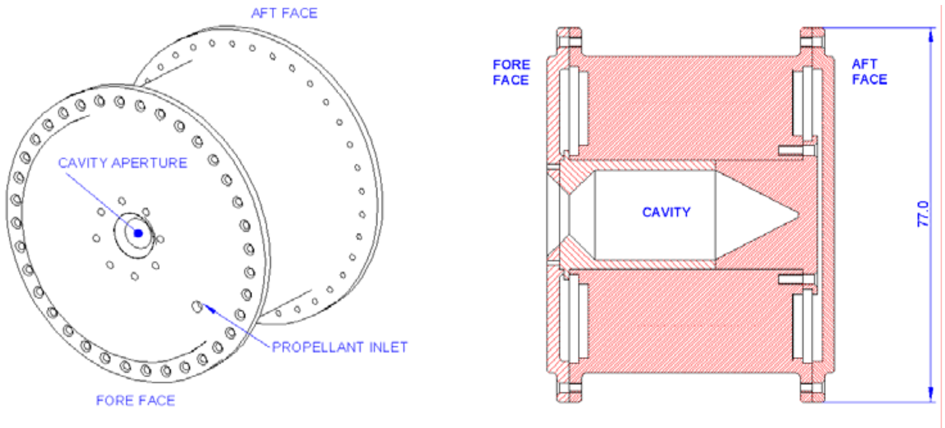

Figure 5-22 Intermediate design, 428 N-s flanged cavity receiver, B_4C particle bed in BN containment, insulation package removed to illustrate mechanical sealing, left. Flanged cavity receiver, engineering drawing cutaway view, insulation package removed, right (dimensions in millimetres).

Bonding BN shapes is essential. The baseline receiver contains complex internal structures that cannot be machined from any single element. Unfortunately, the literature on BN bonding is extremely limited; Nicholas [1990] comments, "…recent work on other nitride ceramics (other than silicon nitride (Si_3N_4) and SiAlON) is sparse." Local and international vendors of BN products have confirmed this [Woodfield, 2002][Lyle, 2002]. Sintec Keramik, a German ceramics vendor with a UK subsidiary in South Wales, produces various BN composites for ceramic heater and vacuum metallization applications. Sintek recommended a mechanical bonding approach over hot-pressing, hot isostatic pressing, or brazing [Woodfield, 2002]. While hot-pressing has been shown to be an effective process for bonding ceramic parts such as alumina and silicon nitride, there is no evidence that pure or composite BN shapes can be reliably bonded in this manner [Schwartz, 1990]. A BN composite (Grade M-26) consisting of 60% BN and 40% silica—suggested by Lyle [2002] at St. Gobain Advanced Ceramics in Amherst, New York—could be heated to high temperatures to produce a silica glassy phase that will melt and flow, potentially providing a ceramic-to-ceramic bond. However, this material is only useable at temperatures under 1,400 ºC (1,673 K)—substantially less than the target receiver temperature of 2,000-2,500 K.

Brazing is one alternative to solid-state bonding. Unfortunately, as BN is not wetted by many metals, even at elevated temperatures, finding a suitable high-temperature capable braze material will pose a significant challenge. Chiaramonte [1992] notes that two flat pyrolitic BN coupons were bonded using Ticusil, a brazing alloy composed of 68.8% Ag, 26.7% Cu, and 4.5% Ti. However, Ticusil melts at just 1,562 ºF (1,123 K). A suitable refractory metal braze, with a liquidus of 2,000 K or higher, would be necessary to bond BN elements inside the zirconia insulation package. Potential filler metals include Mo-Ru and Pt-Mo [Rembar, 2002].

Several experts recommended mechanical sealing with multiple caveats [Yeomans, 2002][Prentice, 2002][Woodfield, 2002]. Bolting ceramic elements together will require relatively hard substances (pure BN is soft, with a Knoop hardness[130] of only 3.4-4.9 kg/mm^2), large flange fittings, and screws machined from similar materials (Figure 5-22). The use of refractory metal screws might produce differential thermal expansion, forcing apart ceramic flanges and preventing the formation of a hermetic seal. After initial mechanical bonding trials were conducted, it was discovered that purpose-built ceramic bolts were extremely brittle and subject to failure; these were eventually replaced with molybdenum bolts, which performed well (see Chapter 6).

M-26 grade BN exhibits substantial anisotropy—its coefficient of thermal expansion between room temperature and 1,500 ºC (1,773 K) is 0.57 x 10^{-6} in./in./ºC (parallel to the pressing direction) and –0.46 x 10^{-6} (perpendicular to the pressing direction) [St. Gobain, 2000]. This can be contrasted with the value for molybdenum, a “low-CTE” metal, of 4.8 x 10^{-6} in./in./ ºC—ten times that of BN [Lide, 1995]. Woodfield [2002] indicated that several BN composites might outperform pure BN as a high-temperature structural material. These included (1) zirconia (ZrO_2) strengthened BN (ZSBN), a low-porosity, higher hardness, high-temperature capable composite ceramic with a maximum use temperature of 2,273 K; (2) boron nitride/aluminium nitride; and (3) an Intermetallic Composite (IMC), composed of titanium diboride (TiB_2) and boron nitride. IMC’s coefficient of thermal expansion is higher than that of molybdenum; receiver flanges fabricated from IMC will thus be held in compression during heating, improving hermetic sealing. Section 6.2.1 describes the results of various material compatibility and sealing tests, using ZSBN and IMC.

---

[130] “The resistance of a material to the formation of a permanent surface impression by an indenter is termed hardness.” [Green, 1998] The Knoop hardness test is performed with an elongated pyramidal indenter and the size of the indentation in the test coupon is measured. A Knoop hardness figure is then calculated by dividing the applied force (F) by the area of the indentation (L^2/14.2), where L is the length of the

Hoop (σ_2) and radial (σ_3) stresses in thick-walled pressure vessels, such as the receiver designs under consideration here, are not uniform through the thickness of the vessel [Young, 1989]. Meridional stress (σ_1) is constant through the thickness:

$$\sigma_1 = q\frac{b^2}{a^2 - b^2} \qquad \textbf{(5-26)}$$

Maximum wall stresses, which occur at the inner radius, are given by:

$$\sigma_2 = q\frac{a^2 + b^2}{a^2 - b^2} \qquad \textbf{(5-27)}$$

$$\sigma_3 = -q \qquad \textbf{(5-28)}$$

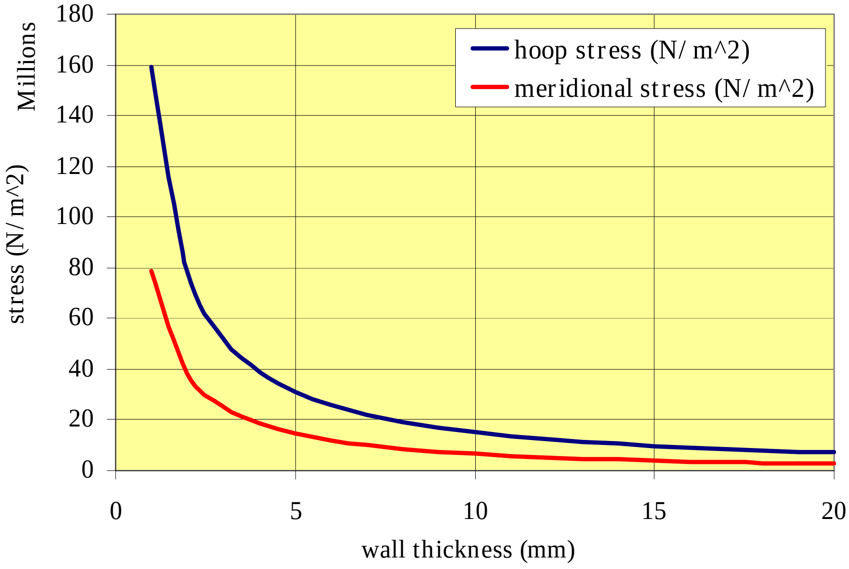

---

indentation. For comparison, tungsten carbide (WC) has a Knoop hardness of 1,000-1,500 kg/mm^2 [NRI,

Figure 5-23 Maximum meridional and hoop stress in 80-mm O.D., thick-walled pressure vessel.

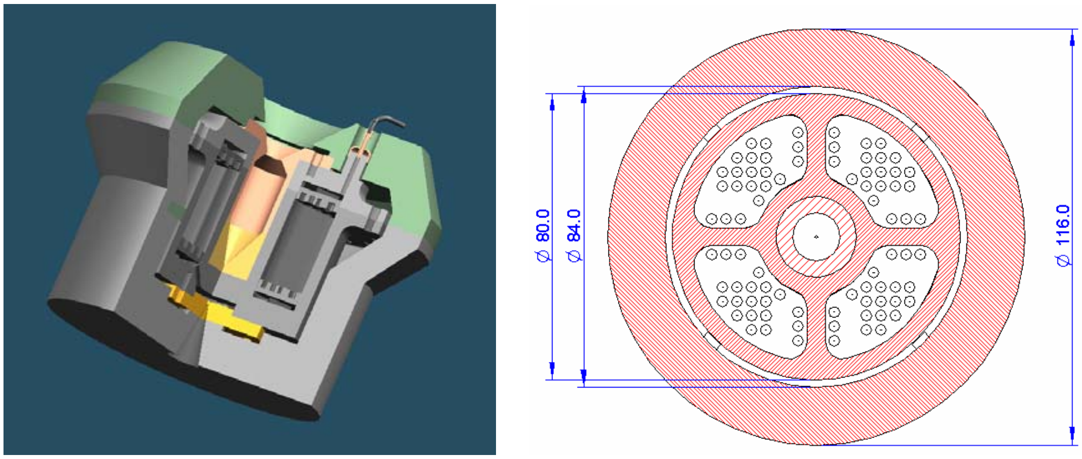

Figure 5-24 Mk. I cavity receiver, 1.3 kg, BN particle bed in ZSBN or IMC containment. Insulation package is 100% graphite foam. Mk. I cavity receiver in cross section, BN particle bed in ZSBN or IMC containment, graphite foam insulation. Dimensions in millimetres.

These are simply functions of the internal pressure, *q*, and the inner (*b*) and outer (*a*) radii of the vessel. For a ceramic vessel with $a = 80$ mm, $b = 75$ mm, and $q = 20$ bar, the maximum value of hoop stress is 31 MPa. Since boron nitride's ultimate tensile strength (UTS) at ambient temperature is approximately 40 MPa—and rises with temperature to over 120 MPa at 2,400 K—a pure BN structure of this size and thickness would appear to be an acceptable solution at pressures of more than 20 bar [Pierson, 1996]. Titanium diboride has a roughly constant UTS (40,000 psi or 272 MPa) to 3,000 °F (1,650 K) [Lynch, 1966]; however, no strength data is available on the BN/TiB_2 composite form.[131] Zirconia's performance is inferior to this: At room temperature, a CaO- or MgO-stabilised ZrO_2 exhibits UTS figures as low as 20,000 psi (136 MPa) but decays to as little as 7 MPa at 3,000 °F.

Of greater concern than wall stresses encountered in the heat exchanger's cylindrical section are those found in the clamped flanges (at top and bottom), including stress concentrations that are likely to occur near the bolt holes. Young [1989] provides the following relations for the maximum moment *M* (occurring at the ends) and stress σ in a beam element of length *L*, subjected to a uniform load *w* (N/m), and clamped at both ends:

$$M = \frac{wL^2}{12} \qquad \textbf{(5-29)}$$

2004]. Titanium diboride has a Knoop hardness of 3,000 kg/mm^2 [Lynch, 1966].

[131] The author will assume a minimum value for IMC's UTS of the mean of its two components' ultimate strengths, or 156 MPa (at room temperature).

$$\sigma = \frac{M}{I/c} = \frac{M}{bh^3/12c} \tag{5-30}$$

The beam's bending moment of inertia (I) is equivalent to the product of the beam section's base, b, and the cube of its height, h. Maximum stress occurs at the periphery of the beam, at a distance $c = ½\,h$ from its centreline. For the top flange of the Mk. I receiver, b = 80 mm and h = 5 mm. The assumed load per unit length w is calculated from the force exerted by an internal pressure of 20 bar over the circular face of the flange; this equates to a figure of 1.256 x 10^5 N/m. Maximum stress is calculated to be 200 MPa, which is above the estimated mean IMC figure at room temperature. Reducing maximum internal pressure below 10 bar (and maximum stress below 100 MPa) will therefore provide a factor of safety of 1.5.

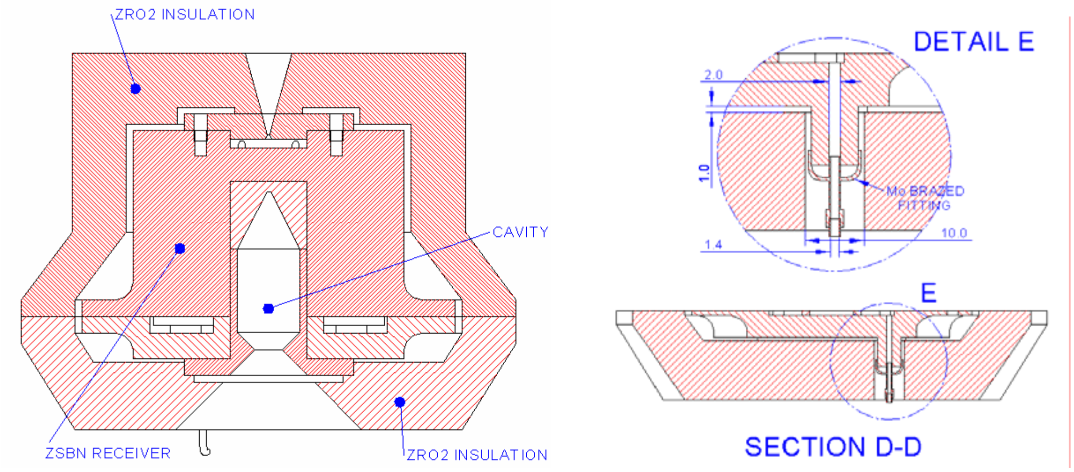

Figure 5-25 Mk. I cavity receiver in cross section, particle bed in ZSBN or IMC containment, ZrO_2 insulation later replaced with graphite foam (left). Feed line pass-through in fore face of receiver, showing brazed Mo fitting, right (all dimensions in millimetres).

Discussions with Sintec Keramik resulted in the inclusion of 5 mm thick ceramic flanges and containment walls, minimum 4 mm holes tapped with M4 thread, and graphite foil seals [Woodfield, 2002]. The use of minimum-thickness (0.1 mm) pyrolitic BN as a seal was determined to be unworkable, as the production method—chemical vapour deposition—produces fully dense (zero porosity) material, unsuitable for seals owing to low compressibility. Painting a BN slurry onto the sealing face so as to form a mortar-like sealant, was suggested as an alternative to graphite foil gaskets. While hydrazine or ammonia decomposition products are likely to react with the graphite foil seals at elevated temperatures, the rate of seal degradation should be relatively low, owing to the small surface area available for seal/propellant contact.

The final design of the Mk. I receiver included a number of alterations to the baseline. Implementing the changes described above increases the micro cavity's total mass by a factor of two, to 1.3 kg The boron carbide particle bed was retained virtually intact, but the particles were replaced with (easier-to-obtain) BN particles, massing 184 g. The boron carbide cavity and cavity plug were also replaced, by IMC, producing a virtually athermal design. The only non-BN elements in the core receiver are (1) graphite foil seals, (2) molybdenum bolts, to seal the upper and lower flanges, and (2) the propellant inlet fitting, also machined from molybdenum..[132]

Morrell [2002] indicated that it would be desirable, from the standpoint of machinability, to minimise the number of flanges, radius corners to remove likely centres of stress concentration, and remove interior webs. Figure 5-24 (right) illustrates the Mk. I cavity receiver's cross-section. The four particle bed containment spaces surrounding the central cavity would be milled out of a single cylindrical ZSBN or IMC billet, without resorting to separately fabricated webs and mounting schemes. The graphite (formerly zirconia/alumina) foam insulation package is simplified; instead of four elements, as in the original design, the Mk. I receiver contains only two. The insulation package provides lateral and axial support for the receiver, but contact is limited to minimize heat losses. Four graphite dowels provide lateral support near the centreline of the receiver; axially, the nozzle and cavity inlet structures mount flush to the insulation walls (Figure 5-25, left). The insulation elements will be clamped together by aluminium mounting rings and a tripod support structure.

A final consideration involves the introduction of propellant into the cavity receiver during firing. Following thermal charging, the micro cavity is expected to attain temperatures of 2,000 K or higher; the propellant inlet fitting (Figure 5-25, right) brazed directly to a hollow ZSBN or IMC post on the fore face of the receiver, is conductively coupled to the main body of the receiver. Because of this, the inlet fitting and feed are baselined as molybdenum, a low-thermal expansion, high melting point (2,890 K) metal similar in properties to tungsten, but with higher workability. The fitting is likely to achieve temperatures approaching 2,000 K prior to engine firing, but will cool down substantially as relatively low temperature hydrazine (at 863 K) or ammonia (at 300 K) is fed to the system. The post material may require metallisation prior to the attachment of the Mo fitting, to enhance the joint's wettability by brazing filler metal. A molybdenum/manganese oxide mixture is perhaps the most commonly used metalliser, although pure Mo and tungsten (W) are also possible [Schwartz, 1990]. The geometry of the joint includes an expansion cap, which is intended to maintain the ZSBN post in compression following ceramic-to-metal joining.

The fitting will be attached prior to the placement of the ZrO_2 foam end cap on the receiver fore face. After the cap is in place, an angled Mo tube will then be electron beam welded to the fitting stub end. The Mo tube will connect the receiver to the propellant storage and feed system, via (1) a catalyst bed mounted near the front face of the receiver, in the case of hydrazine propellant, or (2) a direct feedline to the gas supply, in the case of ammonia, nitrogen, or helium. This catalyst bed will provide decomposed hydrazine (NH_3, N_2, H_2) to the receiver at 863 K. Candidate materials for the receiver are shown in Figure 5-26.

---

[132] The 428 N-s receiver's thermal storage mass was estimated in Chapter 4 to mass 500 g. The as-built Mk. I receiver core structure was weighed, post-test, and found to mass 948 g (after BN particles were removed). The graphite insulation package was also weighed (202 g).

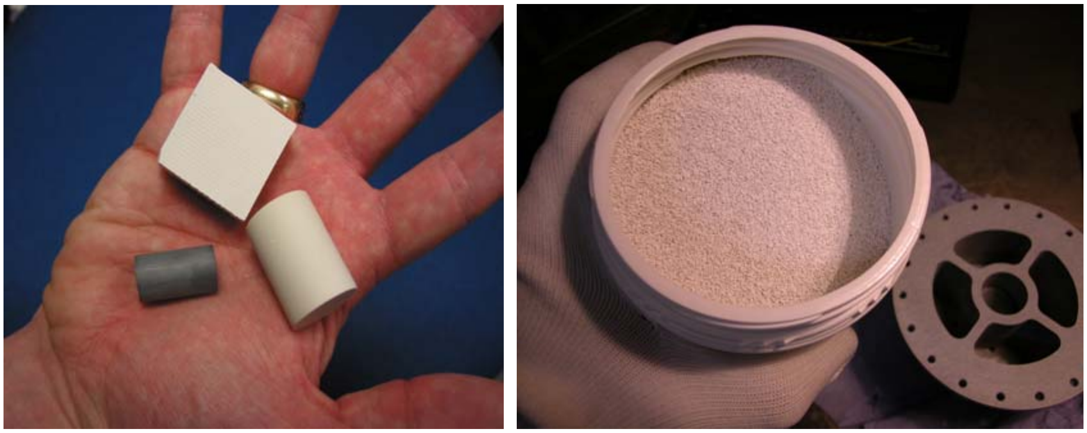

Figure 5-26 Cavity receiver material samples, left photo: (1) Silica/boron nitride composite (M-26 60BN/40SiO$_2$, white block), (2) ZSBN (gray), and (3) BN/AlN (beige cylinder). Boron nitride particles and Mk. I receiver during fill process, right photo. Materials courtesy of St. Gobain Advanced Ceramics and Sintec Keramik.

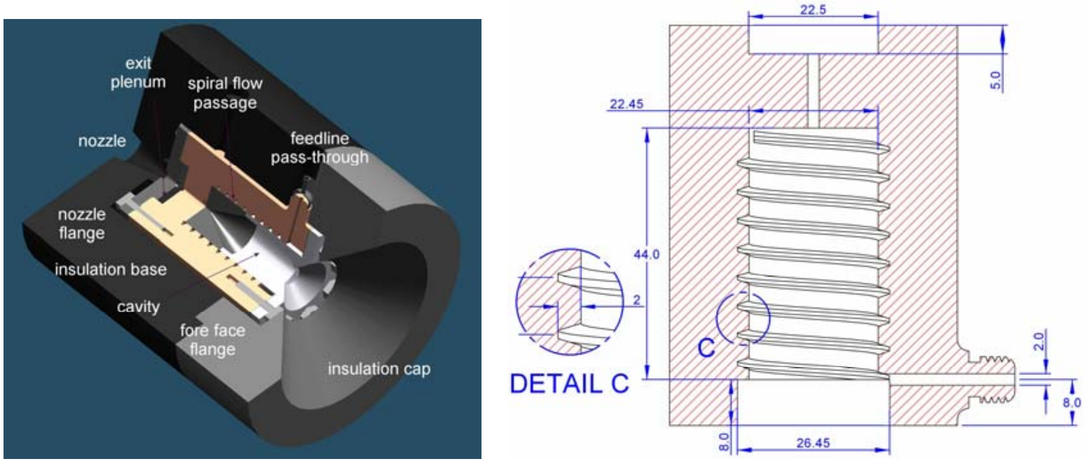
exit plenum
spiral flow passage
nozzle
feedline pass-through
nozzle flange
insulation base
cavity
fore face flange
insulation cap
22.5
5.0
22.45
44.0
2
DETAIL C
C
2.0
8.0
8.0
26.45

Figure 5-27 Mk. II cavity receiver solid model cutaway (left) and engineering drawing (right).

The Mk. II receiver resembles the Mk. I in many important aspects (Figure 5-27, right). Composed of the same composite ceramic as the Mk. I, the Mk. II was designed to be a smaller, simpler receiver with rapid thermal charging capability. Unlike the Mk. I, the Mk. II is a channel-flow heat exchanger, with limited thermal storage mass. A smaller-diameter (50-mm) receiver cap, dimensionally equivalent to the bottom, or nozzle, cap, replaces the wide top flange of the

Mk. I. This strengthened the design of the top of the pressure vessel significantly.[133] The propellant inlet post, which is placed on the fore face of the Mk. I receiver, was moved to the cylindrical side face for ease of positioning the feedline following assembly of the insulation package halves.[134] The pre-test weight of an assembled Mk. II receiver (without insulation, but with molybdenum bolts and feedline cap included) was determined to be 446.1 g.

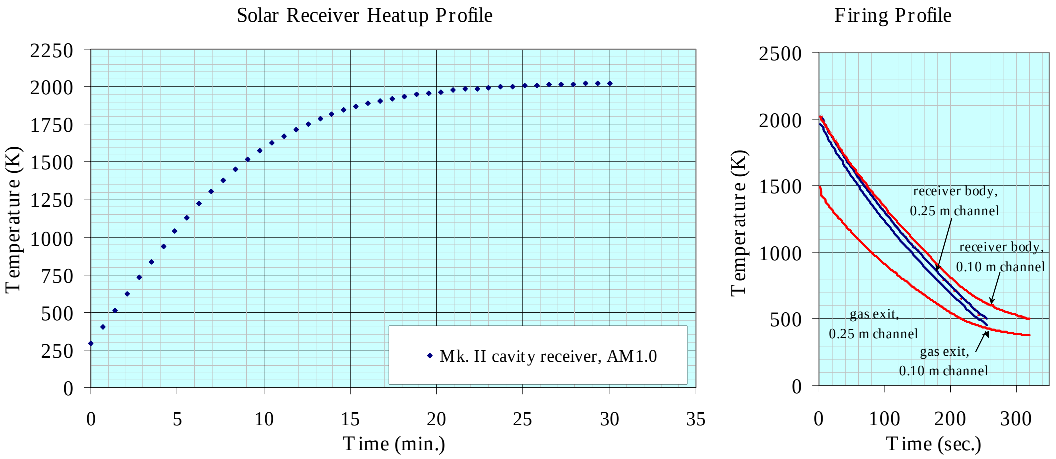

Figure 5-28 Mk. II receiver heatup profile, 1,200 W input power (left), peak cavity temperature = 2,022 K after 30 minutes. Firing profile (right) demonstrates the heating efficiency of the receiver for two channel lengths (10 and 25 cm), with ammonia propellant. The 56 cm case is not shown; gas exit temperature tracks receiver body temperature.

The Mk. II receiver's flow channel is approximately 56 cm in length and 2 mm in diameter. MSTISM simulation indicates that this is sufficient to bring any of several candidate propellants to receiver temperature prior to exiting through the collection plenum (Figure 5-27, left). Figure 28 (right) indicates that shorter-length channels will adversely affect engine performance. For a minimum firing temperature of 500 K, halving the channel length reduces the Mk. II system's burn-average specific impulse from 286 s to 270 s (in ammonia), while burn time increases from 251 to 256 seconds. Further reductions in channel length take a greater toll; for a channel of 10 cm length, I_{sp} falls to 203 s (with an increased burn time, 320 seconds).

---

[133] The applied moment (along the Mk. II's flange perimeter) at an internal pressure of 20 bar is reduced by a factor of four (Eq. 5-29). The maximum stress in the flange is reduced to just 78.5 MPa (Eq. 5-30). This is well within the predicted range of the composite ceramic's capabilities.

[134] The Mk. I design does not allow for non-destructive disassembly of the insulation package sections once the feedline cap is sealed to the feedline post.

5.7 Detailed Design Summary

Two concentrating mirror and two receiver designs were selected for fabrication and testing, following extensive modelling with commercial optical and thermal simulation codes (OSLO LT and WinTherm). The author developed a system-level modelling tool, the Microscale Solar Thermal Integrated System Model, as a means of performing broad sensitivity analyses and understanding performance trends for a variety of system configurations. This tool incorporates concentrator and attitude control system impacts, orbital mechanics, propellant management, and a detailed receiver design model.

Two types of rigid concentrating mirrors, possessing respective diameters of 56 cm and 14 cm, were designed and constructed from aluminium plate, and, in the case of the smaller mirror, PMMA. Both incorporate a steep (fractional f-number) paraboloidal form, with a rim angle of 45º. This maximises achievable concentration ratio on a flat plate cavity absorber/receiver. The small mirrors are to be used in a ganged assembly, with multiple optical fibres transmitting incident, concentrated sunlight to a single cavity receiver.

Two cavity receivers, designated Mk. I and Mk. II, were designed and fabricated from a high-temperature ceramic composite material, BN/TiB_2. The heavier Mk. I receiver incorporates a boron nitride particle bed, maximising heat transfer between the receiver body and inflowing propellant gas. The Mk. II, approximately half the size of the Mk. I, was designed to improve structural soundness at all temperatures, while permitting rapid thermal charging. This receiver utilises a channel flow heat exchange mechanism, which, while not as efficient as the Mk. I's, was designed to extend gas residence time and achieve near-parity between propellant and receiver side wall temperatures at the exit.

Chapter 6

6 Component Test Campaign

This chapter discusses a series of tests conducted on the solar receiver and concentrator elements, and their subcomponents. Receiver testing includes coupon oxidation, high temperature survivability, thermal cycling, bonding, hermetic sealing, and full flow trials. Concentrator testing includes mirror form metrology, spot size determination, power throughput, and optical fibre assessment. Limited component coupling tests, to include small receiver body heating trials with concentrator input, were also conducted.

6.1 Test Strategy

Surrey propulsion research activities, including recent investigations into hybrid rocket systems [Sellers, 1996], resistojets [Lawrence, 1998] and nitrous oxide mono- and bipropellant systems [Zakirov, 2001], differ from the present effort in solar thermal propulsion as a result of STP's reliance on long-term, elevated temperature operation (2,000-2,500 K). These temperatures are essential to STP's high-I_{sp} performance with storable propellants. Previous efforts, such as Zakirov's, tend to focus on a middle temperature regime (<1,500 K) where steel and steel alloys are still permissible material options.[135] Haag [2001] and Coxhill [2002] achieve 2,500 K+ gas exit temperatures through oxidizer film cooling of the thrust chamber wall; this approach is obviously not possible in a resistojet or STP engine.

The STP engine designer must examine a host of "exotic" materials such as refractory metals and ceramics. The author's choice of several boron-based ceramics is only one approach among many; the key point to be made here is that testing at these elevated temperatures virtually demands vacuum as a prerequisite, due to the extremely high oxidation rates—and consequent degradation—for almost any material of choice.[136] Simulation of space conditions (i.e., no convective heat losses to the ambient environment) for cavity receiver thermal charging and firing will also require vacuum operation. It will be valuable to experimentally verify the degradation of selected materials by testing coupons at temperature, at various pressures in air.

---

[135] Haynes nickel-based alloys achieve maximum operating temperatures of 1,260 °C (1,533 K), with good oxidation resistance and structural strength [Gotzig, 2000].

[136] Among the nitrides, for instance, boron nitride and silicon nitride are considered to have good oxidation resistance "to 2,000 °F," or 1370 K [Lynch, 1966]. Peak STP engine temperatures will be nearly double this figure. Pierson [1996] calls hexagonal BN "one of the most outstanding corrosion-resistant materials."

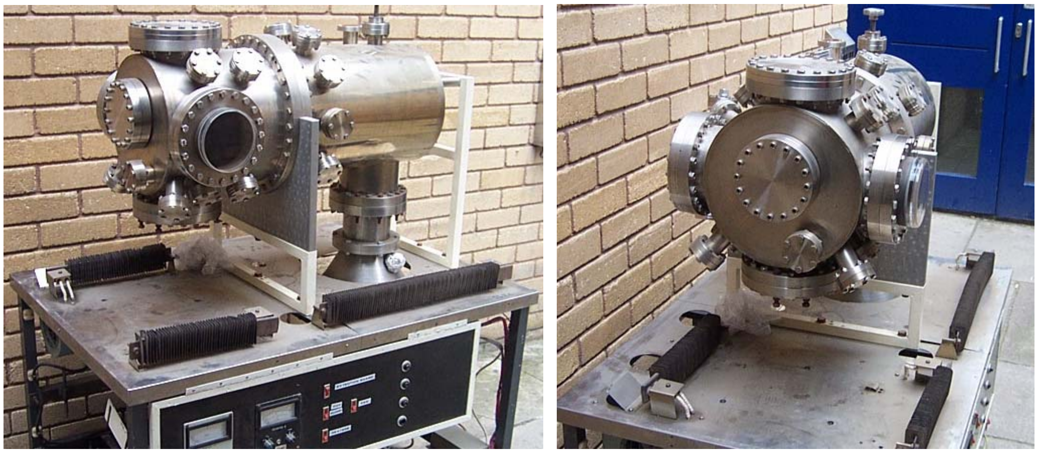

Figure 6-1 SSTL vacuum test chamber with rotary first stage and oil diffusion pump.

Surrey's past propulsion research activities used ambient testing almost exclusively. Of the research programmes discussed above, only Lawrence [1998] performed *in vacuo* testing, and this was conducted entirely at the U.S. Air Force's Rocket Propulsion Laboratory at Edwards Air Force Base, California. Surrey's primary facility for propulsion testing is located at the Ministry of Defence's (MoD) Westcott E-Site; University of Surrey Safety Office representatives have forbidden hydrogen peroxide testing on the campus proper [Haag, 2001]. The Westcott E-Site, located near Aylesbury, northwest of London, is historically associated with British rocket developments and is fitted with an in-air test stand, data acquisition system, gas and liquid bottle storage facility, and protected viewing. A small high-vacuum chamber, 30 cm in diameter, has been obtained by SSTL from the University of Surrey's Department of Materials Science and will be used for initial coupon degradation and heating tests (Figure 6-1).

As noted, receiver heating and cooling rates can only be experimentally verified in a vacuum, due to losses associated with convective cooling in air. Flow characterization experiments with non-toxic or low-toxicity propellants (e.g., He, N_2, and ammonia gas) will be conducted at Westcott's E and F Sites. Ambient checks on non-flight receiver hardware (e.g., PMMA, Al, or stainless steel materials) could be performed at Surrey or Westcott with N_2 propellants—thus folding in propellant storage and seal verification. Full flow testing, at temperature, and/or with hydrazine, will require vacuum operations—perhaps at a nearby facility[137] or overseas.

---

[137] Atlantic Research Corporation's (ARC) Westcott facility includes vacuum and high-altitude chambers for rocket testing [ARC, 2002]. Qinetiq's Farnborough facility performs long-duration testing of low thrust electric propulsion systems in vacuum. Either of these are alternative locations for high-temperature

Initial concentrator characterization was conducted at the Surrey Space Centre using a commercially available sun-tracking mount. Subsystem tests included verification of the concentrator's optical performance over a range of temperatures, offset angles, focal length errors, and simulated contamination or surface degradation. Key figures of merit include concentration ratio, focal spot geometry, and optical efficiency. For some tests, it was possible to use Surrey's solar simulator[138] or low-power lasers.

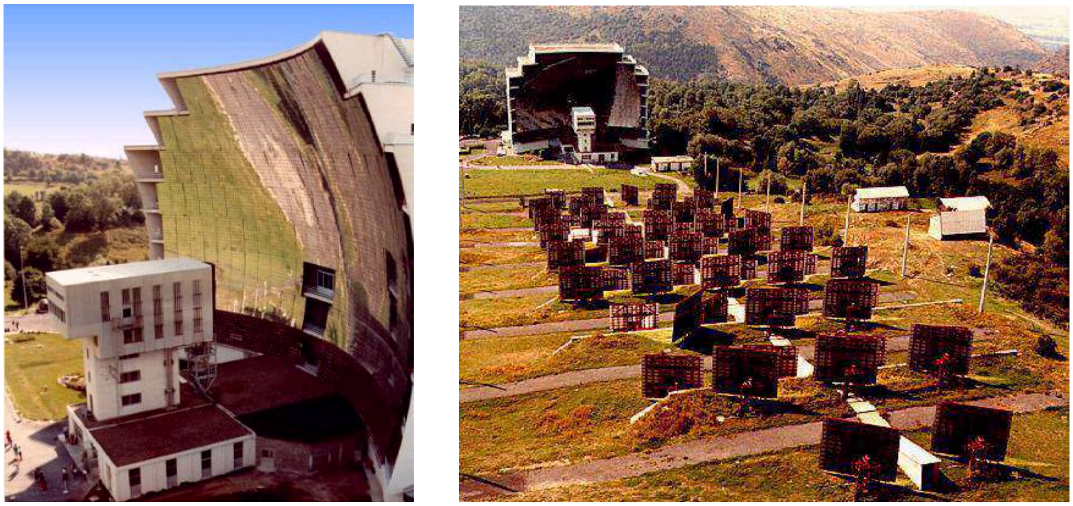

Solar furnace, Odeillo, France [IMP-CNRS, 2001]

Odeillo 1000 kW solar furnace showing heliostat farm and parabolic concentrator mirror [IMP-CNRS, 2001].

Figure 6-2 Odeillo Solar Furnace Facility, near Perpignan, France.

System testing, to include full optical path testing (sun or simulated source to receiver aperture via the concentrator) *in vacuo*, flow with representative propellants, tankage, and feed lines, and test durations nearing or equalling nominal mission profiles, will be highly desirable as a precursor to flight, but was not essential to the present research program. Direct solar insolation requires a dedicated facility, such as the Odeillo furnace in Perpignan, France (Figure 6-2), the DLR furnace (Cologne, Germany [Neumann, 1999]), or Edwards Air Force Base's Rocket Propulsion Laboratory's Solar Thermal Propulsion test facility [Frye, 1992]. These sites have exceedingly large heliostat/concentrator assemblies[139] and limited on-sun capability per day. Solar simulator test facilities include NASA Glenn Research Center's Tank 6 Facility (Figure 6-3), used for solar

---

receiver testing or full-flow tests. The ARC F-Site vacuum chamber was used to conduct full-flow tests on the Mk. I and Mk. II receivers.

[138] The existing simulator is primarily intended for individual solar cell tests and therefore cannot project a sufficiently large area of collimated light to fully illuminate even the micro (30-cm diameter) concentrator surface. Therefore, a "map" of the concentrator's focal plane spot would have to be built up by illuminating various sections of the mirror. Something similar might be performed with a commercially available laser source.

[139] For example, Kreider [1979] indicates that the Odeillo furnace has a mirror area of 96 m^2.

dynamic power system and Integrated Solar Upper Stage testing [Frye, 1998], and the Arnold Engineering Development Center's 12V (12 x 35 foot) solar simulator and thermal vacuum chamber [AEDC, 2001]. These facilities, while theoretically having 24 hour-per-day capability, tend to suffer from xenon arc lamp degradation and failure over a long-duration test cycle. They are also large, highly subscribed, and expensive to operate.

One alternative to conducting a system test in a large facility might be to construct a purpose-built small-scale solar simulator and pair it with an existing thermal vacuum test facility (e.g., QinetiQ or Rutherford Appleton Laboratories)—this would require the test chamber to either have an existing port for introduction of simulated sunlight, or allow for one to be added. Construction of a small simulator is likely to be a lower-cost approach than renting a large facility (e.g., Tank 6) for the necessary test campaign period. While this approach was not adopted during the present research and flight demonstration development activity, it may be useful for future characterisation of operational STP systems.

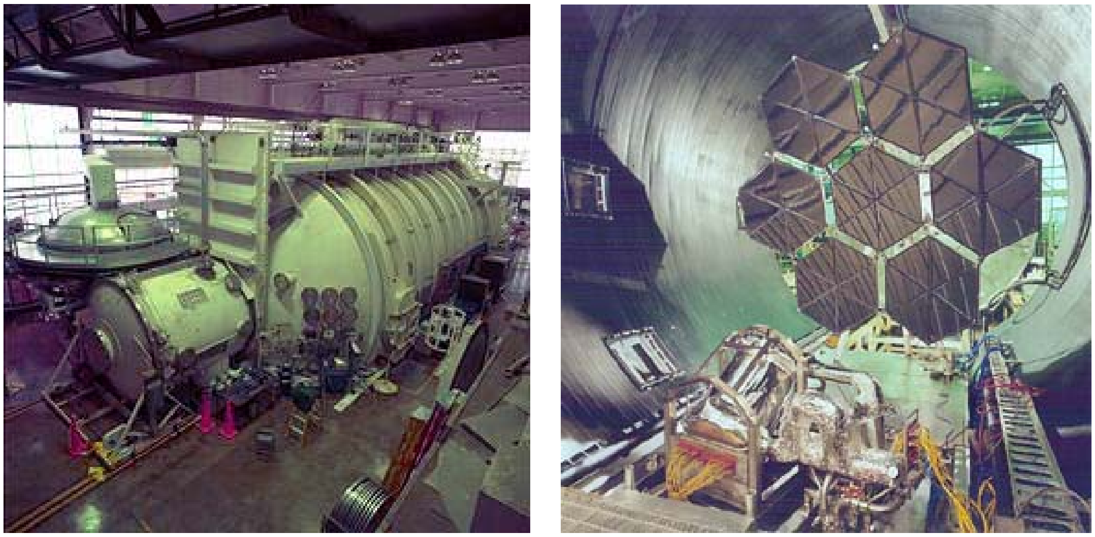

Exterior view of Glenn Research Center's Tank 6 Facility [NASA GRC, 2000]

Tank 6 interior, with 15-foot (4.57 m) concentrator [NASA GRC, 2000]

Figure 6-3 Solar Simulator Test Chamber at the NASA Glenn Research Center.

6.2 Receiver Testing

The receiver subsystem received the greatest amount of attention during the component test phase. Initial material characterisation and bonding tests—needed to determine the efficacy of selected materials at 2,000 K and in vacuum—were followed by heating and thermal cycling trials, and, later, full flow testing in representative propellants (He, N_2, and NH_3). These will be addressed in detail in the following sections.

6.2.1 Material Survivability, Bonding, and Sealing Tests

The solar receiver should be capable of surviving repeated cycling between ambient (290 K) and peak operating temperatures of 2,000-2,500 K. Ideally, it will also be capable of withstanding chemical attack from hot ammonia, hydrazine, or various decomposition products (e.g., N_2, H_2).

Two composite ceramics were selected for further consideration as receiver structural materials: (1) Zirconia-Strengthed Boron Nitride (ZSBN), a blend of 45% zirconia (ZrO_2), 7% silicon carbide, and 48% boron nitride by weight; and (2) an Intermetallic Composite (IMC) of 46% titanium diboride (TiB_2) and 49% boron nitride. Both are low porosity ceramics with good machinability characteristics, high thermal shock resistance, low coefficients of thermal expansion (CTE), and high temperature strength [GE, 2000][St. Gobain, 2000]. IMC was retained as an alternative due to vendor concerns over possible evaporation and chemical reaction in ZSBN at 2,300 K [Woodfield, 2002][Lyle, 2002].

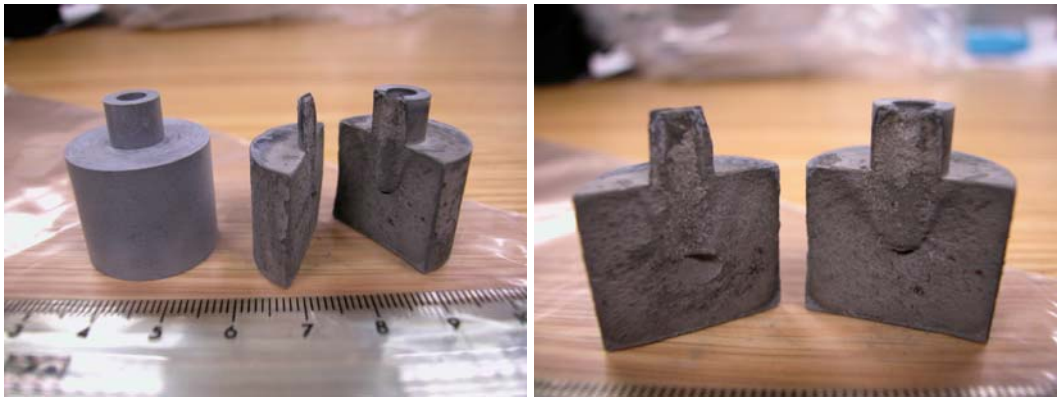

Figure 6-4 Left: Pristine and heated samples of ZSBN ceramic composite, 40 minutes at 2,300 K, 20 mbar He environment, graphite furnace. Right: Fractured ZSBN specimen.

Several specimens of each material were exposed to temperatures of approximately 2,300 K for up to 40 minutes in a low-pressure He atmosphere (20 mbar). Figure 6-4 demonstrates the poor high-temperature performance of ZSBN—both tested samples lost in excess of 40% of their pre-test mass during their short exposure. One of the ZSBN elements fractured into two sections, displaying evidence of heating-induced vaporization and porosity. The IMC specimens performed significantly better; while they experienced some darkening due to surface graphitisation, they lost just 0.35% and 2.3% of their pre-test mass, respectively. Other than this single ZSBN fracture, neither set of samples suffered significant dimensional changes.

Both sets of samples produced a flaky white residue that precipitated out on various elements of the graphite furnace, which post-test X-Ray Photoelectron Spectroscopy (XPS) examination of the specimens revealed to be boric oxide (B_2O_3), a binder material present in small amounts in both ceramics. A dark residue precipitated out on the surface of the IMC elements, which XPS analysis demonstrated to be elemental carbon (Figure 6-5). Based on these results, the author selected IMC as the primary receiver structural material for the component test phase.

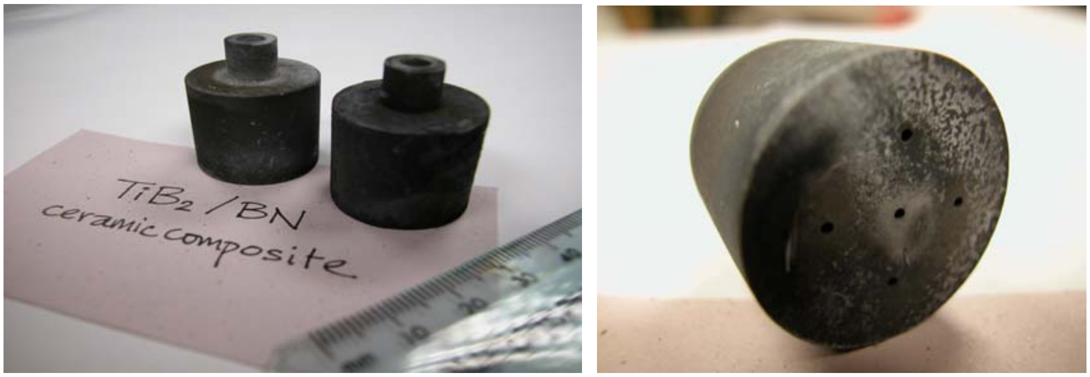

Figure 6-5 Left: Post-test samples of IMC ceramic composite, 40 minutes at 2,300 K, 20 mbar He environment, graphite furnace. Right: Close-up reveals evidence of graphite precipitation.

In addition to surviving at temperature in vacuum, the solar receiver must be capable of being assembled from a selection of subcomponents, with hermetic outer seals preventing the release of propellant gas into space. While metallic structures enjoy a variety of options for sealing, to include welding, mechanical bonding, and brazing, the nitride ceramics investigated by the author for use in a solar thermal engine are typically inert at high temperatures, sublime rather than melt, and are fairly brittle. While BN is notable in that its tensile strength rises considerably with temperature, its inertness makes it very difficult to bond to itself, other ceramics, or metals [Nicholas, 1990][Pierson, 1996]. Its use in crucibles and metallising boats attests to its lack of chemical reactivity, even at elevated temperatures.

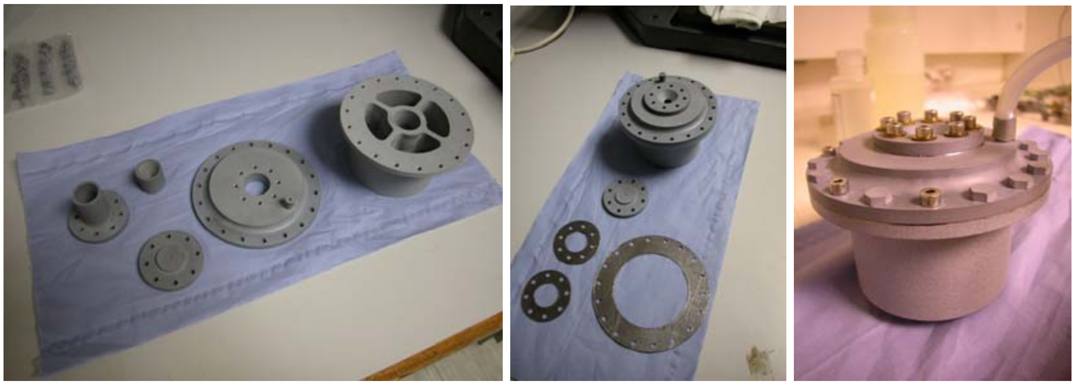

Mk. I receiver components, from left: cavity aperture, cavity plug, nozzle, top flange, and cavity can.	**Partially-assembled solar receiver and graphite foil gaskets.**	**Sealed solar receiver undergoing 3.9 bar leak check in nitrogen.**

Figure 6-6 IMC (TiB_2/BN) solar receiver subcomponents during assembly and initial hermeticity testing.

After conferring with a number of materials experts, the author concluded that the approach with the greatest chance of success consisted of mechanically bonding flanged ceramic sections with ceramic bolts and graphite foil gaskets. The bolts, machined from the same material as the solar receiver, would have the same CTE as the main body[140] and should neither fracture the flange (in compression) or open it to leakage (in tension).

Figure 6-6 illustrates details of the mechanical bonding scheme used in the construction of the solar receiver. The photo at far right shows the assembled Mk. I receiver fitted with a silicone line for leak testing. This receiver withstood nearly 4 bar (gauge) of internal pressure without any leakage around the three graphite seals. There was some apparent leakage around the heads of several bolts; during assembly, it was found that the IMC bolts (4-mm diameter) are extremely brittle, fracturing at torque levels of between 0.2 and 0.4 N-m. This makes it difficult to fully tighten the bolts onto the flange faces.[141]

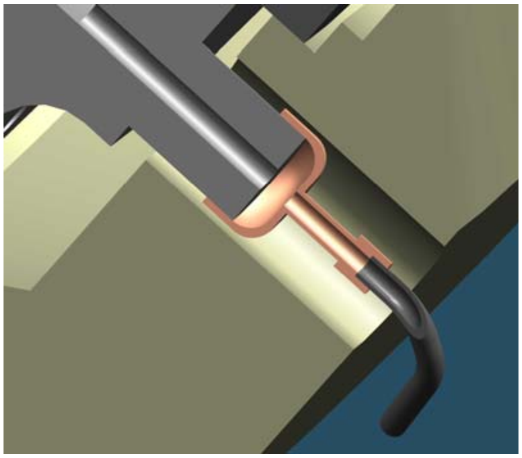

Cavity receiver feedline detail (cutaway)

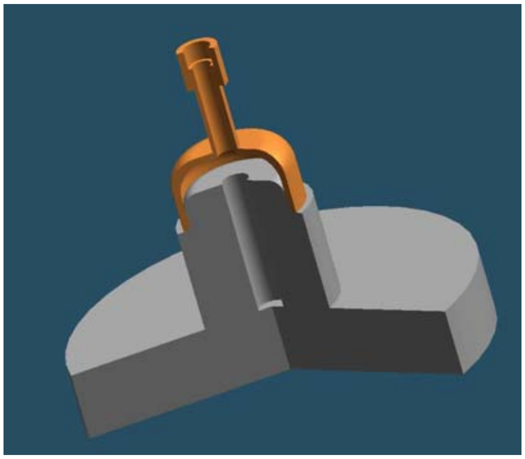

Brazing configuration for test specimen (molybdenum cap on ceramic post)[142]

---

[140] For IMC, this figure is 7.0 x 10^{-6} in/in/°C [GE, 2000]. This is slightly higher than two key refractory metals, tungsten (4.5 x 10^{-6}) and molybdenum (5.1 x 10^{-6}) [Lide, 1995].

[141] Ceramic fasteners were soon thereafter replaced by molybdenum bolts and nuts, which, given molybdenum's lower coefficient of thermal expansion, should expand less than the IMC flange material. This will place the vessel sections in compression at operating temperatures.

[142] The ceramic element used in this test is 30 mm in diameter, with a 10-mm diameter post. The Mo cap fits snugly onto the lip of the post. The cap's minimum internal diameter is 2 mm, matching the outer diameter of Mo tubing procured for use as a propellant feedline.

Figure 6-7 Brazed feedline for high-temperature bond survivability.

Introducing propellant into the solar receiver necessitates a ceramic-to-metal joint capable of withstanding very high temperatures (Figure 6-7). The author selected molybdenum as the feedline material, given its workability, relatively low cost, and refractoriness. Molybdenum's melting point is 2,883 K.

Brazing Filler Metal	°F	°C (K)
Ag	1,760	960 (1,233)
Cu	1,980	1,052 (1,325)
Ni	2,650	1,454 (1,727)
Pd-Mo	2,860	1,571 (1,844)
Pt-Mo	3,225	1,774 (2,047)
Ag-Cu-Mo	1,435	779 (1,052)
Ni-Cu	2,460	1,349 (1,622)
Mo-Ru	3,450	1,899 (2,172)
Pd-Cu	2,200	1,204 (1,477)
Au-Cu	1,625	885 (1,158)
Au-Ni	1,740	949 (1,222)

Table 6-1 Brazing filler metal liquidus temperatures [Rembar, 2002].

Options for joining molybdenum to TiB_2/BN include mechanical assembly (e.g., bolted flanges or screw fittings), high-temperature adhesives, and brazing. All of these approaches—and some combinations thereof—have been examined for application to the receiver feedline connection. Several ceramic adhesives with use temperatures of up to 2,033 K were purchased and tested. Gasketed screw fittings were also designed, fabricated, and tested. As the latter two approaches were likely to suffer more from leakage, the author first undertook an examination of high-temperature brazing.

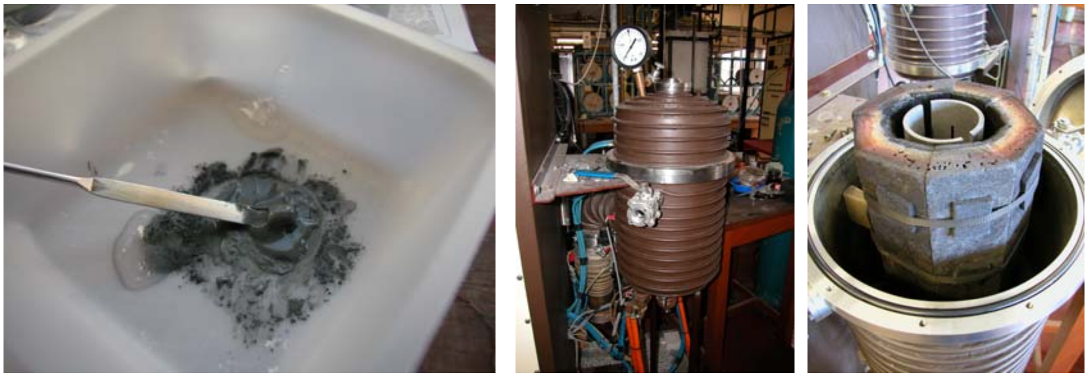

The author mixes Mo (57 wt. %) /Ru (43) braze filler metal powder with a glycerin/water solution prior to application to the test specimens.

High-temperature, vacuum graphite furnace used for Mo/Ru braze trials.

Graphite furnace, open, showing insulation and oven detail.

Figure 6-8 Brazing trials at the University of Manchester's Material Science Institute.

Potential braze filler materials were investigated (Table 6-1), and one selected for further examination: eutectic molybdenum/ ruthenium (Mo/Ru). A second approach, suggested by B.

Derby of the Manchester Materials Science Institute, utilised a mixture of pure Mo, silicon, and molybdenum disilicide ($MoSi_2$), potentially creating a high-temperature solid phase intermediate between the ceramic and metal surfaces. This approach, an example of partial transient liquid phase bonding (PTLPB), was recommended due to $MoSi_2$'s low coefficient of thermal expansion, intermediate between that of the molybdenum feedline cap and ZSBN receiver structure. Mo/Ru, with a melting point of 2,320 K, was successfully used to bond single-crystal molybdenum solar receiver elements in a Japanese test programme conducted in the late 1990s. [Shimizu, 1997] While there was no specific evidence in the literature that suggested that such a bond would be achievable, Mo/Ru represented just one of a very few non-proprietary metal brazes available with a eutectic above the projected receiver use temperature of 2,000 K. It was believed that long experience with molybdenum/manganese metallisation of ceramic elements might make such a bond feasible. [Nicholas, 1998]

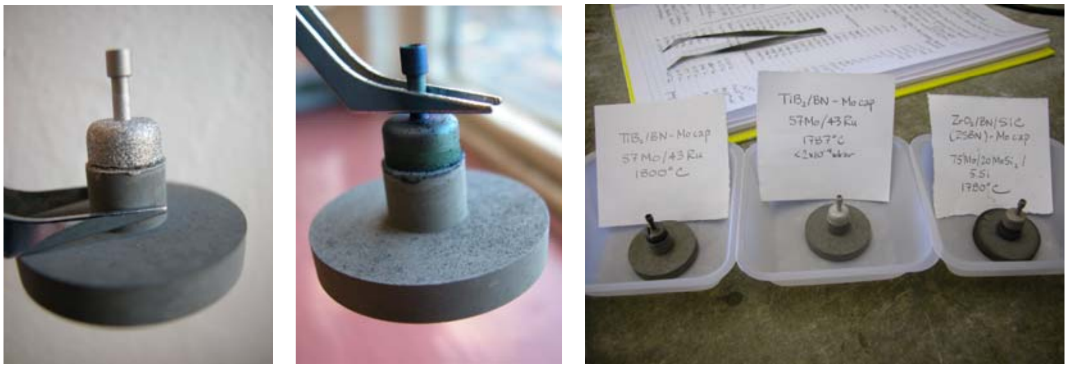

Braze test specimen, Mo/Ru filler, Mo cap, IMC post. Pressure < 10^{-4} mbar.

Braze test specimen, Mo/Ru filler, Mo cap, IMC post. Pressure = 1-2 mbar.

Collection of three braze test specimens. At right: ZSBN specimen with Mo/$MoSi_2$/Si braze, which failed to bond.

Figure 6-9 Post-furnace treatment of several braze specimens, University of Manchester.

Vacuum and low pressure brazing trials were conducted at the University of Manchester in March 2003. Both furnaces used in this test series were water-cooled and graphite-lined, with evidence of prior contaminants present in the lining (Figure 6-8, right). Pure powder samples of molybdenum, ruthenium, $MoSi_2$, and silicon were procured and mixed with a glycerin/water binder for ease of application to the cap and post specimens (Figure 6-8, left). The glycerin/water binder rapidly evaporates upon heating. Prior to application, the Mo/Ru mixture's constituents were weighed on a precision balance to ensure the eutectic composition (57 wt. % Mo, 43 wt. % Ru) [Massalski, 1986]. The Mo (75 wt. %)/$MoSi_2$(20)/Si (5) sample was similarly prepared. To prevent contamination, handling of the cap and post materials was performed only with gloves. The first test article, a cap/ZSBN post specimen with Mo/$MoSi_2$/Si braze filler, was placed in a graphite furnace, the furnace sealed, and the pressure lowered to 10^{-4} mbar (absolute). The specimen was then heated to 1,779 °C (2,052 K) over a period of 4 ½ hours. The specimen was then allowed to cool overnight. After re-examination of the cap/post the following morning, it was found that the Mo/$MoSi_2$/Si filler had not wet the molybdenum cap and no bond was achieved. However, the ZSBN post showed visible cracks and emerged coated with an ash-coloured deposit.

The second test article, a cap/IMC post specimen with Mo/Ru filler, was placed in a second furnace with a single-stage rotary pump and thus only a limited vacuum capability (0.1 mbar). Following a two-hour heating regimen and subsequent cooldown, this article was removed and a very weak bond found to have been formed. This bond was achieved at 2,078 K at fluctuating pressure levels of 1-2 mbar, with clear evidence of purple, blue, and green discoloration, implying oxidation of the molybdenum due to high oxygen partial pressures (Figure 6-9, middle). An attempt to section the specimen and assess the quality of the bond was unsuccessful; the cap separated from the ceramic post soon after the diamond saw was applied to the cap.

The third test article, identical to the second, was tested in the vacuum furnace at a maximum pressure of 2×10^{-4} mbar (absolute). This final trial achieved a relatively strong bond (Figure 6-9, left).[143] Peak furnace temperature attained during this last test was 2,060 K, short of the Mo/Ru eutectic by several hundred degrees. The braze filler material was nevertheless seen to clearly wet the metal cap but refused to flow freely over the ceramic. This specimen was later tested at the Surrey Space Centre for hermeticity. The cap was sealed to a section of silicone tubing with cyanoacrylate glue and pressurized to 2 bar with nitrogen. Liquid soap was applied to the interface between cap and post and clearly indicated leakage through the brazed seam. While the level of leakage was not quantified at this time, this braze trial failed to achieve the desired hermetic seal needed for a flight-type solar receiver.

Further testing at the University of Manchester was suspended, owing to the lack of high-temperature capability achievable with the two furnaces available. The author later conducted several brazing trials with MAST Carbon of Guildford, to determine if higher temperatures might provide a more consistent, hermetic bond.

---

[143] Vacuum furnace temperatures higher than 1,780 ºC (2,052 K) were unobtainable at the University of Manchester, owing to limitations on the furnaces' power supply.

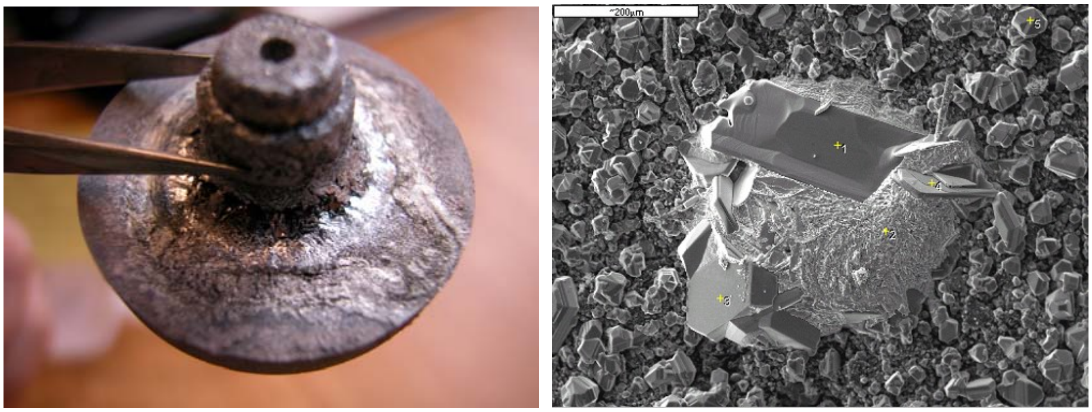

Figure 6-10 MAST Carbon's bonding attempt at 2,320 K melts molybdenum cap.

The first attempt to improve the seal quality of the Mo/Ru bond utilised temperatures approaching the braze filler liquidus of 2,320 K. The author provided two cap/post specimens and applied braze filler and binder using materials prepared at the University of Manchester for the previous test series. MAST Carbon then heated these specimens separately (Mo/MoSi$_2$/Si braze with ZSBN post, Mo/Ru braze with IMC post) to 2,000 ºC (2,273 K) in 50 minutes, in a low-pressure furnace (He purge at < 20 mbar (absolute) pressure). This effort proved unsuccessful, owing to the unexpected destruction of the Mo cap in both instances, over 500 degrees below the accepted melting point of molybdenum (Figure 6-10, left). Both caps appear to have melted and flowed down the sides of the ceramic post, collecting around the base. Energy-dispersive X-ray Scanning electron microscopy (EDX/SEM),[144] conducted by the University of Surrey's Chemistry Department, provided photos such as that shown in Figure 6-10 (right). Silicon crystals—presumably from the Mo/MoSi$_2$/Si filler, are identified by the EDX technique here, embedded in a molybdenum "splatter" found on the graphite oven cap used for the brazing test. Traces of other impurities (e.g., vanadium, carbon) were also detected but not in sufficient quantities necessary to lower the melting point of the molybdenum cap [Massalski, 1986]. The caps were also tested and their purity confirmed through SEM analysis. The author conferred with various experts on possible causes of the premature melt—to include melting point suppression by elemental boron migration, infiltration of molybdenum grain boundaries by titanium, undetected temperature excursions, and the potential inclusion of impurities in the cap material itself—but no conclusion could be drawn until a pristine cap was tested alone [Derby, 2003][Baker, 2003][Yeomans, 2003].

---

[144] Energy-dispersive X-ray analysis relies on electron bombardment of the target specimen (e.g., by a scanning electron microscope). The energy of X rays emitted from the specimen provide elemental composition information [Ritchie, 2003].

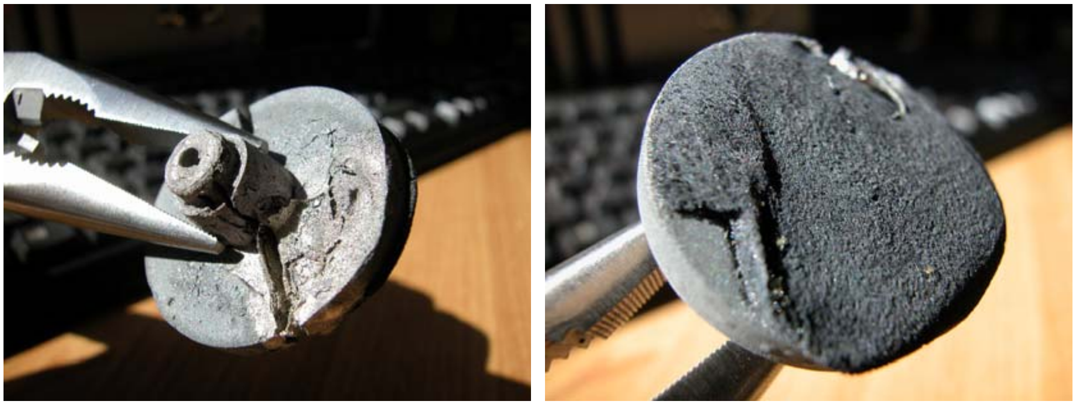

Figure 6-11 ZSBN ceramic post with Mo cap and Mo/$MoSi_2$/Si braze filler material. Graphite felt has bonded to bottom of ceramic post (right).

No braze or ceramic was present in the final test. A molybdenum cap was placed inside a graphite oven in the MAST Carbon low-pressure furnace. The cap rested on a pad of graphite felt, similar to that shown in Figure 6-11, at right. MAST ramped the cap to 2,320 K over 60 minutes. As in previous tests, a helium purge was used to prevent oxidation of the sample. Following removal from the furnace, the cap showed some evidence of melting, albeit only along the interface between the molybdenum cap and the graphite felt base the cap rested on. This tends to validate the thesis that impurity migration (i.e., contaminants present in the carbon felt from previous test runs) may be responsible for the local melting observed. Further brazing trials were not conducted, although there is evident promise in the Mo/Ru braze. Successful application will require a rigorous, long-term programme of investigation beyond the scope of the current research.

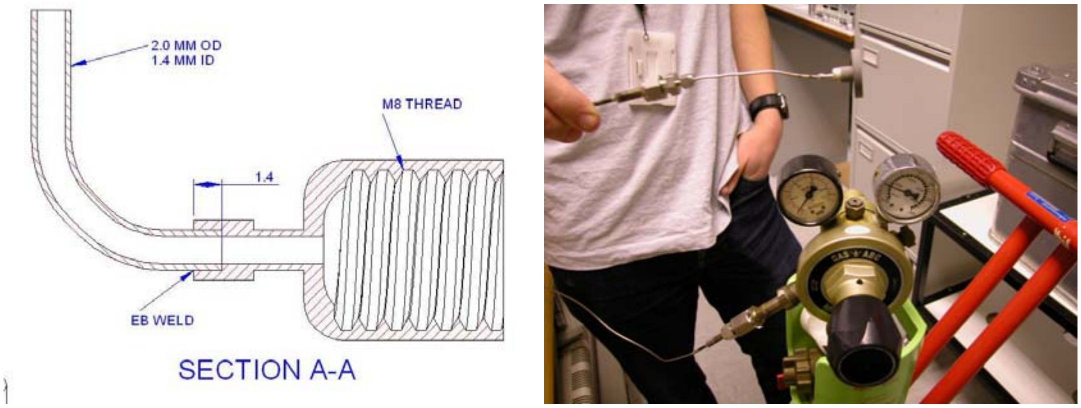

Figure 6-12 Screw-fit molybdenum cap and qualitative leak testing.

A selection of ceramic adhesives was purchased from a UK ceramic materials distributor, Pi-Kem, during the summer of 2003, including a proprietary two-element adhesive, “Ceramabond 552,” produced by Aremco, Inc. [Aremco, 2003] This adhesive is high-temperature capable (to

1,650 ºC or 1,923 K) and can be used for both ceramic-to-ceramic and ceramic-to-metal bonding. The adhesive paste was applied to an IMC element identical to those used in the Manchester and MAST Carbon trials with one exception: the post was fabricated with an internal thread (standard M8) to allow for mechanical as well as adhesive and/or braze sealing. A screw-fit molybdenum cap (Figure 6-12, left) was attached to the post and the assembly cured in at 100 ºC and 260 ºC for two hours at each temperature plateau, then removed and cooled to room temperature overnight. The next day, a silicone gas line was attached to the distal end of the molybdenum cap and pressures of up to 15 bar (N_2, gauge) applied (Figure 6-12, right). Unfortunately, the ceramic adhesive did not provide a hermetic seal even under ambient conditions; painting the interface with liquid soap revealed significant leakage. Immersing the assembly in water, and collecting the released nitrogen gas, permitted a leak rate to be estimated; in this instance, the leak rate over a six-minute immersion test was determined to be 0.444 ml/s or 0.00054 g/s of nitrogen (10 bar). While small in comparison with predicted Mk. I and Mk. II receiver flow rates (0.3 g/s), it is possible that the interface will degrade (a) over time, or (b) at higher temperatures and over successive thermal cycles, owing to erosive effects in the leak region.

A second screwfit cap and post assembly was constructed and sealed using a 0.5 mm thick gasket of high-purity graphite foil acquired from UCAR, Ltd., of Sheffield, Yorkshire, UK. The base of the threaded cap compresses the foil and provides a near-leakproof seal. An example of such a seal can be seen in Figure 6-13. In a manner nearly identical to that used for the adhesive-bonded cap/post hermeticity test, this cap/post was immersed in water and tested at pressures of up to 14 bar (compressed air, gauge). A leak rate test was conducted at 10 bar, over a thirty-minute period. The leak rate for this sealing methodology was determined to be much less than that for the adhesive-bonded cap, .0806 ml/s or 0.000098 g/s. This equates to a leakage rate of just three parts in ten thousand, assuming a flow rate of 0.3 g/s.

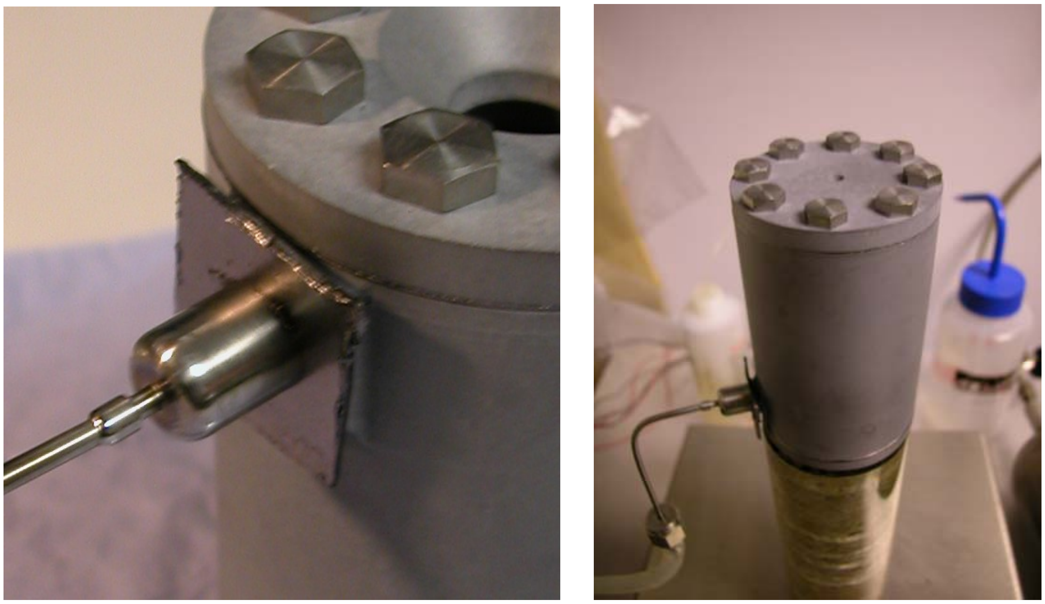

Figure 6-13 Mechanical feedline bonding with screwfit caps and graphite foil gaskets (Mk. II receiver).

The mechanical bonding approach clearly demonstrated hermetic performance superior to either the brazed or the adhesive-bonded fitting. Additionally, mechanical bonding permits disassembly and reconstruction; neither brazing nor adhesive bonding allows for anything but destructive disassembly.

Prior to full flow testing with the Mk. I and Mk. II receivers in December 2003, a final set of checks was performed on the Mk. II receiver to validate its mechanical bonding scheme. The Mk. I receiver bodies were delivered with bare feedline posts—unlike the Mk. II, no M8 thread had been cut into the Mk. I's posts (see Figure 6-14, left).[145] Its nozzle section sealed, the Mk. II receiver was fixed to a silicone gas supply line and placed inside a steel-walled chamber used for low-pressure testing. N_2 gas pressures of up to 20 bar (gauge) were applied to the receiver with no evidence of mechanical failure, although clear evidence of leakage was seen above 15 bar (using liquid soap for leak detection). As the receiver material is very hygroscopic, it was deemed unadvisable to perform an immersion leak rate test, as the inclusion of water in the matrix might damage the receiver structure during outgassing and make it unusable for future high temperature flow testing.

---

[145] At the time of the Mk. I's fabrication, the selected feedline bonding approach (brazed fitting) was still thought to be achievable without significant additional research. Hence, it was delivered with a bare post for braze application.

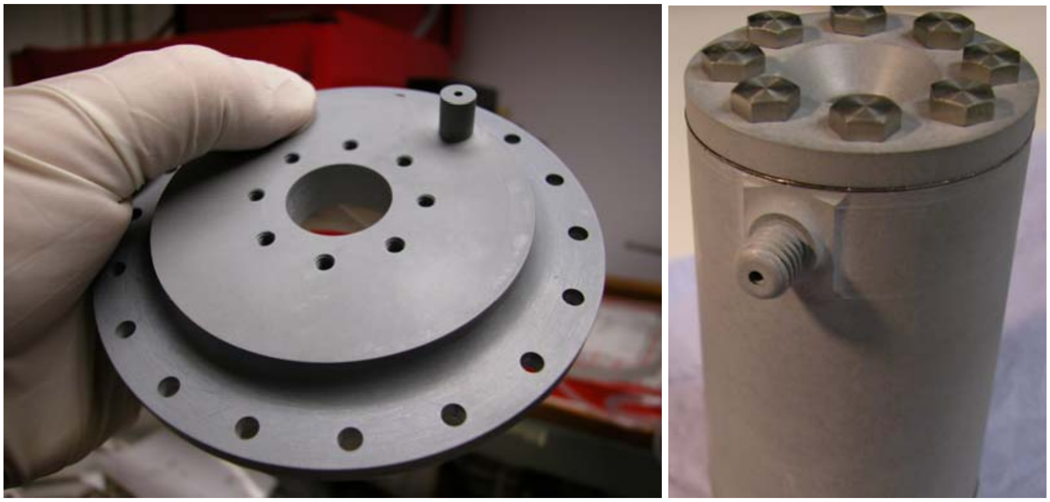

Figure 6-14 Feedline post detail, Mk. I and Mk. II receivers.

The Mk. II receiver's nozzle was then unsealed and placed upside-down on a precision balance (Figure 6-13, right), accurate to ±0.1 g. Pressures of 1, 2, 3, 4, and 5 bar (N_2, gauge) were applied and weight measurements taken at each pressure plateau. Theoretically, any weight increase will be directly attributable to gas departure through the nozzle, and concomitant downward thrust. Close agreement between predicted and measured thrust figures should, in principle, provide a level of confidence that the receiver is reasonably leakproof. Derived thrust measurements and approximate flow rates are shown in Table 6-2. Mass flow rate is first estimated from the well-known relation for characteristic velocity, or c^* [Hill, 1992]:

$$\dot{m} = \frac{P_c A_t}{c^*}$$

Pressure loss in the receiver flow path is neglected for this analysis; the chamber pressure P_c is assumed to be equivalent (or nearly so) to the supply pressure. The throat area A_t is known. Characteristic velocity is a function only of chamber conditions, which, for nitrogen gas at ambient temperature, is calculable via [Hill, 1992]:

$$c^* = \sqrt{\frac{1}{\gamma}\left(\frac{\gamma+1}{2}\right)^{\frac{\gamma+1}{\gamma-1}}\left(\frac{RT_c}{M}\right)}$$

For nitrogen gas at 20 ºC (293 K), $\gamma = 1.4$ and $M = 28$. N_2's c^* is therefore 429 m/s. Then, for a given pressure, an ideal mass flow rate for this receiver configuration can be determined.

Pressure (bar, gauge)	Weight during firing – Quiescent weight (g)	Thrust (mN)	Estimated characteristic velocity (c^*, m/s)	Predicted mass flow rate (g/s)	Predicted thrust (mN), $C_f = 1.0$	Actual/ predicted thrust
1.0	**1.1 ± 0.1**	**10.8 ± 1.0**	**429**	**0.18**	**77.2**	**0.14**

2.0	**3.8**	**37.2**	**429**	**0.27**	**115.8**	**0.32**
3.0	**8.9**	**87.2**	**429**	**0.36**	**154.4**	**0.56**
4.0	**13.6**	**133.3**	**429**	**0.45**	**193.1**	**0.69**
5.0	**18.9**	**185.2**	**429**	**0.54**	**231.7**	**0.80**

Table 6-2 Mk. II receiver mass flow rate check.

Since thrust is simply the product of mass flow rate, characteristic velocity, and the coefficient of thrust (C_f), a predicted thrust value can be calculated and compared to the actual data. C_f is assumed here to be equal to 1, the nominal value for an orifice with no divergent section. Typical values for vacuum thrust coefficient, in nozzles with substantial divergent sections, can range as high as 1.8-2.0 (i.e, isentropic expansion of the effluent gas roughly doubles thrust).

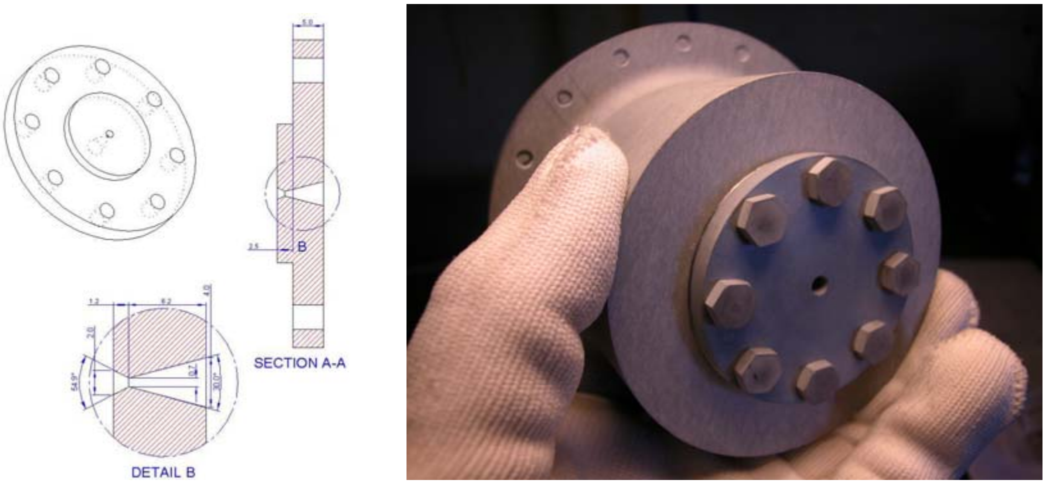

Figure 6-15 Nozzle section, Mk. I and Mk. II receivers.

For the test data in question, it can be seen that, for low supply pressures, the ratio of actual to predicted thrust is very low. This is not entirely surprising: for a sharp-edged orifice, a vena contracta (or "aerodynamic throat") forms downstream of the physical throat, due to the inability of the flow to follow the throat's curvature (Figure 6-15, left).[146] This implies a smaller effective throat area and a lower mass flow rate (and lower thrust). As the pressure differential becomes more favourable, the vena contracta migrates backwards up the nozzle towards the throat; in the limit, the vena contracta area asymptotically approaches the area of the physical throat. Zucrow [1976] notes that this phenomena gives rise to a delayed onset in choked flow; normally, in air (or in N_2), an ambient-to-chamber pressure differential of 1.89 is sufficient to choke the flow in the nozzle and allow for transition to supersonic flow within its divergent section. In experiments performed by Thornock and Brown [1972], pressure differentials of 4.0 or more are required to achieve "truly choked" flow. However, a reduction in throat area cannot completely account for the discrepancies seen in the measured thrust data.

---

[146] For sharp-edged orifices, the curvature is infinite at the throat. Thus, a vena contracta must form.

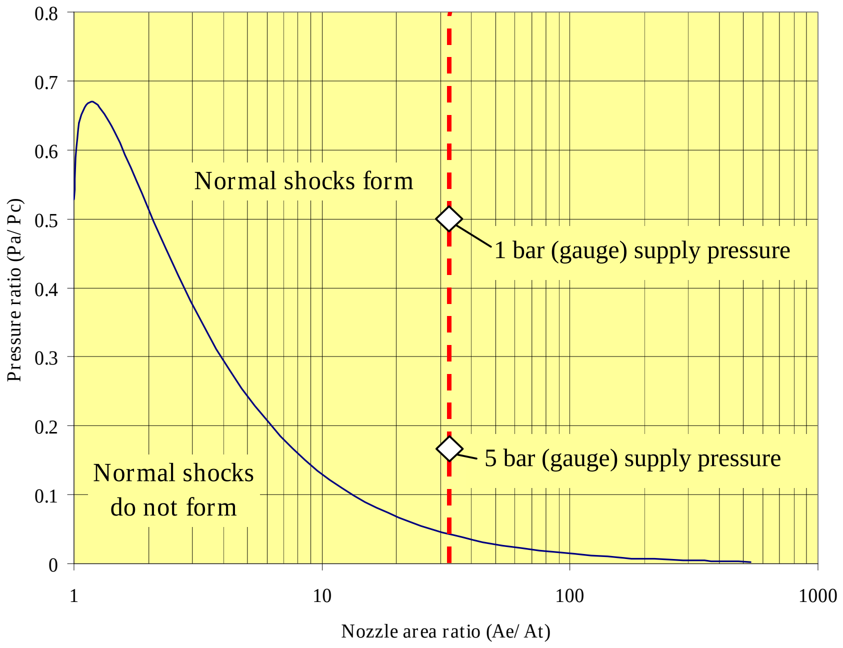

Figure 6-16 Normal shock formation in overexpanded nozzles. Dotted red line represents A_e/A_t = 33.

A further reduction in thrust (but not *c**) can arise as a result of the high back pressure at the nozzle exit plane. For both the Mk. I and Mk. II receivers, the nozzle was designed with a 15° divergent conical section and an area ratio of 33.[147] The isentropic flow relation for nozzle area ratio is a function of the specific heat ratio γ and the exit Mach number [Hill, 1992]:

$$\frac{A_e}{A_t} = \frac{1}{M_e}\left[\frac{2}{\gamma+1}\left(1+\frac{\gamma-1}{2}M_e^2\right)\right]^{\frac{\gamma+1}{\gamma-1}}$$

In the ideal case for nitrogen, with no flow separation, the exit Mach number can be found to be approximately 5.35. The pressure ratio for this Mach number can then be calculated:

$$\frac{P_c}{P_e} = \left(1+\frac{\gamma-1}{2}M_e^2\right)^{\frac{\gamma}{\gamma-1}}$$

For normal shock formation,

$$\frac{P_a}{P_e} = \frac{2\gamma}{\gamma+1}M_e^2 - \frac{\gamma-1}{\gamma+1}$$

---

[147] The Mk. I graphite foam nozzle extension raises the effective area ratio of the nozzle still further, to 375.

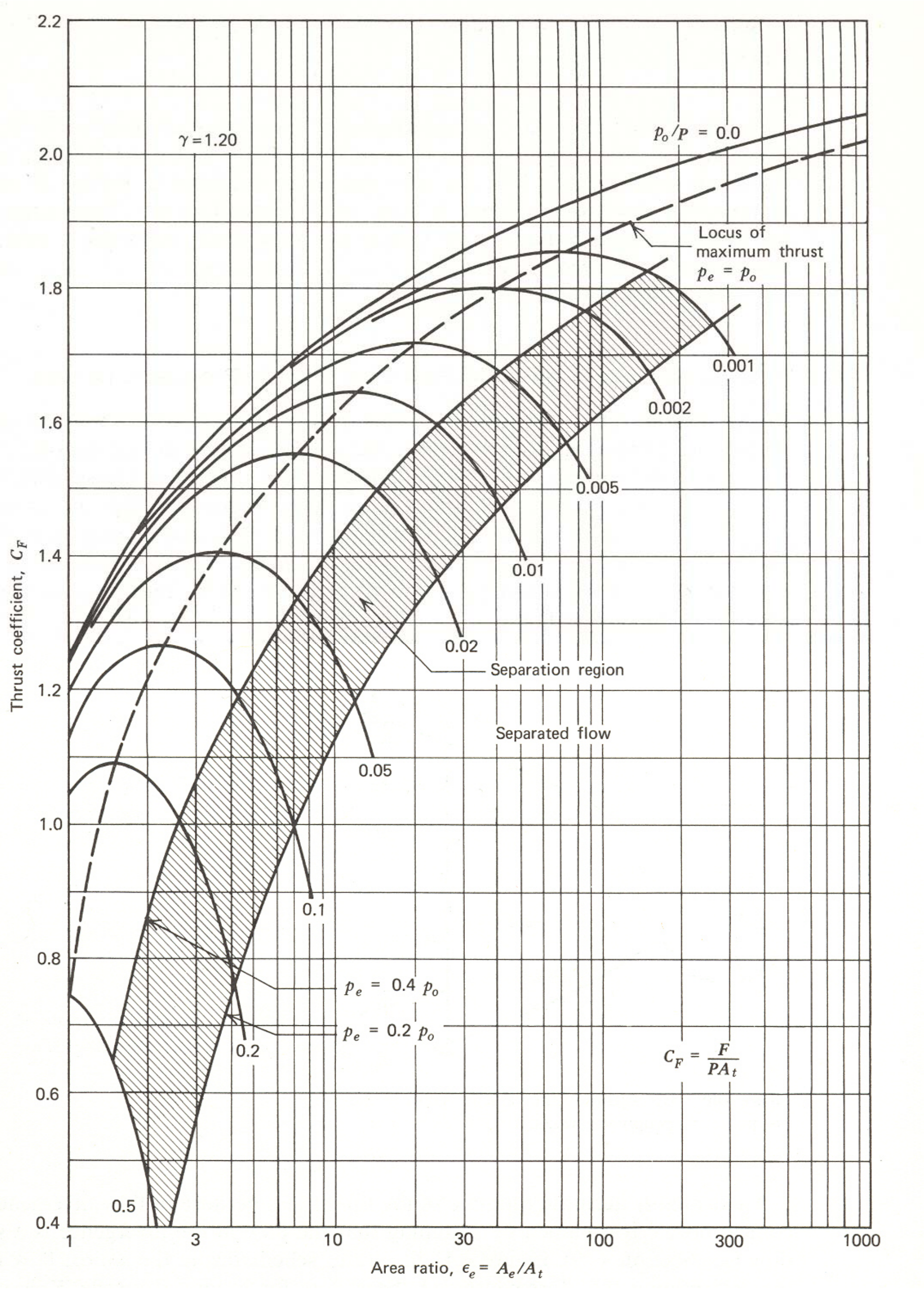

Figure 6-17 Coefficient of thrust as a function of nozzle area ratio, indicating flow separation regime (γ = 1.2) [Zucrow, 1976].

Combining these two relations allows one to determine the highest pressure ratio P_a/P_c for which normal shocks will not form within the nozzle (i.e., the shock forms at the exit plane). For the area ratio = 33 case, P_a/P_c = .045; therefore, to avoid normal shock formation inside the nozzle when exhausting to ambient pressure (1 bar absolute), the chamber pressure must be in excess of 22 bar (Figure 6-16). As these tests were conducted well below this threshold, normal shocks appear very likely to form, potentially deep inside the nozzle. Figure 6-17 confirms that this first flow test was conducted far below the separation regime, and low (< 1) thrust coefficients are to be expected.[148] At more favourable pressure gradients, normal shocks gradually migrate toward the nozzle exit plane. Nevertheless, flow separation and oblique shocks may be present, with complex internal structure [Hill, 1992]. This makes the intended determination of receiver seal efficacy highly problematic. From this analysis, it is not possible to discover whether the receiver is or is not leaking, or to what extent; the thrust discrepancies seen are plausibly the result of unfavourable pressure gradients, flow separation, and normal/oblique shock formation.[149] Thus, this test can only be properly performed in atmosphere at high chamber pressures or, alternatively, under vacuum conditions: in either case, the pressure gradient will be highly favourable. Zucrow [1976] offers:

> "The exact separation point, as well as the thrust developed after separation occurs, can be determined only by experiment."

Although this method met with little success when applied to flow measurement and seal validation, this problem lays theoretical groundwork for similar discrepancies encountered during the hot firing tests. This issue will thus be examined in further detail when the problem of thrust and mass flow measurement is discussed in Section 6.2.3.

6.2.2 Receiver Cavity Heating Profile and Survivability Tests

The two receivers discussed in Chapter 5, the Mk. I and Mk. II, were developed with somewhat different objectives in mind. The Mk. I, which masses nearly 1.5 kg, was intended to maximise gas-body heat transfer through the use of a packed bed of ceramic particles. Modelling indicated that the use of the packed bed would provide for substantially higher gas exit temperatures. The Mk. II receiver, at less than 1 kg, was constructed to maximise body temperature and provide data on high-temperature survivability and potential failure modes. The machined spiral flow path, as demonstrated, is not capable of matching the Mk. I's heat transfer performance. Resistive heating, rather than direct solar insolation, laser heating, or induction heating, was selected as the simplest approach for achieving test aims under vacuum conditions. While power leads must be routed through a feedthrough in the vacuum chamber, this is not especially difficult. Dissipation of an appropriate amount of heat, inside the receiver cavity, becomes the principal difficulty, due to the high energy densities being simulated.[150] Direct insolation requires sunlight to be optically routed inside the vacuum chamber, either via optical fibre (part of the experimental research undertaken in this programme) or an assembly of collimating mirrors.[151] Laser heating would require the acquisition of a high-power (kilowatt-class) laser source, and would still require optical routing to allow the laser light to heat a target inside the vacuum chamber. While these alternatives were briefly investigated, they were quickly seen to be high-cost approaches with significant performance risk and without any distinct advantages.

---

[148] This figure is valid for $\gamma = 1.2$, while, as noted above, nitrogen's value at 293 K is 1.4. Plotting this figure at $\gamma = 1.4$ has the effect of depressing the curves slightly downward, such that the maximum obtainable thrust coefficient is reduced. The flow test under consideration is still well below the separation regime.

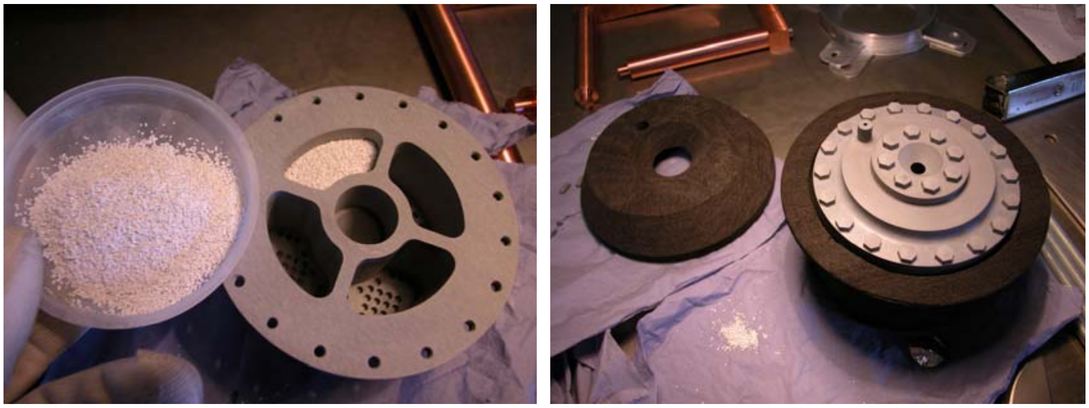

Figure 6-18 Packed bed preparation and assembly of Mk. I solar receiver for heating tests.

The first tests of the insulated solar receiver concentrated on the validation of WinTherm, CHUPS, and MSTISM modelling results for the thermal charging phase. All of the 25 profiling tests were conducted at the ARC UK Westcott E Site in Oxfordshire, UK. Although E Site contains a firing bay, flow measurement and data recording devices, none of these were required for the initial heating tests. The standalone test rig includes (a) a 30-cm diameter high vacuum chamber with multiple ports and feedthroughs (including a quartz window for viewing and optical temperature measurement), (b) a single-stage rotary pump, (c) an oil diffusion pump, (d) a dual-phenomenology wide-range pressure gauge capable of measurements between atmospheric and 10^{-9} mbar, (d) three C-type (tungsten-rhenium) thermocouples with a peak temperature capability of 2,320 ºC (2,593 K), (e) a variable (60 V/50 A maximum) power supply, and (f) a handheld infrared thermometer (for surface temperature measurements above 600 ºC).

Prior to testing, the Mk. I receiver was assembled, its bed cavities filled with boron nitride particles, foil seals and ceramic bolts installed, and placed in its insulation package (Figure 6-18).

---

[149] Coxhill [2004] notes that, although his engines were test-fired in ambient air, chamber pressures would typically rise to 20 bar. Thus, it is highly unlikely that he would have encountered the discrepancies seen here.
[150] On the order of 600 W/cm^3. For comparison, Pueschner [1999] describes a microwave heater for research applications, “with typical…values” of power density, delivering 2.8 W/cm^3.

The receiver assembly was then suspended between two aluminium mounting rings and attached to the cavity heating rig (Figure 6-19). The heating rig is fitted with two large copper bus bars, insulated from the lower aluminium mounting plate by Macor® ceramic elements. Power leads are connected to screw fittings at the rear faces of the bus bars, near the edge of the mounting plate. For the initial series of heating tests, tungsten, tungsten-rhenium, molybdenum-rhenium, and molybdenum wire (<1.5 mm diameter) coils were mounted between the two copper electrodes and the coil inserted inside the IMC ceramic cavity aperture. Care was taken to ensure that the coil did not touch the IMC material, due to IMC's conductivity and the potential for coil-to-receiver body shorting and failure.

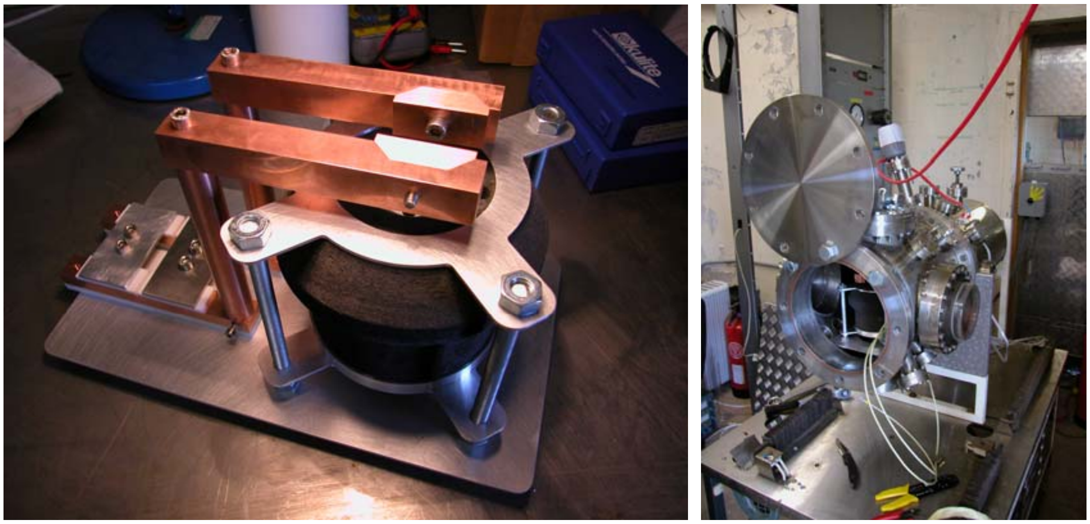

Figure 6-19 Mk. I receiver in cavity heating rig (left). Cavity heating rig installed in chamber (right).

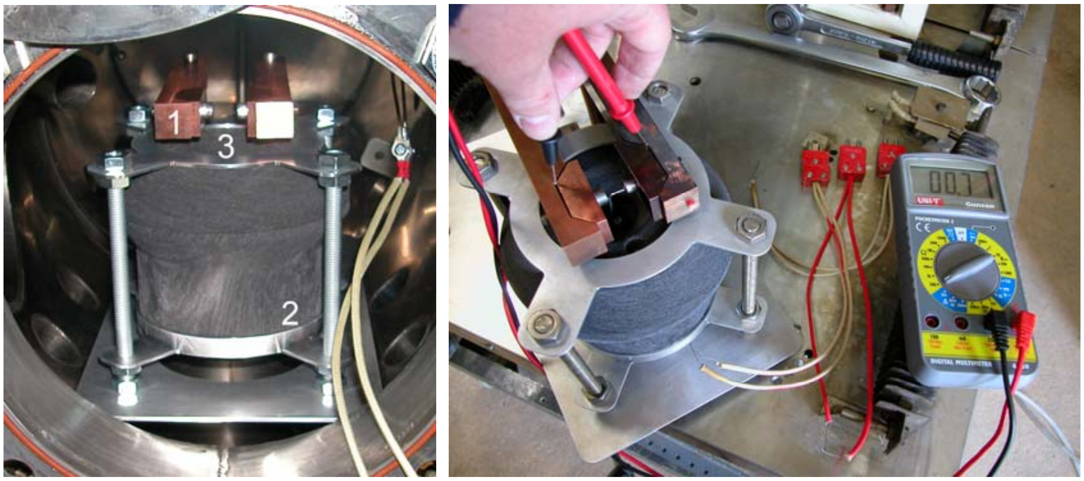

---

[151] Clearly, using ambient sunlight for ground testing severely limits the time available for testing, especially at high latitudes and in a region that typically experiences substantial inclement weather.

Figure 6-20 Thermocouple locations for Mk. I cavity heating profile tests (left). Resistance check on receiver heating element (right).

Once the cavity heating rig was assembled, it was placed on an aluminium mounting floor for insertion into the vacuum chamber. Power leads were connected to the bus bars. Bare thermocouples (sheathed in electrically insulated, high temperature silica fabric along most of their length) were placed at three locations (Figure 6-20, left): (1) at the end of one of the copper electrodes, directly over the cavity aperture; (2) at the interface of the insulation package and the bottom aluminium mounting ring; and (3) inserted in the feedline post on the top flange of the Mk. I receiver. Alignment of the heating coil was verified by a resistance check with a standard multimeter (Figure 6-20, right). Thermocouple transmitters mounted on the exterior of the vacuum chamber included two-line displays calibrated to the C-type thermocouple response curve (mV/ºC) [Dataforth, 2004]. Values were read directly from the displays and recorded. The wide-range pressure gauge was connected to a dial-type gauge display and values from this display recorded in the same manner.

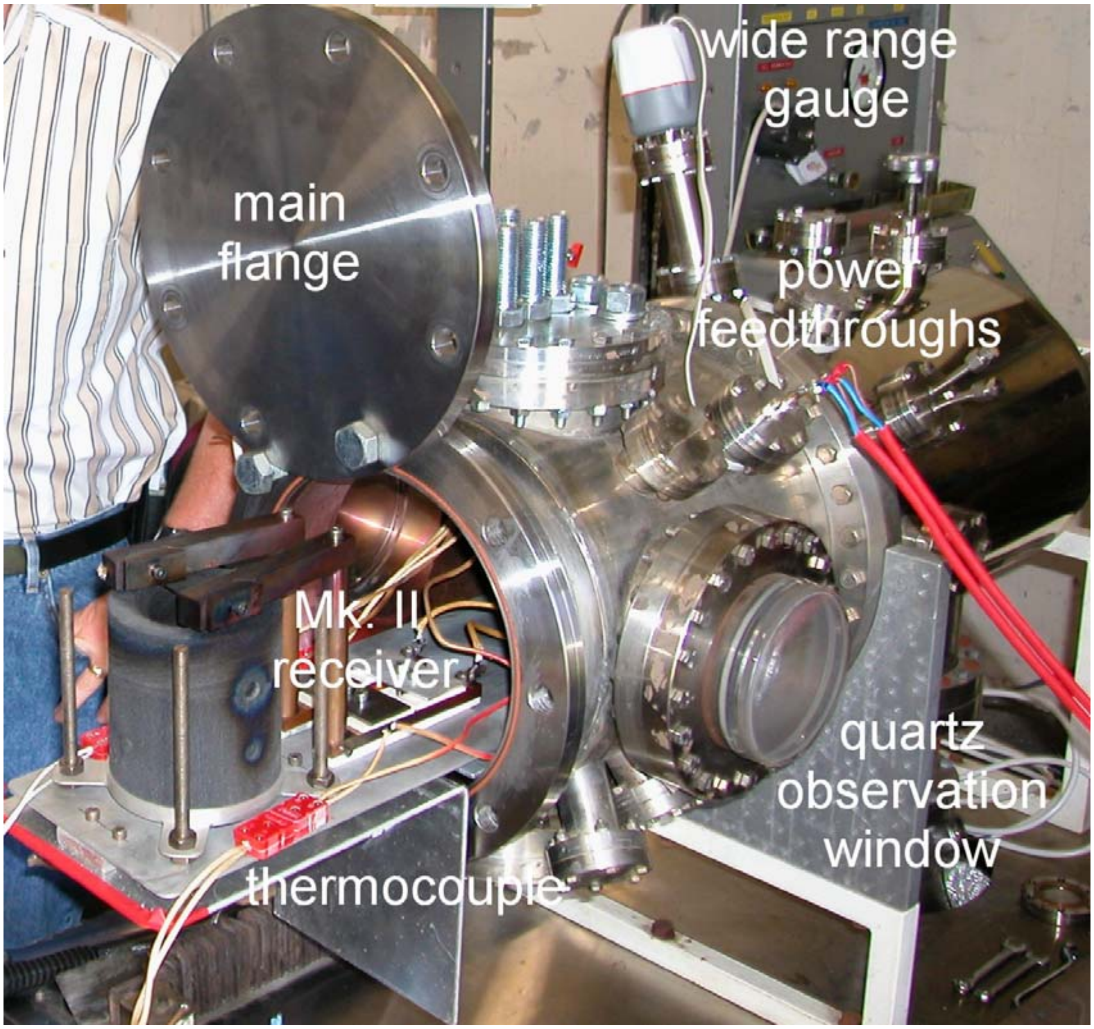

Figure 6-21 Vacuum heating test rig, Westcott E Site.

Unlike some high vacuum systems, the Westcott E Site vacuum chamber contained no roughing line for evacuation of the chamber bypassing the oil diffusion pump. The chamber was roughed through the oil diffusion pump, with care taken to ensure no backstreaming and contamination of the chamber could occur during pumpdown or venting. Therefore, the chamber was always vented to atmosphere before the oil diffusion pump, by means of a large isolation valve between the oil diffusion pump and main chamber. The cavity heating profile test procedure consisted of the following steps:

1. Placement of the instrumented cavity heating test rig in the vacuum chamber (Figure 6-21).
2. Powering on the thermocouple transmitters, wide-range gauge, and gauge display.
3. Verification of heating element resistance with multimeter followed by brief power throughput test. Power supply is turned on and set to 10V/10A for several seconds, then powered down.
4. Sealing of the vacuum chamber main flange.
5. Re-verification of power throughput in case of heating element shift during main flange sealing.
6. Closing the vent valve to the chamber and the foreline vent valve.
7. Opening the isolation valve above the oil diffusion pump.
8. Opening the foreline valve between the oil diffusion pump and the mechanical (rotary) pump.
9. Powering on the mechanical pump and waiting for chamber pressure to asymptotically approach 2 x 10^{-2} mbar (typically 15-20 minutes after startup).
10. Startup of the oil diffusion pump water cooling loop. Powering on the oil diffusion pump and waiting for chamber pressure to approach 1 x 10^{-4} mbar or less (typically 30 minutes).
11. Recording initial temperature readings from thermocouples (1), (2), and (3). Recording chamber pressure from wide-range gauge display.
12. Powering on the power supply and recording thermocouple, pressure, current, voltage, and infrared thermometer readings throughout the course of the test.
13. Powering down the power supply and continuing to record data through the cooldown phase. Once the receiver feedline temperature drops below 200 ºC, the chamber can be isolated from the diffusion pump and vented to atmosphere. The oil diffusion pump can be powered down and the chamber’s main flange removed for post-test inspection of the receiver.

The combination of rotary and oil diffusion pumps permitted pressures as low as 10^{-5} mbar to be attained after approximately 45 minutes, although receiver outgassing during thermal charging raised this significantly, occasionally as high as 5 x 10^{-2} mbar. No evidence of receiver or heating element lead oxidation was seen during the conduct of any of the tests. Several factors combined to complicate the process of resistively heating the solar receiver: (1) cavity volumetric constraints and small aperture diameter (8-11 mm); (2) IMC's natural conductivity, which requires the heating elements to be separated from the cavity walls; and (3) deterioration of heating element lead material in vacuum, through vaporisation, leading to element failure. Tests with bare metal coil elements generally failed rapidly, leading to an open-circuit condition and subsequent test shutdown. Various approaches at producing reliable, high-efficiency heating elements were attempted (Figure 6-22).[152] Practical problems included manual lead bending, which introduces stress concentrations, numerous failures during fabrication, and an increased likelihood of premature failure during test. Tungsten leads, while inexpensive to procure, were eventually discarded in favour of molybdenum and tantalum leads (1.5 mm diameter). Tungsten's brittleness made it extremely difficult to form coils or bends; molybdenum leads were far more ductile and less prone to failure.

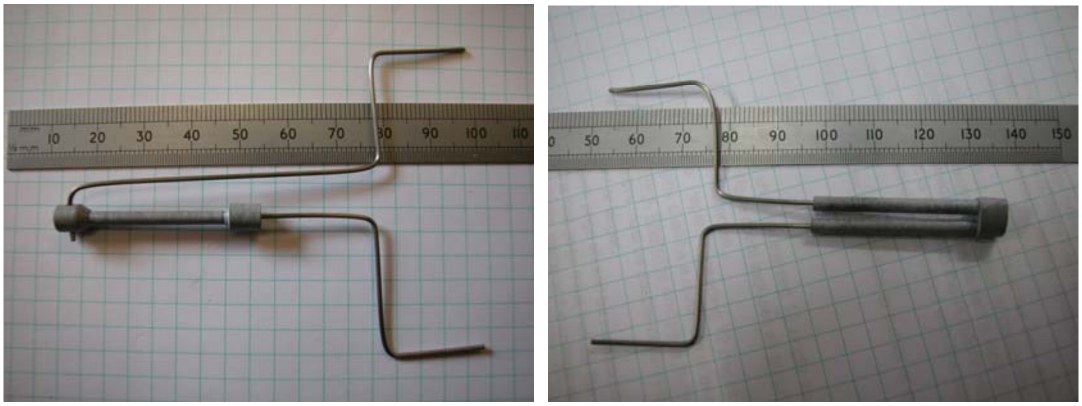

Figure 6-22 IMC heating element, tungsten leads (left). 2-path IMC heating element, 2nd version, tungsten leads (right).

A summary of profile test results can be found in Table 6-3. The Mk. I receiver, 1,131 g in mass, saw nine documented excursions in external cavity temperature above 1,000 K and, in its final heating test, reached 1,424 K. The Mk. II receiver body, roughly half the mass of the Mk. I (563 g), was heated seven times to temperatures above 1,500 K and, in the final test, reached 1,974 K. Example profile data is shown in Figure 6-23 and Figure 6-24.

The figures illustrate a critical problem with the heater element designs—primarily coils of refractory metals (e.g., Mo-Re, Mo, W-Re, and W)—used in early profile testing. There is evidence of substantial conductive loss to the copper electrodes, which were heated to 613 K in the first test and over 750 K in the second test. The MSTISM lumped-capacity model (Figure 6-24, red line) predicts that an input of approximately 600 W will produce the heatup profile seen in Test 2; thus, nearly 300 W of dissipated power were lost through conduction or radiation external to the cavity aperture.[153] The estimated heating efficiency (received power at the cavity divided by total power dissipated in the circuit) is only 0.67. This drove the quest for ever-higher power dissipation, in the attempt to produce high receiver temperatures, but which instead led to numerous, premature shutdowns. Much of the subsequent effort was undertaken with the objective of improving the efficiency of the heating elements by depositing the greater portion of generated heat inside the cavity, without degrading element reliability.

---

[152] No heating elements of the size and power throughput required could be procured commercially.

Test No.	Receiver Type	Heating Element	Peak feedline temp (ºC/K)	Peak penetration temp (IR) (ºC/K)	Power at peak penetration temp (W)	Time to reach peak temp (minutes)
1	Mk. I	Mo/Re coil	855 / 1,128	835 / 1,108	704	93
2	Mk. I	Mo/Re coil	987 / 1,250	950 / 1,223	872	102
3	Mk. I	Mo/Re coil	732 / 1,005	*	1,239	20
4	Mk. I	W/Re coil	*	*	**	--
5	Mk. I	W/Re coil	*	*	**	--
6	Mk. I	W coil	283 / 556	*	784	15
7	Mk. I	W coil	*	*	647	--
8	Mk. I	IMC/W lead	530 / 803	*	495	53
9	Mk. I	IMC 2-Path/W lead	604 / 877	610 / 883	669	101
10	Mk. I	IMC 2-Path/W lead	804 / 1,077	775 / 1,048	810	101
11	Mk. I	4-Path IMC/W lead	907 / 1,180	882 / 1,155	983	34
12	Mk. I	4-Path IMC/W lead	897 / 1,170	890 / 1,163	965	70
13	Mk. I	8-Path C/W lead	768 / 1,041	818 / 1,091	800	27
14	Mk. I	8-Path C/W lead	1,010 / 1,283	994 / 1,267	1,267	36
15	Mk. I	8-Path C/Mo lead	*	*	**	--
16	Mk. I	8-Path C/Mo lead	*	*	**	--
17	Mk. I	8-Path C/Mo lead	*	1,151/ 1,424	1,575	73
18	Mk. II	8-Path C/Mo lead	*	*	**	--
19	Mk. II	8-Path C/Mo lead	1,230 / 1,503	1,175 / 1,448	1,250	17
20	Mk. II	8-Path C/Mo lead	1,237 / 1,510	1,183 / 1,456	1,320	30
21	Mk. II	8-Path C 2/Ta lead	1,515 / 1,788	1,432 / 1,705	1,368	76
22	Mk. II	8-Path C 2/Ta lead	1,515 / 1,788	1,476 / 1,749	1,440	71
23	Mk. II	8-Path C 2/Ta lead	*	1,317 /1,590	1,680	39
24	Mk. II	8-Path C 2/Mo rod	1,346 / 1,619	1,537 / 1,810	1,360	39
25	Mk. II	8-Path C 2/Mo rod	1,404 / 1,677	1,701 / 1,974	1,429	93

*** = no data** **** = failure during power ramp**

Table 6-3 Summary of cavity heating profile tests (April – September 2003).

The author experimented with metal coils of various materials, lengths, and diameter, but none showed substantial promise. Several tests (8, 9, and 10) were conducted with a conductive IMC element attached to 1-mm diameter tungsten leads. These elements exhibited rapid resistivity decay with increasing temperature, which, following cooldown, was demonstrated to be irreversible. Despite these shortcomings, the multi-material (lead/resistive element) approach paved the way towards higher-efficiency designs made from graphite, which were found to be reusable over multiple tests, evincing no significant resistivity decay or mechanical damage.

---

[153] This data also verifies that MSTISM, which does not account for C_p variability with temperature, tends to underpredict cavity temperature at low temperatures, while overpredicting at high temperatures.

Test 10 (Figure 6-25), performed in April 2003, illustrates an attempt to achieve higher temperatures with multi-material heating elements. Over the course of this test, the resistivity of the IMC element decayed from 611 mΩ to 394 mΩ, requiring the test conductor to constantly adjust the voltage supply upward to maintain a constant power input. During the 85th minute, the power supply fuse open-circuited.[154] After replacing the fuse, the test was resumed at a higher power level (810 W) within two minutes, but a second blown fuse halted the test in the 101st minute.[155]

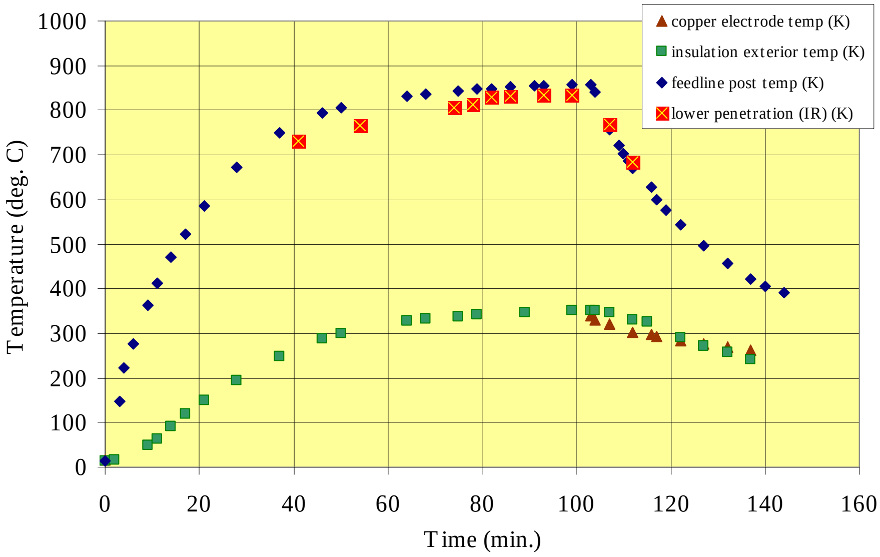

Figure 6-23 Test 1 Heating Profile (Mk. I receiver, peak external cavity temperature (PECT) = 1,128 K, peak power dissipation in circuit = 704 W). Test date: 14 April 2003.

---

[154] At fuse failure, the current supply registered over 40 amps (at 15.75 V).

[155] During the two-minute power supply outage, the temperature of the receiver dropped nearly 50 K.

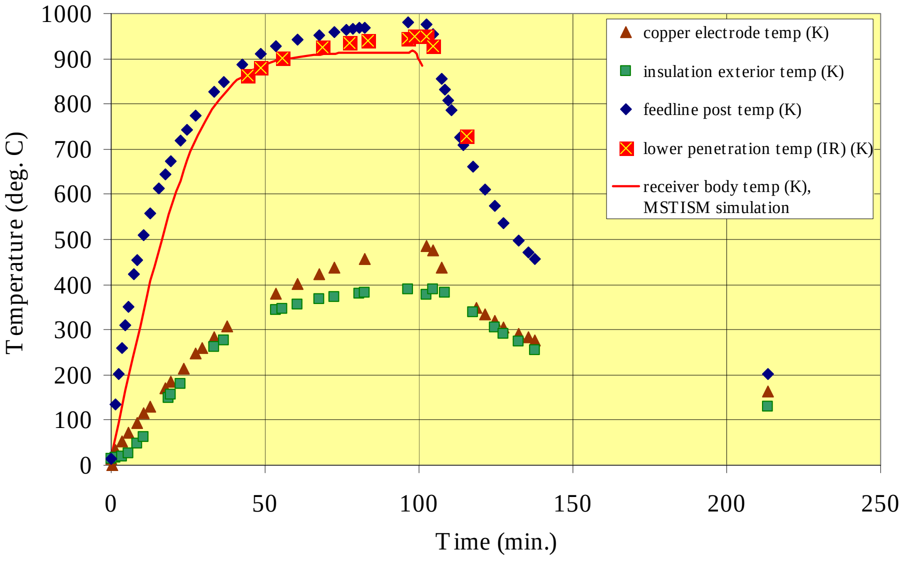

Figure 6-24 Test 2 Heating Profile (Mk. I receiver, PECT = 1,250 K, peak power dissipation in circuit = 872 W). Test date: 16 April 2003. MSTISM power = 595 W.

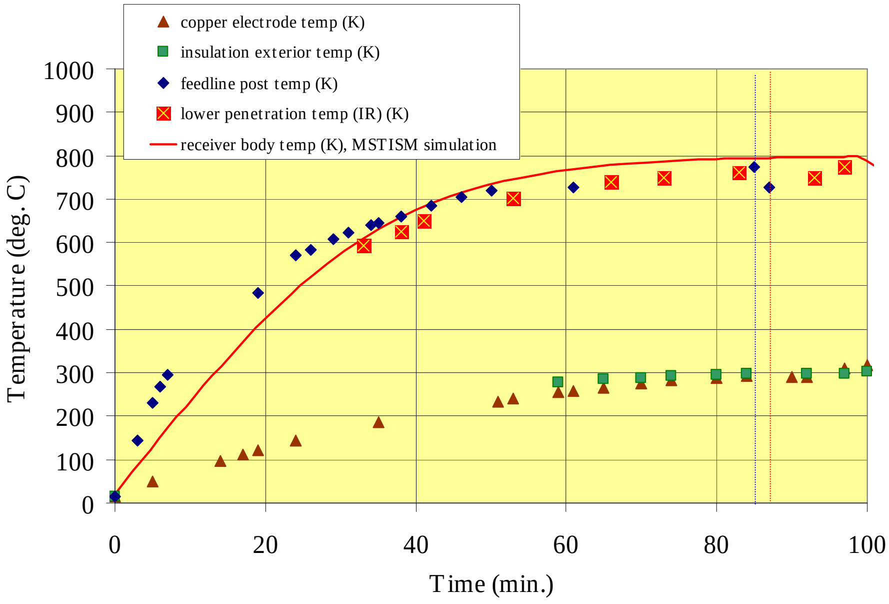

Figure 6-25 Test 10 Heating Profile (Mk. I receiver, PECT prior to first shutdown (85 minutes) = 1,047 K, peak power dissipation in circuit = 630 W; PECT following first shutdown = 1,077 K, peak power dissipation after first shutdown = 810 W). Test date: 13 May 2003. MSTISM power = 414 W. Dashed blue line: First shutdown (85 minutes). Dashed red line: Restart (87 minutes).

The MSTISM model revealed the efficiency of the IMC/tungsten lead heating element to be no better than the refractory metal coils, estimated at 414 W / 630 W, or 0.66. Further, these elements, as a result of their inherently low (and highly temperature-sensitive) resistivity, provided comparatively low power dissipation. The author investigated variants of the IMC element with an extended circuit path—respectively two and four times that of the original element—in an attempt to increase the element's total resistance and produce higher power dissipation inside the cavity aperture.[156]

The author finally abandoned IMC and turned to graphite, despite reservations regarding potential graphite contamination of the receiver surface during heating. The first of these elements, produced by Sintec-Keramik, demonstrated immediate promise; Test 14, conducted on 18 June 2003, produced the highest peak external cavity temperature (PECT) yet seen, at 1,283 K (Figure 6-27).[157] The heating element failed in the 36th minute (Figure 6-26, left), apparently due to a local "runaway" resistance increase and subsequent melting of the tungsten lead at the graphite element interface.[158] The MSTISM model for this test indicated that, were the element to have remained intact, the receiver would have reached 1,350 K by the 60th minute.

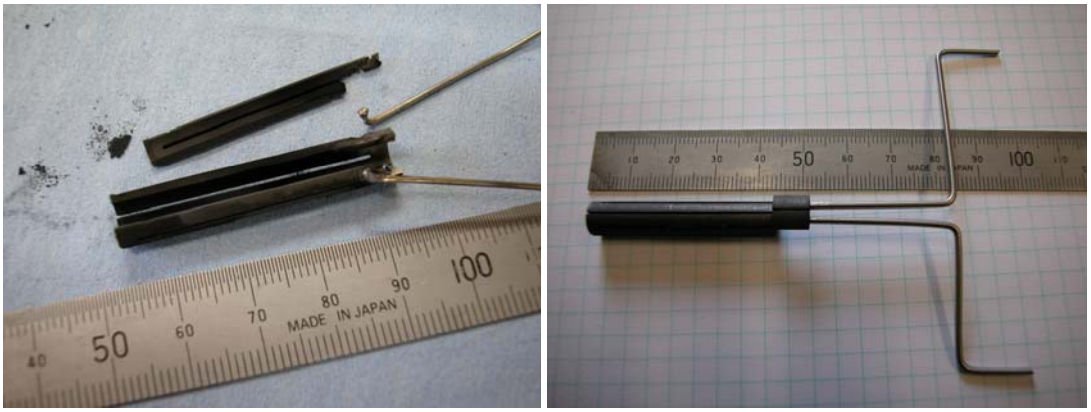

Figure 6-26 Eight-path graphite elements.

---

[156] These repeatedly suffered from brittle failure during assembly, and were difficult to fabricate.

[157] Peak power and heating efficiency (0.74) are also higher.

[158] The test conductor has repeatedly observed this sudden and rapid voltage rise followed by an open-circuit failure.

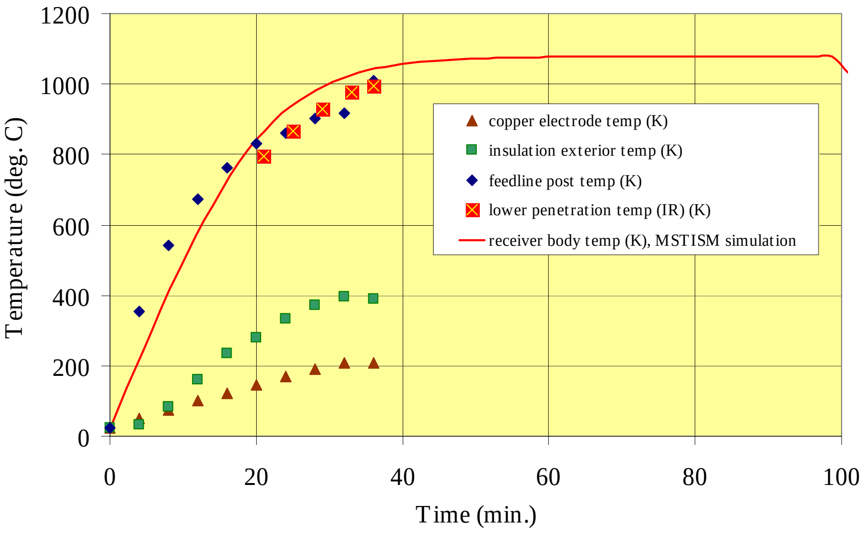

Figure 6-27 Test 14 Heating Profile (Mk. I receiver, PECT = 1,283 K, peak power dissipation in circuit = 1,267 W). Test date: 18 June 2003. MSTISM power = 939 W.

Preliminary bare element survival trials were conducted on 4-path glassy carbon heating elements, obtained from MAST Carbon, although none of these showed sufficient promise to use during receiver heating tests. Upon application of current, the element rapidly deformed and short-circuited, usually within two to three minutes. Given their poor performance and severe machining difficulty,[159] this avenue of investigation was halted and the effort focused on improving the reliability of Sintec's graphite elements.

The results of the final heating test conducted on the Mk. I cavity receiver, Test 17, are shown in Figure 6-28.[160] Thermocouple (T/C) 1, measuring the feedline post temperature (internal side), appears to begin fluctuating at about the 16th minute. The erratic response seen here is most likely the result of reuse and repeated contamination of the W/Re T/C bead with precipitated receiver materials (e.g., boric oxide). These materials are thought to diffuse through and embrittle the thermocouple, causing them to change composition, drift in voltage output, and eventually fracture [Levick, 2003]. At high temperatures (>1,500 K), most thermocouples were rendered unusable after a single test. While this problem could in theory be overcome with thermocouple sheathing such as molybdenum or tantalum, the sheath diameter is much larger than the thermocouples, demanding larger penetrations, higher radiative losses, and would therefore contribute to substantially greater conductive losses than the small-diameter thermocouple beads.

---

[159] The brittle, glassy nature of the carbon base material resulted in substantial breakage during machining.
[160] No external insulation thermocouple data was recorded for this test.

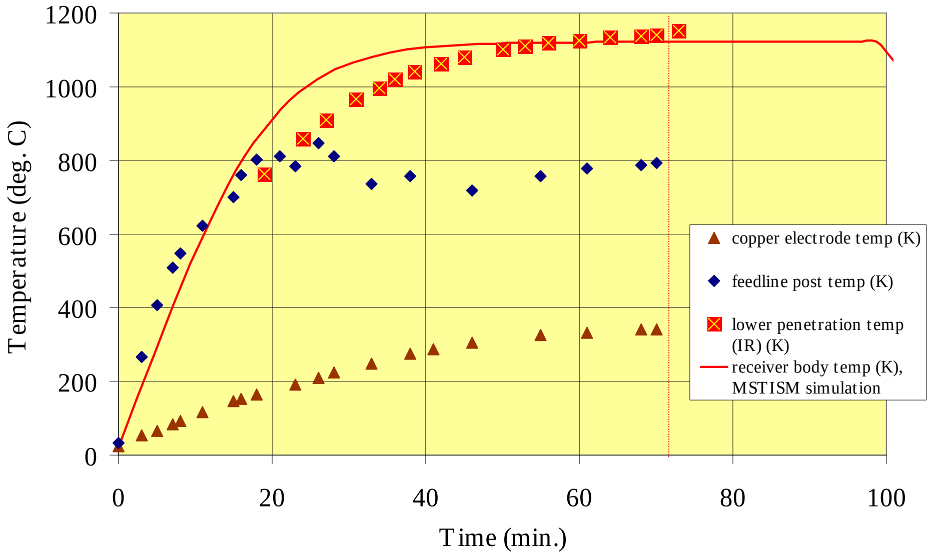

Figure 6-28 Test 17 Heating Profile (Mk. I receiver, PECT = 1,424 K, peak power dissipation before final ramp = 1,267 W; after ramp = 1,575 W). Test date: 27 June 2003. MSTISM power = 1,050 W.

Despite this instance of thermocouple failure, it was still possible to monitor the upward trend in external cavity temperature during this test, with the handheld infrared thermometer (Figure 6-29) shows penetrations in the receiver insulation package, allowing visual access to two points on the receiver surface).[161] Prior to the initial series of receiver heating tests, the infrared thermometer was calibrated against an IMC element instrumented with a thermocouple and heated to high temperature. IMC emissivity was measured at approximately 0.55; this setting was retained throughout subsequent tests.

---

[161] The apparent rate of temperature increase, as measured by the infrared thermometer, is slower than that seen by the thermocouple (or predicted by the MSTISM code). This is due to the positioning of the lower penetration, which exposes a section of receiver farther from the heating element than the feedline post.

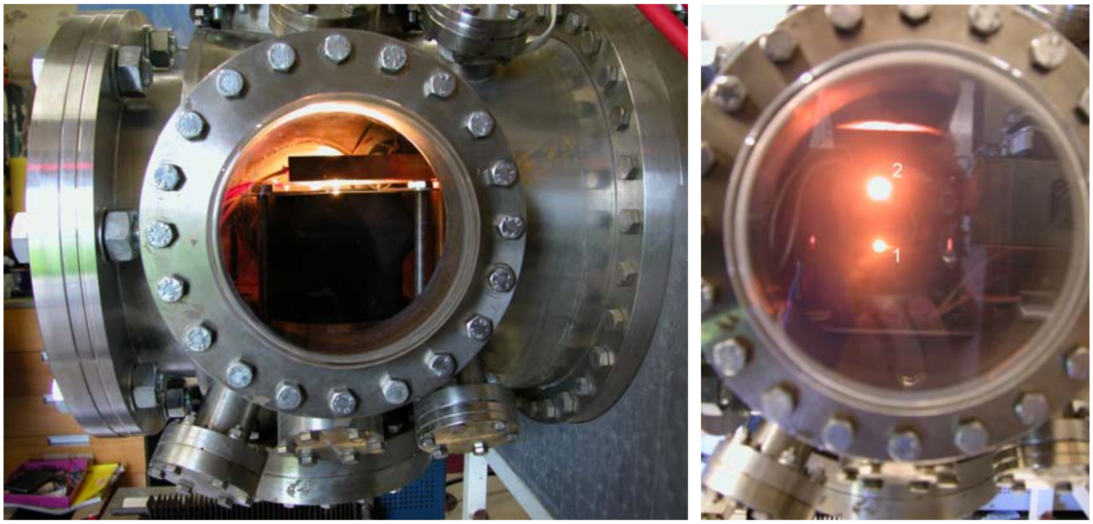

Figure 6-29 Mk. I cavity receiver undergoing heating test in vacuum (left). Mk. II cavity receiver in similar test, showing lower (1) and upper (2) penetrations (right).

Heating efficiency for this test was estimated at 1,050 W / 1,267 W, or 0.83. Note the disparity between the MSTISM model (which accurately tracks the temperature of the receiver in Figure 6-27) and the WinTherm shell simulation (Figure 6-29). The WinTherm model consistently overpredicts cavity temperatures for a given power dissipation; in this instance, WinTherm results suggest that a radiative input of just 325 W is sufficient to heat the Mk. I receiver to almost 1,100 C (1,373 K) in 100 minutes. WinTherm also implies that power input levels on the order of that applied in Test 17 (~1 kW) would raise the cavity temperature to nearly 2,000 K. This was not borne out by test results, and invalidates the WinTherm model as a predictive tool for "thick" non-shell structures (where there is substantial conductive coupling between radiative surfaces).[162]

The Mk. I receiver underwent observable changes during the heating profile test campaign. Most noticeable, following the first test, was the accumulation of flecks of black deposit on the external surfaces of the cavity receiver body. Over the course of testing, this gradually subsided, to be replaced by dark speckling (roughly 1 mm in diameter) over much of its top surface. Additionally, the colour of the structure, initially a uniform grey, became variegated: Near the cavity aperture, the structure became noticeably yellow-orange; the sides retained their initial dull grey appearance (Figure 6-31). No cracks, deformation, or mass loss occurred during the test series.

---

[162] See Section 5.2 for details. The author attempted to circumvent this shortcoming in WinTherm by constructing concentric shell (external and internal surface) models of the receiver, with conductively-coupled fins connecting the two.

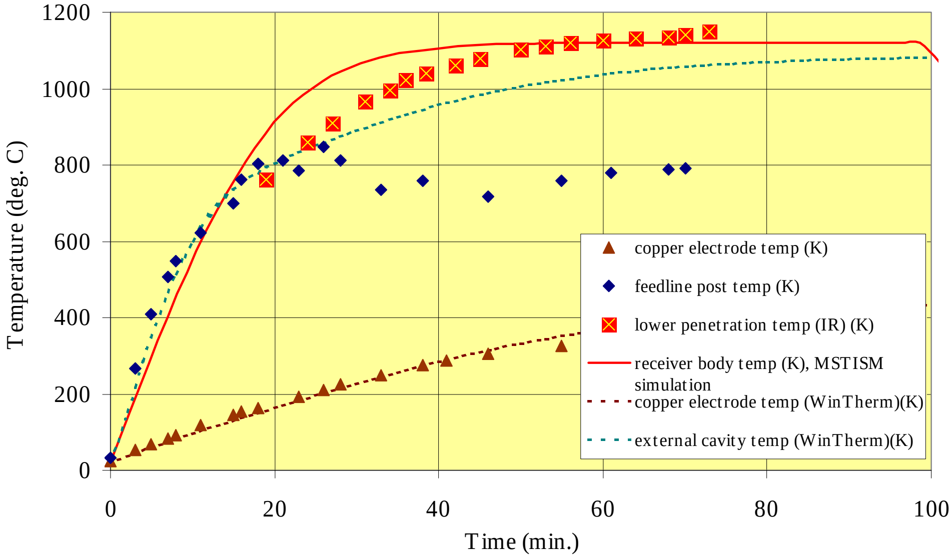

Figure 6-30 WinTherm overprediction of cavity temperature for a given circuit power dissipation. Test 17 (Mk. I receiver). MSTISM power = 1,050 W. WinTherm radiative power to receiver = 325 W.

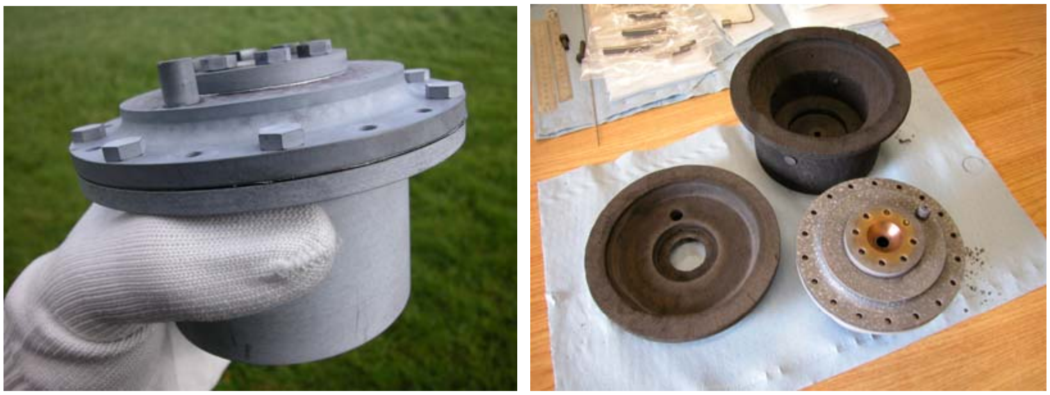

Figure 6-31 Mk. I receiver after completion of Test 1 (left). Mk. I receiver at end of test series (right).

Samples of the Mk. I receiver were examined by Prof. N. Ward in the University of Surrey's Department of Chemistry, in order to ascertain the makeup of the black deposit and copper-coloured coating observed around the cavity aperture. The author prepared these samples, as well as Mk. II receiver samples, for testing via induction-coupled plasma mass spectrometry (ICPMS), a technique for elemental composition determination. All samples were powdered with mortar and pestle and diluted with concentrated nitric acid (HNO_3), then baked to dryness over several hours. Organic materials were digested or during this process, evolving gas; only heavy elements remain. Nitrogen is masked by the nitrogen content of any remaining nitric acid in the sample, and cannot therefore be reliably measured. A blank control sample, consisting only of the concentrated acid, was also prepared.

Both Mk. I samples exhibited elevated titanium content, but indicated little if any contamination by other metals, or even boron (a major constituent of the ceramic). Ward [2003] suggested that the black deposit might be primarily carbon, although the test is obviously inconclusive in this respect, owing to the HNO_3 digestion process. The colour of the coating surrounding the aperture is similar to that of titanium nitride (TiN), a compound that is likely to form at elevated temperatures in the TiB_2/BN matrix. Mk. II results will be discussed later in this chapter.

Tests 18-25 were conducted on the Mk. II receiver, using improved graphite element heaters (Figure 6-32). Two test profiles (Figure 6-33 and Figure 6-34) are shown, illustrating the higher temperatures achieved with the smaller cavity receiver. Test 21 is representative of early tests on the Mk. II. A peak external cavity temperature of 1,515 ºC (1,788 K) is reached in the 76th minute, following two increases in delivered power.[163] Heating efficiency varies between 0.52 and 0.73, trending higher with higher power output (and heating element temperature).

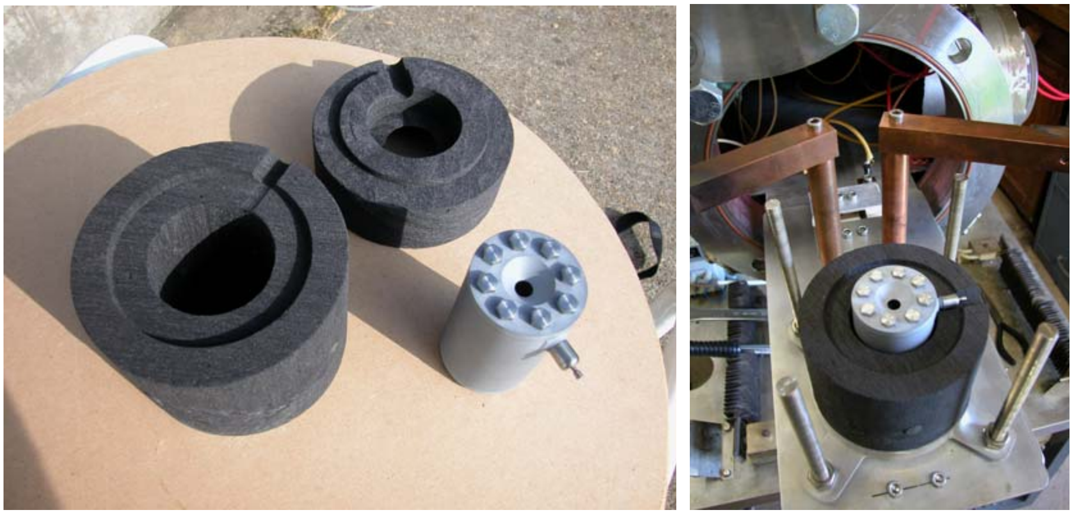

Figure 6-32 Mk. II receiver with insulation package sections, pre-assembly (left). Mk. II receiver on cavity heating rig prior to Test 18, insulation cap removed (right).

The MSTISM code was used to determine radiated power (incident on the receiver walls) for all three power levels. Near the end of the test, the feedline post temperature plateaus, then begins to climb slightly; this appears to be a harbinger of imminent heater failure. Heater output climbs just prior to element failure, increasing receiver temperature.

Test 25 details are shown in Figure 6-34. This test produced the highest peak temperature recorded during the test series, 1,701 ºC (1,974 K), observed by infrared thermometer in the 93rd minute. Feedline post thermocouple data climbs upward steadily, until approximately the 20th minute, after which the readings fluctuate and become unreliable. This is likely due to the high-temperature contamination of the thermocouple bead, also seen in Test 17.[164]

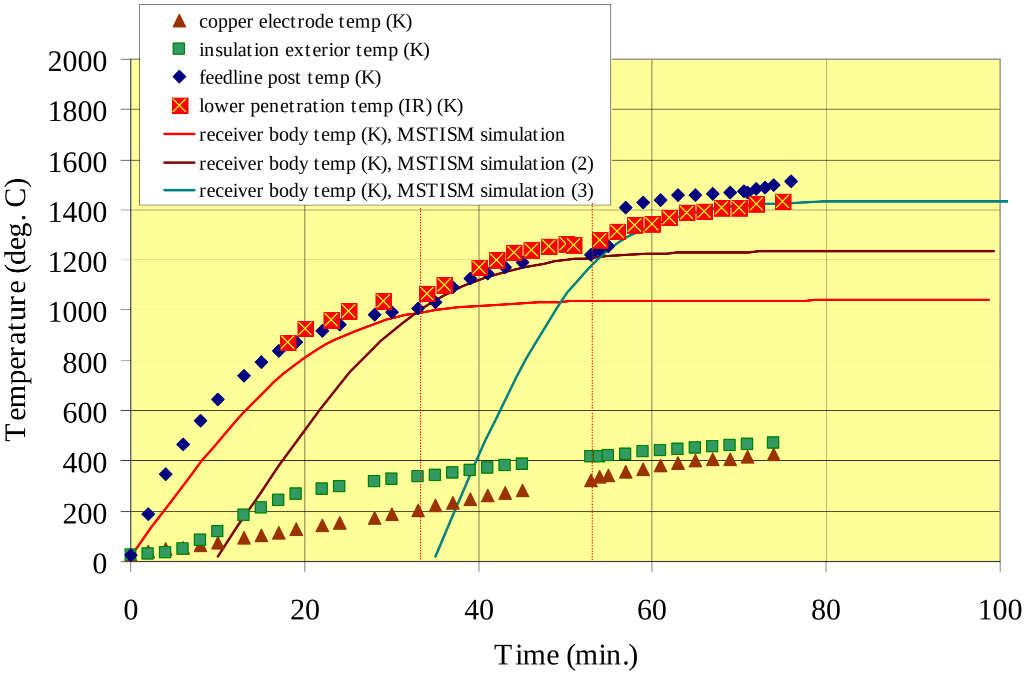

Figure 6-33 Test 21 Heating Profile (Mk. II receiver, PECT = 1,788 K, peak power dissipation (ramp 1) = 773 W; (ramp 2) = 1,080 W; (ramp 3) = 1,368 W). Test date: 10 July 2003. MSTISM power = 400 W. MSTISM power (2) = 654 W. MSTISM power (3) = 1,000 W.

Heating efficiencies in Test 25 were the highest observed during the entire campaign. Prior to the first power ramp, circuit dissipation was recorded as 1,080 W, indicating an efficiency of 0.93. After the first ramp, circuit power was increased to almost 1,430 W, with an estimated received power of 1,294 W (for an efficiency of 0.91).[165]

Like the Mk. I, the Mk. II receiver's outward appearance was observed to change over the course of the test series, although the changes seen in the Mk. II arose more quickly, and were more pronounced. Silver-grey blisters formed over the cylindrical section of the receiver following the

---

[163] Dashed red vertical lines in Figure 6-33 depict these increases.

[164] Following cooldown and removal of the receiver from the vacuum chamber, the feedline post thermocouple was removed and examined, but broke during the attempt to extricate the bead from the feedline penetration. This lends credence to the theory that receiver materials precipitated at high temperatures diffuse into the thermocouple bead, altering its mechanical and electromotive properties.

[165] This last figure may in fact be somewhat higher. Suspect feedline thermocouple data required the author to rely entirely on IR data to model the upper portion of the heatup curve; a conservative estimate of received power was therefore used.

first test (Figure 6-35). The molybdenum bolts used to compress graphite foil seals between the cap and cylinder sections showed signs of darkening. By the final heating trial, several of the bolt tops were coated liberally with a black deposit, which was not susceptible to removal. As was also observed in tests of the Mk. I, the Mk. II exhibited a colour change around the cavity aperture, from an initial grey to yellow-orange.

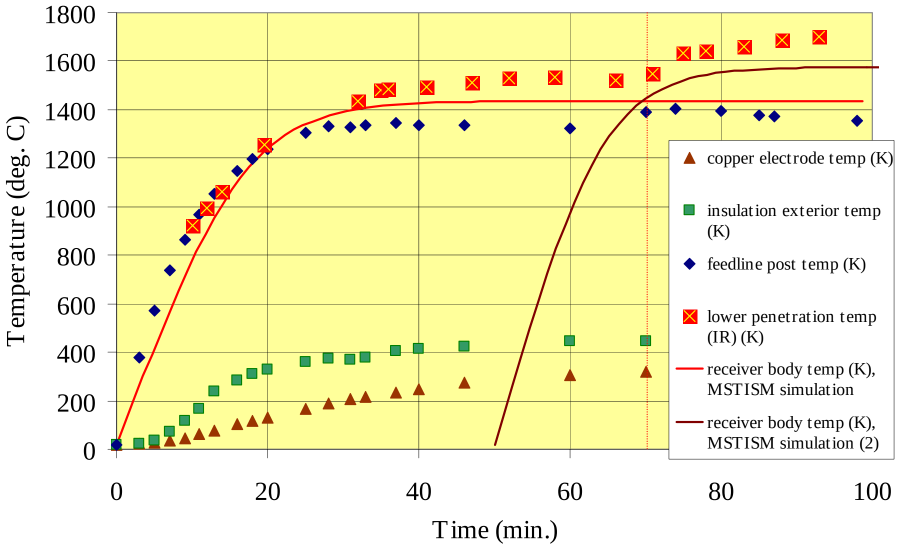

Figure 6-34 Test 25 Heating Profile (Mk. II receiver, PECT = 1,974 K, peak power dissipation before final ramp = 1,080 W; after ramp = 1,429 W). Test date: 9 September 2003. MSTISM power = 1,000 W. MSTISM power (2) = 1,294 W.

Discussions with the vendor of the IMC ceramic material, Sintec-Keramik, revealed that both pure and composite boron nitride ceramics are susceptible to the leaching of binder (boric oxide, B_2O_3) at high temperatures [Oliver, 2003]. When high-purity samples of BN are heated, B_2O_3 is driven out of the matrix and forms white, bead-like formations on the surface of the material. The surface deposits on the Mk. II receiver appeared to be boric oxide contaminated with trace amounts of titanium from the TiB_2 component; this will be demonstrated later when mass spectrometry results of receiver test samples are reviewed.

No mass loss, deformation, or evidence of fracture was observed in the Mk. II receiver's structure following the test series. These results have validated the receiver designs and have demonstrated their robustness and survivability to high temperatures and over multiple thermal cycles. In addition, test results have validated the MSTISM model and demonstrated that both early, simplified codes (e.g., the Cavity Heatup Sequence, or CHUPS) and the commercially-procured WinTherm modeller are inadequate for solar thermal receiver modelling. The next step in solar receiver design verification, full flow testing at temperature and in vacuum, will be discussed presently.

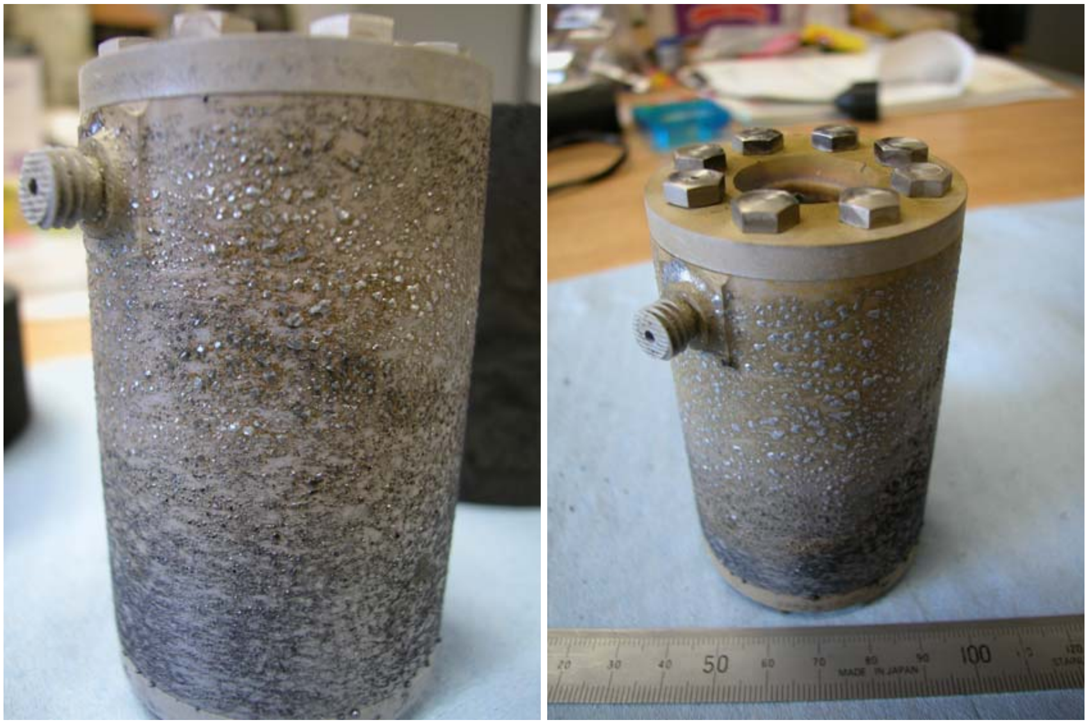

Figure 6-35 Mk. II cavity receiver following initial heating trials (Test 18/19), left. Mk. II cavity receiver after final heating trial (Test 25).

6.2.3 Receiver Cavity Hot Flow Tests

Following the success of the receiver heating trials, the author began work on the conduct of full flow testing, in vacuum, at representative temperatures (~2,000 K). Initially, it was thought that the full flow tests could be conducted in the E Site high vacuum chamber used for the heating trials; unfortunately, the chamber's small diameter and volume, already a problem for heating tests, could not accommodate the added plumbing required to perform a full-up flow test. Additionally, the pumping capacity of the rotary and oil diffusion pumps would have been quickly overwhelmed by even a short-duration firing inside the chamber, limiting tests to very short durations. While this could be overcome by isolating and removing engine exhaust with a sealed flow line, this would further add to plumbing requirements and potentially invalidate the experiment itself.[166]

---

[166] A sealed flow line would itself have to empty into an evacuated chamber, in order to maintain a favourable pressure gradient through the receiver nozzle and prevent flow separation, normal and oblique

The decision was made to investigate alternative test facilities with appropriate vacuum capability. The most convenient of these was the ARC High Altitude Test Facility (HATF) chamber, located at Westcott's F Site in Oxfordshire. This large (1-m diameter) chamber is evacuated by a Leybold-Heraeus Ruvac 5001 Roots blower backed by a rotary forepump [Schooonver, 2003]. Once the forepump has reduced chamber pressure to roughly 1/3 of a millibar, the Roots blower starts automatically (Figure 6-36). Ultimate pressures obtained can be lower than 3 x 10^{-2} mbar. During testing, pressures as low as 2 x 10^{-2} mbar were observed.

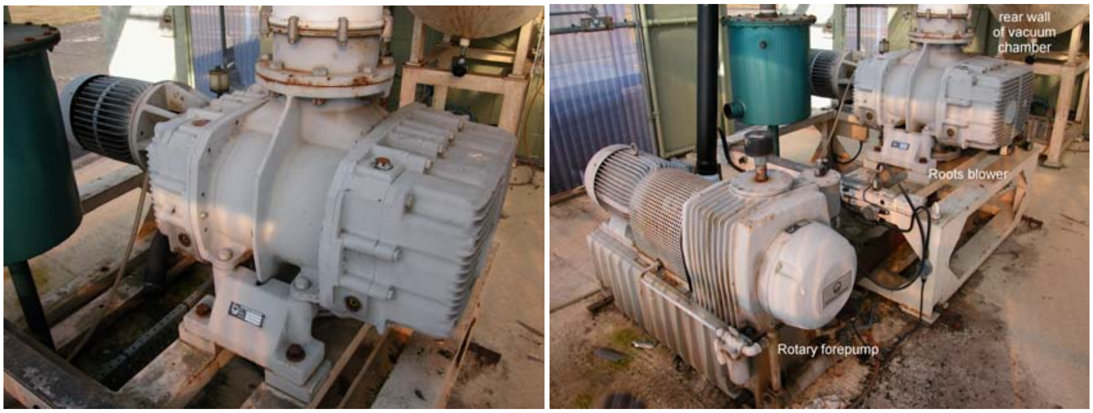
rear wall
of vacuum
chamber
Roots blower
Rotary forepump

Figure 6-36 Rotary forepump (left) and forepump/blower assembly at Westcott F Site (right).

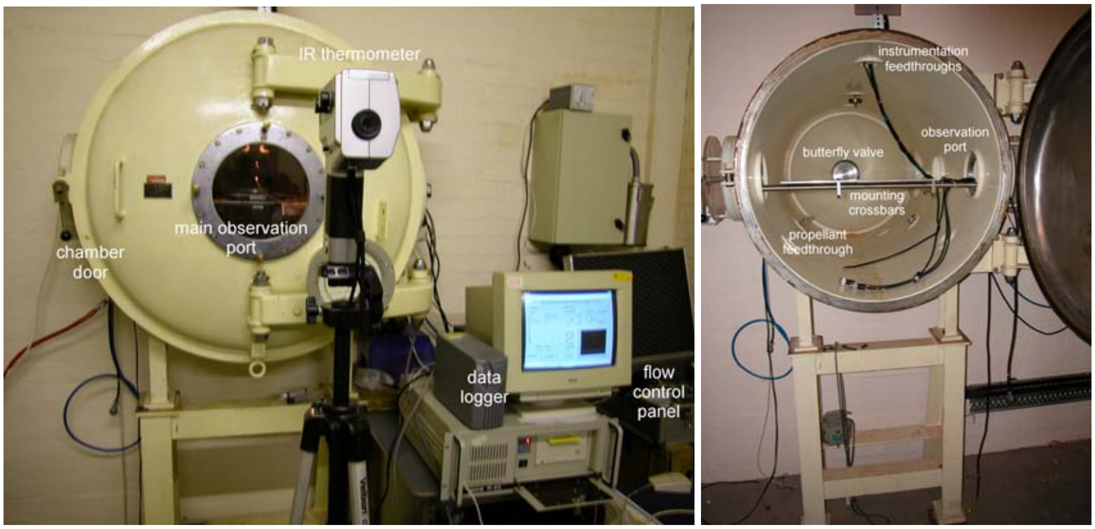
IR thermometer
main observation
port
chamber
door
data
logger
flow
control
panel
instrumentation
feedthroughs
observation
port
butterfly valve
mounting
crossbars
propellant
feedthrough

Figure 6-37 Westcott F Site high altitude test facility (HATF) chamber.

The test rig, as initially configured, included (a) the 1-metre chamber with medium vacuum capability, (b) the dual-phenomenology wide range pressure gauge used during the heating tests, (c) a portable flow control panel for regulating gas bottle feed systems, (c) an Aalborg thermal

---

shocks, and an artificially low thrust coefficient. The alternative, venting to atmosphere, is likewise problematic for the reasons just mentioned.

mass flow measurement device, calibrated to N_2 over a range of 0-100 standard litres per minute (SLPM), with a stated accuracy of ±1.5% (1.5 SLPM) full-scale, (d) three C-type (tungsten-rhenium) thermocouples, (e) a variable (60 V/60 A maximum) power supply, (e) LabView v5.0 software, resident on a personal computer, acting as data logger for temperature and mass flow rate measurements, and (f) a handheld infrared thermometer (Figure 6-37, left). Later tests were augmented by the inclusion of a thrust stand, cantilever-mounted to a 10-kg capacity load cell, in addition to inlet and chamber pressure transmitters (10 or 16 bar (gauge) capacity) and a solenoid valve placed on the thrust stand.

The mass flow meter, thermocouples and pressure transmitters were connected to the data logger. These devices were all capable of producing a linear 4-20 mA current response over their respective ranges, and were connected to the data logger connector block and output voltage translated into a mass flow, temperature, and pressure traces (bar, absolute). During thrust testing, the millivolt-level signal from the load cell was amplified through a transducer amplifier and visually recorded from a Keithley digital multimeter (Figure 6-38, right).

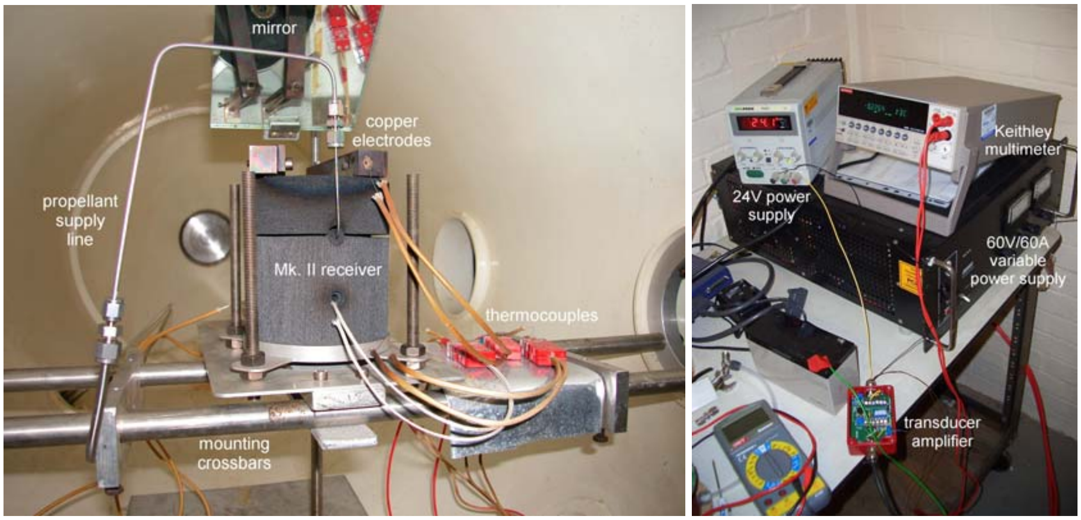

Figure 6-38 Initial flow characterisation test setup, Westcott F Site (left). Thrust stand electronics (right) with visual display on digital multimeter.

As no Mk. I receiver had been fabricated with a screwfit post for mechanical assembly, flow testing commenced with the smaller Mk. II receiver. A pristine receiver was first assembled, seals and molybdenum bolts installed, and placed in its insulation package (cap removed). The assembly was then placed on the lower aluminium mounting ring of the cavity heating rig and the rig mounted on steel crossbars in the vacuum chamber (Figure 6-38, left). C-type thermocouples were inserted at or near locations used in previous heating tests: (1) on the end of one of the copper electrodes, (2) at the interface of aluminium mounting ring and insulation package, and (3) through the lower insulation package penetration, touching the external surface of the IMC cavity receiver. The propellant feedline assembly, consisting of a 2-mm diameter molybdenum tube electron-beam welded to a screwfit molybdenum cap, was attached to the screwfit post on the receiver's cylindrical face. The interface between the cap and post base was tightly sealed with a 0.5-mm graphite foil gasket. The tube end was then connected to the 1/8-inch gas supply line with a standard reducer union fitting.

Pressurized gas bottles (including nitrogen, helium, and ammonia) were stored outside, near the pump room (Figure 6-36). The gas supply was routed through the control room wall and into the flow control panel (Figure 6-37, left), exiting through the thermal mass flow meter and returning back through the wall. The propellant feed line enters the vacuum chamber near the rear end cap (Figure 6-37, right). Just prior to the chamber inlet point, there is a tap-off for a 10-bar (gauge) pressure transmitter and corresponding dial gauge, registering supply pressure. Later the supply transmitter was replaced with a 16-bar (gauge) unit, due to a need to measure inlet pressures in excess of 10 bar.

Full flow tests with gas bottle supply and mass flow meter were conducted according to the following procedure:

1. Startup of water cooling loop for Roots blower.
2. Placement of the instrumented cavity heating test rig in the vacuum chamber. Attachment of propellant supply line.
3. Powering on the thermocouple transmitters, pressure transmitter (inlet), mass flow meter, wide-range gauge, and gauge display. The mass flow meter required several minutes to initialise and settle to its zero value before flow could be introduced.
4. Verification of heating element resistance with multimeter followed by brief power throughput test. Power supply is turned on and set to 10V/10A for several seconds, then powered down.
5. Sealing of the vacuum chamber door.
6. Re-verification of power throughput in case of heating element shift during main flange sealing.
7. Opening of the butterfly valve at the rear of the vacuum chamber and startup of the mechanical pump.
8. Automatic startup of the Roots blower once chamber pressure decreases below 1/3rd of a millibar.
9. Chamber pressure asymptotically approaches 2×10^{-2} mbar (within five minutes of Roots blower startup).
10. Powerup of the data logger and initialisation of the LabView v5.0 virtual instrument for recording temperature, pressure, and mass flow readings.
11. Visual recording initial temperature readings from thermocouples (1), (2), and (3). Recording chamber pressure from wide-range gauge display. Recording of propellant inlet pressure.

12. Powering on the power supply and recording thermocouple, pressure, current, voltage, and infrared thermometer readings throughout the course of the test.
13. Introducing gas at specific receiver temperature plateaus (e.g., 590 K, 1000 K, 1600 K) and at regulated inlet pressures for flow characterisation. Mass flow data and inlet pressure was recorded during these operations.
14. Powering down the power supply and continuing to record data through the cooldown phase. Once the receiver lower penetration temperature drops below 200 ºC, the rotary pump and Roots blower are turned off. The chamber door can then be removed and the receiver inspected.

Initial tests (26-A, B) were conducted at ambient temperatures, in vacuum, to calibrate the mass flow meter and to compare vacuum test data with the inconclusive results of the seal check test discussed at the end of section 6.2.1. A summary of early flow tests is shown in Table 6-4.

Test No.	Receiver Type	Heating Element	Gas type	Penetration temp (ºC/K), at flow test start	Peak characteristic velocity (c*), m/s, estimated	Thrust stand
26-A	**Mk. II (2)**	**-- (cold flow test, vacuum)**	**N_2**	**ambient**	**429**	**No**
26-B	**Mk. II (2)**	**-- (cold flow test, vacuum)**	**N_2**	**ambient**	**429**	**No**
26-C	**Mk. II (2)**	**8-Path C 2/Ta lead**	**N_2**	**321 /594**	**582**	**No**
26-D	**Mk. II (2)**	**8-Path C 2/Ta lead**	**N_2**	**1,382 / 1,655**	**892**	**No**
26-E	**Mk. II (2)**	**-- (cold flow test, ambient)**	**N_2**	**ambient**	**429**	**No**
26-F	**Mk. II (2)**	**-- (cold flow test, ambient)**	**N_2**	**ambient**	**429**	**No**
27-A	**Mk. II (2)**	**8-Path C 2/Ta lead**	**N_2**	**492 / 765**	**709**	**No**
27-B	**Mk. II (2)**	**8-Path C 2/Ta lead**	**N_2**	**1,394 / 1,667**	**1,050**	**No**
27-C	**Mk. II (2)**	**8-Path C 2/Ta lead**	**NH_3**	**1,433 / 1,706**	**1,909**	**No**
28-A	**Mk. II (2)**	**-- (cold flow test, ambient)**	**N_2**	**ambient**	**429**	**No**
28-B	**Mk. II (2)**	**-- (cold flow test, ambient)**	**He**	**ambient**	**1,070**	**No**
28-C	**Mk. II (2)**	**-- (cold flow test, ambient)**	**N_2**	**ambient**	**429**	**No**
28-D	**Mk. II (3)**	**-- (delta-P test, ambient)**	**N_2**	**ambient**	**429**	**No**
28-E	**Mk. II (3)**	**-- (delta-P test, ambient)**	**N_2**	**ambient**	**429**	**No**
28-F	**Mk. II (3)**	**-- (delta-P test, ambient)**	**N_2**	**ambient**	**429**	**No**
28-G	**Mk. II (3)**	**-- (delta-P test, ambient)**	**N_2**	**ambient**	**429**	**No**
28-H	**Mk. II (3)**	**-- (delta-P test, ambient)**	**N_2**	**ambient**	**429**	**No**
28-I	**Mk. II**	**-- (delta-P test,**	**He**	**ambient**	**1,070**	**No**

28-J	**(3) Mk. II (3)**	**ambient) -- (delta-P test, ambient)**	**He**	**ambient**	**1,070**	**No**

Table 6-4 Ambient and high-temperature flow testing in Westcott F Site HATF (first series).

Data from the 26-A and B cold flow vacuum tests are shown in Figure 6-39. At low inlet pressures, the data show significant divergence from predicted mass flow rates.[167] At an inlet pressure of 1.5 bar (absolute), the ratio of measured to predicted mass flow rate is only 0.45. This rises to 0.98 at 10.5 bar. Since we can assume choked flow at the nozzle throat, disturbances in the diverging (supersonic) section of the nozzle cannot propagate upstream. The only rationale for the observed mass flow deficit is the formation of a strong vena contracta at low inlet pressures, due to the sharp edge at the throat. Losses in the nozzle can reduce the thrust coefficient but not mass flow rate (or, consequently, *c**). As pressure rises in the inlet, the vena contracta migrates upstream, the flow constriction's diameter asymptotically converging on that of the throat itself.

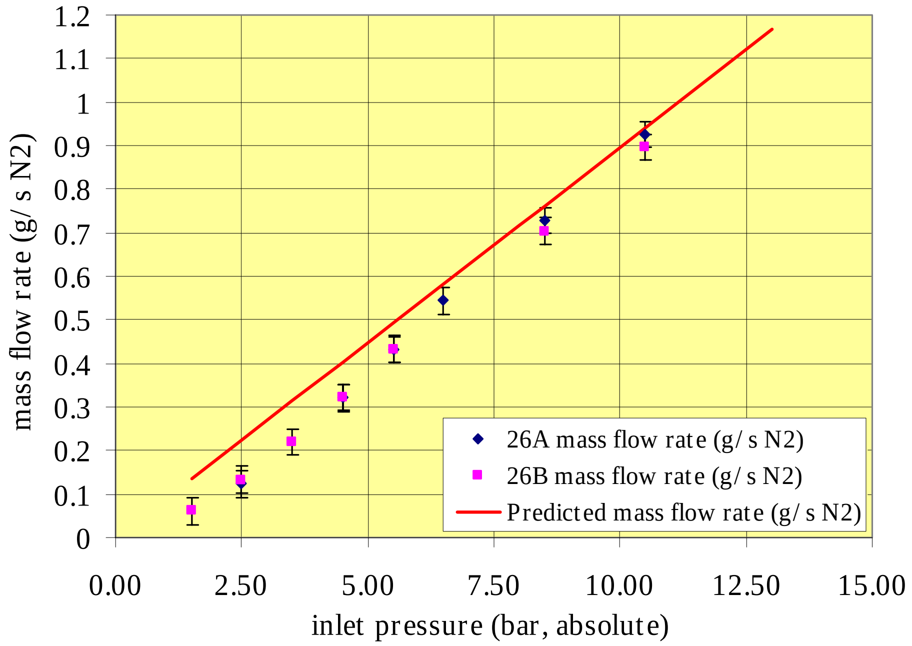

Figure 6-39 Mass flow rate data versus inlet pressure (Tests 26-A, B results, 28-29 October 2003).

Test 26-C was conducted in medium-temperature vacuum with nitrogen propellant. The purpose of this test was to determine the Mk. II receiver's steady-state heat removal capacity. After pumping down the chamber, the receiver temperature (as measured by the lower penetration thermocouple) was slowly raised by 300 ºC to 321 ºC (594 K). Once this was achieved, nitrogen was introduced into the receiver at flow rates of up to 9 SLPM (0.19 g/s). Power input was then increased to achieve a steady temperature under flow conditions. Results (Table 6-5) show good agreement with predicted values.

---

[167] Calculated from inlet pressure, throat area, and estimated characteristic velocity *(c*)*.

	Flow rate (g/s)	**Steady state power (W)**	**Corrected power (W)**	**Calculated power to flow $(Q = mC_p\Delta T)$(W)**
Prior to flow	**--**	**81.3**	**40.7**	**--**
During flow (9 SLPM)	**0.19**	**188.2**	**94.1**	**58.9**

Table 6-5 Test 26-C, Power-To-Flow test results.

In this instance, the author saw an increase in steady state (electrical) power of just over 100 W. However, if we multiply these power figures by the lowest observed element heating efficiency (0.52), corresponding to a low temperature (and low radiated power) heater element, the actual differential is very close to 55 W, approximately the amount of input power required to heat the incoming nitrogen flow from 293 K to 593 K.

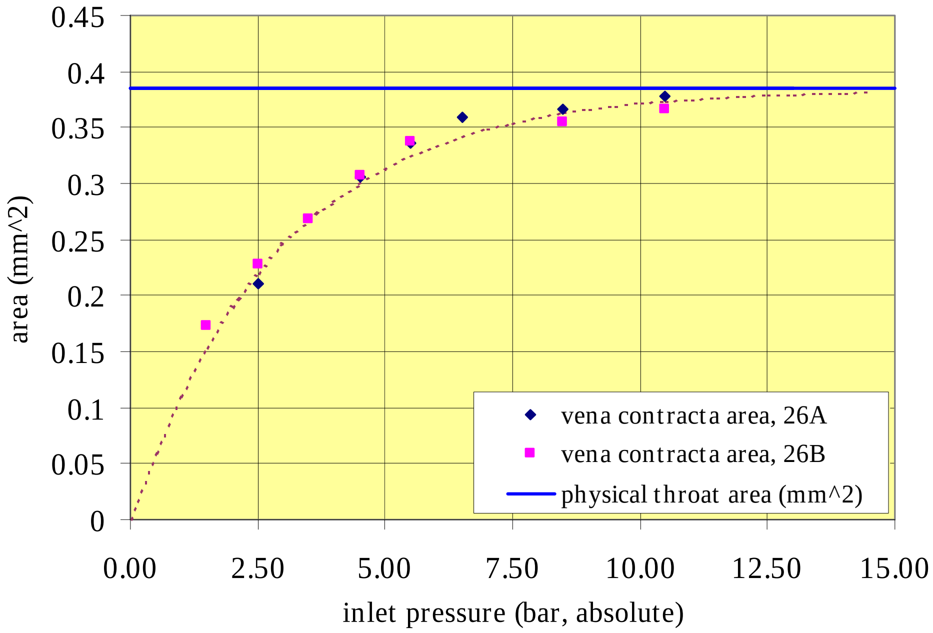

Figure 6-40 Derived vena contracta area (mm^2), Tests 26-A, B (28-29 October 2003).

Given the measured flow rate and correcting for flow constriction effects at the nozzle throat, a characteristic velocity for Test 26-C can be estimated. At an inlet pressure of 4.5 bar (absolute), the trendline in Figure 6-40 provides an estimate of vena contracta throat area, permitting the calculation of nitrogen's c^* at a receiver temperature of 594 K.[168] This value can be compared to the ideal *c** value for N_2 at the receiver temperature (i.e., 613 m/s), and provides an estimate of the Mk. II's *c** efficiency. The value obtained is relatively high (0.909), indicating that, at the relatively low temperatures of this test, the Mk. II receiver is an acceptable heat transfer device.

---

[168] An empirical fit for this data (dashed line in Figure 6-40) is:

A similar calculation can be carried out on test data acquired in Test 26-D, the first high temperature flow test. The Mk. II receiver reached 1,655 K in 43 minutes; at this point, N_2 was introduced in a series of steps (1, 2, 3, 5, 7.5, 10, and 12.5 bar (gauge) inlet pressure).[169] The test conductor held the inlet pressure steady at 5 bar (gauge) for 30 seconds, as indicated in Figure 6-41. The pressure drop through the spiral flow passage of the receiver can be estimated by applying the following pipe flow correlation [Lienhard, 1987]:

$$\Delta P = f \frac{L}{D} \frac{\rho V^2}{2}$$

Here, the pressure drop ΔP is a function of the Darcy-Weisbach friction factor f, channel length L, hydraulic diameter D, gas density, and gas velocity. For smooth pipes, the friction factor in the turbulent regime is typically expressed as:

$$f = \frac{.0115}{\mathrm{Re}_D^{0.2}}.$$

The flow Reynolds number (see Section 4.4.4) is dependent on the propellant's dynamic viscosity μ (which increases with the square root of temperature), density (inversely proportional to temperature), and flow sound speed (proportional to the square root of temperature).[170] The ρV^2 term can be shown to be independent of temperature, assuming choked flow conditions; flow velocity can be related directly to mass flow rate and therefore characteristic velocity (another square root temperature-dependent function).

Since (assuming constant L/D):

$$\Delta P \propto \left(\frac{1}{\mathrm{Re}_D^{0.2}}\right)\left(\frac{\rho V^2}{2}\right)$$

$$A_t = .38485\left[1-\left(1.4^{-P_c}\right)\right]$$

For an estimated engine chamber pressure of 3.92 bar, A_t (effective) = 0.282 mm^2. Therefore, *c** = 582 m/s and *c** efficiency (measured/ideal) = 0.949. This calculation assumes a pressure drop through the receiver of almost 0.6 bar, based on ambient receiver delta-P data acquired later in the test campaign. No pressure drop correction was made to account for the elevated propellant temperature.

[169] This was the first flow test at high temperature; the author wished to ensure that the hot structure suffered no thermal shock by the introduction of high-pressure cold propellant and fractured as a result.

[170] For a selected gas, sound speed is also related to the ratio of specific heats γ, which is only weakly dependent on temperature and is therefore ignored for the purposes of the present analysis.

It can be shown that:

$$\Delta P \propto \left(\frac{\mu}{\rho \sqrt{\gamma R T}} \right)^{0.2} \left(\frac{\dot{m}^{2}}{\rho} \right),$$

and (utilising the mass flow rate relationship to characteristic velocity):

$$\Delta P \propto \left(\frac{\sqrt{T}}{T \sqrt{T}} \right)^{0.2} \left(\frac{\frac{1}{\left(\sqrt{T}\right)^{2}}}{\frac{1}{T}} \right)$$

Therefore:

$$\Delta P \propto T^{\,0.2}$$

This permitted the author to roughly estimate the pressure drop for a given receiver temperature and inlet pressure (Figure 6-41 and Figure 6-42), given the pressure drop and inlet pressure for ambient conditions (Figure 6-43).[171] Figure 6-45, Figure 6-46, and Figure 6-47 show temperature, pressure and $c*$ estimation data for Test 26-D.

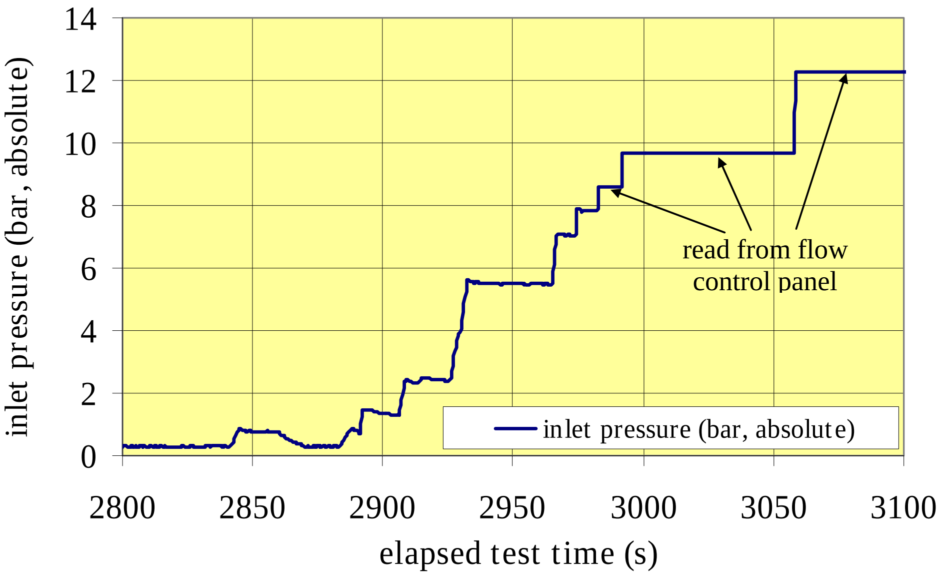

Figure 6-41 Inlet pressure trace from Test 26-D, high temperature N_2 flow trial (29 October 2003).

---

[171] Pressure drop across the receiver was directly measured only in later flow trials (beginning with Test 28-D). The data shown in Figure 6-43 are from Test 29, conducted with a drilled tap hole in the bottom face of the nozzle section. A pressure transmitter was sealed to the tap hole and chamber pressure visually read from a digital display in bar (gauge).

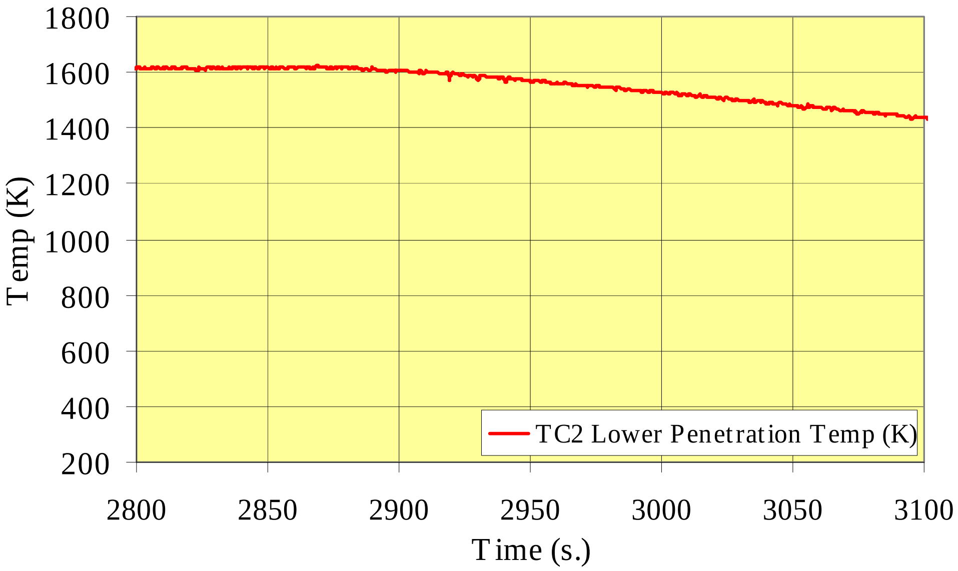

Figure 6-42 Lower penetration temperature trace, Test 26-D, high temperature N_2 flow trial.

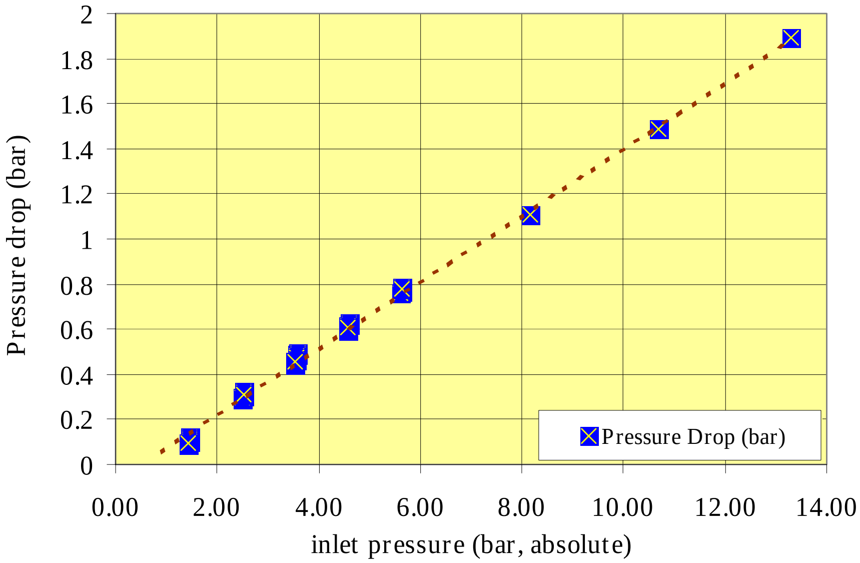

Figure 6-43 Ambient pressure drop trials, Mk. II receiver, Test 29 (19 November 2003).

Below approximately 10 bar (gauge) inlet pressure, the characteristic velocity trendline is unreliable. The data appear to indicate that one or more of the following problems was present: (a) the chamber pressure was substantially lower (and the pressure drop higher) at low inlet pressures than the author’s estimate, (b) the effective throat area was smaller than estimated, due to a partial blockage of the throat itself (Figure 6-44), or (c) the mass flow meter was reading erroneously low. Either (b) or (c) are compatible with the data, although (b) conforms to visual observations of the receiver exit both during and after the test.[172] C^* efficiency is highest (0.884) at the beginning of the test and declines steadily until, at the end of data logging, it has fallen to 0.747. Maximum c^* (at an estimated 9.7 bar chamber pressure) was estimated to be 892 m/s.

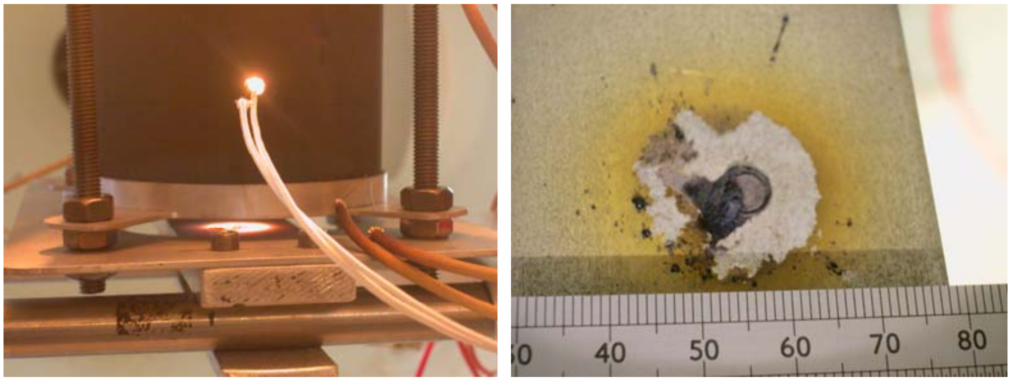

Figure 6-44 Mk. II receiver undergoing N_2 flow testing (left). Residue observed on mounting plate beneath nozzle exit, following N_2 flow testing (right).

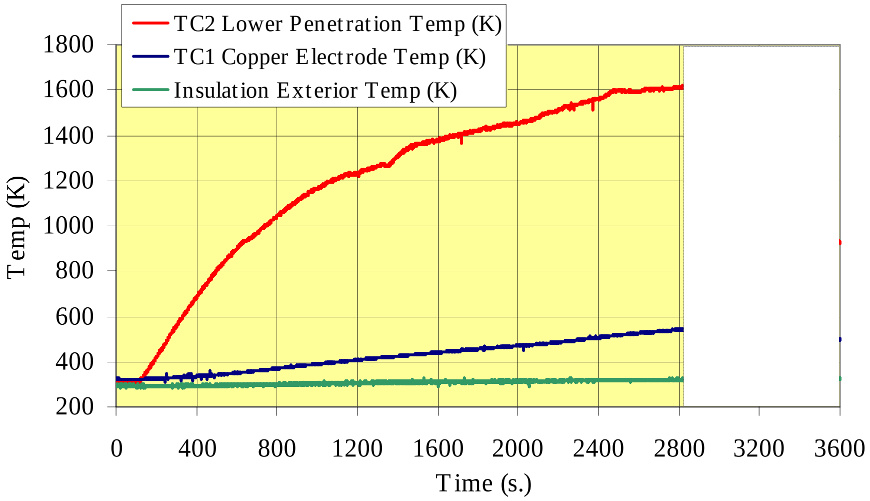

Figure 6-45 Heatup/cooldown profile for N2 flow trial, Test 26-D. Shaded area = flow test period.

---

[172] During this flow test, the nozzle was observed to occasionally discharge sparks, apparently a solid particulate precipitating from an interior receiver surface. Above the 9.7 bar threshold, the author contends, the flow obstruction was dislodged and the trendline becomes consistent.

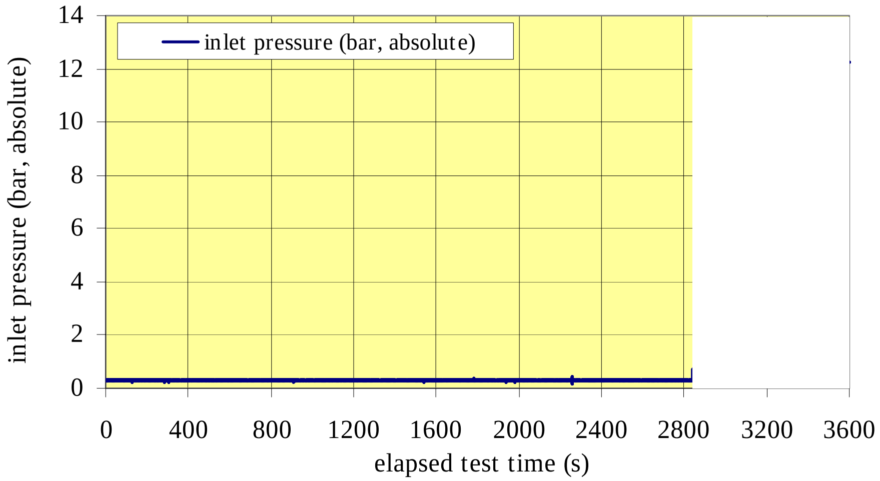

Figure 6-46 Inlet pressure trace for N_2 flow trial, Test 26-D. Shaded area = flow test period.

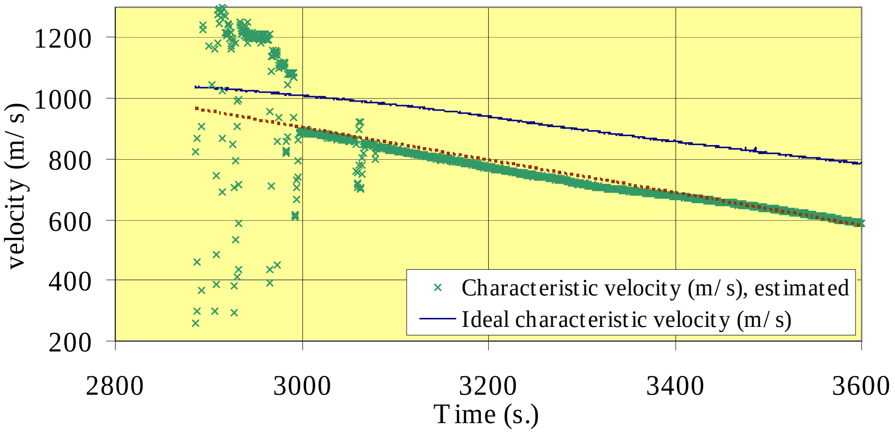

Figure 6-47 Estimated characteristic velocity profile for N_2 flow trial, Test 26-D.

Results from Test 27-A provided insight into mass flow measurement problems at low inlet pressures. Following the Test 27 series, the meter was removed from the test rig and brought to the Surrey Space Centre for calibration. Results of this calibration are shown in Figure 6-48; for sufficiently high mass flow rates (and, typically, high supply pressures), the meter tended to read accurately. At reduced flow rates (i.e., less than 0.3 g/s), the meter proved increasingly inaccurate. Flow meter readings were adjusted to correct for this measurement error, and performance results shown in Figure 6-49. These discrepancies at low pressures finally prompted the author to return the thermal mass flow meter for recalibration; unfortunately, the device’s performance was not significantly improved, still suffering a deficit at low flow rates.

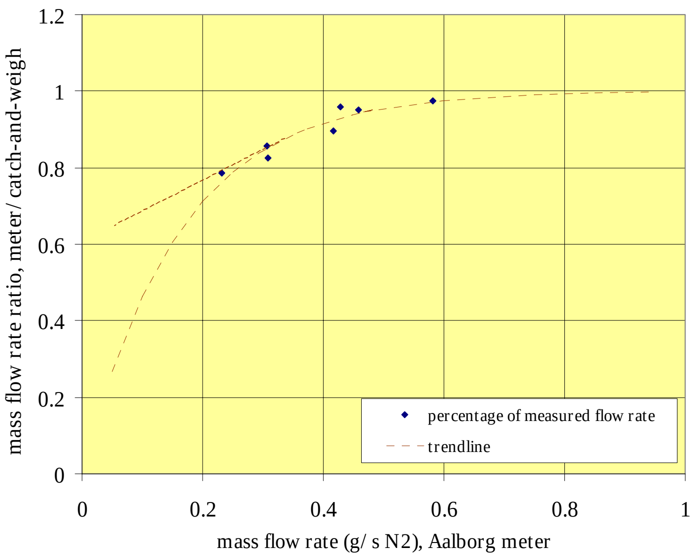

Figure 6-48 Calibration of Aalborg thermal mass flow meter versus catch-and-weigh, nitrogen gas (2-10 bar supply pressure).

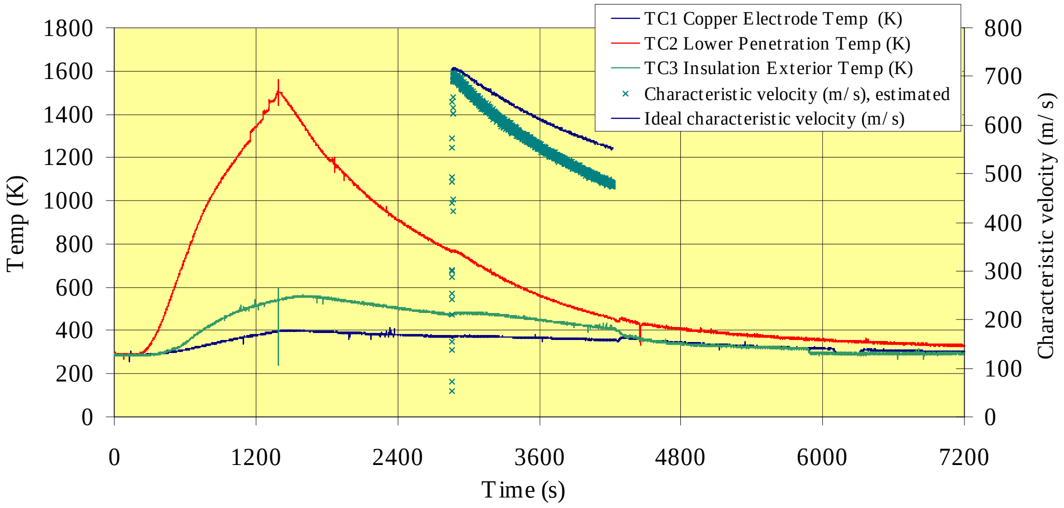

Figure 6-49 Temperature and characteristic velocity (estimated and ideal), Test 27-A (3 November 2003).

After mass flow rate readings for adjusted for calibration data, the author was able to calculate a maximum *c** of 709 m/s and a *c** efficiency of 0.992. Over the course of the test, *c** efficiency falls to 0.861. The most likely reason for the observed decay in efficiency is the cooling taking place in the receiver structure during the firing, immediately adjacent to the flow passages. This would have the effect of shortening the effective heating length of the spiral flow passage, preventing the nitrogen from reaching peak receiver temperature.

Similar results for Test 27-B are shown in Figure 6-50 and Figure 6-51. Characteristic velocity decays from 1,050 m/s to 685 m/s at test end, while *c** efficiency declines from nearly 1.0 to 0.88.

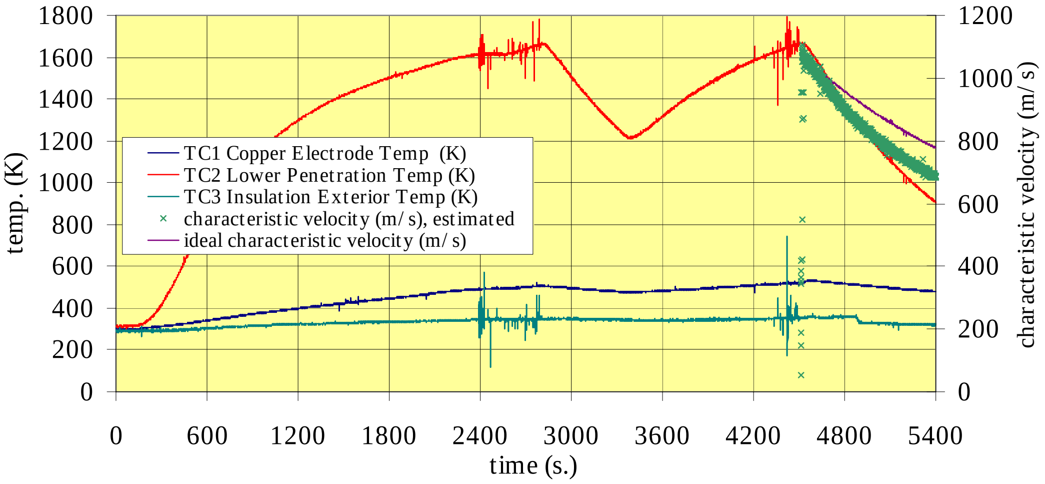

Figure 6-50 Temperature and characteristic velocity (estimated and ideal), Test 27-B (3 November 2003).

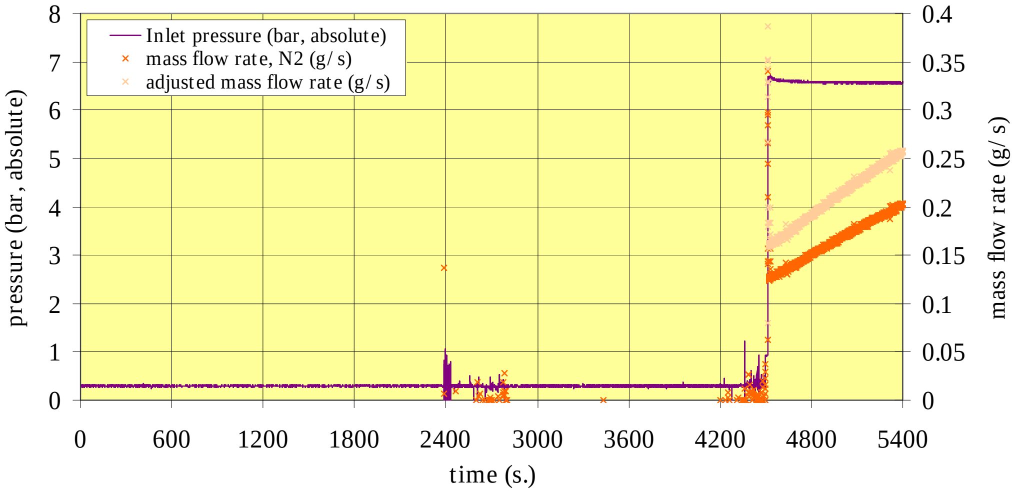

Figure 6-51 Inlet pressure and mass flow (measured and adjusted), Test 27-B (3 November 2003).

A final test was conducted with ammonia propellant. Unlike N_2, ammonia is stored as a liquefied gas; therefore, supply vapour pressure will vary with supply bottle temperature. Due to ammonia's high heat of vaporisation (1,372 kJ/kg),[173] substantial heat is drawn from the supply vessel during a long firing trial. This can lower the vessel's temperature (particularly when the vessel is small, as will be noted in thrust stand trials) and decrease the supply pressure. Ammonia is also toxic in concentrations of greater than a few hundred parts per million, necessitating safety precautions to be taken in advance of, during, and following flow testing. The nominal test procedure (p. 116) was modified to account for additional steps needed to safeguard test conductors. All personnel wore faceshields during connection and disconnection of the ammonia supply tank. Furthermore, the vacuum vessel was left evacuated considerably longer than was usual, to ensure that any remaining ammonia in the propellant lines and receiver was scavenged by the pumps and vented.

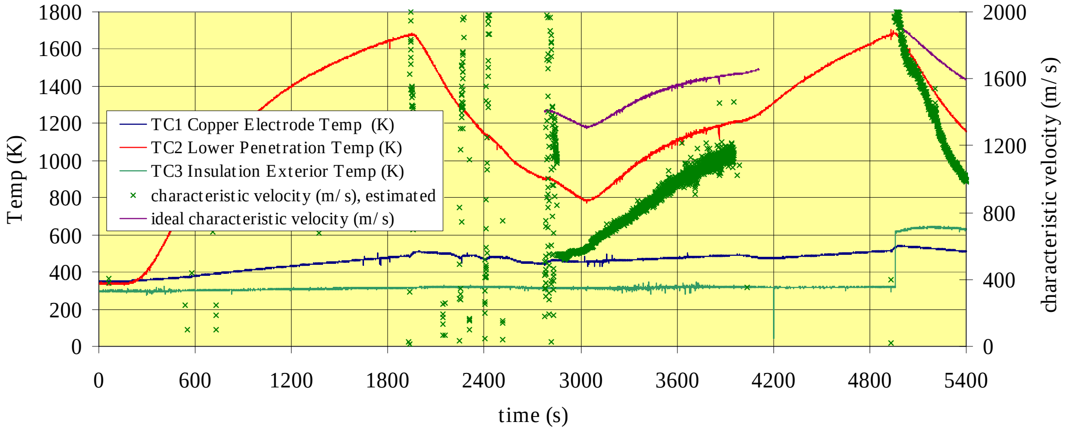

Figure 6-52 Temperature and characteristic velocity (estimated and ideal), ammonia flow trial, Test 27-C (3 November 2003).

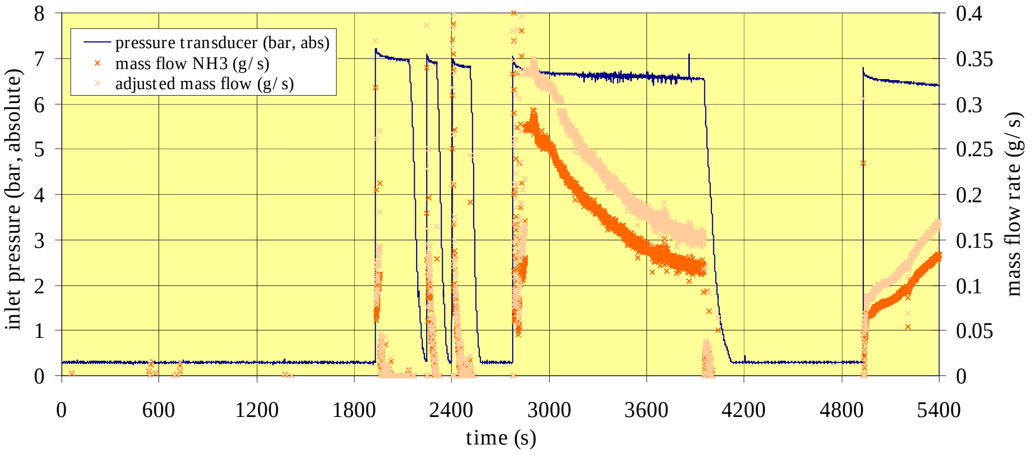

Figure 6-53 Inlet pressure and mass flow (measured and adjusted), Test 27-C (3 November 2003).

Test 27-C was conducted over a 90-minute period. The Mk. II receiver was heated to approximately 1,700 K and electrical power shut off before NH_3 was introduced. As can be seen

---

[173] Compared with, for example, butane (387 kJ/kg), methane (512 kJ/kg), acetylene (614 kJ/kg), and xenon (96.3 kJ/kg) [Lide, 1995][Air Liquide, 2004].

from Figure 6-53, the supply tank valve was opened during the 32nd minute. Monitoring of the mass flow meter indicated a brief pulse of flow and then a rapid decrease to zero, within three minutes. Two additional attempts were made to introduce ammonia, with the same result. The receiver was then allowed to cool to 900 K. The supply tank valve was reopened in the 46th minute; at this point, the mass flow meter registered a continuous mass flow rate of 0.28 g/s. In the 50th minute, electrical power was re-applied and the receiver heated to its previous peak temperature of 1,700 K.[174]

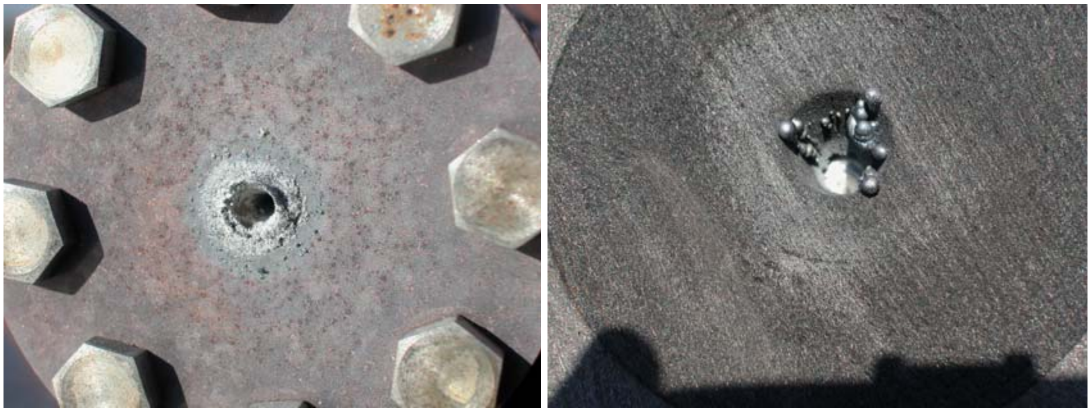

Figure 6-54 Boric oxide precipitate surrounding receiver nozzle exit (left) and dark globules on graphite foam insulation bottom (right) following Test 27-C (high-temperature NH_3 flow trial).

Flow was re-introduced at peak temperature without any evidence of the stoppage seen during the first hot cycle. Sparks were observed occasionally being ejected from the nozzle during this phase of the test. The author also noted molten droplets falling from the graphite foam insulation package, near the receiver nozzle. Peak c^* was estimated at 1,909 m/s, at essentially 100% efficiency.[175] Unlike the nitrogen tests, c^* efficiency decayed rapidly (Figure 6-52), falling to 0.62 at test's end. This appears to be due to two factors: (1) ammonia's substantially higher C_p, which draws proportionally more heat from the receiver than a similar mass flow rate of nitrogen, and (2) ammonia's tendency to thermally dissociate into nitrogen and hydrogen, a strongly endothermic reaction. While this dissociation is advantageous in one important respect—since it increases the flow's c^* for a given temperature—it is undesirable in that it extracts a great deal of heat energy, limiting burn times and total applied impulse. Calculated c^* efficiency during the low-temperature run ranged between 0.46 and 0.72.

The 27-C test ran to nearly thirty minutes of total firing time in ammonia. When the Mk. II receiver was removed from its insulation package and examined, it was found that it had undergone superficial changes, more pronounced than those seen during the heating profile tests conducted earlier. The author noted that a white particulate precipitate surrounded the receiver nozzle exit, while large (up to 0.5 cm) globules of hard, dark material formed in the nozzle extension of the graphite foam insulation package (Figure 6-54). Blistering on the receiver sides appeared more pronounced than that seen during heating tests, with large raised spots on the surface, silver-grey in colour (Figure 6-55). These blisters did not form on the cavity aperture section or the nozzle, and were confined primarily to the ends of the cylindrical section. The middle of the cylindrical section was coated in material with colours ranging from purple to orange-yellow.

---

[174] Ammonia flow was shut off in the trial's 66th minute to permit more rapid heating to peak temperature.

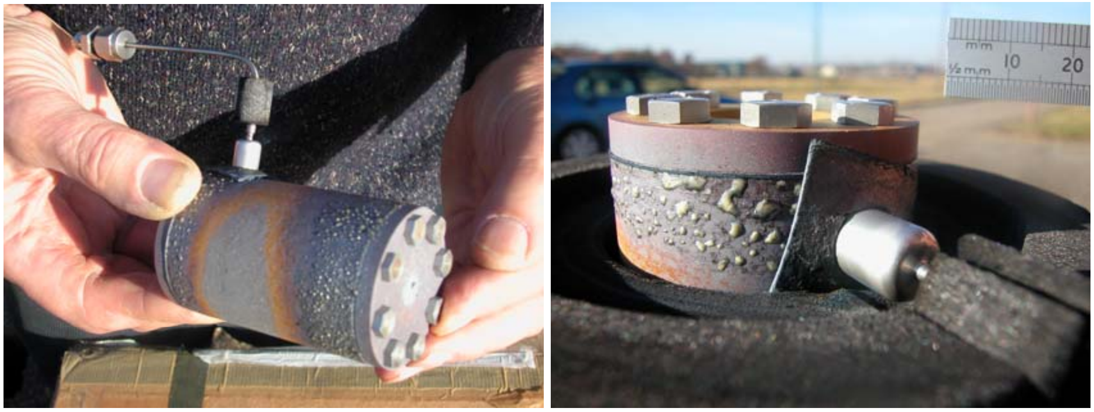

Figure 6-55 Mk. II receiver following Test 27-C (left). Detail of precipitate blisters near feedline (right).

Samples of the particulate precipitate, dark globules, and surface coating were delivered to the University of Surrey's Chemistry Department for characterisation. The samples were prepared in a manner similar to that described in Section 6.2.2 and analysed to determine elemental composition. Results were roughly similar to those seen for the Mk. I cavity; all samples contained elevated levels of titanium metal, in some cases constituting 3% of the sample's initial mass. As noted previously, the particular mass spectrometry technique utilised is not capable of providing carbon or volatile gas composition, since these elements are either digested during the initial preparation of samples or are masked by the nitric acid used for the digestion process.

Samples shown in Table 6-6 are numbered and refer to the following:

1. Sample 1: iridescent orange deposit on Mk. II receiver following N_2 and NH_3 flow tests.
2. Sample 2: same as (1), from different area of receiver.
3. Sample 3: white precipitate around nozzle exit, Mk. II receiver.
4. Sample 4: black deposit on Mk. I cavity fore plenum surface (Figure 6-31).

---

[175] Full ammonia decomposition to N_2 and H_2 was assumed, which accords well with the measured data.

5. Sample 5: copper-coloured deposit on Mk. I cavity fore plenum surface.
6. Sample 6: dark globules from Mk. II insulation package bottom.
7. Sample 7: same as (6).
8. Sample 8: silver-grey deposit on Mk. II receiver side.
9. Sample 9: same as (8).

Titanium-bearing, coloured precipitate appeared to emerge from most of the exposed surfaces on the Mk. II receiver during flow testing (samples 1, 2, and 3). This was most likely boric oxide binder exuded from the surface, carrying with it some of the matrix material (TiB_2 and BN) or chemical re-combinations, such as TiN. The dark globules seen on the insulation package contain a relatively small fraction of titanium. They are most likely boric oxide with a graphitic component, providing the dark colour. The author has surmised that these materials are precipitated during the initial heatup, potentially blocking the propellant flow passages. This may be the cause of the three flow stoppages seen in Test 27-C.

Element/ Sample	1	2	3	4	5	6	7	8	9
B (ppm)	1,604	2763	5,041	432	3,968	342	101	601	880
Al	1,038	1,644	3,281	401	3,860	169	266	578	712
Ti	10,068	15,938	32,908	1,355	3,604	1,318	1,176	291	322
V	41	32	45	4.4	32.7	0.6	0.9	2.1	3.1
Cr	129	182	375	30	340	5.7	12.6	47	73
Mn	333	462	1,050	95	1,073	17	37	159	222
Fe	2,238	3518	7,324	652	6,492	112	231	966	1,302
Co	3.7	5.6	10.9	2.4	36.5	1.4	1.5	1.3	1.7
Ni	328	317	954	443	2714	7.8	16.3	294	264
Cu	33.4	40.5	76.1	8.2	60.4	1.6	2.9	8.6	11.6
Mo	13.1	17.1	23.7	2.2	185.8	2.8	3.9	5.2	3.3
Ta	< 0.1	< 0.1	< 0.1	< 0.1	< 0.1	< 0.1	< 0.1	< 0.1	< 0.1
Zn	300	309	1,252	46	350	7.3	11.5	87.6	112.3

Table 6-6 Induction-coupled mass spectrometry results from Mk. I and Mk. II receiver samples.

Pressure drop calibrations, necessary for performing analysis on flow test data, were acquired during Tests 28 and 29, which were run under ambient pressure conditions. Both nitrogen and helium were used. A pristine Mk. II receiver was assembled and the nozzle section tapped, permitting a direct measurement of chamber pressure.

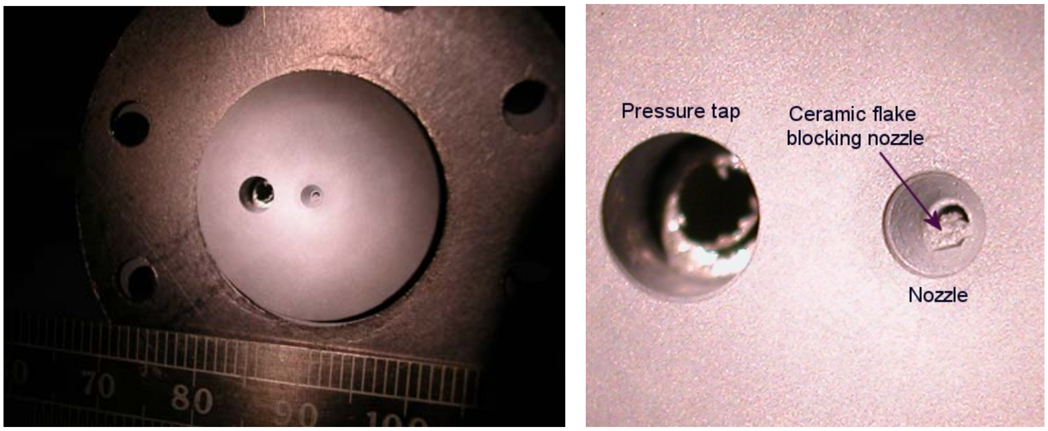

Figure 6-56 Mk. II nozzle section (left) utilised for ambient pressure drop tests, with detail (right).

Test 29 specifically examined the role of the nozzle in vena contracta formation. Both a full nozzle and an orifice (with no divergent section) were tested, with no appreciable difference between measured mass flow and inlet/chamber pressures.[176] Following the final Test 28 run, a flake of ceramic material was discovered in the nozzle (Figure 6-56, right). This lent credence to the theory that a sufficiently large fragment of receiver material could break away from the main body during firing, partially or fully blocking the nozzle.

---

[176] With test equipment occasionally registering discharge coefficients (i.e., ratio of measured mass flow to ideal mass flow rate) below the theoretical minimum of 0.6, the author wanted to confirm that nozzle losses could not be responsible for this effect. Test 29 results led to the identification of the mass flow deficit problem in the thermal mass flow meter, subsequently confirmed in calibration runs.

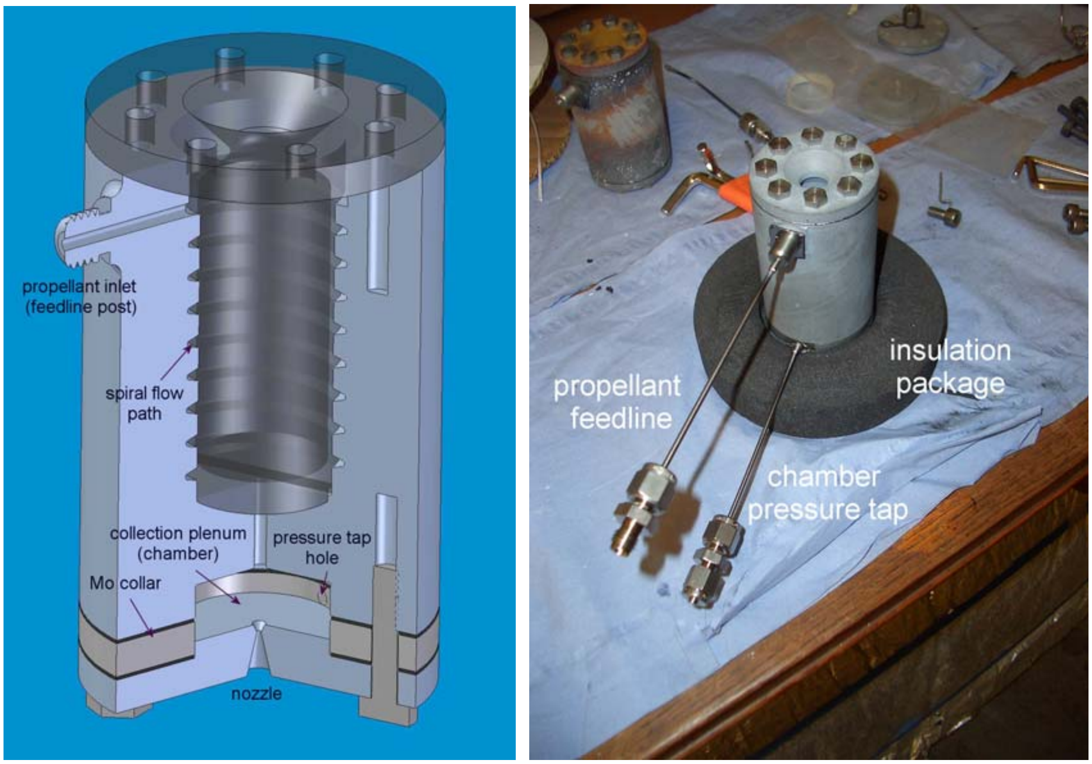

Figure 6-57 Cutaway view of Mk. II receiver with chamber pressure tap collar (left). Assembled receiver prior to beginning Test 30 series (right).

The final round of flow testing was intended to rectify some of the shortcomings in test results found during Test 27. These included (a) an inability to record chamber pressures during firing, necessitating an estimate based on either a theoretical or measured pressure drop, (b) reliance on a potentially faulty mass flow measurement device, and (c) a lack of thrust data, which prevents an estimation of vacuum specific impulse. In order to overcome the problem of measuring chamber pressure at high temperatures, a refractory metal pressure tap was devised and welded to molybdenum tube, which in turn was connected to a 16-bar (gauge) pressure transmitter (Figure 6-57). The pressure tap was sealed to a molybdenum collar extension on the Mk. II receiver. The suspect thermal mass flow meter was discarded in favour of a catch-and-weigh scheme: a small gas bottle was filled from one of the large gas supply bottles, then placed on a precision scale and the difference between pre- and post-firing weights recorded, providing a time-averaged mass flow rate over a specified period. Finally, a thrust stand, fabricated by Mr. M. Paul (Figure 6-58) of Surrey Satellite Technologies, Ltd., was assembled inside the F Site vacuum chamber. The stand was designed around a 10-kilogram load cell; propellant exiting the receiver nozzle applied an upward force to the cavity heating test rig, reducing the load on the load cell. This difference was noted on a precision multimeter (Figure 6-38, right).

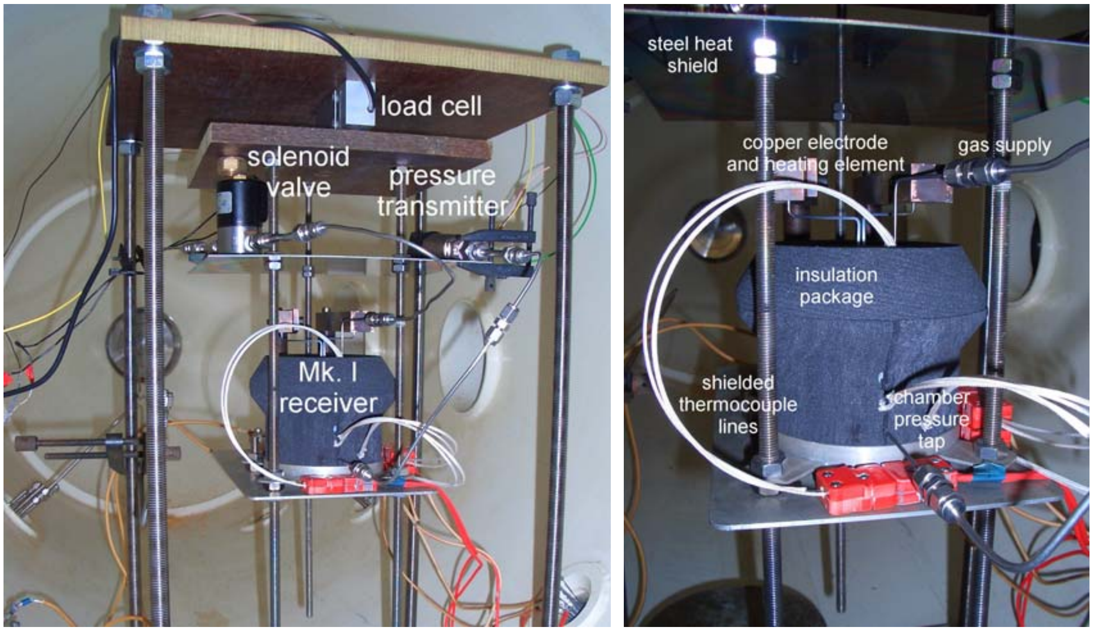
load cell
solenoid valve
pressure transmitter
Mk. I receiver
steel heat shield
copper electrode and heating element
gas supply
insulation package
shielded thermocouple lines
chamber pressure tap

Figure 6-58 Flow testing with installed thrust stand.

The solenoid valve and chamber pressure transmitter were mounted to a stainless steel heat shield above the receiver. The intent of this was to mitigate line stiffening (and concomitant weight changes) following pressurization. The thrust stand was initially calibrated without an amplifier; therefore, the largest unamplified signal received at the multimeter was on the order of just 0.01 mV. The calibration, performed with several 10 gram weights, provided a thrust scale factor of 4.31 ± 0.17 N/mV (±3.9%) over fifteen trials.[177] After installing a transducer and amplifying this signal by a factor of over 850, a similar trial series resulted in a scale factor of 3.72 ± 0.06 N/V (±1.6%).

Table 6-7 lists a series of preliminary thrust measurement trials and their associated results, performed at the Westcott F Site. Initial testing at ambient pressure duplicated the results of the flow rate validation test performed earlier and discussed in Section 6.2.1: Namely, at supply pressures of as high as 12.5 bar (gauge), sub-unity thrust coefficients were measured. Once the chamber door was closed and pressure reduced, thrust increased substantially. Vena contracta effects, as noted previously, were accounted for by an adjustment factor to throat area based on chamber pressure.[178] An engine's thrust coefficient can be determined from thrust and chamber pressure measurements:

$$C_f = \frac{T}{P_c A_t} - \frac{A_e}{A_t}\frac{P_a}{P_c} \qquad (6\text{-}14)$$

---

[177] Weights of up to 72.3 g (709 mN equivalent thrust) were used.

[178] The nitrogen adjustment factor for effective throat area was not applied to He or NH_3 cases.

The second term in this equation can be ignored when vacuum conditions obtain ($P_a << P_c$). It can also be calculated from the equivalent formulation [Hill, 1992]:

$$C_f = \sqrt{\frac{2\gamma^2}{\gamma - 1}\left(\frac{2}{\gamma + 1}\right)^{\frac{\gamma+1}{\gamma-1}}\left[1 - \left(\frac{P_e}{P_a}\right)^{\frac{\gamma-1}{\gamma}}\right]} + \frac{P_e - P_a}{P_c}\frac{A_e}{A_t} \tag{6-15}$$

The exhaust velocity of a rocket (u_e) was introduced in Section 4.1.1, and is simply:

$$u_e = C_f c^* \tag{6-16}$$

Thus, if C_f and c^* are known, u_e (and therefore I_{sp}) can be determined directly.

Test No.	Receiver Type	Gas type	Peak thrust (mN)	Coefficient of thrust (C_f)	Penetration temp (°C/K), at flow start	Peak c*, m/s, estimated / I_{sp}, s (estimated)	Thrust stand
30	**Mk. II (3)**	**N_2**	**460**	**1.65**	**ambient**	**429 / 72**	**Yes**
30-A	**Mk. II (3)**	**N_2**	**471**	**--**	**ambient**	**429 / ***	**Yes**
30-A2	**Mk. II (3)**	**N_2**	**468**	**1.61**	**ambient**	**429 / 70**	**Yes**
30-B	**Mk. II (3)**	**He**	**442**	**1.48**	**ambient**	**429 / 162**	**Yes**
30-C	**Mk. II (3)**	**He**	**445**	**--**	**ambient**	**1,070 / ***	**Yes**
30-C2	**Mk. II (3)**	**He**	**435**	**1.45**	**ambient**	**1,070 / 158**	**Yes**
30-C3	**Mk. II (3)**	**He**	**435**	**1.42**	**ambient**	**1,070 / 155**	**Yes**
30-C4	**Mk. II (3)**	**He**	**(1) 438**	**1.58**	**ambient**	**1,070 / 173**	**Yes**
			(2) 453	**1.58**			
30-C5	**Mk. II (3)**	**He**	**(1) 241**	**1.56**	**ambient**	**1,070 / 170**	**Yes**
			(2) 245	**1.52**			
30-C6	**Mk. II (3)**	**He**	**(1) 128**	**1.50**	**ambient**	**1,070 / 164**	**Yes**
			(2) 128	**1.47**			

* = Specific impulse not calculated (no pressure trace data available)

Table 6-7 Ambient (no heating) thrust measurement tests, Mk. II receiver, in nitrogen and helium.

C_f figures tabulated in Table 6-7 are accurate to ± 3.75%.[179] Since these trials were conducted at ambient temperatures, c^* is known to within ± 15 m/s (3.5%) for nitrogen, ± 19 m/s (1.8%) for helium, and ± 10 m/s (1.8%) for ammonia.[180] Here, thrust coefficients are found to be within the margin of error of the calculated ideal values: 1.71 for nitrogen, 1.60 for helium, and 1.71 for ammonia. Specific impulse figures, with a margin of error of ± 7.25%, are also close to ideal.[181]

Test No.	Receiver Type	Gas type	Peak thrust (mN)	Coeff. of thrust (C_f)	Penetration temp (°C/K), at flow start	Peak c*, m/s, estimated / I_{sp}, s (estimated)	Thrust stand
30-D	**Mk. II (3)**	**NH_3**	**(1) 245**	**1.76**	**ambient**	**548 / 98**	**Yes**
			(2) 197	**1.76**		**548 / 98**	

---

[179] This includes the aforementioned thrust measurement error, in addition to errors on pressure measurement (± 909 Pa) and throat diameter (± .05 mm). As will be seen, thrust measurement during hot flow trials introduces additional error.

[180] This presumes an ambient temperature of 293 ± 10 K.

[181] Theoretical performance in vacuum is 76 s for nitrogen and 179 s for helium [Sutton, 2001].

30-E	**Mk. II (3)**	**NH_3**	**(1) 303**	**1.80**	**ambient**	**548 / 101**	**Yes**
			(2) 226	**1.81**		**548 / 101**	
30-F	**Mk. II (3)**	**N_2**	**(1) 500**	**1.50**	**315 / 588**	**550 / 84**	**Yes**
			(2) 482	**1.45**	**664 / 937**	*** / ***	
			(3) 500	**1.49**	**694 / 967**	**551 / 84**	
			(4) 511	**1.59**	**1,007 / 1,280**	**647 / 105**	
			(5) 472	**1.46**	**1,013 / 1,286**	**662 / 99**	
30-G	**Mk. II (3)**	**He**	**(1) 446**	**1.42**	**379 / 652**	**1,428 / 207**	**Yes**
			(2) 460	**1.42**	**427 / 700**	**1,511 / 219**	
			(3) 380	**1.23**	**925 / 1,198**	**1,572 / 197**	
			(4) 400	**1.26**	**960 / 1,233**	**1,675 / 215**	
			(5) 330	**1.06**	**1,090 / 1,363**	**1,753 / 190**	
			(6) 402	**1.26**	**1,005 / 1,278**	**1,669 / 215**	
30-H	**Mk. II (3)**	**NH_3**	**(1) 237**	**1.65**	**358 / 631**	**792 / 133**	**Yes**
			(2) 220	**1.74**	**437 / 710**	**755 / 133**	
			(3) 183	**1.56**	**760 / 1,033**	**874 / 139**	
			(4) 186	**1.78**	**783 / 1,056**	**904 / 164**	
			(5) 165	**1.18**	**1,121 / 1,394**	**1,188 / 143**	
			(6) 146	**1.11**	**1,085 / 1,358**	**1,001 / 114**	
			(7) 172	**1.36**	**1,121 / 1,394**	**1,576 / 219**	
			(8) 164	**1.44**	**1,348 / 1,621**	**1,610 / 237**	
			(9) 164	**1.51**	**1,354 / 1,627**	**1,483 / 229**	
			(10) 135	**1.34**	**1,309 / 1,582**	**1,534 / 210**	
31-A	**Mk. I (2)**	**NH_3**	**(1) 274**	**1.70**	**ambient**	**548 / 95**	**Yes**
			(2) 223	**1.76**		**548 / 98**	
31-B	**Mk. I (2)**	**NH_3**	**197**	**1.79**	**ambient**	**548 / 100**	**Yes**
31-C	**Mk. I (2)**	**NH_3**	**(1) 219**	**1.42**	**366 / 639**	**1,103 / 160**	**Yes**
			(2) 223	**1.38**	**392 / 665**	**1,077 / 152**	
			(3) 183	**1.11**	**730 / 1,003**	**1,389 / 157**	
			(4) 190	**1.12**	**735 / 1,008**	**1,360 / 155**	

Table 6-8 Hot flow thrust measurement trials in helium, nitrogen, and ammonia.

Results of the hot flow trials utilising both the Mk. I and Mk. II receivers are shown in Table 6-8. The first of these tests to be performed (Test 30-F), was conducted in nitrogen, reaching nearly 1,300 K, an output of over 500 mN of thrust, but a peak specific impulse of only 105 seconds (Figure 6-59). *C** efficiency peaked during the first firing (0.90); thereafter, measured *c** dropped to just 70% of the ideal value and never recovered. Thrust coefficients decayed during this run, but only slightly. This observation, coupled with the anomalously low *c** efficiency figures, led the author to theorise that, at high temperatures and chamber pressures, a leak path developed in the receiver, presumably along one of the five graphite foil seals,[182] increasing the effective throat area. The addition of the molybdenum pressure tap collar (contributing two extra sealing interfaces, Figure 6-60) increased the likelihood of a leak. This leak path appeared to reseal as temperatures declined, resulting in near-theoretical low-temperature performance. As recorded mass flow rates did not decline with temperature as rapidly as theory predicts, this would also tend to confirm that the discrepancy was most likely due to the introduction of leak paths through seals.

---

[182] The five include a ceramic-to-ceramic and two ceramic-to-metal face seals, the propellant feedline connection, and the chamber pressure tap interface to the molybdenum collar.

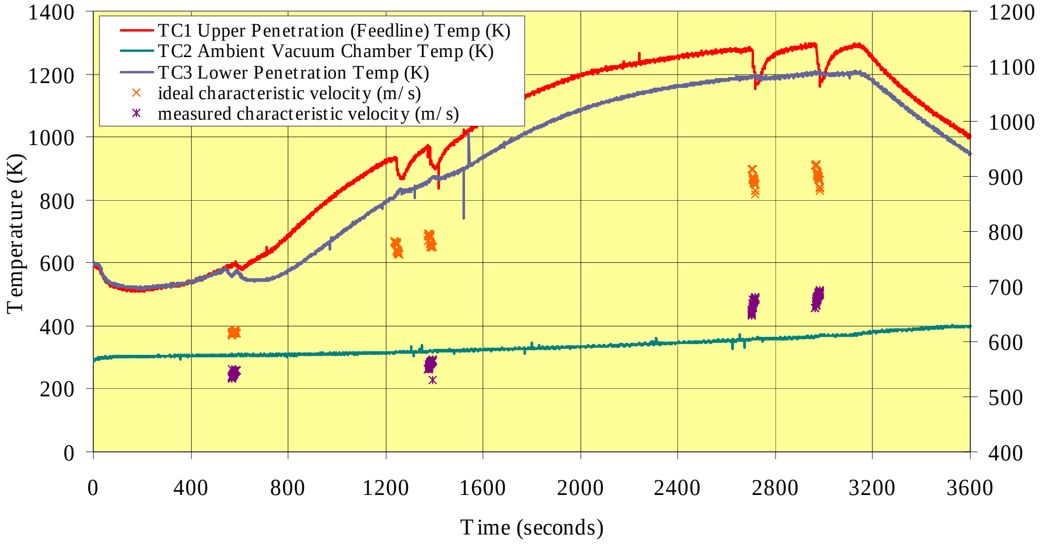

Figure 6-59 Temperature and characteristic velocity (measured and ideal), nitrogen flow trial, Test 30-F (12 December 2003).

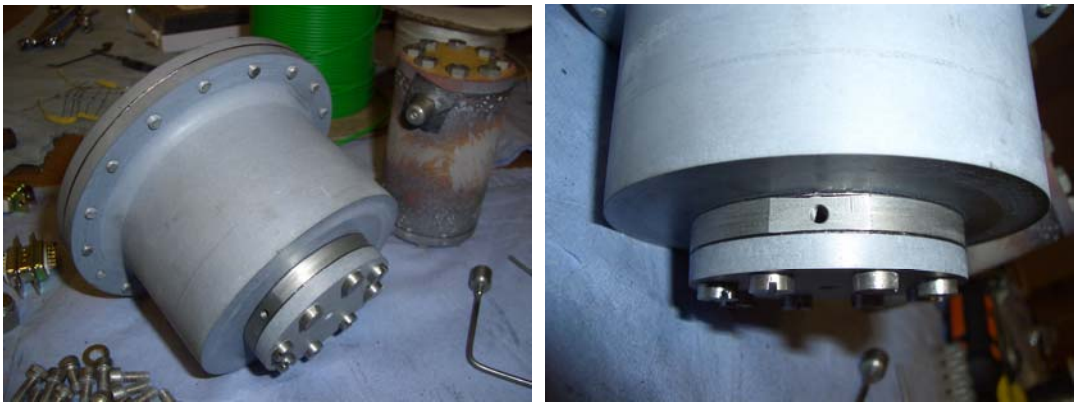

Figure 6-60 Mk. I receiver with chamber pressure tap collar.

This theory was borne out by additional hot flow trials in helium and ammonia. Test 30-G (helium) demonstrated similar thrust coefficient decay, at temperatures exceeding 1,000 K. While ambient testing in helium exhibited C_f figures of between 1.42 and 1.58,[183] high-temperature testing recorded values as low as 1.06. Similarly, Test 30-H (ammonia) produced the highest specific impulses recorded (237 s) but highly variable thrust coefficients at higher temperatures. Several anomalously low values (i.e., 1.18 and 1.11, respectively) were seen at intermediate temperatures. These can be compared to ambient tests and corresponding theoretical predictions, which agree with each other to within 6%.[184] These discrepancies substantially impact specific impulse: Since exhaust velocity (Equation 6-16) is directly proportional to the product of C_f and c*, a 15% drop in C_f translates to an I_{sp} loss of over 40 seconds at 1,621 K.

---

[183] The theoretical value of C_f for helium, at 293 K and zero ambient pressure, is 1.60.

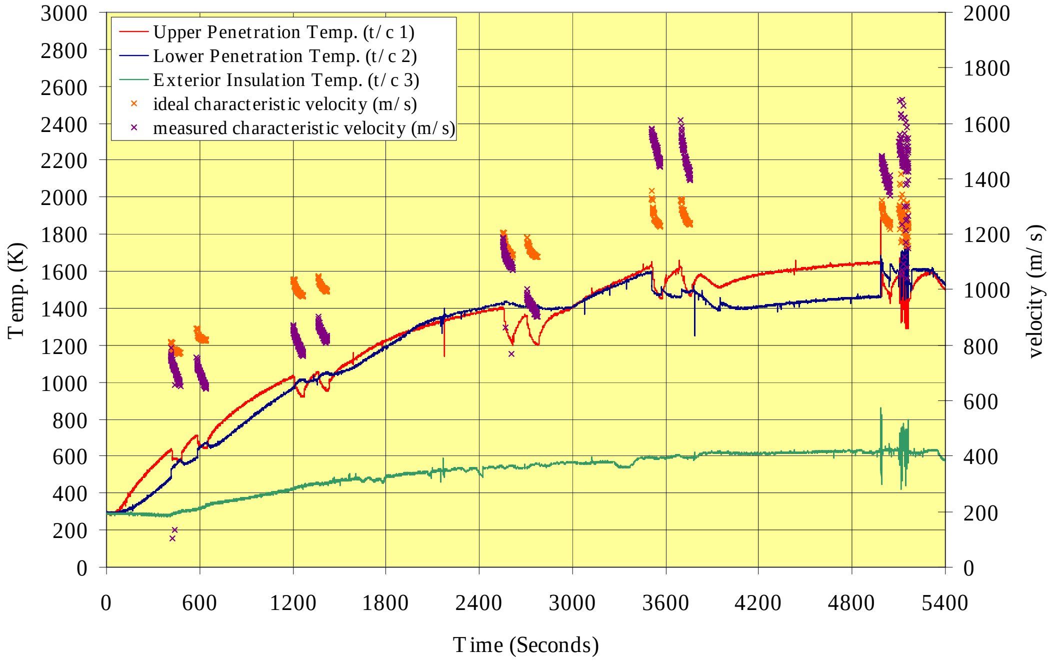

Figure 6-61 Temperature and characteristic velocity (measured and ideal), ammonia flow trial, Test 30-H (8 January 2004).

Characteristic velocity was observed to rise slowly near 1,000 K and then increase rapidly above this temperature, apparently exceeding ideal c* estimates (Figure 6-61). The rapid rise was most likely due to the strongly endothermic ammonia decomposition occurring at these temperatures, which, once overcome, lowers the gas mixture's molecular weight from 17 g/mol to as little as 8.5 g/mol, increasing c*.[185] Pressure traces from these trials indicated a substantial fall in supply (vapour) pressure during the course of the 60-second test firings. Ammonia's high heat of vaporisation extracts a large quantity of heat from the small supply bottle, lowering its temperature and vapour pressure (Figure 6-63). The temperature dropped sufficiently for ice to form on the outer surface of the tank within 30 seconds. Application of heat to the tank, via a hot air dryer, was required to re-establish nominal supply pressure.

---

[184] Ammonia's theoretical C_f is approximately 1.70 at ambient temperatures and zero ambient pressure. At higher temperatures, ammonia will dissociate. Thrust coefficient rises slightly (to 1.80).

[185] This figure presumes no ammonia dissociation takes place in the receiver. Below 1,600 K, this assumption holds true (see Section 5.4). Above this temperature, ammonia dissociation becomes significant and c* efficiencies appear to rise above unity. In actuality, decomposition lowers the mean molecular weight of the propellant gas, raising ideal c* (Figure 6-62). At 1,600 K, gas residence time in the receiver is insufficient to produce substantial dissociation. At 1,825 K, dissociation is nearly total.

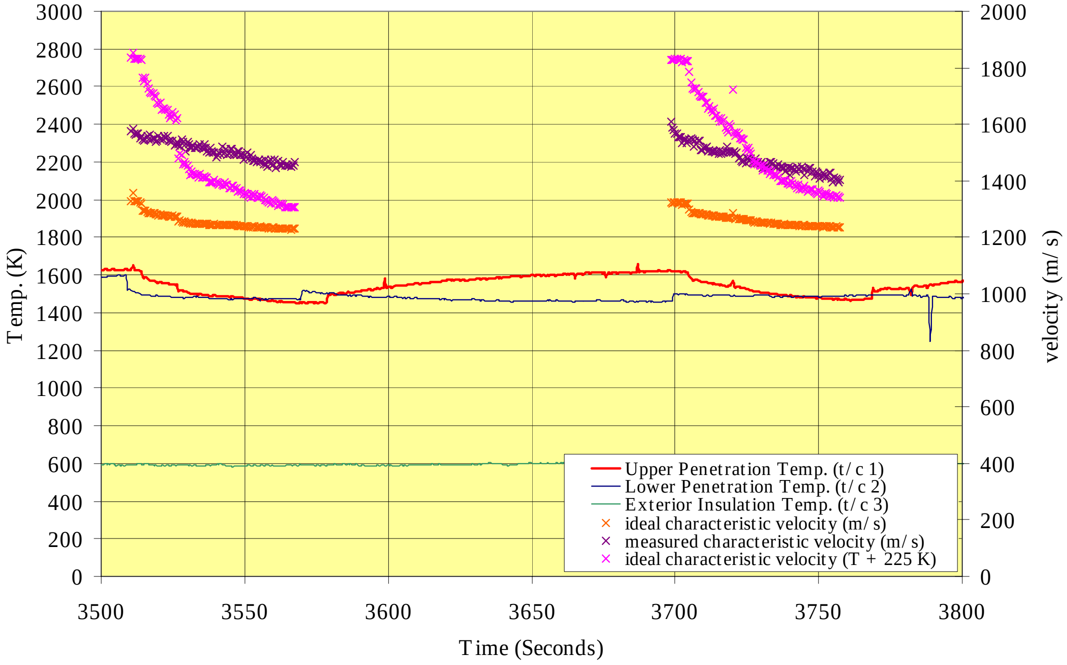

Figure 6-62 Test 30-H detail, with ideal *c estimates (no dissociation and partial dissociation).**

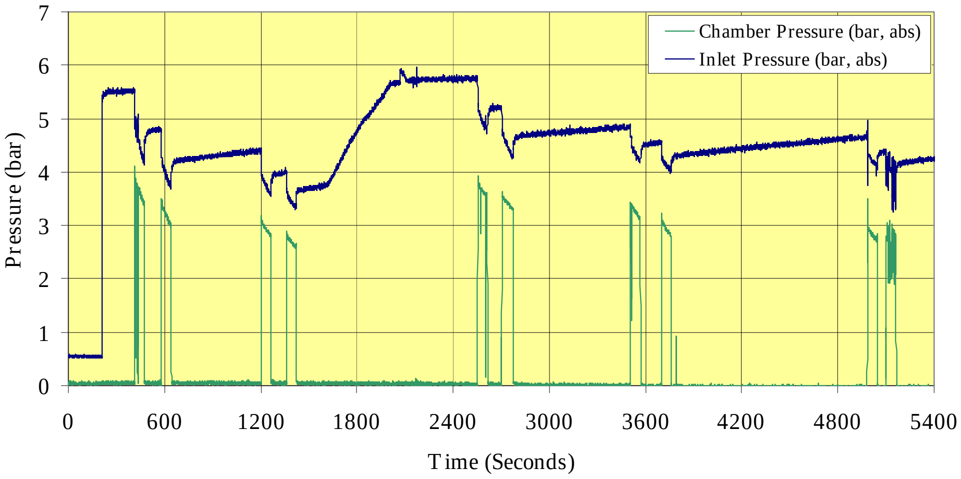

Figure 6-63 Inlet and chamber pressure trace measurements, ammonia flow trial, Test 30-H.

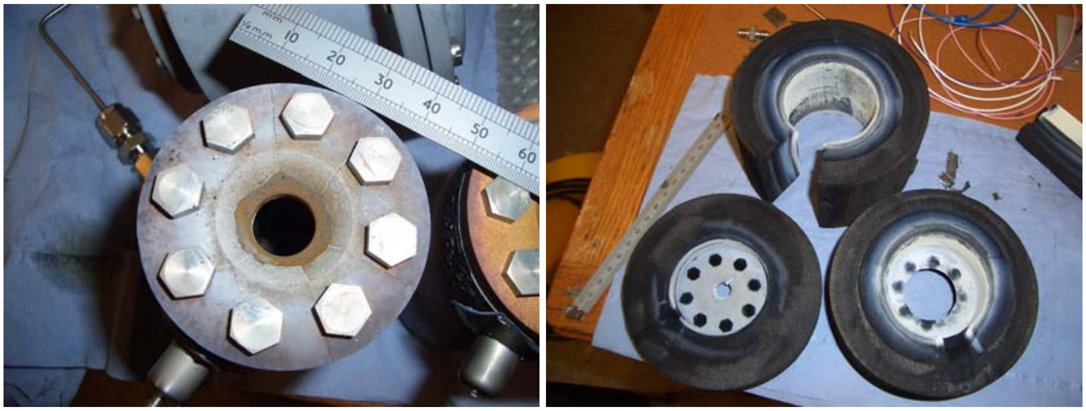

Figure 6-64 Mk. II solar receiver, top surface detail showing circumferential and radial cracking (left). Mk. II receiver insulation package displaying white powder precipitate (right).

Following this final test of the Mk. II cavity receiver, the insulation package was removed and the assembly inspected. As before, a discolouration of the receiver body about its circumference, dark red in colour, was noted. The internal surface of the receiver insulation package was coated with a white, powdery substance; this material was also found on the tantalum leads of the heater element. This was most likely due, as seen with previous tests, to boric oxide binder outgassing. The top of the receiver displayed several fine cracks, including one running entirely around the circumference of the cavity aperture, with multiple radial cracks (Figure 6-64). These cracks did not extend through the thickness of the aperture section; furthermore, while several of the radial cracks emanated from a bolt location, some did not, and so it was not possible to conclude that the cracks resulted only from over tightening of the bolts prior to testing. The surface of the aperture between the circumferential crack and the aperture edge was also discoloured. Despite these superficial changes, there was no indication of mass loss or deformation, and no observational evidence that the Mk. II receiver's seals suffered any degradation or breach.

Following this last Mk. II trial, a second Mk. I cavity receiver was prepared for flow testing. Since these receivers were initially designed to take brazed feedline fittings, the receiver was modified to accept a screwfit molybdenum cap. It was then placed in an insulation package and tested twice at ambient temperatures with ammonia propellant. In both cases, performance was seen to approximate the theoretical: C_f values ranged between 1.70 and 1.79. During the heating trial (Test 31-C), thrust coefficient was seen to drop significantly, to 1.38 (at 665 K) and 1.11 (at 1,003 K), indicating the opening of a leak path similar to that seen in Mk. II testing.

The Mk. I's particle bed permitted near-theoretical characteristic velocities at low temperatures. At the 1,000 K plateau, c^* efficiency remained near unity (Figure 6-65). The calculation of c^* in this case was not complicated by the effects of ammonia dissociation (seen in Test 30-H); peak temperature did not rise sufficiently to permit significant decomposition to take place.

A total of four successful firings were made (Figure 6-67, left); the fifth attempt, in the 116th minute of the test, resulted in a rupture of the top flange of the receiver, fracture of the insulation package top cap, and subsequent failure of the electrical heating element. The receiver temperature at failure was above 1,200 K.

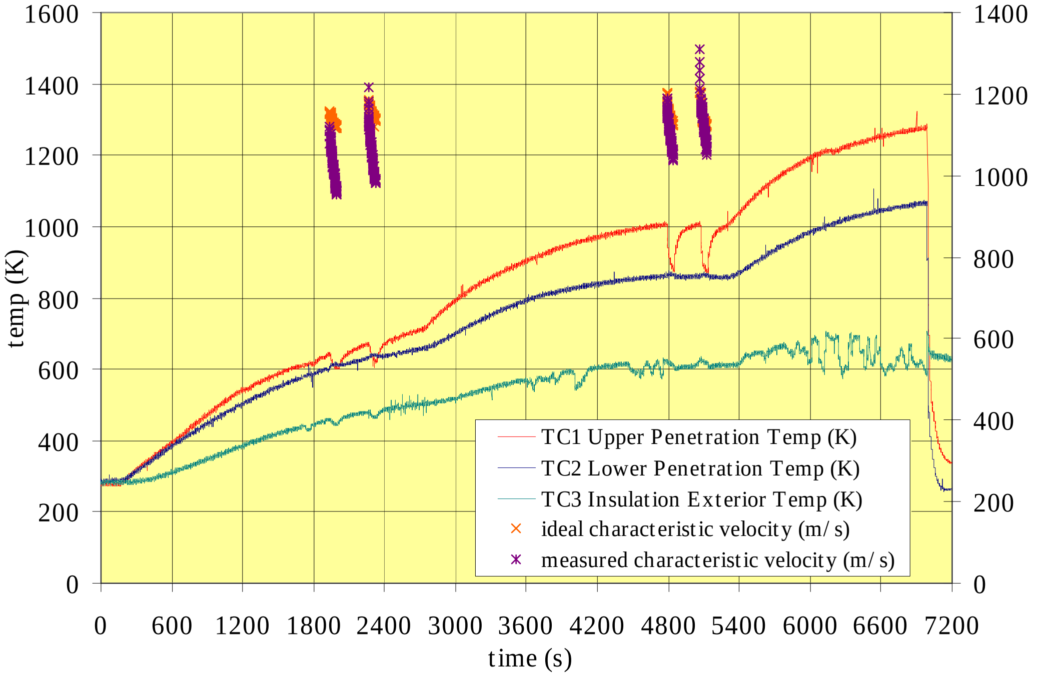

Figure 6-65 Temperature and characteristic velocity (measured and ideal), ammonia flow trial, Test 31-C (14 January 2004).

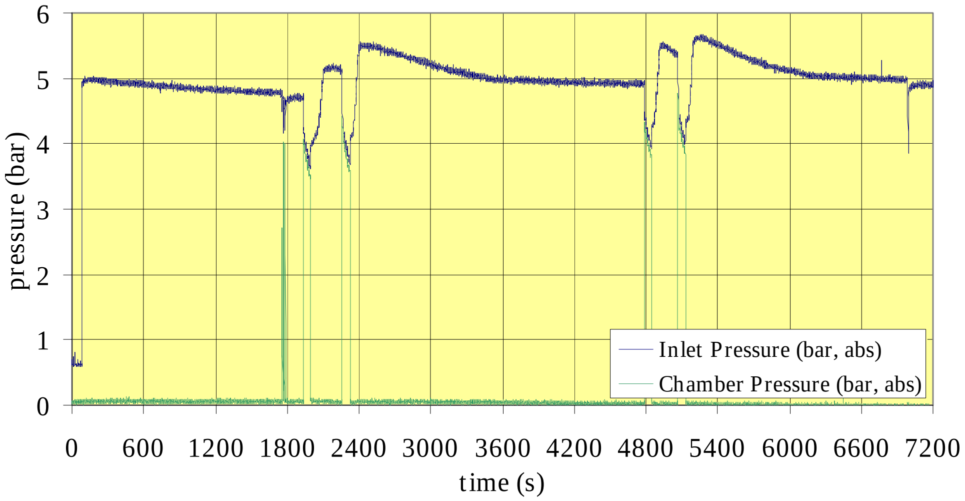

Figure 6-66 Inlet and chamber pressure trace measurements, ammonia flow trial, Test 31-C.

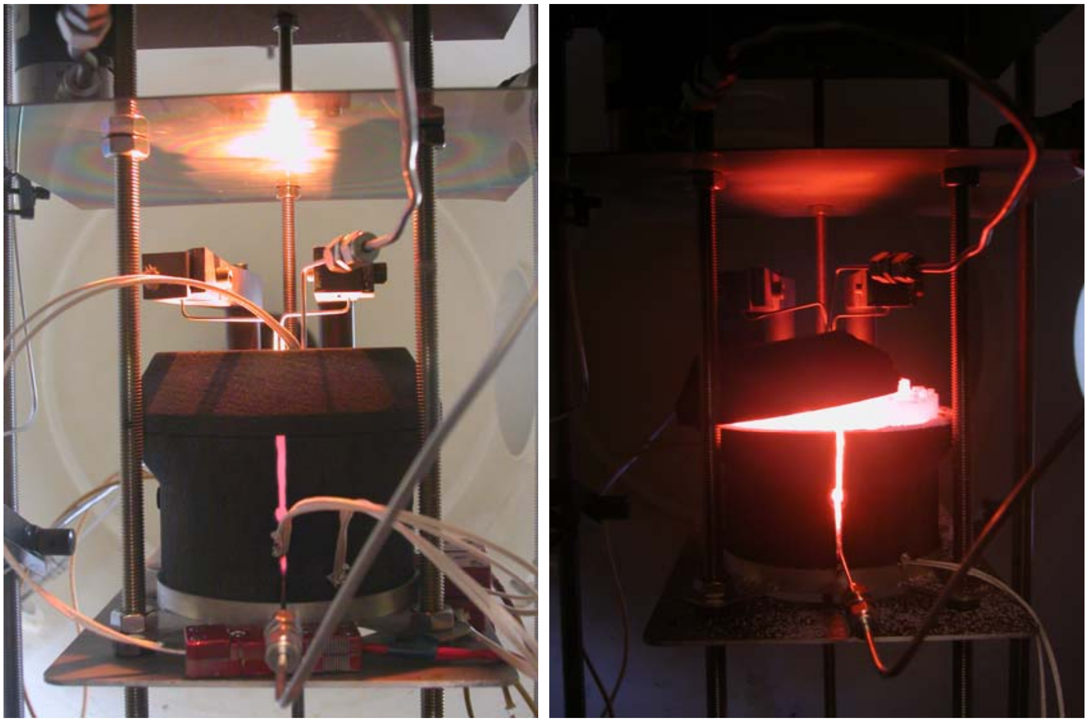

Figure 6-67 Mk. I receiver in ammonia flow testing (left) and following flange failure (right).

The failure occurred precisely when flow was introduced to the Mk. I and appeared to have originated at one or two bolt sites on the top flange of the receiver (Figure 6-68, left). The feedline post was sheared away following this event, interrupting propellant flow, and upper/lower receiver penetration thermocouples were thrown free. The boron nitride particle bed was exposed, and the particles themselves scattered around the vacuum chamber. Post-test examination of the structure led the author to conclude that directly bonding metal screws to threaded holes in the (relatively brittle) ceramic structure's outsize top flange led to cracking of the threads, bolt loosening, and potential pre-failure leaks. A superior solution would have involved the use of molybdenum nuts to direct tensile stress away from the ceramic structure.[186]

The results of the hot flow trials provided substantial test data on two novel all-ceramic solar thermal rocket engines. Both receivers performed well in ambient testing but showed signs of moderate leakage (i.e., thrust coefficient decay) at higher temperatures when outfitted with chamber pressure taps. While the author encountered a number of difficulties in properly engineering ceramic structures for mechanical bonding and subsequent operation at high temperatures and pressures, many of these problems were either overcome or appear to have ready solutions. For example, the Mk. I nozzle (Figure 6-68, right) evinced no signs of precipitate deposition following ammonia propellant flow at high temperatures, possibly due to the boron nitride particle bed's action as a filter for boric oxide departing the matrix. A flight-type Mk. III receiver, similar in design to its predecessors, could incorporate the advantageous design aspects of both the Mk. I (high heat transfer capability, low pressure drop, filtration of precipitates) and Mk. II (structural stability, rapid thermal charging).

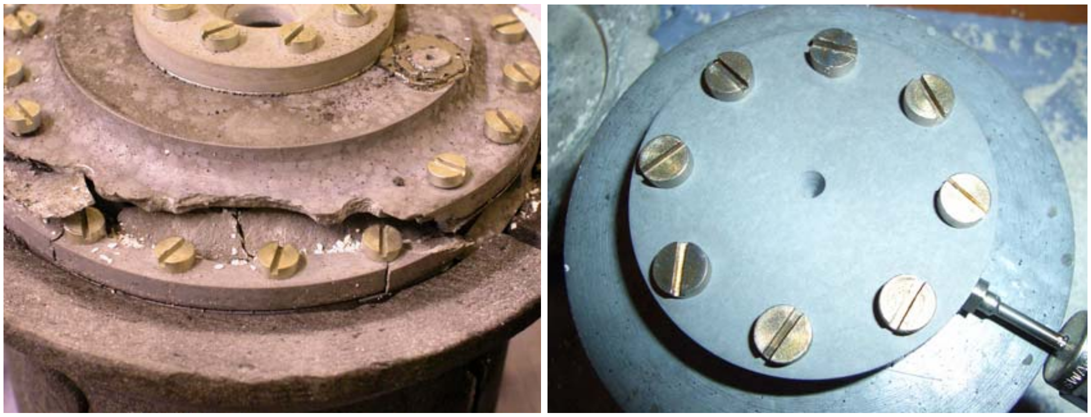

Figure 6-68 Mk. I receiver flange failure detail (left). Mk. I nozzle detail, post-firing (right).

6.3 Concentrator Testing

As noted in Section 6.2, the primary focus of the present research effort fell on the development a small, reliable, moderate-temperature (~2,000 K) receiver subsystem. Nevertheless, a substantial amount of effort was expended on the design, fabrication, and testing of several low-cost rigid concentrator schemes suitable for mounting on a small satellite. The two schemes selected for test were: (1) a large primary (56-cm diameter) aluminium concentrator, *f*/0.6, with no secondary concentration; and (2) multiple small primary (14-cm diameter) concentrators, fabricated from aluminium and PMMA, *f*/0.6, for remote receiver heating via optical fibre transmission of sunlight.

Both schemes offer maximum concentration ($\geq$10,000:1) without the need for secondary concentrators, but which demand accurate solar tracking, typically to within 0.1º. To facilitate ground testing of the concentrator mirrors, a Losmandy G-11 telescopic tracking mount (Figure 6-69) was purchased and modified to accept an outsize concentrator support structure. The Losmandy mount is capable of tracking in various modes—with solar, celestial object, and lunar rate being among the options available—and at pointing accuracies theoretically exceeding $\pm$0.00014º (one-half of an arc-second). The G-11 is rated to 60 lbm (27 kg) and is equipped with an axis polar scope for precision alignment with the polar axis.

---

[186] The receiver structure was designed to cope with stresses significantly higher than that applied during the hot flow trials. See Chapter 5.

The concentrator support structure was fabricated from aluminium plate and fixed to the G-11's saddle plate with a custom dovetail bar (Figure 6-70, right). Pass-throughs in the backing structure were created for two sensor mounts: (1) a small *f*/5 mini-Borg ranging/spotting scope with a 4.55º field-of-view, to permit manual telescopic centring of the structure's axis on the solar disk; and (2) a Kipp & Zonen CH-1 pyrheliometer, or direct solar flux measurement device, in order to gauge instantaneous flux while performing power throughput measurements. A copper heating target was mounted on an adjustable stand in the focal plane to assist in spot size and power throughput measurements, in conjunction with the 56-cm diameter concentrator. The copper target was initially plumbed to facilitate calorimetry with water flow, although this feature was later found to be unnecessary, owing to alternate power measurement methods used.

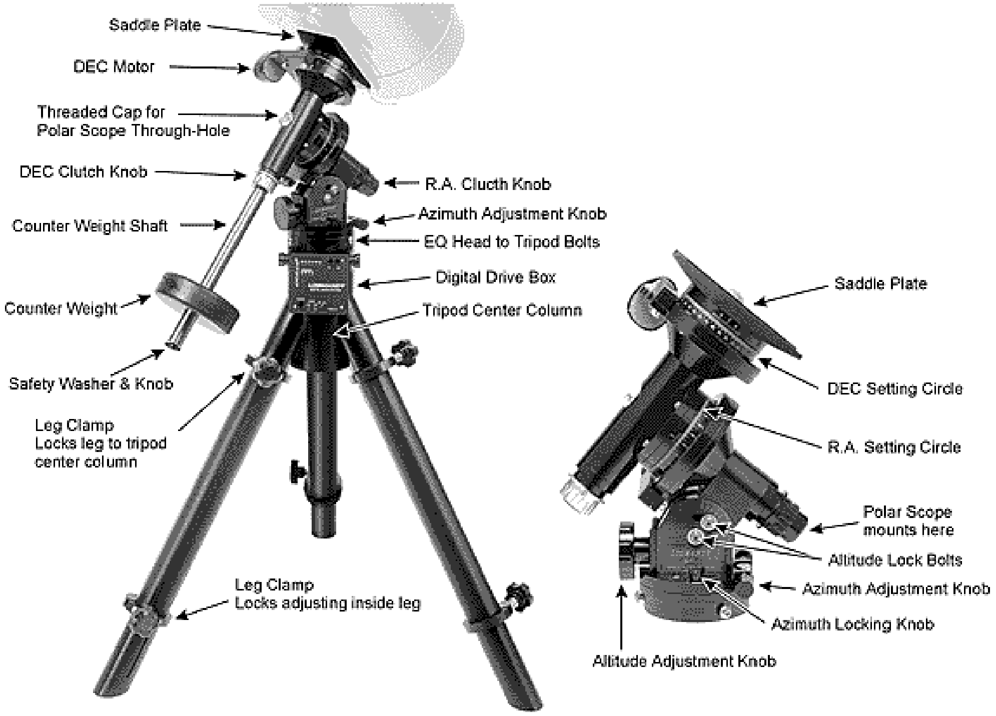
Saddle Plate
DEC Motor
Threaded Cap for Polar Scope Through-Hole
DEC Clutch Knob
R.A. Clucth Knob
Azimuth Adjustment Knob
Counter Weight Shaft
EQ Head to Tripod Bolts
Digital Drive Box
Counter Weight
Tripod Center Column
Safety Washer & Knob
Leg Clamp Locks leg to tripod center column
Leg Clamp Locks adjusting inside leg
Saddle Plate
DEC Setting Circle
R.A. Setting Circle
Polar Scope mounts here
Altitude Lock Bolts
Azimuth Adjustment Knob
Azimuth Locking Knob
Altitude Adjustment Knob

Figure 6-69 Losmandy G-11 German Equatorial Mount, with declination/right ascension axes at right [Losmandy, 2004].

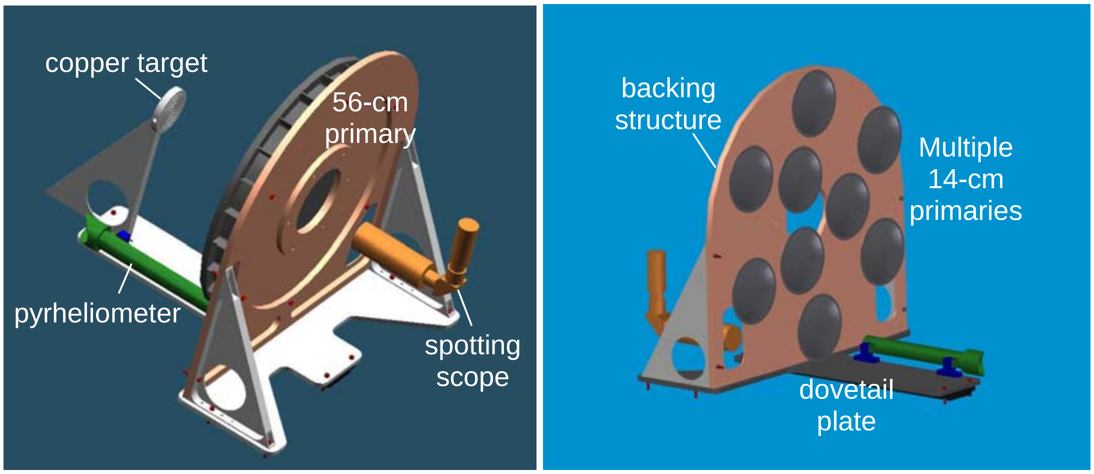

Figure 6-70 Concentrator support structure for on-sun test, in single mirror configuration (left) and multiple small mirror configuration (right).

6.3.1 Large Concentrator Properties Testing

As noted in previous sections, the Mk. I and Mk. II cavity receivers behave as near-perfect blackbodies with an aperture emissivity approaching unity. To minimise heat loss from the body, both low thermal conductivity insulation and a small optical aperture are required. At 2,500 K, a 12-mm diameter aperture will radiate approximately 250 W to space. Given that the 56-cm mirror fabricated for this effort is only capable of generating about 270 W under AM0 conditions, and that there are other significant sources of heat loss in the system—to include radiative losses from the insulation surface and conductive losses along the feedline and structural supports, it is clear that the smallest achievable aperture—and thus the highest concentration ratio, is needed.

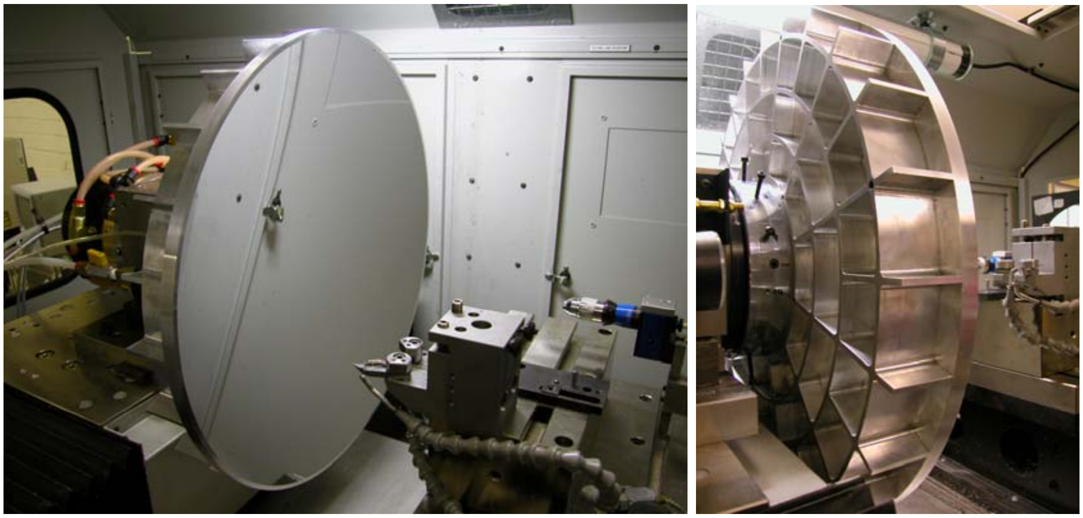

Figure 6-71 56-cm aluminium concentrating mirror on diamond turning tool following fabrication.

The 56-cm, 15-kg aluminium mirror (Figure 6-71) is an uncoated, diamond-turned optic procured from Precision-Optical Engineering (P-OE) in Hitchin, Hertfordshire, UK. The diamond-turning process permits relatively rapid fabrication of aspheric surfaces, although at form errors slightly in excess of that required for imaging optics (Chapter 4). This concentrator is a fast (fractional *f*/#) mirror with a rim angle (Φ) of 45°, a focal length of 33.7 cm, and an areal density of approximately 60 kg/m^2—slightly heavier than the solid model estimate (15 kg). Designed for maximum concentration, it should theoretically produce a solar image at the focal plane 4.9 mm in diameter.

P-OE provided interferogram and form error data for the central portion of the concentrator but was unable to sample a full diameter with their test probe. This data indicated that the mirror's peak-to-valley (PV) form error[187] is just 1.25 μm (1250 nm); the deviation from an ideal paraboloid is shown in Figure 6-72. A rough estimate of the mirror's RMS wavefront error can be determined from the form data; it is found to be approximately 1.34 microns.

Using the ray-trace software package OSLO LT (Chapter 5), the author was able to demonstrate that this level of optical performance is sufficient to produce concentration ratios of 10,000 or greater. A form error profile (i.e., the smooth curve in Figure 6-72) similar in shape to P-OE's test data produces a spot size of almost precisely 5 mm, while a similar error profile (but with an RMS form error of almost 60 microns) produces a spot nearly 10 mm in diameter. A doubling of spot size reduces effective concentration by a factor of four; thus, a mirror with 60 microns of form error can do no better than a concentration ratio of 3,250. The 60-micron figure, while not a firm upper bound, provides an order-of-magnitude estimate for acceptable form error.[188]

---

[187] P-V form error is defined here as the difference between the largest-magnitude positive and negative deviations from the ideal parabolic profile. Root-mean-square (RMS) form error and P-V form error are two common measures of mirror surface accuracy; P-V error provides a conservative (if less accurate) estimate of accuracy than does RMS error.

[188] Carbon fiber composite and ceramic mirrors for space applications, which exhibit form errors on the order of microns, should therefore be capable of concentrating sunlight to the level desired.

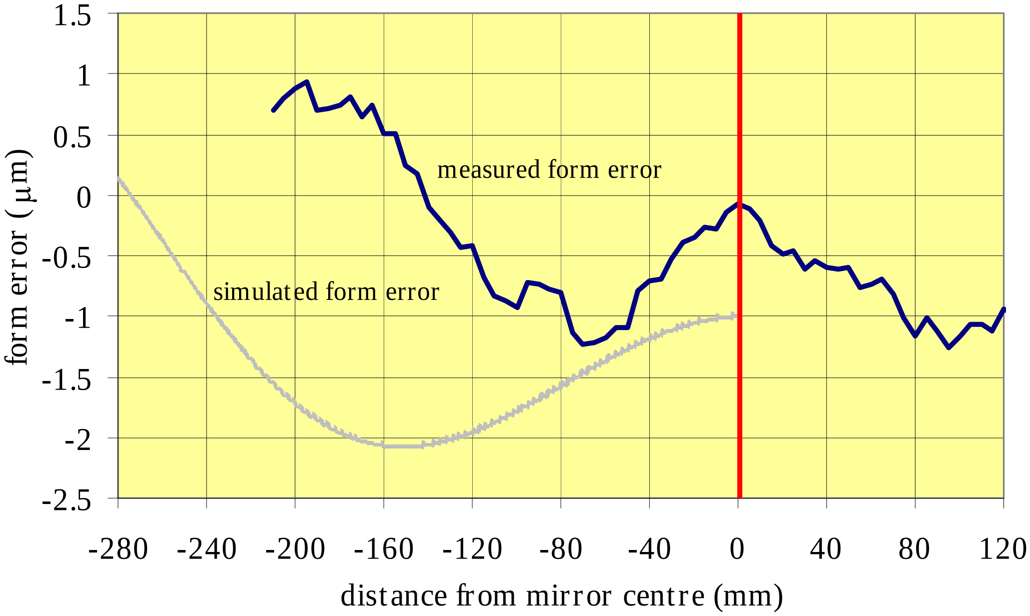

Figure 6-72 56-cm mirror form error (sag) data [Parker, 2003]. Bold line represents mirror centre.

For several days in early May 2003, the Losmandy GM-11 mount was placed on its tripod in the courtyard of the Surrey Space Centre and its right ascension axis aligned with the North Celestial Pole. To facilitate precise solar tracking, the mount's digital drive was connected to a 12-volt battery and activated prior to testing; the drive tracks only in right ascension, not declination, and can be moved while tracking (Figure 6-73). Initial tests were conducted to measure solar image size at the focal plane; a copper target engraved with concentric rings was mounted at the focus to allow the measurement to take place. The rings are spaced 5 mm apart, with a centre ring 10 mm in diameter (Figure 6-75, right).

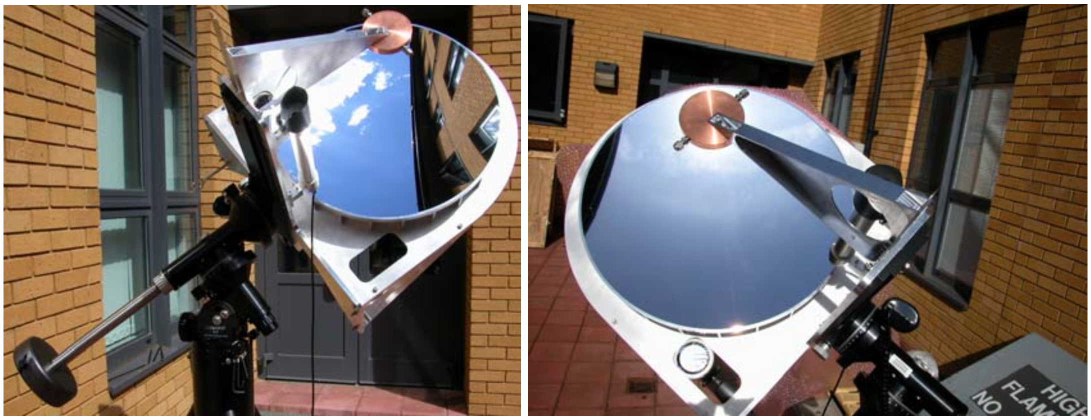

Figure 6-73 Optical test rig mounted on Losmandy GM-11 mount.

Photographs of the copper target during on-sun testing, taken through welding glass, confirmed that the diameter of the spot is slightly less than 5 mm (Figure 6-75, left), which implies a geometric concentration ratio (C_g) of more than 12,500. However, due to non-unity mirror reflectance and imperfect specularity, received flux at the target will lower actual concentration ratio (C), despite its near-ideal C_g.[189]

Several methods were used in an attempt to measure received power and, thus, the the mirror's effective value of C. These included (1) direct measurement of incident radiation with a thermopile-based heat flux sensor;[190] (2) indirect calorimetry using a copper target; and (3) direct measurement with a laser power meter, designed for power levels of up to 250 W.

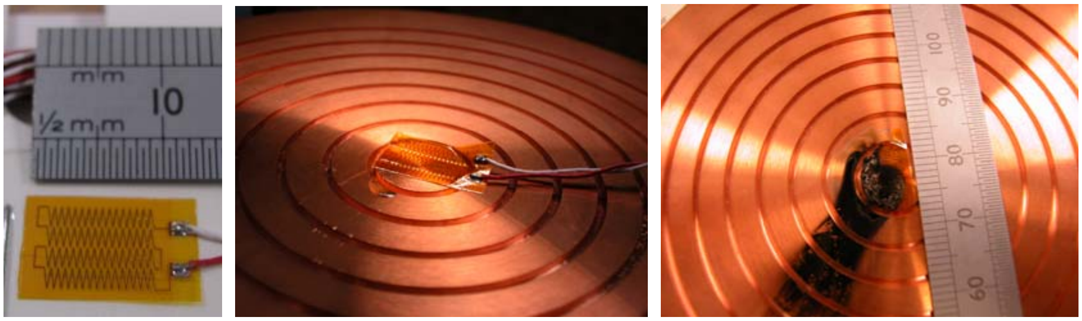

Figure 6-74 RdF micro-foil heat flux sensor, Type 27133-1, 50 W/cm^2 maximum (left); sensor glue-mounted to copper target, prior to on-sun test (middle); and result of short on-sun exposure (right).

An RdF heat flux sensor (Figure 6-74) rated to 50 W/cm^2 was mounted on the copper target and the mirror exposed to direct sunlight for several seconds. The sensor briefly reported heat flux values of up to 33 W/cm^2 before failing. Since expected heat flux values at the target range between 500 and 1,000 W/cm^2, this failure was not unexpected.

---

[189] Recall that C is defined on a power throughput basis (the ratio of received power at the aperture to mirror intercepted power), while C_g is based only on geometric considerations.

[190] Essentially a collection of thermocouples, connected in series.

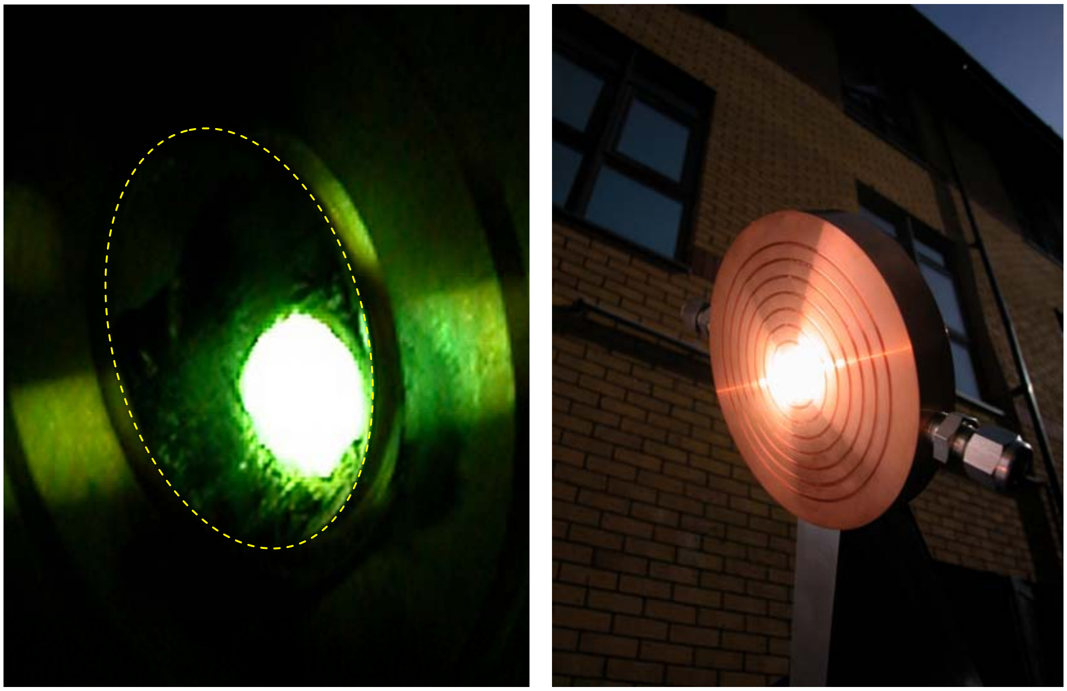

Figure 6-75 Photograph of centre of copper target during on-sun testing, through welding glass (left) and without (right). Spot size is clearly less than half the diameter of the inner ring, which is marked in yellow in the left-hand photo (10 mm).

As an alternative to direct measurement, the author conducted a second on-sun test while measuring bulk copper target temperature. The target was coated with high-temperature black paint to increase its absorptance.[191] A C-type (tungsten/rhenium) thermocouple used for cavity receiver testing was inserted into the interior of the target, with its bead placed directly behind the focal point. After an equilibrium temperature was reached, the mirror was covered and temperature data was recorded (). Pyrheliometer output voltages, visually read from a Keithley multimeter, provided solar flux measurements.[192] To determine effective concentration ratio, a mean solar flux figure was calculated, based on measurements taken over the first 46 minutes of the trial. The standard deviation of the flux over this period was found to be 24 W/m^2. Several times during the test, thin cloud cover briefly obscured the sun's disk and lowered the measured flux from its mean value of 742 W/m^2 to as little as 560 W/m^2. This had little effect on the equilibrium temperature of the target.

Copper's thermal conductivity is high (401 W/m-K at 300 K). Even at 1,000 K, the target's effective Biot number (*Bi*, see Equation 5-10) is much smaller than unity; this indicates that the target can be treated as a lumped-capacity object, its surface temperature (*T*) approximately equal to its bulk temperature:

---

[191] Lampblack—at incidence angles of up to 50°—has an absorptance of 0.95-0.96 [Goswami, 2000].
[192] The pyrheliometer was accompanied by a calibration certificate noting its output at 10.8 μV/W/m^2.

$$\frac{dT}{dt} = \frac{Q}{\rho C_p V} \qquad \textbf{(6-17)}$$

Here, $\rho C_p V$ is the target's heat capacity in joules (J). At equilibrium, the power radiated and/or convected away from the target is equivalent to the incident power. Therefore, upon covering the mirror, target heat loss will be essentially equivalent to the heat flux falling on the target just prior to the shutoff. This loss was calculated using temperatures at both shutoff and 30 seconds afterwards. The 120-minute test, conducted at an average solar flux of 742 W/m^2, resulted in (1) an intercepted flux of 183 W at the mirror, and (2) a heat flux figure at the target of 147 W, or roughly 750 W/cm^2. This produced an optical efficiency of 0.803 and an effective concentration ratio of 10,072—in line with the stated requirement of 10,000.

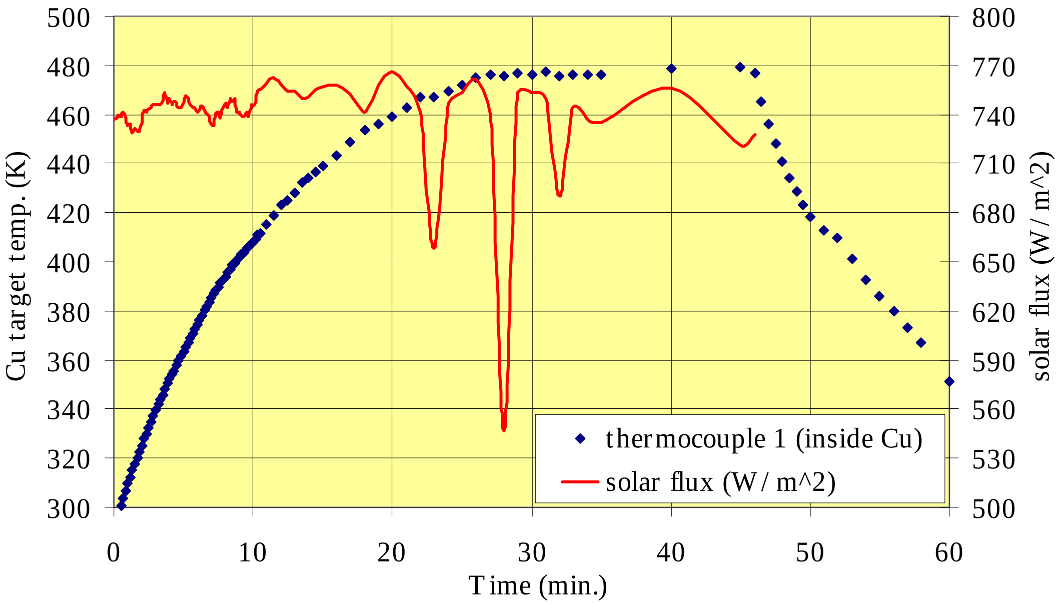

Copper target temperature (left axis) and solar flux measurements (right axis) as function of time, on-sun heating test, 9 July 2003.

Laser power meter tests confirmed these results. The power meter's sensor head—a high-absorptance black disk—was placed in the focal spot for several seconds and the displayed power reading recorded. Representative test data from a mid-July 2003 trial is shown in Table 6-9. Since the meter's sensor head has an absorptance of approximately unity, the measured optical efficiency, η (far right column of Table 6-9), should be equivalent to the concentrating mirror's reflectance. The mean value of η was found to be 0.89; if the single outlier figure of 0.748 is dropped, this rises to 0.92. For comparison, the specular reflectance of bare aluminium surfaces in the visible spectrum is usually quoted as 0.82 to 0.92 [Goswami, 2000].

Test No.	Time (BST)	Measured solar flux (W/m^2)	Intercepted power (W)	Received power at focal spot	Optical efficiency (η)

				(W)	
1	**15:46:00**	**574**	**141.4**	**126**	**0.891**
2	**15:47:00**	**559**	**137.7**	**103**	**0.748**
3	**15:48:00**	**528**	**130.0**	**121**	**0.931**
4	**15:49:00**	**538**	**132.5**	**120**	**0.906**
5	**15:58:00**	**588**	**144.8**	**136**	**0.939**
6	**16:00:00**	**551**	**135.7**	**126**	**0.929**

Table 6-9 Laser power meter characterisation of large (56-cm) concentrating mirror, 15 July 2003.

6.3.2 Small and Ganged Mirror Testing

To validate the hypothesis that multiple small (plastic or metal) concentrating mirrors might duplicate the performance of a single large mirror, but at significantly reduced weight, the author procured a number of 14-cm, f/0.6 paraboloidal dishes for initial trials. Ten of these were diamond-turned from polymethyl methacrylate (a hard plastic) by Carville, Ltd., of Dorking, Surrey. Following visual inspection of the form and discussion with the coating supplier, it was decided to ask Carville to hand-polish their mirrors to improve their quality (the mirrors were covered with numerous fine scratches, flaws which would be amplified by metallic coating). This was done and the resulting mirrors delivered to Kendall-Hyde (of Basingstoke, Hampshire) for coating with aluminium and overcoating with magnesium fluoride. Despite the additional effort expended on polishing, fine scratches were still visible on the mirror's surface following the coating procedure (Figure 6-76). All plastic mirrors weighed approximately 130 g.

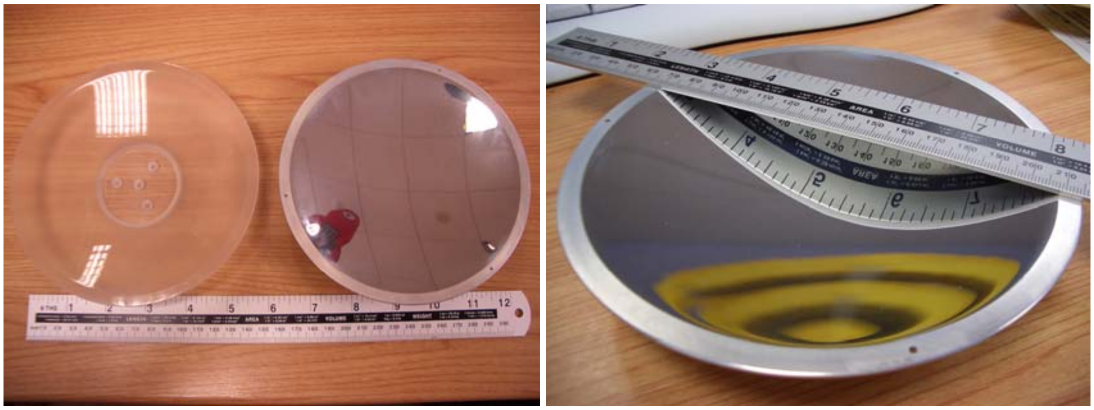

Figure 6-76 Uncoated and coated (Al/MgF$_2$) 14-cm concentrating mirror (left). Mirror detail (right).

Precision Optics was asked to produce three 14-cm diameter aluminium mirrors (uncoated) and provide form error measurement data on each. P-OE was also requested to provide form error data on three of Carville's PMMA mirrors. The results of the aluminium mirror testing are shown in Figure 6-77. While there are clearly zonal (asymmetrical) defects in the mirror form, the peak-to-valley form error was measured at less than 2.5 μm (for a test wavelength of 490 nm). The RMS figure of 570 nm is significantly less than P-OE was able to obtain with the large (56-cm) paraboloidal mirror [Whelton, 2003]. This strongly suggests that the small mirrors' performance should equal or exceed that of the large mirror, with concentration ratios near the theoretical maximum of 13,000. The aluminium mirrors are heavier than their plastic counterparts, weighing approximately 300 g.

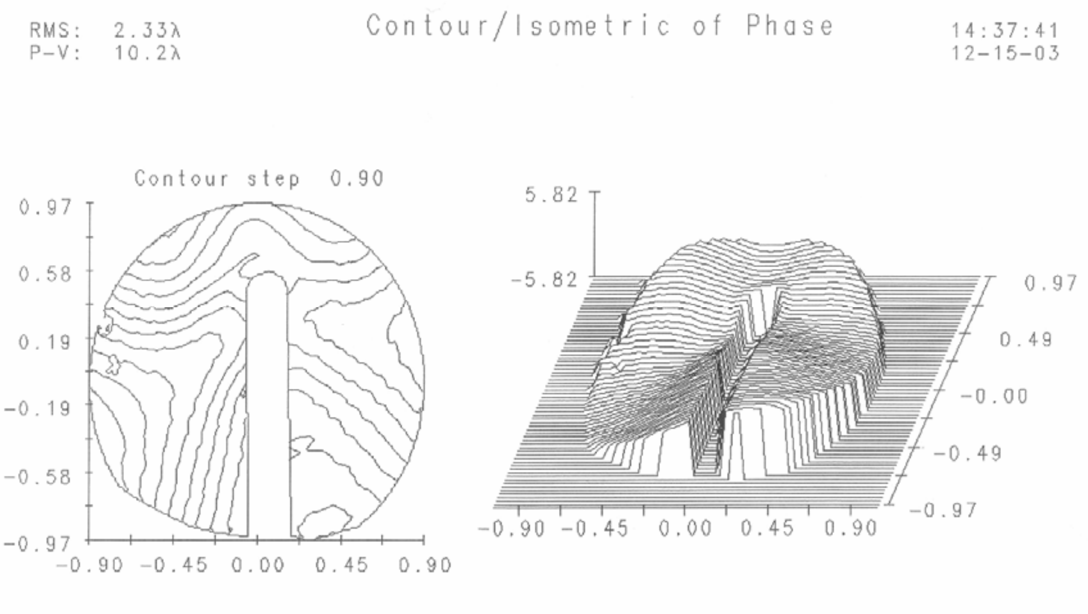

Figure 6-77 14-cm aluminium concentrator form error test results. Peak-to-Valley (PV) form error is 2.5 μm; RMS form error is significantly less, 0.57 μm (λ = 0.490 μm) [Whelton, 2003].

Precise form error measurements of the plastic mirrors were not obtainable, owing to large surface flaws. Whelton [2003] attempted to perform a probe test similar to that conducted for the large metal optic (Figure 6-72) but the test could not be concluded; the probe repeatedly was halted at obstructions on the order of 40 microns in height or more. From the limited data obtained, one can reasonably assume that peak-to-valley form error is at least 40 microns, and may in fact be significantly higher.

Figure 6-78 Small PMMA mirrors undergoing spot size testing at SSTL solar simulator facility (left). Geometric concentration ratio estimate based on focal spot size measurement (right).

Spot size measurements were obtained under simulated sun in the late autumn of 2003. SSTL's solar simulator facility, composed of a high-power xenon arc lamp, parabolic reflector, and collimating lens, is capable of providing a circular spot beam (AM0 intensity and higher) of 14-cm diameter. Beam divergence half-angle $\Delta\theta$, estimated at $\leq 2°$ [Eade, 2003], will tend to spread the incident light, artificially increasing focal length and focal spot diameter. Equation 4-9, which defines the maximum permissible concentration for a given source half-angle θ, can be used to estimate concentration with a divergent beam (the divergence half-angle is simply added to the source half-angle). For $\Delta\theta = 2°$, $C_{max} = 649$ and the focal spot size—assuming perfect optics--will be at least 5.5 mm in diameter.[193] For $\Delta\theta = 1°$, C_{max} increases to 2,100, while estimated spot diameter decreases to just over 3 mm.

Test results bear out these calculations. A 14-cm diameter PMMA mirror was mounted with its symmetry axis aligned to that of the solar simulator's exit beam, behind a collimating lens (Figure 6-78, left). The arc lamp was then switched on and a steel rule placed at the focal plane of the mirror. Photographs, such as that shown in Figure 6-78 (right) indicate that the focal spot was between 4 and 5 mm in diameter. It was discovered during similar tests with the aluminium mirror that the focal spot size was smaller—3 mm in diameter, with a bright centre 1 mm wide (Figure 6-79, left). Geometric concentration ratios of up to 2,000 appear to be achievable with the solar simulator.[194] This is insufficient for high-temperature testing, but could be utilised for other benchmarking tasks.

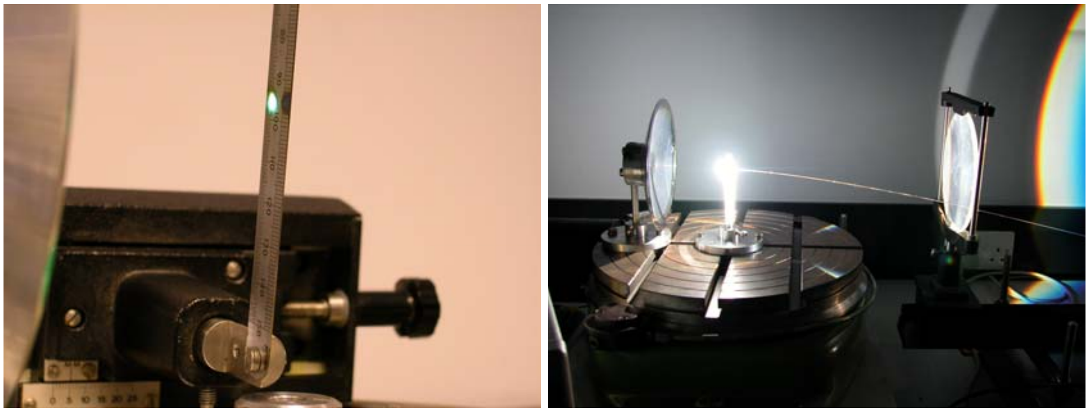

---

[193] In practice, this will be somewhat larger. C_{max} is a peak figure; the mean concentration C is one-fourth this value, for a 45° rim-angle (*f*/0.6) mirror.

[194] On-sun testing with plastic mirrors indicates a spot size of 2 mm or less ($C_g = 4{,}900$). Metal mirror tests indicated spot sizes of approximately 1 mm.

Figure 6-79 Focal spot size measurement, 14-cm aluminium mirror, utilising solar simulator (left). Optical fibre transmission testing with solar simulator (right).

At an estimated C_g = 2,000, the author was able to measure incident radiation at the focal spot with the laser power meter discussed in Section 6.3.1; these results gave a mean power level of 19.2 W, an estimated incident flux of 1,386 W/m^2,[195] and an estimated intensity at the focal spot of 277 W/cm^2. One end of a two-metre length of 0.75-mm core diameter silica optical fibre, donated by Polymicro Technologies, LLC, of Phoenix, Arizona, was placed at the focal spot and the distal end embedded in a graphite post massing 1 g (Figure 6-79, right). No special preparations for this test were made; the fibre ends were left unpolished and alignment was performed manually, without the use of micrometer stages. Figure 6-80 indicates the results of the test. Using temperature data in conjunction with Equation 6-17, it was found that the heating rate, Q, climbed from 0.35 to 0.69 W over the first minute of testing; the mean heating rate was 0.59 W. One can compare this heating rate with the incident flux on the fibre tip—for a numerical aperture of 0.66 and an intensity of 277 W/cm^2, the fibre will intercept 1.22 W. The optical efficiency η, defined as the received power at the graphite element divided by the intercepted power at the entrance tip, is therefore 0.57.[196]

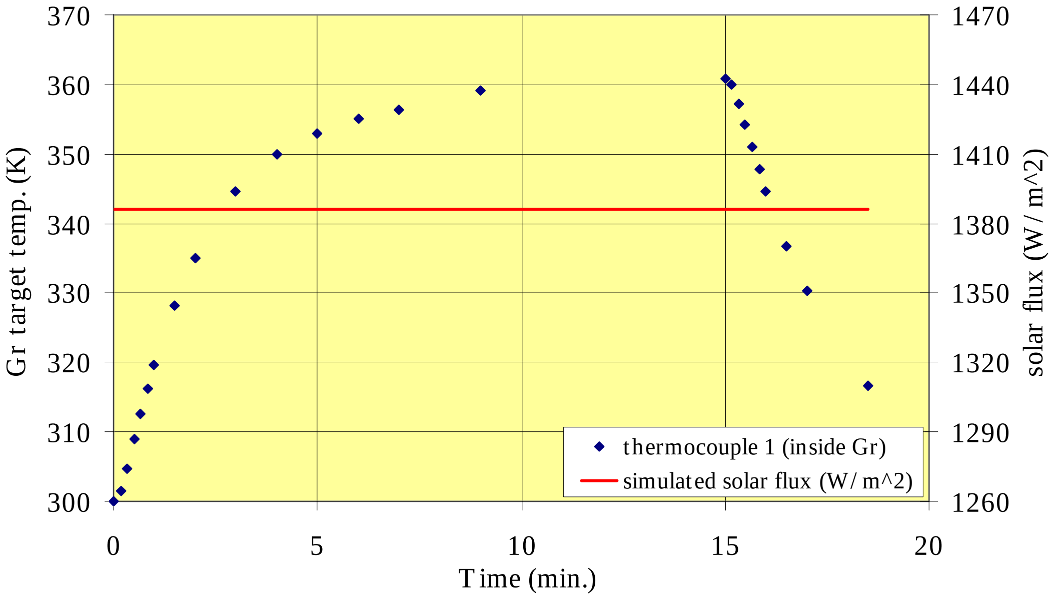

Figure 6-80 0.75-mm (NA = 0.66) optical fibre heating test, using SSTL's solar simulator.

---

[195] This calculation presumes a mirror reflectance of 0.9.

[196] Liang [1998] notes that unprepared (unpolished, imprecisely aligned) fibres transmit as little as 30% of incident sunlight.

Henshall and Lock [2004] performed several laser testing trials at the University of Surrey's Optoelectronics Lab to verify power throughput estimates. A 980-nm laser source was boresighted on the entrance tip of the 0.75-mm (NA=0.66) optical fibre described above (Figure 6-81). The distal end was terminated inside an integrating sphere; a silicon photodiode, with a fixed responsivity at the laser's wavelength of operation, captures a fraction of the incident light from the sphere. Knowing the sphere's multiplication factor (due to multiple internal reflections, as a result of the sphere's high internal reflectance) permits one to calculate the power incident on the sphere surface. Boresighted (on-axis), the fibre was able to transmit between 59% and 75% of incident laser flux, at power levels of between 1.2 and 16 mW. With the laser firing 30° off the fibre axis, this figure (at 1.2 mW input power) fell to 46%.

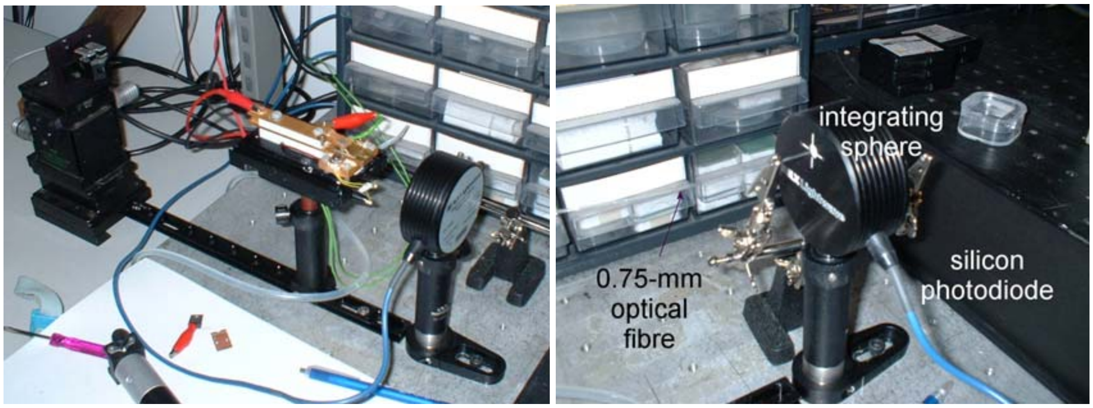

Figure 6-81 Optical fibre laser power throughput measurement test rig, University of Surrey Optoelectronics Laboratory (February 2004) [Lock, 2004].

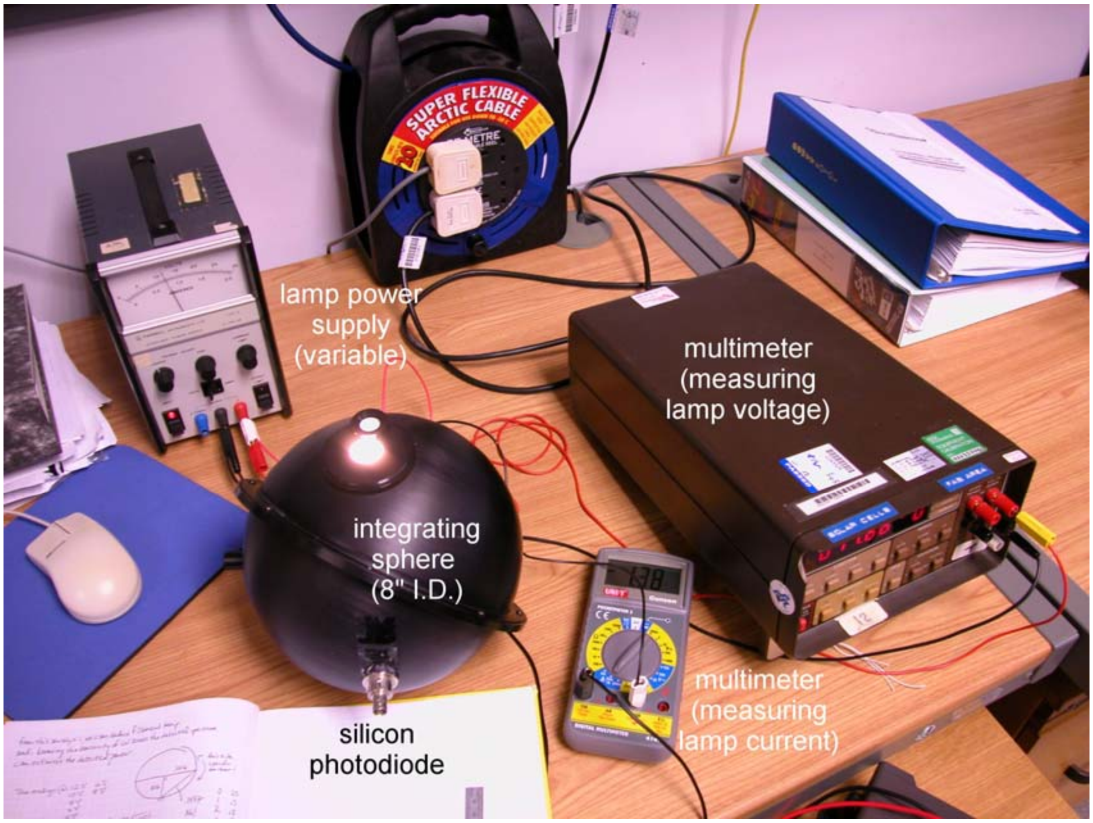
lamp power supply (variable)
multimeter (measuring lamp voltage)
integrating sphere (8" I.D.)
multimeter (measuring lamp current)
silicon photodiode

Figure 6-82 Incandescent lamp calibration for integrating sphere power throughput testing.

An analogous test rig was constructed at the Surrey Space Centre to measure power throughput with broad spectrum sources, rather than narrow bandwidth lasers. To calibrate the rig, a 12-V incandescent lamp was inserted in an 8” (20.32 cm) integrating sphere (Figure 6-82), donated by H. Newell of SSTL, Ltd. An Oriel 71648 silicon photodiode (UV-enhanced) was mounted to a side port behind a light baffle, to prevent direct light transmission from the lamp to the photodiode (Figure 6-83, left).[197] The lamp (Figure 6-83, right) was connected to a direct-current power supply and tested at powers of between 5 and 45 W. Input current, voltage, and photodiode current were measured for each power level.

---

[197] A preferred solution would utilise a thermopile in place of the photodiode, which has a flat (constant) spectral responsivity. None were available at the time of testing.

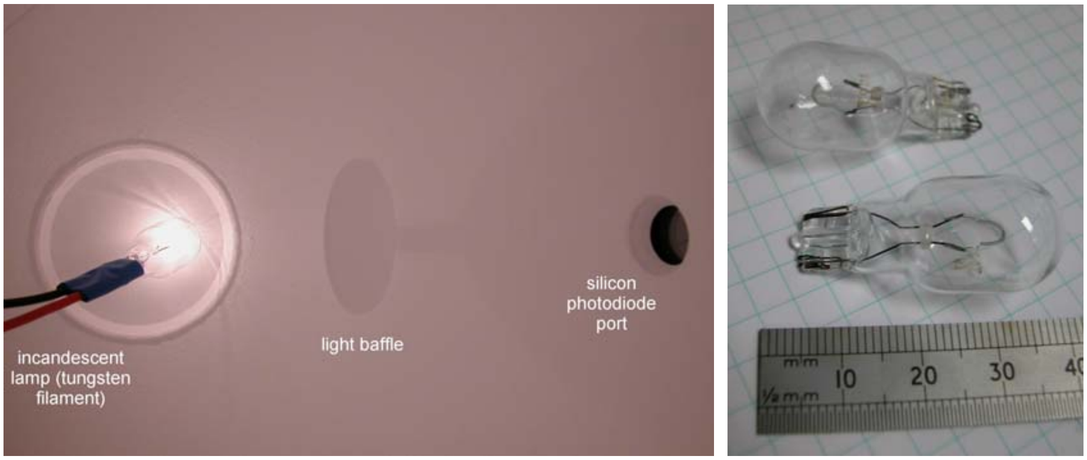

Figure 6-83 Interior of integrating sphere, demonstrating light baffling between source and sensor (left), 12-V test lamps (right).

It is important to note that variable photodiode response and lamp colour temperature must be accounted for when calculating power output. The photodiode is only sensitive to a relatively narrow range of incident light and will severely underestimate lamp power; its responsivity (measured in A/W) is dependent on wavelength, and varies from 0.075 A/W at 200 nm to a peak of 0.561 A/W between 880 and 900 nm.[198] A photodiode's spectral responsivity, *R*, can be computed from [Melles Griot, 2004]:

$$R = \frac{q \eta_q \lambda}{hc} \qquad \textbf{(6-18)}$$

This relates responsivity to electron charge, *q* (1.6022 x 10^{-19} coulombs), the quantum efficiency η_q, wavelength λ, Planck's constant, *h*, and the speed of light, *c*. Quantum efficiency, a measure of the number of photoelectrons generated as a result of impingement by an incident photon, reaches a maximum of 0.80 between 850 nm and 900 nm. Silicon is transparent to infrared radiation (l $\geq$ 1,100 nm) and ultraviolet radiation below approximately 200 nm.

A lamp source such as the tungsten filament test article described above can be modelled as a blackbody source with a temperature-dependent emissivity [Harang, 2003]. The blackbody curve for a typical lamp source, derived from Equation 2-2, demonstrates that it will radiate most strongly in the infrared, with only 8-14% of its output in the visible spectrum. As power increases, the filament temperature increases and the curve shifts towards the visible (Figure 6-84). However, even at temperatures approaching 3,000 K, the emission characteristics of tungsten are unrepresentative of sunlight (Figure 2-15). The emissivity of tungsten varies with both wavelength and with filament temperature; at 1,600 K, the mean emissivity (between 250 and 700 nm) is 0.465, while at elevated temperature, visible spectrum emissivity decays slightly (at 2,800, mean emissivity drops to 0.441) [Lide, 1995]. Tungsten's total emissivity is tabulated and can be computed by using the following formula for temperatures between 1,200 and 2,500 K [Harang, 2003]:

---

[198] For a representative Type 71648 photodiode.

$$\varepsilon(T) = -5\times10^{-8}T^{2} + 3.11\times10^{-4}T - 0.161 \qquad \textbf{(6-19)}$$

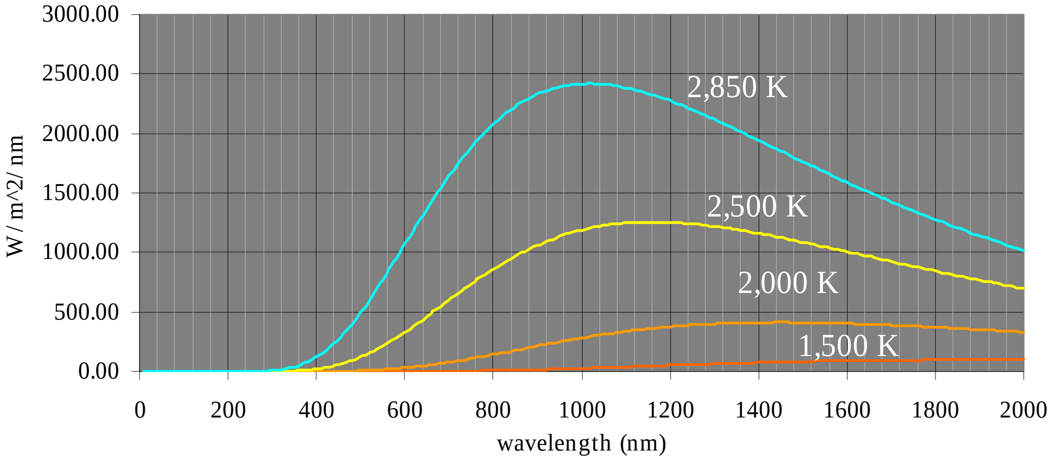

Figure 6-84 Blackbody emission curves (monochromatic emissive power) for tungsten filament temperatures between 1,500 and 2,850 K.

To determine emissive power, one must first estimate filament temperature. This can be found by comparing the element resistivity (ρ_e, in μΩ-cm) during operation with its zero-power value at room temperature. Since resistivity is a known function of temperature, it is possible to calculate the filament temperature from this ratio [Harang, 2003]. The product of total emissivity and integrated blackbody emissive power is filament radiated power; at these temperatures, efficiencies are high and virtually all dissipated power is radiated away, so it is possible to equate this figure with the amount of power dissipated in the circuit.

Table 6-10 provides the results of the lamp calibration testing. The measured photodiode current is compared to the predicted current produced by a representative UV-enhanced photodiode viewing a tungsten filament lamp of a known power output and given colour temperature at a separation distance of 4" (the integrating sphere's radius, 10.16 cm). A sphere multiplier, shown in the final column, is the ratio of measured to predicted filament power. This multiplier was seen to decline from roughly 7 at low temperatures (1,500 K) to 2 at moderate temperatures (2,500 K).[199]

---

[199] The integrating sphere's multiplier, *M*, is a function of both its internal reflectance, ρ, and the port fraction, *f* (the amount of internal surface area occupied by apertures for sources and sensors):

Test No.	Current (A)	Voltage (V)	Power (W)	Si photodiode current (mA)	Estimated filament temperature (K)	Sphere Multiplier
1	1.35	12.02	16.2	3.13	2,035	3.24
1	1.20	9.83	11.8	2.22	1,896	4.02
1	1.07	8.02	8.6	1.50	1,759	4.98
1	0.91	5.98	5.4	0.81	1,573	6.90
1	1.46	13.96	20.4	3.96	2,161	2.70
1	1.58	15.78	24.9	5.06	2,242	2.54
1	1.71	18.14	31.0	6.55	2,358	2.30
2	1.35	12.22	16.5	3.16	2,063	3.07
2	1.22	9.88	12.1	2.27	1,878	4.80
2	1.09	8.08	8.8	1.59	1,742	5.34
2	0.93	6.11	5.7	0.92	1,573	7.52
2	1.54	15.08	23.2	4.65	2,205	2.63
2	1.67	17.20	28.7	5.89	2,300	2.39
2	1.82	19.99	36.4	7.74	2,428	2.16
2	1.96	22.72	44.5	9.77	2,540	1.99

Table 6-10 Incandescent lamp calibration test results, 1 and 4 May 2004.

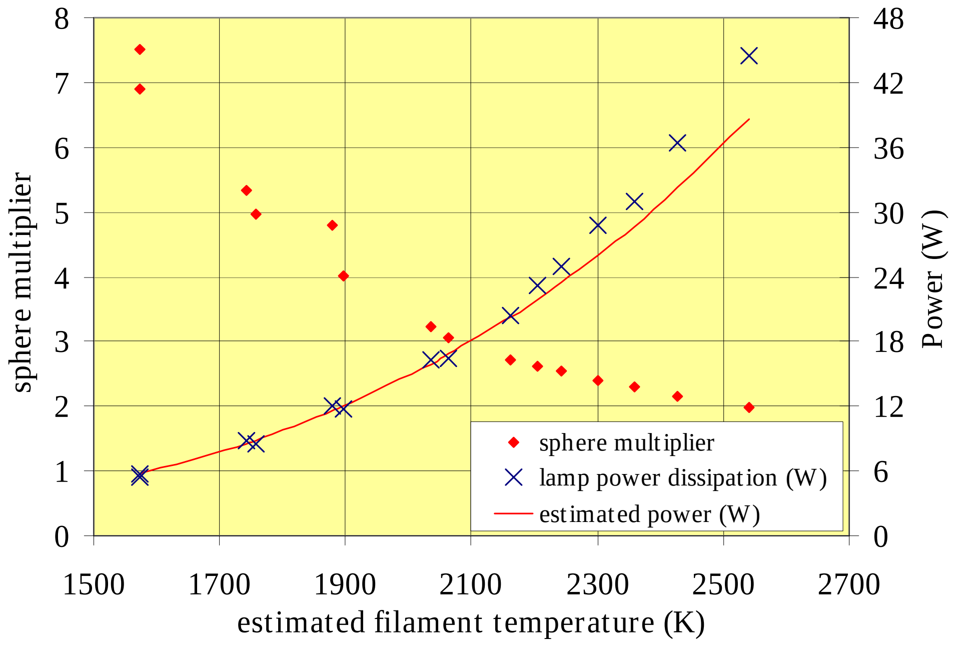

Figure 6-85 Sphere multiplier and power dissipation (estimated and actual) versus predicted filament temperature, 1 and 4 May 2004.

Test results are displayed graphically in Figure 6-85. The apparent deviation from the expected cT^4 curve (power vs. temperature, displayed in red) at higher temperatures and powers is likely to

---

$$M = \frac{\rho}{(1-\rho)(1-f)} \tag{6-20}$$

have resulted from increasing resistance—and power dissipation—in the remainder of circuit. The sphere multiplier, M, appears to asymptote slightly below 2.0, as filament temperature increases. The author used a value of $M = 2.0$ as a conservative estimate for follow-on solar power throughput tests.

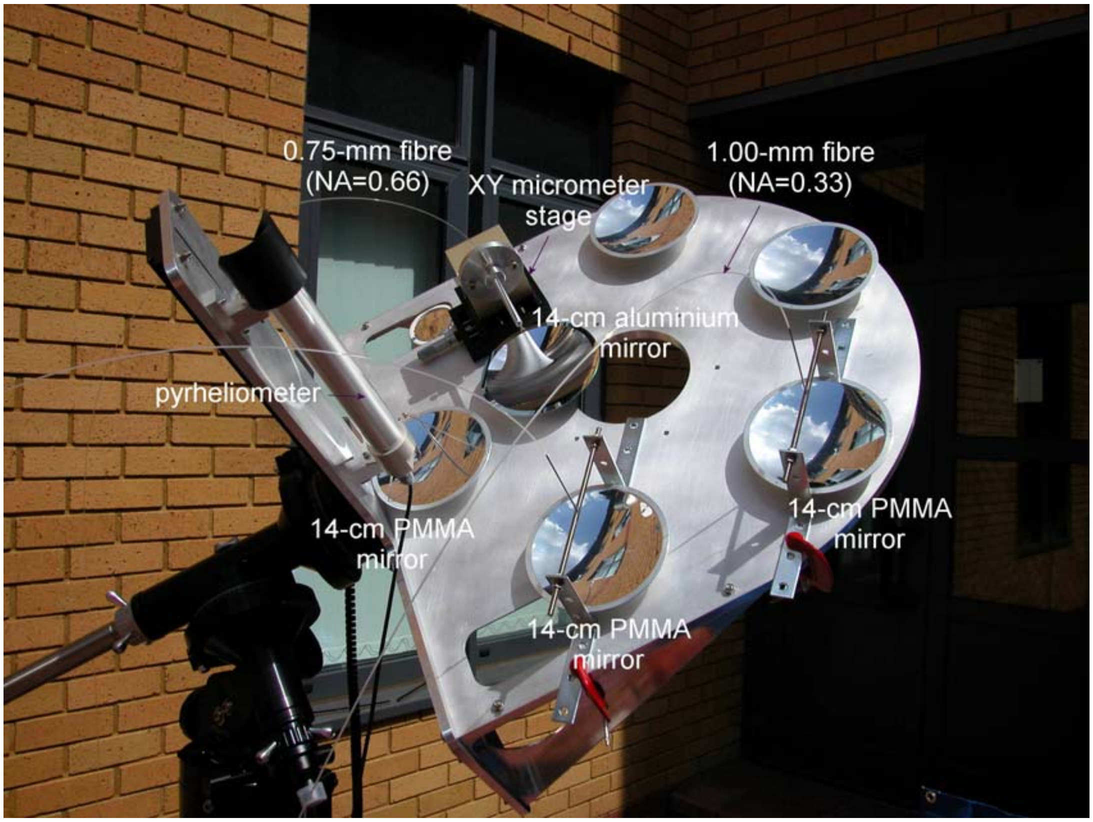
0.75-mm fibre
(NA=0.66)
XY micrometer
stage
1.00-mm fibre
(NA=0.33)
14-cm aluminium
mirror
pyrheliometer
14-cm PMMA
mirror
14-cm PMMA
mirror
14-cm PMMA
mirror

Figure 6-86 Ganged mirror power throughput test, three optical fibres, 14 May 2004.

On-sun fibre power throughput testing commenced in May 2004. The optical test rig, shown in Figure 6-86, includes a number of 14-cm diameter PMMA and aluminium mirrors mounted to the backing structure of the telescope mount. A two-axis micrometer stage permits fine control over fibre tip position, crucial for proper alignment of the small-diameter (0.75-mm) optical fibre with the aluminium mirror's focal spot.[200] While mean concentration ratio C can be expected to approach the flat-plate limit of 13,000, the concentration ratio in the core region of this spot was calculated to reach a much higher figure of 26,000 (from Equation 2-5). The plastic mirrors exhibit greater optical inaccuracy and, consequently, will not be able to produce a high-concentration core region. Low numerical aperture (NA = 0.33) fibres were placed at the foci of two of the PMMA mirrors. These fibres have larger core diameters (1.00 mm).

---

[200] The focal spot is composed of a high-concentration core region of radius $f \sin \theta$ [Feuermann, 1999]. For the 14-cm diameter aluminium mirror, $f = 8.4$ cm and the core region is predicted to be 740 microns in diameter. This is essentially equivalent to the core diameter (750 microns) of the NA = 0.66 optical fibre.

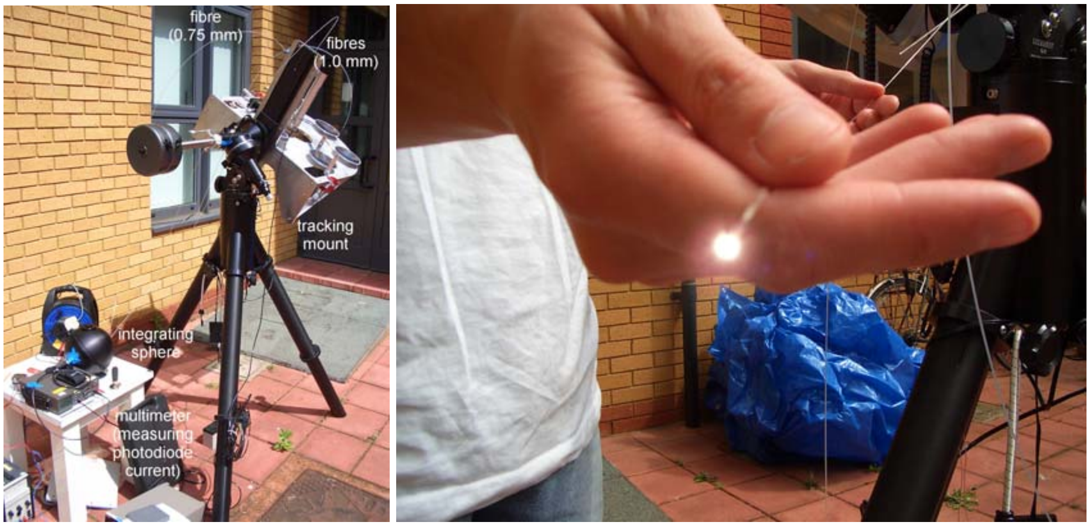

Figure 6-87 Ganged mirror power throughput test setup (left). Concentrated sunlight emerging from 0.75-mm core diameter optical fibre (NA = 0.66).

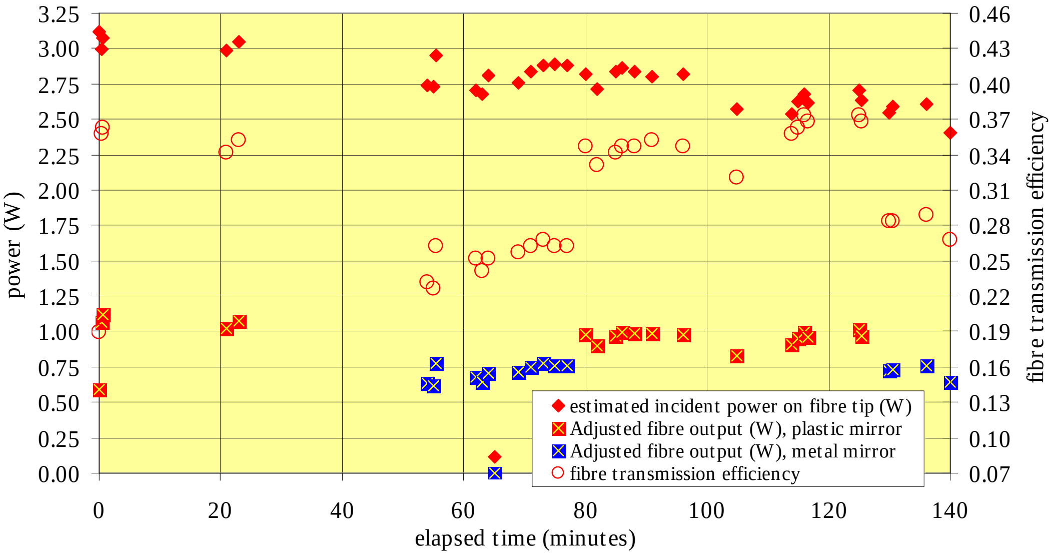

Figure 6-88 Fibre power transmission test results, 11 May 2004.

Multiple fibres were inserted into a small aperture on the side of the 8” integrating sphere (Figure 6-87). A multimeter was attached to the silicon photodiode at middle left and provided current measurement during the test. Pyrheliometer flux measurements and photodiode output were recorded simultaneously, first for a combination of PMMA primary mirror and 0.75-mm (NA = 0.66) optical fibre, then substituting the metal mirror for the plastic mirror to ascertain any differences in power throughput resulting from improved form accuracy.

The mean responsivity (200-1,100 nm) of the silicon photodiode varies slightly, depending on whether the spectral distribution is (1) a blackbody at 5,700 K, in which case R = 0.364 A/W; (2) a blackbody at 5,900 K (R = 0.356 A/W); or (3) an AM1.5 source, based on standard solar spectra data (R = 0.398 A/W) [NREL, 2001]. Additionally, the ratio of detected power to emitted power varies, from 0.76 for a 5,700 K blackbody to 0.79 for the AM1.5 source. Test results (Figure 6-88) indicate that fibre transmission efficiencies[201] of up to 0.37 were achieved.

A second series of measurements were taken on the 14th of May, utilising multiple mirrors and fibres. The author recorded single mirror/fibre outputs of as much as 2.1 W at a measured solar flux level of 691 W/m^2. While the amount of incident flux on the fibre's entrance tip cannot be precisely estimated, it is likely that these high figures (twice the output of the 11 May 2004 tests) resulted from precise alignment of the centre of the metal mirror's focal spot with the fibre tip. If the concentration at centre approaches the theoretical ideal for this rim angle (26,000:1), the amount of incident flux on the 750-micron fibre can be calculated to be 7.9 W and the total fibre transmission efficiency is at least 0.27.[202]

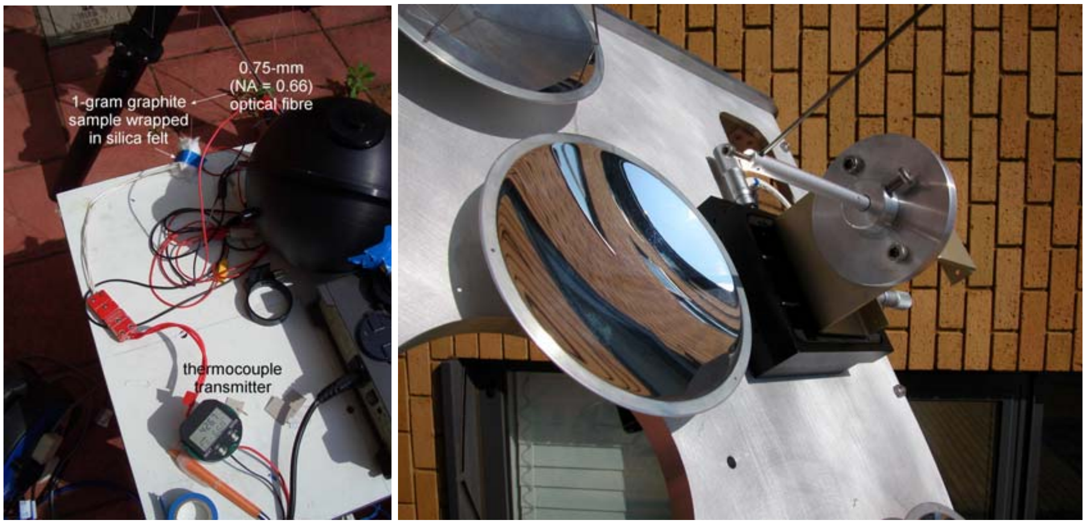

Figure 6-89 Graphite element heating with fibre-transmitted sunlight (left); detail of precision fibre placement rig (XY micrometer stage) with 14-cm plastic mirror and 0.75-mm fibre (right).

Lower-NA fibres (1-mm core diameter), coupled to PMMA mirrors, were used to provide a ganged input. At a numerical aperture of 0.33, only 19% of the flux incident on the fibre end strikes the fibre at a sufficiently low entrance angle to ensure its transmission.[203] One can separate this *acceptance fraction* from *fibre loss* (due to Fresnel losses at the air-fibre interfaces and internal absorption); combined, they provide the fibre transmission efficiency. If the in-fibre loss is 0.55 (45% of accepted light emerges at the far end), the total fibre transmission efficiency is just 0.07. This estimate is borne out by the relatively small amount of light observed emerging from the coupled PMMA mirror/low-NA fibre package, detected by the integrating sphere test rig. The maximum output measured from the low-NA fibre was 0.16 W at a flux level of 561 W/m^2. Estimated fibre transmission efficiency is therefore only 0.035.

---

[201] The author distinguishes between the optical efficiency η (defined as an end-to-end figure of merit, comparing flux incident on the fibre with receiver heating power) and fibre transmission efficiency, which compares fibre input and output power.

[202] This is a minimum estimate for fibre transmission efficiency. If the concentration ratio is lower than this, the efficiency is obviously higher.

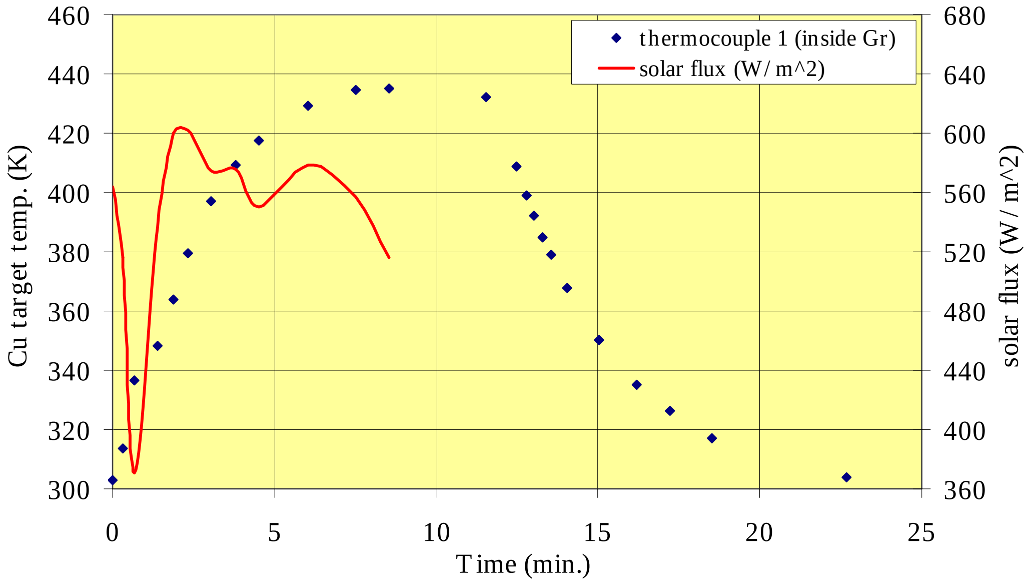

Figure 6-90 1-g graphite element heating test, single 750-micron optical fibre, NA = 0.66 (14 May 2004).

Maximum ganged output (three mirrors) was measured at 2.27 W at an incident flux level of 667 W/m^2. A mean efficiency, calculated on the basis of total received power divided by total estimated incident flux at the tips of the three fibres (17 W), was low: 0.13.

A final pair of on-sun, in-air tests was conducted to determine the end-to-end efficiency of the coupled fibre/mirror approach to receiver heating, resulting in two heating profiles similar to that shown in Figure 6-80. In the first of these, the distal tip of the 0.75-mm optical fibre was inserted into a 1-gram graphite sample, which was then covered by silica felt to inhibit natural convective cooling (Figure 6-89). A C-type thermocouple was affixed to the external surface of the sample.

---

[203] The vast majority of the incident flux strikes the fibre at less than the fibre's critical angle and will only be partially reflected at the core-clad interface [Hecht, 1992]. Equation 2-4 allows one to determine the fraction of the incident light cone that will be accepted at the fibre's entrance tip. The NA = 0.66 fibre has a much wider acceptance cone; 85% of light incident from a 45° rim angle paraboloid will be accepted.

The entrance tip was placed in the focal spot of the 14-cm aluminium *f*/0.6 mirror. Solar flux levels were recorded from pyrheliometer readings and temperature measurements taken from the C-type thermocouple's transmitter display, over the course of the 25-minute test (Figure 6-90). The fibre reached a maximum temperature of 162 °C (435 K) after 8 ½ minutes of heating, at a mean flux level of 545 W/m^2.[204] The heating rate was calculated to be 1.14 W (over the first 20 seconds), with an end-to-end efficiency of 0.18.[205]

A second test was conducted without fibre transmission (Figure 6-91). The graphite element was placed in the focal spot of the metal mirror and the mirror uncovered at time $t = 0$. After 3 ½ minutes, the sample reached a maximum temperature of 283 °C (556 K), at a mean flux level of 708 W/m^2. In this instance, the element sees the entire focal spot (not simply a 0.75-mm diameter circular portion); the heating rate was calculated to be 9.63 W, with an estimated end-to-end efficiency of 0.88.

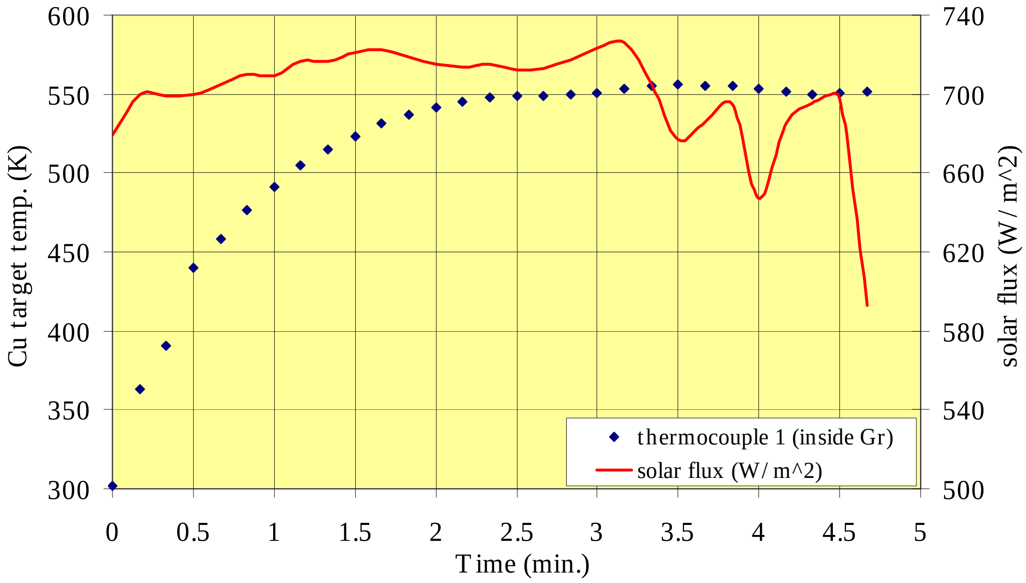

Figure 6-91 1-g graphite element heating test, direct heating (14 May 2004).

6.4 Summary of Test Results

The bulk of the effort's testing activities was concerned with the miniaturisation and simplification of high-temperature solar receivers and rigid, fixed concentrators, suitable for microsatellite use. Initial tests focused on the bonding and sealing of ceramic elements to themselves and to metallic fixtures. Brazing tests were conducted on ceramic-to-metal seals at high temperatures (>1,780 °C, or 2,053 K) using refractory alloy braze filler metals (molybdenum and ruthenium) as well as combinations of molybdenum, molybdenum disilicide, and silicon. These tests were only partially successful; while a strong Mo/Ru bond was achieved between a composite boron nitride ceramic and a molybdenum fitting, the seal was not leaktight. Ceramic adhesives and mechanical bonding (utilising graphite seals) were also attempted, with the best results being obtained with gasketed, flanged systems. This approach was carried forward into the detailed design phase and resulted in the Mk. I and Mk. II solar receivers—essentially flanged, bolted cans of composite ceramic—discussed earlier in this chapter.

---

[204] The effects of passing cloud cover during the first minute of the test can be seen—flux drops to less than 400 W/m^2 and the heating rate drops substantially, then returns to roughly its previous rate of increase.

[205] Assuming a peak concentration of 26,000:1 and perfect spot-fibre tip alignment. Without proper alignment, the local concentration at the tip could be 10,000:1 or even lower.

Testing of ceramic coupons in vacuum and at high temperatures (> 2,000 °C, or 2,273 K) provided the basis for the selection of an intermetallic composite (BN/TiB_2) as the primary structure for the solar receiver. Coupons fabricated from BN/TiB_2 displayed no appreciable mass loss, deformation, or damage after an hour of exposure. The Mk. I receiver, an all-ceramic system, was designed as a container for a boron nitride[206] particle bed; the Mk. II receiver, a simpler, smaller design, substituted a spiral flow channel in place of the particle bed.

Both receivers were repeatedly heated to high temperatures in vacuum and examined for damage. The large (Mk. I) receiver reached temperatures in excess of 1,600 K; the Mk. II receiver briefly topped 2,000 K. Both receivers showed signs of boric oxide binder precipitation on their surfaces following heating, but no evidence of cracking, deformation, or mass loss. Both closely followed heating profiles predicted by the author’s MSTISM code for solar thermal propulsion system modelling.

Full flow tests with helium, nitrogen, and ammonia were conducted in vacuum, at receiver temperatures of up to 1,700 K. At high temperatures and moderate ($\leq$ 12 bar) pressures, both receivers showed signs of moderate leakage, resulting in thrust coefficient decay. Some cracking was observed around the cavity aperture in both receiver types after high-temperature exposure with propellant, as well as precipitate formation similar to that seen in electrical heating tests. Thrust stand measurements at temperature indicate maximum specific impulse performance in ammonia of 237 s. Thrust levels were measured at between 130 and 500 mN. The large (Mk. I) receiver suffered a catastrophic failure, during the introduction of ammonia at 1,200 K, along its top flange. The failure appears to have resulted from stress concentrations in the top flange’s molybdenum bolts, which were attached not to nuts (which would have diverted the loading) but directly to the lower ceramic flange. The receiver testing clearly indicated that low-cost, all-ceramic designs are feasible but that care must be taken to ensure that these systems (1) maintain seal integrity, even at elevated temperatures, and (2) incorporate stress-relieving features to minimise the possibility of mechanical failure.

Two concentration schemes were tested. This included a direct-incidence heating approach with a single large (56-cm diameter) paraboloidal primary mirror with the solar receiver placed at the focal plane. Form error measurements following mirror fabrication confirmed that the mirror, which was diamond-turned from a single aluminium billet, would easily meet or exceed previously discussed thresholds for surface non-uniformity. Flux concentration was measured, on-sun, at greater than 10,000:1. Power throughput at terrestrial flux levels exceeded 140 W; mirror reflectance was shown to be better than 0.9 at low incidence angles.

The large mirror's as-fabricated mass (15 kg) and surface area (0.25 m^2) made its placement onboard a 100-kg microsatellite problematic. A novel alternative concentration scheme, intended to minimise design and operational impact on a small spacecraft, was devised to overcome this problem. Building on theoretical predictions and terrestrial test efforts from researchers in Japan [Nakamura, 1976] and Israel [Feuermann, 2002], the author adapted a proposal for optical fibre transmission of concentrated sunlight to the specific problem of solar thermal propulsion on microsatellites. A number of researchers over the past 30 years have reported significant power throughput in optical fibre runs of many metres. If the output of multiple mirrors could be conjoined and deposited on a single solar receiver, several significant advantages accrue: (1) the solar receiver can be decoupled from the mirror focal point, allowing it to be placed anywhere on the spacecraft; and (2) multiple small mirrors potentially allow substantial weight savings over a single large mirror, due to the fourth-power empirical scaling relationship between space mirror diameter and mass.

Ten 14-cm diameter plastic mirrors and three aluminium mirrors were fabricated by two separate vendors and tested. The plastic mirrors were found to be inferior to the metal in probe tests (conducted by the vendor) and solar simulator tests. The aluminium mirrors were found to have form errors of less than 600 nm, surpassing the performance of the 56-cm optic, while the plastic mirrors were estimated to have RMS errors of at least 40 microns, a factor of 70 worse than the metal. Geometric concentration ratios in solar simulator testing were found to be on the order of 600 (plastic) to 2,000 (metal); on-sun observations indicate that the plastic mirror achieves a geometric concentration ratio of 4,900. The metal mirrors' focal spot size was observed to be on the order of 1 mm, although the spot was sufficiently small as to make a precise estimate difficult.

Boresight laser testing of high-NA optical fibre demonstrated power throughputs of up to 75%. This same fibre was found to transmit 57% of intercepted (simulated) sunlight in a heating test

---

[206] Initially, boron carbide.

with a 1-gram graphite receiver element and 14-cm metal primary mirror. Direct power measurements with an integrating sphere and silicon photodiode indicated single fibre transmission efficiencies of 20-37%, with lower ganged fibre efficiencies resulting from the use of low-NA (0.33) optical fibre. On-sun graphite element heating tests appeared to demonstrate relatively low transmission efficiencies (< 20%), while a final direct-incidence heating test (no fibre) with this same graphite element and mirror produced heating rates of over 9 W and an end-to-end efficiency of nearly 90%. This testing has shown that there is significant potential in the fibre optic transmission of sunlight for solar thermal propulsion applications, although the maintenance of precision alignment on-orbit, as well as the ground preparation of fibre tips, will be crucial in maximising throughput.

In summary, test results from the comprehensive examination of several microsatellite-compatible solar receiver and concentrator approaches confirmed the feasibility of downsizing the concept and have indicated that high performance is possible. An innovative all-ceramic solar receiver, designed for low-cost fabrication and test, performed extremely well over a wide range of temperatures, pressures, and propellant types. Large, diamond-turned paraboloidal mirror systems have been shown to be effective—if outsize—optical elements, available at relatively low cost for ground test, and, in the future, space operations. Smaller, fibre-optic coupled mirror systems, utilising plastic or metal optics and state-of-the-art optical fibre, were shown to transmit a significant fraction of incident sunlight to a receiver body; further efforts are needed to optimise the fibre-mirror coupling and, therefore, power transmission before this approach can be demonstrated on an operational spacecraft. Both the receiver and mirror elements are now ready for final refinement, in preparation for integration and on-orbit test.

Chapter 7

7 Flight System Development

7.1 Mission Applications

Since 1999, the Surrey Space Centre has taken part in the design, fabrication, test, and on-orbit operation of eight satellites augmented with onboard propulsion (Table 7-1). The first of these, UoSAT-12, carried two propulsion systems and was launched successfully in 1999. The 6.5-kg SNAP nanosatellite, with a total delta-V capability of just 3 m/s, was orbited the following year. Five systems are currently operational, four more are in active development, and several additional propulsion systems are undergoing preparation for launch in mid-2005. Without exception, these satellites used onboard propulsion systems for attitude control and minor orbital adjustments—to date, only a single satellite operator (GSTB-v2, see Table 7-1) has stated a requirement to perform major orbit transfers. In the specific case of SSTL's Disaster Monitoring Constellation (DMC) satellites, butane resistojets were deployed to correct launch insertion errors and properly phase individual satellites (including AlSat-1, UK-DMC, NigeriaSat-1, and BilSat-1) [Gibbon, 2003].

Programme	Status	Launch	Propellant	Propellant mass (kg)	Comments
UoSAT-12	**On orbit**	**21 April 1999**	**N_2**	**6.4**	**Cold gas**
UoSAT-12	**On orbit**	**21 April 1999**	**N_2O**	**2.1**	**100-W resistojet**
SNAP-1	**On orbit**	**28 June 2000**	**Butane**	**0.03**	**Cold gas**
AlSat-1	**On orbit**	**28 November 2002**	**Butane**	**2.4**	**Low power resistojet (LPR)**
UK-DMC	**On orbit**	**27 September 2003**	**Butane**	**2.4**	**LPR**
UK-DMC	**On orbit**	**27 September 2003**	**H_2O**	**0.002**	**microresistojet**
NigeriaSat-1	**On orbit**	**27 September 2003**	**Butane**	**2.4**	**LPR**
BilSat-1	**On orbit**	**27 September 2003**	**Butane**	**2.4**	**LPR**
China DMC+4	**Test**	**2005**	**Xe**	**5.7**	**LPR**
GSTB-v2	**Design**	**2005**	**Butane**	**55.0**	**10 x LPR**
PROBA 2	**Design**	**2006**	**Xe**	**0.5**	**LPR**
GEMINI	**Pre-Design**	**To Be Announced**	**Hydrazine**	**90.0**	**In development**

Table 7-1 SSTL microsatellites augmented with propulsion systems (current and planned).

Actual velocity changes for these missions ranged from essentially zero, in the case of the UK-DMC satellite's experimental water microresistojet, to better than 14 m/s, for the AlSat butane thruster. AlSat-1's performance is instructive: Although originally designed to a target delta-V budget of just 4 m/s, AlSat-1 was launched into a non-optimal orbit requiring significant apogee lowering to ensure proper constellation phasing. Instead of the 686-km circular orbit it was intended to achieve, AlSat-1 was placed in a high, slightly eccentric orbit (686 x 745 km). At an estimated burn-average I_{sp} of 100 s, the AlSat-1 thruster was fired 168 times for three-minute durations over the course of two months in 2003. [Gibbon, 2003]

With a "wet" mass of 90 kg and a propellant loading of 2.4 kg, the butane thruster would be theoretically capable of performing a manoeuvre (or series of manoeuvres) of as much as 26.5 m/s before exhausting its propellant. This would have been sufficient to re-phase AlSat-1 for apogees as high as 790 km.[207] If the launch insertion error had necessitated a larger orbit correction than this, however, onboard propulsion would not have sufficed, and the mission at least partially compromised.

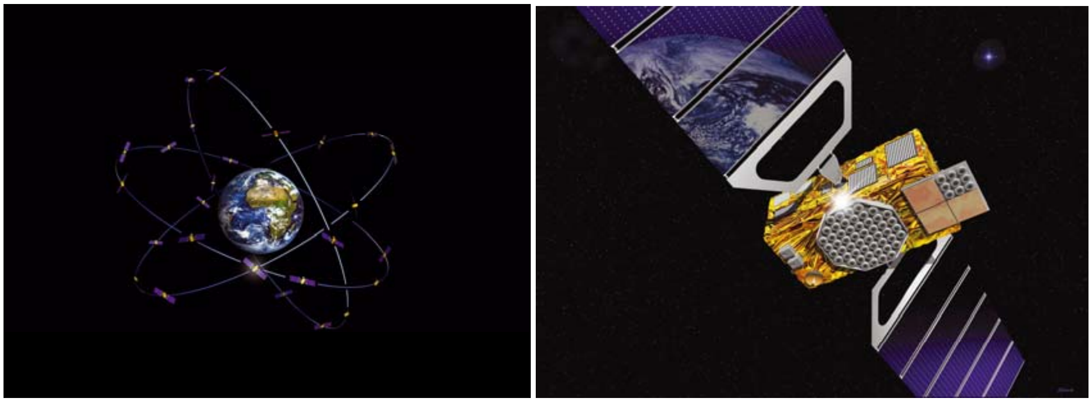

Figure 7-1 30-spacecraft Galileo navigation satellite constellation (left) and satellite detail (right).

Higher delta-V missions, to include low orbit drag makeup, long-term orbit maintenance, and orbit transfer, are under investigation now. The Galileo System Test Bed (GSTB) navigation demonstration satellite, developed by SSTL for the European Space Agency, will launch in 2005 to a moderate-inclination (56°), 23,200-km circular orbit. [Benedicto, 2000] This spacecraft, which will be SSTL's largest to date, will mass more than 500 kg and carry up to 55 kg of butane propellant. The butane system is intended to provide not only initial orbit error correction and fine on-orbit positioning, but also orbit transfer—specifically, for "graveyarding" of the satellite in order to remove it from its operational orbit prior to deployment of the full-up constellation.

---

[207] Presuming a perigee of 686 km. The 26.5 m/s limit would also permit correction from higher-eccentricity orbits centred on the target circular orbit (up to approximately $e = 0.007$, corresponding to an orbit of 636 x 736 km).

[Coxhill, 2004] NASA, ESA, and the U.S. government have published guidelines for re-orbiting post-operational satellites; NASA requires that, for geosynchronous satellites, manoeuvres of this type must place GEO spacecraft in disposal orbits of no less than 300 km above GEO. A 300-km orbit-raising manoeuvre, applied to GSTB, would cost 19 m/s. [Walker, 2002] A 500-km transfer would add to this somewhat, costing 31 m/s. Even at a modest I_{sp} of 80 s, the butane propulsion system on GSTB should be capable of providing more than three times this delta-V, or 90 m/s. This should be sufficient to perform fine positioning and perhaps provide some margin in the event of unforeseen launch injection errors.

Of the current stable of missions under investigation, only GEMINI (see Section 3.1.1) will require a substantially larger delta-V budget than those spacecraft already on-orbit, and this is primarily due to the requirement to achieve fine north-south stationkeeping in geosynchronous orbit.[208] While there do not appear to be any microsatellite missions within the Centre's current planning horizon that would utilise very high delta-V systems (1,000 m/s or more), there are at least two near-term opportunities for flight demonstration of a microscale solar thermal propulsion system: (1) As a minimum-impact experiment on the next DMC spacecraft, modelled on the existing bus and launched into the standard 686 km circular orbit; and (2) as an operational system performing drag makeup and life extension for the Los Alamos National Laboratories' Cibola Flight Experiment satellite (CFESat), an SSTL spacecraft intended to launch in October 2006 from Cape Canaveral in the United States. [Ambrosiano, 2004] The author will review requirements and recommended design options for each of these missions.

7.1.1 A Microscale Solar Thermal Propulsion Experiment on DMC

Any of several Russian launch vehicles are capable of delivering a DMC spacecraft, along with multiple additional payloads, to the standard 98° inclination, 686-km circular orbit. [SSTL, 2004]. The four DMC satellites currently on orbit have sufficient onboard propellant to continue stationkeeping operations for up to five years. After this point, spacecraft-to-spacecraft phasing will deteriorate and the constellation will have to be replenished. However, due to (1) the relatively low atmospheric drag extant at altitudes over 600 km, and (2) the high ballistic coefficient[209] of the standard DMC bus (see Section 7.1.2), DMC spacecraft are predicted to have lengthy orbital lifetimes—potentially as long as a century, were the satellite's gravity gradient boom not to deploy [Larson, 1992]. A pseudo ballistic coefficient, B^*, has been historically defined by the relation [Kelso, 1998]:

---

[208] This could be as much as 50 m/s/year, and is due primarily to the need to offset cyclical solar and lunar perturbations [Larson, 1992].

$$B^* = \frac{\rho_o}{2B} = \frac{\rho_o}{2}\left(\frac{C_D A}{m}\right) \tag{7-1}$$

Here, ρ_o is the standard atmospheric density at 120 km altitude. B^* is usually tabulated in units of (earth radii)$^{-1}$ or r_E^{-1}, and can take on negative values at altitudes for which solar and lunar perturbations impart an apparent "negative drag." The DMC constellation orbits in the transition region, around 700 km, between low altitudes (where atmospheric drag dominates) and higher altitudes (where solar and lunar effects dominate). For AlSat-1, the first of the DMC spacecraft, $B^* = 4.7793 \times 10^{-5}\ r_E^{-1}$ [Peat, 2004]. This corresponds to a ballistic coefficient of greater than 1,600, and would tend to indicate an extremely long orbital lifetime; however, this very high apparent value is due not just to solar and lunar effects, but also to solar activity, which is nearly halfway between two solar maxima (the last occurring in 2000) [Space.com, 2000]. As the next solar maximum approaches, heating of the upper atmosphere will cause B^* to increase.

It would be useful to investigate the possibility of removing decommissioned DMC satellites from the vicinity of the constellation, to mitigate debris proliferation at the orbit of interest. Two alternatives suggest themselves: (1) orbit raising, to 1,000 km or higher,[210] or (2) orbit lowering, followed by rapid decay and re-entry. While orbit raising eliminates the concern over specific interference with the DMC constellation, it nevertheless remains on-orbit, where it represents a potential collision hazard for other spacecraft. For the purposes of this analysis, the author has assumed a series of apogee manoeuvres, designed to lower satellite perigee from 686 to 300 km. At this altitude, orbital lifetime is measured in weeks to months.

To investigate alternative propulsion system configurations that could perform this mission, the author conducted a number of simulation exercises with the Microscale Solar Thermal Propulsion Integrated System Model (MSTISM), a spreadsheet-based model utilising Visual Basic scripts to simulate concentrator properties and solar power input, solar receiver thermal charging, propellant discharge, and resulting rocket performance.

Start Orbit	**686 x 686 km circular**
Target Orbit	**686 x 300 km circular**
Elapsed Time	**324 hrs., 55 min.**
Number of Manoeuvres	**203 (perigee kicks only)**
Total Velocity Change	**112 m/s**
Propellant Consumption	**7.63 kg (ammonia)**
Burn-average I_{sp}	**151 s**
Thrust (mN)	**1,310**
Concentrator properties	**Four 14-cm diameter, aluminium monolith mirrors, 300 g,**

---

[209] A DMC satellite has a maximum ram area of 0.48 m^2 (60 x 80 cm). For the minimum value of spacecraft mass (100 kg) and probable drag coefficient (2-4), a ballistic coefficient of 50-100 kg/m^2 results.

[210] This would place the defunct spacecraft in a sparsely populated region, just inside the first van Allen belt [Brown, 2002].

Receiver properties and heat transfer mode	***f*/0.6 (theoretical concentration ratio > 12,000)** **Receiver dimensions: 3 cm length, 3 cm outer diameter, 0.4 cm inner diameter** **Insulation thickness: 3 cm** **Channel flow (1 mm diameter, 15 cm length)** **Channel ΔP = 6 bar**
Engine "On-Time"	**2 hrs., 17 min.**

Table 7-2 Baseline parameters of a DMC de-orbit mission utilising solar thermal propulsion. Spacecraft "wet" mass = 100 kg.

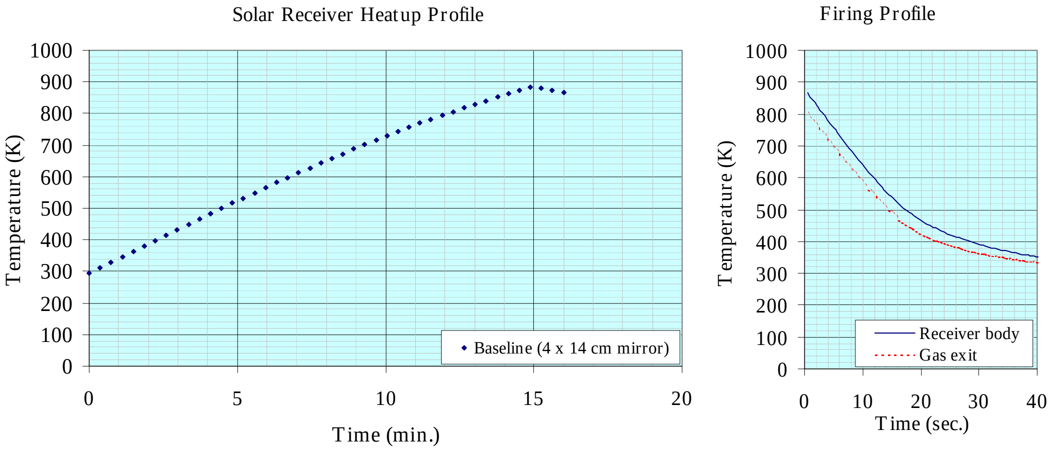

Figure 7-2 Heatup (left) and firing profile (right) for baseline solar thermal demonstrator engine (15-minute charge, 1 minute delay, 40.4 s firing time).

Properties of the baseline solar thermal propulsion experiment are described in Table 7-2. It includes the use of four 14-centimetre diameter aluminium concentrating mirrors, producing 75 W of input power; a 95-gram ceramic heat exchanger, coupled to each of the mirrors via a low attenuation fibre optic feed, and insulated with a jacket of carbon foam; and a vapour-pressure fed ammonia propellant storage and feed system. A single-mirror version of the baseline, shown mounted on a sun-tracking alt-azimuth platform, is illustrated in Figure 7-3.

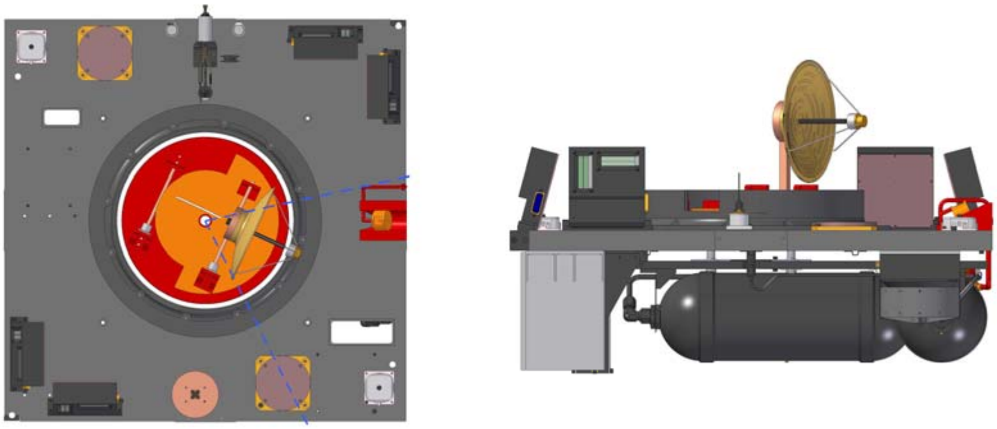

Figure 7-3 Disaster Monitoring Constellation microsatellite augmented with microscale solar thermal propulsion experiment (space-facing facet detail, deployed configuration).

Although the fibre-coupled, multiple-mirror solution provides sufficient power to perform the orbit-lowering mission in just 13 ½ days, surface area on the space-facing facet of DMC is at a premium; while a single mirror could be accommodated within the spacecraft-launcher separation ring (in the figure above), placing multiple mirrors within this ring will prove difficult without complex deployment mechanisms (e.g., folding arrays of mirrors). For this reason, MSTISM was employed to investigate single-mirror alternatives to the baseline, some using alternate propellants.

Concentrator diameter	14 cm		20		30		60	
Input power (W)	19		38		71		318	
Propellant	NH_3	H_2	NH_3	H_2	NH_3	H_2	NH_3	H_2
Elapsed time to orbit (hrs.)	647	634	442	374	333	272	214	188
Number of manoeuvres	403	395	276	233	208	170	134	118
Total velocity change (m/s)	112	112	112	112	112	112	112	112
Propellant Consumption (kg)	8.85	3.68	8.33	3.49	7.70	3.29	6.46	2.95
Tank volume (litres)	14	134	13	128	12	120	10	107
Engine "On-Time" (min.)	2.23	2.49	2.25	2.49	2.28	2.48	2.32	2.47
Burn-average I_{sp} (s)	129	319	138	337	150	358	179	400
Mirror mass (kg)	0.3	0.3	0.6	0.6	1.36	1.36	5.45	5.45
Dry STP system mass (kg)	0.81	5.31	1.09	5.62	1.81	6.37	5.85	10.46
Final payload mass (kg)	90.34	91.01	90.58	90.89	90.49	90.34	87.69	86.59

Table 7-3 Sensitivity of system performance to mirror diameter and propellant choice. The 60-cm option requires a larger receiver aperture (0.75 cm diameter) to accommodate the increase in focal spot size.

Table 7-3 compares the performance of several STP systems, utilising 14-, 20-, 30-, and 60-cm aluminium concentrating mirrors and both ammonia and hydrogen as propellants. While hydrogen's specific impulse advantage greatly reduces propellant mass, storing hydrogen as a high-pressure gas requires tank volumes of more than 100 litres; the current DMC satellite, fitted with two 2.5-litre tanks (Figure 7-4), would be incapable of supporting this vastly increased tank volume without significant re-design [Gibbon, 2004].

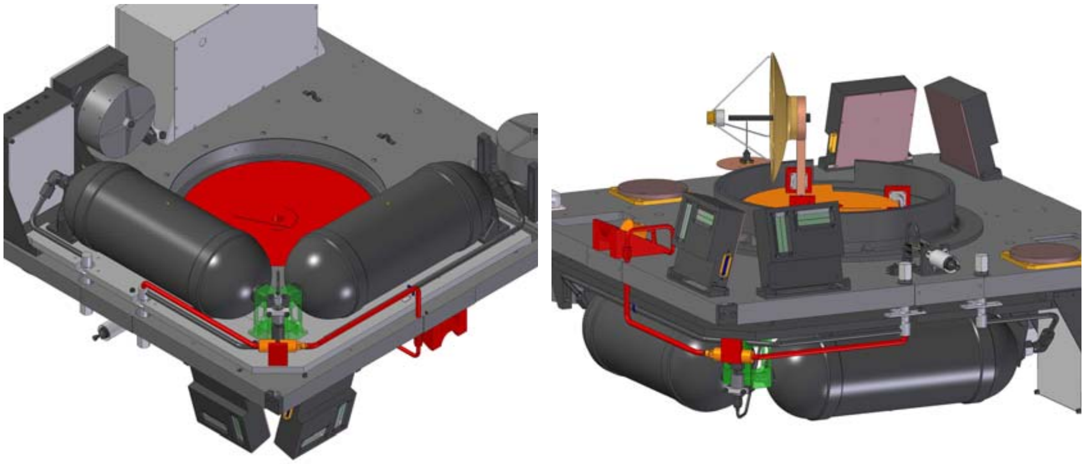

Figure 7-4 Propellant storage and feed system configuration, DMC experiment (left). Solar receiver mounting (right).

The minimum diameter single mirror configuration, shown in Figure 7-4, would have to be augmented with approximately 10 litres of additional ammonia tankage to permit an orbit transfer of the magnitude required. Alternatively, utilising the unmodified existing tankage could permit a low-power STP experiment to lower a DMC satellite's perigee to 536 km (delta-V = 43 m/s).

Unlike the CFESat demonstrator (discussed in the next section), the DMC experiment is not especially sensitive to seasonal changes in sun orientation, due to the satellite's high inclination and the selected deployment scheme. DMC and CFESat are nadir-pointing spacecraft; on DMC, the STP experiment would be initially deployed with the concentrator axis orthogonal to the space-facing facet on which it resides. Therefore, it will be possible to perform thermal chargings and firings on each orbit; there are no firing seasons and eclipse seasons. CFESat, which orbits at a lower inclination, does possess firing seasons, with substantial impacts on manoeuvre strategy.

7.1.2 An Operational Solar Thermal Propulsion Demonstrator on CFESat

The Los Alamos National Laboratories (LANL) are pursuing the development of CFESat, which is intended to survey portions of the Very High Frequency (VHF) and Ultra-High Frequency (UHF) electromagnetic spectrum in low earth orbit. The CFESat platform will be designed and fabricated by SSTL prior to delivery to the United States.

> "The U.S. Department of Defense Space Test Program (STP) is including the CFE satellite as part of the STP-1 space flight mission. The STP-1 mission goal is to provide space-flight opportunity for a maximum number of DoD Space Experiments Review Board payloads on a single launch. The DoD Space Test Program is responsible for the integration of seven satellites into a single payload stack and launch of the STP-1 mission. The STP-1 mission is scheduled for launch in 2006 on a medium-class Lockheed-Martin Atlas-V, a U.S. Air Force Evolved Expendable Launch Vehicle (EELV),

> using the EELV's Secondary Payload Adapter that allows small satellites to be launched as "piggyback" passengers with larger spacecraft." [Nice, 2004]

The U.S. Air Force's Space Test Program (STP)-1 launch vehicle will deliver the 165-kg CFESat and several other experimental payloads to a 35.4° inclination, 560-km circular orbit. [Sakoda, 2002][Ambrosiano, 2004]. At this altitude, atmospheric drag is potentially significant; the orbital lifetime of a small spacecraft at 560 km could be as low as 4 ½ years, assuming solar maximum conditions. For decreased solar activity, this rises to 15 years or more. In the worst-case (solar maximum), onboard propulsion could provide significant drag makeup capability, extending on-orbit lifetime.

For circular orbits, an approximate relation for the change in orbital period ΔP per revolution is [Larson, 1992]:

$$\Delta P = -6\pi^2 \left(\frac{C_D A}{m} \right) \frac{\rho a^2}{v} \tag{7-2}$$

ΔP is thus directly related to the satellite's drag coefficient, C_D, its planform area, A, as well as the local atmospheric density, ρ, and the square of the orbit's semi-major axis, a. It is also an inverse function of the product of the satellite's mass (m) and velocity (v). The second term in the equation is the satellite's ballistic coefficient. This parameter is obviously dependent on the "ram" area of the spacecraft, which can vary significantly if the satellite's aspect ratio is large and/or it experiences attitude changes which permit various vehicle facets to face in the direction of the velocity vector at different times. C_D typically takes on values between 2 and 4 [Larson, 1992]. Integrating this equation with respect to time provides an estimation of orbital altitude and therefore orbital lifetime (Figure 7-5).

Atmospheric density at orbital altitudes fluctuates as a result of thermospheric heating, itself a function of two phenomena: (1) absorption of extreme ultraviolet (EUV) radiation from the Sun, which varies with the 11-year solar activity cycle, and (2) geomagnetic storms, which occur during violent solar activity (e.g., coronal mass ejections), precipitating electrons from the magnetosphere into the lower thermosphere.[211] Measurements of the 10.7-cm radio flux, made daily by a variety of agencies, are generally regarded as a surrogate for EUV intensity; the $f_{10.7}$ index can vary between 50 and perhaps 300 Solar Flux Units (SFU), with the upper end of this range indicating the condition known as "Solar Maximum." Daily measurements of the planetary A (A_p) index for geomagnetic activity are also available [ESTEC, 2004].

---

[211] Nominally between 120 and 600 km [Larson, 1992].

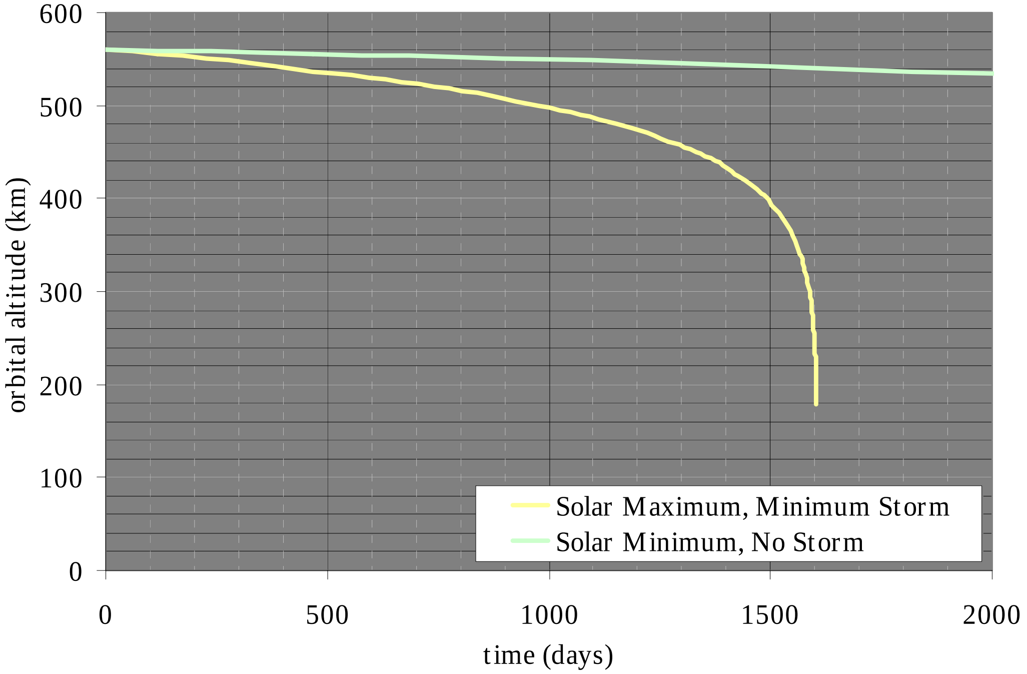

Figure 7-5 Orbital altitude versus time, initial spacecraft altitude = 560 km, planform area = 2 m^2, spacecraft mass = 150 kg . Solar maximum conditions assume a solar flux ($f_{10.7}$) of 225 SFU and a Geomagnetic A index (A_p) of 30. Solar minimum conditions assume a flux of 138 SFU and an A_p of 0.

Kennewell provides the following empirical correlation between solar activity and storm intensity, vehicle altitude (*h*), and atmospheric density [Kennewell, 1999]:

$$\rho(h) = 6\times10^{-10} e^{-\left(\frac{h-175}{\left(\frac{900+1.5A_p+2.5(f_{10.7}-70)}{27-0.012(h-200)}\right)}\right)} \tag{7-3}$$

The analysis that follows is based on solar maximum conditions. The velocity change needed to re-acquire the CFESat mission orbit is determined by stationkeeping requirements and will define an "orbit box" that the vehicle must remain inside to achieve its mission objectives.[212] Figure 7-6 illustrates the variation of delta-V for various wait times. If stationkeeping requirements are stringent (e.g., the satellite must not drop more than 5 km before a reboost is required), then a 2.8 m/s firing will be required every 90 days. As this requirement relaxes, firings can become less frequent but delta-V grows roughly linearly; for a ±10-km orbit box, firings can be performed once every six months, but the total delta-V is roughly double, at 5.5 m/s. For large orbit boxes, increased drag at lower altitudes requires a higher cumulative delta-V: A ±60-km box can be maintained with infrequent firings (every 26 months) at a per-firing cost of 33 m/s.

---

[212] Specifically, the satellite developer must specify a minimum altitude (*h*) under which the satellite is incapable of performing its mission effectively.

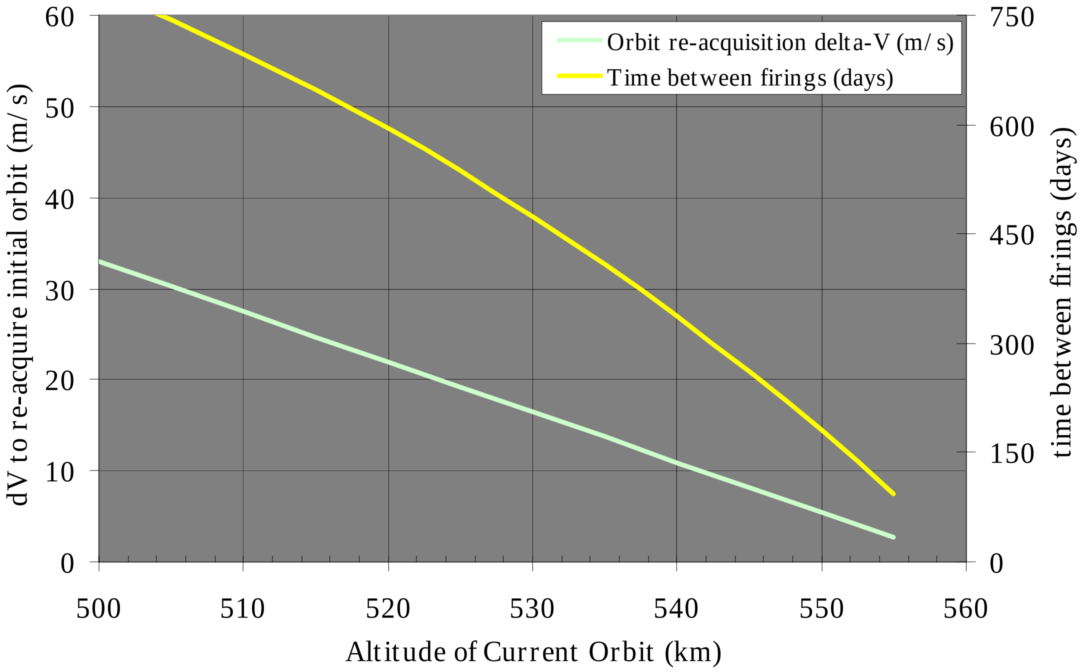

Figure 7-6 Mission orbit re-acquisition delta-V requirements and mean time between firings versus orbital altitude, assuming solar maximum conditions.

Three key constraints appear to drive the mechanical design and operational use of the solar thermal demonstrator on CFESat: (1) a stipulated requirement to place any associated demonstrator hardware on the space-facing facet of the satellite; (2) the satellite's pointing accuracy, which is likely to be on the order of ±1.0° [Oosthuizen, 2004]; and (3) an inability to re-point the satellite for thermal charging. A rigid, fixed mirror is therefore not recommended, even were it operationally feasible to re-orient the satellite; without a fine-pointing capability of ±0.1° or better, the concentrator subsystem will be required to perform its own pointing.

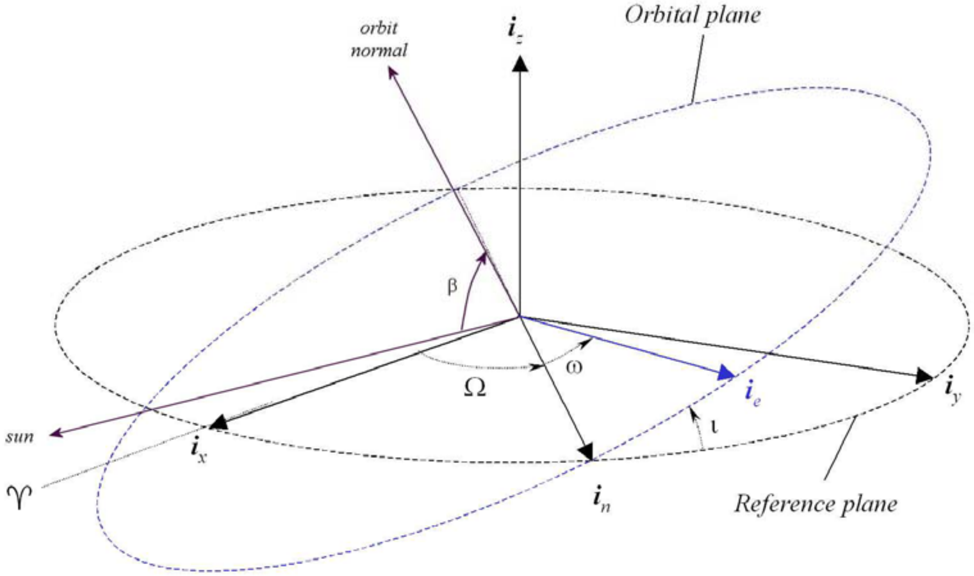

Figure 7-7 Solar beta angle definition [Battin, 1987][Larson, 1992].

Firing opportunities will be further restricted to sunlit portions of the orbit, during certain seasons of the year. The duration of these firing opportunities is determined by the satellite's beta (β) angle, defined as the angle between the vehicle's orbit plane (and the orbit normal, *n*) and the solar vector *s* (Figure 7-7). Additionally, for a nadir-pointing spacecraft in low earth orbit, the zenith angle φ between the space-facing facet normal *f* and *s* can be represented by the dot product of the two unit vectors:

$$\varphi = \cos^{-1}\left[f \cdot s\right] \tag{7-3}$$

Where $f(t)$ = [0.53cos(94.36(t-t_o)) sin(94.36(t-t_o)) 0.85cos(94.36(t-t_o))]. The solar vector $s(t)$ can be represented by [sin(.0172(t-t_o) cos(.0172(t-t_o) 0]. Zenith angle maxima and minima, shown in Figure 7-8, illustrate seasonal firing constraints: For a hypothetical STP system constrained to operate within 40° of zenith, it will be possible to conduct a firing campaign for the first 72 days of satellite operation. The satellite then enters a non-firing season, which extends nearly three months, to mission day 156. Note that a system capable of slewing as far as 60° from zenith would not experience firing seasons, and could be used virtually throughout the year.

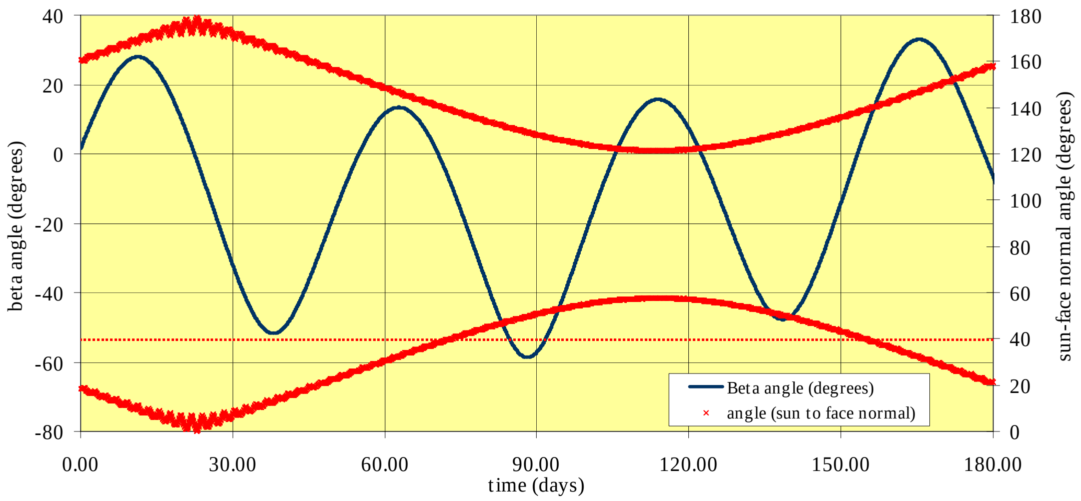

Figure 7-8 Solar beta angle and zenith angle (φ) maxima and minima, 560 km circular orbit, 35.4° inclination, 1 October 2006 to 1 April 2007 (Mission Days 1-180).

For a zenith angle constraint of 40°, the actual firing season will be somewhat shorter than that indicated in Figure 7-8. Due to finite charging time requirements, which could range as high as 15 minutes or more, depending on receiver thermal storage mass and concentrating mirror input power, the first firing season would be constrained to occur between Mission Days (MD) 1 (18 minute thermal charging opportunity) and MD 60 (15 minutes). The longest window occurs on MD 21 (Figure 7-9), with nearly 22 minutes of charging time. Given CFESat's orbital period of 96 minutes, each mission day provides 15 firing opportunities; thus, there are 900 thermal charging windows available during the first firing season. These will repeat every 180 days.

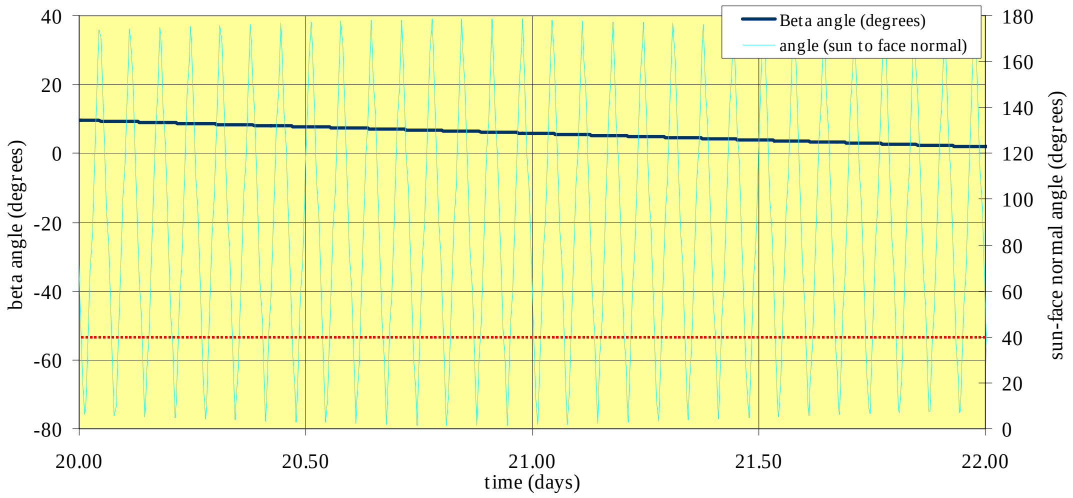

Figure 7-9 Beta angle and zenith angle φ, Mission Days 20-22 (longest-duration thermal charging opportunity).

Start Orbit	**550 x 550 km circular**
Mission Orbit	**560 x 560 km circular**
Elapsed Time	**582 hrs., 41 min.**
Number of Manoeuvres	**366 (184 apogee kicks, 182 perigee kicks).**
Total Velocity Change	**5.8 m/s**
Propellant Consumption	**410 g (ammonia)**
Burn-average I_{sp}	**246 s**
Thrust (mN)	**1,040**
Concentrator properties	**14-cm diameter, aluminium monolith, 300 g**
Receiver properties and heat transfer mode	**Receiver dimensions: 1 cm outer diameter, 0.4 cm inner diameter, 3.5 cm length, 0.3 cm aperture diameter, 3 cm insulation thickness** **Channel flow (1 mm diameter, 15 cm length)** **Channel ΔP = 4.5 bar**
Engine "On-Time"	**15.2 min.**

Table 7-4 Baseline LEO drag makeup mission, key parameters. Spacecraft "wet" mass = 165 kg.

The author's MSTISM model was used to examine excursions from the baseline demonstrator design, described in Table 7-4. The baseline system includes a 300-gram, 14-cm diameter mirror[213] supplying 19 W to a ceramic (TiB_2/BN) solar receiver via coupled fibre optics. The receiver structure masses 11 grams; a 15-minute thermal charging raises the receiver's temperature to almost 1,200 K; this decays to 1,115 K during the one-minute hold prior to firing. Each of the 366 firings lasts just 2 ½ seconds (Figure 7-10). With ammonia propellant, the baseline engine achieves a burn-average I_{sp} of 246 s. This is superior to monopropellant hydrazine.[214] The STP system's total mass (propellant excluded) is very low, less than 0.5 kg.

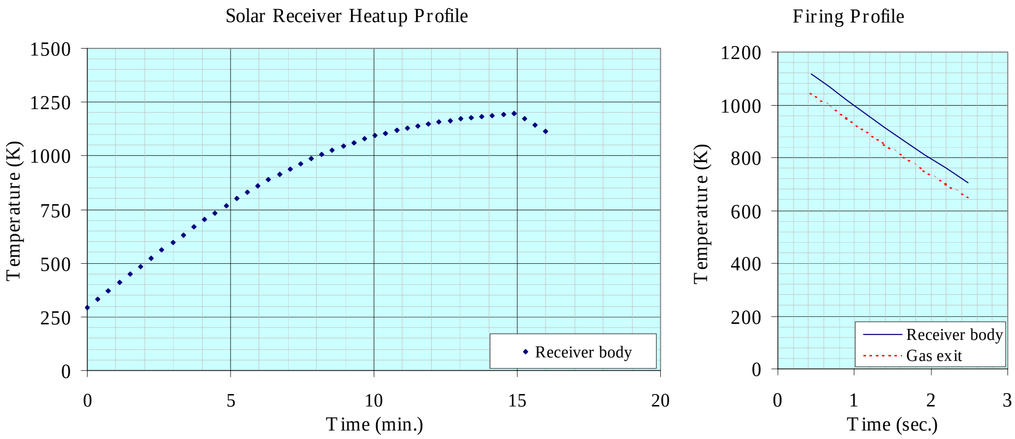

Figure 7-10 Heatup (left) and firing profile (right) for baseline solar thermal demonstrator engine (15-minute charge, 1 minute delay, 2.49 s firing time).

---

[213] This is comparable to the ground test optic's mass properties, discussed in Section 6.3.3. The approximate areal density of this item is 19 kg/m^3.

[214] Representative systems can achieve an I_{sp} of as much as 230 s (Section 3.2.1).

While it is technically feasible to begin firings immediately—due to favourable orbital conditions immediately following launch—it is unlikely to be necessary, unless the system is required to perform an orbit correction upon insertion. The first useful firing season, beginning around MD 171, is 60 days in length (assuming, as stated, an STP tracking capability of up to 40° off zenith). Under solar maximum conditions, orbital altitude is estimated to decay by as much as 10 km during the first six months of the mission; the baseline STP system would fire once per orbit, beginning on MD 188 and completing its last burn just over 24 days later (Figure 7-11).

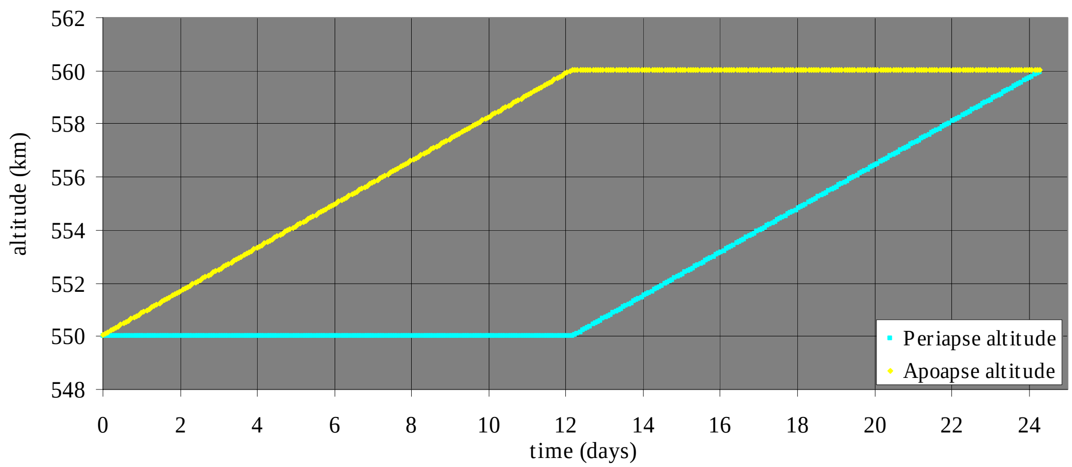

Figure 7-11 Orbital altitude versus time, drag makeup mission. Day 0 = MD 188 (7 April 2007).

Concentrator diameter	14 cm	7	20	30
Input power (W)	19	5	38	71
Elapsed time to orbit (hrs.)	583	429	409	311
Number of manoeuvres (apogee/perigee)	366 (184/182)	270 (136/134)	257 (129/128)	196 (99/97)
Total velocity change (m/s)	5.8	5.8	5.8	5.8
Propellant Consumption (ammonia, g)	410	680	390	380
Engine “On-Time” (min.)	15.2	14.6	14.2	13.7
Burn-average I_{sp} (s)	246	150*	259	264
Mirror mass (kg)	0.30	0.07	0.61	1.36
Dry STP system mass (kg)	0.33	0.11	0.64	1.39
Final payload mass (kg)	164.26	164.21	163.97	163.23

Table 7-5 Sensitivity of STP system performance to mirror diameter. (*The 7-cm mirror option does not achieve the baseline minimum firing temperature (MFT) of 600 K; for this case only, MFT = 350 K).

While it may appear intuitive that larger mirror diameters—and therefore higher radiant flux input, higher peak receiver temperatures, and higher burn-average specific impulses—would significantly improve the baseline, Table 7-5 demonstrates the opposite. For the extremely low delta-V requirement posited for the case at hand, substantial increases or decreases in I_{sp} can do little to affect overall system performance; far more important is the non-linear dependence of space mirror mass on diameter. Replacing the baseline mirror with a 30-cm concentrator increases input power by a factor of nearly five, while increasing mirror mass by the same factor. Halving mirror diameter, to 7 cm, reduces input power, peak firing temperature, and achievable burn-average I_{sp}; nevertheless, the decrease in mirror mass more than makes up for the increase in required propellant. For minor, occasional orbital adjustments, then, a demonstration STP system can be as small as desired, without sacrificing significant performance.[215]

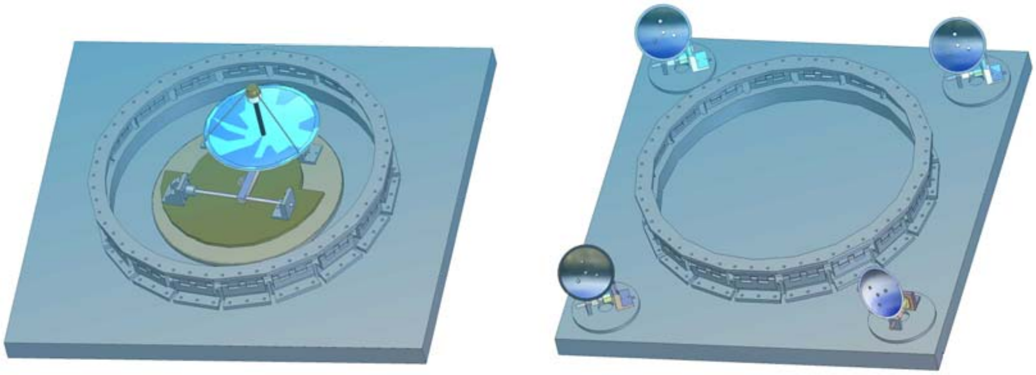

Figure 7-12 Concentrator subassembly mounting schemes on CFESat space-facing facet: baseline 14-cm mirror, alt-azimuth mount (left), ganged mirror alternative, including four 7-cm mirrors (right).

Like the DMC experiment, the CFESat demonstrator will be required to perform fine sun-pointing, which does not permit a receiver placed at the concentrator focal point to fire through the spacecraft centre of gravity without prior re-positioning following thermal charging. The appropriate implementation would therefore include fibre optic transmission from the focal point to a fixed, remote solar receiver.

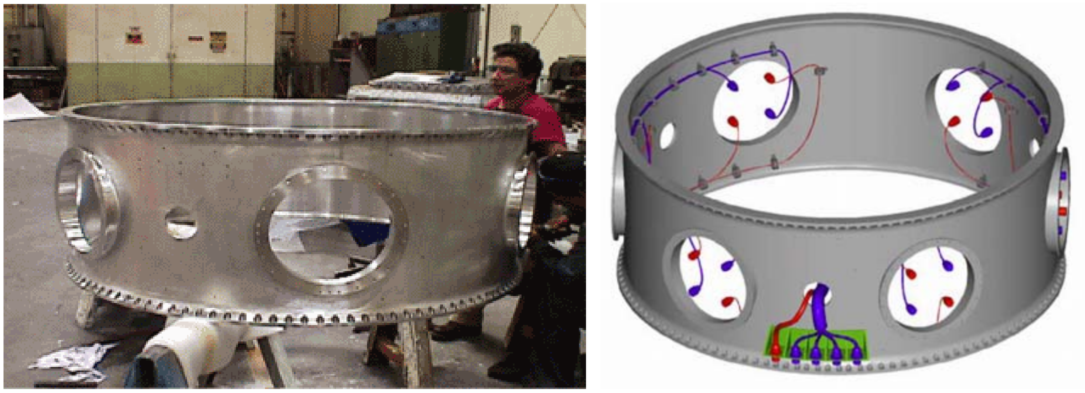

---

[215] Were this drag makeup mission performed five times—for a cumulative delta-V requirement of 29 m/s—the difference in propellant consumption between the baseline and the 7-cm case would increase to almost a kilogram, favouring the larger mirror.

Figure 7-13 EELV secondary payload adapter ring undergoing final machining, left [Ganley, 2002]. Example electrical harness layout, right [Goodwin, 2001].

With limited vehicle surface available, the most likely placement point for the demonstration system will be inside the launch vehicle adapter-spacecraft separation ring (Figure 7-12, Figure 7-13), presuming deconfliction with any mission critical hardware. Up to six small satellites (each massing less than 400 lbs., or 182 kg) can be cantilevered off of the EELV's main payload adapter ring [STP, 2001]. While previous Surrey platforms have used this space to stow a gravity gradient boom (prior to deployment), CFESat will use momentum wheels and star trackers to permit full three-axis attitude control of the spacecraft. Therefore, a gravity gradient stabilisation system is not required, and this volume is potentially free to accommodate other subsystems.

The CFESat adapter ring, which mates to one of the six ESPA port shown in Figure 7-13, is only 6 cm in height. Since the baseline mirror's focal length is 8.5 cm, there will be limited intrusion into the ESPA port even with the mirror stowed flush against the spacecraft facet; it is likely that this could conflict with harness placement and therefore may not be an acceptable solution. An alternative approach would be to use one or more smaller-diameter mirrors on separate alt-azimuth mounts, placed either inside or outside the separation ring. Four 7-cm mirrors,[216] supplying radiant power equivalent to the single 14-cm mirror baseline, can be placed outside the separation ring on individual pointing mounts, demonstrating a ganged mirror scheme.[217]

7.2 Baseline Demonstrator Design Issues

The simplest demonstrator would rely on spacecraft attitude control for solar tracking, which would remove the need to provide a fine-pointing mechanism on the STP system. However, for both the DMC and CFESat cases, the operational impact—namely, the requirement to off-point from nadir each orbit for up to 15 minutes to allow STP thermal charging—is sufficiently high to demand an alternative implementation.

The space-facing facets of both DMC and CFESat will host two or more of SSTL's two-axis fine sun sensors, providing analogue output from each axis (0-5V). The onboard computer, or a local controller, could concatenate this output (Figure 7-14) to provide sun angle information and transmit concentrator mirror steering commands. These sensors are capable of providing, at a minimum, coarse pointing knowledge to within one-half of one degree [SSTL 2, 2004].[218] AeroAstro [2004] produces an extremely small (2-cm diameter, 36 grams) quad-photodiode sun sensor but its quoted pointing knowledge is only ±1°. Jena-Optronik [2004] manufactures precise sun sensors (±0.18°, 3σ); however, at 630 grams, these are twice as heavy as SSTL's sensors. As none of these solutions permit fine pointing (≤ 0.1°), the most plausible approach would be to use onboard, already-available sensor data for coarse pointing and closed-loop fine pointing on the mirror assembly itself. Small heat flux sensors, comparable to the elements described in Section 6.3.1, could be affixed to a heat sink mounted in the focal plane, surrounding the nominal focal spot. Spot "drift" would result in excess heating of one or more heat flux sensors; an appropriate control algorithm would then steer the concentrating mirror back into alignment. Because of the extreme fluxes present at the focal point, the heat flux sensors would have to be shielded, perhaps by a thin layer of aluminium.

---

[216] A small mirror, identical in form to the baseline (7-cm diameter, f/0.6), would have a focal length of just 4.25 cm. This should provide sufficient height clearance to permit placement either inside or outside the separation ring.

[217] Placing one or mirrors outside the separation ring simplifies the placement of fibre runs. If the concentrator assembly were to be placed inside the ring, a fibre line would have to penetrate the space-facing facet and re-emerge outside the ring, complicating internal subsystem arrangements.

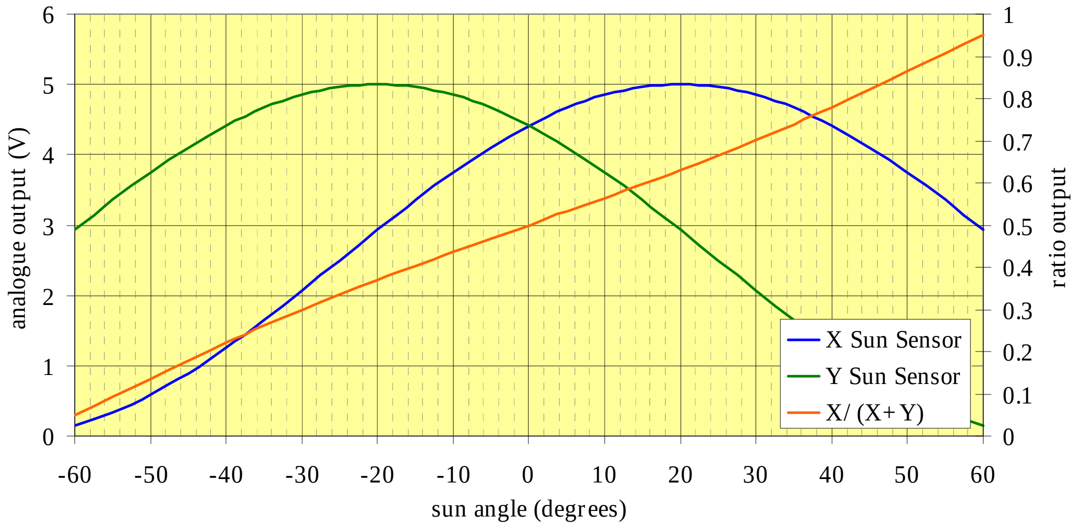

Figure 7-14 SSTL Fine Sun Sensor output, two axes and ratio (X/(X+Y)).

Mussett [2003] describes a coarse-pointing assembly (CPA) for optical intersatellite links. This device is a 2.5-kg, two-axis (altitude-azimuth) tracker using stepper motors in microstepping[219] mode to produce mirror steps of 5 μrad (in altitude) and 2 μrad (azimuth). Positional accuracy is stated at better than ±0.5 mrad in both axes (±0.03°). A combined CPA/FPA (coarse pointing assembly/fine pointing assembly) for intersatellite laser communication is discussed by Barho [2003]; this is substantially heavier (at 12 kg) and uses brushless DC motors to achieve coarse pointing accuracies of ±0.009° and a fine pointing accuracy a factor of ten better. While these systems demonstrate that extreme fine-pointing is possible and practical, system mass is relatively high and the units themselves are volumetrically inefficient, designed as they were for large satellite platforms. Producing and validating a low-cost, low-mass, medium-accuracy pointing system suitable for the baseline demonstrator system represents the single greatest challenge to the designer.

---

[218] Quoted performance is ±0.5°, 3σ.

[219] Microstepping permits stepper motors to increase their resolution by holding at intermediate points between two hardstops. Power is supplied to the stepper motor during microstepping.

Other issues will include:

(1) The development of an appropriate fibre-receiver interface element, to prevent fibre tip contamination by receiver outgassing or fibre slumping and failure upon exposure to extreme temperatures. Since the fibre's numerical aperture is likely to be closely matched to that of the mirror, to permit maximum acceptance of incident flux, it will exhibit an exit NA equal to or greater than the entrance NA. This prohibits the use of Gordon's "overlapping spotlights," whereupon fibre tips can be held at a safe distance from the receiver [Gordon, 2003]. The wide exit light cone produced by a high-NA fibre will require it to be placed either at or inside the receiver aperture, to ensure proper flux transmission and minimise losses. Molded fibre tips, or the placement of high-temperature tolerant secondary refractive elements [Soules, 1997] at the fibre's distal tip, might mitigate this problem.

(2) A methodology for preventing fibre breakage during launch and operation of the solar thermal demonstrator. For fibre-coupled systems with rigid, fixed mirrors, the fibre can be placed (and set) prior to launch; however, a moving mirror assembly pre-supposes some slack in the fibre, in order to allow for mirror tracking. Large azimuthal mirror motions could cause the fibre to twist and break. Improperly-made fibre support assemblies could induce stress concentrations and crack fibres.[220] These events would be catastrophic for the subsystem; flux transmission to the solar receiver would fall to zero.

(3) The use of secondary concentrators (e.g., hyperboloidal mirror elements) and Cassegrain-like schemes to improve fibre support at the mirror-fibre interface and to relax pointing accuracy requirements.

7.3 Summary

A solar thermal propulsion demonstrator, utilising small metal concentrating mirrors, optical fibre transmission of solar flux, and remote solar receivers, is technically feasible and can augment existing Surrey microsatellites, including the DMC and CFESat spacecraft. Either butane or ammonia could serve as propellant. Such a system could supply 100 m/s of velocity change to a DMC satellite, permitting re-entry, assuming approximately 10 litres of additional tankage volume (ammonia) could be made available. The small demonstrator is also capable of performing limited drag makeup for the CFESat vehicle, although firings would be constrained to occur only during certain seasons, owing to the satellite's solar beta angle variations. The velocity change required to accomplish orbital re-acquisition is just 6 m/s, twice per year. Each re-acquisition would consume approximately 400 grams of ammonia propellant, at a burn-average I_{sp} of 245 s.

---

[220] The author broke several 1-mm core diameter fibre tips while preparing the ganged-mirror power throughput tests described in Section 6.3.2. The fibre tips were placed inside a metal sheath, which, for certain sun angles, would press against the side of the fibre, cracking it.

Chapter 8

8 Summary and Conclusions

8.1 Overview

This chapter summarises the author's three-year investigation of solar thermal propulsion for microsatellites. It discusses some of the highlights of the effort, including key contributions in the areas of microsatellite mission analysis, modelling, design, test, and flight demonstration preparation. This chapter will also make note of specific recommendations for follow-on research.

8.2 Summary

Efforts to determine the utility and feasibility of a small solar thermal propulsion system, suitable for use aboard a microsatellite platform, have shown that it is possible—with some minor modifications to the author's existing test articles—to design a high-performance solar thermal engine that should rival or exceed state-of-the-art bipropellant hydrazine (N_2H_4/N_2O_4) systems, at a fraction of their cost. The author has built and tested practical designs for two critical components of the solar thermal engine, the concentrator and thermal storage receiver. Test results were compared with predictions taken from the author's Microscale Solar Thermal Integrated System Model, showing strong agreement.

A number of candidate missions were examined to determine the applicability of a small-scale solar thermal propulsion system. Spiral transfers, with their substantial delta-V penalties, were rejected in favour of multi-impulse (apogee and perigee "kick") firing plans. Detailed analysis, using Analytical Graphics' Satellite Tool Kit and Astrogator, permitted the author to calculate specific delta-V requirements for a wide variety of orbit transfers, from highly elliptical earth orbits to (1) geosynchronous earth orbit, (2) earth escape (and flyby of several Near Earth Objects, and (3) low lunar orbit.

- For Near-Escape and Lunar Capture mission types, lunar perturbations become sufficiently severe to warrant the selection of special parking orbits to prevent premature re-entry or unacceptable variation in orbital elements. The author proposed a novel manoeuvring sequence for a solar thermal engine, specifically designed to avoid these lunar perturbations and permit earth escape along any desired trajectory. This High Altitude Phasing Orbit is expensive, costing as much as 3,000 m/s, but maximises mission flexibility (and launcher selection).

- Given the low thrust-to-weight achievable by the solar thermal engine (typically on the order of 10^{-3}), the author proposes the use of intermediate, low-eccentricity phasing orbits in order to achieve low-thrust insertion upon lunar approach without encountering the lunar perturbation difficulties discussed above.

After performing a number of optical and thermal analyses with the validated codes OSLO (optical ray-tracing) and WinTherm (coupled heat transfer in shell bodies), the author constructed MSTISM, a Microsoft Windows-based solar thermal propulsion system model incorporating numerous aspects of the solar thermal engine and its interfaces. For a specified orbit transfer and initial microsatellite mass, MSTISM provides a user with the capability of assigning values to such variables as concentrating mirror diameter, number of mirrors, rim angle or numerical aperture, surface form error, attitude control accuracy, and receiver characteristics such as material densities and thermal conductivities, thicknesses and sizes, heat transfer modes, firing times, propellant types, and supply pressures. Some plausible propellants (notably butane and water) were not included as a result of their complex dissociation chains (butane) and requirement for two-phase flow modelling (water).

- MSTISM uses an explicit finite difference formulation to compute the receiver energy balance and determine the correct heating profile. While explicit approaches suffer from instability and divergence, the author has mitigated this problem by introducing “self-policing,” in the form of a lookup table for characteristic receiver thicknesses and time steps required to achieve convergent solutions. A similar formulation is used to compute receiver-gas energy transfer during propellant flow. Dissociation models for hydrazine and ammonia, based on equilibrium constant calculations, were included.
- Test data and MSTISM heatup profile predictions match remarkably well (Chapter 6). The agreement between MSTISM and firing data from hot flow tests is not as close, owing to MSTISM’s lumped-capacity assumptions; during firing, channel or bed temperatures diverge substantially from external receiver surface temperatures, resulting in an optimistic performance prediction.
- The author was able to use the MSTISM code to perform sensitivity analyses on solar thermal propulsion systems for a number of applications, including demonstration on two upcoming Surrey microsatellites for end-of-life re-entry and life extension with drag

makeup. The comprehensive nature of the MSTISM code permitted optimisation of the solar thermal engine system and an understanding of key trends (e.g., the utility of higher incident power versus increasing mirror size, for a range of delta-V requirements).

The solar receiver is inherently a high-temperature device and demands the use of exotic, refractory ceramics and metals to survive repeated exposure to temperatures of 2,000 K or more. This precludes the use of stainless steel or other alloys, even high-temperature tolerant, oxidation resistant materials ones such as the Haynes 230 (Ni-Cr-W-Mo) employed by Coxhill [2, 2002] on a series of hydrogen peroxide ground test engines. Historically, rhenium, molybdenum, and graphite have been used; for this activity, the author selected an ammonia- and hydrogen-resistant intermetallic composite of titanium diboride (TiB_2) and boron nitride (BN) as the primary structure and thermal storage material of the Mk. I and Mk. II solar receivers.

- This material proved to be both inexpensive to procure and easily machined with commonly available workshop tools; the material cost to assemble a Mk. I receiver was less than £2,500. Rhenium or single-crystal molybdenum structures of similar dimensions might cost upwards of £30,000 to fabricate.
- Material coupon tests, performed in vacuum, demonstrated conclusively that TiB_2/BN elements exposed to temperatures as high as 2,000 °C (2,273 K) for one hour suffered essentially zero mass loss, deformation, or cracking. An alternative material, ZrO_2/BN/SiC, exhibited substantial mass loss and deformation over this same duration.
- Mechanical bonding tests, using low thermal expansion molybdenum bolts and graphite gaskets to hold together TiB_2/BN flanged sections, demonstrated negligible leakage at ambient pressures and temperatures. This performance was seen to be superior to both ceramic adhesives and refractory metal braze systems. The mechanical bonding and sealing technique had the added advantages of (1) low cost, and (2) the potential for non-destructive disassembly following test.
- Repeated exposures to high temperatures (up to 2,000 K) and vacuum resulted in minor boric oxide binder migration and precipitation on TiB_2/BN surfaces, but no mass loss or damage. Some evidence of titanium nitride (TiN) formation around the receiver aperture exists; this was borne out by mass spectrometry tests conducted by the University of Surrey's Department of Chemistry.
- Repeated exposure to hot ammonia, at temperatures of up to 1,700 K, resulted in no damage to the Mk. I or Mk. II receivers. Some cracking around the cavity aperture was evident in both cases, but neither resulted in failure. Blistering of the cylindrical section of the receiver appears to have been the result of boric oxide precipitation (contaminated with titanium).

- The Mk. I receiver's top flange failed at 1,200 K, immediately following the opening of an ammonia supply valve. This catastrophic failure appears to have resulted from stress concentrations at the bolted flanges; the molybdenum bolts were designed to be anchored directly to the flange material, rather than matching nuts, which might have diverted the loading during high-temperature test and prevented the failure. The smaller Mk. II receiver, designed without an outsize top flange, survived repeated tests. Future ceramic receiver designs will exclude large-diameter flanges.
- Characteristic velocity (c^*) measurements taken during full-flow testing closely matched predictions, with a maximum figure (in ammonia) of 1,909 m/s at a peak external cavity temperature of 1,706 K.[221] C^* efficiency figures ranged as high as 0.992; in some cases, the measured c^* efficiency exceeded unity, but this appears to be due to uncertainties involving the effects of ammonia dissociation and the precise molecular weight of exiting propellant gases. Without intrusive mass spectrometry of decomposition products, made untenable by the need to minimise heat losses from the solar thermal receiver, ideal c^* can only be estimated. The author has calculated that ammonia dissociation rises from essentially zero to 100% between 1,600 and 1,825 K.
- C^* efficiency decayed substantially over the course of engine firings, in some cases declining by 40%. Since temperature measurement is conducted at the external surface of the receiver, it is likely that a significant ΔT between the surface and the channel (or bed) arises over the duration of the firing. This contributes to the disparity between predicted and measured c^*. As above, only intrusive temperature measurement devices could provide more precise knowledge of interior bed and channel temperatures, at the cost of introducing additional heat loss paths into the receiver design, and lowering achievable peak temperature.
- Thrust stand measurements enabled the author to calculate engine specific impulse, which fell short of the values predicted by the MSTISM code. This occurred because of an observed decay in thrust coefficient (C_F) at high temperatures, which appears to have resulted from leakage in the gasketed flanges. Upon returning to ambient conditions, the leaks reseal and thrust coefficients return to their predicted values. Maximum measured specific impulse utilising ammonia propellant was 237 s, at a C_F of just 1.44 (82% of ideal).

Two types of concentrating mirror were selected for fabrication and test, corresponding to the two concentration schemes under investigation for small satellite application. The first scheme, a direct-incidence heating approach with a single large (56-cm diameter, 15 kg) paraboloidal primary mirror, required a blackbody solar receiver to be mounted with its aperture at the focal point.

---

[221] This corresponds to an ideal specific impulse in vacuum of 341 s ($C_F = 1.75$).

- Form error measurements (via probe testing and interferogram) indicated that the large mirror had been manufactured at near optical quality. Flux concentration was measured, on-sun, at greater than 10,000:1. Ground testing with a solar tracking mount permitted the author to measure power throughputs. For flux levels of over 700 W/m^2, measurements of greater than 140 W were obtained. The diamond-turned mirror surface, bare (uncoated) aluminium, exhibited a reflectance in excess of 0.9.
- This mirror's areal density (60.9 kg/m^2) was too high for use as a space demonstration concentrator, and its dimensions would require it to cover all of a standard microsatellite space-facing facet.

While investigating alternatives to the standard single mirror, the author became aware of historical proposals that suggested the use of optical fibre for the transmission of high-flux sunlight. The author confirmed that the output of multiple concentrating mirrors was capable of being efficiently ganged and relayed to a (remote) solar receiver, permitting a decoupling of mirror and receiver (allowing the microsatellite designer to place the receiver anywhere on the host spacecraft) and, due to the strongly non-linear relationship between space mirror mass and diameter, replacing single large mirrors with arrays of smaller ones, saving significant mass.

- A number of 14-centimetre diameter, aluminium-coated plastic (polymethyl methacrylate) mirrors, designed by the author and fabricated by a local optical vendor, were tested to determine their effective concentration ratio and power throughput. These mirrors exhibited visible scratches and warpage, and were of sufficiently poor surface form that probe testing of the mirror surface was unable to determine the error (> 40 μm RMS). They were tested with SSTL's collimated solar simulator and achieved concentration ratios of several hundred. Despite this poor initial showing, on-sun testing indicated performance at least a factor of nearly a factor of ten better than this (C_g ~ 4,900).
- Three bare aluminium metal mirrors, identical in plan to the PMMA ones described above, were fabricated and tested. Form errors were found to be less than 600 nm. Focal spot size was observed at approximately 1 mm; concentration ratio should approach the theoretical limit for the mirror's form (13,500).

- Both the small plastic and aluminium mirrors were produced at superior areal densities. The plastic mirrors (130 g, 8.45 kg/m^2) outperformed the metal mirrors (300 g, 19.5 kg/m^2) by a wide margin.
- On-axis laser testing with a 980-nm low-power laser demonstrated power throughputs of up to 75% through low-attenuation, high numerical aperture (0.66) optical fibres. In a simulated solar heating test at the Surrey Space Centre, this same fibre was found to transmit nearly 60% of incident sunlight from the focal spot of a 14-cm paraboloidal concentrator to a small graphite sample.
- The author performed a number of direct power measurements with an integrating sphere and silicon photodiode, indicating single fibre transmission efficiencies of 20-37%, with lower ganged fibre efficiencies resulting from the use of low-NA (0.33) optical fibre. Power throughputs of over 2 W were obtained from multiple fibres. The measured efficiencies compare favourably with results from the literature, suggesting that unpolished, imprecisely aligned fibres transmit as little as 30% of incident sunlight.
- On-sun graphite element heating tests exhibited relatively low transmission efficiencies (< 20%), while a final direct-incidence heating test (no fibre) with a graphite element and 14-centimetre mirror produced heating rates of over 9 W and an end-to-end efficiency of nearly 90%. This difference in efficiency clearly demonstrates the need to investigate simple, low-cost methods for improving throughput; without such methods, the ganged-mirror concept cannot be competitive.

8.3 Recommendations for Further Research

The comprehensive nature of the present research effort required the author to pursue multiple avenues of investigation that could benefit strongly from additional examination. These include:

- Additional high-temperature brazing trials with molybdenum-ruthenium. While the present effort was unable to produce a hermetic seal, the Mo-Ru braze filler metal wet the TiB_2/BN ceramic coupons and provided a strong bond. Experimentation with heating rates, peak temperatures, hold durations, vacuum quality, and variable braze mixtures (smaller particle sizes) might permit the development of an optimal, strong seal. This could be used to replace the mechanical connections between the receiver feedline and receiver body, as well as the graphite gaskets between receiver flanges.
- A detailed investigation into the hermeticity of bolted ceramic composite flanges at elevated temperatures. This could include alternative bolt materials (e.g., tungsten) with lower coefficients of thermal expansion than molybdenum. Since high-temperature

hermeticity is absolutely essential in determining peak specific impulse capability, this would represent a highly useful follow-on activity.

- Examination of canned receiver structures composed primarily of ceramic or ceramic composite but having an outer (thin) refractory metal pressure vessel. This could be composed of any ductile refractory, including rhenium, molybdenum, or tantalum, or an alloy of these metals. This would permit an all-welded assembly, without the need for (potentially experimental) ceramic-to-metal or ceramic-to-ceramic joining.
- Procurement and test of large-core (1-2 mm diameter), high-NA fibre for ganged mirror testing. Since power throughput is absolutely critical to the performance of fibre-coupled solar thermal engines, it is more important to accept all incident flux than it is to accept only the high-concentration flux at the focal spot's centre. Multiple fibre tips can be placed at the focal spot, but there will be substantial loss between the fibres unless they are sculpted and joined. Large-core fibres with numerical apertures matched to that of typical concentrating mirrors are not commercially available, and must be specially ordered.
- Low-mass, low-footprint fine-pointing arrays to permit small solar thermal engine placement on satellite platforms which either (1) are incapable of meeting the engine's strict solar tracking requirement, or (2) is operationally constrained from long-duration solar tracking. This might include closed-loop steering with heat flux sensors or photodiodes.
- The use of secondary concentration systems to simplify mechanical design of solar thermal engine demonstrators. Hyperboloidal secondaries and Cassegrain optical arrangements, after Gordon [2003], permit optical fibres to be placed at the concentrator apex (rather than suspended above the mirror surface), although they can contribute to decreased end-to-end power throughput. Furthermore, a small secondary concentrator can increase pointing tolerance, relaxing requirements on the spacecraft or mirror fine pointing assembly.

References

[Ackermann, 1915] "The Utilization of Solar Energy," Annual Report Smithsonian Institution, pp. 141-166, Ackermann, A., 1915.

[ACS, 1994] http://www.a-m.de/englisch/literatur/cb0694.htm, American Ceramic Society Bulletin, 73 (1994) 6, American Ceramic Society, June 1994 [accessed 22 March 2002].

[AEDC, 2002] http://www.arnold.af.mil/aedc/factsheets/12vcham.pdf, "12V Space Chamber web page," Arnold Engineering Development Center (AEDC), Arnold Air Force Base, Tennessee, 2002 [accessed July 2002].

[AeroAstro, 2004] http://www.aeroastro.com/Data_Sheets/Medium_Sun_Sensors.pdf, "Medium Sun Sensors," AeroAstro, Ashburn, Virginia, 2004 [accessed 25 May 2004].

[AFRL, 2004] http://www.vs.afrl.af.mil/images/programs.html, Air Force Research Laboratory Photo Archives, Kirtland Air Force Base, New Mexico, 2004 [accessed 6 May 2004].

[Air Liquide, 2004] http://www.airliquide.com/en/business/products/gases/gasdata/index.asp, "Gases," Air Liquide, Paris, France, March 2004 [accessed 26 March 2004].

[Amass, 2000] http://www.lanternroom.com/misc/freslens.htm, "Description of a Fresnel lens for lighthouses," web page, Amass, P., 2000 [accessed July 2002].

[Ambrosiano, 2004] "Los Alamos Surrey Satellite contract for Cibola Flight Experiment platform," http://www.lanl.gov/orgs/pa/newsbulletin/2004/03/11/text10.shtml, Ambrosiano, L., Los Alamos National Laboratories, Los Alamos, New Mexico, 11 March 2004 [accessed 22 April 2004].

[APL, 2002] http://www.contour2002.org, "CONTOUR mission home page," Applied Physics Laboratory, Johns Hopkins University, 2002 [accessed July 2002].

[Apogee, 2002] http://www.apogeeinc.com/scopeoptics.html, "Apogee amateur telescope optics," Apogee, Inc., web page, 2002 [accessed July 2002].

[ARC, 2001] *Rocket Propulsion Data Handbook, 5th edition*, Atlantic Research Corporation (ARC), May 2001.

[ARC, 2002] http://www.atlanticresearchcorp.com/docs/space.shtml, "Space web page," Atlantic Research Corporation (ARC), Gainesville, Virginia, 2002 [accessed 24 April 2002].

[Aremco, 2003] http://www.aremco.com/PDFs/A2.pdf, "High Temperature Ceramic Adhesives and Pastes, Technical Bulletin A2," Aremco, Inc., Valley Cottage, New York, undated [accessed May 2003].

[Ashby, 1980] *Engineering Materials: An Introduction to their Properties and Applications*, Ashby, M., and Jones, D., Pergamon Press, Oxford, 1980.

[Astro-Physics, 2002] http://www.astro-physics.com/, "German Equatorial mount 1200GTO web page," Astro-Physics, Inc., Rockford, Illinois, 2002.

[ATSDR, 1997] http://www.atsdr.cdc.gov/tfacts100.html, "ToxFAQs for hydrazine, 1,1-dimethylhydrazine, and 1,2-dimethylhydrazine," Agency for Toxic Substances and Disease Registry (ATSDR) web page, September 1997 [accessed July 2002].

[Atkins, 1997] *Chemistry: Molecules, Matter, and Change*, Atkins, P., and Jones, L., W.H. Freeman and Company, New York, 1997.

[Backer, 2001] http://astron.berkeley.edu/~ay203/2001/Leuschner/hartman.01mar14.html, "Leuschner Infrared Telescope Testing web page," Backer, D., Astronomy Department, University of California, Berkeley, 2001.

[Baker, 2002] Private Communication, Baker, A., Surrey Satellite Technologies, Ltd., March 2002.

[Baker, 2003] Private Communication, Baker, A., Surrey Satellite Technologies, Ltd., April 2003.

[Barho, 2003] "Coarse Pointing and Fine Pointing Mechanism (CPA and FPA) for an Optical Communications Link," *Proceedings of the 10th European Space Mechanisms and Tribology Symposium*, San Sebastian, Spain, 24-26 September 2003, Barho, R., and Schmid, M., Astrium GmbH, Friedrichshafen, Germany, 2003.

[Bate, 1971] *Fundamentals of Astrodynamics*, Bate, R., Mueller, D., and White, J., Dover Publications, New York, 1971.

[Battin, 1987] *An Introduction to the Mathematics and Methods of Astrodynamics*, Battin, R., American Institute of Aeronautics and Astronautics Education Series, Washington, D.C., 1987.

[Belbruno, 1993] "Sun-Perturbed Earth-to-Moon Transfers with Ballistic Capture," *J. Guidance, Control, and Dynamics* **16**, *No. 4*, pp. 770-775, Belbruno, E., Miller, J., Jet Propulsion Laboratory, Pasadena, California, 1993.

[Bendt, 1980] "Effect of Circumsolar Radiation on Performance of Focusing Collectors," Bendt, P., Rabl, A., SERI Report TR-34 -093, April 1980.

[Bendt, 1981] "Optical Analysis of Point Focus Parabolic Radiation Concentrators," *Applied Optics* **20**, *No. 4*, pp. 674-683, Bendt, P., Rabl, A., Solar Energy Research Institute, Golden, Colorado, February 1981.

[Benedicto, 2000] "Galileo: Satellite System Design and Technology Developments," http://esamultimedia.esa.int/docs/galileo_world_paper_Dec_2000.pdf, Benedicto, J., Dinwiddy, S., Gatti, G., Lucas, R., Lugart, M., European Space Agency, November 2000.

[Biesbrock, 2001] "Study on Lunar Trajectories from GTO by Using Weak Stability Boundary Transfers and Swing-bys—Part III," http://wirescript.com/magazine/rb9901P3.htm, Biesbrock, R., European Space Research and Technology Centre (ESTEC), undated [accessed October 2001].

[Blanchard, 1994] "Target Temperature Prediction for Plasma Source Ion Implantation," Blanchard, J., *Vacuum Science B* **12**, *No. 2*, p. 910, 1994.

[Boeing, 1996] “Delta II Payload Planner’s Guide,” Boeing Company, Huntington Beach, California, 1996.

[Boeing, 1999] “Solar Orbit Transfer Vehicle (SOTV) artist’s conception,” Boeing Company, Rocketdyne Division, Canoga Park, California, 1999.

[Borell, 1996] “ISUS Solar Concentrator Development,” AIAA 96-3045, Borell, G., and Campbell, J., Harris Corporation, July 1996.

[Brooks, 2002] Private Communication, Brooks, D., University College London, Dept. of Physics and Astronomy, London, 30 May 2002.

[Brown, 1996] *Spacecraft Propulsion*, Brown, C., American Institute of Aeronautics and Astronautics Education Series, Washington, D.C., 1996.

[Brown, 2002] *Elements of Spacecraft Design*, Brown, D., American Institute of Aeronautics and Astronautics Education Series, Washington, D.C., 2002.

[Brush Wellman, 2002] http://www.brushwellman.com/ehs/msdsweb.nsf/, “Brush Wellman Material Safety Data Sheet for Beryllia,” Brush Wellman, January 2002 [accessed 21 March 2002].

[Burnett, 1998] http://www.stargazing.net/kepler/kepler.html, “Kepler’s Equation solution web page,” Burnett, K, 1998 [accessed July 2002].

[Cady, 1996] “Cryogen Storage and Propellant Feed System for the Integrated Solar Upper Stage (ISUS) Program,” AIAA 96-3044, Cady, E., and Olsen, A., July 1996.

[Calabro, 2001] “Solar Thermal Propulsion,” *International Conference on Green Propellant for Space Propulsion*, Noordwijk, The Netherlands, June 2001.

[Calogeras, 1992] “The Ground Testing of a 2kWe Solar Dynamic Space Power System,” Proceedings of the 27th Intersociety Energy Conversion Engineering Conference, Vol. 1, pp. 455-460, Calogeras, J. E. and Dustin, M. O., 1992.

[Cariou, 1982] “Transport of Solar Energy with Optical Fibres,” *Solar Energy* **29**, Vol. 5, pp. 397-406, Cariou, J., Dugas, J., and Martin, L., Laboratoire de Physique des Solides Associé au CNRS, Université Paul Sabatier, Toulouse, France, 1982.

[Cariou, 1985] “Theoretical Limits of Optical Fibre Solar Furnace,” *Solar Energy* **34**, Vol. 4/5, pp. 329-339, Cariou, J., Dugas, J., and Martin, L., Laboratoire de Physique des Solides Associé au CNRS, Université Paul Sabatier, Toulouse, France, 1985.

[CfA, 2001] http://cfa-www.harvard.edu/iau/lists/CloseApp.html, “Forthcoming Close Approaches to the Earth,” Harvard Smithsonian Center for Astrophysics (CfA), 24 October 2001 [accessed July 2002].

[Chiaramonte, 1992] “Joining Ceramics by Brazing,” NASA Technical Briefs, Chiaramonte, F., Sudsina, M., Washington, D.C., October 1992.

[Claasen, 1980] “Introduction to Solar Materials Science, Ch. 1,” *Solar Materials Science,* pp. 3-51, Claasen, R., Butler, B., Academic Press, Inc., 1980.

[Clark, 1972] *Ignition! An Informal History of Liquid Rocket Propellants*, Clark, J., Rutgers University Press, New Brunswick, New Jersey, 1972.

[CNN, 2001] http://www.cnn.com/2001/TECH/space/07/13/ariane.orbit/, "Ariane Rocket in Orbit Blunder," Cable News Network (CNN) web page, July 2001 [accessed July 2002].

[COI, 2000] http://www.coi-world.com/first.htm, "Composite Optics, Inc., Successfully Completes the World's Largest, Lightest Weight, Composite Mirror," Composite Optics, Inc., web page, August 2000 [accessed July 2002].

[CGA, 1966] *Handbook of Compressed Gases*, Compressed Gas Association, Hawes, G., Ed., Reinhold Publishing Corporation, 1966.

[Content, 2001] Private Communication, Content, D., NASA Goddard Spaceflight Center, Greenbelt, Maryland, December 2001.

[Cowie, 2001] "BILTENSat Solid Edge Model," Solid Edge file, Cowie, L., et. al., Surrey Satellite Technologies, Ltd., 2001.

[Coxhill, 2002] "An Investigation of a Low Cost HTP/Kerosene 40 N Thruster for Small Satellites," *Proceedings of the 38th Joint Propulsion Conference*, Indianapolis, Indiana, Coxhill, I., Richardson, G., and Sweeting, M., Surrey Space Centre, 2002.

[Coxhill 2, 2002] "Hydrogen peroxide/kerosene engine test firing photo," Coxhill, I., Surrey Space Centre, University of Surrey, 2002.

[Coxhill 3, 2002] *An Investigation of a Low-Cost Bi-Propellant Rocket Engine for Small Satellites*, Ph.D. Thesis, Coxhill, I., Surrey Space Centre, University of Surrey, November 2002.

[Coxhill, 2004] Private Communication, Coxhill, I., Surrey Satellite Technologies, Ltd., 16 March 2004.

[Coxhill 2, 2004] Private Communication, Coxhill, I., Surrey Satellite Technologies, Ltd., 22 April 2004.

[Dataforth, 2004] http://www.dataforth.com/catalog/bb/193_806659937.pdf, "Practical Thermocouple Data Measurements," Dataforth Corporation, Tucson, Arizona, undated [accessed 18 March 2004].

[Da Silva Curiel, 1996] http://www.ee.surrey.ac.uk/CSER/UOSAT/products/gstn.html, "Ground Station Products, University of Surrey web page," Da Silva Curiel, A., 1996 [accessed July 2002].

[Davila, 1998] http://www.ngst.nasa.gov/public/unconfigured/doc_0089/rev_02/3356-79.pdf, "Optical Design of the Developmental Cryogenic Active Telescope Testbed," Davila, P., et. al., NASA Next Generation Telescope (NGST) web site, Goddard Spaceflight Center, Greenbelt, Maryland, 1998 [accessed July 2002].

[DCATT, 2000] http://dcatt.gsfc.nasa.gov/gallery.html, "Developmental Cryogenic Active Telescope Testbed (DCATT) Program," DCATT Home Page, NASA Goddard Space Flight Center, 2000 [accessed July 2002].

[DelaRosa, 1993] "Design and Fabrication of a Solar-Powered Rocket Engine," 29th Annual AIAA/SAE/ASME/ASEE Joint Propulsion Conference, Monterey, California, DelaRosa, M., Tuffias, R., 1993.

[Derby, 2003] Private Communication, Derby, B., University of Manchester Materials Science Centre, March 2003.

[Dierickx, 2000] http://astrosun.tn.cornell.edu/, "Telescope Optics and Mirror Technologies," Dierickx, P., Astronomy Department, Cornell University, Ithaca, NY, 2000 [accessed July 2002].

[Donovan, 1997] http://www.grc.nasa.gov/WWW/RT1997/5000/5490donovan.htm, "Refractive Secondary Solar Concentrator Being Designed and Developed," Donovan, R., NASA Glenn Research Center, Cleveland, Ohio, 1997.

[Dowd, 2001] http://www.spaceelectronics.com/pdf/technical/radiation_guarantees.pdf, "How Rad Hard do You Need? The Changing Approach to Space Parts Selection," Dowd, M., Space Electronics web site, 2001 [accessed July 2002].

[Eade, 2003] Private Communication, Eade, G., Surrey Satellite Technologies, Ltd., October 2003.

[El-Genk, 1994] *A Critical Review of Space Nuclear Power and Propulsion: 1984-1993,* El-Genk, M., AIP Press, New York, 1994.

[ESA, 2000] http://sci.esa.int/content/doc/be/1982_.htm#P12_1774, "Cluster: The Launch," ESA science missions web page, , European Space Agency (ESA), October 2000 [accessed July 2002].

[ESA 2, 2000] http://sci.esa.int/content/doc/35/23605_.htm, "Fregat-Cluster launch and orbit maneuvers web page," European Space Agency (ESA), August 2000 [accessed July 2002].

[ESA 3, 2000] http://spdext.estec.esa.nl/content/doc/e3/2275_.htm, "Rosetta mission profile web page," European Space Agency (ESA), 2000 [accessed July 2002].

[ESA 4, 2000] http://astro.esa.int/herschel/overview.html, "Herschel mission overview web page," European Space Agency (ESA), December 2000 [accessed July 2002].

[ESA 5, 2000] http://www.sci.esa.int/content/doc/0f/19215_.htm, "SMART-1 Multicolour micro-camera (AMIE)," European Space Agency (ESA), 24 May 2000 [accessed July 2002].

[ESA, 2001] http://sci.esa.int/content/doc/c4/27844_.htm, "The SMART-2 Orbit" web page," European Space Agency (ESA), 2001 [accessed July 2002].

[ESA 2, 2001] http://spdext.estec.esa.nl/content/doc/3c/6204_.htm, "GAIA: To Chart the Billion Brightest Objects,", European Space Agency (ESA), December 2001 [accessed July 2002].

[ESA, 2002] http://sci.esa.int/content/doc/10/2320_.htm, "SMART-1 mission data web page," European Space Agency (ESA), 2002 [accessed July 2002].

[ESA, 2003] "Galileo: European Satellite Navigation System," http://europa.eu.int/comm/dgs/energy_transport/galileo/intro/index_en.htm, European Space Agency, December 2003.

[ESA, 2004] http://www.esa.int/export/SPECIALS/SMART-1/, "The SMART Way to Travel," European Space Agency web site, 2004 [accessed 11 March 2004].

[ESI, 2001] http://www.esidirectory.org/eid/consultation/productdetail.jsp?retour=genList, "Stationary Plasma Thrusters," European Space Industry (ESI) Directory, November 2001 [accessed July 2002].

[ESTEC, 2004] "Daily Geomagnetic A_p Index, Wednesday, 21 April 2004," http://www.estec.esa.nl/wmwww/wma/Data_Plots/noaa/ap_plot.html, European Space Research and Technology Centre, Noordwijk, Netherlands, 21 April 2004 [accessed 22 April 2004].

[Etheridge, 1979] "Solar Rocket System Concept Analysis," AFRPL-TR-79-79, Final Technical Report, Etheridge, F., Satellite Systems Division, Space Systems Group, Rockwell International, Edwards AFB, California, December 1979.

[Feuermann, 1999] "High-flux solar concentration with imaging designs," *Solar Energy* **65**, p. 83, Feuermann, D., Gordon, J.M. and Ries, H., Center for Energy Environmental Physics, Jacob Blaustein Institute for Desert Research, Ben-Gurion University of the Negev, Israel, 1999.

[Feuermann, 1999] "Solar Fiber-Optic Mini-Dishes: A New Approach to the Efficient Collection of Sunlight," *Solar Energy* **65**, No. 3, pp. 159-170, Feuermann, D., and Gordon, J., Center for Energy Environmental Physics, Jacob Blaustein Institute for Desert Research, Ben-Gurion University of the Negev, Israel, 1999.

[Feuermann, 2002] "Solar Fiber Optic Mini-Dish Concentrators: First Experimental Results and Field Experience," *Solar Energy* **72**, No. 6, pp. 459-472, Feuermann, D., and Gordon, J., Center for Energy Environmental Physics, Jacob Blaustein Institute for Desert Research, Ben-Gurion University of the Negev, Israel, 2002.

[Freeland, 1997] "Large Inflatable Deployable Antenna Flight Experiment Results," IAF-97-1.3.01, *48th International Astronautical Congress*, Turin, Italy, Freeland, R., Jet Propulsion Laboratory, Pasadena, California, Bilyeu, G., Veal, G., L'Garde, Tustin, California, and Steiner, M., Carson, D., NASA Goddard Spaceflight Center, Greenbelt, Maryland, 1997.

[Friedman, 1996] "Compact High-Flux Two-Stage Solar Collectors Based on Tailored Edge-Ray Concentrators," Solar Energy 56, No. 6, pp. 607-615, Friedman, R., Gordon, J., Center for Energy Environmental Physics, Jacob Blaustein Institute for Desert Research, and the Pearlstone Center for Aeronautical Engineering Studies, Department of Mechanical Engineering, Ben-Gurion University of the Negev, Israel, and Ries, H., Paul Scherrer Institute, Villigen, Switzerland, 1996.

[Frye, 1992] "Innovative Applications of Solar Thermal Propulsion," AIAA 92-3081, Frye, P., and Shoji, J., Rocketdyne, July 1992.

[Frye, 1998] "Integrated Solar Upper Stage Engine Ground Demonstration Test Results and Data Analysis," AIAA 98-3958, Frye, P., and Kudija, C., Rocketdyne, July 1998.

[Fujii, 1991] "Corrosion behavior of sintered pellet of graphite and boron carbide in helium containing water vapor," IAEA-TECDOC-690, pp. 169-176, *Specialists' Meeting on the Status of Graphite*

Development for Gas Cooled Reactors, Tokai, Fujii, K.; Nomura, S.; Shindo, M., Imai, H., Japan Atomic Energy Research Institute, Tokai, Ibaraki, Japan, Dept. of Fuels and Materials Research, and the Research Association for Nuclear Facilities Decommissioning, Tokai, Ibaraki, Japan, 9-12 September 1991.

[Ganley, 2002] “Small Satellite Technology: Researchers are developing affordable and reliable small satellite launch opportunities,” http://www.afrlhorizons.com/Briefs/Dec02/VS0202.html, Ganley, J., and Wegner, P., U.S. Air Force Research Laboratory Space Vehicles Directorate, Kirtland Air Force Base, New Mexico, December 2002 [accessed 27 April 2004].

[Garber, 2002] “Nuclear Rocket Engine Being Transported to Test Stand,” http://grin.hq.nasa.gov/ABSTRACTS/GPN-2002-000143.html, Garber, S., NASA History Office, October 2002 [accessed 5 May 2004].

[GE, 2000] http://www.advceramics.com/acc/downloads/, “Titanium Diboride/Boron Nitride, Intermetallic Composite Powder Material Safety Data Sheet (MSDS),” GE Advanced Ceramics, web page, Cleveland, Ohio, 12 April 2000 [accessed July 2002].

[Gibbon, 2000] “The Design, Development, and In-Orbit Performance of a Propulsion System for the SNAP-1 Nanosatellite,” *Proceedings of the 3rd International Conference on Spacecraft Propulsion*, ESA SP-465, Cannes, France, Gibbon, D., Charman, P., Surrey Satellite Technology, Ltd., Kay, N., Polyflex Aerospace Ltd., 2000.

[Gibbon, 2002] Private Communication, Gibbon, D., Surrey Satellite Technologies, Ltd., January 2002.

[Gibbon, 2003] “The Design, Development, and In-Flight Performance of a Low Power Resistojet Thruster,” *Proceedings of the 39th Joint Propulsion Conference*, Huntsville, Alabama, Gibbon, D., Baker, A., Surrey Satellite Technologies, Ltd., Guildford, Nicolini, D., Robertson, D., European Space Agency, Noordwijk, the Netherlands, Dye, C., H&B Sensors, Bognor Regis, 2003.

[Gibbon, 2004] Private Communication, Gibbon, D., Surrey Satellite Technologies, Ltd., 26 April 2004.

[Gierow, 2000] “Solar Thermal Propulsion,” http://www.stg.srs.com/atd/STP.htm, Gierow, P., SRS Corporation, Huntsville, Alabama, 2000 [accessed 6 May 2004].

[Goodwin, 2001] “Evolved Expendable Launch Vehicle Secondary Payload Adapter: A New Delivery System for Small Satellites,” *15th Annual AIAA/Utah State University Conference on Small Satellites*, Logan, Utah, Goodwin, J, and Wegner, S., August 2001.

[Gordon, 2003] “Solar Surgery,” Applied Physics **93**, No. 8, pp. 4843–4851, Gordon, J., Feuermann, D., Huleihil, M., Center for Energy Environmental Physics, Jacob Blaustein Institute for Desert Research, Mizrahi, S., Department of Surgery, Soroka Medical Center, and Shaco-Levy, R., Department of Pathology, Soroka Medical Center, Ben-Gurion University of the Negev, Israel 15 April 2003.

[Gordon 2, 2003] “New Optical Systems for the Solar Generation of Nanomaterials,” *SPIE Symposium on Non-Imaging Optics*, San Diego, California, Gordon, J., Feuermann, D., Huleihil, M., Center for Energy Environmental Physics, Jacob Blaustein Institute for Desert Research, and the Pearlstone Center for

Aeronautical Engineering Studies, Department of Mechanical Engineering, Ben-Gurion University of the Negev, Israel, 2003.

[Goswami, 2000] *Principles of Solar Engineering, 2nd Edition*, Goswami, Y., Kreith, F., Kreider, J., Taylor & Francis, Philadelphia, Pennysylvania, 2000.

[Gotzig, 2000] "Development of a Low Cost 22N Thruster," *Proceedings of the 3rd International Conference on Spacecraft Propulsion*, Cannes, France, Gotzig, U., Astrium GmbH, October 2000.

[Green, 1998] *An Introduction to the Mechanical Properties of Ceramics*, Green, D., Pennsylvania State University, State College, Pennsylvania, Cambridge University Press, Cambridge, 1998.

[Haack, 2002] http://www.porvair.com/pfc/papers/, "Novel Lightweight Metal Foam Heat Exchangers," Haack, D., et. al., Porvair Fuel Cell Technology, Hendersonville, North Carolina, and the Department of Engineering, University of Cambridge, undated [accessed 22 March 2002].

[Haag, 2000] "Low Cost Propulsion Developments for Small Spacecraft at the Surrey Space Centre," *Space Technology* **20**, *No. 3,* pp. 87-98, Haag, G., Sweeting, M., and Richardson, G., Surrey Space Centre, 2000.

[Haag, 2001] *Alternative Geometry Hybrid Rockets for Spacecraft Orbit Transfer*, Haag, G., Ph.D. thesis, University of Surrey, Guildford, UK, 2001.

[Hampsten, 2001] Revised Space Test Program (STP) Propulsion Module Requirements, *Small Business Innovative Research (SBIR) Announcement*, Hampsten, K., et. al., Air Force Research Laboratory, August 2001.

[Hansen, 2002] http://www.dsri.dk/roemer/pub/sat_tech/Space_Environment.pdf, "Satellite Technology Course, Space Environment," Hansen, F., Danish Space Research Institute, Danish Small Satellite Program, June 2002 [accessed July 2002].

[Harang, 2003] "Absolute Optical Calibrations Using a Simple Tungsten Bulb: Theory," *Sodankyla Geophysical Observatory Publications* **92**, pp. 121-123, Harang, O., University of Tromso, Norway, and Kosch, M., University of Lancaster, Lancaster, United Kingdom, 2003.

[Harris, 2004] "JCSAT-9 Geostationary Telecommunications Satellite," http://www.govcomm.harris.com/solutions/, Government Communications Systems Division, Harris Corporation, Melbourne, Florida, 2004.

[Haskett, 1999] "EELV Secondary Payload Adapter (ESPA)," *13th AIAA/USU Conference on Small Satellites*, Haskett, S., Doggrell, L., et. al., Logan, Utah, 1999.

[Hastings, 1990] "Monopropellant Microthrusters and Electrothermal Augmentation," *Space Propulsion and Power Generation Course Notes*, Hastings, D., Massachusetts Institute of Technology, 1990.

[Hecht, 1998] *Optics, 3rd Ed.*, Hecht, E., Addison Wesley Longman, Inc., Reading, Massachusetts, 1998.

[Hextek, 2000] http://www.hextek.com/, "Hi-Tek Gas Fusion Mirror" Hextek, Inc., web page, July 2000 [accessed July 2002].

[Hill, 1992] *Mechanics and Thermodynamics of Propulsion, 2nd Ed.*, Hill, P., and Peterson, C., Addison-Wesley, Reading, Massachusetts, 1992.

[Holmes, 2001] "Solar Rocket Propulsion: Ground and Space Technology Demonstration," 12th Annual Advanced Space Propulsion Workshop, University of Alabama-Huntsville, Huntsville, Alabama, Holmes, M., Air Force Research Laboratory, Edwards Air Force Base, California, 2001.

[Hottel, 1967] *Radiative Transfer*, Hottel, H., and Sarofim, A., McGraw-Hill, 1967.

[Humble, 1995] *Space Propulsion Analysis and Design*, Humble, R., Henry, G., and Larson, W., McGraw-Hill, New York, 1995.

[IMP-CNRS, 2001] http://www.imp.cnrs.fr/foursol/index.shtml, IMP-CNRS (Material Science and Process Engineering, Centre Nationale de la Recherche Scientifique), Odeillo/Perpignan, France, December 2001 [accessed July 2002].

[ISAS, 2002] http://www.muses-c.isas.ac.jp/English/index.html, "MUSES-C homepage," ISAS (Japan Institute of Space and Astronautical Science), 2002 [accessed July 2002].

[ISC Kosmotras, 2001] http://www.kosmotras.ru/rndnepr2.htm, "Kosmotras Dnepr launch vehicle specification page," ISC Kosmotras, Moscow, Russian Federation 2001 [accessed July 2002].

[Jaffe, 1989] "Test Results on Parabolic Dish Concentrators for Solar Thermal Power Systems," *Solar Energy* **42**, pp. 173-187, Jaffe, L., Jet Propulsion Laboratory, 1989.

[Jason, 2000] "Low Cost Planetary Exploration: Surrey Lunar Minisatellite and Interplanetary Platform Missions," IAF-00-Q.4.02, *51st International Astronautical Congress*, Jason, S., da Silva Curiel, A., Gomes, L., Phipps, A., Ward, J., and Sun, W., Surrey Satellite Technologies, Ltd., October 2000.

[Jena-Optronik, 2004] http://www.jena-optronik.de/sensors/fss.pdf, "FSS: Fine Sun Sensor," Jena-Optronik, Jena, Germany, April 2004 [accessed 25 May 2004].

[JPL, 2001] http://sim.jpl.nasa.gov/mission/index.html, "Space Interferometry Mission (SIM) mission data web page," Jet Propulsion Laboratory (JPL), 30 October 2001 [accessed July 2002].

[JPL 2, 2001] http://ssd.jpl.nasa.gov/dastcom.html, "DASTCOM (Database of ASTeroids and COMets) database web site," Jet Propulsion Laboratory, 2001 [accessed July 2002].

[JPL, 2002] http://echo.jpl.nasa.gov/asteroids/4179_Toutatis/toutatis.html, "Asteroid 4179 Toutatis," Jet Propulsion Laboratory, 2002 [accessed July 2002].

[JPL, 2002] http://neo.jpl.nasa.gov/neo.html, "NEO Program web page," Jet Propulsion Laboratory, 2002 [accessed July 2002].

[JPL 2, 2002] http://neo.jpl.nasa.gov/neo/pha.html, "Potentially Hazardous Asteroids web page," Jet Propulsion Laboratory, 2002 [accessed July 2002].

[Johnson, 1992] "Combined Release and Radiation Effects Satellite (CRRES): Spacecraft and Mission," *J. Spacecraft and Rockets* **29**, *Vol. 4*, pp. 556-563, Johnson, M., and Ball, J., July-August 1992.

[Johnston, 1998] "Focal Region Measurement of the 20 m^2 Tiled Dish at the Australian National University," *Solar Energy* **63**, *No. 2*, pp. 117-124, Johnston, G., Centre for Sustainable Energy Systems, Dept. of Engineering, Australian National University, Canberra, 1998.

[J.T. Baker, 2000] http://www.jtbaker.com/msds, "Material Safety Data Sheet for Nitromethane (CH_3NO_2)," J.T. Baker, Mallinckrodt Baker, Inc., September 2000 [accessed July 2002].

[Kasl, 1997] "A Critical Review of Ultralightweight Composite Mirror Technology, *Proceedings of the Conference on Advanced Materials for Optics and Precision Structures*, San Diego, California, Kasl, E., Crowe, D., Composite Optics, July 1997.

[Kato, 1976] "Application of Optical Fibres to the Transmission of Solar Radiation," *Applied Physics* **47**, No. 10, Kato, D., and Nakamura, T., Electrotechnical Laboratory, The Agency of Industrial Science and Technology, Ministry of International Trade and Industry, Tanashi, Tokyo, Japan, October 1976.

[Katscher, 1986] "Graphite Corrosion Under Severe HTR Accident Conditions," *IAEA Specialists' Meeting on Graphite Component Structural Design*, JAERI, Tokai-Mura, Japan, Katscher, W., Moormann, R., Institute for Nuclear Safety Research, Federal Republic of Germany, 1986.

[Kawaguchi, 1998] "Synthesis of Muses-C Low Thrust Sample and Return Trajectory," IAF-98-A.4.01, *49th International Astronautical Congress*, Kawaguchi, J., Yamakawa, H., September-October 1998.

[Kelso, 1998] Frequently Asked Questions: Two Line Element Set Format, http://celestrak.com/columns/v04n03/, Kelso, T., Center for Space Standards and Innovation, Colorado Springs, Colorado, 1998.

[Kennedy, 1995] "The Integrated Solar Upper Stage (ISUS) Program," AIAA 95-3628, Kennedy, F., Jacox, M., U.S. Air Force Phillips Laboratory, Kirtland AFB, New Mexico, 1995.

[Kennedy, 2001] "Revised Proposal for Doctoral Research on Solar Thermal Propulsion for Small Satellites at the Surrey Space Centre," Kennedy, F., University of Surrey, Guildford, UK, unpublished, 2001.

[Kennewell, 1999] "Orbital Decay Calculations," http://www.ips.gov.au/, Kennewell, J., IPS Radio and Space Services, Australian Space Weather Agency, Sydney, Australia, 1999.

[Kerslake, 1993] "Analysis of Thermal Energy Storage Material With Change-of-Phase Volumetric Effects," *J. Solar Energy Engineering* **115**, *No. 1*, pp. 22-31, Kerslake, T. W. and Ibrahim, M. B., February 1993.

[Kessler, 2000] Solar Thermal OTV: Applications to Reusable and Expendable Launch Vehicles, *Acta Astronautica* **47**, *Issues 2-9*, pp. 215-226, Kessler, T., Frye, P., and Partch, R., Boeing, U.S. Air Force Research Laboratory, July-November 2000.

[Kreider, 1979] *Medium and High Temperature Solar Processes*, Kreider, J., Academic Press, New York, 1979.

[Kreith, 1997] *Principles of Heat Transfer, 5th Ed.*, Kreith, F., and Bohn, M., PWS Publishing Company, Boston, Massachusetts, 1997.

[KSC Online, 2001] http://www-pao.ksc.nasa.gov/kscpao/shuttle/summaries/sts108/ index.htm, "STS-108 page," Kennedy Space Center (KSC) Online, December 2001 [accessed July 2002].

[KSC Online, 2002] http://www-pao.ksc.nasa.gov/kscpao/schedule/schedule.htm, "Launch Assessment page," Kennedy Space Center (KSC) Online, January 2002 [accessed July 2002].

[LRC, 2001] *Optics Software for Layout and Optimisation (OSLO)*, Optics Reference Version 6.1, Lambda Research Corporation, Littleton, Massachusetts, 2001.

[Larson, 1992] *Space Mission Analysis and Design, 2nd Ed.*, Larson, W., and Wertz, J., Microcosm, Inc., Kluwer Academic Publishers, Dordrecht, Netherlands, 1992.

[Latham, 1969] "Criticality Studies of a Nuclear Light Bulb Engine," *Journal of Spacecraft* **6**, No. 19, Latham, T., 1969.

[Latham, 1971] "Summary of the Performance Characteristics of the Nuclear Light Bulb Engine," AIAA 71-642, Latham, T., 1971.

[Lawrence, 1998] *Research into Resistojet Rockets for Small Satellite Applications,* Ph.D. thesis, Lawrence, T., University of Surrey, Guildford, UK, 1998.

[Lee, 1998] "The Need of Adaptive Optics in Future Space Optical Instruments," ESO/OSA Topical Meeting on Astronomy with Adaptive Optics, Present Results and Future Programmes—European Southern Observatory, Munich, Germany, Lee, J., Yan, P., Walker, D., and Bingham, R., 7-11 September 1998.

[Levick, 2003] Private Communication, Levick, A., National Physical Laboratory, Teddington, UK, 10 Jaunary 2003.

[L'Garde, 2004] "Inflatable Antenna Experiment," http://www.lgarde.com/programs/iae.html, L'Garde, Tustin, California, 2004 [accessed 6 May 2004].

[Liang, 1998] "Fiber-optic solar energy transmission and concentration," *Solar Energy Materials and Solar Cells* **54**, pp. 323-331, Liang, D., Monteiro, L., Teixeira, M., Departamento de Fisica, Universidade Nova de Lisboa, Monteiro, M., Departamento de Fisica, Universidade de Lisboa, and Collares-Pereira, Departamento de Fisica, Universidade Tecnica de Lisboa, Portugal, 1998.

[Lide, 1995] *CRC Handbook of Chemistry and Physics, 76th Edition,* CRC Press, Lide, D., Ed., Boca Raton, Florida, 1995.

[Lienhard, 1987] *A Heat Transfer Textbook, 2nd Ed.*, Lienhard, J., Prentice-Hall, Englewood Cliffs, New Jersey, 1987.

[Lock, 2004] 980-nm Laser Power Throughput Testing Data, Private Communication, Lock, D., and Henshall, P., 24 February 2004.

[Losmandy, 2004] http://www.losmandy.com/g-11.html. Losmandy Astronomical Products: Equatorial Mounts, Losmandy, S., Los Angeles, California, 2004 [accessed 18 May 2004].

[Lot-Oriel, 2004] "Short DC Arc Lamps," http://www.lot-oriel.com/pdf_it/all/light_arc_speci1.pdf, Lot-Oriel, Leatherhead, 2004 [accessed 7 May 2004].

[LUNARSAT, 2002] http://www.lunarsat.de/mission.htm, "LUNARSAT mission web page," 2002 [accessed July 2002].

[Lyle, 2002] Private Communication, Lyle, S., St. Gobain Advanced Ceramics, Amherst, New York, November 2002.

[Lynch, 1966] *Engineering Properties of Selected Ceramic Materials*, Lynch, J., ed., American Ceramic Society, Inc., Columbus, Ohio, 1966.

[Malacara, 1992] *Optical Shop Testing, 2nd Ed.*, Malacara, D., John Wiley & Sons, Inc., New York, 1992.

[Marcus, 2002] http://www.mcelwee.net/html/hardness_comparisons.html, "Marcus Materials Co., Hardness Comparisons web page," Marcus Materials, Newark, Delaware, undated [accessed 25 July 2002].

[Martinez-Sanchez, 1990] "Electrothermal Arcjets," *Space Propulsion and Power Generation Course Notes*, Martinez-Sanchez, M., Massachusetts Institute of Technology, 1990.

[Massalski, 1986] *Binary Alloy Phase Diagrams, Vol. 2*, T. Massalski, ed., American Society for Metals, Metals Park, Ohio, 1986.

[MatWeb, 2002] http://www.matweb.com/, "MatWeb, The Online Materials Information Resource," Automatic Creations, Inc., 2002 [accessed July 2002].

[McLafferty, 1970] "Gas-Core Nuclear Rocket Engine Technology Status," *Journal of Spacecraft* **7**, No. 12, McLafferty, G., 1970.

[Meadors, 1999] "The Design and Construction of a Gas Extraction Probe for a Hybrid Rocket Gas Extraction System," AIAA 99-2535, Meadors, C., Wright, A., Department of Applied Science, University of Arkansas, 1999.

[Melles Griot, 2004] "Understanding Photodiode Detector Performance," http://beammeasurement.mellesgriot.com/tut_photo_det.asp, Melles Griot, Carlsbad, California, 2004 [accessed 20 May 2004].

[Miller, 2000] http://www.minerals.sk.ca/atm_design/aluminum.html, Aluminum web page, Miller, D., Northern Lights Optics Amateur Telescope Makers, 2000 [accessed July 2002].

[Mills, 1992] "Reflections on the 'Burning Mirrors of Archimedes,' with a Consideration of the Geometry and Intensity of Sunlight Reflected from Plane Mirrors," *European Journal of Physics* **13**, pp. 268-279, Mills, A., and Clift, R., Leicester University, Leicester, 1992.

[Morrell, 2002] Private Communication, Morrell, R., National Physical Laboratory, Teddington, 28 June 2002.

[Moore, 1999] "Ultra-Lightweight Precision Membrane Optics," The Ultra-Lightweight Space Optics Challenge Workshop, Napa, California, Moore, J., SRS Technologies, Huntsville, Alabama, 1999.

[Mugnier, 2000] *Ariane Structure for Auxiliary Payload 5 User's Manual, Issue 1, Rev. 0*, Mugnier, D., Arianespace, Evry, France, May 2000.

[Munz, 1999] *Ceramics: Mechanical Properties, Failure Behaviour, Material Selection*, Munz, D., Karlsruhe University, Fett, T., Institute of Materials Research, Forschungszentrum, Karlsruhe, Germany, Springer Verlag, Berlin, 1999.

[Mussett, 2003] "Contraves Optical Terminal—Coarse Pointing Assembly (CPA)," *Proceedings of the 10th European Space Mechanisms and Tribology Symposium*, San Sebastian, Spain, 24-26 September 2003, Mussett, D., Humphries, M., Henzelin, F., and Szekely, G., Contraves Space AG, Zurich, Switzerland, 2003.

[Nakamura, 1998] "Development of the Optical Waveguide Solar Lighting System for Space-Based Plant Growing," *Intl. J. of Earth\Space* **5** (2), pp. 205-215, Nakamura, T., Case, J., and Mankamyer, M., 1998.

[NASA, 2002] http://spaceflight.nasa.gov/shuttle/reference/shutref/orbiter/tps/hrcitiles.html, "Shuttle Thermal Protection Systems," NASA Spaceflight web site, August 2001 [accessed 22 March 2002].

[NASA ARC, 2002] TPSX Materials Database, http://tpsx.arc.nasa.gov/tpsx3/main.html, Thermal Protection Materials and Systems Branch, NASA Ames Research Center, 2001 [accessed 22 March 2002].

[NASA GRC, 2002] http://www.grc.nasa.gov/WWW/tmsb/dynamicpower/doc/sd_gtd.html, "Solar Dynamic Ground Demonstration web page," NASA Glenn Research Center (GRC), January 2000 [accessed 28 February 2002].

[NASA GSFC, 1999] *The Magnetospheric Multiscale Mission…Resolving Fundamental Processes in Space Plasmas*, NASA/TM 2000-209883, NASA Science and Technology Definition Team for the Magnetospheric Multiscale Mission, NASA Goddard Spaceflight Center (GSFC), Greenbelt, Maryland, December 1999.

[NASA GSFC, 2002] http://stp.gsfc.nasa.gov/missions/mms/mms.htm, "Magnetospheric Multiscale web page," NASA Goddard Spaceflight Center (GSFC), June 2002 [accessed July 2002].

[Nice, 2004] "Los Alamos and Surrey Satellite Contract for Cibola Flight Experiment Platform," http://www.sstl.co.uk/index.php?loc=27&id=741, Nice, A., Surrey Satellite Technologies, Ltd., 12 March 2004 [accessed 22 April 2004].

[NRC, 2000] http://www.nationalacademies.org/ssb/smallsatmenu.htm, *The Role of Small Satellites in NASA and NOAA Earth Observation Programs*, National Research Council (NRC), Committee on Earth Studies, Space Studies Board, Commission on Physical Sciences, Mathematics, and Applications, 2000 [accessed July 2002].

[NREL, 2001] http://rredc.nrel.gov/solar/spectra/, "Solar Spectra," National Renewable Energy Laboratory, Golden, Colorado, 2001.

[NRI, 2004] http://www.carbideprocessors.com/Brazing/book/03.htm, "Tool Tipping Materials, Northwest Research Institute, Tacoma, Washington, 2004 [accessed 16 May 2004].

[Neumann, 1999] "The influence of sunshape on the DLR Solar Furnace beam," *Solar Energy* **66**, *Issue 6*, pp. 447-457, Neumann, A., Witzke, A., September 1999.

[New Brunswick Lighthouses, 2001] http://66.96.244.85/~nblight/fresnel.html, "New Brunswick Lighthouses web page," 2001 [accessed July 2002].

[Nicholas, 1990] "Some Observations on the Wetting and Bonding of Nitride Ceramics," *Materials Science* **25,** *No. 6*, Nicholas, D., Mortimer, L., 1990.

[Nicholas, 1998] *Joining Processes: Introduction to Brazing and Diffusion Bonding,* Nicholas, M., Kluwer Academic Publishers, Dordrecht, The Netherlands, 1998.

[NIST, 2000] http://kinetics.nist.gov/, Kinetics web site, National Institute of Standards and Technology, Gaithersburg, Maryland, 2000 [accessed 6 April 2004].

[O'Gallagher, 1988] "Performance Model for Two-Stage Optical Concentrators for Solar Thermal Applications," Solar Energy 41, No. 4, pp. 319-325, O'Gallagher, J., and Winston, R., Enrico Fermi Institute, University of Chicago, 1988.

[Oliver, 2003] Private Communication, Oliver, R., Sintec-Keramik UK, Newport, Wales, November 2003.

[Omega, 2001] http://www.omega.com/toc_asp/frameset.html?book=Temperature&file=XTA-W5R26, "Exotic Thermocouple Probes web page," Omega Engineering, Inc., 2001 [accessed July 2002].

[Oosthuizen, 2004] Private Communication, Oosthuizen, P., Surrey Satellite Technologies, Ltd., 23 April 2004.

[Optiforms, 1999] http://www.optiforms.com/products/coatings-grid.html, "OptiForms coatings page," Optiforms, Inc., 1999 [accessed 20 February 2002].

[OSC, 2000] http://www.orbital.com/LaunchVehicles/Pegasus/peg-user-guide.pdf, *Pegasus User's Guide, Release 5.0,* Orbital Sciences Corporation (OSC), August 2000 [accessed July 2002].

[Ostro, 1995] http://www.planetscapes.com/solar/cap/ast/toutathi.htm, "Asteroid 4179 Toutatis," Planetscapes web site, from *Science* **270**, pp. 80-83, Ostro, S., et. al., 1995.

[Parker, 2003] 56-Centimetre Solar Concentrating Mirror Probe Data, Private Communication, Parker, R., Precision Optical Engineering, January 2003.

[Partch, 1999] "Solar Orbit Transfer Vehicle Space Experiment Conceptual Design," AIAA 99-2476, Partch, R., and Frye, P., U.S. Air Force Research Laboratory, Boeing Company, June 1999.

[Peat, 2004] AlSat-1 Two Line Element Set, http://www.heavens-above.com/, Peat, C., Munich, Germany, 2004 [accessed 26 April 2004].

[Pedrotti, 1987] *Introduction to Optics, 2nd Ed.,* Pedrotti, F., and Pedrotti, L., Prentice-Hall, Upper Saddle River, New Jersey, 1987.

[Pierson, 1996] *Handbook of Refractory Carbides and Nitrides,* Pierson, H., Noyes Publications, Westwood, New Jersey, 1996.

[Pilbratt, 2000] "The Herschel Mission, Scientific Objectives, and this Meeting," *Proceedings of 'The Promise of the Herschel Space Observatory,'* ESA SP-460, pp. 13-20, Toledo, Spain, Pilbratt, G., Cernicharo, J., Heras, A., Prusti, T., Harris, R., ed., 12-15 December 2000.

[Pletka, 1998] "Indirectly Heated Fluidized Bed Biomass Gasification Using a Latent Heat Ballast," Pletka, R., Brown, R., and Smeenk, J., Center for Coal and the Environment, Iowa State Unversity, 1998.

[POE, 2002] http://www.p-oe.co.uk/home.html, Precision Optical Engineering (POE), Hitchin, Hertsfordshire, United Kingdom, May 2002 [accessed July 2002].

[Polyflex, 1999] http://www.polyflex.co.uk/spacesystems.htm, "Xenon Feed Systems for Electric Propulsion," Polyflex Aerospace, 1999 [accessed July 2002].

[Polymicro, 2004] http://www.polymicro.com/products/opticalfibers/products_opticalfibers_spec5.htm, "Silicon/Teflon AF Clad Optical Fiber," Polymicro Technologies, LLC, Phoenix, Arizona, 2004 [accessed 7 May 2004].

[Prentice, 2002] Private Communication, Prentice, C., QinetiQ, Farnborough, 30 May 2002.

[Pueschner, 1999] http://www.pueschner.com/engl/basics/calculations_en.html, "Basic Calculations," Pueschner Microwaves, Bremen, Germany, 1999 [accessed 18 March 2004].

[Purdue, 1998] http://www.ccm.ecn.purdue.edu/tfd/testing_methods/vickers_and_knoop.htm, "Vickers and Knoop Hardness testing," Purdue University, Center for Collaborative Manufacturing, 1998 [accessed July 2002].

[PIC, 2000] http://www.pyrometer.com/Products/frame_sets/opticalframeset.htm, "PYRO Optical Pyrometer web page," Pyrometer Instrument Company, Inc. (PIC), Northvale, New Jersey, 2000 [accessed July 2002].

[Rabl, 1976] "Optical and Thermal Properties of Compound Parabolic Concentrators," *Solar Energy* **18**, pp. 497-511, Rabl, A., Solar Energy Group, Argonne National Laboratory, Illinois, 1976.

[Rembar, 2001] http://www.rembar.com/tech2.htm#chart11, "Rembar Brazing Filler Metals web page," Rembar Company, September 2001 [accessed 28 March 2002].

[Rhodes, 2001] http://www.erpt.org/012Q/rhod-07.htm, "Heat Transfer in Fluidized Beds," Rhodes, M., 2001 [accessed 22 March 2002].

[Ritchie, 2003] "X-Ray Based Measurement of Composition during Electron Beam Melting of AISI 316 Stainless Steel: Evaporation Processes and Simulation," Ritchie, M., Lee, P., Mitchell, A., Cockcroft, S., and Wang, T., *Metallurgical and Material Transactions A* **34A**, p. 863, March 2003.

[Robbins, 1966] "An Analytical Study of the Impulsive Approximation," *AIAA Journal*, Robbins, H., August 1966.

[Roberts, 2001] http://www.hia.nrc.ca/pub/staff/cbt/XLT/Reports/XLT-SiC.pdf, "Primary Mirror Substrate Materials for the XLT Telescope," Roberts, S., National Research Council, Herzberg Institute of Astrophysics, Victoria, British Columbia, Canada, 2001 [accessed July 2002].

[Saccocia, 2000] "European Activities in Electric Propulsion," *Proceedings of the 3rd International Conference on Spacecraft Propulsion*, pp. 49-63, ESA SP-465, Saccocia, G., Cannes, France, December 2000.

[Safa, 1997] "Silicon Carbide Technology for Submillimetre Space-Based Telescopes," *48th International Astronautical Congress*, Turin, Italy, Safa, F., Levallois, F., Matra Marconi, and Bougoin, M., Castel, D., SiCSpace, October 1997.

[Sakoda, 2002] "Overview of the NPS Spacecraft Architecture and Technology Demonstration Satellite, NPSAT-1," SSC-02-I-4, *16th Annual AIAA/USU Conference on Small Satellites*, Logan, Utah, Sakoda, D., Horning, J., Naval Postgraduate School, Monterey, California, 2002.

[Sandorff, 1960] *Orbital and Ballistic Flight*, Sandorff, P., MIT Department of Aeronautics and Astronautics (unpublished paper), Cambridge, Massachusetts, 1960.

[Schleinitz, 1987] "Solar Thermal OTVs in Comparison with Electrical and Chemical Propulsion Systems," IAF 87-199, Schleinitz, J., and Lo, R., October 1987.

[Schoonover, 2003] http://www.schoonoverinc.com/PDFs/c07e_ruvac.pdf, "Ruvac Roots Vacuum Pumps, Single Stage," Schoonover, Inc., Atlanta, Georgia, 2003 [accessed 22 March 2004].

[Schwartz, 1990] *Ceramic Joining*, Schwartz, M., ASM International, Materials Park, Ohio, 1990.

[Sellers, 1996] *Investigation into Low-Cost Propulsion Systems for Small Satellite Missions*, Ph.D. thesis, Sellers, J., Department of Electrical Engineering, University of Surrey, Guildford, UK, June 1996.

[Shaltens, 2002] "RSC Shooting Star," http://www.grc.nasa.gov/WWW/tmsb/secondaryconc/doc/rsc_sse.html, Shaltens, R., NASA Glenn Research Center, Ohio, 2002 [accessed 6 May 2004].

[Shimizu, 1997] "Fabrication and Testing of Single Crystal Mo Solar Thermal Thruster," *48th International Astronautical Congress*, Shimizu, M., Itoh, K., and Sato, H., National Aerospace Laboratory (NAL), National Research Institute of Metals (NRIM), and Tokyo Tungsten Co., Ltd., Turin, Italy, October 1997.

[Shoji, 1983] "Performance Potential of Advanced Solar Thermal Propulsion," AIAA-83-1307, *19th Annual AIAA/SAE/ASME Joint Propulsion Conference*, Seattle, Washington, Shoji, J., June 1983.

[Shoji, 1986] "Windowed Porous Material Absorption Concept – A New Solar Thermal Propulsion Concept," 1986 JANNAF Propulsion Meeting, New Orleans, Louisiana, Shoji, J., Perry, F., Lim, D., and Pard, A., Rockwell International, Rocketdyne Division, August 1986.

[Shoji, 1992] "Advanced Absorber/Thruster Concepts for Solar Thermal Propulsion," Shoji, J., Frye, P., Chwiedor, T., and Lim, D., Rockwell International, Rocketdyne Division, unpublished technical paper, 1992.

[Sinclair Optics, 2001] http://www.sinopt.com, OSLO LT Rev. 6.1, Sinclair Optics, Inc., 2001.

[Soules, 1997] "Design and Fabrication of a Dielectric Total Internal Reflecting Solar Concentrator and Associated Flux Extractor for Extreme (2,500 K) High Temperature Applications," NASA Contractor Report 204145, Soules, J., Castle, C., and Macosko, R., Analex Corporation, Buchele, D., ADF Corporation, Brook Park, Ohio, 1997.

[Space.com, 2000] http://www.space.com/scienceastronomy/solarsystem/large_sunspot_000921.html, "Largest Sunspot Group in Nine Years Visible," Weinstock, M., Space.com, 21 September 2000 [accessed 26 April 2004.

[SpaceandTech.com, 2001] http://www.spaceandtech.com/spacedata/elvs/athena_image1.shtml, "Athena launch vehicle specifications page," SpaceandTech.com, Andrews Space and Technology, 2001.

[SpaceandTech.com 2, 2001] http://www.spaceandtech.com/spacedata/motors/star37_sum.shtml, "STAR 37 Solid Rocket Motor Summary page," SpaceandTech.com, Andrews Space and Technology, 2001.

[Space Today, 2004] http://www.spacetoday.org/SolSys/Comets/Rosetta.html, "Europe Sends Rosetta to Comet," Space Today web site, Space Today Online, 2004 [accessed 11 March 2004].

[SSC, 2002] http://www.ee.surrey.ac.uk/SSC/SSHP/launcher/launch_asap.html#launcher, "Small Satellites Home Page, Ariane ASAP image," Surrey Space Centre, 2002 [accessed July 2002].

[SSTL, 2001] http://www.sstl.co.uk/datasheets/Platform_GEMINI_HQ.pdf, "Geosynchronous MINIsatellite Datasheet," Surrey Satellite Technologies Ltd., (SSTL), 2001 [accessed July 2002].

[SSTL 2, 2001] "BILTENSat On Orbit image," Surrey Satellite Technologies, Ltd., 2001.

[SSTL 3, 2001] "UoSAT-12 image," Surrey Satellite Technologies, Ltd., 2001.

[SSTL, 2004] "Surrey's DMC Satellites Reach Targeted Orbit Station," http://www.sstl.co.uk/index.php?loc=6, Surrey Satellite Technologies, Ltd., 30 March 2004 [accessed 26 April 2004].

[SSTL 2, 2004] http://www1.sstl.co.uk/datasheets/Subsys_ASS.pdf, "SSTL 2-Axis Fine Sun Sensor," Surrey Satellite Technologies, Ltd., 2004 [accessed 25 May 2004].

[St. Gobain, 2000] "Boron Nitride," company brochure with technical data, St. Gobain Advanced Ceramics, Amherst, New York, November 2000.

[STK, 2002] http://www.stk.com/products/explore/products/astrogator_prod_desc.htm, "Satellite Tool Kit (STK), Astrogator Product Description," STK web site, Analytical Graphics, Inc., 2002 [accessed July 2002].

[STP, 2001] *Secondary Payload Planner's Guide for Use of on the EELV Secondary Payload Adapter*, Draft Version 1.0, Department of Defense Space Test Program, Kirtland Air Force Base, New Mexico, June 2001.

[Sutton, 2001] *Rocket Propulsion Elements, 7th Edition*, Sutton, G., and Biblarz, O., Wiley-Interscience, New York, 2001.

[Technical Glass, 2003] http://www.technicalglass.co.uk/macor_composition.html, "Macor®," The Technical Glass Company, Haverhill, Suffolk, undated [accessed 18 March 2004].

[Thermoanalytics, 2001] http://www.thermoanalytics.com/products/radtherm/index.html, "RadTherm 6.0, Thermal Modeling and Heat Transfer Software," Thermoanalytics, Inc., 2001 [accessed July 2002].

[Thornock, 1972] "An Experimental Study of Compressible Flow Through Convergent-Conical Nozzles, Including a Comparison with Theoretical Results," *Journal of Basic Engineering, Transactions ASME* **94**, Series D, No. 4, pp. 926-932, Thornock, R., and Brown, E., December 1972.

[Tucker, 2001] "Solar Thermal Engine Tests: An Overview," Advanced Space Propulsion Workshop," 12th Annual Advanced Space Propulsion Workshop, University of Alabama-Huntsville, Huntsville, Alabama, Tucker, S., Marshall Spaceflight Center, Huntsville, Alabama, 2001.

[UBC, 2004] http://www.mmat.ubc.ca/courses/mmat382/, "Body of Basic Knowledge for Materials Engineering Courses," University of British Columbia, March 2004 [accessed 10 May 2004].

[Ultramet, 2002] http://www.ultramet.com/, "Ultramet Lightweight Composite Reflectors for Space Optics," Ultramet, Inc., Pacoima, California, undated [accessed May 2002].

[Ultramet 2, 2002] http://www.ultramet.com/foamtech.htm, "Ultramet Foam Technology," Ultramet, Inc., Pacoima, California, undated [accessed March 2002].

[Ultramet 3, 2002] http://www.ultramet.com/rhenium.htm, "Rhenium Properties," Ultramet, Inc., Pacoima, California, undated [accessed 6 April 2002].

[Ultramet 4, 2002] http://www.ultramet.com/, "Platinum Group Metals," Ultramet, Inc., Pacoima, California, undated [accessed May 2002].

[Ultramet 5, 2002] http://www.ultramet.com/, "Ultra-Refractory Carbides," Ultramet, Inc., Pacoima, California, undated [accessed May 2002].

[U. Missouri, 2002] http://www.ece.umr.edu/areas/power/solarth1.htm, "JPL Edwards Parabolic Dish Test Site," University of Missouri (Rolla), undated [accessed 12 February 2002].

[USACE, 2001] http://www.sam.usace.army.mil/PA/January2001/0101pen.html, "District Helps Redstone Rid of 'Green Dragon,'" U.S. Army Corps of Engineers (USACE), Mobile District web page, January 2001 [accessed July 2002].

[Venkateswaran, 1992] "Analysis of Direct Solar Thermal Rocket Propulsion," *Journal of Propulsion and Power* **8**, No. 3, Venkateswaran, S., Merkle, C., and Thynell, S., Pennsylvania State University, University Park, Pennsylvania, 1992.

[Villefranche, 1997] "Rosetta: the ESA comet rendezvous mission," *Acta Astronautica* **40**, *Issue 12,* pp. 871-877, Villefranche, P., Evans, J., and Faye, F., June 1997.

[Voltaix, 2000] http://www.voltaix.com/msds/newb2h6.htm#sec10, "Material Safety Data Sheet for Diborane (B_2H_6)," Voltaix, Inc., December 2000 [accessed July 2002].

[Wassom, 2000] "Revolutionary Propulsion Concepts for Small Satellites," *15th Annual AIAA/USU Conference on Small Satellites*, Wassom, S., Space Dynamics Laboratory, Utah State University, Logan, Utah, 2000.

[Weisstein, 1999] http://mathworld.wolfram.com/, "Mathworld™ web site," Weisstein, E., Wolfram Research, 1999 [accessed July 2002].

[Walker, 2002] "ESA Space Debris Mitigation Handbook, Executive Summary," http://www.esa.int/gsp/completed/execsum00_N06.pdf, Walker, R., et. al., Qinetiq, Farnborough, July 2002.

[Ward, 2003] Private Communication, Ward, N., Department of Chemistry, University of Surrey, 27 November 2003.

[Wells, 2001] "Minimising the Size and Mass of Interplanetary Spacecraft," *52nd International Astronautical Congress*, Toulouse, France, Wells, N., and Fearn, D., Space Department, QinetiQ, Farnborough, United Kingdom, October 2001.

[Westerman, 1998] "Testing of a Receiver-Absorber-Converter (RAC) for the Integrated Solar Upper Stage (ISUS) Program," *Proceedings of the 1998 Space Technology and Applications International Forum,* pp. 375-380, Westerman, K., and Miles, B., Albuquerque, New Mexico, 1998.

[Whelton, 2003] 14-Centimetre Aluminium Mirror Form Error Test Data, Private Communication, Whelton, D., Precision Optical Engineering, Hitchin, Hertfordshire, UK, December 2003.

[Winston, 1974] "Principles of Solar Concentrators of a Novel Design," *Solar Energy* **16**, pp. 89-95, Winston, R., Enrico Fermi Institute and Department of Physics, University of Chicago, 1974.

[Wong, 2001] http://www.grc.nasa.gov/WWW/RT2000/5000/5490wong.html, "High Efficiency Solar Thermal Vacuum Demonstration Completed for Refractive Secondary Concentrator," Wong, W., NASA Glenn Research Center, Cleveland, Ohio, 2001 [accessed 10 May 2004].

[Woodfield, 2002] Private Communication, Woodfield, M., Sintec-Keramik (UK) Ltd., Newport, South Wales, 20 June 2002.

[Wright, 1999] "Pressure Measurement in the Post-Combustion Section of a Hybrid Rocket Motor," AIAA 99-2536, Wright, A., Tomany, A., Wright, A., and Hudson, M., Department of Applied Science, University of Arkansas, 1999.

[Wyant, 2000] http://www.optics.arizona.edu/jcwyant/optics513(2000).htm, "Optics 513 Course Materials," Wyant, J., University of Arizona, 2000 [accessed July 2002].

[Wysong, 2004] Private Communication, Wysong, I., United States Air Force European Office of Aerospace Research and Development, London, 2 February 2004.

[Yeomans, 2002] Private Communication, Yeomans, J., University of Surrey, Guildford, 13 June 2002.

[Yeomans, 2003] Private Communication, Yeomans, J., University of Surrey, Guildford, April 2003.

[Young, 1989] *Roark's Formulas for Stress and Strain, 6th Edition,* Young, W., McGraw-Hill International, New York, 1989.

[Zakirov, 2001] "Nitrous Oxide as a Rocket Propellant," *Acta Astronautica* **48**, *No. 5-12*, pp. 353-362, Zakirov, V., and Sweeting, M., Lawrence, T., and Sellers, J., Surrey Space Centre and the European Office of Aerospace Research and Development, 2001.

[Zucrow, 1976] *Gas Dynamics, Vol. 1*, Zucrow, M., and Hoffman, J., John Wiley & Sons, Inc., New York, 1976.

Research Publications

[1] "Solar Thermal Propulsion for Microsatellites," *6th International Symposium: Propulsion for Space Transportation of the 21st Century*, Versailles, France, Kennedy, F., and Palmer, P., May 2002.

[2] "Preliminary Design of a Micro-Scale Solar Thermal Propulsion System," AIAA 2002-3928, *38th Joint Propulsion Conference*, Indianapolis, Indiana, Kennedy, F., and Palmer, P., July 2002.

[3] "Design and Proto-Flight Test Strategy for a Microscale Solar Thermal Engine," *Space Technology* **23**, No. 1, pp. 11-26, Kennedy, F., and Palmer, P., June 2003 (updated version of paper initially presented at the 53rd International Astronautical Conference, Houston, Texas, 10-19 October 2002).

[4] "An Analysis of Preliminary Test Campaign Results for a Microscale Solar Thermal Engine," *17th Annual AIAA/Utah State University Small Satellite Conference*, Logan, Utah, Kennedy, F., August 2003.

[5] "Prometheus: A Low-Cost Microsatellite Flyby Mission of 4179 Toutatis," *J. British Interplanetary Society* **56**, No. 9/10, pp. 299-307, Kennedy, F., Coxhill, I., Imre, E., Fielding, J., Atek, S., Lappas, V., Kormos, T., and Freebody, M., September/October 2003 (updated version of paper initially presented at the 10th Student Satellite Design Competition, Japan Space Forum, Tokyo, Japan, October 2002).

[6] "A Comparison of Simulation and Test Campaign Results for a Microscale Solar Thermal Engine," *54th International Astronautical Conference*, Bremen, Germany, Kennedy, F., Palmer, P., Surrey Space Centre, and Paul, M., Surrey Satellite Technologies, Ltd., October 2003.

[7] "Preparing for Flight: The Surrey Space Centre's Microscale Solar Thermal Propulsion Experiment (MSPeX)," Kennedy, F., Henshall, P., Surrey Space Centre, and Gibbon, D., Surrey Satellite Technologies, Ltd., June 2004.

[8] "Results of a Microscale Solar Thermal Engine Ground Test Campaign at the Surrey Space Centre," *40th Joint Propulsion Conference*, Ft. Lauderdale, Florida, Kennedy, F., Palmer, P., and Paul, M., Surrey Satellite Technologies, Ltd., July 2004.

Appendix A: Astrodynamics

The mission analysis in Chapter 3 relies on calculations involving basic astrodynamical principles. There are excellent texts that treat this subject in detail. The most notable (and rigorous) is Richard Battin's *An Introduction to the Mathematics and Methods of Astrodynamics,* published as part of the American Institute of Aeronautics and Astronautics' Education Series. Perhaps slightly more approachable is *Fundamentals of Astrodynamics* (Bate, Mueller, and White), which includes numerous examples and case studies.

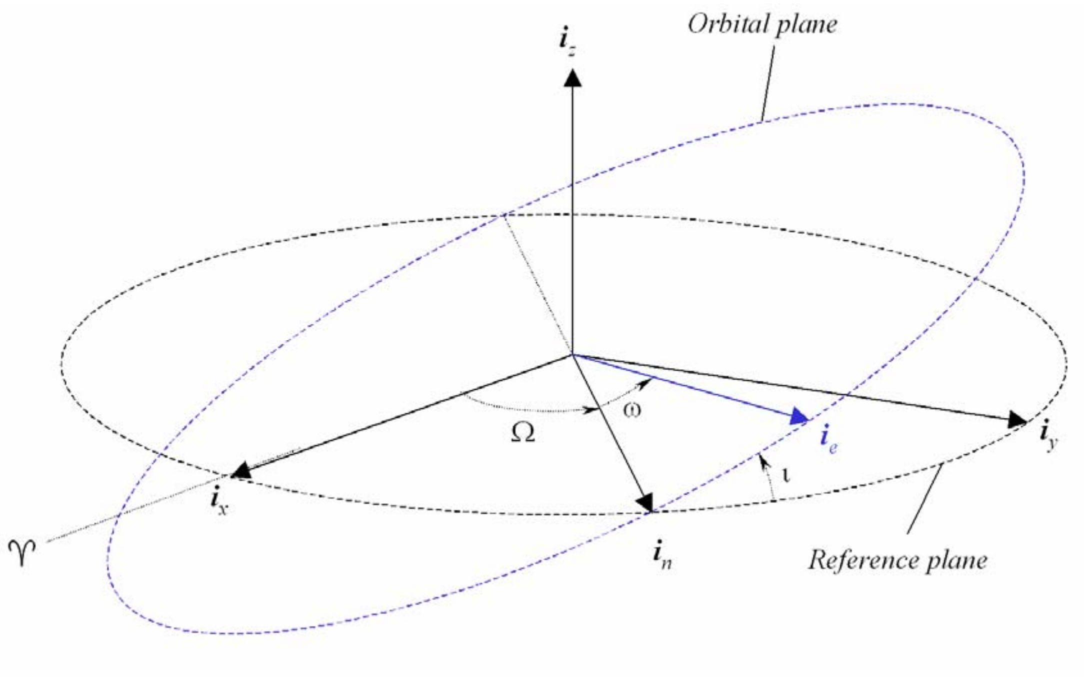

Figure A-1 Coordinate system geometry [Battin, 1987]

The author assumes the reader is familiar with the two-body problem and the vector differential equations of relative motion. The usual Keplerian orbital elements—six integration constants of a two-body orbit—are displayed in Figures A-1 and A-2. The reference axis i_x points towards the vernal equinox (the "first point" of Aries the Ram, signified by the symbol ♈). Due to long-period precession of the earth's axis, this direction is not constant; however, i_x can be uniquely specified by a time, or *epoch,* for which the direction is known. These include the J2000 epoch, based on the direction of i_x on 1 January 2000 at 12:00:00.00 Universal Time.[222] The STK

---

[222] This is equivalent to the Julian Date (JD) 2451545.0.

Astrogator simulations performed by the author make use of the J2000 epoch for establishing a reference coordinate system.

The intersection of the reference plane—in this case, the earth's ecliptic or plane of revolution about the sun—and the orbital plane is the apsidal line or line of nodes (i_n). The angle between i_x and i_n is referred to as either the *longitude of the ascending node* (LAN) or the *right ascension of the ascending node* (RAAN).[223] In either case, this angle is designated by the symbol Ω. The angle between the reference plane and the orbital plane is the *inclination angle* (i). For inclination angles of 0 degrees (e.g. heliocentric orbits that lie within the ecliptic), there is no defined angle Ω. The *argument of periapse*, ω, is an angle within the orbital plane and is measured from to the eccentricity vector, which will be discussed presently. These three angles (Ω,i, and ω) are referred to as Euler angles, uniquely defining the orbit's spatial orientation.

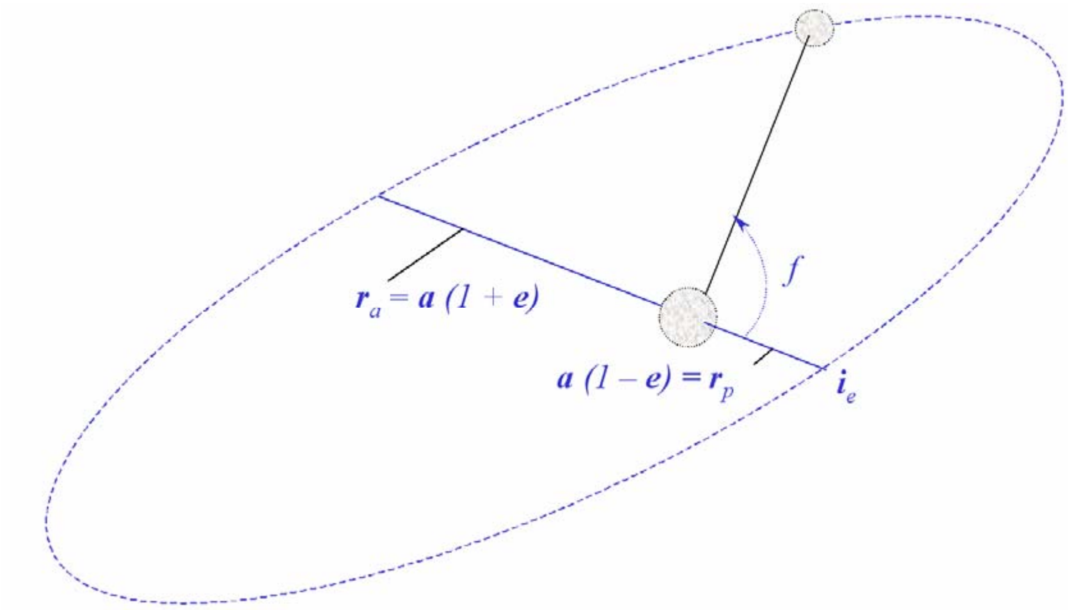

Figure A-2 Orbital elements.

The remaining three Keplerian elements are the orbit's *semi-major axis*, a, its *eccentricity*, e, and the *true anomaly*, f. The semi-major axis and eccentricity describe the orbital shape—hyperbolic, parabolic, or elliptic—while the true anomaly provides information about a body's position in the orbit. Periapse and apoapse radii (r_p and r_a, respectively) for elliptical orbits can be determined from the relations shown in Fig. A.2, if a and e are known.

---

[223] For purposes of this discussion, we are assuming that a body in the orbit of interest is moving counterclockwise (i.e., is in a *prograde* orbit) in Figures A-1 and A-2. Therefore, $\boldsymbol{i}_n$ points toward the ascending node, where a body would cross from north to south as it passes through the node. Objects moving in a clockwise direction would be termed *retrograde*.

Often, orbital elements databases for celestial objects (e.g., near-earth objects such as asteroids) do not provide f. Instead, observers indicate the object's *mean anomaly*, M, which is derived from its *mean motion*, n. Another angle, the *eccentric anomaly*, E, is intermediate in the calculation of the true anomaly from the mean anomaly.[224] The following relations[225] can be solved iteratively to provide f [Burnett, 1998]:

$$M = E - e \sin E$$

$$\tan\left(\frac{f}{2}\right) = \sqrt{\frac{1+e}{1-e}}\tan\left(\frac{E}{2}\right)$$

The Jet Propulsion Laboratory's DASTCOM database[226] is a searchable, online repository of up-to-date orbital elements for a number of objects [JPL (2), 2001]. To conduct an analysis of potential Near Earth Object flybys on STK Astrogator, it was necessary to verify DASTCOM elements for several Potentially Hazardous Asteroids (PHAs). This was done by comparing existing close approach data (which provides the time of approach to within approximately 15 minutes)[227] to simulations created by the author on STK Astrogator. The STK and close approach data agreed within the limits of accuracy imposed by the time of approach information. Specific DASTCOM elements for 4179 Toutatis and 2000 UK11 follow:

	4179 Toutatis	**2000 UK11**
Mean Anomaly (M), deg.	**86.2812009**	**70.3968054**
Argument of Perigee (ω), deg.	**274.7794758**	**292.5602815**
Longitude of the Asc. Node (Ω), deg.	**128.2491025**	**238.1008351**
Inclination (i), deg.	**0.4695832**	**0.7761772**
Eccentricity (e)	**0.634227437**	**0.248142893**
Semi-Major Axis (a), AU[228]	**2.510053675**	**0.884675531**

Table A.1. Orbital Element Data for two Near Earth Objects (NEOs)

These data are valid for the epoch 2452000.5 (1 April 2001). They are updated regularly, as additional observations are made. Sufficient significant digits are available to obtain sub-kilometre position accuracy.

STK Astrogator

---

[224] "The relation between the mean anomaly and the eccentric anomaly…is called Kepler's Equation." [Battin, 1987]

[225] These equations, and their derivations, can also be found in [Battin, 1987].

[226] Database of ASTeroids and COMets.

[227] Available on the Harvard-Smithsonian Center for Astrophysics web page [CfA, 2001].

[228] One Astronomical Unit (AU) = 149,597,871 kilometres.

The author made extensive use of STK Astrogator (an "add-on" module for Satellite Tool Kit 4.2) to simulate the mission scenarios discussed in Section 2, Detailed Mission Analysis. Astrogator permits the user to define engine and thruster models, impulsive or finite duration burns, and to specify the direction of the firing in a coordinate system of his choice.

Astrogator permits the user to select any of a number of "force models," to include geocentric, heliocentric, and selenocentric versions, and to swap models "on the fly" when one becomes more applicable than another. The author used the "Earth Full" model for most near-Earth analysis, which includes first- and second-order oblateness effects, as well as the moon, Sun, and all major planetary bodies. For Near-Escape missions, the author selected the default heliocentric model following the final escape maneuver. For missions terminating at, or interacting significantly with, the moon, STK's default selenocentric force model, with zonal J2 effects[229] (lunar oblateness) was used during approach and/or lunar orbit.

The software also permits the selection of specific numerical integrators. In all cases, the default integrator (an 8th-order Runge-Kutta-Verner algorithm with 9th-order error control) was used.[230]

A Note on Third-Body Perturbations

The ideal low-thrust escape trajectory consists of ellipses of increasing eccentricity; all manoeuvres are performed near perigee in an attempt to minimize finite burn losses. As e increases and the orbital apogee r_a extends beyond 200,000 km, lunar perturbations begin to become significant enough to cause mission failure. Initial attempts to produce escape trajectories with STK Astrogator resulted in eccentric re-entry at earth or lunar gravity "assists" which, despite their name, often provided little in the way of astrodynamic assistance. Fundamentally, these perturbations can be understood, and their approximate magnitude estimated, from Gauss' variational equations for i, a, and e:

$$\frac{di}{dt} = \frac{r cos\theta}{na^2\sqrt{1-e^2}} F_\perp$$

$$\frac{da}{dt} = \frac{2e sin f}{n\sqrt{1-e^2}} F_r + \frac{2a\sqrt{1-e^2}}{nr} F_f$$

---

[229] Earth asphericity results in perturbing accelerations due to equator bulging, pole flattening, and other asymmetries. The J terms (J2, J3, etc.) are empirically-determined zonal coefficients of a potential function describing the Earth's gravitational field. J2 is the most significant of these, resulting from Earth's oblateness. The value of J2 is on the order of 1000 times greater than J3 ("pear-shaped" earth) and J4.

[230] STK Astrogator's Manual declares their heliocentric 8th-Order RKV with 9th-Order error control to have "tolerances suitable for interplanetary missions."

$$\frac{de}{dt} = \left[\frac{\sqrt{1-e^2}}{na} sinf\right] F_r + \left[\frac{\sqrt{1-e^2}}{na^2 e}\left(\frac{a^2\left(1-e^2\right)}{r} - r\right)\right] F_f$$

Here, F_r, F_f, and $F_\perp$ represent the orthogonal components of a disturbing acceleration in a modified "perifocal" coordinate system [Bate, 1971], where i_r is the instantaneous radius vector, i_f is rotated 90 degrees from i_r in the direction of increasing true anomaly, f. The third axis, $i_\perp$, is orthogonal to the orbital plane (i_r x i_f). θ is the orbiting object's *argument of latitude* ($\omega + f$), the angle between the object's ascending node and the instantaneous radius vector.

From these relations, it can be seen that inclination changes will result only from out-of-plane disturbances, and that increasingly eccentric orbits (e approaching 1) cause this term to grow dramatically. The following geocentric orbits were examined:

	GTO (i = 7 deg.)	**HEO 1**	**HEO 2**
Mean Anomaly (M), deg.	**0.00000**	**0.00000**	**0.00000**
Argument of Perigee (ω), deg.	**180.000**	**180.000**	**180.000**
Longitude of the Asc. Node (Ω), deg.	**0.00000**	**0.00000**	**0.00000**
Inclination (i), deg.	**7.00000**	**7.00000**	**7.00000**
Eccentricity (e)	**.724392**	**0.94082**	**0.95403**
Semi-Major Axis (a), km	**24411.5**	**121793**	**156793**
Period (hrs.)	**10.5**	**117.5**	**171.7**

Table A.2 Three high-e orbits.

The effect of the moon's gravitation on inclination is roughly 12 times greater in HEO 1 than the standard GTO (Figure A-3). At the higher HEO 2, the lunar influence grows by an additional factor of 1.5.[231] HEO 2's long period—roughly seven days—is almost 50% greater than HEO 1's and allows for a much greater time to be spent near apogee, magnifying the effect per orbit. STK Astrogator simulations demonstrate that HEO 1 is a relatively stable phasing orbit; HEO 2, with an apogee of 306,000 km, is much more susceptible to orbital element change as a result of lunar perturbations.

---

[231] These calculations assume the moon is at roughly minimum separation from the spacecraft at the spacecraft's apogee, (i.e., directly behind it), with zero f-axis separation ($M = f = 180$ degrees).

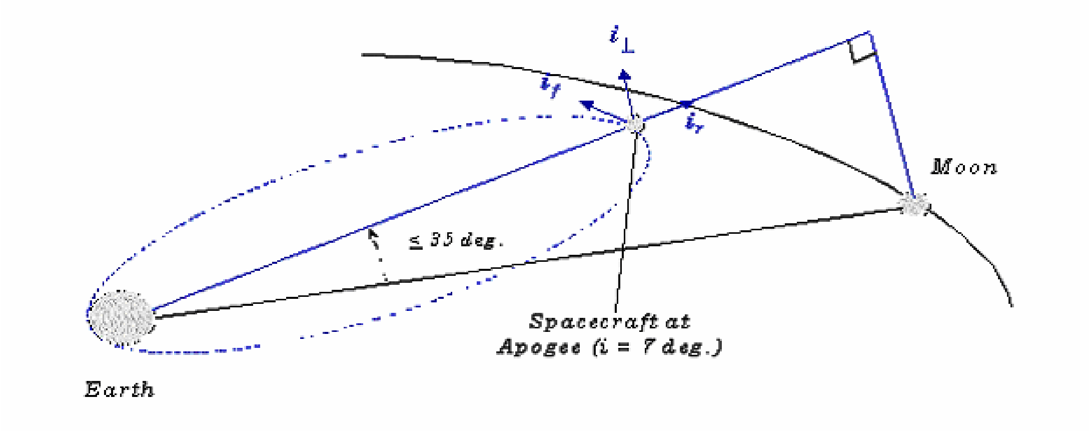
$i_\perp$
i_f
i_r
Moon
≤ 35 deg.
Spacecraft at
Apogee (i = 7 deg.)
Earth

Figure A.3 Modified perifocal coordinate system. The moon's orbit is inclined from the Earth's rotational axis by 18-28 degrees. For a spacecraft at roughly 7 degrees inclination, the moon will never be inclined at an angle greater than 35 degrees.

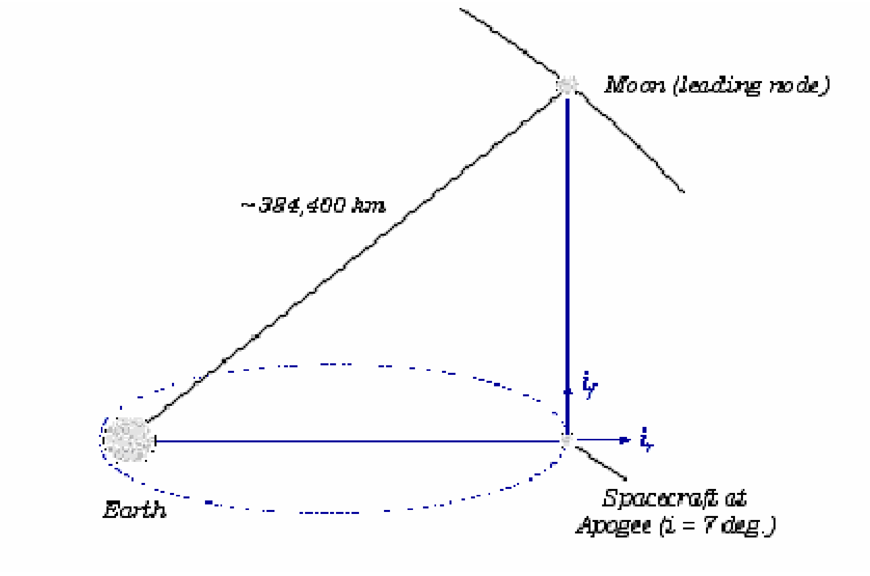
Moon (leading node)
~384,400 km
i_f
i_r
Spacecraft at
Apogee (i = 7 deg.)
Earth

Figure A-4 Potentially catastrophic lunar perturbations to a highly eccentric earth-orbiting spacecraft can occur near the moon's points of intersection of the f-axis (modified perifocal coordinates). If this intersection occurs near apogee, spacecraft-moon separation is likely to be small and significant semi-major axis (a) changes can occur.

Similar results occur for semi-major axis and eccentricity effects. The most significant perturbation to the semi major axis *a* occurs when the instantaneous *f*-axis is pointed at or near the moon. If the spacecraft is near apogee, and the moon is leading or lagging the spacecraft as shown (Figure A-4), significant semi-major axis impacts can occur. At an apogee distance of

236,000 km, *da/dt* exceeds ±1.25 m/s (±108 km/day). At the "lagging node,"[232] the moon causes *a* to decrease by this amount—while eccentricity rises slightly. If perigee is sufficiently low (e.g., 350 km), this can result in an eccentric re-entry. These estimates agree with the results of the author's STK Astrogator simulations.

---

[232] The moon is shown at the "leading node" in Fig. A.4, where it sits astride the *f*-axis. For a spacecraft at an apogee of 236,000 km, the moon is over 300,000 km distant. This is far larger than the lunar SOI, which is approximately 66,000 km. [Bate, 1971] Nevertheless, lunar effects appear long before a spacecraft enters its SOI.

Appendix B: Development of a System Requirements Document

Mission Summary

The author investigated three high delta-V missions, including: (1) GTO-to-GEO, assuming launch aboard both Ariane (i = 7°) and Atlas (i = 18°) into a 350 x 35,717 km orbit; (2) GTO-to-Near Escape, which places the host satellite in a heliocentric near-Earth orbit, suitable for missions to many Near Earth Objects (NEOs); and (3) Other Body Capture, or, more specifically GTO-to-Lunar Orbit, with final placement in a 1,000 km x 13,000 km polar lunar orbit. All of these missions were baselined for a 100-kilogram (wet mass) microsatellite, and all demand between 1,600 and 2,400 m/s of velocity change from an initial GTO. Placement of a standard 100-kilogram microsatellite into a high altitude phasing orbit was also addressed; this mission is intended to overcome the difficulties of achieving flybys of selected NEO targets when the initial orbit is unfavourable for escape. This mission, a type of Near Escape, requires a relatively large velocity change—approximately 3,000 m/s.

A final mission is addressed here. The host vehicle would be substantially smaller than the 100-kilogram platform discussed above—with a probable initial (wet mass) target of 20 kilograms and a final (dry mass) of no less than 10 kilograms. This satellite, intended either for experimental verification of the solar thermal propulsion system or as a modular transfer stage for LEO payloads, would be deposited in a 352 km LEO by one of several launch systems, and then perform a series of orbit raising manoeuvres to achieve a final circular orbit at 704 km. This mirrors stated requirements for a Shuttle Small Payload (SPL) Propulsion Module [Hampsten, 2001].

System Performance[233]

Threshold requirements—considered as lower bounds—and *objective* requirements, or goals, are presented wherever possible. The underpinning rationale and derivation of requirements are provided.

System Volume **.*09* m^3 threshold / .*045* m^3 objective**[234]

---

[233] Many of these requirements are also—perhaps unsurprisingly—criteria used by Sellers [1996] in his *Nine-Dimensional Cost Paradigm* for selecting a satellite propulsion system.

The solar thermal propulsion system's available volume is highly constrained by spacecraft and launch vehicle limitations. For purposes of baselining the system, a representative 100-kg class Surrey enhanced microsatellite was assumed. The Surrey microsatellite is configured to fit within the specified volume constraints imposed by Ariane 5's Ariane Structure for Auxiliary Payloads (ASAP)—a rectangular space of 60 cm (width) x 60 cm (length) x 71 cm (height) for each of up to 8 satellites. The spacecraft's allowable footprint on the ASAP is limited to 60 cm x 60 cm; the height of the spacecraft, nominally 71 cm, can exceed this threshold if it can be shown that a taller microsatellite will not interfere structurally with the primary payload. The volume of this static envelope is .2556 m^3. Fig. B.1 illustrates the placement scheme for microsatellites on ASAP.

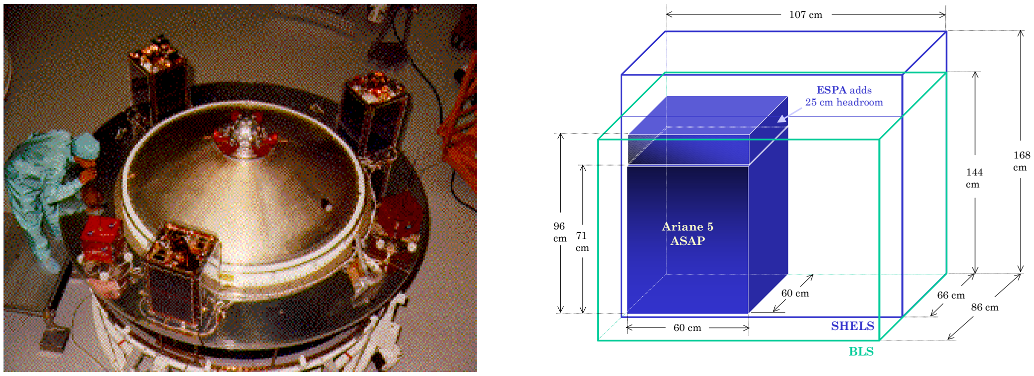

Fig. B.1. SSTL's KITSAT-2, PoSAT-1, and HealthSAT-2 arrayed on the Ariane Structure for Auxiliary Payloads (Ariane 4 ASAP), at left. The primary payload, the French SPOT-3 imaging satellite, is not shown. SPOT would mount to the central adapter cone (inside the white circle). A successful launch was conducted in 1993 [SSTL, 2002]. Several examples of small satellite static envelopes, at right [Hampsten, 2001].

Ariane 5's ASAP is a limiting case; all other launch systems under investigation provide larger spacecraft volumes. Figure B.1 (right) shows the relative sizes of the ASAP static envelope and three other potential providers' systems—the Evolved Expendable Launch Vehicle (EELV) Secondary Payload Adapter (ESPA),[235] the Shuttle's Bridge Launch System (BLS) and the Shuttle Hitchhiker Experiment Launch System (SHELS). Figure B.2 illustrates the size of larger envelopes—Pegasus XL and Athena, for comparison. Table B.1 provides static envelope volumes for a number of launch vehicles.[236]

Jason [2000] notes that a Surrey minisatellite—similar to UoSAT-12[237]—may nominally budget 180 litres (.18 m^3) of space for propulsion. The vast majority of this is propellant tankage.

---

[234] 100-kg. microsatellite requirement. Small microsatellite (20-kg) value not stated.
[235] ESPA will be available no earlier than US Government fiscal year 2003. [Haskett, 1999]
[236] These include, when applicable, the conical space near the top of the payload fairing.
[237] 400 kg., exterior dimensions: 1.1 x 1.1 x .885 m.

Assuming linear scaling, an enhanced microsatellite (100 kg) will have roughly 45 litres available for propulsion.

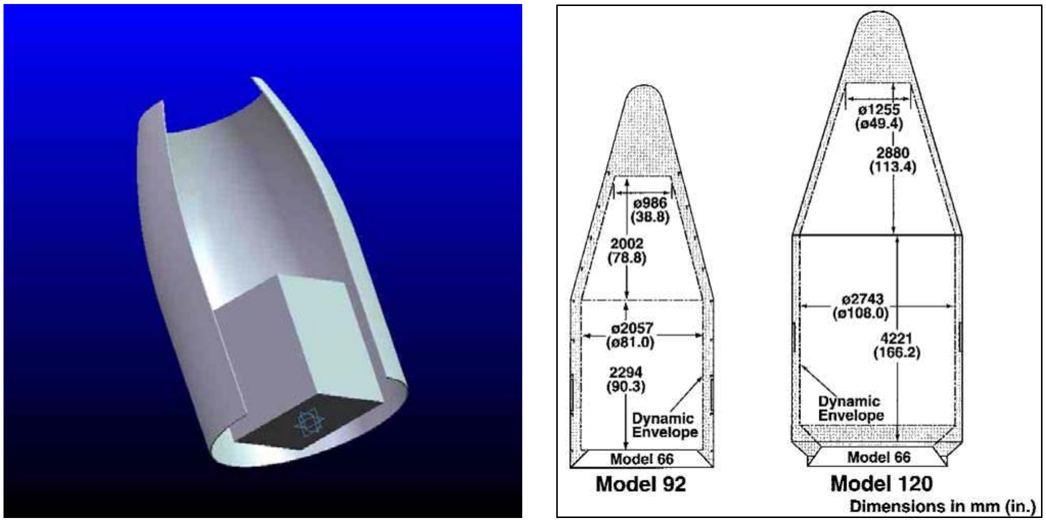

Figure B.2. Static envelope comparison: Ariane 5 ASAP inside Pegasus XL (110 cm diameter payload volume, 188 cm height), left. Athena launch vehicle dynamic envelopes (206- and 274-cm diameter payload volumes) [SpaceandTech.com, 2001].

For a nominal, 71-cm microsatellite, the potentially useful zone (shown in Figure B.3 in yellow) constitutes approximately 180 litres[238]. However, as can be seen at left, this space is used by other satellite subsystems, to include payloads (cameras), attitude control (reaction wheels and star trackers), and power (batteries). The BilSat system has many of the elements necessary for conducting one of the three primary missions discussed in Chapter 3. Therefore, it is almost certain that something less than 180 litres will be available for the missions under consideration.

Launcher	Dimensions (cm)	Payload volume (m^3)
Ariane 5 ASAP	**60 (w) x 60 (l) x 71 (h)**	**.2556**
ESPA	**61 x 61 x 96**	**.3572**
SHELS	**66 x 107 x 168**	**1.1864**
BLS	**86 x 107 x 144**	**1.3251**
Pegasus XL	**111.8 (radius) x 188 (cone height)**	**1.5306**
Minotaur[b]	**116.8 (radius) x 223.5 (cone height)**	**< 2.4[a]**
Athena Model 92[b]	**205.7 (radius) x 429.6 (cone height)**	**11.41**
Dnepr[c]	**270.0 (radius) x 461 (cone height)**	**16.91**

[a] Precise dimensions unavailable
[b] Dynamic values
[c] Unknown if dynamic or static value

Table B.1. Static envelopes of various small launch vehicles

The 45-liter figure will be addressed as an objective. This value does not take into account the unique volumetric issues raised by a solar thermal propulsion system's concentrating mirror and high-temperature receiver. A threshold figure of 90 litres—double the goal value—is intended to account for the additional volume necessary to accommodate these items.

For the smaller (20-kg) satellite, a volume requirement will not be imposed. The author assumes that the small microsatellite mission is experimental in nature, and that its primary purposes may very well be to validate the propulsion system under investigation. Therefore, this smaller system will respond to the required volumetrics of the STP engine.

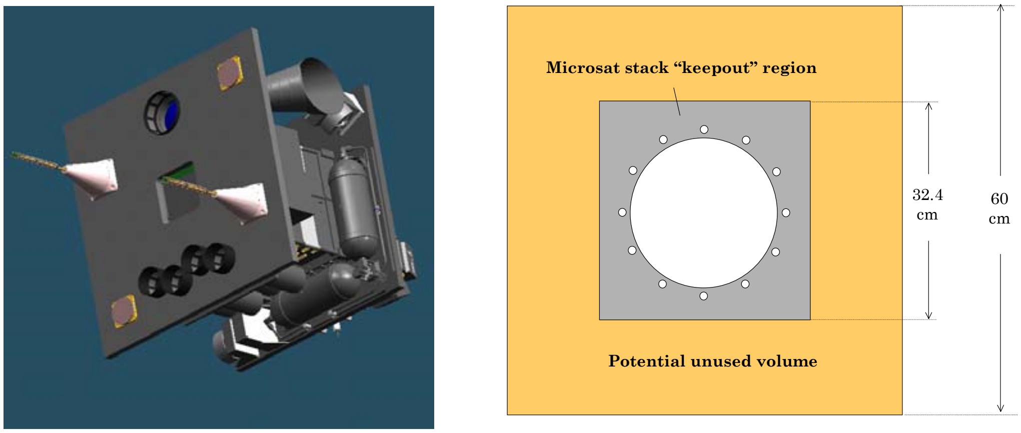

Figure B.3. BILTENSat butane propulsion system on lower shelf of enhanced microsatellite (solar arrays removed from view). Lower shelf structure is shown at right [Cowie, 2001].

System Dry Mass *15 kg* **threshold /** *10 kg* **objective (microsat-class)**
10 kg **threshold /** *7 kg* **objective (small microsat-class)**

This requirement is highly coupled with the determination of a target engine specific impulse. As specific impulse rises, the solar thermal engine becomes increasingly favourable vis-à-vis competitive systems (e.g., monopropellant hydrazine or bipropellant monomethylhydrazine [MMH/N_2O_4]).

Why select these systems for comparison? Monopropellant N_2H_4 and bipropellant MMH/N_2O_4 certainly appear to be appropriate competitors from a cost and heritage standpoint—higher performance is typically only available through the use of cryogenic fuels or oxidizers (e.g., liquid oxygen and kerosene, liquid oxygen and liquid hydrogen), infeasible for small satellite missions. Electric propulsion (EP), while in principle feasible for orbit transfer and providing very high specific impulses, must contend with the severe power limitations of a small satellite—typically dictated by dedicated space for solar arrays.[239] Body-mounted silicon arrays, similar to those used

---

[238] Incidentally, this figure, which represents all available space on a microsatellite, is identical to the propellant budget for the significantly larger minisatellite.

[239] As these systems use spiral orbit transfer strategies, they are “always on,” and cannot rely on stored energy (in the form of batteries) to provide high power for short durations. Thus, the main constraint on the

by SSTL's microsatellites, achieve on the order of 134 W/m^2. [Wertz, 1992] A single SSTL microsatellite face—60 x 71 cm—can thus provide a steady state power of ~57 W. More expensive, but more radiation-tolerant indium phosphide or gallium arsenide arrays might conceivably double this performance. Higher power levels will require stowed, deployable arrays of increased complexity and/or greater conversion efficiency. Such systems have been proposed,[240] but they are likely to be substantially more expensive to build and test than the simple, body-mounted silicon system discussed above. These factors tend to drive EP systems to very low thrust—in the tens of milliNewtons—and correspondingly lengthy transfer times.[241] This will be addressed in detail.

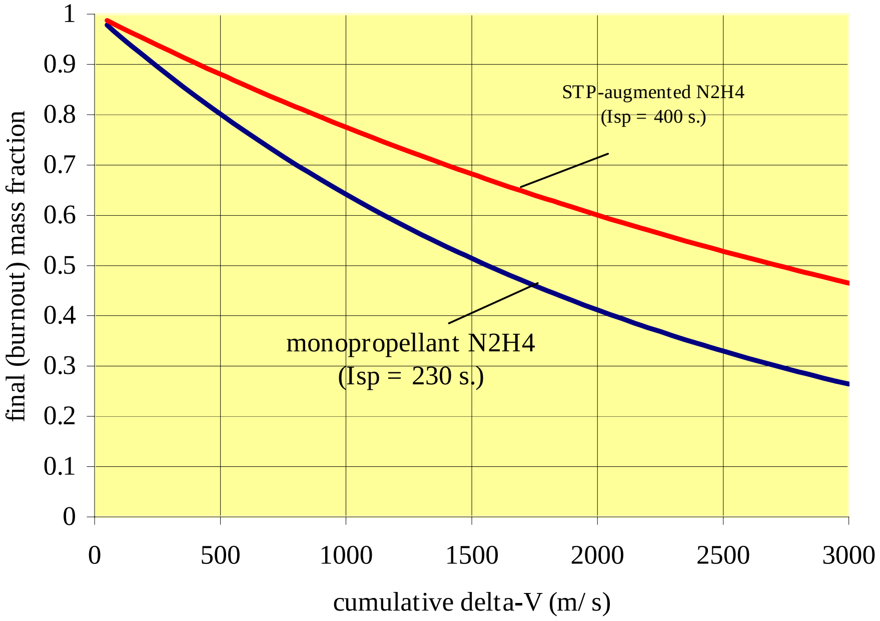

Figure B.4. Mass fractions for monopropellant hydrazine and STP-augmented hydrazine. A 100-kg microsatellite can perform a velocity change of 1,500 m/s by consuming 49 kg of hydrazine (I_{sp} = 230 s) or 31 kg of hydrazine with STP augmentation (I_{sp} = 400 s).

Results of System-to-System Comparisons

A 100-kg microsatellite is assumed as the baseline host. For velocity changes on the order of 1,250 m/s—somewhat less than the mission requirements discussed in Chapters 2 and 3—a

---

electric propulsion system is likely to be solar input power. This tends to restrict their use on small satellites to orbit maintenance.

[240] QinetiQ's proposal for SIMONE, a 120-kg microsatellite, would use a 25 mN, 670-W xenon ion engine to rendezvous with a near earth object in 26 months. A 1-1.5 kW deployable, flexible, high-efficiency (25-35%) array is assumed. [Wells, 2001]

hydrazine-based solar thermal system[242] breaks even with its conventional monopropellant partner for an augmentation mass of 15 kg (Figure B.4).[243] This breakeven occurs at 10 kg for 750 m/s. For higher velocity changes, less efficient (heavier) solar thermal engines become increasingly competitive. This trade-off is straightforward inasmuch as the engine cycle is an "add-on"—the STP augmented hydrazine system uses all of the hardware of the conventional monopropellant hydrazine system, but includes additional hardware (concentrator array, receiver structure) which must be offset by its increased engine performance to be effective. Figure B.5 illustrates the allowable margin provided by STP-augmented hydrazine.

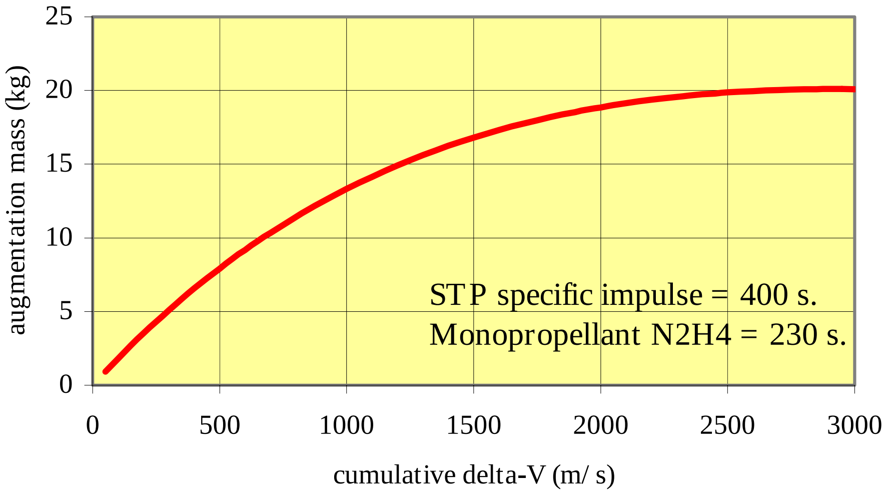

Figure B.5. Permissible STP augmentation mass for breakeven with a monopropellant hydrazine thruster, for a 100-kg "wet" satellite.

A similar trade can be performed against bipropellant hydrazine/N_2O_4 or MMH/N_2O_4.[244] In this instance, however, the STP system is not simply "additional mass." The bipropellant system will

---

[241] ESA's SMART-1 mission, which requires 15-17 months to achieve lunar orbit, uses Snecma's PPS-1350 Hall effect thruster. The PPS-1350 consumes 1350 W and produces 80 mN of thrust. [ESI Directory, 2001]

[242] The solar thermal system adds heat to the decomposed monopropellant hydrazine flow. Monopropellant hydrazine specific impulse is approximately 230 s. STP engine heat addition would raise the I_{sp} to approximately 400 s (corresponding to an average temperature of 2,000 K).

[243] This figure represents the most mass that the solar thermal system can "add" to the monopropellant hydrazine thruster (at a higher specific I_{sp}). Additional weight will make the system a worse performer than the stand-alone monopropellant system.

[244] Atlantic Research Corporation's LEROS 1B bipropellant thruster provides 645 N of thrust at 318 s. It masses 4.1 kg (not including tanks, valves, and lines). Lower thrust engines (e.g., LEROS 10 and LTT) are lighter but provide lesser performance, with specific impulses of around 270-290 s. [ARC, 2001]

require somewhat more tankage mass than the comparable monopropellant STP system.[245] This is partially offset by MMH/N_2O_4's higher bulk density.

Figure B.6 illustrates an imposed constraint on solar thermal engine mass for velocity changes of up to 3,000 m/s. To break even with bipropellant hydrazine/N_2O_4, a solar thermal engine must weigh less than 10 kg for a cumulative mission delta-V of 1,250 m/s. This figure does not include tankage mass—which, at this delta-V, is likely to be 2-3 kg.

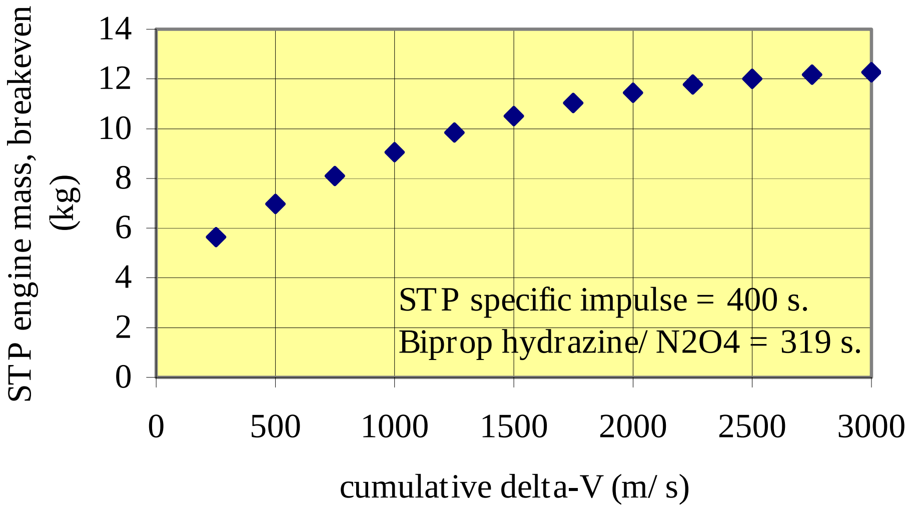

Figure B.6. STP engine mass constraint for breakeven with ARC LEROS 1B N_2H_4/N_2O_4 thruster. A 10-kg engine will outperform the bipropellant combination for velocity changes of $\geq$ 1,250 m/s.

---

[245] To simplify this trade, the author assumes identical storage pressure requirements for the STP and bipropellant systems, and the use of spherical aluminium tanks. No additional tank—for pressurant gas—is assumed; initial storage pressure is 600 psi (4.1 MPa, or roughly 40 atm). A factor of safety of 1.3 is used for all calculations. A 30% margin for bosses and/or fittings is added to the total membrane weight. MMH/N_2O_4's bulk density is 1170 kg/m^3 [Brown, 1996].

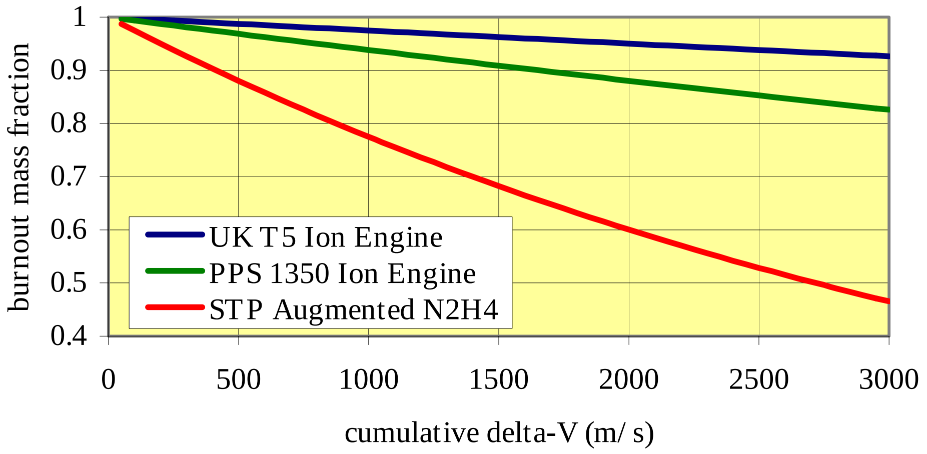

Figure B.7. STP augmented N_2H_4 versus two state-of-the-art ion engines, Snecma's PPS 1350 (I_{sp} ~ 1,600 s.) and the UK T5 (I_{sp} ~ 4,000 m/s).

Both of the previously discussed trades indicate that the STP system mass (with tankage and lines) must fall below ~15 kg to *ensure* the system is competitive with heritage mono- and bipropellant systems on 100-kg class microsatellites. This sets the threshold value. The objective value is selected as 10 kg—this would permit a 400-s. STP engine to outperform monopropellant hydrazine even at very low velocity changes (as low as 750 m/s, roughly equivalent to the ideal earth escape requirement from GTO).

A final comparison—between the STP engine and a microsatellite-compatible electric propulsion system—is of interest, since EP systems represent the highest achievable performance (in terms of I_{sp}) potentially available to the small satellite builder. Figure B.7 demonstrates the substantial advantage of high I_{sp}—for a delta-V of 2,000 m/s, the PPS 1350 consumes only 30% of the propellant required by STP-augmented N_2H_4 (or, alternatively, an ammonia-based STP system).[246]

---

[246] The author has noted that the use of electric propulsion normally dictates a spiral orbit transfer strategy, which proscribes the use of elliptical starting orbits such as the Geosynchronous Transfer Orbit. Firing over small portions of the orbital arc will incur extremely large transfer time penalties, often on the order of years. Battin [1987] has shown that, for constant tangential thrusting from a *circular* starting orbit,

$$t_{esc} - t_o = \frac{v_o}{a_{Tt}}\left[1 - \left(\frac{20 a_{Tt}^2 r_o^2}{v_o^4}\right)^{\frac{1}{8}}\right]$$

where $t_{esc} - t_o$ is time to escape, v_o and r_o are the velocity and radius of the initial orbit, and a_{Tt} is acceleration. Clearly, a delta-V figure can be computed from the product of $t_{esc} - t_o$ and a_{Tt}. For sufficiently small values of a_{Tt}, a low-thrust propulsion system tends toward a delta-V of v_o. This compares with a single-impulse (or multiple near-impulsive) escape requirement from this same circular orbit of $(2^{½} - 1)v_o$, or approximately 0.414 v_o. Others have made note of this "spiral penalty" [Sandorff, 1960]. In a 350 x

This somewhat simplistic analysis neglects (1) penalties associated with using a spiral transfer strategy and circular starting orbits, which is almost unavoidable for electric propulsion, (2) differences in the dry masses of the propulsion systems discussed, and (3) the significant coupling between electric propulsion and the satellite electrical power system that supports it, which—when ignored—tends to skew results in favour of higher-I_{sp} EP systems. The first issue is discussed in Footnote 15, and we will return to it later. The second issue can be left aside—the UK T5 ion engine, with electronics, tankage, fittings, and piping, is expected to mass 18 kg [Wells, 2001]. This is already larger than the threshold mass figure established for the STP system. (3) will be explored further. The author assumes a baseline microsatellite power budget of 50 W at a specific power of 25 W/kg [Wertz, 1992]. This represents the least efficiency (and likely lowest cost) available to small satellite builders today. To generate sufficient steady-state power for the UK T5 ion engine, the array size must increase substantially—accommodating a power output of 1 kW or greater. The additional 950 W is produced by an advanced photovoltaic system (100 W/kg), which reduces available payload weight by 9.5 kg.

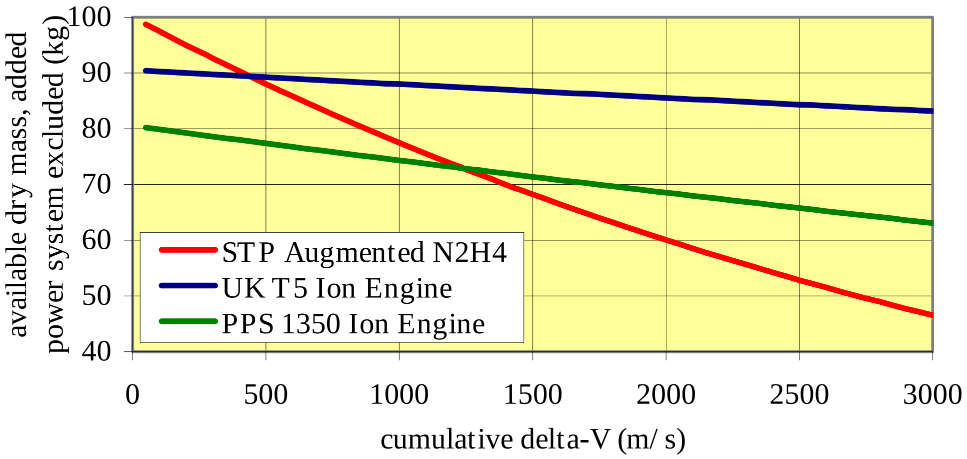

Figure B.8. STP augmented N_2H_4 versus two state-of-the-art ion engines, Snecma's PPS 1350 (I_{sp} ~ 1,600 s.) and the UK T5 (I_{sp} ~ 4,000 m/s). The additional power system mass required to support the electric propulsion systems has been subtracted from the burnout mass.

A similar trade can be performed for the PPS 1350, a 1,350 W system Hall effect thruster that would require a solar power production capability of 2 kW. The additional power system would

---

35,717 km GTO, a single-impulse or multiple near-impulse escape requires an even smaller velocity increment of 778 m/s—roughly 0.10 v_o. More generally, escaping from an elliptical orbit will require $[2^{½} - (1 + e)^{½}]\, v_o$, where e is the elliptical orbit's eccentricity; the ratio of spiral to impulsive escape is therefore $[2^{½} - (1 + e)^{½}]^{-1}$. For GTO, $e = .7244$. Therefore, delta-V_{spiral} (350 km circular to escape) = 10.1 × delta-$V_{impulsive}$ (GTO-to-escape). This large difference in required delta-V is not accounted for in Fig. B.7.

mass on the order of 20 kg. Figure B.8 shows the effect of excluding this power system penalty mass from the dry mass available to EP-assisted spacecraft at the end of the mission.

The results are now much less clear-cut. With its 20 kg of additional power system mass, the PPS 1350 is oversized for a 100-kg mission, and thus—at these low delta-V requirements—appears to be a relatively poor performer. On larger satellites (i.e., ESA's SMART-1), or with significantly larger delta-V budgets, this mass penalty would be less of a concern. For small velocity changes (< 400 m/s), the STP engine actually outperforms the lightweight T5; if the STP engine can be built within its objective budget (10 kg), this regime would be extended to 1,000 m/s or beyond. Orbit transfer strategy considerations—which would favour the STP system—have been neglected for now.

This assessment has been made entirely on a mass basis, and ignores the value of (1) arriving in mission orbit in as short a period of time as is possible (transfer time), and (2) the added cost of developing, fabricating, and testing a 100 W/kg solar power system to support EP (system cost). These factors would, if weighted heavily, tend to favour the STP system. The small satellite regime tends to favour compact, low-cost solutions over high-performance systems, which tend to scale poorly at these sizes. This permits relatively low-performance propulsion systems (e.g., butane, N_2O, H_2O_2, hybrid liquid/solid) to rate as highly competitive.

To be effective in the 100-kg and smaller satellite class, a solar thermal propulsion system must incorporate the advantages of low-performance chemical systems (high density-I_{sp}, low fabrication costs) while preserving moderate specific impulses (greater than bipropellant hydrazine/N_2O_4). Lack of any requirement for additional power—over and above what is required by the spacecraft—permits the STP engine to compete with (and potentially beat) proposed small satellite electric propulsion systems.[247]

Transfer Time

Mission Class	**Threshold**	**Objective**
GTO-to-GEO	**100 days**	**10 days**
Lunar Capture	**100 days/240 days**[a]	**10 days/120 days**[a]
Near Escape	**100 days/390 days**[b]	**10 days/195 days**[b]
Small Microsatellite Orbit Raising	**5.5 days**	**3 days**

[a] These values (e.g., 100 days/240 days) represent, respectively, required time to translunar injection and required time to final encounter.

[b] These values (e.g., 100 days/390 days) represent, respectively, required time to earth escape and required time to final encounter.

---

[247] For low delta-V requirements—up to approximately 3,000 m/s.

High thrust-to-weight ratio chemical propulsion systems can reach geosynchronous altitudes from LEO in roughly 5 hours.[248] A microsatellite with onboard electric propulsion—for instance, the UK T5 ion engine—requires a substantially longer period of time to achieve GEO, owing to its low thrust-to-weight (2.55×10^{-5}). If we assume a delta-V of roughly 6,000 m/s [Schleinitz, 1987], a 100-kg microsatellite equipped with the T5 will require almost 260 days (over 8 months) to reach GEO.[249] Likewise, the author has elsewhere noted that ESA's SMART-1 spacecraft, scheduled for launch in late 2002, will require 15-17 months to achieve lunar orbit from GTO. SMART-1 uses Snecma's PPS-1350 Hall thrusters.

A key advantage of solar thermal propulsion is its moderate thrust-to-weight capability. This permits faster transfer times than electric propulsion but at higher performance (i.e., I_{sp}) levels than chemical propulsion. Solar thermal engines take advantage of relatively high thrust-to-weight ratios ($\sim 10^{-3}$) to perform near-impulsive manoeuvres—permitting low propellant usage while achieving transfer times substantially smaller than electric propulsion.

Detailed mission analysis (Section 2) demonstrates that a 500 mN STP engine can reach GEO from GTO in 35 days. A slightly higher-thrust system (3 N) should achieve lunar orbit from GTO in 178 days (6 months). This is substantially faster than SMART-1.

Principal factors driving the selection of a threshold transfer time include loss of mission functionality or a decrease in mission lifetime as a result of "loitering" in transfer orbits. GTO, the initial orbit for each of the mission cases analysed in Section 2, is a relatively high-risk orbit. A low-thrust orbit transfer strategy—either via thrusting at the apses or via spiral transfers—exposes satellite systems to substantially more radiation (due to significant, repeated radiation doses imparted by the belts at 1.3 and 5 R_E) than the standard high-thrust transfer. This dosage is likely to be the driving requirement for transfer time in the orbits of interest. A vehicle in GTO receives approximately 20 times the radiation dose of a satellite in an 850-km altitude polar orbit [Hansen, 2002]. Radiation-hardened ("rad-hard") electronics typically tolerate up to 10^5 rads.[250] Commercial, off-the-shelf (COTS) components are highly variable in radiation tolerance—Table B.2 illustrates some of their features versus rad-hard elements.

---

[248] A single-burn Hohmann transfer from a circular, 350 km altitude LEO to a 350 x 35,717 km geosynchronous transfer orbit has a half-period of 5 hrs., 16 min.

[249] Hill [1992] provides an impulsive delta-V figure for LEO-to-GEO transfer of 4,200 m/s. As thrust-to-weight tends to zero, a spiral transfer strategy's delta-V requirement tends toward $v_{LEO} - v_{GEO}$. For a 350 km circular starting orbit, $v_{LEO} - v_{GEO} = 4{,}619$ m/s, not all that much greater than the impulsive (two-burn) requirement. Schleinitz' simulation of such a transfer resulted in a value of 11,916 m/s for LEO-GEO and return, and presumably includes losses associated with non-ideal firing. Half of this value (5,958 m/s) is required to raise the orbit from LEO to GEO. This velocity change can be achieved at a (constant) average acceleration of .00027 m/s^2 in 256 days.

[250] From Dowd [2001]. 1 rad ("radiation absorbed dose") = .01 J/kg. The 2-year total dose in GTO—primarily due to electron fluence—is approximately 10^8 rads, or 4.17×10^6 rads/month [Hansen, 2002].

Characteristics	COTS	Rad Hard
Total Dose	**$10^3 - 10^4$ rads**	**$10^5 - 10^6$ rads**
Dose Rate Upset	**$10^6 - 10^8$ rads (Si)/sec.**	**$> 10^9$ rads (Si)/sec.**
Dose Rate Induced Latchup	**$10^7 - 10^9$ rads (Si)/sec.**	**$> 10^{12}$ rads (Si)/sec.**
Neutrons	**$10^{11} - 10^{13}$ n/cm^2**	**$10^{14} - 10^{15}$ n/cm^2**
Single Event Upset (SEU)	**$10^{-3} - 10^{-7}$ errors/bit-day**	**$10^{-3} - 10^{-7}$ errors/bit-day**
Single Event Latchup/Single Event Burnout (SEL/SEB)	**< 20 MeV-cm^2/mg (linear energy transfer)**	**37-80 MeV-cm^2/mg (linear energy transfer)**

Table B.2. Radiation tolerance of commercially available and radiation-hardened electronics for space applications [Hansen, 2002].

Unprotected, "soft" electronics in GTO will experience single-day doses in excess of their total dose constraints—more than 100 Krads. The use of unshielded COTS elements in microsatellite systems would require limiting stationing in GTO (on the order of hours)—impossible to meet with low-thrust orbit transfer systems. A combination of spot shielding and rad-hard components would permit longer on-station time in high-radiation transfer orbits. A total dose limit of 10^6 rad—near the top of rad-hard component tolerances without additional shielding—would translate to 10 days in GTO. This is a reasonable transfer time objective (GTO-to-GEO).

Aluminum spot-shielding of 1-mm thickness reduces the total dose by more than a factor of ten [Hansen, 2002]. Critical electronics can be shielded to this level, permitting transfer times of 100 days or longer at the expense of some added weight. The 100-day figure is selected as a threshold requirement for GTO-to-GEO orbit transfer.

Near-Escape and Lunar Capture missions, like the GTO-to-GEO mission, begin in highly elliptical, low-inclination earth orbits and are susceptible to equivalent radiation dose rates during their outbound transfer phase. Therefore, similar constraints (10 and 100 days, respectively) can be selected for the initial portions of these missions.

Selecting a transfer time requirement for the post-escape portion of these missions is more subjective, and substantially more mission dependent. As very long transfers may account for a substantial portion of the entire mission life, failures of key subsystems may occur before the spacecraft reaches its final orbit (or encounter phase, for near-escape missions), rendering the spacecraft useless. The author chooses to target lunar and NEO missions currently under consideration or construction—ESA's SMART-1 and QinetiQ's SIMONE—and perform them in 50% of the time or less. Therefore, the lunar capture mission threshold transfer time requirement is selected to be 8 months. The objective requirement is half of the threshold figure, or 4 months.

The Near Escape mission threshold requirement is selected to be 13 months, one-half the estimated mission duration for SIMONE's excursion to the near-earth asteroid 4660 Nereus. The objective requirement is chosen, as above, to be half of this figure, or 195 days.[251]

The small microsatellite mission is not constrained by high radiation dose—circular orbits below 1,000 km have relatively low dose rates. Furthermore, the source requirements for this mission, taken from AFRL's STP Propulsion Module need statement for Space Shuttle secondary payloads, does not ask offerors to observe any limitations on transfer time from initial orbit (352 km) to final orbit (704 km). The author is therefore free to assign threshold and objective requirements—and selects 5.5 days (threshold) and 3 days (objective), respectively.[252] The threshold value is one-half the duration of current[253] Space Shuttle missions—potentially permitting retrieval of a host satellite in the event of failure. [KSC Online, 2002] Of course, this presumes that payload ejection occurs at the beginning of the Shuttle mission. Safety concerns may prohibit early ejection.

Thrust

Mission Class	**Threshold**	**Objective**
GTO-to-GEO	**150 mN**	**1.45 N**
Lunar Capture	**5.2 N**	**22 N**
Near Escape	**5.2 N**	**22 N**
Small Microsatellite Orbit Raising	**1 N**	**6 N**

Specification of STP engine volume, mass, and transfer time permit the derivation of additional requirements, shown above.

High-thrust chemical engines (e.g., Thiokol's STAR-37 solid motor [SpaceandTech.com 2, 2001]) provide kilonewtons or greater thrust. Electric propulsion systems, as discussed previously, provide thrust levels orders of magnitude smaller—typically on the order of millinewtons. The common two-burn Hohmann transfer, which represents the minimum energy for movement between two orbits, and which is readily adapted to high-thrust systems, must be modified in order to accommodate the much smaller delta-V increments imparted by low thrust systems. Two basic orbit transfer strategies—sequential apogee and perigee boosting, and constant firing or spiral transfer—are available to the low-thrust engine designer.

---

[251] Note that this is not a requirement for reaching 4660 Nereus, but a more generic requirement—the solar thermal engine must permit its host spacecraft to reach a near earth encounter in less than 390 days (threshold) or 185 days (objective). This may require judicious selection of the target object (closer approaches being preferable) and a rendezvous strategy different from that proposed by SIMONE's engineers—specifically, a flyby rather than a rendezvous (q.v., Chapter 2).

[252] To calibrate expectations, the author has performed an ideal simulation of this mission, applying basic astrodynamic relationships in Microsoft Excel. Total mission delta-V = 194 m/s. Number of burns = 14. Thrust = 3 N. Specific impulse = 400 s. Burn time (per burn) = 920 s. If the STP system were capable of firing once per orbit (whether this is the case will be highly dependent upon the choice of engine size and mode), this mission would require as little as 22 hours to perform. Low-altitude circular orbits will constrain the STP system's performance, due to long per-orbit eclipses.

[253] E.g., STS-109, a Space Shuttle *Columbia* flight, intended for Hubble Space Telescope servicing, slated for launch in February 2002. Mission duration = 11 days. [KSC Online, 2002]

Apogee and perigee boosting over multiple orbits allows the engine designer to approximate an impulsive (Hohmann) transfer. The host spacecraft is constrained to fire only near the apses of the orbit and the duration of the firing is limited by the impulsive requirement—as the spacecraft moves away from orbital perigee or apogee, delta-V penalties accrue rapidly. This occurs whenever the spacecraft velocity vector and the local gravity vector are not orthogonal—thrusting along the velocity vector then entails a certain amount of gravity *loss*. This penalty can be held to arbitrarily small levels [Robbins, 1966]. For long-period earth orbits (e.g., GTO), wait time between firings will be 10½ hours. For escape missions, this wait time will at first increase gradually as the orbit becomes increasingly eccentric.[254] As the spacecraft approaches escape, this wait time will become quite lengthy –Table B.5 illustrates a 195-hour escape mission, of which over 100 hours is spent waiting in the fifth and final orbit. Similarly, a GTO-to-GEO mission will see wait times rise from 10½ to 24 hours.

Mission	Ideal Hohmann Transfer from GTO, no plane changes	Ideal Spiral Transfer from LEO, no plane changes
Initial Orbit-to-GEO	**1,461 m/s**	**4,619 m/s**
Initial Orbit-to-Escape	**778 m/s**	**7,695 m/s**

Table B.3. Idealized delta-V requirements for GEO and Escape missions.

Spiral transfer missions accept delta-V penalties associated with non-impulsive thrusting—normally due to the very high specific impulse of the thruster, which more than offsets the penalty [Hill, 1992]. Spiral transfers from circular orbits to escape have delta-V requirements approaching 2.414 times[255] that of comparable impulsive (or a sequence of near-impulsive) transfers from the same circular orbit [Sandorff, 1960]. Unfortunately, a direct comparison between systems using spiral and multiple near-impulsive boosting is not possible: Spiral transfer systems cannot normally use elliptical starting orbits, which are highly favourable for systems using near-impulsive boosting. The figures shown in Table 3 can be calculated from the following identity:

---

[254] Sequential apogee boosting from an initial GTO to a 350 x 206,000 km orbit—ideally requiring 600 m/s of velocity change at perigee—can require a month or longer at thrust levels of 3,000 mN. The final orbit has a period of 100 hrs. (4 days).

[255] At thrust-to-weight ratios of $\leq 10^{-5}$ [Sandorff, 1960].

$$\frac{\Delta v_{Spiral,Circular-Circular}}{\Delta v_{Impulsive,Elliptical-Circular}} = \frac{\left(1-\sqrt{\frac{r_0}{r_1}}\right)}{\left(1-\sqrt{1-e}\right)\left(\sqrt{\frac{r_o}{r_1}}\right)}.$$

The values r_0 and r_1 are the radii of the initial and final orbits. The radius r_0 also corresponds to the perigee radius of the initial elliptical orbit for multiple-kick systems. The eccentricity of this elliptical orbit is denoted by e. Note that the value of the radical $[(r_0/r_1)^{½}]$, which appears in both numerator and denominator, is approximately 0.40 for the orbits of interest: r_0 = 6,728 km and r_1 = 42,095 km. The delta-V ratio for these values (spiral/impulsive) is 3.16. A similar identity can be found for spiral and impulsive manoeuvres to earth escape (see Chapter 3).

Transfer time constraints for GTO-to-GEO and GTO-to-Escape can be translated directly into thrust level requirements for 100-kg and 20-kg microsatellites. Delta-V requirements for GEO and earth escape (ignoring inclination changes and perturbations such as lunar influence) are:

An approximate spiral transfer thrust requirement is relatively straightforward to obtain for an initial circular orbit. Given the delta-V figures above, an average acceleration can be calculated, assuming 10- and 100-day transfer time constraints for LEO-to-GEO missions. For a 10-day transfer, a 100-kg spacecraft will have to achieve an average acceleration of 5.35×10^{-3} m/s^2 (and an average thrust of 535 mN). This is somewhat conservative, as it does not account for propellant consumption during the transfer.[256] For a 100-day transfer, average acceleration (and average thrust) is an order of magnitude smaller (54 mN). LEO-to-escape requires thrust levels on the order of 890 mN (10 days to escape) and 89 mN (100 days to escape). A GTO-to-GEO or GTO-to-Escape, utilizing spiral (or, more accurately, long-arc “near-spiral”) transfers, has not been considered.

In order to assess thrust requirements for apogee and perigee thrusting strategies, the author will select firing time constraints to minimize delta-V penalties. At GTO apogee, a spacecraft’s angular rate of motion ($d\theta/dt$) is approximately .002°/s. This can be calculated from:

$$\frac{d\theta}{dt} = \frac{h}{r^2}$$

---

[256] At an Isp of 400 s., a 100-kg “wet” spacecraft in GTO deposits 59.6 of burnout mass in GEO. Average spacecraft mass = 79.7 kg. Therefore, the thrust requirement is actually somewhat lower than the conservative figure stated above.

Where *h* represents orbital angular momentum and *r* is the instantaneous orbital radius. [Battin, 1987] This angular rate is approximately one-half that of a spacecraft in GEO, but varies significantly over the course of the orbit.[257]

Using Robbins' analysis of near-impulsive manoeuvres [1966], and using the (constant) GEO angular rate as a conservative measure, we may obtain a burn time limitation for a pre-specified finite burn delta-V penalty.[258] This value is 6,710 sec. (1 hr., 52 min.) for a 1% penalty. The author selected a 5,000 sec. burn time for the following analysis.

Delta-V imparted (m/s)	S/C mass (start of burn)	S/C mass (end of burn)	Apogee velocity (m/s)	Semi-major axis (km)	Perigee altitude (km)	Period at end of burn (hrs.)	Time since end of burn 1 (hrs.)	Cumulative delta-V (m/s)
73.18	100 kg	98.15 kg	1688.1053	24778.54	1084.07482	10.79	0	73.18
74.57	98.15	96.30	1762.674	25181.61	1890.22769	11.05	10.79	147.75
76.01	96.30	94.45	1838.6887	25625.09	2777.17493	11.34	21.84	223.76
77.52	94.45	92.60	1916.2066	26114.07	3755.14176	11.67	33.18	301.28
79.08	92.60	90.75	1995.2883	26654.6	4836.20254	12.03	44.85	380.36
80.71	90.75	88.90	2075.9983	27253.86	6034.71746	12.44	56.88	461.07
82.41	88.90	87.05	2158.405	27920.45	7367.89918	12.90	69.33	543.48
84.18	87.05	85.20	2242.5812	28664.78	8856.55685	13.42	82.23	627.65
86.02	85.20	83.35	2328.6047	29499.54	10526.086	14.01	95.65	713.68
87.95	83.35	81.51	2416.5582	30440.4	12407.8046	14.69	109.66	801.63
89.97	81.51	79.66	2506.5305	31506.89	14540.7848	15.47	124.35	891.6
92.09	79.66	77.81	2598.6164	32723.7	16974.4095	16.37	139.81	983.69
94.30	77.81	75.96	2692.9175	34122.51	19772.0132	17.43	156.18	1078
96.63	75.96	74.11	2789.5431	35744.59	23016.1807	18.69	173.61	1174.6
99.07	74.11	72.26	2888.6106	37644.83	26816.6616	20.20	192.30	1273.7
101.64	72.26	70.41	2990.2468	39897.77	31322.5386	22.04	212.50	1375.3
104.34	70.41	68.56	3094.5882	42607.29	36741.5807	24.32	234.54	1479.7

Table B.4. 17-burn, 235-hour GTO-to-GEO transfer, ideally applied velocity increments (no delta-V losses, no inclination change). Burn time (5,000 sec.) is based on the assumption of a 1% finite burn delta-V penalty, ~15 m/s. This firing strategy meets the 10-day transfer time requirement with margin.

Table B.4 illustrates a 17-burn transfer from GTO to GEO. At a thrust level of 1.45 N, and an average specific impulse of 400 s, this series of manoeuvres can be accomplished just under ten days, using 32 kg of hydrazine or ammonia propellant. Note that this thrust level (1.45 N) is approximately three times the spiral transfer thrust requirement. A 100-day mission requires 164 firings at a thrust level of 150 mN.

---

[257] Satellites in Molniya orbits take advantage of this relatively low angular rate near apogee. Such spacecraft "hang" overhead for up to 8 hours out of a 12-hour orbit, especially useful for communications to high-latitude locations. [Wertz, 1992] The angular rate of motion of a spacecraft in GEO is .0042°/sec.—obviously, not apparent to the earth-based viewer.

[258] Robbins provides an identity for relating burn time (τ_b) in a circular orbit to acceptable delta-V penalty (as a fraction of the total delta-V imparted during the manoeuvre). For values of the product $(d\theta/d\tau)\tau_b < 1$, Robbins' approximation holds. A 5,000-sec. burn in GTO gives a figure of 0.19, well below 1.

Table B.5 shows a similar set of calculations for an earth escape mission. Here, burn time constraints are significantly greater, as thrusting must occur at orbital perigee. Angular rate of motion at GTO perigee (350 km) is approximately .164°/s.[259] For a 1% delta-V penalty per burn, burn time must be limited to just 171 s—this will drive thrust levels into the hundreds of newtons to achieve 10-day transfer times. Allowing for a 10% penalty raises the burn time limitation to approximately 540 s.

Delta-V imparted (m/s)	S/C mass (start of burn)	S/C mass (end of burn)	Perigee velocity (m/s)	Semi-major axis (km)	Perigee altitude (km)	Period at end of burn (hrs.)	Time since end of burn 1 (hrs.)	Cumulative delta-V (m/s)
29.61	100	99.25	10133.72	25342.21	37578.4	11.15633	0	29.61
138.43	99.25	95.80	10272.14	30894.17	48682.3	15.01652	11.156	168.04
143.49	95.80	92.36	10415.63	40134.61	67163.2	22.23479	26.173	311.53
148.94	92.36	88.92	10564.58	58578.10	104050	39.20645	48.408	460.47
154.83	88.92	85.47	10719.41	113657.32	214209	105.9621	87.614	615.3
161.19	85.47	82.03	10880.6	--	--	--	193.58	776.5

Table B.5. 6-burn, 194-hour GTO-to-Escape transfer, ideal applied velocity increments (no losses, no inclination change). Burn time is based on a 10% finite burn delta-V penalty, ~78 m/s.

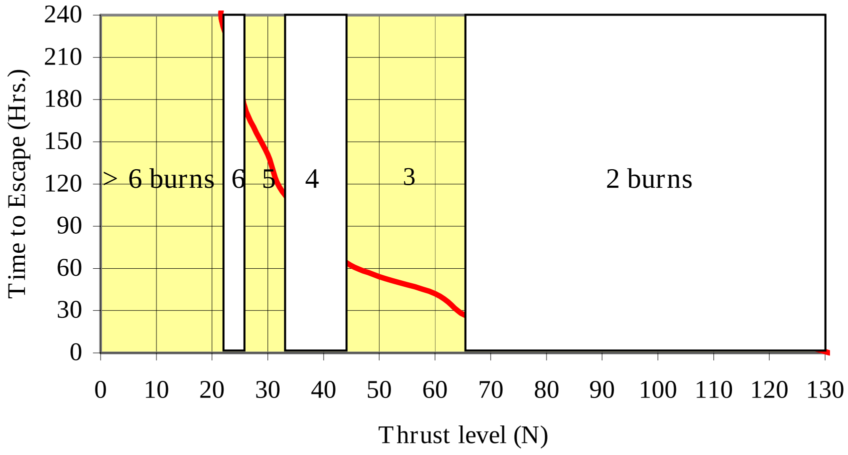

Figure B.9. Time to escape versus engine thrust level, for successive apogee boosts (at perigee). For the stated burn time limit (540 s), delta-V penalty is as stated in Table B.5.

The six-burn transfer strategy in Table B.5 requires a 25 N thrust level, one burn of 118 sec. duration, and five successive burns of 540 s each. This transfer can be accomplished in 194 hours (8 days). A given thrust level dictates the number of discrete firings that must be performed; to achieve a 10-day transfer, the threshold thrust is ~ 22 N. This can be seen in Figure B.9.[260]

---

[259] This is 3 times higher than the circular orbit angular rate at 350 km—.066 deg./sec.

[260] Also note that a single-impulse transfer to escape requires a thrust of 131 N or greater.

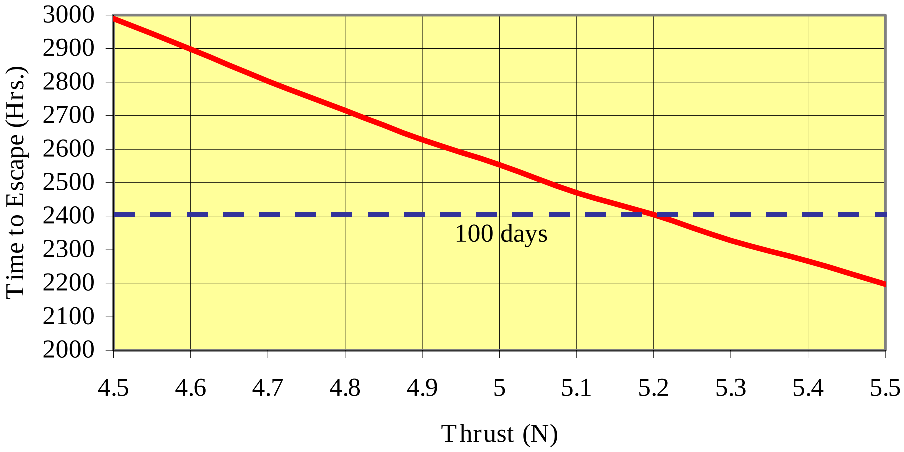

Figure B.10. Time to escape versus engine thrust level, for successive apogee boosts (at perigee), 540-sec. burn time limit. At 4.5 N, 29 burns are required. At 5.5 N, only 24 burns are needed. See Table B.5 for delta-V penalty information.

A 100-day transfer will require a thrust level of greater than 5.2 N (Figure B.10) and 24 firings. Note that the thrust indicated is on the order of six times that of the spiral transfer requirement, for the same transfer time.

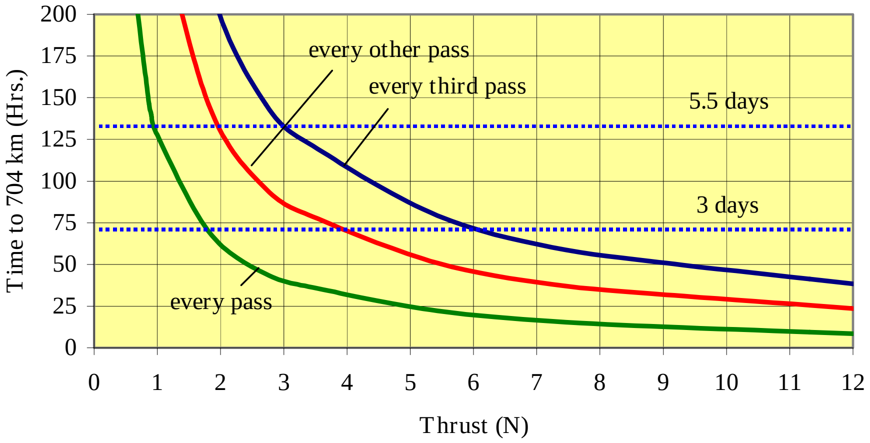

Figure B.11. Time to perform an orbit-raise and circularisation (352 – 704 km circular) vs. thrust level, for successive apogee and perigee boosts, 428-sec. burn time limit (1% delta-V penalty). Three orbit transfer strategies are shown.

Based on the foregoing analysis, the author selects a threshold thrust requirement for GTO-to-GEO transfer missions of 150 mN, based on a 100-day transfer time limit. For an objective of 10 days, a thrust level of 1.45 N is selected. Missions that depart earth orbit (lunar capture and near-escape) will be required to produce 5.2 N (threshold) and 22 N (objective), respectively.

The final mission of interest involves small microsatellite orbit-raising from 352 to 704 km. Threshold transfer time requirements dictate required thrust levels, as before. The spiral transfer value is, as has been shown in the previous analysis, likely to be an order of magnitude below the value obtained for impulsive firings at the apses. Figure B.11 illustrates breakpoints for this second firing strategy, assuming the STP engine is capable of firing (1) on every pass, (2) on every other pass, and (3) on every third pass.[261]

For a circular low earth orbit (352 km), the angular rate of motion is only .066 deg./sec. For a 1% allowable delta-V penalty, burn times must be constrained to 428 sec. Threshold and objective thrust levels can be determined from the above figure:

(1) 3-day (72-hour) transfer: *1.75 N* (firing on each pass)
4 N (firing on every other pass)
6 N (firing on every third pass)
(2) 5.5-day (132-hour) transfer: *1 N* (firing on each pass)
2 N (firing on every other pass)
3 N (firing on every third pass)

The values in bold indicate the selected threshold and objective values. A 6-N thrust level will be capable of achieving the objective transfer time of 3 days—even if it can only be fired on every third pass. A level of 1 N will require thrusting on each pass, and will just meet the threshold time requirement.

Specific Impulse *350 s.* threshold / *400 s.* objective

Determination of an appropriate specific impulse target relies on previously accepted goals—namely, providing greater performance than monopropellant hydrazine and bipropellant hydrazine/N_2O_4 systems, for delta-V figures of interest, and competing head-to-head with electric propulsion systems in this same regime.

The author will expand upon the system-to-system comparison performed earlier in this, in order to encompass a range of potential I_{sp} targets for the solar thermal engine. The graphs in Figure B.14 indicate performance of the STP-augmented hydrazine system versus a monopropellant hydrazine thruster (I_{sp} = 230 sec.). At an objective mass of 10 kg, a 300-sec. system breaks even with monopropellant hydrazine in the 2,500 m/s delta-V regime. Most missions of interest fall below this figure (1,500-2,500 m/s)—thus, there is little or no trade space for system mass at this low specific impulse. At 350 sec., a threshold breakeven (15 kg.) occurs at roughly 2,000 m/s, an objective breakeven (10 kg.) at 1,000 m/s. This roughly brackets the missions of interest, although lunar capture and insertion into a high-altitude phasing orbit (Section 2, q.v.) fall above this regime.

---

[261] This will be dictated by engine mode and sizing considerations. Direct-gain systems will be capable of firing on every orbit. Thermal storage systems—depending on their size—may have to wait additional orbits before firing.

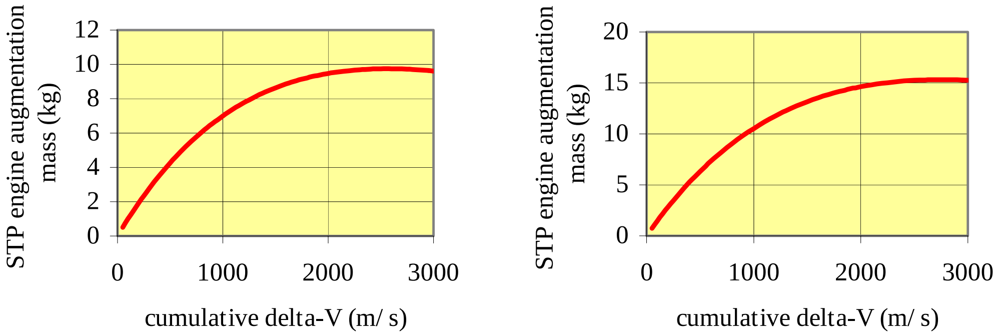

Figure B.12. STP engine augmentation mass limit for a specific impulse of 300 s (left). STP engine augmentation mass limit for a specific impulse of 350 s (right).

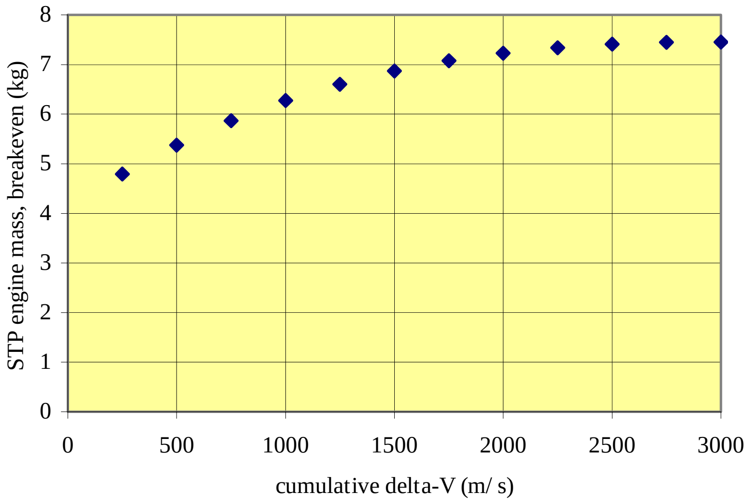

Figure B.13. STP engine mass constraint for breakeven with ARC LEROS 1B bipropellant hydrazine/N_2O_4 thruster. A 10-kg, 350 s engine cannot outperform the bipropellant combination for the delta-V regime under investigation. Breakeven occurs for a 7-kg engine—the smallest objective engine under consideration—at 1,750 m/s.

A comparison of a 350-sec. STP engine with bipropellant hydrazine/N_2O_4 reveals little room for tradeoffs. At 10 kg., the objective microsatellite engine is too large; it cannot beat the bipropellant engine at any delta-V. A system built to the small microsatellite objective mass requirement (7 kg.) can meet N_2H_4/N_2O_4's performance but not beat it. (Fig. B.13).

Fig. B.14 shows that decreased STP engine performance results in a smaller regime in which STP outperforms electric propulsion alternatives on a strict delta-V basis. Previously, at 400 sec., the

STP engine provided for more dry mass than the PPS 1350 above approximately 1,250 m/s. In this instance, the PPS 1350 breaks even with STP at roughly 1,000 m/s. Further, the UK T5 expands its predominance to lower delta-Vs—above 300 m/s.[262]

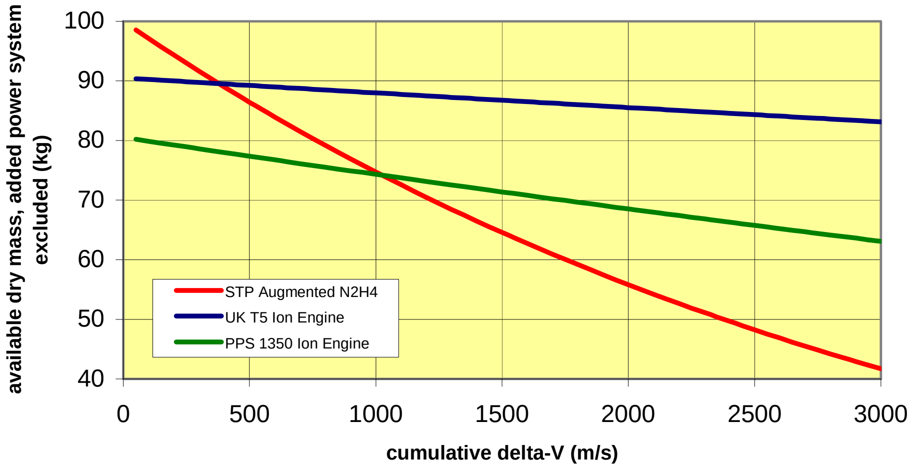

Figure B.14. STP augmented N_2H_4 (350 s I_{sp}) versus two state-of-the-art ion engines, Snecma's PPS 1350 (I_{sp} ~ 1600 s.) and the UK T5 (I_{sp} ~ 4000 m/s). This chart subtracts the weight of the ion engines' augmented power systems from the available dry mass on the spacecraft.

The author concludes that 350 sec. represents a lower bound for STP engine performance. An objective value of 400 sec., corresponding to the performance of decomposed N_2H_4 at 2,500 K, is desirable.[263]

Density I_{sp} *330 g-s/cm³* **threshold** / *400 g-s/cm³* **objective**

The product (ρ x I_{sp}),[264] known as density I_{sp} or DI_{sp}, is of fundamental importance to the small satellite propulsion system designer. Mass and volumetric constraints impair the designer's ability to place bulky propellant tanks, feed lines, and other items. As discussed earlier in this Appendix, SSTL's enhanced microsatellites provide for a small useable region surrounding the main satellite electronics "stack" of electronics. This region sets system volume threshold and objective requirements (.09 and .045 m^3, respectively). Table B.6 provides specific impulse, density, DI_{sp}, and delta-V capability for a variety of propellant choices.

---

[262] The author stresses that this chart, like the previous one (Figure B.10), does not take into account the substantial difference in required delta-V between the electric systems (which require spiral transfers) and an STP system (which, nominally, would use a series of near-impulsive firings to simulate a Hohmann or minimum-energy transfer).

[263] Higher specific impulses, if achievable, will improve performance substantially. If a microsatellite-based STP system could achieve propellant temperatures of 3,000 K (near material limits), specific impulses of nearly 500 sec. could be obtained.

[264] ρ is here expressed in units of g/cm^3.

Total impulse (I) is calculated from:

$$I = M_p u_e$$

I is the product of the volume-constrained propellant mass (M_p) and exhaust velocity (u_e). This is a useful figure of merit, as it is independent of host spacecraft specifics, unlike delta-V (which is dependent on spacecraft mass, or, more correctly, burnout mass fraction—the ratio of post-burn to pre-burn spacecraft mass). The chart above indicates that an STP engine, using N_2H_4 propellant and operating at its objective I_{sp} requirement of ~400 s, outperforms all other combinations save the Xenon ion thruster.[265]

Propellant Type	Density (g/cm^3)	I_{sp} (s.)	DI_{sp} ($g\text{-}s/cm^3$)	Total Impulse (kN-s)	Delta-V (m/s), volume-constrained (.045 m^3)	Delta-V (m/s), mass-constrained (50 kg.)
Xe (3000 psi)[a]	2.00	1600	3200	1,410	36,104	10,868
Xe (882 psi)[b]	1.10	1600	1760	776	10,712	10,868
STP H_2[c]	0.071	917	65	29	292	6,229
STP-augmented N_2H_4[c]	1.0045	402	404	178	2,370	2,731
STP NH_3[c]	0.60	449	270	119	1,385	3,050
STP H_2O[c]	1.00	372	372	164	2,180	2,527
MMH/N_2O_4[d]	1.159	319	370	163	2,305	2,167
H_2O_2/Kerosene[d]	1.279	305	390	172	2,562	2,072
Hybrid H_2O_2/ Polyethylene[d]	1.297	300	389	175	2,577	2,038
N_2O	0.75	206	155	68	831	1,399
H_2O_2 (89%)	1.38	179	247	109	1,702	1,216

[a] 3,000 psi storage pressure [Polyflex, 1999], UK T5 I_{sp} [Wells, 2001]
[b] 882 psi storage pressure [Gibbon, 2002], UK T5 I_{sp}
[c] Heated to 2,500 K. C_p and γ values are at 1,500 K, ideal expansion to vacuum assumed
[d] Oxidizer/fuel ratio optimised for maximum I_{sp}

Table B.6. Density-I_{sp}, volume-constrained total impulse, and potential delta-V (aboard a 100-kg. spacecraft) available for a volume limit of .045 m^3 and—in the final column—a mass limit of 50 kg., for a representative variety of monopropellant and bipropellant combinations.

For a spacecraft mass of 100 kg, dense propellant combinations (H_2O_2 /kerosene and H_2O_2/polyethylene hybrid) are extremely competitive—unless mass limitations are imposed. The author has selected 50 kg as a propellant mass limit, based on discussions found in both Jason [2000] and Haag [2001]. The smaller of the two delta-V figures in Table B.6 represents maximum performance.[266] To ensure the system's competitiveness aboard microsatellites, STP engines should maintain high density-I_{sp}, on the order of 400 g-s/cm^3 or better. This will permit the STP system to perform most of the missions analysed in Section 2 within the objective volume constraints.

---

[265] The first Xenon figure is actually somewhat misleading, insofar as the high storage density (and resultant high DI_{sp}) allows for very high propellant mass fractions on a 100-kg satellite. In this instance (3000 psi storage pressure, 2 g/cm^3 density), the 100-kg satellite includes 90 kg of Xe. The remaining 10 kg is insufficient to hold the thruster hardware and tank—much less the 1 kW power system necessary to operate it, other key subsystems, or payloads. A lower (882 psi) storage pressure provides a more reasonable propellant mass fraction and delta-V capability—roughly equivalent to QinetiQ's proposed SIMONE mission (9.9 km/s). [Wells, 2001]

A threshold value of 330 g-s/cm^3 provides for the investigation of several propellant choices, and still permits volume-constrained delta-V figures of approximately 2,000 m/s.

Firing Duration

Mission Class	Threshold	Objective
GTO-to-GEO	**5,000 sec. (83 min., 20 sec.)**	**11,250 s. (187 min., 30 sec.)**
Lunar Capture	**540 s. (9 min.)**	**1,215 s. (20 min., 15 sec.)**
Near Escape	**540 s. (9 min.)**	**1,215 s. (20 min., 15 sec.)**
Small Microsatellite Orbit Raising	**428 sec. (7 min., 8 sec.)**	**963 s. (16 min., 3 sec.)**

This requirement is applicable to near-impulsive (non-spiral) transfers. Spiral transfer strategies will drive firing durations on the order of total mission durations (10-100 days).

The driving requirement for firing duration is confined to apogee firings during circularisation (GTO-to-GEO). At GTO apogee, long firings can be conducted owing to the spacecraft's low orbital velocity and resultant small delta-V penalties for finite burn manoeuvres. A threshold value of 5,000 sec. is selected, corresponding with the analysis in a previous section discussing required thrust levels. The objective is set at 2.25 times the threshold value to allow for full qualification testing with margin.[267] Values for other mission cases are likewise drawn from the thrust requirement analysis, and objectives set at 225% of the threshold value.

Number of Firings

Mission Class	Threshold	Objective
GTO-to-GEO	**17**	**39**
Lunar Capture	**26**	**59**
Near Escape	**26**	**59**
Small Microsatellite Orbit Raising	**40**	**90**

---

[266] This is captured in *red*. Note H_2's low performance for the applied volume constraint; were volume were not a limiting factor, this propellant would be twice as effective as all other combinations except electric propulsion utilizing Xenon.

[267] For recurring builds of the STP engine (non-proto qualification hardware), this would allow for a "makeup" burn of double the normal duration (with some additional losses) in the event of a missed manoeuvre opportunity.

As is the case for the previous requirement (firing duration), firing number is primarily applicable to non-spiral orbit transfer strategies. Spiral transfers will typically be composed of a single, long-period firing, although restart capability will be needed in the event of spacecraft or system failures.

The number of firings required for each mission class is fixed by the top-level threshold values for transfer time and engine thrust level. Objective values are, in the same way as firing duration, set at 225% of threshold, permitting qualification of a space engine prior to launch.

Thermal Charging Time

Mission Class	Threshold	Objective
GTO-to-GEO	**4 hrs.**	**2 hrs.**
Lunar Capture	**5 hrs.**	**2.5 hrs.**
Near Escape	**5 hrs.**	**2.5 hrs.**
Small Microsatellite Orbit Raising	**2 hrs.**	**40 min.**

This quantity, like the two previous, is of main interest for thermal storage systems, which require "on-sun" heating prior to firing. For missions with initial orbits in GTO, a useful threshold charging time is slightly less than half the orbital period (5 hrs.), as it allows for a pair of apogee and perigee boosts to be conducted in a single orbit. This is applicable to GTO-to-lunar orbit and GTO-to-escape, where stringent constraints at perigee limit the amount of thrusting time to just over 500 sec. For GTO-to-GEO, the charging time is significantly reduced as a result of long firings at orbital apogee (5,000-6,000 sec.). Circularisation missions will therefore require charging times on the order of 3.5-4 hours. Objective requirements are chosen to be 50% of the threshold value.

The small microsatellite mission's charging time is highly constrained by the nature of the initial low earth orbit. At 352 km altitude, slightly greater than half of the orbital period (45 min., 48 sec.) is spent in sunlight. To provide for thrusting outside of eclipse (i.e., in sunlight, reducing potential charging time but allowing greater mission flexibility), this figure is further reduced by the thrusting time (428 s. in this orbit). This sets an approximate objective of 40 minutes. Multiple orbits may be required to charge the thermal storage system to its target temperature. Previously, the author considered up to three orbits of charging prior to engine firing—this sets a threshold charging time of 120 minutes.

System Reliability *.95* **threshold /** *.99* **objective**

The missions under consideration require substantial delta-V increments and are therefore "propulsion-heavy." Mission success criteria will include, among other things, reaching the orbit of interest—GEO, lunar orbit, higher LEO, or a NEO encounter. The propulsion system is central to the conduct of the overall mission and high reliability is essential. For comparison, launch system reliabilities tend to cluster in the 90-95% regime.[268]

System Function

Startup NA[269]

The specifics of the solar thermal engine's startup sequence, and impact on spacecraft mission operations and/or testing, were not part of the scope of the present research, although startup will have to be addressed prior to a demonstration launch.

Restart *The system must be restartable.*

Restart is obviously required for the sequential apogee and/or perigee boosting strategy. The number of restarts is at least equal to n_f - 1, where n_f is the required number of firings to produce a needed velocity change. Restart is less important for the spiral transfer strategy, but is still clearly necessary in the event of inadvertent shutdown or spacecraft failures and safe holds.

Throttling NA

The solar thermal engine has no current throttling requirement.

Shutdown NA

Details of the solar thermal engine's shutdown sequence, and its impact on spacecraft mission and test operations, remains to be addressed.

Additional Guidance

These statements represent goals for the engineer to keep in mind in the initial design phase, but do not support numerical targets (e.g., system mass and volume limits, I_{sp}). These include manufacturability, testability, the use of proto-qualification/proto-flight hardware, operations, and safety.

Manufacturability and Ease of Procurement

Where possible, the solar thermal engine will be designed to incorporate commercially available components, avoiding the use of rare materials and propellants, items with highly specialized machining requirements, and custom-built hardware. Efforts will be focused on finding regional (i.e., EU or UK) vendors for critical items—thus reducing the amount of effort spent on meeting criteria for import and export control. This should tend to reduce overall cost and schedule requirements.

---

[268] Ariane's cumulative reliability—for all of its launch vehicles—is 0.943 (133 successes for 141 launch attempts), as of July 2001. [CNN, 2001] Atlas I/II (between 1990 and 2000) demonstrated a reliability of 0.95 (57 successes/60 attempts). [Astronautix.com, 2001] The Space Shuttle—a system driven by safety concerns in the wake of the 1986 *Challenger* disaster and further exacerbated by the loss of *Columbia* in 2003—presently stands at 0.982 (111 successes for 113 attempts). [KSC Online, 2001]

[269] Not Addressed.

Testability and Test Safety

The solar thermal engine must be designed with a specific qualification and/or acceptance-testing program in mind. This will require the creation of a detailed test plan early in the course of the development activity. The design should attempt, wherever possible, to simplify test operations and test apparatus design, and to minimize the overall extent of the testing program—performing only those tests that are necessary for assessing performance and flightworthiness.

Figure B.15. High-temperature coupon testing at MAST Carbon, Guildford, Surrey, 2003 (left). Sectioning of a brazed ceramic-to-metal seal, University of Manchester, 2003 (right).

A relatively simple propulsion test program—using “green” (i.e., non-toxic, non-flammable) propellants to simplify test procedures and increase test safety, eschewing purpose-built hardware in favour of existing test stands,[270] and constructing flight-like or flight-capable hardware wherever possible–is likely to result in a lower cost activity and a shorter schedule overall.

Proto-Qualification/Proto-Flight

The solar thermal propulsion system will—as far as possible—be designed and built as a proto-qualification/proto-flight unit (i.e., tested to qualification levels and subsequently used in on-orbit operations). This is intended to minimize the number of experimental iterations prior to flight and reduce development cost.

---

[270] with previously-tested processes and procedures.

Minimal Impact to Host Spacecraft Design, Test, and Integration

The solar thermal propulsion system must be designed in such a way as to minimize the impact of its addition to the host microsatellite. The Integrated Solar Upper Stage [Kennedy, 1995] was an attempt to provide two critical functions—propulsive thrust for orbit transfer and on-station electrical power production—with a single subsystem, minimizing propulsion and power hardware, and thereby increasing available payload mass to the satellite's owner. This approach, while deemed feasible, falls outside the present satellite design paradigm—which consists of decoupled subsystems with heavily managed interfaces—and will likely face hurdles in implementation.

Imposing significant requirements on the host satellite—stringent pointing, an added command and telemetry burden, substantial power augmentation, or severe structural modifications—could make a *prima facie* "useful" system worthless to the owner and/or operator. A principal goal of this activity will be to search for creative ways to limit these imposed requirements, simplifying the satellite designer's task.

Similarly, the solar thermal engine must be designed so as to minimize the burden on the spacecraft testing program. Stringent cleanliness requirements (e.g., the use of optical surfaces requiring Class 100[271] facilities) and structural incompatibilities (which could impact vibration testing and force spacecraft structural modifications) are examples of problem areas that should be addressed early in the preliminary design.

---

[271] Such "ultra-clean" facilities have less than 100 particles per cubic foot of air. [Wertz, 1992]

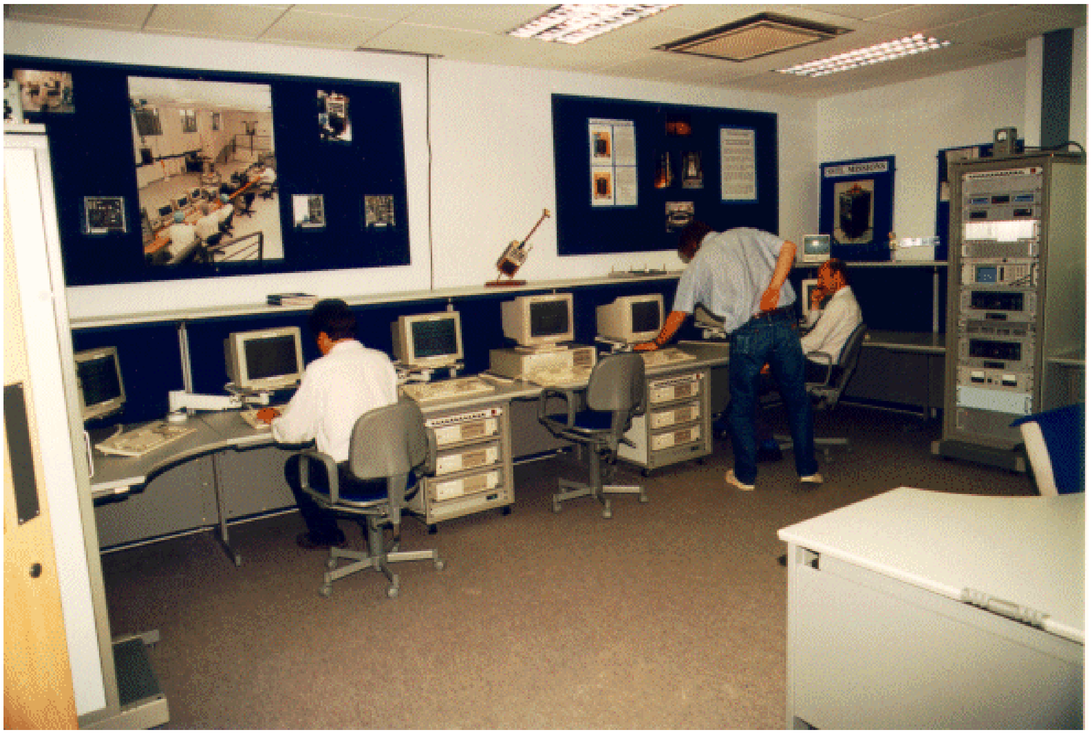

Figure B.15. Surrey Satellite Technology, Ltd., ground station, University of Surrey, Guildford, Surrey, United Kingdom [da Silva Curiel, 1996].

Minimal Impact to Mission Operations

The solar thermal engine will be designed and constructed so as to ensure compatibility with host spacecraft operational protocols. SSTL ground operations are "autonomous and self-checking," requiring the equivalent of 1 1/3 operators per day for 75 satellite passes [da Silva Curiel, 1996]. Figure B.18 depicts the SSTL ground station at the University of Surrey. It is important that an advanced propulsion system not compromise the existing operational paradigm by requiring significantly increased oversight at the satellite ground station, or additional insight and/or approvals from other entities (e.g., Air Force Satellite Control Network).

Externally Imposed Constraints

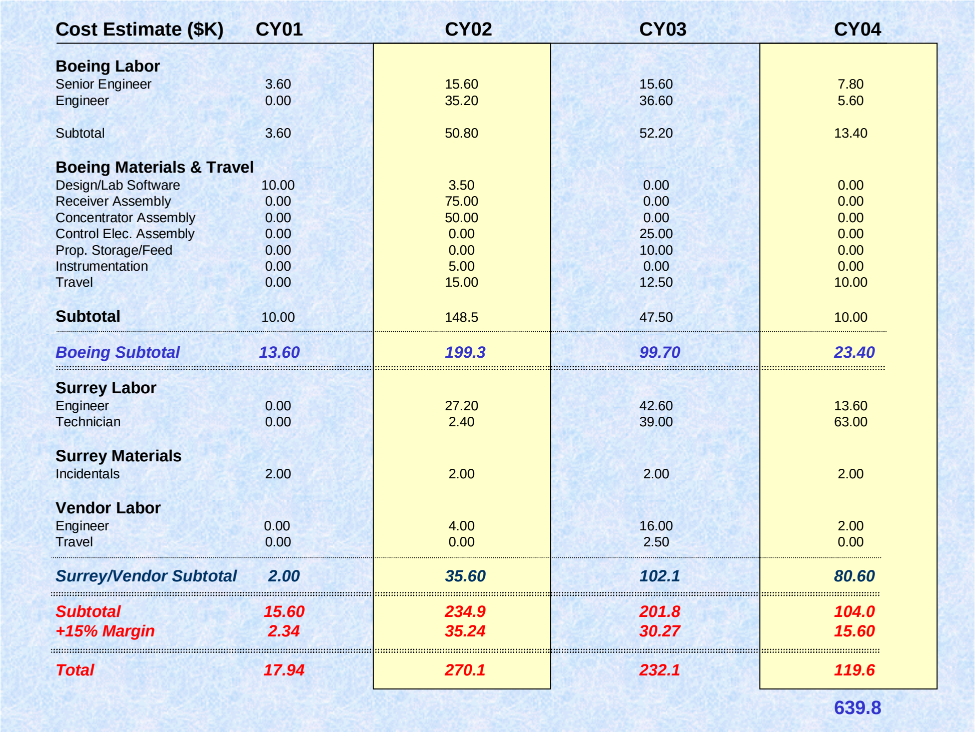

Cost Estimate ($K)	CY01	CY02	CY03	CY04
Boeing Labor				
Senior Engineer	3.60	15.60	15.60	7.80
Engineer	0.00	35.20	36.60	5.60
Subtotal	3.60	50.80	52.20	13.40
Boeing Materials & Travel				
Design/Lab Software	10.00	3.50	0.00	0.00
Receiver Assembly	0.00	75.00	0.00	0.00
Concentrator Assembly	0.00	50.00	0.00	0.00
Control Elec. Assembly	0.00	0.00	25.00	0.00
Prop. Storage/Feed	0.00	0.00	10.00	0.00
Instrumentation	0.00	5.00	0.00	0.00
Travel	0.00	15.00	12.50	10.00
Subtotal	10.00	148.5	47.50	10.00
Boeing Subtotal	***13.60***	***199.3***	***99.70***	***23.40***
Surrey Labor				
Engineer	0.00	27.20	42.60	13.60
Technician	0.00	2.40	39.00	63.00
Surrey Materials				
Incidentals	2.00	2.00	2.00	2.00
Vendor Labor				
Engineer	0.00	4.00	16.00	2.00
Travel	0.00	0.00	2.50	0.00
Surrey/Vendor Subtotal	***2.00***	***35.60***	***102.1***	***80.60***
Subtotal	***15.60***	***234.9***	***201.8***	***104.0***
+15% Margin	***2.34***	***35.24***	***30.27***	***15.60***
Total	***17.94***	***270.1***	***232.1***	***119.6***
				639.8

Figure B.16. Author's cost assessment—in dollars—of a three-year microsatellite-based solar thermal engine development program. Spacecraft integration is not included in the estimate. [Kennedy, 2001]

Development cost *(through spacecraft integration)*

£1M ($1.5M) to launch (microsatellite),

£250,000 ($375,000) to launch (small microsatellite)

These figures include design, component and system test, and integration costs with the host spacecraft. They represent between 1% and 4% of the estimated cost for a U.S. solar orbit transfer vehicle flight experiment. They are based on Boeing and Surrey proposal data and the author's original cost breakdown for the design, component hardware procurement and test, and integrated system test of a small satellite-compatible STE. Recurring costs have not been investigated.

Development schedule *3 yrs.* **to launch (microsatellite),**
2 yrs. **to launch (small microsatellite)**

These figures are based on schedules developed for a three-phase developmental activity, in the author's doctoral research proposal. SSTL has released data sheets that indicate an enhanced microsatellite can be available in as little as 15 months after contract award. The solar thermal engine will likely be the principal schedule driver. The author presumes that a small microsatellite development will operate on a compressed schedule.

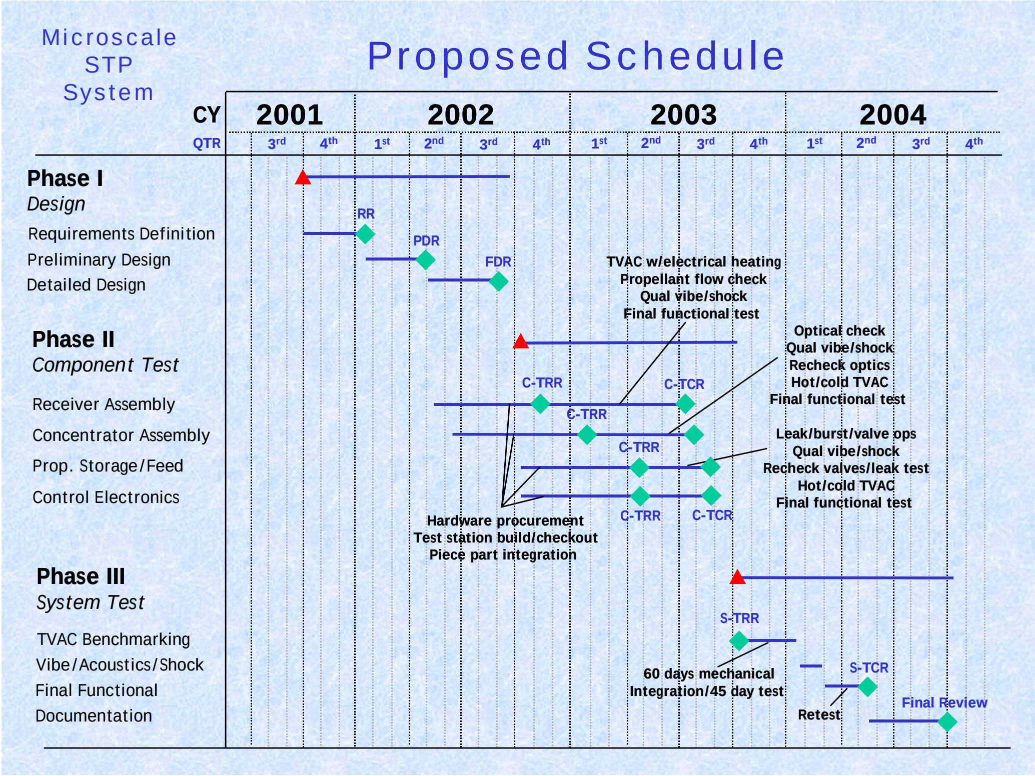

Figure B.20. Author's proposed schedule details for a three-year microsatellite-based solar thermal engine development program. Host spacecraft integration and test, as well as a microsatellite launch campaign, is not included [Kennedy, 2001].

Host Spacecraft Launch Environment

The solar thermal engine will be tested to required qualification levels prior to integration with a host spacecraft. This may include acoustic, sinusoidal, and random vibration tests. Likely values are shown in Table B.7. The Ariane 5 ASAP requires the highest small spacecraft natural frequencies (90 and 45 Hz, respectively) and produces sound pressure levels in excess of any other booster investigated. As the SSTL enhanced microsatellite is specifically designed for an ASAP launch, these figures represent excellent baseline values for preliminary design efforts.

Launch environment factors include payload and launch processing facility humidity, temperature, contamination and cleanliness level, thermal[272] and electromagnetic interference[273] constraints.

---

[272] Delta II's 9.5-ft. payload fairing rises to a maximum temperature of 500 °F (260 °C), 100 s. after launch. An acoustic blanket also serves as insulator—its internal wall temperature never exceeds 50 deg. C. [Boeing Company, 1996]

[273] Pegasus XL uses 7 separate RF transmitters or receivers, at UHF, C-, L-, and S-band for telemetry, tracking, command destruct, GPS navigation, and camera data downlink. [OSC, 2000] Delta II transmits on S- and C-bands for similar functions. [Boeing Company, 1996] Electromagnetic interference—from spacecraft to booster and vice versa—must be carefully avoided.

Payload user guides provide detailed guidance on these elements. These are not driving requirements for the solar thermal engine and specific values will not be assigned at this time.

	Pegasus XL	**Athena 1 (Mod 92)**	**Delta II 7920 (9.5' fairing)**	**Dnepr**	**Ariane 5 ASAP (microsat)**	**Space Shuttle**
Max. Acceleration **(axial)** **(lateral)**	**< 13 g** **< ± 6 g**	**< 4/-8 g** **< ±2.5g**	**< 6.8 g** **< ±2 g**	**< 7.5 g** **< 0.8 g**	**< 5.5/-7.5 g** **< ± 6 g**	**< 3.5 g** **< 3.4 g**
Spacecraft/ adapter natural frequencies **(longitudinal)** **(lateral)**	**> 18 Hz** **> 20 Hz**	**> 15 Hz** **> 30 Hz**	**> 35 Hz** **> 15 Hz**	**N/A** **N/A**	**> 90 Hz** **> 45 Hz**	**> 13 Hz** **> 13 Hz**
Shock (staging and/or separation)	**50 g[c]** **3,500 g[e]** **3,500 g[g]**	**N/A**	**40 g[c]** **1,100 g[e]** **4,100 g[f]**	**N/A**	**60 g[d]** **1,000 g[e]** **4,500 g[g]**	**N/A**
Sound Pressure Level (dB)	**< 130.8**	**< 133.5**	**< 139.6**	**<140**	**<146[a]** **<142[b]**	**N/A**

N/A = Not Available **[c] at 100 Hz** **[f] at 3,000 Hz**
[a] Qualification test level **[d] at 200 Hz** **[g] at 10,000 Hz**
[b] Acceptance test level **[e] at 1,000 Hz**

Table B.7 Launch environment limit loads for a selection of booster types. Acceleration values include dynamic and static components. Compiled from multiple sources, including Wertz [1992], Ariane 5 ASAP User's Manual [Mugnier, 2000], ISC Kosmotras [2001], Pegasus User's Guide [OSC, 2000], Delta II Payload Planner's Guide [Boeing Company, 1996], and the National Research Council's Small Satellite Report [NRC, 2000].

Space Environment

Long-term operations in a Geosynchronous Transfer Orbit will result in high radiation doses (due to proton and electron fluences). Transfer time requirements are based partially on the need to minimize these doses—and dose rates—and therefore minimize the impact on the host spacecraft design. 10- and 100-day dose levels in GTO are 1.37 x 10^6 and 1.37 x 10^7 rads, respectively. Solar thermal engine control electronics will require shielding and/or radiation hardening to operate under these conditions.

A second space environment factor is contamination. The solar thermal engine relies on a high-reflectivity concentrator to function properly. Contaminants settling on optical-quality surfaces (or, in the case of atomic oxygen, chemically combining with or spalling the surface) will degrade the concentrator's performance—reducing the amount of sunlight incident on the solar thermal engine. Precise knowledge of outgassed products, as well as mitigation strategies (heating the optics to drive out precipitated contaminants) are items of interest to the engine designer. No specific requirements on contamination will be assigned at this time.

Interface Requirements

These will be spacecraft-specific in many instances, but will include items such as: (1) telemetry downlink (e.g., engine and tank pressure and temperature data), and associated data formatting (2) commanding uplink requirements (throttling, startup and shutdown, pointing), also with associated data formatting (3) power requirements for valve and control electronics, (4) on-orbit safety requirements—in the event of a Shuttle launch, additional safety precautions will have to be taken into account during the design, (5) spacecraft pointing accuracy and knowledge limits, due to precise concentrator array pointing accuracy needs, (6) vehicle-specific mechanical and electrical interfaces (e.g., bolt patterns, mounting locations, centre-of-gravity limitations, pin numbers), and (7) ground station procedures and software (and/or hardware) changes for engine operation, as well as health and safety status monitoring.

Requirement	*Threshold*	*Objective*
(1) STP System Volume	The solar thermal propulsion system's enclosed volume shall be no greater than .09 m^3. (100-kg microsat)	The solar thermal propulsion system's enclosed volume shall be no greater than .045 m^3. (100-kg microsat)
(2) STP System Mass	The solar thermal engine's total mass, to include tankage and feed systems, system-specific structural supporting mechanisms, control electronics, concentrator, and receiver elements, shall be no greater than 15 kg (100-kg microsat host) or 10 kg (20-kg small microsat orbit transfer stage).	The solar thermal engine's total mass, to include tankage and feed systems, system-specific structural supporting mechanisms, control electronics, concentrator, and receiver elements, shall be no greater than 10 kg (100-kg microsat host) or 7 kg (20-kg small microsat or orbit transfer stage).
(3) Transfer Time	The solar thermal propulsion system must be capable of effecting the following orbit transfers within the specified time: (a) GTO-to-GEO (350 x 35717 km, *i* = 7 deg., to circular 35717 km, *i* = 0 deg.), in 100 days. (100-kg microsat) (b) GTO-to-lunar orbit, in 240 days, achieving translunar injection in 100 days. (100-kg microsat) (c) GTO-to-near earth object encounter, in 390 days, achieving earth escape in 100 days. (100-kg microsat) (d) 352 km circular to 704 km circular, in 5.5 days. (20-kg small microsat, 181-kg maximum mass of microsat/payload)	The solar thermal propulsion system must be capable of effecting the following orbit transfers within the specified time: (a) GTO-to-GEO (350 x 35717 km, *i* = 7 deg., to circular 35717 km, *i* = 0 deg.), in 10 days. (100-kg microsat) (b) GTO-to-lunar orbit, in 120 days, achieving translunar injection in 10 days. (100-kg microsat) (c) GTO-to-near earth object encounter, in 195 days, achieving earth escape in 10 days. (100-kg microsat) (d) 352 km circular to 704 km circular, in 3 days. (20-kg small microsat, 181-kg maximum mass of microsat/payload)
(4) Thrust	The solar thermal propulsion system shall be capable of producing: (a) 150 mN of thrust for GTO-to-GEO transfer (b) 5.2 N of thrust for GTO-to-lunar orbit and GTO-to-near-escape (c) 1 N of thrust for small microsat orbit raising from 352 to 704 km circular.	The solar thermal propulsion system shall be capable of producing: (a) 1.45 N of thrust for GTO-to-GEO transfer (b) 22 N of thrust for GTO-to-lunar orbit and GTO-to-near-escape (c) 6 N of thrust for small microsat orbit raising from 352 to 704 km circular.

(5) Specific Impulse (I_{sp})	The solar thermal engine shall be capable of achieving propellant temperatures sufficient to produce an effective I_{sp} of 350 s.	The solar thermal engine shall be capable of achieving propellant temperatures sufficient to produce an effective I_{sp} of 400 sec.
(6) Density-I_{sp} (DI_{sp})	The solar thermal engine shall be capable of achieving a density-I_{sp} of 330 g-s/cm^3	The solar thermal engine shall be capable of achieving a density-I_{sp} of 400 g-s/cm^3
(7) Firing Duration	The solar thermal engine shall be capable of firing continuously for no less than: (a) 5,000 s., for GTO-to-GEO missions (b) 540 s., for GTO-to-lunar orbit and GTO-to-near-escape missions (c) 428 s., for small microsat orbit raising from 352 to 704 km —or— 10 days for a spiral transfer (continuous firing throughout transfer) strategy	The solar thermal engine shall be capable of firing continuously for no less than: (a) 11,250 s., for GTO-to-GEO missions (b) 1,215 s., for GTO-to-lunar orbit and GTO-to-near-escape missions (c) 963 s., for small microsat orbit raising from 352 to 704 km —or— 100 days for a spiral transfer (continuous firing throughout transfer) strategy
(8) Number of Firings/Restarts	The solar thermal engine shall be capable of firing no less than: (a) 17 times, 5,000 s. per firing (85,000 s. on-time) (b) 26 times, 540 s. per firing (14,040 s. on-time) (c) 40 times, 428 s. per firing (17,120 s. on-time) —or— for a spiral transfer strategy, TBD times.	The solar thermal engine shall be capable of firing no less than: (a) 39 times, 5,000 s. per firing (195,000 s. on-time) (b) 59 times, 540 s. per firing (c) (31,860 s. on-time) (d) 90 times, 428 s. per firing (38,520 s. on-time) —or— for a spiral transfer strategy, TBD times.

(9) Thermal Charging Time	*If thermal storage is used*, the solar thermal engine must be capable of attaining a "fully charged" (maximum operating temperature) state within: (a) 4 hrs., for GTO-to-GEO missions (b) 5 hrs., for GTO-to-lunar orbit and GTO-to-near escape missions (c) 2 hrs., for small microsat orbit-raising from 352 to 704 km	*If thermal storage is used*, the solar thermal engine must be capable of attaining a "fully charged" (maximum operating temperature) state within: (a) 2 hrs., for GTO-to-GEO missions (b) 2.5 hrs., for GTO-to-lunar orbit and GTO-to-near escape missions (c) 40 min., for small microsat orbit-raising from 352 to 704 km
(10) System Reliability	The solar thermal engine shall achieve a per-mission reliability of no less than 95%.	The solar thermal engine shall achieve a per-mission reliability of no less than 99%.
(11) Startup, Restart, Throttling, and Shutdown	The solar thermal engine must be capable of restarting. Startup, throttling, and shutdown requirements are TBD.	The solar thermal engine must be capable of restarting. Startup, throttling, and shutdown requirements are TBD.
(12) Cost of Development	No threshold established.	The solar thermal engine shall be delivered for integration—to include design, component and system test, with: (a) a host microsatellite (100-kg.) for £1M ($1.5M) (b) a small microsatellite (20-kg.) for £250K ($375K)
(13) Development Schedule	No threshold established.	The solar thermal engine shall be delivered for integration—to include design, component and systems test, with: (a) a host microsatellite, in 3 yrs. (b) a small microsatellite, in 2 yrs.
(14) Launch Environment Loading	The solar thermal engine shall be designed to: (a) withstand Ariane 5 ASAP launch loads (i.e., shock, axial and lateral load limits, and sound pressure level), and to (b) conform to Ariane 5 ASAP natural frequency requirements	The solar thermal engine shall be designed to: (c) withstand Ariane 5 ASAP launch loads (i.e., shock, axial and lateral load limits, and sound pressure level), and to (d) conform to Ariane 5 ASAP natural frequency requirements

(15) Launch and Payload Processing Environment	Requirement(s) are TBD. These will include temperature limits, thermal, contamination (cleanliness), humidity, and electromagnetic interference.	Requirement(s) are TBD.
(16) Space Environment Contamination Tolerance	Requirement is TBD.	Requirement is TBD.
(17) Space Environment Radiation Tolerance	The solar thermal engine shall remain functional after exposure to a total dose of 1.37×10^6 rads (electron and proton fluence).	The solar thermal engine shall remain functional after exposure to a total dose of 1.37×10^7 rads (electron and proton fluence).
(18) Interface Requirements	Requirement(s) are TBD. These will include telemetry, command, electrical power, safety, pointing accuracy/knowledge, mechanical and electrical interfaces, and ground station operational procedures.	Requirement(s) are TBD.
(19) Manufacture and Ease of Procurement		(GUIDANCE) The solar thermal engine will be designed to incorporate commercially available components from regional vendors whenever possible, avoid the use of rare materials and propellants, items with highly specialized machining requirements, and custom-built hardware.
(20) Testability and Test Safety		(GUIDANCE) The solar thermal engine shall be designed so as to maximize the use of existing test facilities and hardware, and to conform to locally acceptable test procedures.
(21) Proto-Qualification/ Proto-Flight Build		(GUIDANCE) The solar thermal engine shall be designed to proto-qualification/proto-flight standards.

(22) Spacecraft Design, Test, and Integration		(GUIDANCE) The solar thermal engine shall be designed to minimize host spacecraft modifications and spacecraft testing/integration hardware or procedural changes resulting from the engine's unique requirements.
(23) Mission Operations		(GUIDANCE) The solar thermal engine shall be designed to minimize changes to ground station operational procedures, personnel requirements, support hardware, and software.

Appendix C: Engineering Drawings

This section contains a number of detailed engineering drawings of key items fabricated for component and system level testing, including both large and small concentrating mirrors, the Mk. I and Mk. II solar receivers, and their components.

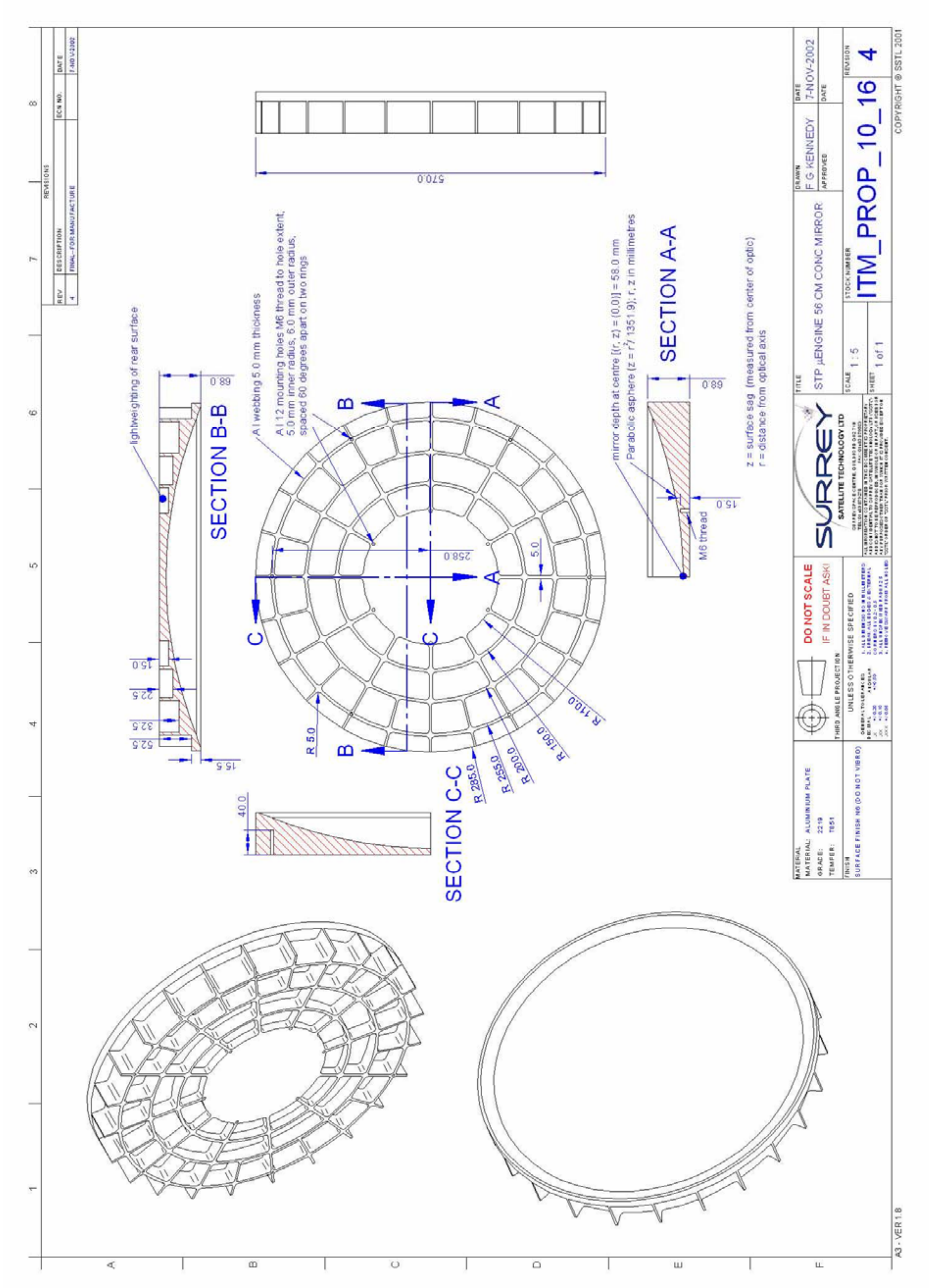
REVISIONS
REV
DESCRIPTION
ECN NO.
DATE
4
FINAL–FOR MANUFACTURE
7-NOV-2002
570.0
lightweighting of rear surface
SECTION B-B
68.0
15.0
22.5
32.5
52.5
15.5
A) webbing 5.0 mm thickness
A) 12 mounting holes M6 thread to hole extent, 5.0 mm inner radius, 6.0 mm outer radius, spaced 60 degrees apart on two rings
258.0
5.0
R 5.0
R 285.0
R 255.0
R 200.0
R 150.0
R 110.0
A
B
C
SECTION C-C
40.0
mirror depth at centre [(r, z) = (0,0)] = 58.0 mm
Parabolic asphere (z = r²/ 1351.9); r, z in millimetres
SECTION A-A
68.0
15.0
M6 thread
z = surface sag (measured from center of optic)
r = distance from optical axis
MATERIAL
MATERIAL: ALUMINIUM PLATE
GRADE: 2219
TEMPER: T851
FINISH
SURFACE FINISH N6 (DO NOT VIBRO)
THIRD ANGLE PROJECTION
UNLESS OTHERWISE SPECIFIED
DO NOT SCALE
IF IN DOUBT ASK!
SURREY
SATELLITE TECHNOLOGY LTD
TITLE
STP μENGINE 56 CM CONC MIRROR
DRAWN
F G KENNEDY
DATE
7-NOV-2002
APPROVED
DATE
SCALE
1 : 5
STOCK NUMBER
ITM_PROP_10_16
REVISION
4
SHEET
1 of 1
COPYRIGHT © SSTL 2001
A3 - VER 1.8
1
2
3
4
5
6
7
8
A
B
C
D
E
F

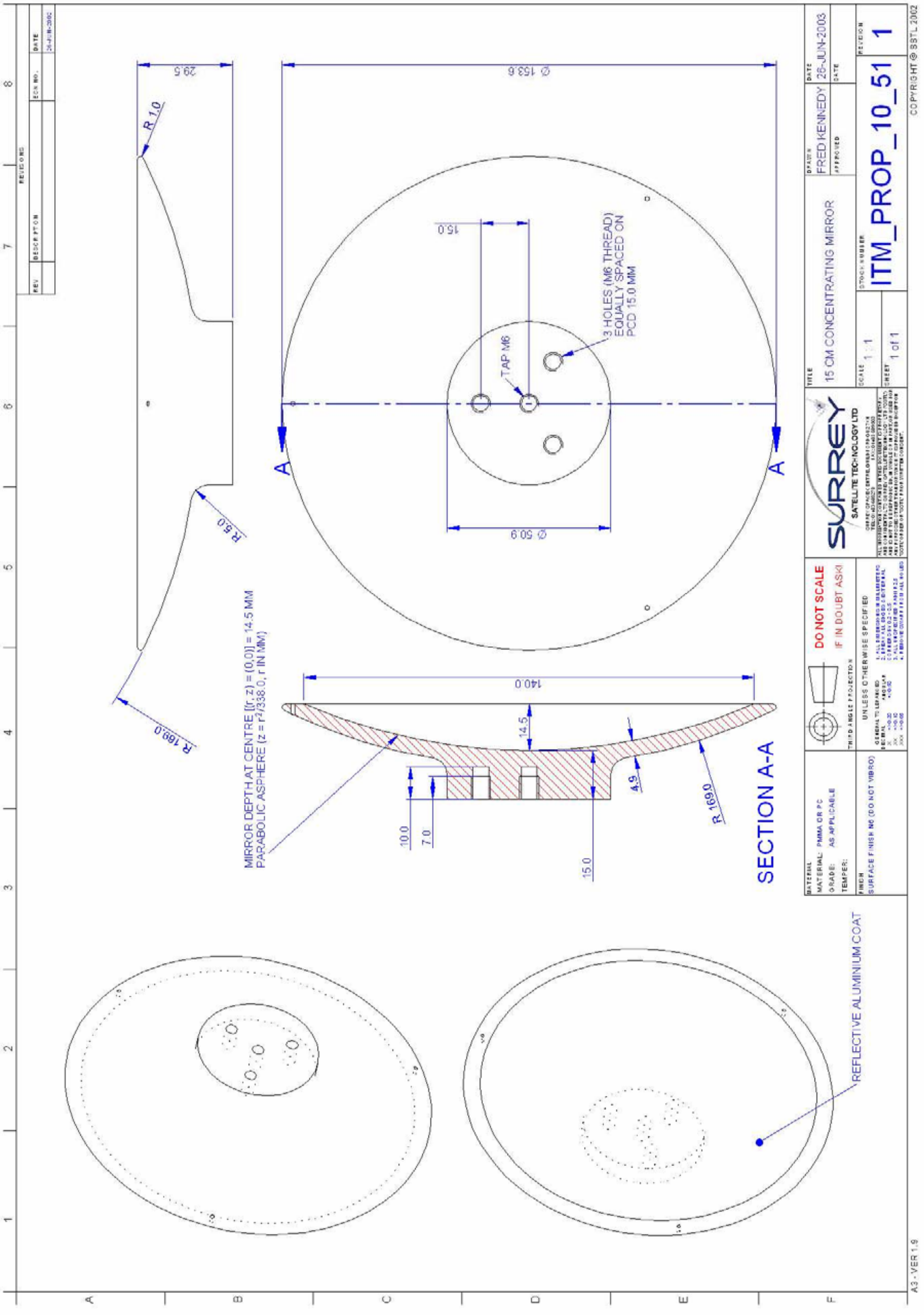

REV
DESCRIPTION
REVISIONS
ECN NO.
DATE
26-JUN-2002
29.5
R 1.0
Ø 153.6
15.0
3 HOLES (M6 THREAD)
EQUALLY SPACED ON
PCD 15.0 MM
TAP M6
A
A
Ø 50.9
R 5.0
R 169.0
MIRROR DEPTH AT CENTRE [(r, z) = (0,0)] = 14.5 MM
PARABOLIC ASPHERE (z = r²/338.0, r IN MM)
140.0
14.5
4.9
R 169.0
10.0
7.0
15.0
SECTION A-A
REFLECTIVE ALUMINIUM COAT
MATERIAL
MATERIAL: PMMA OR PC
GRADE: AS APPLICABLE
TEMPER:
FINISH
SURFACE FINISH NO (DO NOT VIBRO)
THIRD ANGLE PROJECTION
UNLESS OTHERWISE SPECIFIED
DO NOT SCALE
IF IN DOUBT ASK!
SURREY
SATELLITE TECHNOLOGY LTD
TITLE
15 CM CONCENTRATING MIRROR
DRAWN
FRED KENNEDY
DATE
26-JUN-2003
APPROVED
DATE
SCALE
1:1
SHEET
1 of 1
STOCK NUMBER
ITM_PROP_10_51
REVISION
1
COPYRIGHT © SSTL 2002
A3 - VER 1.9
1
2
3
4
5
6
7
8
A
B
C
D
E
F

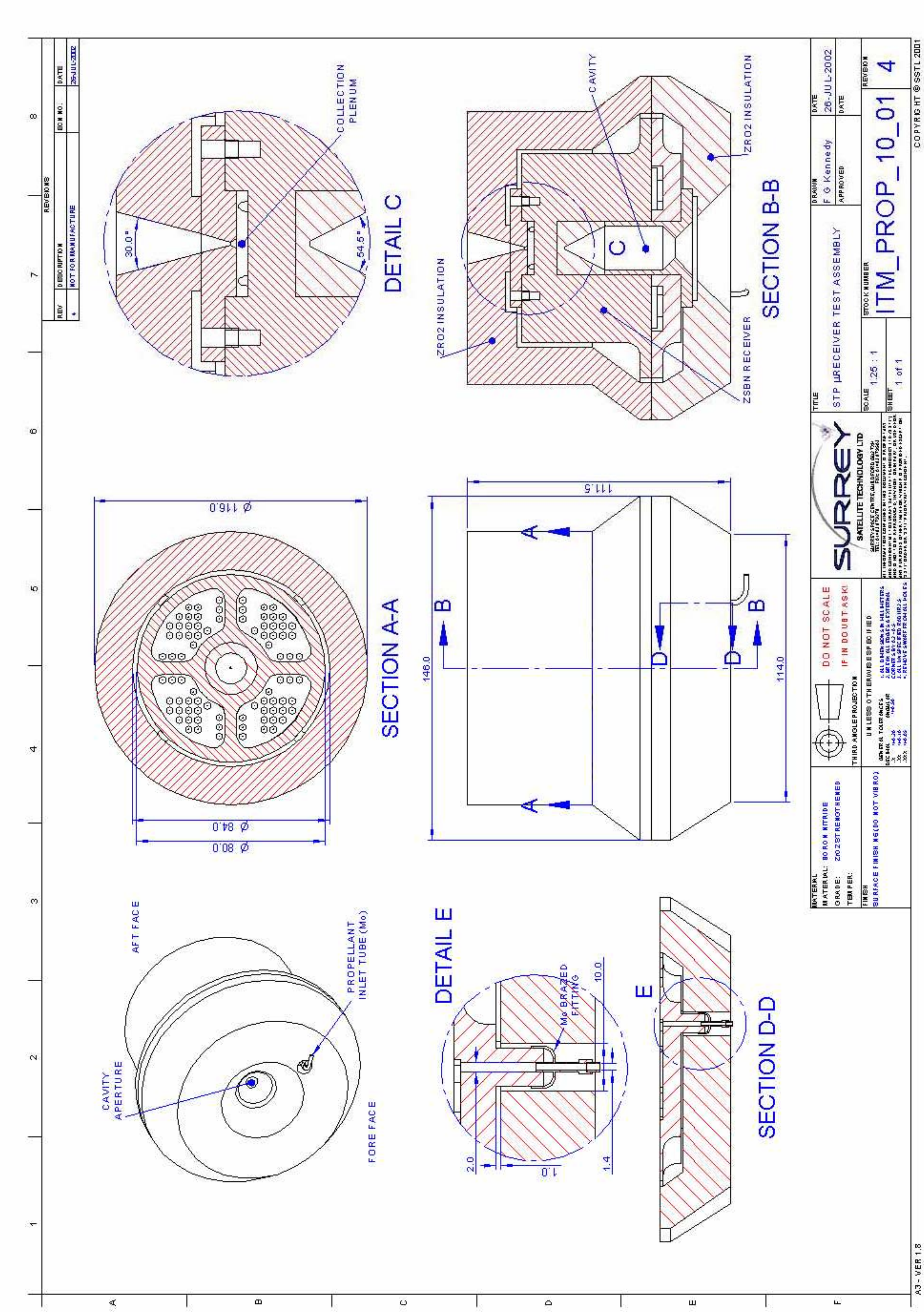
REVISIONS
REV
DESCRIPTION
ECN NO.
DATE
4
NOT FOR MANUFACTURE
26-JUL-2002
COLLECTION PLENUM
30.0°
54.5°
DETAIL C
CAVITY
ZRO2 INSULATION
ZRO2 INSULATION
C
ZSBN RECEIVER
SECTION B-B
Ø 116.0
Ø 84.0
Ø 80.0
SECTION A-A
111.5
146.0
114.0
A
A
B
B
D
D
AFT FACE
PROPELLANT INLET TUBE (Mo)
CAVITY APERTURE
FORE FACE
DETAIL E
Mo BRAZED FITTING
10.0
2.0
1.0
1.4
E
SECTION D-D
MATERIAL
MATERIAL: BORON NITRIDE
GRADE: ZrO2 STRENGTHENED
TEMPER:
FINISH
SURFACE FINISH N6 (DO NOT VIBRO)
THIRD ANGLE PROJECTION
UNLESS OTHERWISE SPECIFIED
GENERAL TOLERANCES
DO NOT SCALE
IF IN DOUBT ASK!
SURREY
SATELLITE TECHNOLOGY LTD
TITLE
STP µRECEIVER TEST ASSEMBLY
DRAWN
F G Kennedy
DATE
26-JUL-2002
APPROVED
DATE
SCALE
1.25 : 1
SHEET
1 of 1
STOCK NUMBER
ITM_PROP_10_01
REVISION
4
COPYRIGHT © SSTL 2001
A3 - VER 1.8

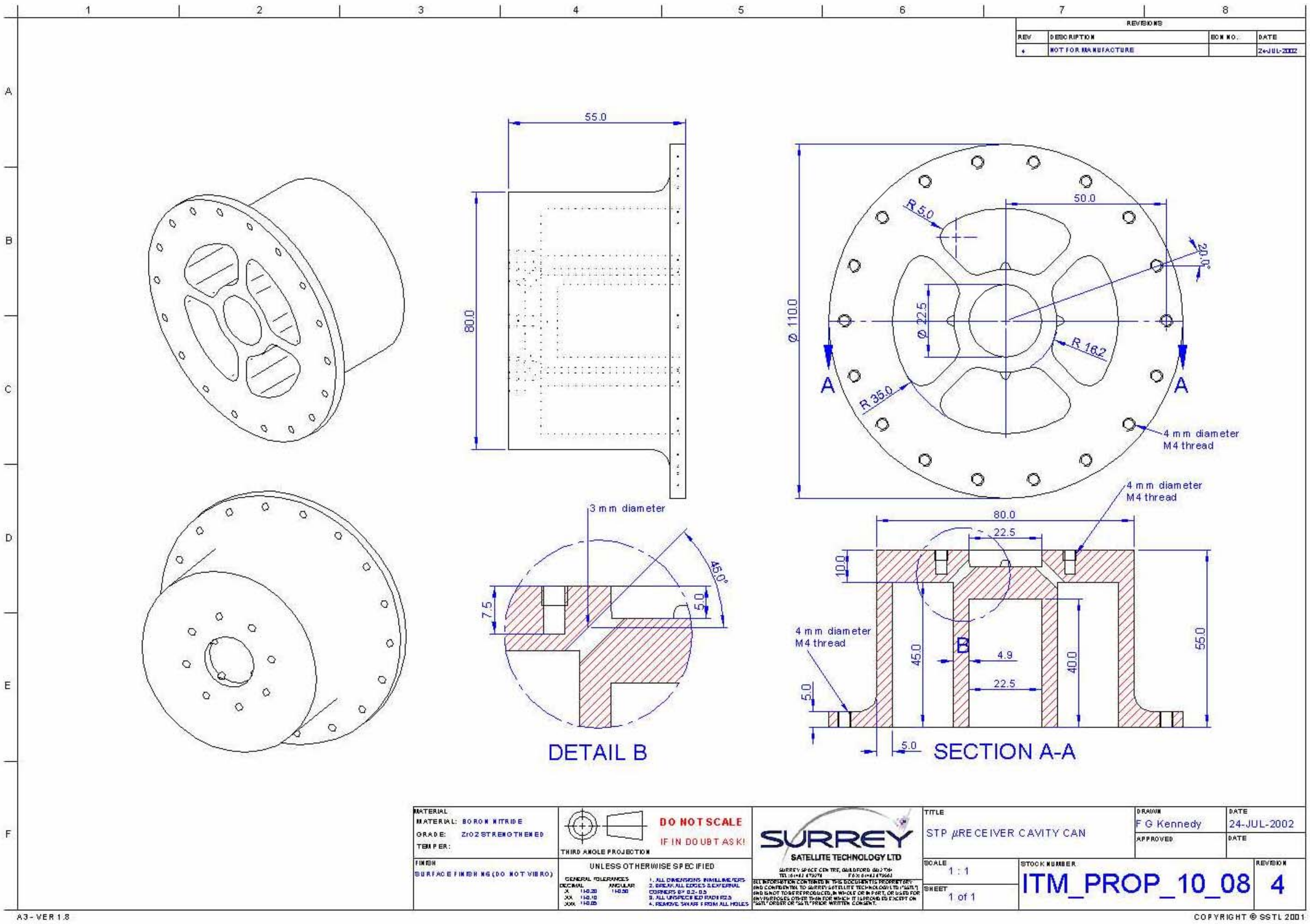
REVISIONS
REV
DESCRIPTION
ECN NO.
DATE
4
NOT FOR MANUFACTURE
24-JUL-2002
55.0
80.0
Ø 110.0
50.0
20.0°
R 5.0
Ø 22.5
R 16.2
R 35.0
A
A
4 mm diameter
M4 thread
4 mm diameter
M4 thread
3 mm diameter
45.0°
7.5
5.0
DETAIL B
80.0
22.5
10.0
4 mm diameter
M4 thread
45.0
B
4.9
22.5
40.0
55.0
5.0
5.0
SECTION A-A
MATERIAL
MATERIAL: BORON NITRIDE
GRADE: ZrO2 STRENGTHENED
TEMPER:
FINISH
SURFACE FINISHING (DO NOT VIBRO)
THIRD ANGLE PROJECTION
DO NOT SCALE
IF IN DOUBT ASK!
UNLESS OTHERWISE SPECIFIED
GENERAL TOLERANCES
DECIMAL
X ±0.20
XX ±0.10
XXX ±0.05
ANGULAR ±0.50
1. ALL DIMENSIONS IN MILLIMETERS
2. BREAK ALL EDGES & EXTERNAL CORNERS BY 0.2 - 0.5
3. ALL UNSPECIFIED RADII R2.5
4. REMOVE SWARF FROM ALL HOLES
SURREY
SATELLITE TECHNOLOGY LTD
SURREY SPACE CENTRE, GUILDFORD GU2 7XH
ALL INFORMATION CONTAINED IN THIS DOCUMENT IS PROPRIETARY AND CONFIDENTIAL TO SURREY SATELLITE TECHNOLOGY LTD ("SSTL") AND IS NOT TO BE REPRODUCED, IN WHOLE OR IN PART, OR USED FOR ANY PURPOSES OTHER THAN FOR WHICH IT IS PROVIDED EXCEPT ON "SSTL" ORDER OR "SSTL" PRIOR WRITTEN CONSENT.
TITLE
STP µRECEIVER CAVITY CAN
DRAWN
F G Kennedy
DATE
24-JUL-2002
APPROVED
DATE
SCALE
1 : 1
SHEET
1 of 1
STOCK NUMBER
ITM_PROP_10_08
REVISION
4
A3 - VER 1.8
COPYRIGHT © SSTL 2001
1
2
3
4
5
6
7
8
A
B
C
D
E
F

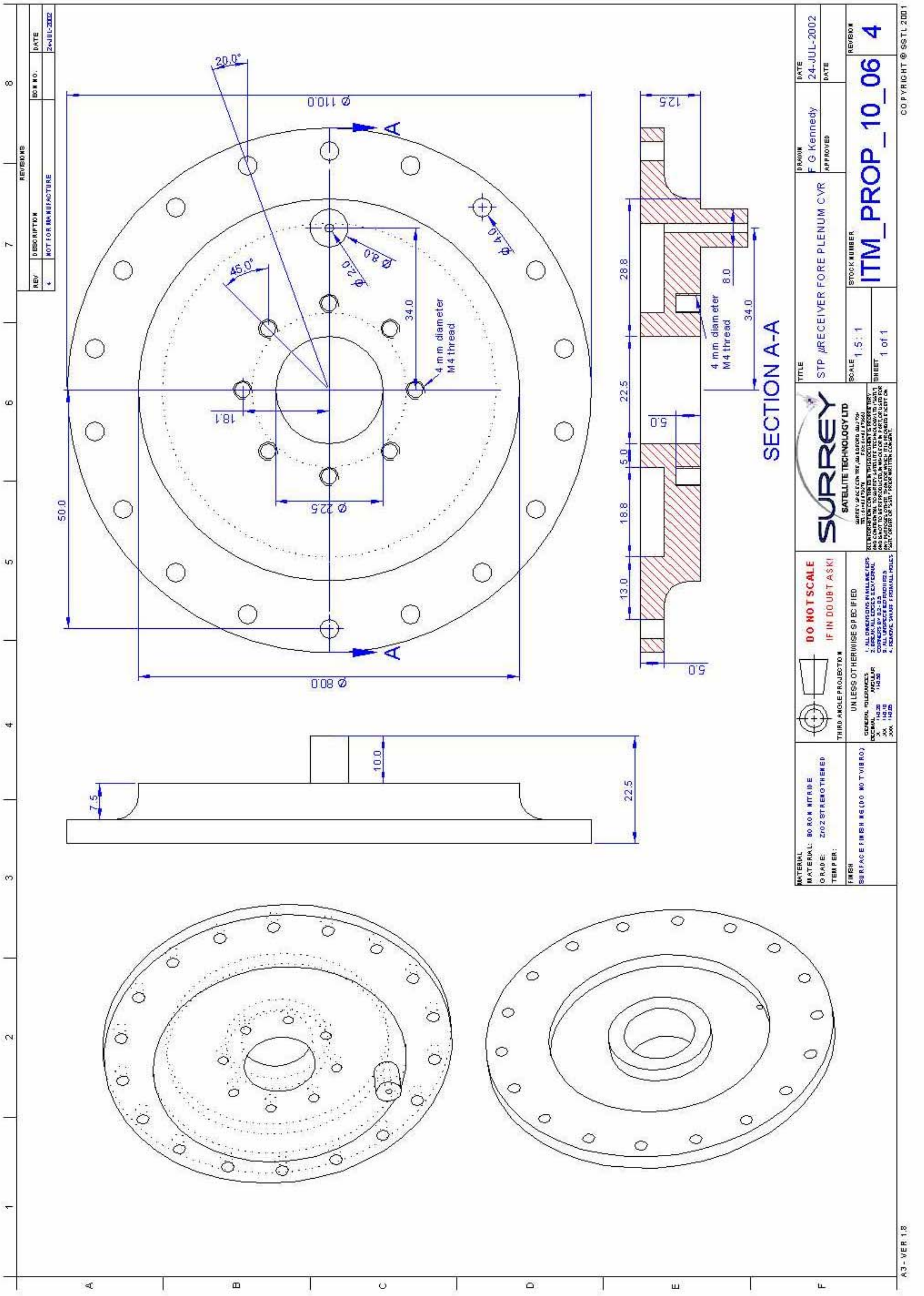

REVISIONS
REV
DESCRIPTION
ECN NO.
DATE
4
NOT FOR MANUFACTURE
24-JUL-2002
20.0°
Ø 110.0
A
45.0°
Ø 2.0
Ø 8.0
Ø 4.0
34.0
4 mm diameter
M4 thread
18.1
Ø 22.5
50.0
Ø 80.0
12.5
28.8
8.0
22.5
5.0
5.0
18.8
13.0
34.0
SECTION A-A
7.5
10.0
22.5
TITLE
STP μRECEIVER FORE PLENUM CVR
DRAWN
F G Kennedy
DATE
24-JUL-2002
APPROVED
DATE
SCALE
1.5 : 1
SHEET
1 of 1
STOCK NUMBER
ITM_PROP_10_06
REVISION
4
COPYRIGHT © SSTL 2001
SURREY
SATELLITE TECHNOLOGY LTD
DO NOT SCALE
IF IN DOUBT ASK!
THIRD ANGLE PROJECTION
UNLESS OTHERWISE SPECIFIED
MATERIAL
MATERIAL: BORON NITRIDE
GRADE: ZrO2 STRENGTHENED
TEMPER:
FINISH
SURFACE FINISHING (DO NOT VIBRO)
A3 - VER 1.8
A
B
C
D
E
F
1
2
3
4
5
6
7
8

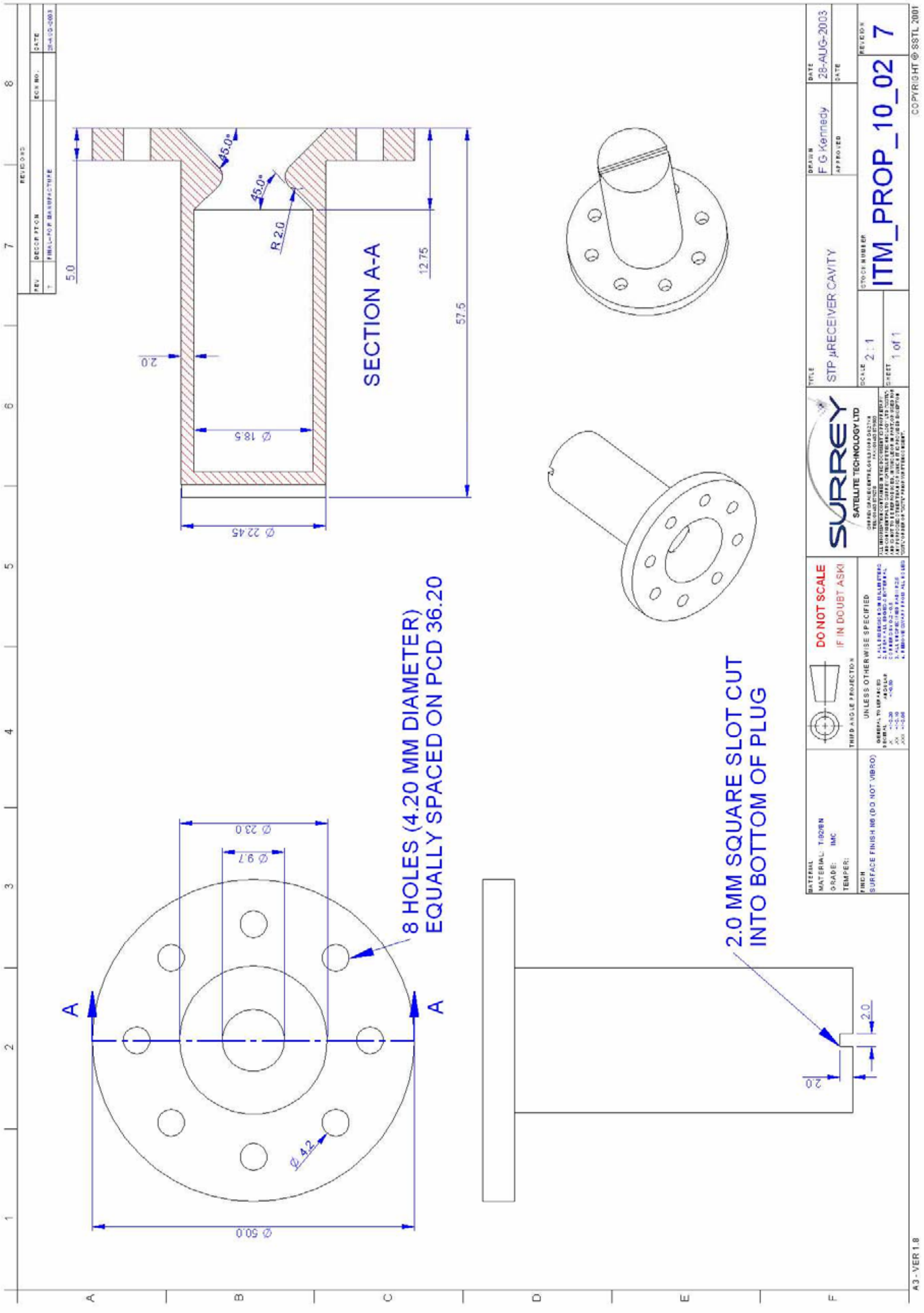
SECTION A-A
45.0°
45.0°
R 2.0
5.0
12.75
57.5
2.0
Ø 18.5
Ø 22.45
A
A
Ø 50.0
Ø 23.0
Ø 9.7
Ø 4.2
8 HOLES (4.20 MM DIAMETER)
EQUALLY SPACED ON PCD 36.20
2.0 MM SQUARE SLOT CUT
INTO BOTTOM OF PLUG
2.0
2.0
REVISIONS
REV
DESCRIPTION
ECN NO.
DATE
7
FINAL-FOR MANUFACTURE
28-AUG-2003
MATERIAL
MATERIAL: T-92/BN
GRADE: IMC
TEMPER:
FINISH
SURFACE FINISH N6 (DO NOT VIBRO)
THIRD ANGLE PROJECTION
DO NOT SCALE
IF IN DOUBT ASK!
UNLESS OTHERWISE SPECIFIED
SURREY
SATELLITE TECHNOLOGY LTD
TITLE
STP µRECEIVER CAVITY
SCALE
2 : 1
SHEET
1 of 1
DRAWN
F G Kennedy
APPROVED
DATE
28-AUG-2003
DATE
STOCK NUMBER
ITM_PROP_10_02
REVISION
7
COPYRIGHT © SSTL 2001
A3 - VER 1.8
1
2
3
4
5
6
7
8
A
B
C
D
E
F

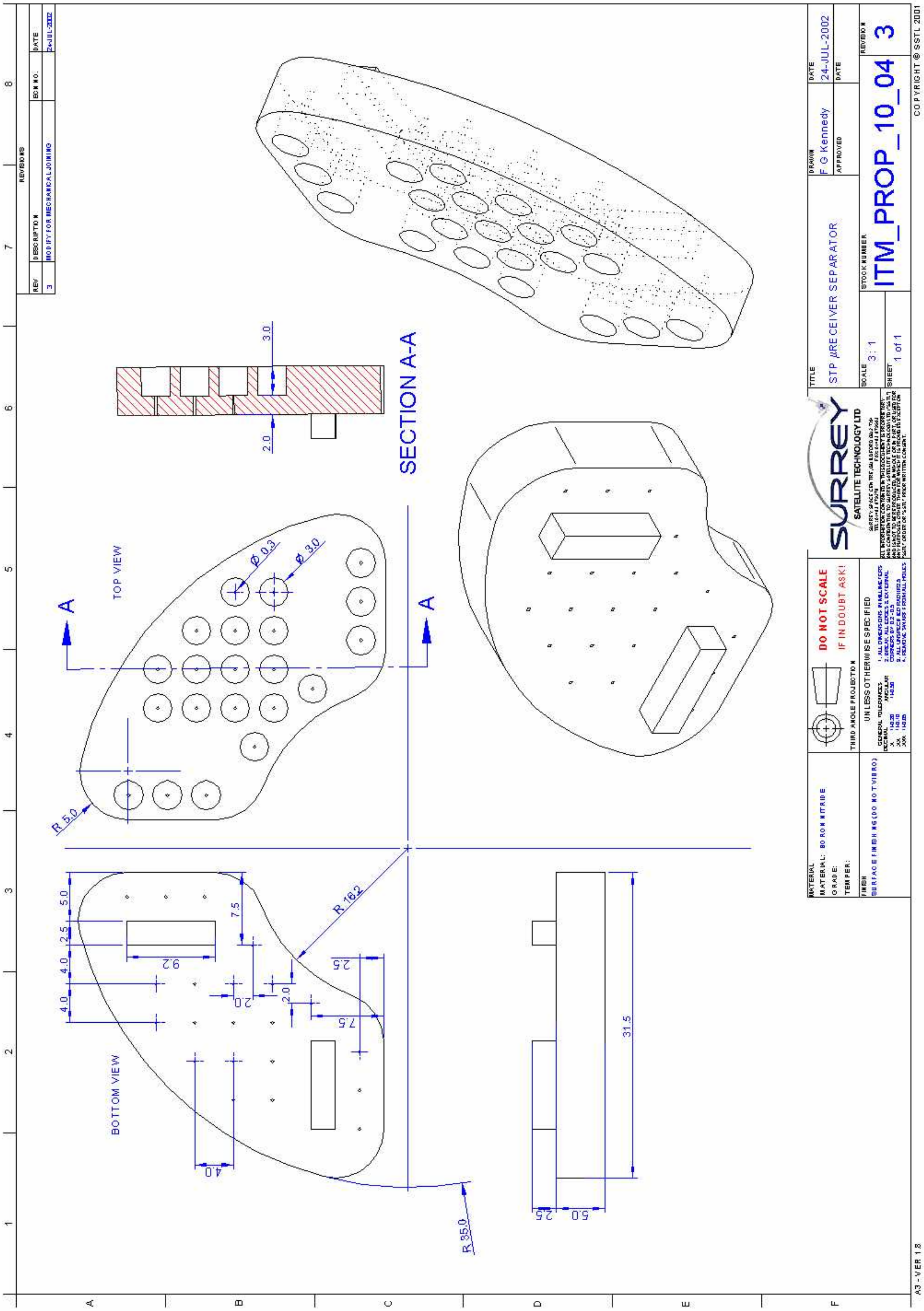
REVISIONS
REV
DESCRIPTION
ECN NO.
DATE
3
MODIFY FOR MECHANICAL JOINING
24-JUL-2002
SECTION A-A
3.0
2.0
TOP VIEW
A
A
Ø 0.3
Ø 3.0
R 5.0
BOTTOM VIEW
5.0
2.5
4.0
4.0
9.2
7.5
2.0
2.0
2.5
7.5
4.0
R 16.2
R 35.0
31.5
2.5
5.0
MATERIAL
MATERIAL: BORON NITRIDE
GRADE:
TEMPER:
FINISH
SURFACE FINISHING (DO NOT VIBRO)
THIRD ANGLE PROJECTION
UNLESS OTHERWISE SPECIFIED
DO NOT SCALE
IF IN DOUBT ASK!
SURREY
SATELLITE TECHNOLOGY LTD
TITLE
STP µRECEIVER SEPARATOR
DRAWN
F G Kennedy
APPROVED
DATE
24-JUL-2002
DATE
SCALE
3 : 1
SHEET
1 of 1
STOCK NUMBER
ITM_PROP_10_04
REVISION
3
COPYRIGHT © SSTL 2001
A3 - VER 1.8
1
2
3
4
5
6
7
8
A
B
C
D
E
F

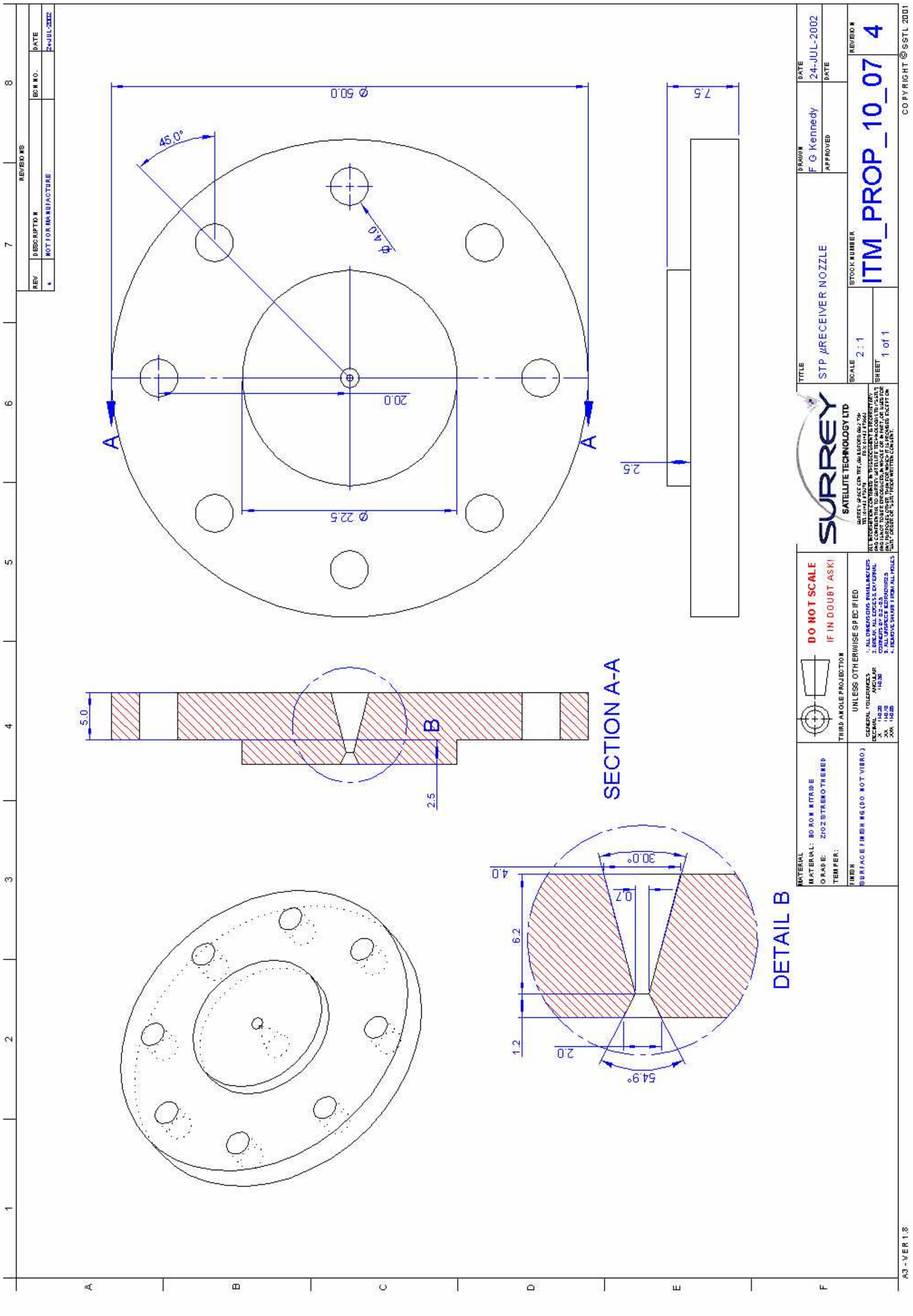
REVISIONS
REV
DESCRIPTION
ECN NO.
DATE
4
NOT FOR MANUFACTURE
24-JUL-2002
Ø 50.0
45.0°
Ø 4.0
20.0
Ø 22.5
7.5
2.5
A
A
5.0
B
2.5
SECTION A-A
30.0°
4.0
0.7
6.2
1.2
2.0
54.9°
DETAIL B
MATERIAL
MATERIAL: BORON NITRIDE
GRADE: ZrO2 STRENGTHENED
TEMPER:
FINISH
SURFACE FINISHING (DO NOT VIBRO)
THIRD ANGLE PROJECTION
UNLESS OTHERWISE SPECIFIED
DO NOT SCALE
IF IN DOUBT ASK!
SURREY
SATELLITE TECHNOLOGY LTD
TITLE
STP µRECEIVER NOZZLE
SCALE
2 : 1
SHEET
1 of 1
STOCK NUMBER
ITM_PROP_10_07
REVISION
4
DRAWN
F G Kennedy
APPROVED
DATE
24-JUL-2002
DATE
COPYRIGHT © SSTL 2001
A3-VER1.8
A
B
C
D
E
F
1
2
3
4
5
6
7
8

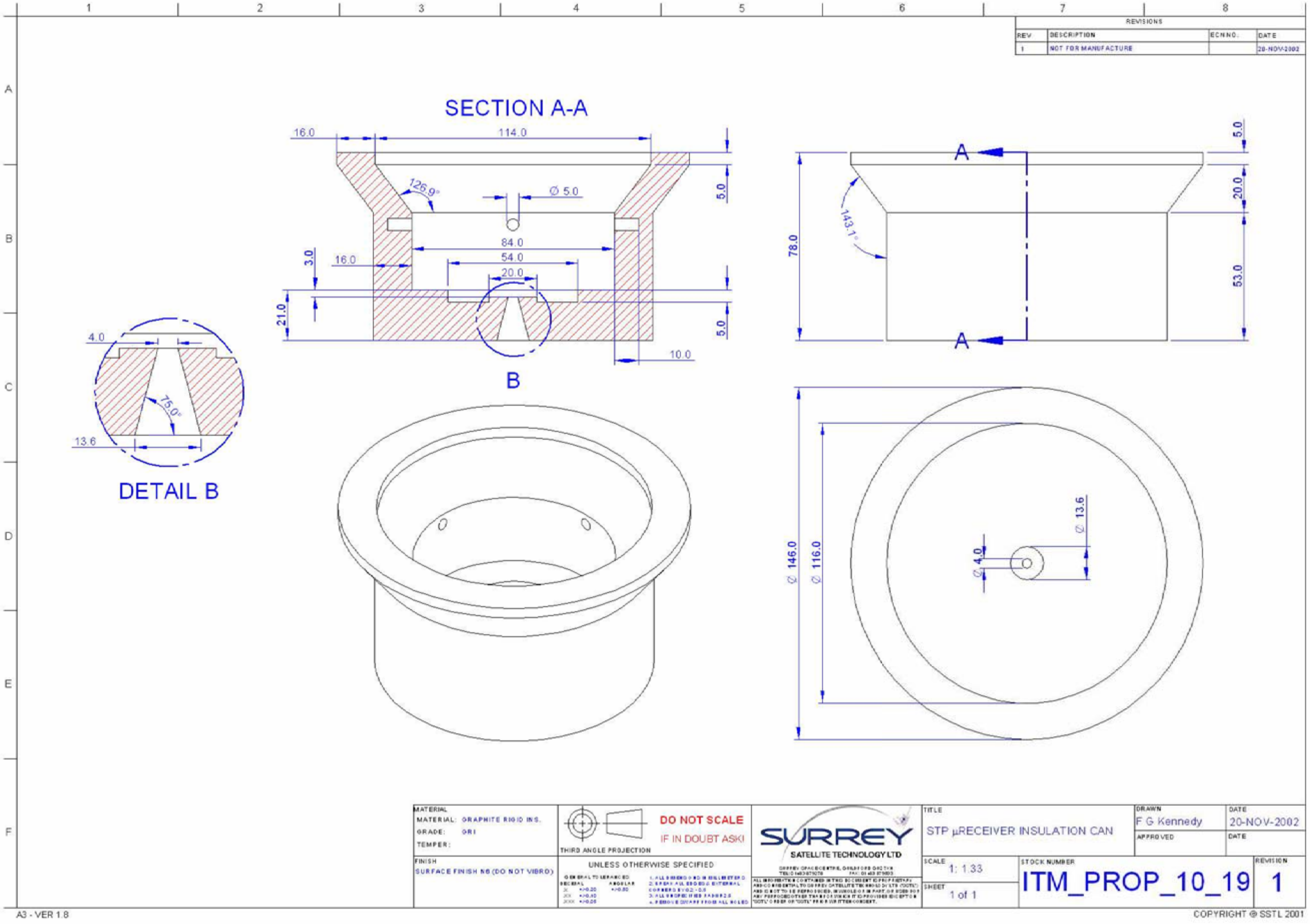
REVISIONS
REV
DESCRIPTION
ECN NO.
DATE
1
NOT FOR MANUFACTURE
20-NOV-2002
SECTION A-A
16.0
114.0
126.9°
Ø 5.0
5.0
84.0
54.0
20.0
3.0
16.0
21.0
5.0
10.0
B
DETAIL B
4.0
75.0°
13.6
A
A
5.0
20.0
53.0
78.0
143.1°
Ø 146.0
Ø 116.0
Ø 4.0
Ø 13.6
MATERIAL
MATERIAL: GRAPHITE RIGID INS.
GRADE: GRI
TEMPER:
FINISH
SURFACE FINISH N6 (DO NOT VIBRO)
THIRD ANGLE PROJECTION
DO NOT SCALE
IF IN DOUBT ASK!
UNLESS OTHERWISE SPECIFIED
SURREY
SATELLITE TECHNOLOGY LTD
TITLE
STP µRECEIVER INSULATION CAN
DRAWN
F G Kennedy
DATE
20-NOV-2002
APPROVED
DATE
SCALE
1: 1.33
SHEET
1 of 1
STOCK NUMBER
ITM_PROP_10_19
REVISION
1
COPYRIGHT © SSTL 2001
A3 - VER 1.8

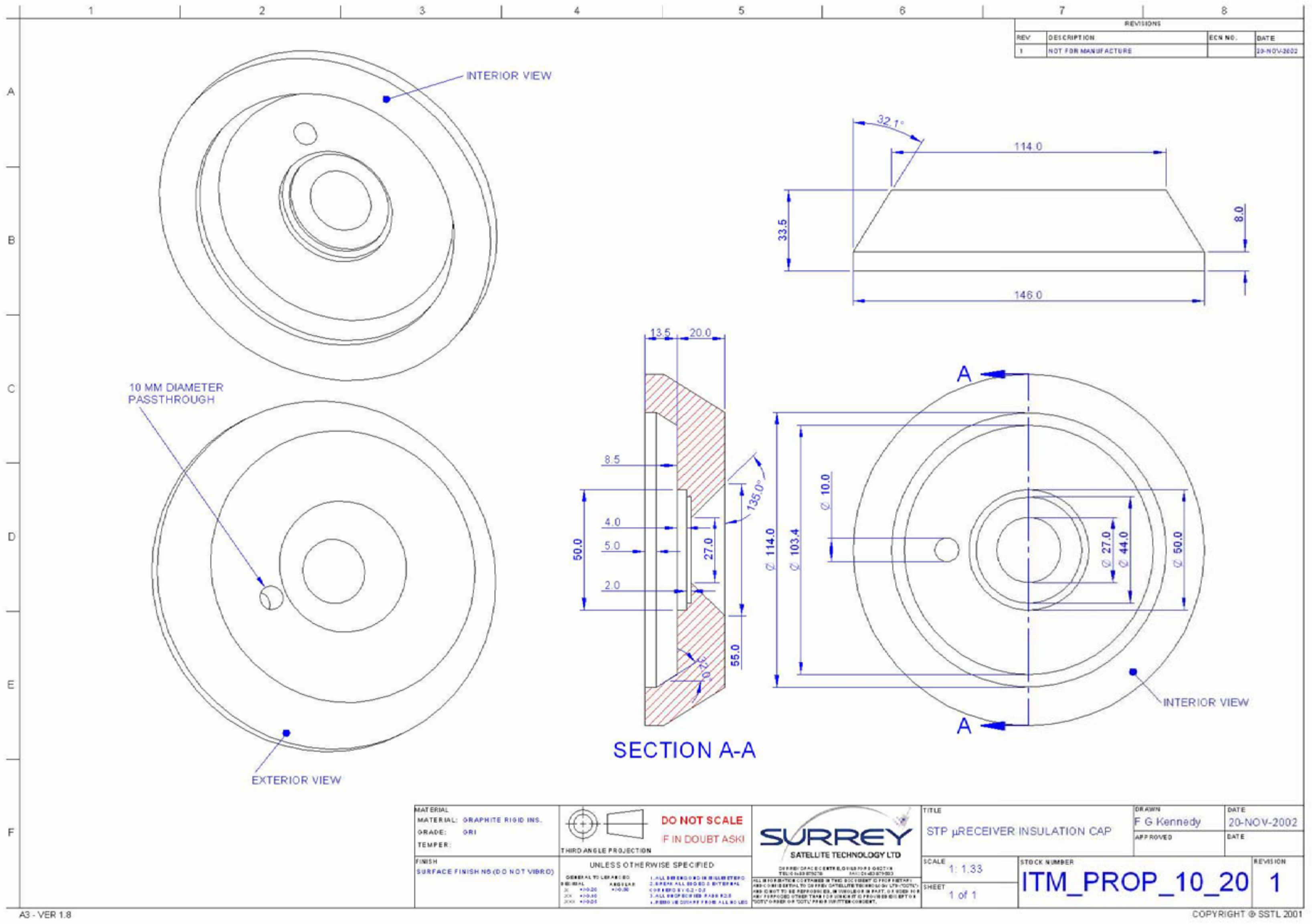
REVISIONS
REV
DESCRIPTION
ECN NO.
DATE
1
NOT FOR MANUFACTURE
20-NOV-2002
INTERIOR VIEW
32.1°
114.0
33.5
8.0
146.0
13.5
20.0
10 MM DIAMETER PASSTHROUGH
8.5
4.0
5.0
2.0
50.0
27.0
135.0°
32.0°
55.0
Ø 114.0
Ø 103.4
Ø 10.0
Ø 27.0
Ø 44.0
Ø 50.0
A
A
INTERIOR VIEW
SECTION A-A
EXTERIOR VIEW
MATERIAL
MATERIAL: GRAPHITE RIGID INS.
GRADE: GRI
TEMPER:
FINISH
SURFACE FINISH N6 (DO NOT VIBRO)
THIRD ANGLE PROJECTION
DO NOT SCALE
IF IN DOUBT ASK!
UNLESS OTHERWISE SPECIFIED
SURREY
SATELLITE TECHNOLOGY LTD
TITLE
STP μRECEIVER INSULATION CAP
DRAWN
F G Kennedy
APPROVED
DATE
20-NOV-2002
DATE
SCALE
1: 1.33
SHEET
1 of 1
STOCK NUMBER
ITM_PROP_10_20
REVISION
1
A3 - VER 1.8
COPYRIGHT © SSTL 2001

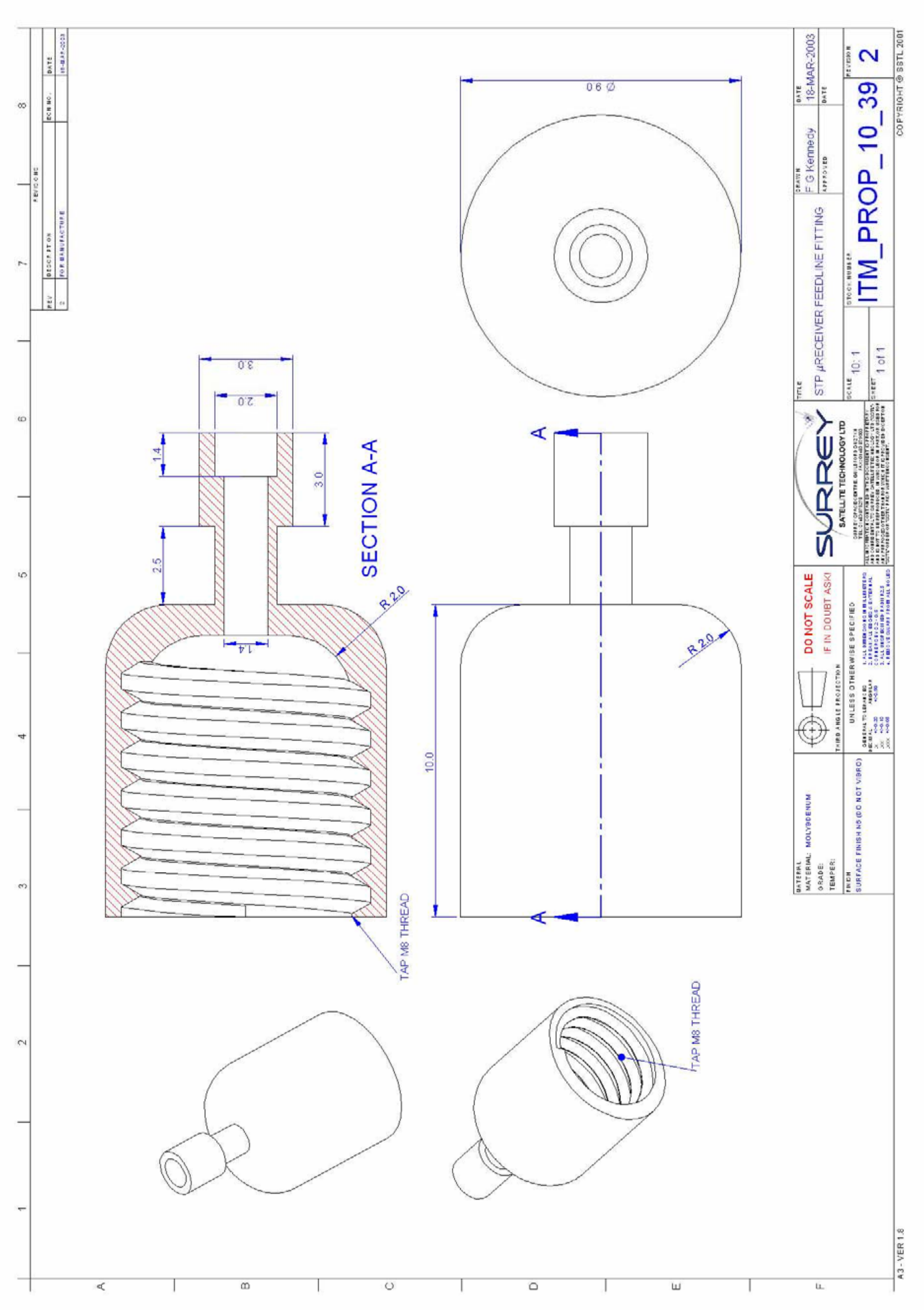
SECTION A-A
3.0
2.0
1.4
3.0
2.5
1.4
R 2.0
R 2.0
10.0
9.0 Ø
A
A
TAP M8 THREAD
TAP M8 THREAD
REV
DESCRIPTION
FOR MANUFACTURE
ECN NO.
DATE
MATERIAL: MOLYBDENUM
GRADE:
TEMPER:
FINISH
SURFACE FINISH N5 (DO NOT VIBRO)
THIRD ANGLE PROJECTION
UNLESS OTHERWISE SPECIFIED
DO NOT SCALE
IF IN DOUBT ASK!
SURREY
SATELLITE TECHNOLOGY LTD
TITLE
STP μRECEIVER FEEDLINE FITTING
DRAWN
F G Kennedy
DATE
18-MAR-2003
APPROVED
SCALE
10:1
SHEET
1 of 1
STOCK NUMBER
ITM_PROP_10_39
REVISION
2
COPYRIGHT © SSTL 2001
A3 - VER 1.8
A
B
C
D
E
F
1
2
3
4
5
6
7
8

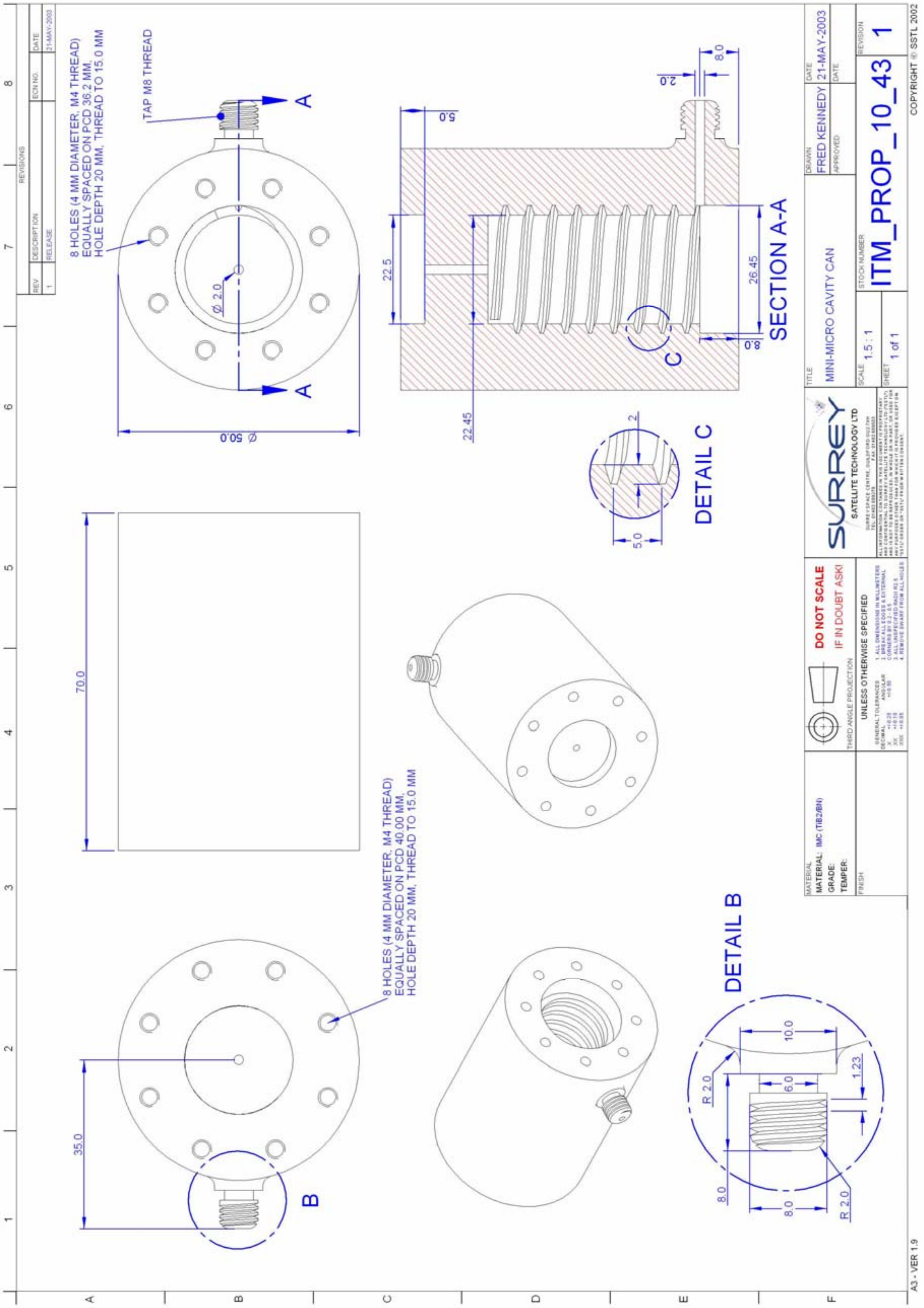
8 HOLES (4 MM DIAMETER, M4 THREAD) EQUALLY SPACED ON PCD 36.2 MM. HOLE DEPTH 20 MM, THREAD TO 15.0 MM
TAP M8 THREAD
Ø 2.0
Ø 50.0
A
A
5.0
2.0
8.0
22.5
22.45
26.45
8.0
C
SECTION A-A
DETAIL C
2
5.0
70.0
35.0
B
8 HOLES (4 MM DIAMETER, M4 THREAD) EQUALLY SPACED ON PCD 40.00 MM. HOLE DEPTH 20 MM, THREAD TO 15.0 MM
DETAIL B
10.0
R 2.0
6.0
1.23
8.0
8.0
R 2.0
REV
DESCRIPTION
ECN NO.
DATE
1
RELEASE
21-MAY-2003
REVISIONS
MATERIAL: IMC (TiB2/BN)
GRADE:
TEMPER:
FINISH
THIRD ANGLE PROJECTION
DO NOT SCALE
IF IN DOUBT ASK!
UNLESS OTHERWISE SPECIFIED
SURREY SATELLITE TECHNOLOGY LTD
TITLE
MINI-MICRO CAVITY CAN
SCALE 1.5 : 1
SHEET 1 of 1
DRAWN FRED KENNEDY
DATE 21-MAY-2003
APPROVED
STOCK NUMBER
ITM_PROP_10_43
REVISION 1
COPYRIGHT © SSTL 2002
A3 - VER 1.9
1
2
3
4
5
6
7
8
A
B
C
D
E
F

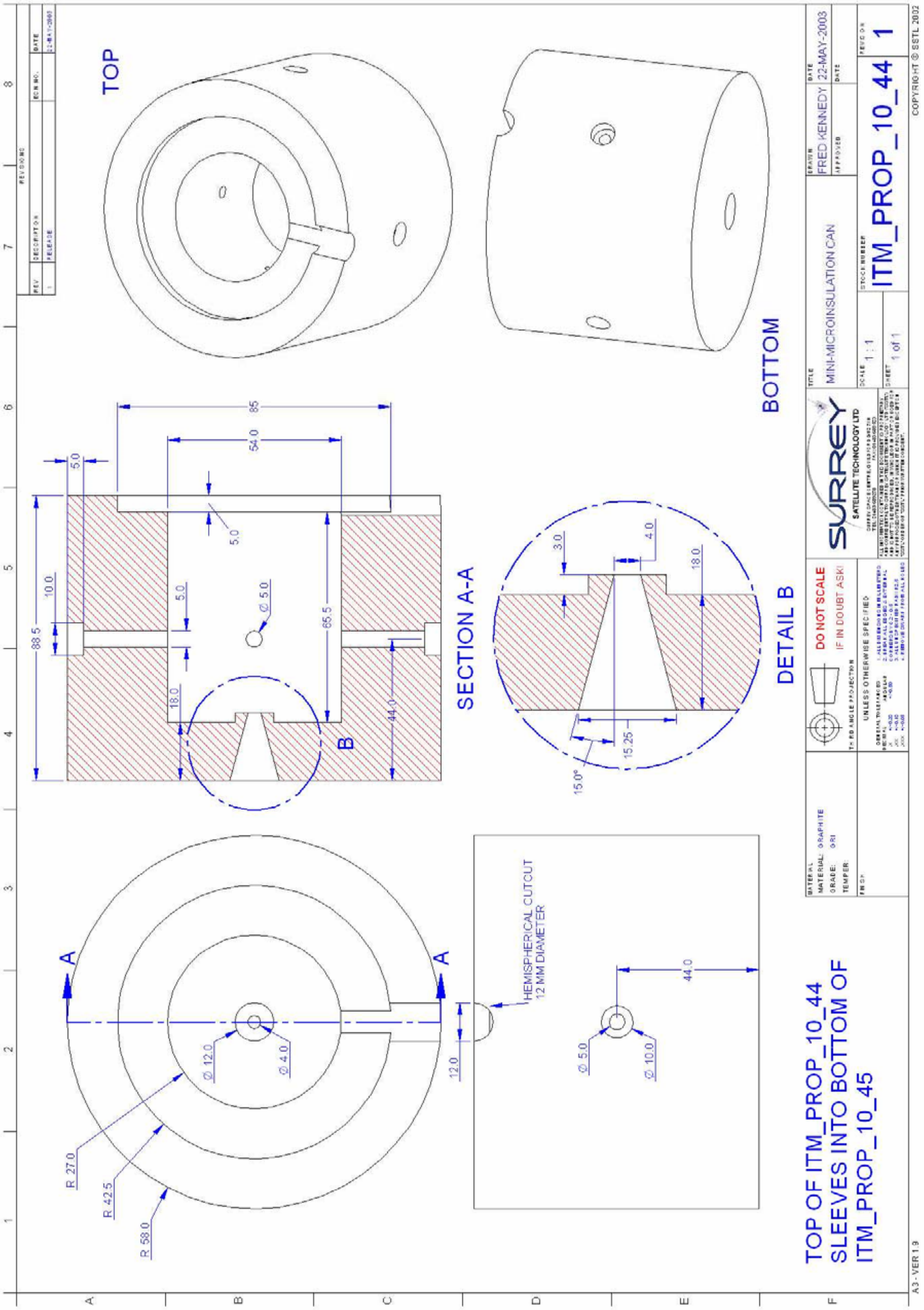
TOP
BOTTOM
SECTION A-A
DETAIL B
A
A
B
85
54.0
5.0
5.0
10.0
5.0
88.5
65.5
∅ 5.0
18.0
44.0
3.0
4.0
18.0
15.25
15.0°
R 27.0
R 42.5
R 58.0
∅ 12.0
∅ 4.0
12.0
HEMISPHERICAL CUTOUT 12 MM DIAMETER
44.0
∅ 5.0
∅ 10.0
TOP OF ITM_PROP_10_44 SLEEVES INTO BOTTOM OF ITM_PROP_10_45
REV
DESCRIPTION
ECN NO.
DATE
REVISIONS
1
RELEASE
22-MAY-2003
MATERIAL
MATERIAL: GRAPHITE
GRADE: GRI
TEMPER:
FINISH
THIRD ANGLE PROJECTION
DO NOT SCALE
IF IN DOUBT ASK!
UNLESS OTHERWISE SPECIFIED
SURREY
SATELLITE TECHNOLOGY LTD
TITLE
MINI-MICROINSULATION CAN
DRAWN
FRED KENNEDY
DATE
22-MAY-2003
APPROVED
DATE
SCALE
1:1
SHEET
1 of 1
STOCK NUMBER
ITM_PROP_10_44
REVISION
1
COPYRIGHT © SSTL 2002
A3 - VER 1.9
A
B
C
D
E
F
1
2
3
4
5
6
7
8

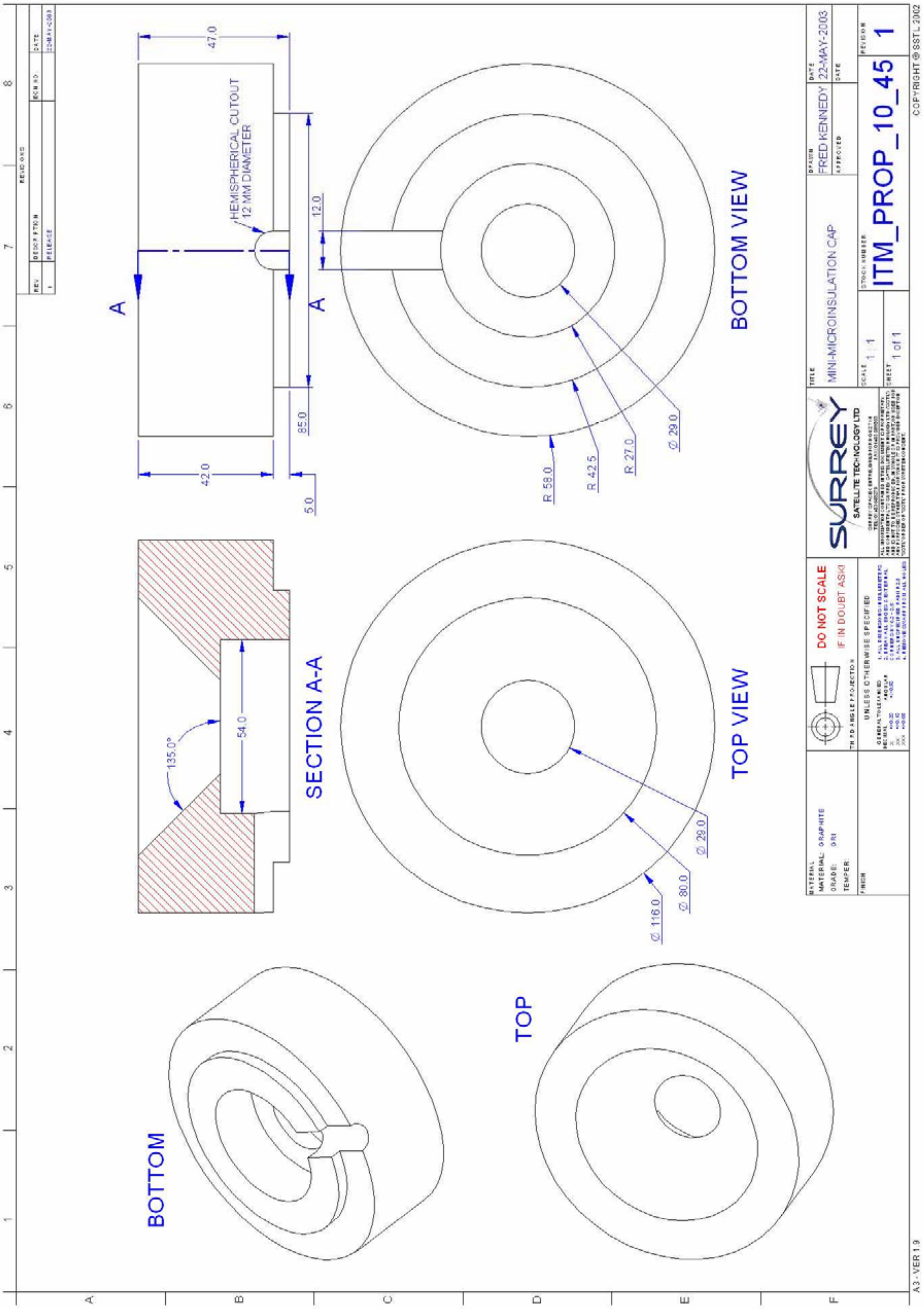
BOTTOM
TOP
SECTION A-A
TOP VIEW
BOTTOM VIEW
A
A
HEMISPHERICAL CUTOUT
12 MM DIAMETER
47.0
12.0
85.0
42.0
5.0
54.0
135.0°
Ø 116.0
Ø 80.0
Ø 29.0
R 58.0
R 42.5
R 27.0
Ø 29.0
REVISIONS
REV
DESCRIPTION
ECN NO.
DATE
1
RELEASE
22-MAY-2003
MATERIAL
MATERIAL: GRAPHITE
GRADE: GRI
TEMPER:
FINISH
THIRD ANGLE PROJECTION
UNLESS OTHERWISE SPECIFIED
DO NOT SCALE
IF IN DOUBT ASK!
SURREY
SATELLITE TECHNOLOGY LTD
TITLE
MINI-MICROINSULATION CAP
DRAWN
FRED KENNEDY
DATE
22-MAY-2003
APPROVED
DATE
SCALE
1:1
SHEET
1 of 1
STOCK NUMBER
ITM_PROP_10_45
REVISION
1
COPYRIGHT © SSTL 2002
A3 - VER 1.9
1
2
3
4
5
6
7
8
A
B
C
D
E
F

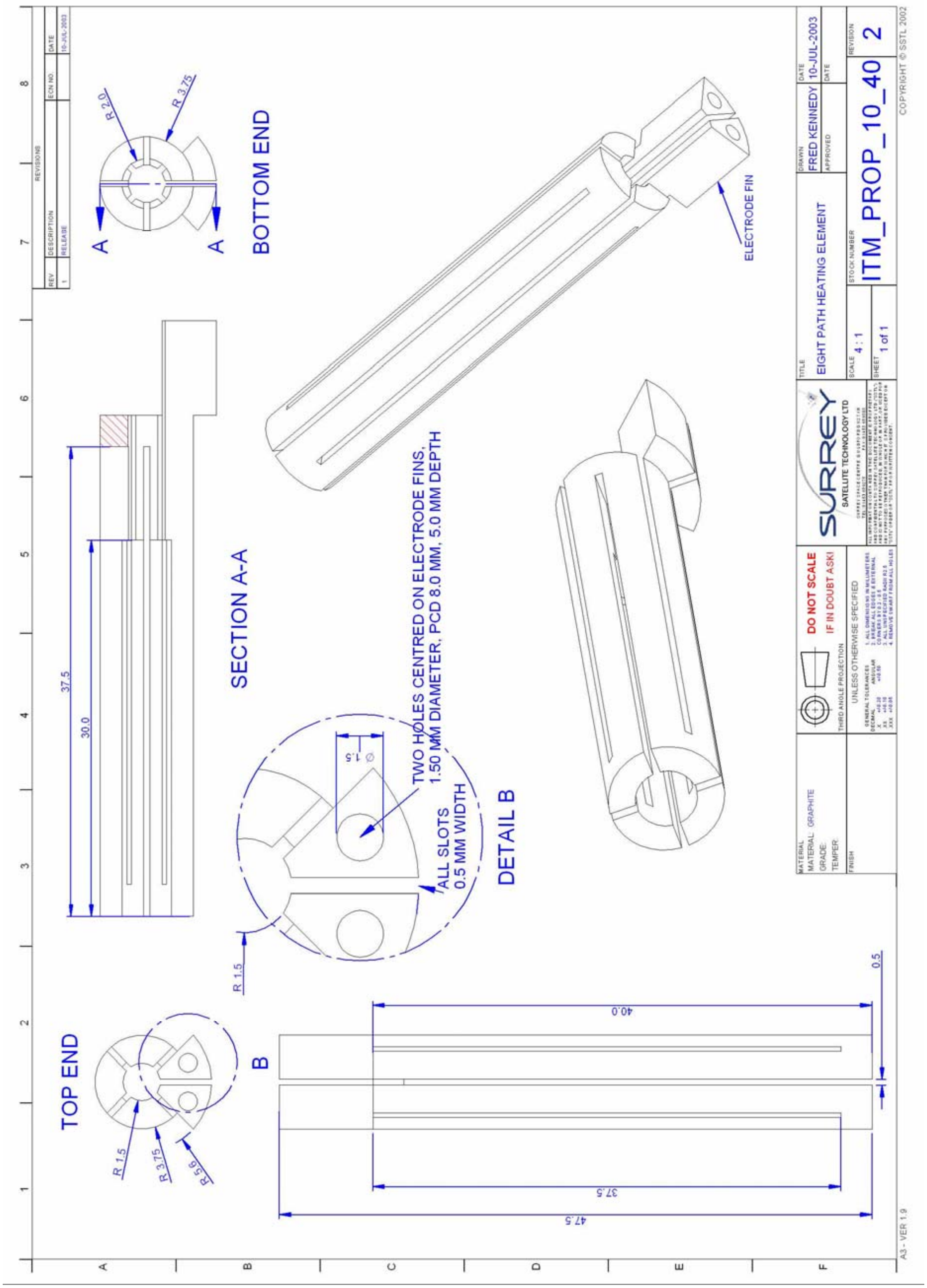
TOP END
R 1.5
R 3.75
R 5.6
B
47.5
37.5
40.0
0.5
R 1.5
DETAIL B
ALL SLOTS 0.5 MM WIDTH
TWO HOLES CENTRED ON ELECTRODE FINS, 1.50 MM DIAMETER, PCD 8.0 MM, 5.0 MM DEPTH
Ø 1.5
SECTION A-A
37.5
30.0
BOTTOM END
A
A
R 2.0
R 3.75
ELECTRODE FIN
REVISIONS
REV
DESCRIPTION
ECN NO.
DATE
1
RELEASE
10-JUL-2003
MATERIAL
MATERIAL: GRAPHITE
GRADE:
TEMPER:
FINISH
THIRD ANGLE PROJECTION
DO NOT SCALE
IF IN DOUBT ASK!
UNLESS OTHERWISE SPECIFIED
SURREY
SATELLITE TECHNOLOGY LTD
TITLE
EIGHT PATH HEATING ELEMENT
SCALE
4 : 1
SHEET
1 of 1
STOCK NUMBER
ITM_PROP_10_40
DRAWN
FRED KENNEDY
DATE
10-JUL-2003
APPROVED
DATE
REVISION
2
COPYRIGHT © SSTL 2002
A3 - VER 1.9
1
2
3
4
5
6
7
8
A
B
C
D
E
F